University of Jyväskylä
Department of Mathematics
Laboratory of Scientific Computing

Report 3/1994

PROCEEDINGS OF THE 5TH FINNISH MECHANICS DAYS

Raino A. E. Mäkinen Pekka Neittaanmäki
(editors)

University of Jyväskylä
Laboratory of Scientific Computing
P.O. Box 35
FIN-40351 Jyväskylä
FINLAND
tel. +358-41-602732
fax +358-41-602731

Organizer

University of Jyväskylä
Department of Mathematics
Laboratory of Scientific Computing

ISBN 951-34-0284-3
ISSN 1236-6919

Preface

These proceedings contain the papers presented at the Fifth Finnish Mechanics Days held in Jyväskylä, Finland, 26–27 May 1994. The First Finnish Mechanics Days were held in Oulu in 1982, the Second in Tampere in 1985, the Third in Otaniemi (Helsinki) in 1988 and the Fourth in Lappeenranta in 1991.

The aim of the Finnish Mechanics Days is to bring together researchers and doctoral students whose interest lies in mechanics and scientific computing. The program of the seminar consisted of invited lectures given by Ü. Lepik and E. Stein and contributed papers.

The organizers are grateful to the participants of the meeting and to the speakers who contributed their lectures to these proceedings.

Jyväskylä, May 1994

Raino A. E. Mäkinen Pekka Neittaanmäki

Contents

SECTION 3 – VIBRATIONS

SECTION 4 – FINITE ELEMENT METHOD

SECTION 5 – STRUCTURAL OPTIMIZATION

SECTION 6 – PAPER TECHNOLOGY

SECTION 7 – FLUID FLOW

SECTION 8 – MATERIAL BEHAVIOUR

SECTION 9 – BASIC PRINCIPLES

SECTION 10 – APPLICATIONS

A CONTINUUM MECHANICAL APPROACH FOR ANALYTICAL SENSITIVITY ANALYSIS IN STRUCTURAL OPTIMIZATION

FRANZ–JOSEPH BARTHOLD & ERWIN STEIN
Institute for Structural Mechanics and Computational Mechanics
University of Hannover
Appelstraße 9A, D-30167 Hannover, GERMANY

ABSTRACT

We present a differential geometry based formulation of structural optimization which links continuum mechanics and computer aided design closely together to obtain very naturally fundamental sensitivity data for the optimization procedure.

A variational principle based on a variation of the covariant basis vector in each point of the deformed or undeformed configuration is formulated to obtain analytical sensitivity data both for lagrangean and eulerian description of structural mechanics.

1. A CONTINUUM MECHANICAL FRAMEWORK

In this section we introduce the basic notations and mappings used in this paper. For details see books on continuum mechanics e.g. *Malvern* [9], *Marsden, Hughes* [10]. We freely use Einstein' s summation convention on repeated indices.

1.1 The configurations of material bodies. The material body $\mathcal{B}$ consists of a compact set of material points $\mathcal{M}$. For each time t from the space of time T_t the material points are mapped into the points $\mathcal{P}$ of the euclidean space $I\!E^3$ by a continuous mapping and can be identified by their position in space.

At reference time $t = t_\circ$ the undeformed and unstressed material body occupies a reference configuration $\mathbf{B}_\circ$. Using a fixed cartesian frame $\mathbf{E}_1, \mathbf{E}_2, \mathbf{E}_3$ at reference time $t_\circ$ we obtain $\mathbf{X} = X^A \mathbf{E}_A$. The coordinates X^A are called *material* or *lagrangean coordinates*. All quantities of the reference configuration are labeled by capital letters. At current time $t > t_\circ$ the material body has a deformed current configuration $\mathbf{B}_t$ and using the cartesian frame $\mathbf{e}_1, \mathbf{e}_2, \mathbf{e}_3$ at time t the position of the material points is denoted by $\mathbf{x} = x^k \mathbf{e}_k$.

The coordinates x^k are called *spatial* or *eulerian coordinates*. All quantities of the current configuration are labeled by small letters.

The deformation of the material body from the undeformed reference configuration $\mathbf{B}_o$ at reference time t_o into the current configuration $\mathbf{B}_t$ at time t is given by the mapping

$$\varphi_{t,t_o} : \left\{ \begin{array}{ccc} \mathbf{B}_o & \rightarrow & \mathbf{B}_t \\ \mathbf{X} & \mapsto & \mathbf{x} = \varphi_{t,t_o}(\mathbf{X}). \end{array} \right. \tag{1}$$

The mapping φ_{t,t_o} is assumed to be continuous differentiable and for each fixed time t invertible. For notational convenience we write φ without indices. Furthermore we assume the cartesian frames of the reference and current configuration to be identical, i.e. $\mathbf{E}_i = \mathbf{e}_i$. The theory can fully be developed only by using the mapping φ from an undeformed reference configuration into a deformed current configuration. In this context the coordinates X^A of the material points at time t_o are the independent variables.

1.2 The concept of differential manifold. For any further development towards introducing scalar valued design variables or formulating variational principles for optimization purposes this approach is inconvenient because the reference configuration depends on design and is therefore not fixed. To overcome this problem in an elegant way we introduce concepts of differential geometry to describe the different configurations of the material body, see e.g. *Marsden, Hughes* [10] and *Abraham, Marsden, Ratiou* [1] for further theoretical background on manifold theory.

In the framework of differential geometry a configuration of a material body is considered to be a differential manifold. This means that a finite number of smooth mappings with local support from a fixed cartesian coordinate system into the euclidean space is sufficient to describe any real configuration of the body. We restrict our attention to one chart from the atlas of the differentiable manifold and introduce local coordinates $\Theta^1, \Theta^2, \Theta^3$ to describe the vector $\mathbf{X}$ and thus the material point $\mathcal{M}$ uniquely. Using these ideas the parameter space $T_\Theta := [0,1]^3 \subset I\!R^3$ of local coordinates $\Theta^1, \Theta^2, \Theta^3$ is mapped by

$$\psi : \left\{ \begin{array}{ccc} T_\Theta & \rightarrow & \mathbf{B}_o \\ (\Theta^1, \Theta^2, \Theta^3) & \mapsto & \mathbf{X} = \psi(\Theta^1, \Theta^2, \Theta^3) \end{array} \right. \tag{2}$$

into the space $B := \{\mathcal{B} | \mathcal{B} = \psi(\mathbf{B}_o)\}$ of the reference configurations of all possible material bodies. The cartesian coordinates X^A or x^i, respectively, can be described by the local coordinates using the mapping ψ, i.e. $X^A = \hat{X}^A(\Theta^1, \Theta^2, \Theta^3)$ and $x^i = \hat{x}^i(\Theta^1, \Theta^2, \Theta^3, t)$, respectively. The mapping between the coordinates $\left\{X^A\right\}$ or $\{x^i\}$ and $\left\{\Theta^B\right\}$ is assumed to be sufficiently smooth and invertible for any fixed time t. The tangential space at any point $\mathbf{X} \in \mathbf{B}_t$ is given by the covariant or contravariant basis vectors

$$\mathbf{G}_i = \frac{\partial \mathbf{X}}{\partial \Theta^i} \qquad \text{or} \qquad \mathbf{G}^i = \frac{\partial \Theta^i}{\partial \mathbf{X}} \tag{3}$$

where $\mathbf{G}_i \cdot \mathbf{G}^j = \delta_i^j$, $\mathbf{G}_i \cdot \mathbf{G}_j = G_{ij}$ and $G_{ij}\, G^{jk} = \delta_i^j$. Here G_{ij} and G^{ij} denote the covariant and contravariant metric coefficients. δ_i^j is the Kronecker symbol.

1.3 Computer Aided Design and continuum mechanics. For any practical application of modern computational methods for analyzing or optimizing structural behaviour we should consider computer aided design as a central tool for describing geometry well

established in industry. To implement CAD into a continuum mechanical framework of structural optimization we recall the mathematical concept. A so called *patch* within e.g. a surface description is again a chart of a differentiable manifold mapping locally a parameter space $T_\Theta := [0,1]^3 \subset I\!R^3$ into the real surface, i.e. again $\mathbf{X} = \psi(\Theta^1, \Theta^2, \Theta^3)$ for any point $\mathbf{X}$. Thus, both CAD and continuum mechanics are founded on differential geometry. Using features already available in CAD we can calculate covariant and contravariant basis vectors $\mathbf{G}_i$ and $\mathbf{G}^i$ for any point of the CAD geometry model representing the reference configuration.

1.4 Variation of design using CAD. So far no comment has been made how different designs given by different mappings ψ are interrelated. A sequence of different bodies with a sufficiently smooth change of design must be considered to obtain any optimal solution by improving the objective function within some mathematical programming algorithm. Analyzing CAD geometry representation carefully, e.g. $\mathbf{X} = \psi(\Theta^1, \Theta^2, \Theta^3)$ given by

$$\mathbf{X} = \sum_{j=1}^{n} \hat{M}_j(\Theta^1, \Theta^2, \Theta^3)\, \mathbf{Y}_j \quad \text{and} \quad \mathbf{G}_i = \sum_{j=1}^{n} \frac{\partial \hat{M}_j(\Theta^1, \Theta^2, \Theta^3)}{\partial \Theta^i}\, \mathbf{Y}_j \tag{4}$$

where M_j denote some geometrical shape functions and $\mathbf{Y}_j$ are e.g. control point coordinates of a Bézier surface description, we observe that these requirements are already naturally fulfilled. Introducing the control point coordinates, i.e. $\mathbf{Y}_j = \hat{\mathbf{Y}}_j(s)$, or any other naturally given or improved combination of scalar control parameters as design variables (denoted by s) we end up with the desired sufficiently smooth parametrization of a family of possible bodies. This parametrization is also a discretization in geometry since only a finite number of control points can be used. Therefore once the geometrical shape functions $M_j = \hat{M}_j(\Theta^1, \Theta^2, \Theta^3)$ are chosen we are restricted to a finite dimensional subspace of all possible bodies.

Considering any variation of design $\delta\mathbf{X}$ given for example by changing CAD control points of a Bézier representation of curves or surfaces we end up with variations $\boldsymbol{\omega}_i$ of the covariant vector field $\mathbf{G}_i$ given by

$$\boldsymbol{\omega}_i = \delta\mathbf{G}_i = \delta\left\{\frac{\partial \mathbf{X}}{\partial \Theta^i}\right\} = \frac{\partial}{\partial \Theta^i}\,\{\delta\mathbf{X}\}\,,$$

which are actually the partial derivatives of the covariant basis vectors with respect to design, i.e.

$$\frac{\partial \mathbf{G}_j}{\partial s} = \frac{\partial}{\partial s}\left(\frac{\partial X^i}{\partial \Theta^j}\mathbf{E}_i\right) = \frac{\partial}{\partial s}\left(\frac{\partial X^i}{\partial \Theta^j}\right)\mathbf{E}_i = \frac{\partial^2 X^i}{\partial \Theta^j\, \partial s}\,\mathbf{E}_i. \tag{5}$$

Thus, it is essential for the sensitivity analysis to calculate the mixed partial derivatives of the coordinates X^i of all points of the reference configuration with respect to the local coordinates Θ^j and the design variable s. Calculating these quantities analytically for general design variables in commercial CAD software is the central point for further development of structural optimization.

1.5 Influence of design variables on continuum mechanical functions. These results are leading to a modification of the functional dependencies of the material body and the reference and current configuration. Using $\Theta^1, \Theta^2, \Theta^3$ from the parameter space $T_\Theta = [0,1]^3 \subset I\!R^3$ as discussed above we introduce a design variable s from the parameter

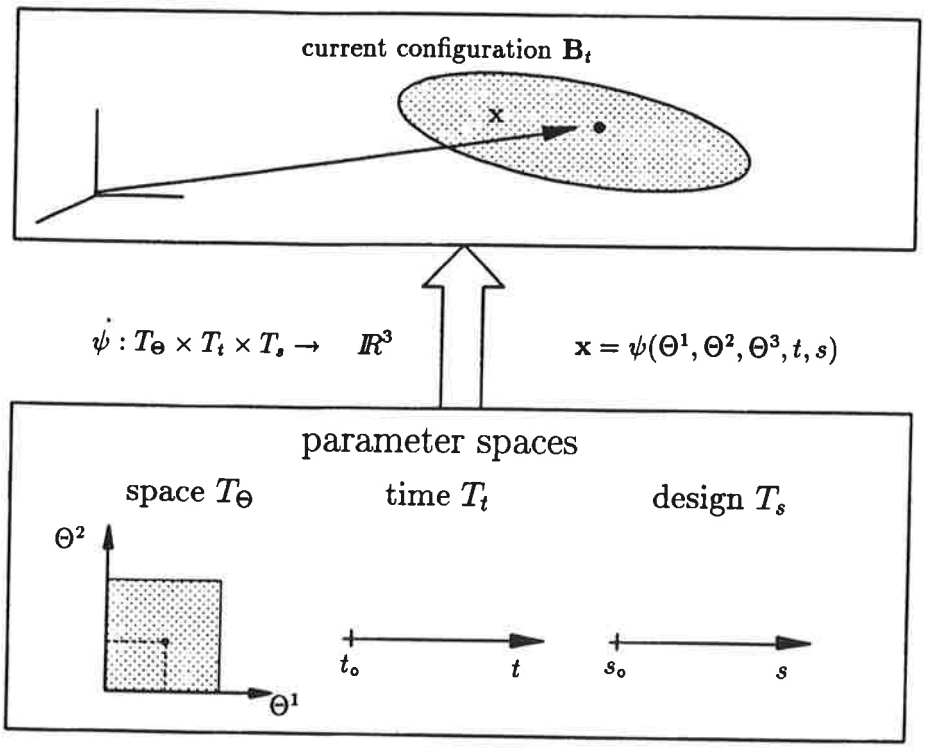

FIGURE 1: Deformation of a body parametrized by local coordinates, time and design

space $T_s := \mathbb{R}$ of the design variables into the definition of the mapping ψ which enhances equation (2). For notational convenience we use again ψ to describe the mapping

$$\psi : \left\{ \begin{array}{rcl} T_\Theta \times T_s & \to & \mathbf{B}_o \\ (\Theta^1, \Theta^2, \Theta^3, s) & \mapsto & \mathbf{X} = \psi(\Theta^1, \Theta^2, \Theta^3, s) \end{array} \right. \tag{6}$$

of local coordinates and design variables into the actual reference configuration. The mapping ψ is assumed to be sufficiently smooth with respect to $\Theta^1, \Theta^2, \Theta^3$ and s and now the deformation is given by

$$\varphi : \left\{ \begin{array}{rcl} T_\Theta \times T_t \times T_s & \to & \mathbb{R}^3 \\ (\Theta^1, \Theta^2, \Theta^3, t, s) & \mapsto & \mathbf{x} = \psi(\Theta^1, \Theta^2, \Theta^3, t, s). \end{array} \right. \tag{7}$$

The cartesian coordinates X^A or x^i, respectively, can be written as

$$X^A = \hat{X}^A(\Theta^1, \Theta^2, \Theta^3, s) \qquad \text{or} \qquad x^i = \hat{x}^i(\Theta^1, \Theta^2, \Theta^3, t, s). \tag{8}$$

Thus the actual configuration of a material body in space and time is parametrized by the local coordinates $\Theta^1, \Theta^2, \Theta^3$, time t and design variable s as shown in figure 1.

Introducing the displacement field $\mathbf{u} = \mathbf{x} - \mathbf{X}$ we observe the functional dependencies

$$\mathbf{u} = \hat{\mathbf{u}}(\mathbf{X}, t, s) = \tilde{\mathbf{u}}(\Theta^1, \Theta^2, \Theta^3, t, s) \tag{9}$$

and $\alpha = \hat{\alpha}(s, \hat{\mathbf{u}}(s))$ for a model function α representing any continuum mechanical objective function or constraint (either scalar, vector or tensor valued). The stated relationship is valid for all elastic materials where the structural response is only a function of the total displacement vector. If sophisticated materials are considered these dependencies must be enlarged to represent the deformation history.

2. STRAINS, STRESSES AND WEAK FORMS

2.1 Strain measurements. The deformation gradient $\mathbf{F} = \mathrm{Grad}\,\mathbf{x}$ with its determinant $J := \det \mathbf{F}$ is used to define strain measurements, e.g. $\mathbf{C} = \mathbf{F}^T\mathbf{F}$, $\mathbf{b} = \mathbf{F}\mathbf{F}^T$, $2\mathbf{E} = \mathbf{C} - \mathbf{1}$. These quantities are used to evaluate invariants and eigenvalues used in finite elasticity.

2.2 Strain energy functions, stresses and elasticities. The strain energy function W of rubberlike materials used in the examples is given as a function of the invariants or eigenvalues of the strain tensor, i.e. $W = \tilde{W}(\mathrm{I}, \mathrm{II}, \mathrm{III}) = \tilde{W}(\lambda_1, \lambda_2, \lambda_3)$. As an example we mention Ogden' s material law

$$W = \tilde{W}(\lambda_1, \lambda_2, \lambda_3) = \sum_{p=1}^{N} \frac{\mu_p}{\alpha_p} \left\{ \lambda_1^{\alpha_p} + \lambda_2^{\alpha_p} + \lambda_3^{\alpha_p} \right\} + g(J). \tag{10}$$

A detailed representation of the stress tensor and the tensor of elastic moduli for isotropic hyperelastic materials is given in *Barthold* [6]. We introduce the notation $\mathbf{T}$ for Cauchy stresses, $\boldsymbol{\tau}$ for Kirchhoff stresses, $\mathbf{P}$ for the first Piola-Kirchhoff stress tensor and $\mathbf{S}$ for the second Piola-Kirchhoff stress tensor and obtain $\boldsymbol{\tau} = J\,\mathbf{T} = \mathbf{F}\,\mathbf{S}\,\mathbf{F}^T = \mathbf{P}\,\mathbf{F}^T$. Using the strain energy function W we can derive the stress tensors and the tensor of elastic moduli

$$\mathbf{T} = \frac{2}{J}\frac{\partial W}{\partial \mathbf{g}}, \quad \mathbf{S} = 2\,\frac{\partial W}{\partial \mathbf{C}}, \quad \mathbb{C} = 2\,\frac{\partial \mathbf{S}}{\partial \mathbf{C}} = 4\,\frac{\partial^2 W}{\partial \mathbf{C}\,\partial \mathbf{C}} \quad \text{and} \quad \mathfrak{c} = \frac{2}{J}\frac{\partial \boldsymbol{\tau}}{\partial \mathbf{g}} = \frac{4}{J}\frac{\partial^2 W}{\partial \mathbf{g}\,\partial \mathbf{g}}.$$

2.3 Weak form of the equilibrium condition. The weak form of the equilibrium condition is given by $g = \hat{g}(s, \hat{\mathbf{u}}(s)) =: \hat{g}_{int}((s, \hat{\mathbf{u}}(s))) - g_{ext} = 0$ where

$$\hat{g}_{int}(s, \hat{\mathbf{u}}(s)) = \int_{\mathbf{B}_t} \mathbf{T} : \mathrm{grad}\,\boldsymbol{\eta}\; dv \quad \text{and} \quad g_{ext} = \left\{ \int_{\mathbf{B}_t} \rho\,\bar{\mathbf{k}} \cdot \boldsymbol{\eta}\; dv + \int_{\partial \mathbf{B}_{t\sigma}} \bar{\mathbf{t}} \cdot \boldsymbol{\eta}\; da \right\}. \tag{11}$$

We concentrate our attention (for notational simplicity) on g_{int} and assume g_{ext} to be deformation independent and constant for any considered design variable s. The variation of the displacement field is given by $\boldsymbol{\eta}$. The internal virtual work can be expressed using the design independent local parameter space T_Θ

$$g_{int} = \int_{T_\Theta} f\, J_\psi\; dV_\Theta \quad \text{and} \quad f = \boldsymbol{\tau} : \mathrm{grad}\,\boldsymbol{\eta} = \mathbf{P} : \mathrm{Grad}\,\boldsymbol{\eta} = \mathbf{S} : \mathbf{F}^T\ \mathrm{Grad}\,\boldsymbol{\eta}. \tag{12}$$

2.4 Linearization of the weak form. The linearization of the weak form with respect to some displacement increment $\Delta\mathbf{u}$ can be obtained by a well known technique, see e.g. [8]

$$Dg(\varphi, \boldsymbol{\eta}) \cdot \Delta\mathbf{u} = \int_{\mathbf{B}_o} \left\{ \mathrm{Grad}\,\Delta\mathbf{u}\,\mathbf{S} + \mathbf{F}\mathbb{C} : \frac{1}{2}\left[\mathbf{F}^T\ \mathrm{Grad}\,\Delta\mathbf{u} + \mathrm{Grad}^T\,\Delta\mathbf{u}\,\mathbf{F} \right] \right\} \cdot \mathrm{Grad}\,\boldsymbol{\eta}\; dV$$

and depends linearly on the virtual displacement $\boldsymbol{\eta}$ and the displacement increment $\Delta\mathbf{u}$.

2.5 Discretization using finite element method. A discretization of the unknown displacement field $\mathbf{u}$ and similarly of the virtual displacement $\boldsymbol{\eta}$ and the displacement increment $\Delta\mathbf{u}$ using the shape functions $N_i = N_i(\Theta^1, \Theta^2, \Theta^3)$ is given by

$$\mathbf{u} \approx \mathbf{u}_h = \sum_i N_i \, \mathbf{v}_i, \quad \boldsymbol{\eta} \approx \boldsymbol{\eta}_h = \sum_i N_i \, \delta\mathbf{v}_i \quad \text{and} \quad \Delta\mathbf{u} \approx \Delta\mathbf{u}_h = \sum_i N_i \, \delta\Delta\mathbf{v}_i \tag{13}$$

where $\mathbf{v}_i$, $\delta\mathbf{v}_i$ and $\delta\Delta\mathbf{v}_i$ denote the node displacement vector, the virtual node displacement vector and the incremental node displacement vector, respectively, of the node i. Assembling these node based vectors to global vectors $\mathbf{V}$, $\delta\mathbf{V}$ and $\delta\Delta\mathbf{V}$ we can write the discretized weak form and the corresponding linearization in the following form

$$g \approx g_h = \delta\mathbf{V}^T \, \mathbf{R} = 0 \quad \text{and} \quad Dg(\varphi, \boldsymbol{\eta}) \cdot \Delta\mathbf{u} \approx Dg_h(\varphi, \boldsymbol{\eta}_h) \cdot \Delta\mathbf{u}_h = \delta\mathbf{V}^T \, \mathbf{K}_T \, \delta\Delta\mathbf{V} \tag{14}$$

where $\mathbf{R}$ and $\mathbf{K}_T$ denote the global residual vector and the global tangent stiffness matrix, respectively.

2.6 A detailed consideration of the deformation gradient. Considering the above introduced quantities it turns out that the deformation gradient $\mathbf{F}$ dominates all continuum mechanical functions. A careful consideration of its functional dependencies with respect to design and displacement is the key for an efficient sensitivity analysis. For this reason we use local coordinates to formulate $\mathbf{F}$ with respect to the deformed and undeformed covariant basis vectors $\mathbf{G}_i$ and $\mathbf{g}_i$, i.e.

$$\mathbf{G}_i = \frac{\partial \mathbf{X}}{\partial \Theta^i} \quad \text{and} \quad \mathbf{g}_i = \frac{\partial \mathbf{x}}{\partial \Theta^i} = \frac{\partial (\mathbf{X} + \mathbf{u})}{\partial \Theta^i} = \frac{\partial \mathbf{X}}{\partial \Theta^i} + \frac{\partial \mathbf{u}}{\partial \Theta^i} = \mathbf{G}_i + \frac{\partial \mathbf{u}}{\partial \Theta^i} = \mathbf{G}_i + \mathbf{u}_{,i}. \tag{15}$$

Using these relationships we can write $\mathbf{F}\,\mathrm{Grad}\,\mathbf{x} = \mathbf{1} + \mathrm{Grad}\,\mathbf{u}$ where $\mathbf{1} = \mathbf{G}_i \otimes \mathbf{G}^i = \mathbf{g}_i \otimes \mathbf{g}^i$ denotes the unity tensor which is independent from design. Therefore, the displacement gradient

$$\mathbf{H} = \mathrm{Grad}\,\mathbf{u} = \frac{\partial \mathbf{u}}{\partial \Theta^i} \otimes \mathbf{G}^i = \mathbf{u}_{,i} \otimes \mathbf{G}^i \tag{16}$$

carries all information both of deformation and geometry into strains and stresses as well as weak forms. Analyzing the displacement gradient we observe the following facts.

1. Geometry is represented by the curvilinear basis vectors $\mathbf{G}_i$ and $\mathbf{G}^i$ which can be calculated using standard features of CAD at any point $(\Theta^1, \Theta^2, \Theta^3) \in T_\Theta$, see equation (4).

2. In any realistic industrial application using CAD the underlying design can be formulated by a finite number of scalar variables. The number of interesting variables, i.e. the design variables which can be modified to improve the design, is also finite. Thus it is very reasonable to restrict the infinite dimensional design space and the space of all considered variations of design to some finite dimensional subspace spanned by the chosen geometrical shape functions M_j.

3. The deformation field $\mathbf{u}$ from the undeformed reference configuration $\mathbf{B}_0$ into the deformed current configuration $\mathbf{B}_t$ can be formulated as function of local coordinates $(\Theta^1, \Theta^2, \Theta^3)$ and time $t \in T_t$. Furthermore it is an implicit function of geometry, i.e. depending on $\mathbf{G}_i$. This part of $\mathbf{H}$ is approximated using e.g. the finite element method.

2.7 Definition of the geometry gradient. The deformation gradient $\mathbf{F}$ is the gradient of the mapping φ from the undeformed reference configuration $\mathbf{B}_o$ into the deformed current configuration $\mathbf{B}_t$. In a similar way we consider the mapping ψ from the parameter space T_Θ into the reference configuration $\mathbf{B}_o$ and define

$$\mathbf{F}_\psi := \frac{\partial \mathbf{X}}{\partial \boldsymbol{\Theta}} = \frac{\partial \mathbf{X}}{\partial \Theta^i} \otimes \mathbf{E}^i = \mathbf{G}_i \otimes \mathbf{E}^i \tag{17}$$

and call this quantity *geometry gradient*. The determinant $J_\psi := \det \mathbf{F}_\psi$ is used to transform the volume elements of $\mathbf{B}_o$ and T_Θ via $dV = J_\psi \, dV_\Theta$ where

$$J_\psi := \det \mathbf{F}_\psi = \det \left[\frac{\partial \psi^i}{\partial \Theta^j} \right] = \det [\mathbf{G}_1, \mathbf{G}_2, \mathbf{G}_3] = \{ \det [\mathbf{G}_i \cdot \mathbf{G}_j] \}^{1/2} = \{ \det [G_{ij}] \}^{1/2}. \tag{18}$$

Furthermore, it is interesting to note that $\mathbf{F}_\psi$ and its inverse and transpose can be used to apply *push-forward* and *pull-back* operations between T_Θ and $\mathbf{B}_o$.

Having these fundamental relationships in mind we proceed to present a variational sensitivity analysis relying on discrete scalar valued design variables naturally introduced by CAD. For further remarks on variational techniques in optimization and on the state of the art on analytical sensitivity analysis see e.g. *Haug, Choi, Komkov* [7], *Banichuk* [3], *Arora* [2], *Tortorelli, Wang* [13], *Souli, Zolesio* [12]. Our formulation improves these known techniques for deriving analytical sensitivity data and the subsequent numerical realisation in several ways which will be outlined later on. We want to concentrate on the basics of this new approach and refer to *Barthold, Stein* [5] for all tensor analytical details.

3. PARTIAL DERIVATIVES WITH RESPECT TO DESIGN

In this section we consider functions depending on some scalar valued design variables s and on the scalar variable time t leading to a close relationship between time derivative and sensitivity. In this section we restrict our attention to derive partial derivatives with respect to the design variable s and refer to the next section on the variational approach for total derivatives, i.e. variations.

3.1 Purely geometrical functions. The partial derivative of J_ψ (see equation (18)) can be calculated using the derivative of a determinant of a tensor with respect to this tensor, i.e.

$$\begin{aligned} \frac{\partial J_\psi}{\partial s} &= \frac{\partial \det \mathbf{F}_\psi}{\partial \mathbf{F}_\psi} : \frac{\partial \mathbf{F}_\psi}{\partial s} = J_\psi \, \mathbf{F}_\psi^{-T} : \frac{\partial \mathbf{F}_\psi}{\partial s} = J_\psi \, \operatorname{tr} \left(\frac{\partial \mathbf{F}_\psi}{\partial s} \, \mathbf{F}_\psi^{-1} \right) \\ &= J_\psi \, \operatorname{tr} \left(\frac{\partial \mathbf{G}_i}{\partial s} \otimes \mathbf{G}^i \right) = J_\psi \left(\frac{\partial \mathbf{G}_i}{\partial s} \otimes \mathbf{G}^i \right) : \left(\mathbf{G}^j \otimes \mathbf{G}_j \right) = J_\psi \, \mathbf{G}^i \cdot \frac{\partial \mathbf{G}_i}{\partial s}. \end{aligned}$$

3.2 Strain measurements. All other strain measurements depend on the deformation gradient $\mathbf{F}$ and their sensitivity can be derived from the sensitivity of $\mathbf{F}$ using chain and product rule. Using either cartesian coordinates X^B or local coordinates Θ^i to describe the deformed configuration we obtain the partial derivatives of the deformation gradient $\mathbf{F} = \mathbf{1} + \operatorname{Grad} \mathbf{u}$ with respect to the design variable s

$$\frac{\partial \mathbf{F}}{\partial s} = \frac{\partial \mathbf{H}}{\partial s} = \frac{\partial \operatorname{Grad} \mathbf{u}}{\partial s} = \frac{\partial}{\partial s} \left(\frac{\partial u^A}{\partial X^B} \right) \mathbf{E}_A \otimes \mathbf{E}^B = \frac{\partial \mathbf{u}}{\partial \Theta^i} \otimes \frac{\partial \mathbf{G}^i}{\partial s}. \tag{19}$$

3.3 Stresses. The stress tensor of any isotropic hyperelastic material is a function of the strain tensors $\mathbf{C} = \hat{\mathbf{C}}(s)$ or $\mathbf{b} = \hat{\mathbf{b}}(s)$, i.e. $\mathbf{S} = \hat{\mathbf{S}}(\hat{\mathbf{C}}(s))$ or $\mathbf{T} = \hat{\mathbf{T}}(\hat{\mathbf{b}}(s))$. It is important to formulate the necessary partial derivatives with respect to the design variables by using the already calculated elasticities and the sensitivity of the strain tensors, i.e. considering $\mathbf{S}$ we obtain

$$\frac{\partial \mathbf{S}}{\partial s} = \frac{\partial \mathbf{S}}{\partial \mathbf{C}} : \frac{\partial \mathbf{C}}{\partial s} = \mathbb{C} : \frac{1}{2}\frac{\partial \mathbf{C}}{\partial s} = \mathbb{C} : \frac{\partial \mathbf{E}}{\partial s}. \tag{20}$$

The partial derivatives of Cauchy's stresses $\mathbf{T}$ with respect to the design variable s can be derived by using the elasticities $\mathfrak{c}$. The Kirchhoff stresses $\boldsymbol{\tau}$ defined as $\boldsymbol{\tau} = J\,\mathbf{T} = \mathbf{F}\,\mathbf{S}\,\mathbf{F}^T$ are used to calculate the partial derivative of Cauchy's stress tensor $\mathbf{T}$

$$\frac{\partial \mathbf{T}}{\partial s} = \frac{\partial}{\partial s}\left(\frac{1}{J}\boldsymbol{\tau}\right) = \frac{-1}{J^2}\frac{\partial J}{\partial s}\boldsymbol{\tau} + \frac{1}{J}\frac{\partial \boldsymbol{\tau}}{\partial s}$$

where

$$\frac{\partial J}{\partial s} = \frac{\partial}{\partial s}(\det \mathbf{F}) = \frac{\partial}{\partial \mathbf{F}}(\det \mathbf{F}) : \frac{\partial \mathbf{F}}{\partial s} = J\mathbf{F}^{-T} : \frac{\partial \mathbf{F}}{\partial s} = J \operatorname{tr}\left(\frac{\partial \mathbf{F}}{\partial s}\mathbf{F}^{-1}\right) = J \operatorname{tr} \mathbf{l}_\Delta,$$

and the notations

$$\mathbf{l}_\Delta := \frac{\partial \mathbf{F}}{\partial s}\mathbf{F}^{-1} \qquad \text{and} \qquad \mathbf{d}_\Delta := \frac{1}{2}\left\{\mathbf{l}_\Delta + \mathbf{l}_\Delta^T\right\} \tag{21}$$

are used. The partial derivative of $\boldsymbol{\tau}$ can be calculated using $\boldsymbol{\tau} = \mathbf{F}\,\mathbf{S}\,\mathbf{F}^T$, i.e.

$$\frac{\partial \boldsymbol{\tau}}{\partial s} = \frac{\partial \mathbf{F}}{\partial s}\mathbf{S}\,\mathbf{F}^T + \mathbf{F}\,\mathbf{S}\frac{\partial \mathbf{F}^T}{\partial s} + \mathbf{F}\frac{\partial \mathbf{S}}{\partial s}\mathbf{F}^T = \mathbf{l}_\Delta\,\boldsymbol{\tau} + \boldsymbol{\tau}\,\mathbf{l}_\Delta + \mathbf{F}\left[\mathbb{C} : \frac{1}{2}\frac{\partial \mathbf{C}}{\partial s}\right]\mathbf{F}^T.$$

The elasticities with respect to the current configuration $\mathfrak{c}$ and the reference configuration $\mathbb{C}$ are related by

$$\mathfrak{c} : \mathbf{a} = \frac{1}{J}\,\mathbf{F}\left[\mathbb{C} : \left(\mathbf{F}^T\,\mathbf{a}\,\mathbf{F}\right)\right]\mathbf{F}^T$$

for each spatial tensor $\mathbf{a}$. Using the transformations

$$\frac{1}{2}\frac{\partial \mathbf{C}}{\partial s} = \mathbf{F}^T\,\mathbf{d}_\Delta\,\mathbf{F} \qquad \text{and} \qquad \mathfrak{c} : \mathbf{d}_\Delta = \frac{1}{J}\,\mathbf{F}\frac{\partial \mathbf{S}}{\partial s}\mathbf{F}^T. \tag{22}$$

we can can calcute the partial derivative of $\mathbf{T}$ with respect to design s by

$$\frac{\partial \mathbf{T}}{\partial s} = \mathfrak{c} : \mathbf{d}_\Delta + \mathbf{l}_\Delta\,\mathbf{T} + \mathbf{T}\,\mathbf{l}_\Delta^T - \operatorname{tr}\mathbf{l}_\Delta\,\mathbf{T}. \tag{23}$$

This results indicates that the already calculated elasticities can be used directly to determine the major part of the sensitivity of Cauchy' s stresses. The above equation indicates the close relationship between time derivative and design sensitivity.

3.4 Equilibrium conditions. The weak form of equilibrium is an integral formulation depending on the domain of interest which is influenced by design variables. We consider only the internal part of the weak form and assume that the virtual work done by the external loads is independent from design. The virtual work of the actual stresses done on virtual strains can be expressed equivalently in different forms (see equation (12)) and we

can use several reference or current configuration descriptions to evaluate the sensitivity. Choosing $f = \mathbf{S} : \mathbf{F}^T \operatorname{Grad} \boldsymbol{\eta}$ we obtain

$$\begin{aligned} \frac{\partial f}{\partial s} &= \mathbf{F}^T \operatorname{Grad} \boldsymbol{\eta} : \frac{\partial \mathbf{S}}{\partial s} + \mathbf{S} : \frac{\partial \mathbf{F}^T \operatorname{Grad} \boldsymbol{\eta}}{\partial s} \\ &= \mathbf{F}^T \operatorname{Grad} \boldsymbol{\eta} : \mathbb{C} : \frac{\partial \mathbf{E}}{\partial s} + \mathbf{S} : \frac{\partial \mathbf{F}^T \operatorname{Grad} \boldsymbol{\eta}}{\partial s} \\ &= \left\{ \mathbf{F}^T \operatorname{Grad} \boldsymbol{\eta} : \mathbb{C} : \frac{\partial \mathbf{E}}{\partial \mathbf{G}_i} + \mathbf{S} : \frac{\partial \mathbf{F}^T \operatorname{Grad} \boldsymbol{\eta}}{\partial \mathbf{G}_i} \right\} \cdot \frac{\partial \mathbf{G}_i}{\partial s}. \end{aligned} \tag{24}$$

It is important to observe that again $\mathbb{C}$ can be used to reduce the sensitivity of stresses to the sensitivity of strain measurements. Finally it is necessary to calculate the the derivatives of $\mathbf{E}$ and $\mathbf{F}^T \operatorname{grad} \boldsymbol{\eta}$ with respect to the covariant basis vectors. Using results from tensor analysis we obtain third order tensors

$$\mathbf{M}^i := \frac{\partial \mathbf{E}}{\partial \mathbf{G}_i} \qquad \text{and} \qquad \mathbf{N}^i := \frac{\partial \left(\mathbf{F}^T \operatorname{Grad} \boldsymbol{\eta} \right)}{\partial \mathbf{G}_i}. \tag{25}$$

Thus, we can formulate the partial derivative of f in the following way

$$\frac{\partial f}{\partial s} = \mathbf{a}^i \cdot \frac{\partial \mathbf{G}_i}{\partial s} \quad \text{where} \quad \mathbf{a}^i := \mathbf{F}^T \operatorname{Grad} \boldsymbol{\eta} : \mathbb{C} : \mathbf{M}^i + \mathbf{S} : \mathbf{N}^i. \tag{26}$$

Finally, the partial derivative of the weak form with respect to s is given by

$$\frac{\partial g}{\partial s} = \int_{T_\Theta} \mathbf{A}^i \cdot \frac{\partial \mathbf{G}_i}{\partial s} \, J_\psi \, dV_\Theta \quad \text{where} \quad \mathbf{A}^i := \mathbf{a}^i + f \, \mathbf{G}^i. \tag{27}$$

We call $\mathbf{A}^i$ the (partial) *sensitivity vector of the weak form* corresponding to a virtual change of covariant basis vectors induced by a virtual change of design.

4. A VARIATIONAL FORMULATION OF SENSITIVITY ANALYSIS

4.1 General formulation of the variational principle. We start of by considering the internal part g_{int} of the weak form as an example for any continuum mechanical function (either scalar, vector or tensor valued) defined on the parameter space T_Θ in the following way

$$g_{int} = \int_{T_\Theta} f(\mathbf{G}_i, \mathbf{u}(\mathbf{G}_i)) \, J_\psi(\mathbf{G}_i) \, dV_\Theta. \tag{28}$$

Performing the total variation with respect to design we obtain

$$\delta g_{int} = \delta \left[\int_{T_\Theta} f \, J_\psi \, dV_\Theta \right] = \int_{T_\Theta} \delta \left[f \, J_\psi \right] \, dV_\Theta = \int_{T_\Theta} \delta f \, J_\psi + f \, \delta J_\psi \, dV_\Theta \tag{29}$$

Thus it is important to calculate the total variation of internal virtual work f with respect to a variation of design which leads to

$$\begin{aligned} \delta f &= \frac{d}{d\epsilon} \left[f(\mathbf{G}_i + \epsilon \, \boldsymbol{\omega}_i, \mathbf{u}(\mathbf{G}_i + \epsilon \, \boldsymbol{\omega}_i)) \right]_{\epsilon=0} \\ &= \left\{ \frac{\partial f}{\partial \mathbf{G}_i} + \frac{\partial f}{\partial \mathbf{u}} \frac{\partial \mathbf{u}}{\partial \mathbf{G}_i} \right\} \cdot \boldsymbol{\omega}_i = \frac{\partial f}{\partial \mathbf{G}_i} \cdot \boldsymbol{\omega}_i + \frac{\partial f}{\partial \mathbf{u}} \frac{\partial \mathbf{u}}{\partial \mathbf{G}_i} \cdot \boldsymbol{\omega}_i. \end{aligned} \tag{30}$$

Since the functional relationship of the displacement field $\mathbf{u}$ for the solution for the structural analysis problem is not known explicitly we cannot determine $\frac{\partial \mathbf{u}}{\partial \mathbf{G}_i}$. But it is important to observe that

$$\overline{\boldsymbol{\eta}} := \frac{\partial \mathbf{u}}{\partial \mathbf{G}_i} \cdot \boldsymbol{\omega}_i \tag{31}$$

is a special variation of the displacement field induced by the chosen variation $\boldsymbol{\omega}_i$. Thus we can write

$$\begin{aligned} \delta f &= \delta_1 f + \delta_2 f = \frac{\partial f}{\partial \mathbf{G}_i} \cdot \boldsymbol{\omega}_i + \frac{\partial f}{\partial \mathbf{u}} \cdot \overline{\boldsymbol{\eta}} \\ &= \frac{d}{d\epsilon} \left[f(\mathbf{G}_i + \epsilon\, \boldsymbol{\omega}_i, \mathbf{u}(\mathbf{G}_i)) \right]_{\epsilon=0} + \frac{d}{d\epsilon} \left[f(\mathbf{G}_i, \mathbf{u}(\mathbf{G}_i) + \epsilon\, \overline{\boldsymbol{\eta}}) \right]_{\epsilon=0} . \end{aligned} \tag{32}$$

Here $\delta_1 f$ denotes a variation of f with respect to geometry (i.e. $\boldsymbol{\omega}_i$) keeping the displacement field $\mathbf{u}$ fixed and $\delta_2 f$ means a variation of f with respect to the special virtual displacement field $\overline{\boldsymbol{\eta}}$ keeping geometry fixed.

4.2 Variation of J_ψ. Since all integrals are transformed to the local parameter space T_Θ using the relation $dV = J_\psi\, dV_\Theta$ we must supply the variation

$$\delta J_\psi = \frac{d}{d\epsilon} \left[J_\psi(\mathbf{G}_i + \epsilon\, \boldsymbol{\omega}_i) \right]_{\epsilon=0} = \frac{\partial J_\psi}{\partial \mathbf{G}_i} \cdot \boldsymbol{\omega}_i \tag{33}$$

which is linear in $\boldsymbol{\omega}_i$.

4.3 Variation of objective function, constraints and the weak form. After introducing the general framework of a total variation with respect to design we can apply the developed technique to all functions modelling the optimizing problem. The variation of weak form with respect to design must vanish for all $\boldsymbol{\omega}_i$ since the equilibrium state has to be fulfilled for every design, i.e.

$$\delta g = \delta \left[\int_{T_\Theta} f(\mathbf{G}_i, \mathbf{u}(\mathbf{G}_i))\; J_\psi(\mathbf{G}_i)\; dV_\Theta \right] = 0. \tag{34}$$

This equation is valid for all variations $\boldsymbol{\omega}_i$ of geometry and for the induced variation $\overline{\boldsymbol{\eta}}$ of the displacement field and can therefore be used to evaluate $\overline{\boldsymbol{\eta}}$ for any given variation $\boldsymbol{\omega}_i$. This procedure will be explained after formulating the corresponding discretized sensitivity equation.

Considering any other continuum mechanical function α we can determine the total variation via

$$\delta\alpha = \frac{\partial \alpha}{\partial \mathbf{G}_i} \cdot \boldsymbol{\omega}_i + \frac{\partial \alpha}{\partial \mathbf{u}} \cdot \overline{\boldsymbol{\eta}} =: \mathbf{b}^i \cdot \boldsymbol{\omega}_i + \mathbf{c} \cdot \overline{\boldsymbol{\eta}}, \tag{35}$$

if for given $\boldsymbol{\omega}_i$ the induced variation $\overline{\boldsymbol{\eta}}$ was calculated. It is important to observe that $\delta\alpha$ depends linearly on $\boldsymbol{\omega}_i$ and $\overline{\boldsymbol{\eta}}$.

The necessary (partial) variations with respect to design or displacement can be calculated using standard tensor analytical arguments, e.g. as outlined in section 3.

Our discrete CAD based geometry model is an important application of the variational formulation since it can be considered to be a finite dimensional approximation of all

possible shapes. Thus limiting the whole variety of infinite many possible shapes to all shapes from a finite dimensional space of possible CAD based geometry models can be seen as a discretization process similar to the finite element approach of approximating the unknown displacement field $\mathbf{u}$ by $\mathbf{u}_h$. Now, it is important to distinguish geometrical shape functions M_i from shape functions N_k used to approximate the displacement field.

5. A DISCRETE FORMULATION OF THE SENSITIVITY ANALYSIS

The above derived sensitivity equations must be discretized corresponding to the given finite element scheme. It is necessary to divide the discretization process up into a discretization in space using some triangulation of the reference configuration and a discretization of the unknown displacement field. First of all we only consider the discretization in space and assume the exact displacement field to be given over the actual domains.

5.1 Considering different domains. The problem of discretizing structural analysis as well as sensitivity data can be discussed efficiently by introducing the following four domains of interest, see Fig , which are connected by well known mappings. It is important to note that these mappings are purely geometrical and independent from any continuous or discretized solution of the structural analysis problem.

1. $T_\square := [-1,1]^3$ quadrilateral element reference domain with local coordinates ξ_1, ξ_2, ξ_3.
2. $T_\Theta := [0,1]^3$ space of local coordinates $\Theta^1, \Theta^2, \Theta^3$.
3. $\mathbf{B}_o$ reference configuration with coordinates X^1, X^2, X^3.
4. $\mathbf{B}_{oh}$ discretized reference configuration with coordinates X_h^1, X_h^2, X_h^3.

An effective finite element formulation is almost formulated with respect to the local coordinates ξ_1, ξ_2, ξ_3 of the standard quadrilateral reference domain $T_\square$ and we recall that a finite element is called isoparametric if the geometry and the displacement field are approximated using the same shape functions. Otherwise the element is called subparametric or superparametric, respectively, depending on the actual choice of different shape functions for geometric mapping and displacement approximation.

Furthermore the mesh generator and the mesh refinement strategy operate on the parameter space T_Θ to create first of all the local coordinates Θ^i for each node of the finite element mesh. Finally the actual point $\mathbf{X}$ is calculated by inserting $\Theta^1, \Theta^2, \Theta^3$ into the mapping ψ.

The local coordinates $(\xi_1, \xi_2, \xi_3) \in T_\square = [-1,1]^3$ can be mapped into T_Θ via

$$\Theta^j = \sum_{k=1}^{4} \hat{L}^k(\xi_1, \xi_2, \xi_3)\, \Theta_k^j \tag{36}$$

where L^k denote bilinear functions which are identical to the shape functions if four noded elements are used and Θ_k^j is the j-th component of the local coordinates of the k-th element node.

5.2 Discretization of the displacement field. The displacement ficld $\mathbf{u}$ is approxima ted by $\mathbf{u}_h$ using shape functions $N^k = \hat{N}^k(\xi_1, \xi_2, \xi_3)$ in the following way

$$u_h^i = \hat{u}_h^i(\xi_1, \xi_2, \xi_3, s) = \sum_{k=1}^{nkel} \hat{N}^k(\xi_1, \xi_2, \xi_3)\, \hat{v}_k^i(s), \tag{37}$$

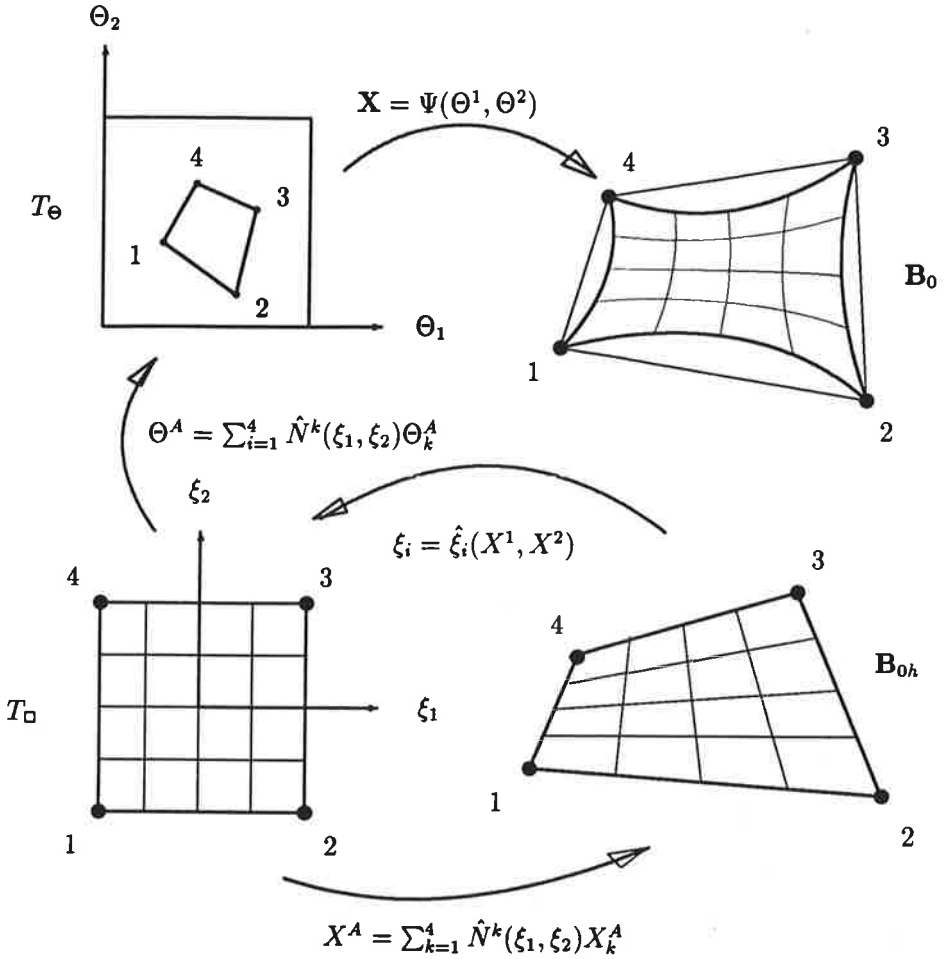

FIGURE 2: Geometrical mappings connecting four domains of interest

with v_k^i denoting the i-th displacement component of the k-th node.

5.3 Discretization representing the exact geometry. It is important to observe that an exact triangulation of the reference configuration without introducing any discretization error is possible by using the mapping ψ on each triangle or quadrilateral. Thus, it is possible to formulate some superparametric finite element method using exact CAD formulated geometrical shape functions M_i.

In this case it is appropriate to use local coordinates $\Theta^1, \Theta^2, \Theta^3$ and we obtain second mixed partial derivatives of the cartesian coordinates with respect to local coordinates and design variable

$$\frac{\partial^2 \hat{X}^A}{\partial \Theta^j \partial s} = \frac{\partial^2}{\partial \Theta^j \partial s}\left[\sum_{i=1}^{n} \hat{M}^i(\Theta^1, \Theta^2, \Theta^3)\,\hat{Y}_i^A(s)\right] = \sum_{i=1}^{n}\left[\frac{\partial \hat{M}^i(\Theta^1, \Theta^2, \Theta^3)}{\partial \Theta^j}\,\frac{\partial \hat{Y}_i^A(s)}{\partial s}\right]. \quad (38)$$

Analyzing the result it is necessary to evaluate the local coordinates $\Theta^1, \Theta^2, \Theta^3$ at the quadrature points ξ_1, ξ_2, ξ_3 using equation (36) and the partial derivatives of the geometrical shape functions M_i with respect to the local coordinates for these values as the

continuum mechanical part of the information. The structural optimization part is given by the partial derivative of the control point coordinates with respect to design varibale s. Both parts are linked multiplicatively to give the partial derivative of the local basis vectors.

In computational mechanics cartesian coordinate systems are often easier to handle than curvilinear coordinate systems given by $\mathbf{G}_i$, introducing the extra transformation between $T_\square$ and T_Θ, i.e. we obtain

$$\frac{\partial}{\partial s}\left(\frac{\partial u^A}{\partial X^B}\right) = \frac{\partial}{\partial s}\left(\frac{\partial u^A}{\partial \xi_k}\cdot\frac{\partial \xi_k}{\partial \Theta^j}\cdot\frac{\partial \Theta^j}{\partial X^B}\right) = \frac{\partial u^A}{\partial \xi_k}\cdot\frac{\partial \xi_k}{\partial \Theta^j}\cdot\left\{\frac{\partial}{\partial s}\left(\frac{\partial \Theta^j}{\partial X^B}\right)\right\}$$

where the sensitivity

$$\frac{\partial}{\partial s}\left(\frac{\partial \Theta^l}{\partial X^B}\right) = -\left(\frac{\partial \Theta^l}{\partial X^A}\right)\cdot\left(\frac{\partial^2 X^A}{\partial \Theta^j \partial s}\right)\cdot\left(\frac{\partial \Theta^j}{\partial X^B}\right)$$

is independent of the displacement field. Thus any discretization of the displacement field $\mathbf{u}$ is separated from the sensitivity information.

5.4 Discretization using the isoparametric concept. Using on the other hand some standard isoparametric finite element schemes we introduce an approximation error on the geometry and on the displacement field. Considering the geometry approximation we observe that the nodes of the finite element mesh are lying on the exact geometry with equation (8) defining their nodal coordinates. Since the local coordinates $\Theta^1, \Theta^2, \Theta^3$ are fixed for all nodes they depend only on the design variable s, i.e. $X_k^A = \hat{X}_k^A(s)$. The interior of each element is defined using shape functions N^k in the following way

$$X_h^A = \hat{X}_h^A(\xi_1, \xi_2, \xi_3, s) = \sum_{k=1}^{nkel} \hat{N}^k(\xi_1, \xi_2, \xi_3)\, \hat{X}_k^A(s) \tag{39}$$

and the covariant basis vectors $\mathbf{G}_i$ of the exact geometry are approximated by $\mathbf{G}_{hi}$. Using local coordinates we obtain

$$\frac{\partial \mathbf{G}_{hi}}{\partial s} = \frac{\partial^2 \hat{\mathbf{X}}_h}{\partial \Theta^j\, \partial s} = \frac{\partial^2}{\partial \Theta^j\, \partial s}\left[\sum_{k=1}^{nkel} \hat{N}^k\, \hat{\mathbf{X}}_k\right] = \sum_{k=1}^{nkel}\left[\frac{\partial \hat{N}^k}{\partial \Theta^j}\,\frac{\partial \hat{\mathbf{X}}_k}{\partial s}\right] = \sum_{k=1}^{nkel}\left[\frac{\partial \hat{N}^k}{\partial \xi_i}\,\frac{\partial \hat{\xi}_i}{\partial \Theta^j}\,\frac{\partial \hat{\mathbf{X}}_k}{\partial s}\right].$$

The partial derivative of the covariant basis vectors $\mathbf{G}_i$ with respect to design, i.e. the variation of $\mathbf{G}_i$ which is $\boldsymbol{\omega}_i = \delta \mathbf{G}_i$, is approximated by the partial derivatives of finite element node coordinates using local shape functions N^k, i.e.

$$\boldsymbol{\omega}_{hi} = \delta \mathbf{G}_{hi} = \sum_{k=1}^{nkel}\left[\frac{\partial \hat{N}^k}{\partial \xi_i}\,\frac{\partial \hat{\xi}_i}{\partial \Theta^j}\,\delta \mathbf{X}_k\right]. \tag{40}$$

The vector $\delta \mathbf{Z} := \{\delta \mathbf{X}_1, \cdots, \delta \mathbf{X}_{nnode}\}^T$ collecting the variation of all finite elemente node coordinates $\delta \mathbf{X}_k$ must be supplied using CAD and the mesh generator.

5.4 A discretized variational sensitivity analysis. A discretization step can be performed for the variation of the weak form δg and for the variation of any objective function $\delta \alpha$ using standard isoparametric finite elements. Since the variation depends linear on $\boldsymbol{\omega}_i$

or ω_{hi}, respectively, it is possible to separate $\delta\mathbf{Z}$ (used in the discrete variation ω_{hi}) from the integral part using the same procedure done for the discretized virtual displacement η_h to separate $\delta\mathbf{V}$. Thus finally we end up with

$$\delta g_h = \delta\mathbf{V}^T \left[\mathbf{A}_h \, \delta\mathbf{Z} + \mathbf{K}_T \, \delta\overline{\mathbf{V}} \right] = 0 \tag{41}$$

and we can calculate $\delta\overline{\mathbf{V}}$ via

$$\overline{\mathbf{V}} = -\mathbf{K}_T^{-1} \, \mathbf{A}_h \, \delta\mathbf{Z}. \tag{42}$$

Here $\mathbf{A}_h \, \delta\mathbf{Z}$ denotes the discretization of equation (27). Inserting this relationship in the discretized form of the variation of α we obtain by discretizing (35)

$$\delta\alpha = \mathbf{b}_h^T \, \delta\mathbf{Z} + \mathbf{c}_h^T \delta\overline{\mathbf{V}} = \left[\mathbf{b}_h^T + \mathbf{c}_h^T \left[-\mathbf{K}_T^{-1} \, \mathbf{A}_\mathbf{h} \right] \right] \, \delta\mathbf{Z} \tag{43}$$

Here $\mathbf{b}_h^T \delta\mathbf{Z}$ and $\mathbf{c}_h^T$ denote the discretization of $(\partial\alpha/\partial\mathbf{G}_i) \cdot \boldsymbol{\omega}_i$ and $\partial\alpha/\partial\mathbf{u}$ respectively. Analyzing the above obtained matrix representation of a model function α we seperated the influence of the virtual change of geometry from the discretized sensitivity. Here $\mathbf{A}_h$ denotes the discretized partial sensitivity matrix of the total residual vector with respect to the coordinates of the FE nodes which is analytical available and independent of the actual choice of design variables. It is important to observe that both $\mathbf{K}_T$ (and $\mathbf{K}_T^{-1}$) and $\mathbf{A}_h$ are sparse matrizes, i.e. $\mathbf{K}_t^{-1} \, \mathbf{A}_h$ can be calculated efficiently being itself sparse.

6. SOFTWARE REALIZATION AND EXAMPLES

The proposed concept of structural optimization has been realized in our research analysis tool INA-OPT (INelastic Analysis and OPTimization). The described sensitivity analysis was applied in various intermediate stages of its development to solve optimization problems considering rubberlike materials under large strains. The overall structural optimization algorithm and numerical details concerning the sensitivity analysis and the used mathematical programming algorithm can be found in *Barthold* [6].

We present very briefly an example, where a plate with dimensions $a = 36\,mm$, $b = 20\,mm$, thickness $d = 1\,mm$ and a circular hole with radius $r = 5\,mm$ was optimized to reduce weight under displacement and stress constraints. The plate consists of an incompressible rubber material which can be modeled by Ogden' s material law, see equation (10). Using symmetry only a quarter of the systems was considered. The plate was deformed to an overall elongation of three times the initial length. The geometry of the plate was modelled using Bézier curves and a Coons surface model. The control point coordinates of the outer surfaces are design variables. The radius is fixed.

The finite element mesh consists of 255 elements and 364 nodes with 698 d.o.f. The mesh was derived by using adaptive mesh refinement strategies, see Rust [11], Zienkiewicz and Zhu [14].

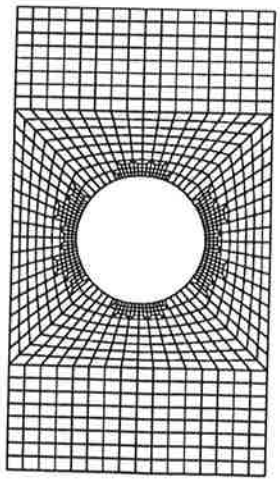

The deformed mesh of the initial design and the optimal design as well as the distribution of maximal normal Cauchy stresses for the optimal design are given in figure 3.

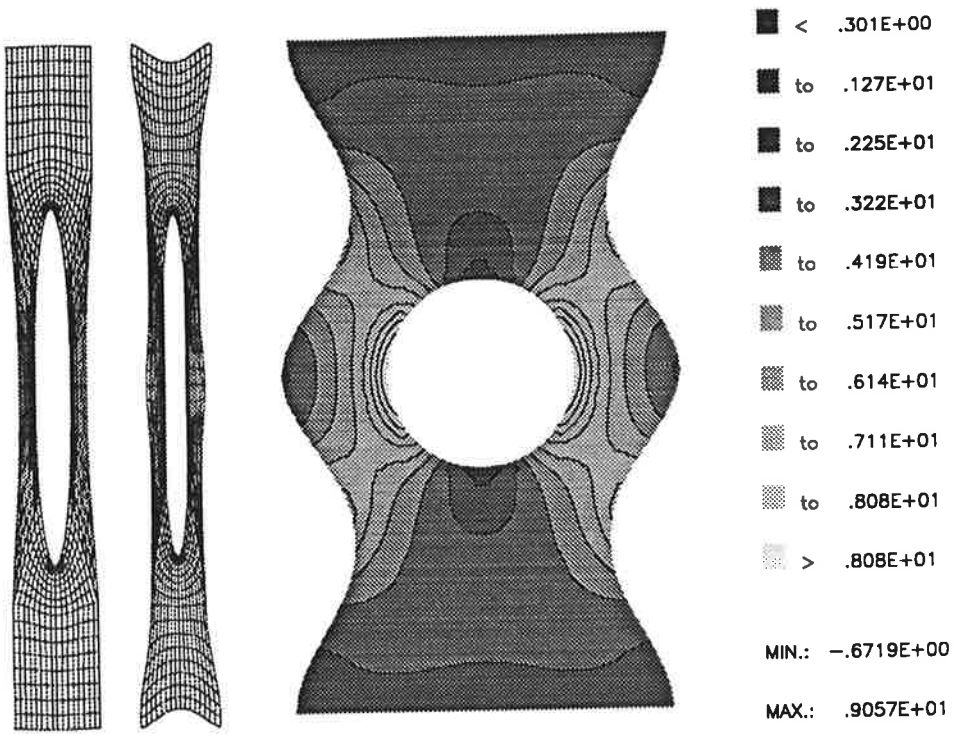

FIGURE 3: Displacements and stresses of initial and optimal design

7. CONCLUSIONS

In this paper a continuum mechanical theory of structural optimization is developed. Considering the geometrical properties of a material body in the continuum mechanical context and of patches in computer aided design we linked these two important foundations of structural optimization together.

This theory is an important application of the modern variational formulations in structural optimization. Here we consider the well established CAD software systems as a tool for discretizing the continuously derived sensitivity analysis towards an applicable discrete geometry model. The step from any variation of shape to this proposed family of possible shapes parametrized with well known control parameters is similar to discretizing the unknown displacement field by finite element approximants.

The variation of continuum mechanical functions with respect to geometrical design variables can be written using the covariant basis vectors in each point of the body and their sensitivity.

A discretization process using isoparametric elements end up with a new elegant matrix formulation of sensitivity analysis reducing the total computational effort drastically.

REFERENCES

[1] R. Abraham, J. E. Marsden und T. Ratiu. *Manifolds, Tensor Analysis and Applications.* Addison-Wesley, 1983.

[2] J. S. Arora. An exposition of the material derivative approach for structural shape sensitivity analysis. *Computer Methods in Applied Mechanics and Engineering*, 105:41–62, 1993.

[3] N. V. Banichuk. *Introduction to Optimization of Structures.* Springer-Verlag, New York, Berlin, Heidelberg, 1990.

[4] F.-J. Barthold, A. Falk und E. Stein. Structural optimization of rubberlike materials using analytical sensitivity analysis. In *Proceedings of the 20th ASME Design Automation Conference, Minneapolis, September 11–14, 1994*, to appear, 1994.

[5] F.-J. Barthold und E. Stein. A continuum mechanical theory of structural optimization. *Structural Optimization*, to appear, 1994.

[6] F.J. Barthold. Theorie und Numerik zur Berechnung und Optimierung von Strukturen aus isotropen, hyperelastischen Materialien. Technischer Bericht F 93/2, Forschungs- und Seminarberichte aus dem Bereich der Mechanik der Universität Hannover, 1993.

[7] E. J. Haug, K. K. Choi und V. Komkov. *Design Sensitivity Analysis of Structural Systems.* Academic Press, Orlando, 1986.

[8] T. J. R. Hughes und K. S. Pister. Consistent linearization in mechanics of solids and structures. *Computers and Structures*, 8:391–397, 1978.

[9] L. E. Malvern. *Introduction to the Mechanics of a Continuous Medium.* Prentice-Hall, Inc., Englewood Cliffs, 1969.

[10] J. E. Marsden und T. J. R. Hughes. *Mathematical Foundations of Elasticity.* Prentice-Hall, Inc., Englewood Cliffs, 1983.

[11] W. Rust. Mehrgitterverfahren und Netzadaption für lineare und nichtlineare statische FE-Berechnungen von Flächentragwerken. Technischer Bericht F 91/2, Forschungs- und Seminarberichte aus dem Bereich der Mechanik der Universität Hannover, 1991.

[12] M. Souli und J. P. Zolesio. Shape derivative of discretized problems. *Computer Methods in Applied Mechanics and Engineering*, 108:187–199, 1993.

[13] D. A. Tortorelli und Z. Wang. A systematic approach to shape sensitivity analysis. *International Journal of Solids & Structures*, 30(9):1181–1212, 1993.

[14] O. C. Zienkiewicz und J. Z. Zhu. A simple error estimator and adaptive procedure for practical engineering analysis. *International Journal for Numerical Methods in Engineering*, 24:334–357, 1987.

CHAOS IN STRUCTURAL MECHANICS

ÜLO LEPIK
Institute of Applied Mathematics
Tartu University
Vanemuise str. 46-250, EE2400 Tartu, ESTONIA

ABSTRACT

The main aim of this report is to give an overview about chaotic processes in structural dynamics. The paper begins with an introduction, where main features of a chaotic motion are described. After that we shall examine chaotic vibrations of elastic and elastic-plastic systems. In the last part of the paper some results of the author are presented.

1. ABOUT CHAOS

What is chaos? To give an answer to this question is not quite easy, since up to now an mathematically exact definition of chaos is wanting. A somewhat simplified definition is: chaos is an unpredictable motion.

Investigation of chaos began with the famous work of Edward Lorenz from 1960 (although the term "chaos" was introduced somewhat later, by James York in 1975). Lorenz solved numerically the following system of equations

$$\begin{aligned} \dot{x} &= 10(y-x) \\ \dot{y} &= xz + 28x - y \\ \dot{z} &= xy - \frac{8}{3}z. \end{aligned} \tag{1}$$

It turned out that this system is very sensitive to small changes of initial conditions (e.g. the initial values 0.506 and 0.506127 brought to quite different solutions). Figuring the solution in three-dimensional space Lorenz got the well-known "butterfly" diagram.

Next contribution to chaos belongs to James York and Robert May (1975–76). They investigated the mapping

$$x_{n+1} = rx_n(1-x_n), \tag{2}$$

which characterizes the growth of populations for different values of the parameter r. It

turned out that if $r < 2.7$, the process $n \to \infty$ has a unique solution. By increasing the value of r a period doubling takes place and we have two values for x_∞ . If r rises further another period doubling is observed, after that the system turns chaotic and we get infinitely many different values for x_∞ . It is interesting to mark that inside the chaotic region there are "windows" where the motion is deterministic.

An import step was made in 1977 by Benoit Mandelbrot, who introduced the concept of "fractals". A fractal can be defined as a continuous function which does not have a derivative in the common sense. Many objects of nature have fractal pattern (coastline, snowflakes, ice cristals, metal allows); fractal are also cracks in a concrete. The boundaries of fractal structures are generally compound lines (i.e. they exist in the form of several lines). By zooming this picture it remains fractal and more and more new lines become evident (self-similarity effect).

There are several methods for establishing chaotic motions. For shortness sake we shall consider here only two of them. Let us take an autonomous dynamic system

$$\dot{x}_1 = f(x_1, x_2) \qquad , \qquad \dot{x}_2 = g(x_1, x_2)$$

and compose the phase portrait in the plane (x_1, x_2). In the case of periodic or quasiperiodic vibrations we get a closed curve. For chaotic motions we shall have in the phase plane orbits which never close or repeat; the trajectories of these orbits tend to fill up a definite section in the phase plane (cf. Fig. 1a).

The other possibility is to put together a power spectrum diagram. For this purpose we shall transform the time variable $f(t)$ with the help of a discrete Fourier transform into the frequency domain

$$F(\omega_n) = \Delta t \sum_{k=0}^{2N-1} f(t_k) e^{-\omega_n t_k i} \tag{3}$$

and calculate the power spectrum

$$P(\omega_n) = |F(\omega_n)|^2.$$

Periodic and quasi-periodic vibrations can be recognized by discrete line spectra; chaotic motions - by a broad, continuous band of frequencies (cf. Fig. 1b).

From other criteria for chaotic behavior of dynamical systems we shall mention here a positive Lyapunov exponent, a Poincare map of fractal dimension, Melnikov method for homoclinic trajectories. One can learn about these methods of the text-books, from which some are presented in the list of references [1-7] .

One of the equations of motion for which regular and chaotic motions are investigated in detail is the Düffing's equation

$$\ddot{y} + k\dot{y} - \beta y + \alpha y^3 = A \cos \omega t. \tag{4}$$

This equation was first examined by Georg Düffing in 1918. A more detailed analysis was given by Ueda [8] , who cleared out the regions in the parameters plane (A, k) for which

chaotic motion takes place. The equation (4) is important to structural dynamics, since many problems about nonlinear vibrations of structures can be reduced to the solution of this equation.

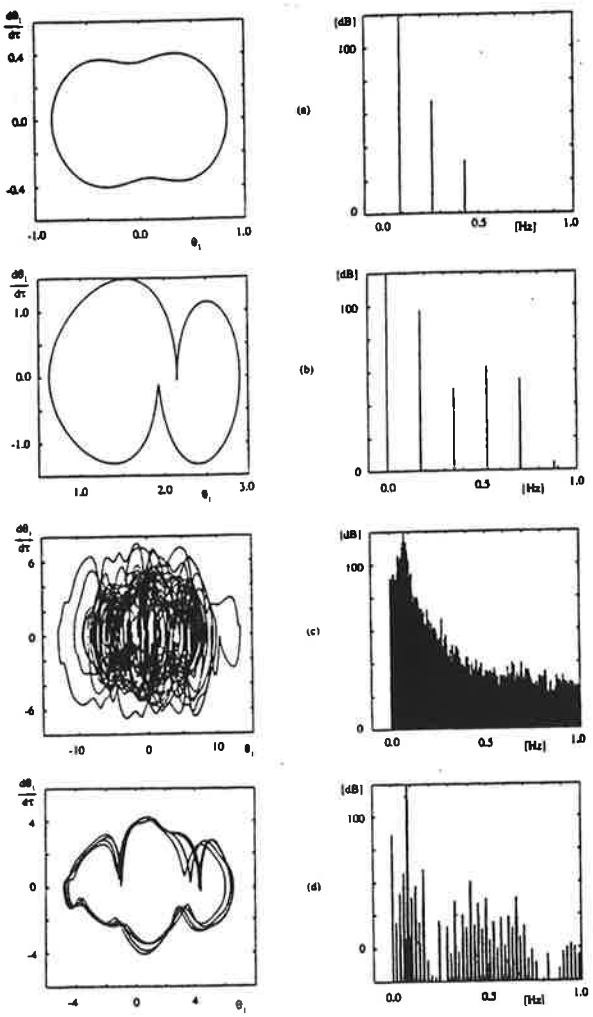

FIGURE 1. Phase portraits and power spectra for regular and chaotic motions (Thomsen [19])

2. CHAOTIC BEHAVIOR OF ELASTIC STRUCTURES

Chaotic motion can take place only in nonlinear dynamic systems. In structural dynamics nonlinear effects can be introduced in two ways: (i) due to large displacements: we must take into account nonlinear terms in the equations of motion (geometric nonlineary); (ii) from external forces or boundary conditions. Both cases are illustrated in Fig. 2.

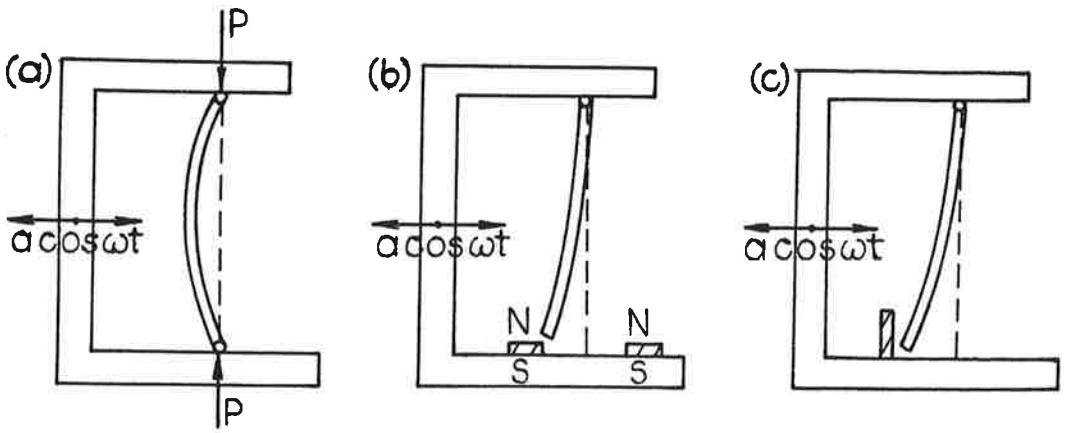

FIGURE 2. Three elastic periodically excited beams

Here we have three elastic beams which are placed on a vibrostand carrying out forced vibrations $a\cos\omega t$. The first beam is compressed by the end load P_0 and, if we assume that the axial load T is constant along the beam, then the equation of motion is

$$EI\frac{\partial^4 w}{\partial x^4} - T\frac{\partial^2 w}{\partial x^2} + C\dot{w} + \rho A\ddot{w} = a\cos\omega t, \tag{5}$$

where

$$T = -P_0 + \frac{EA}{2L}\int_0^L (\frac{\partial w}{\partial x})dx. \tag{6}$$

Here E is the Young's modulus, I – moment of inertia, A – cross-sectional area, ρ – density, C – damping coefficient, L – length of the beam. If we take

$$w = f(t)\sin\pi\frac{x}{L} \tag{7}$$

and solve the equation (5) by the Galerkin's method, we get the Düffing's equation (4).

As to the other two problems then the beam in Fig. 2b vibrates between two magnets, nonlinearity is caused by the magnetic forces. In Fig. 2c there is a stop near the free end of the beam; so for source of nonlinearity is the boundary condition.

These three problems were solved by Moon, Shaw and Holmes [4, 14, 15]. It follows from their analysis that for certain values of the beam and load parameters chaotic vibrations take place; also the period doubling was stated. Tang and Dowell [18] showed that the one

degree of freedom formula (7) may lead to significant errors and therefore higher modes should be taken into account. Dowell [10] found chaos in the flutter of a buckled plate.

Bifurcations and chaotic behavior of elastic strings in three dimensional space were examined by O'Reilly and Holmes [16, 17] ; their results were confirmed by experiments carried out by Molteno and Tufillaro [13].

Bifurcation analysis of a rotating elastic beam was examined by Gross et al. [12]. Chaotic dynamics of a double pendelum was investigated by Thomsen [20]; the pendelum consists of two rigid bars, which carry concentrated masses and are connected by elastic springs. For establishing chaotic motion the Ljapunov exponents, Poincare sections phase portraits and power spectra have been used (some characteristic diagrams are shown in Fig. 1). In another paper by Thomsen [19] chaotic vibrations of non-shallow arches are examined.

Goncalves [11] has investigated the dynamic non-linear behavior of a pre-loaded shallow spherical shell under a harmonic excitation. The equations of motion are solved by the Galerkin's method. Different physical situations are identified in which period-doubling phenomena and chaos can be observed.

Irregular vibrations of compressed beams under lateral excitation are discussed in several papers from which we shall note here the paper by Tseng and Dugundij [21] . These results were developed further by Abhuankar et al. [9] . They considered a beam which is compressed by an axial load greater than the Euler buckling load and then is fixed in its compressed position. After that a transverse load $F = F(x,t)$ will be applied, besides a base excitation $w_B(t)$ may act (Fig. 3). Now the equations (5)-(6) hold if we shall substitute the right side of (5) by the term $F(x,t) - \rho A \ddot{w}_B$.

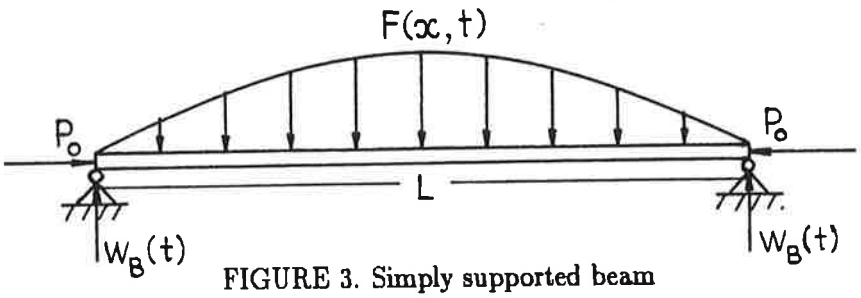

FIGURE 3. Simply supported beam

The equation (5) was solved in two ways: (a) making use of the Galerkin's procedure; (b) solving this partial differential equation by an explicit finite difference scheme. The results, which were carried out for $F(x,t) = a \sin \pi \frac{x}{L} \cos \omega t$ and $\ddot{w}_g = 0$ according to these two methods, showed good accordance. Also a problem where $|w(x,t)| < \delta$ (i.e. deflections are constrained by two stops) is considered. Chaotic behavior of the solutions follows from phase portraits and period doubling bifurcations.

3. ELASTIC-PLASTIC PROBLEMS

In 1985 Symonds and Yu [34] considered the following problem: a fixed-ended beam is

subjected to a short intensive pulse of transverse loading that produces plastic deformation. Since the ends of the beam are fixed then also membrane forces must be taken into account. For simplicity sake the real beam was replaced by a Shanley-type model with a single degree of freedom. This model consists of two rigid beams, which are connected by a small elastic-plastic "cell" (Fig. 4a). Solving the equations of motion Symonds and Yu found that permanent deflection may be in the direction opposite to that of load. Such a phenomenon they called "the anomalous" or "counter-intuitive behavior" of the beam. They established that such a behavior takes place only in a narrow region of beam and load parameters.

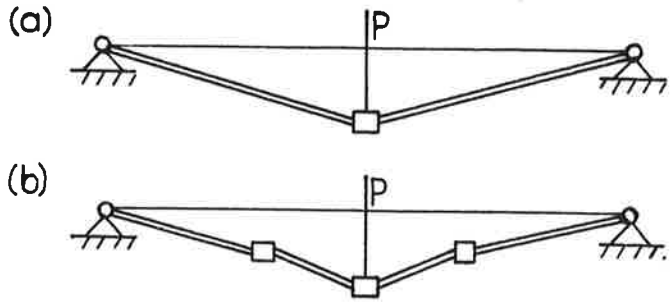

FIGURE 4. Shanley-type beam models

A different single degree of freedom model was proposed by Yu and Xy [35] in 1989. This model consists of a rigid concentrated mass and two tiers of elastic-plastic strings, which connect the mass to the fixed pin ends. The model describes the same effects as the model of Symonds and Yu.

Counter-intuitive behavior of the beam was observed also in experiments which were carried out in 1991 by Kolsky et al. [25] ; here the impact loading was simulated by pulling the specimen to an initial deflection and then releasing it abrubtly.

For counter-intuitive behavior of the beam the question, if the vibrations in a pin-ended beam may be chaotic, arises. Lee and Symonds [26], making use of energy approach, showed that in the case of a single degree of freedom model the motion is fully determined and there cannot be chaotic vibrations.

So if we want to get chaotic motion we must go out from a model which has two degrees of freedom at least. Such a model was proposed by Symonds and his coworkers and is shown in Fig. 4b (here three rigid bars are connected by three elastic-plastic shells). This model has been applied in several papers of Symonds et al.; for shortness sake we have brought in the list of references only some of them [22, 27, 33]. A brief survey of the obtained results is as follows.

Symonds et al. showed that at after some first vibrations the motion "shakes down", so that the plastic strains remain constant and the following motion is wholly elastic. The solution is very sensitive to small changes of load. This is demonstrated in Fig. 5a

where permanent deflections of midpoint of the beam are shown; Fig. 5b shows the same for an expanded scala. As to the black regions in these figures then if we shall go to more expanded scales they are decomposed to positive and negative subintervals of very small size. From here the fractality and self-similarity, which are characteristic to chaotic processes, follow. Symonds and Lee [33] calculated also the fractal dimensions for this problem. They found for the similary dimension the value 0.78 and for the correlation fractal dimension ~ 1.44 (in the non-chaotic case these values are 0 and 1, respectively). Symonds and his coworkers have used also other methods for establishing chaotic character of vibrations (e.g. Poincare' diagrams, Lyapunov exponents).

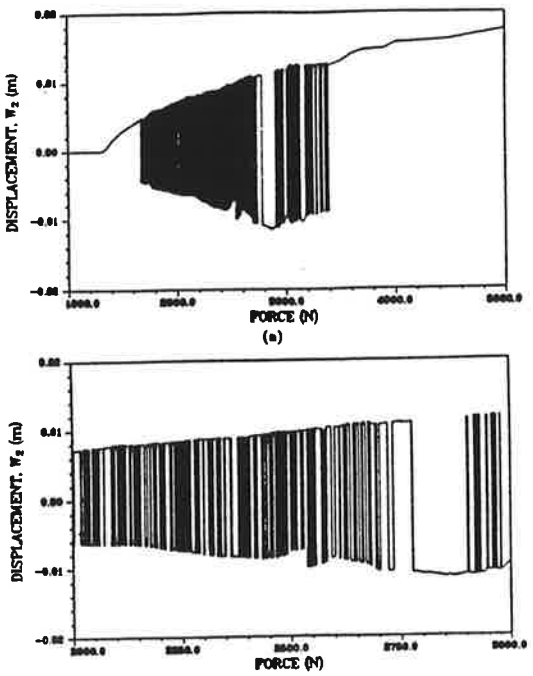

FIGURE 5. Final midpoint deflections plotted as function of pulse force (Symonds and Lee [32])

Elastic-plastic response of circular plates was examined by Galiev and Nechitailo [22-23]. The equations of motion were integrated by the second order difference method. The yield condition of Huber-Mises has been applied. It follows from the calculations that also for this problem counter-intuitive behavior can be realized.

Of course, it would be important to get solutions for continuous beams (i.e. without making use of Shanley-type or analogical models). For this purpose FEM-type technics could be used, but this requires a lot of computation time. Therefore it is essential to work out some simplified methods of solution. Such an attempt has been done by the author [28-31] . The method of solution proposed in these papers is reported below.

If a transverse pressure $p(x)$ acts to the beam, then the equations of motion are

$$\Phi_1 \equiv \frac{\partial T}{\partial x} - \rho h B \frac{\partial^2 u}{\partial t^2} = 0$$
$$\Phi_2 \equiv \frac{\partial^2 M}{\partial x^2} + \frac{\partial}{\partial x}(T\frac{\partial w}{\partial x}) + p(x) - \rho B h \frac{\partial^2 w}{\partial t^2} = 0 \tag{8}$$

It is assumed that the beam has a rectangular cross-section (B – is the beam width, h – height). Axial force T and bending moment M we shall calculate from the formulae

$$T = \int_{-\frac{h}{2}}^{\frac{h}{2}} \sigma(x,z)dz, \qquad M = \int_{-\frac{h}{2}}^{\frac{h}{2}} \sigma(x,z)zdz. \tag{9}$$

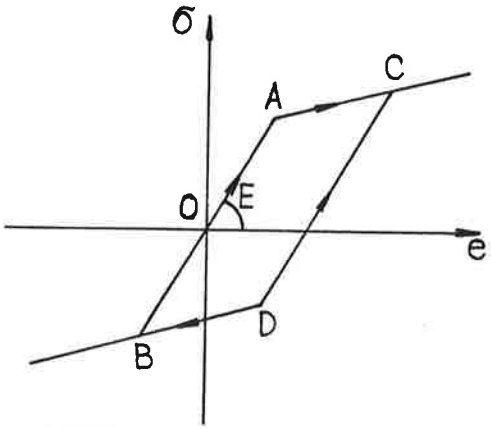

FIGURE 6. Stress-strain diagram

For simplicity sake we shall take the stress-strain diagram in the form as shown in Fig. 6 (material with linear strain-hardening), elastic unloading (line CD) is also taken into account. To the equations (8) we shall apply the Galerkin's procedure

$$\int_0^{\frac{L}{2}} \Phi \delta u dx = 0, \qquad \int_0^{\frac{L}{2}} \Phi_2 \delta w dx = 0. \tag{10}$$

Displacements u and w we shall seek in the form

$$u = \sum_{i=1}^{n} b_i \sin 2i\pi \frac{x}{L}, \qquad w = \sum_{i=1}^{n} f_i \cos(2i+1)\pi \frac{x}{L}. \tag{11}$$

The integrals (9) and (10) we shall evaluate numerically doing this we find the second derivatives $\ddot{b}_i$ and $\ddot{f}_i$. For evaluating the quantities $b_i, \dot{b}_i, f_i, \dot{f}_i$. we shall use the scheme of central finite differences (it was shown by Mikkola et. al. [32] , that with this simple method high accuracy can be achieved). To get a stable solution the time increment must be sufficiently small. Calculations have shown that it is enough to take two terms from the series (11). The results obtained by our method are quite close to the solutions, obtained by Abacus technic (see [30]). Now let us briefly discuss some results obtained by this method. Most of the elastic solutions go out from the assumption that the axial

force is constant along the beam (see (6)). In paper [28] it was shown, that for plastic beams it does not hold(see Fig. 1-3 of this paper). Still more, in the elastic case examples can also be brought, where the assumption $T = const$ brings to quite different deflection-load diagrams to be compared with the real solution. Therefore one should be careful by making use of the solution $T = const$ even in the case of elastic beams. Computations show that plastic deformations take place only during the first vibrations; after that the system "shakes down" and the subsequent motion is wholly elastic. This enables us to put together an approximate solution (elastic recovery type solution). If we assume that $u \equiv 0$ and w can by approximated by one term in the equation (11) we get again a Düffing-type equation. Details of this approximate method can be found from papers [28-30] . It follows from papers [28-31] that in the case of continuous beams also counterintuitive behavior takes place. Weak chaotic effects in the response of the beam may exist, especially in the initial phase; as to the long-term motion then it transitates to periodic vibrations of smaller amplitude. In paper [31] also vibrations of flat elastic-plastic arches are considered.

References

A About chaos:

1. J.Argyris, G.Faust and M.Haase, An adventure in chaos, Comp. Meth. in Appl. Mech. and Engng, 91 (1991), 997-1091.

2. L.Glass and M.C.Mackey, From clocks to chaos. The rythms of life, Princeton University Press, 1988.

3. J.Gleick, Chaos: Making a new science. Viking Press, New-York, 1987.

4. F.C.Moon, Chaotic vibrations: an introduction for applied scientists and engineers. J. Wiley, New-York et al., 1987.

5. H.O.Pertgen and P.H.Richter, The beauty of fractals: images of complex dynamical systems, Springer, Berlin et. al., 1986.

6. H.G.Schuster, Deterministic chaos: an introduction. Physik- -Verlag GmbH, D-6940, Weinheim, 1984.

7. J.M.T.Thompson and H.B.Stewart, Nonlinear dynamics and chaos: geometrical methods for engineers and scientists. J.Wiley, Chichester et al., 1986.

8. Y.Ueda, Steady motions exhibited by Duffing's equation: a picture book of regular and chaotic motions. In "New Approaches to Non- linear Problems in Dynamics", P. J. Holmes (Ed.), SIAM, Philadelphia, 1980.

B Elastic problems:

9. N.S.Abhyankar, E.K.Hall and S.V.Hanagud, Chaotic vibrations of beams: numerical solution of partial differential equations. ASME, J. Appl. Mech., 60, (1993), 167-174.

10. E.H.Dowell, Flutter of a buckled plate as an example of chaotic motion of a deter-

ministic autonomous system. J. Sound and Vibration, 85, (1982), 333-344.

11. P.B.Goncalves, Jump phenomena, bifurcations and chaos in a pressure loaded spherical cap under harmonic excitation. "Mechanics Pan-America, 1993 (ed. C. da Silva, C. Mazzilli)", Appl. Mech. Rev. 46, N 11, part 2, (1993), S 279 - S 288.

12. P.Gross, M.Gürgöze and W.Kliem, Bifurcation and stability analysis of a rotating beam. The Technical University of Denmark, report N 432, 1991.

13. T.C.A.Molteno and N.B.Tufillaro, Torus doubling and chaotic string vibrations: experimental results, J. Sound and Vibration, 135, (1990), 327-330.

14. F.C.Moon and P.J.Holmes, Strange attractors and chaos in nonlinear systems, ASME J. Appl. Mech., 50, (1983), 1021-1032.

15. F.C.Moon and S.W.Shaw, Chaotic vibrations of a beam with nonlinear boundary conditions, Int. J. Non-Linear Mechanics, 18, (1983), 465-477.

16. O.O'Reilly, Global bifurcations on the forced vibration of a damped string, Int. J. Non-Linear Mechanics, 28, (1993), 337-351.

17. O.O'Reilly and P.Holmes, Nonlinear, nonplanar and nonperiodic vibrations of a string, J. Sound and Vibrations, 153, (1992), 413-435.

18. D.M.Tang and E.H.Dowell, On the threshold force for chaotic motions for a forced buckled beam, ASME, J. Appl. Mech., 55, (1988), 190-196.

19. J.J.Thomsen, Chaotic vibrations of nonshallow arches, J. Sound and Vibration, 153, (1992), 239-258.

20. J.J.Thomsen, Chaotic dynamics of the partially follower-loaded elastic double-pendelum. The Technical University of Denmark report, N 455, 1993.

21. W.Y.Tseng and J.Dugundji, Nonlinear vibrations of a buckled beam under harmonic excitation, ASME J. Appl. Mech., 38, (1971), 467-476.

C Elastic-plastic problems:

22. G.Borino, U.Perego and P.S.Symonds, An energy approach to anomalous damped elastic-plastic response to short pulse loading, ASME J. Appl. Mech., 56 (1989), 430-438.

23. Sh.U.Galiev and N.V.Nechitailo, Unexpected behavior of plates under impulsive and hydrodynamic loading (in Russian), Problemy Prochnosti, N 12, (1986), 63-72.

24. Sh.U.Galiev, J.N.Babitch, S.V.Zhuravski, N.V.Nechitailo and V.A.Romastshenko, Numerical modelling wave processes in limited media (in Russian), Kiev, Naukova Dumka, 1989.

25. H.Kolsky, P.Rush and P.S.Symonds, Some experimental observations of anomalous response of fully clamped beams, Int. J. Impact Engng., 11, (1991), 445-456.

26. J.-Y.Lee and P.S.Symonds, Extended energy approach to chaotic elastic-plastic response to impulsive loading, Int. J. Mech. Sci., 34, (1992), 139-157.

27. J.-Y.Lee, P.S.Symonds and G.Borino, Chaotic responses of a two-degree-of-freedom

elastic-plastic beam model to short pulse loading, ASME, J. Appl. Mech., 59, (1992), 711-721.

28. Ü.Lepik, Dynamic response of elastic-plastic beams with axial constraints, Int. J. Impact Engng, 15, (1994), 3-16.

29. Ü.Lepik, Impulsively loaded fully fixed-ended elastic-plastic beams by Galerkin's method, Int. J. Impact Engng, 15, (1994), 17-23.

30. Ü.Lepik, Dynamic response of elastic-plastic pin-ended beams by Galerkin's method (to appear in Int. J. Solids and Structures).

31. Ü.Lepik, Vibrations of elastic-plastic fully clamped beams and flat arches under impulsive loading (to appear in Int. J. Nonlinear Mech.).

32. M.J.Mikkola, M.Tuomala and H.Sinisalo, Comparisons of numerical integration methods in the analysis of impulsively loaded elastic-plastic and viscoplastic structures. Computers and Structures, 14, (1981), 469-478.

33. P.S.Symonds and J.-Y-Lee, Fractal dimensions in elastic-plastic beam dynamics (to appear in the Proceedings of the 14th Biennal ASME Conference on Vibration and Noise, Sept. 1993, Albuquerque, New Mexico).

34. P.S.Symonds and T.X.Yu, Counterintuitive behavior in a problem of elastic-plastic beam dynamics, ASME, J. Appl. Mech., 52, (1985), 517-522.

35. T.X.Yu and Y.Xu, The anomalous response of an elastic-plastic structural model to impulsive loading. ASME, J. Appl. Mech., 56, (1989), 868-873.

PRODUCT DEVELOPMENT PROCESS OF A SANDWICH PANEL, STRUCTURAL MECHANICS

MARKKU HEINISUO
Finnish Academy

SIMO MALMI
Structural Mechanics
Tampere University of Technology
P.O.Box 600,FIN-33101 Tampere,FINLAND

1. INTRODUCTION

The paper deals with the studies of the mechanics of a new Sandwich panel, Composer. The faces of the panel can be made of steel, copper, aluminium or some other metal. The core material is plastic foam. The panel is used as a covering of the outer walls of buildings. The panel is usually a rectangular plate which is joined to the wall by using the special connectors developed to this purpose. Fig. 1 presents a typical panel connection to the wall and the use of the panel in buildings.

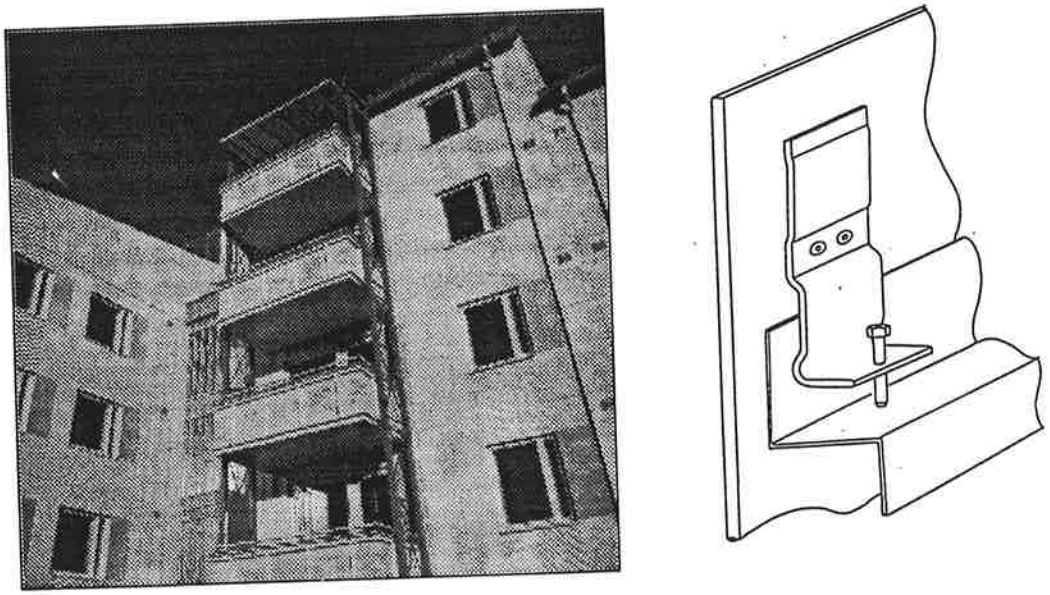

FIGURE 1. The panel developed.

The product development process is going on in Tampere University of Technology in co-operation with the company Teräselementti Oy, which is the fabricator of the panel. The research project has been divided into two parts: the durability and fabrication of the panel and the mechanics of the panel. The first part is done in the department of material science and the second part is done in the department of civil engineering. The paper deals with the second part of the project.

2. DESIGN CRITERIA OF THE PANEL

The design criteria of the panel were taken from the reference [2] because there are no similar criteria available in the Finnish codes for the Sandwich panels. The following equation must be satisfied at both the ultimate limit state and the serviceability limit state

$$F_d = \gamma_f \left(F_{wind} + 0.5\, F_T \right) \leq \frac{R}{\gamma_m}$$
$$F_d = \gamma_f \left(F_T + 0.5\, F_{wind} \right) \leq \frac{R}{\gamma_m} \qquad (1)$$

where

F_d = design value of action
γ_f = relevant load factor according to Table 1
F_{wind} = calculated value of the action of wind
F_T = calculated value of the effect of temperature
R = value of resistance at relevant limit state
γ_m = relevant material factor according to Table 1

	Ultimate limit state	Serviceability limit state
Load factor γ_f	1.5	1.0
Material factor γ_m		
yielding of metal face	1.1	1.0
wrinkling of metal face at a support	1.5	1.2
shear of the core	1.25	1.0
crushing of the core	1.25	1.0
failure of fasteners	1.25	1.0
failure of an element at a point of connection	1.25	1.0

TABLE 1. Load factors and material factors for Sandwich panels [2].

3. LOADING OF THE PANEL

The panel is loaded mainly by the variable short-time actions like wind loads and temperature gradients when the panel is used in buildings. The self weight of the panel can be ignored when designing the panel. The wind loads and corresponding shape factors are taken from the national codes. Instead, the temperature and its gradient between the faces must be studied, because there are no exact rules for this loading e.g. in the Finnish codes.

The surface temperatures at the outer side of the panel, i.e. at the sunshine, can be found from [2]. There are some facts which must be taken into account when designing this kind of panels. Firstly, the temperature values in [2] are given for the use of panels in the middle Europe. Secondly, the heat flow between the panel faces is remarkable, because the thickness of the panels studied is only 4-6 mm.

Temperature-measurements of a panel in the building of Fig. 1 were done in site to get relevant information of the actual temperature loadings. Fig. 2 shows the variations of temperature of the inner and outer surface of a panel and in the structure behind a panel and the variations of air temperature during a cold and sunny winter day.

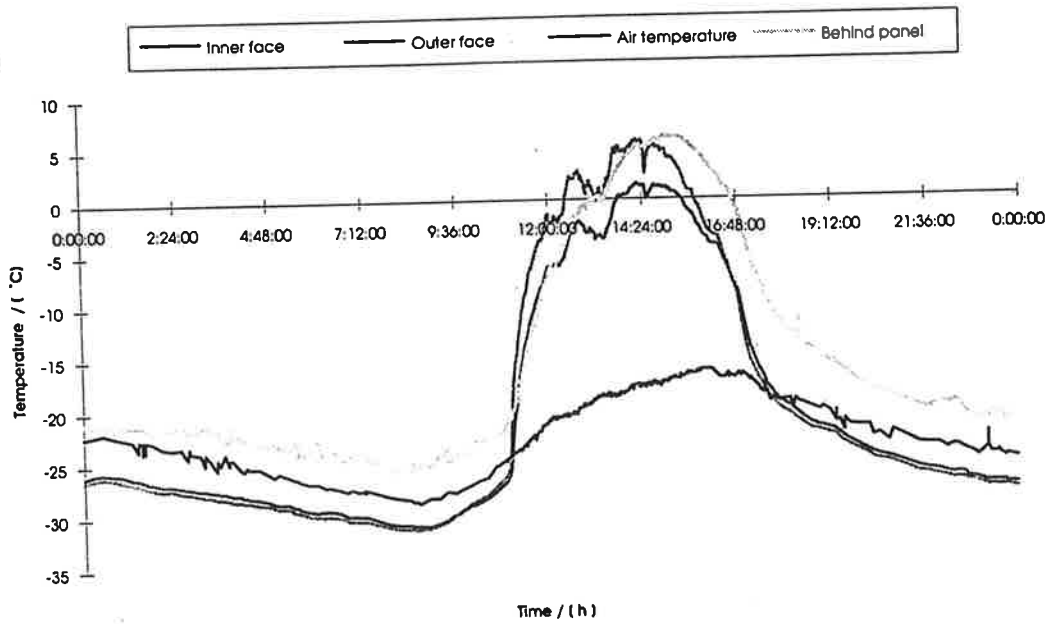

FIGURE 2. An example of measured temperature values of a sandwich panel

Some more tests were done in the laboratory of TUT and in the factory of Teräselementti Oy. The calculation model proposed in [1] was used to verify the experiments.

As a result the design values in Table 2 were found to be proper for the design of these panels for the use in Finland.

Maximum summer temperature values at serviceability limit state	T °C
- very light colours, R_G=75-90 %	45
- ligth colours, R_G=40-74 %	50
- dark colours, R_G=8-39 %	55
Maximum summer temperature values at ultimate limit state	
- dark colours, R_G=8-39 %	60
R_G= degree of reflection relative to magnesium oxide=100 %	
Maximum temperature difference between metal faces	10

TABLE 2. Design values of temperature load [7]

The equations 2 ([1],[8]) can be used for the calculation of the temperatures of the outer and inner faces of the panel.

$$T_{up} = \frac{a\,I + \frac{T_s}{m_o} + \frac{T_u}{m_u}}{\frac{1}{m_o} + \frac{1}{m_u}} \quad , \quad T_{sp} = T_s + \frac{T_{up} - T_s}{m_o + m_s}\, m_s \qquad (2)$$

where

a = absorption coefficient of surface
I = intensity of shortwave radiation(W/m^2)
T_s = temperature of inside air (°C)
T_u = temperature of outside air (°C)
m_o = coefficient of heat resistance from inner surface to outer surface
m_s = coefficient of heat resistence of inner surface
m_u = coefficient of heat resistence of outer surface
T_{sp} = surface temperature of inner surface
T_{up} = surface temperature of outer surface

4. MATERIAL PROPERTIES OF THE PANEL

The material properties of the faces are well known because they are metal. The glue between the faces and the core is supposed to be at least as good as the core material. The deformation of the glue is included into the material behaviour of the core, because all material tests were done by using the whole sandwich structure (i.e. the core is not tested alone but always with the faces glued to it). The core material is plastic foam which material properties are dependent on the temperature, the period of loading and the level of stress.

The shear modulus of the core is the main parameter when designing the panel. The reduction of the shear modulus is done following [2] by using the Eq. 3

$$G_{ST} = \frac{G_S}{1 + \varphi_t} \tag{3}$$

where φ_t= creep coefficient and G_S= initial shear modulus.

The shear modulus of the core material was determined from the maximum deflections of test beams by means of a four-point bending test at temperatures -20 °C,+20 °C and +60 °C. The level of stress used in tests was taken as the approximated maximum to be reached in the ultimate limit state.

The shear modulus was calculated from the equations [2]

$$\begin{aligned} w_B &= \frac{F\ L^3}{56.34\ B_S} \\ w_s &= w - w_B \\ G_S &= \frac{F\ L}{6\ B\ H_S\ w_S} \end{aligned} \tag{4}$$

where

B_S = flexural rigidity

F = total load on test specimen

L = length of test specimen

w = deflection (measured) at mid-span for a load F

w_B = bending deflection

w_s = shear deflection

H_S = depth of core material

B = width of test specimen

Deflections were measured at seven time-points during the test, namely 0.1 , 1, 2, 10, 100, 500 and 1000 hours. Curve fitting was used to find a time-dependence function for the shear modulus. The determined redused shear modulus G_{ST} was verified by running some test using the general purpose FEM-program,ABAQUS.

Table 3 shows the determined shear modulus G_s and the creep coefficients φ_t at temperatures -20 °C,+20 °C and +60 °C as a function of time t.

Tempe-rature T	shear modulus G_s	creep coefficient φ_t				
°C	MPa	t=50 h	t=100 h	t=500 h	t=2000 h	t=100000 h
- 20	5.1	0.3	0.35	0.45	0.5	0.6
+ 20	2.4	0.6	0.7	0.9	1.0	1.2
+ 60	1.2	0.6	0.7	0.9	1.0	1.2

TABLE 3. Initial shear modulus G_s (at t=0 h) and creep coefficient φ_t [7]

5. DESIGN OF THE PANEL

The design criteria of the panel are at the ultimate limit state: yielding in a face, wrinkling in a face, shear failure of the core and crushing of the core at a support and at the seviceability limit state: first yield or wrinkling at a support or a single point and the attainment of a specified limiting deflection .

5.1 Ultimate limit state. The yield stress of the face material is the guaranteed minimum value for the metal quality. The wrinkling stress may be calculated [3] using

$$\sigma_w = 0.823 \sqrt[3]{E\, E_{ST}\, G_{ST}} \qquad (5)$$

where

E = elastic modulus of metal face

E_{ST} = characteristic value of the elastic modulus of the core

G_{ST} = characteristic value of the shear modulus of the core

E_{ST} and G_{ST} are characteristic values of the material properties of the core at the relevant temperature [7]. The value of E_{ST} is taken from the tensile tests [7]. Tests also showed that the shear failure of the core would not be the critical design criterion. Other criteria are explaned in the next chapter.

5.2 Serviceability limit state. In a flat face, the wrinkling stress σ_w may be calculated using equation 5. The specified limiting deflections are span/100 concerning the wind loading and span/150 concerning the temperature loading.

6. DESIGN OF THE JOINT

As it can be seen from Fig. 1, the behaviour of the connection of a fastener to the panel and to supporting Z-profile is not linear. When the support reaction is tensile, only the fasteners are in contact with the supporting Z-profile (point supports, prying effect), but when the support reaction is compressive, the panel lies on the Z-profile and the fasteners are not active (line supports).

The ultimate tension capacity of the joint was verified by tests. The material and sizes of the rivets were as variables. The pull-out capacity of the rivet from the steel face (t= 0.6 mm) was the critical value. The mean capacity of the joint was approximately 780-930 N. The compression capacity of the joint can be calculated by using the equation [4]

$$\sum_i \gamma_{fi}\, \sigma_{si} \leq \frac{f_{sc}}{\gamma_m} \qquad (6)$$

where γ_{fi}= load factor (Table 1.), γ_m= material factor (Table 1.),f_{sc}= characteristic valuc of compression strength of core (information from the fabricator) and σ_{si}= compressive stress from the support action i. The last variable can be calculated from

$$\sigma_{si} = \frac{R_i}{L_s + \frac{h}{2}} \qquad (7)$$

where R_i= support reaction, L_s= width of the support and h= thickness of the panel. The interaction between stresses of the compressed panel face due to bending moment (eq. 5) and the compressive support reaction (Eq. 6.) must be taken into account e.g. by using the interaction diagams of [5].

7. DESIGN PROGRAMMES

The panel was first considered as a beam structure. A calculation program based on the exact finite element method for linear elastic analysis of the continuous sandwich beam [6] was implemented on a PC-computer. The program was extended by an iteration prosedure which took into account the special action of the fasteners, when the support reaction is tensile. The program prints maximum deflections, maximum shear stresses of the core and maximum normal stresses of the faces at each span of the beam. The temperature, the period of loading and the level of stress are taken into account by using the reduced shear modulus G_{ST} of the core (Eq. 3.).

The second calculation program was based on the linear elastic analysis of the sandwich plates. The program is based on the plate theory of Reissner and Mindlin and it is a finite element program, which uses eight-node plate bending elements (AIZ- elements) with three degrees of freedom per node. The fasteners are implemented by using special elements. The program generates automatically element mesh and takes into account the iteration of the tensile support reaction when needed. The user interfaces of the program are made by the company Teräselementti Oy. It runs on a VAX-computer. The calculation results were verified by the general purpose FEM-program, ABAQUS.

8. CONCLUSIONS

This product development of a new sandwich panel will be continued. It can be concluded that in this kind of geometrically very simplified structural unit there are many interesting details when considering the research activity. It can also be concluded that the sophisticated methods such as the solution of the contact problems and the behaviour of the time and temperature dependent materials are needed. It is our belief that the product developed shows its competitiness on the domestic market and abroad.

REFERENCES

1. D. Björkholtz, Lämpö ja kosteus: Rakennusfysiikka,Rakentajain kustannus,Helsinki,1987

2. European Convention for Constructional Steelwork Commetee TWG 7.4, Preliminary European Recommendations for Sandwich Panels,Part I: Design,ECCS Publication No. 66, 1991, Brussels

3. P. Hassinen, Evaluation of design stersses in the compressed face layers of sandwich panels, Proc. of Nordic Composites and Sandwich Meeting - Nov. 19-20,1991

4. P. Hassinen, Metalliohutlevypintaisten sandwich-elementtien staattinen mitoitus, Rakentajain kalenteri, Rakentajain kustannus, 1993

5. P. Hassinen and L. Martikainen, Jatkuvan sandwich-palkin kestävyys välituella, Rakenteiden Mekaniikka, Vol. 27, No. 1,1994,pp. 14-25.

6. M. Heinisuo, An exact finite element technique for layered beams, Computers and Structures, Vol. 30, No. 3, 1988, pp. 615-622.

7. M. Häkkinen, S. Malmi, M. Heinisuo, I. Hiekkanen, T. Tiainen, Composer-levyn lujuustarkastelu ja pitkäaikaiskestävyys,Tampere University of Technology, 1993

8. I. Höglund, Rapport: Metod för beräkning av extrema yttemperaturer hos isolerade ytterkonstruktioner, Stocholms Statens råd för byggnadsforskning,1973

NONLINEAR FEM-ANALYSIS AND DESIGN OF COMPOSITE BEAM-COLUMN

VILLE HYTTINEN
Laboratory of Structural Engineering
University of Oulu
P. O. Box 191, FIN-90101 Oulu, FINLAND

ABSTRACT

This paper presents nonlinear FEM-analysis of concrete encased steel columns subjected to combined axial compression and bending. A materially and geometrically nonlinear model is used to analyse the ultimate strength of columns. The results of FEM-analysis are in a good agreement with test results. Different combinations of axial and transverse loads are used in FEM-analysis in order to determine the M-N-interaction curve of the column. Comparison is made with the results of FEM-analysis and the design resistances based on the Finnish design code for composite structures. It was observed that the design method based on the code for composite structures underestimates the strength of columns due to overestimated eccentricities of the compressive axial force. A corrected design method is proposed. Results calculated according to this method are in a good agreement with the test results and the results of FEM-analysis.

1. INTRODUCTION

During the years 1990 and 1991 tests on the strength of composite columns were conducted at the University of Oulu. Tests were carried out with five different combinations of axial and transverse loads in columns. Due to the practical limitations of test equipment, the bending moment (M) caused by transverse loads was relatively high compared to the axial force (N), i.e. the eccentricity of the normal force ($e=M/N$) had a relatively high value.

In this study the columns tested are analysed by using a materially and geometrically nonlinear model. A nonlinear FEM-analysis using several eccentricities ($e=M/N$) of normal force is carried out in order to determine the M-N-interaction curve as a whole. In this way more information is gained on columns tested earlier especially under loading conditions when the normal force eccentricity is relatively small. Comparison is made with the strengths obtained by the FEM-analysis and the design strengths based on the Finnish design code for composite structures. The observation of the earlier study [6] is confirmed. The design method based on

the code for composite structures underestimates the strength of columns. In this study a corrected design method is proposed.

Consider the strength of a slender composite column under combined axial compression and bending in a plane which is parallel to the loads (Figure 1). In the ultimate limit state the strength of the column is equal either to the flexural buckling strength or the cross-sectional strength of the column depending on the slenderness and the loading condition of the column. If the eccentricity of the normal force ($e=M/N$) is small the flexural buckling is obvious to happen. When the eccentricity e is great the cross-sectional strength is dominant. An additional secondary bending moment due to the deflection of the column and an eccentric normal force (Figure 1) have to be taken into account in an exact analysis.

Side view of loading **Cross-section of column**

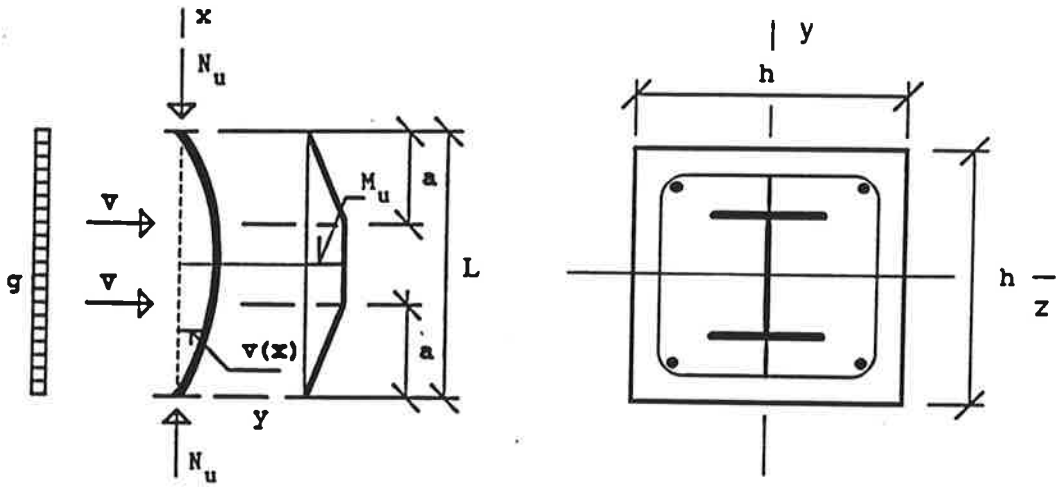

Figure 1. Composite column under combined compression and bending.

In this study a nonlinear FEM-analysis is carried out on the following basis: A bending theory with the assumption of plane cross-sections remaining plane and normal during bending is used. The plasticity of reinforcement steel and the nonlinear stress-strain relation for concrete in compression are taken into account. Tensile resistance of concrete has a significant meaning in estimating beam-column deflections and secondary bending moment due to the eccentric normal force. Tensile strain softening of concrete is taken into account. Tension stiffening of steel bars is neglected.

The above described model has been used recently in analysing deflections of non-prestressed and partially prestressed concrete beams [3], [4]. Results of these analyses are in a good agreement with test results. In this study the above described model is used for the reinforced concrete part of the composite column. In the concrete encased composite columns under consideration both the concrete part and the structural steel are located symmetrically about both axes of the cross section as indicated in Figure 1. Full composite action is assumed between structural steel and concrete. An ideally plastic material model is used for structural steel. Geometric nonlinearity and second order effects are taken into account.

2. FEM-ANALYSIS MODEL

Calculations of the analysis were carried out by using a finite element program ABAQUS. The modified Riks-method was used in FEM-calculations to obtain the load-displacement relation of the columns up to the ultimate limit state and beyond it. A local unstability is not possible for the columns under consideration. When the eccentricity of compressive normal force $e=M/N$ is small a flexural buckling of the column is possible at the ultimate state. When the structural behaviour of columns is studied with the finite element method an initial effect must be added for the centrally loaded and ideally straight element model to take into account the possible loss of stability of the column. An initial deformed shape of the column can be used to model the geometrical imperfections and the small eccentricity of loads due to the construction tolerances and the residual stresses in the actual column. In the tests [6] the columns were in a horizontal position (Figure 4). In this study the transverse self weight load of the structure will cause the needed perturbation in the perfect geometry of the model.

The columns were modelled with three node 3-dimensional beam elements. The I-section beam elements shown in Figure 2 were used to model the structural steel part of the columns. The concrete part was modelled with a rectangular cross section element. Steel ribs, welded in the structural steel, were used as additional shear connectors in the tests [6]. The ribs were modelled with eccentric rectangular elements. Part of the ribs have holes as shown in Figure 4. These ribs were modelled with narrower rectangular elements having the same cross-sectional area as the ribs. The elements for the concrete, the structural steel and the ribs have common nodal points. The integration points used in the cross sections of elements to take into account the material properties, strain and stresses, cracking of concrete and plastification of concrete and steel are shown in Figure 2.

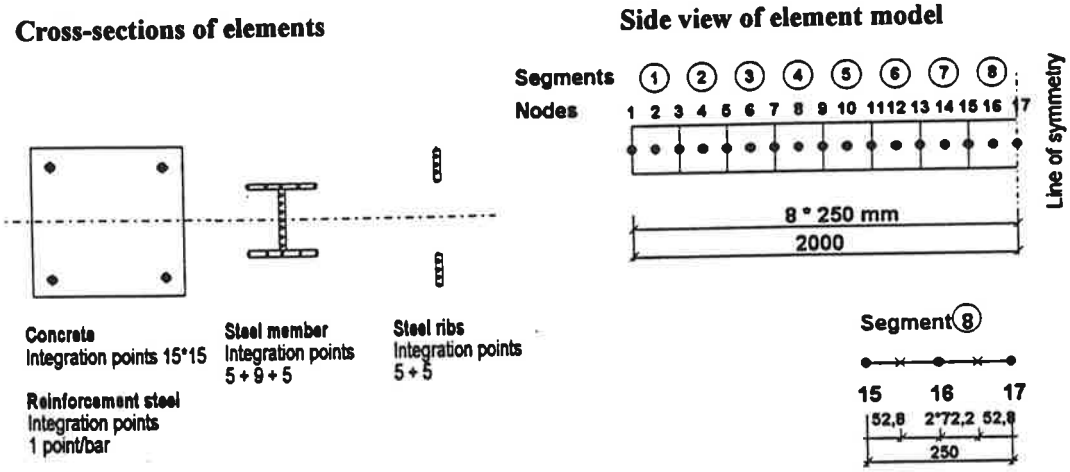

Figure 2. Element model of the composite column.

When analysing a reinforced concrete beam by the finite element method with beam elements the constitutive laws with strain softening are shown to lead to false sensitivity of results to the chosen finite element size [1], [2]. According to references [1] and [2] the finite element length, L_e, may not be smaller than approximately the beam depth h. At the same time, to include the effect of full curvature localization, the minimum element length must be used in the softening regions of beams. In this study the strain softening constitutive laws are used for

the concrete part of the columns. For this reason the element length 250 mm was chosen, the depth h of the columns being 240 mm. The element model is shown in Figure 2.

The stress-strain relation used in [3] is adopted for concrete in tension:

$$\text{For } \varepsilon \le \varepsilon_{tp}: \quad \sigma = E_c \varepsilon \tag{1}$$

$$\text{For } \varepsilon_{tp} < \varepsilon < \varepsilon_{tf}: \quad \sigma = f_t' - (\varepsilon - \varepsilon_{tp})(-E_t) \tag{2}$$

$$\text{For } \varepsilon \ge \varepsilon_{tf}: \quad \sigma = 0 \tag{3}$$

$$E_t = \frac{-0{,}48 E_c}{0{,}39 + f_t'} \tag{4}$$

where σ, ε are uniaxial stress and strain, f'_t is direct tensile strength, E_c is modulus of elasticity of concrete, E_t is tangent strain softening modulus of concrete, ε_{tp} is strain at peak tensile stress, ε_{tf} is strain at zero stress after strain softening. In formula (4) E_c, f'_t, and E_t are in MPa. According to reference [8] $E_c = 5000\sqrt{K}$, where K is the cubic strength of concrete. The stress-strain relation in figure 3 for concrete in tension is obtained from equations (1) - (4). For concrete in uniaxial compression, the well known expression is used [10]:

$$\sigma = \frac{E_c \varepsilon}{1 + \left(\frac{E_c \varepsilon_{cp}}{\sigma_{cp}} - 2\right)\left(\frac{\varepsilon}{\varepsilon_{cp}}\right) + \left(\frac{\varepsilon}{\varepsilon_{cp}}\right)^2} \tag{5}$$

in which σ_{cp} is peak stress (compression strength f_{ck}) and ε_{cp} is strain at peak stress. For the FEM-analysis the stress-strain relation of equation (5) is modified to a curve that is composed of several linear parts (Figure 3). In the curve the compression strength [8] $f_{ck} = 0{,}7K$ is reached at the strain value ε_{cp} = -2.0 ‰. As the strain exceeds ε_{cp}, concrete will exhibit compressive strain softening. The reinforcement steel and the structural steel are assumed as elastic - plastic, characterized by modulus of elasticity E_s and uniaxial yield stress f_y (Figure 3).

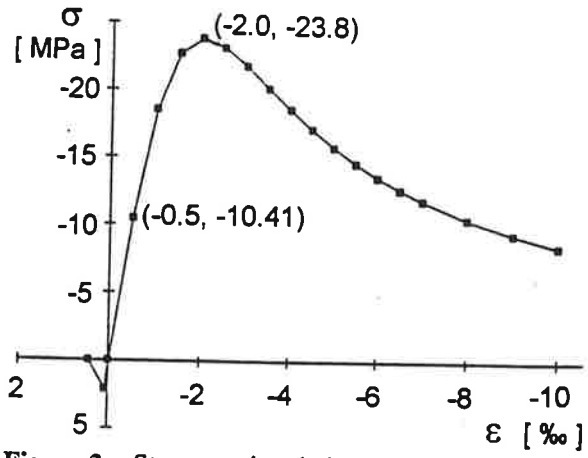

Figure 3. Stress-strain relation for concrete

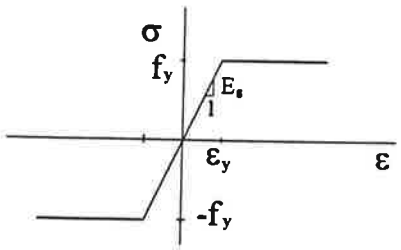

Stress-strain relation for structural steel and reinforcement steel.

2.1 Verification of analysis model. The model used in FEM-analysis is verified by comparing the test results in reference [6] and the results of FEM-calculations in the Table 1. The loading arrangement and the dimensions of the columns for both test series are shown in Figure 4.

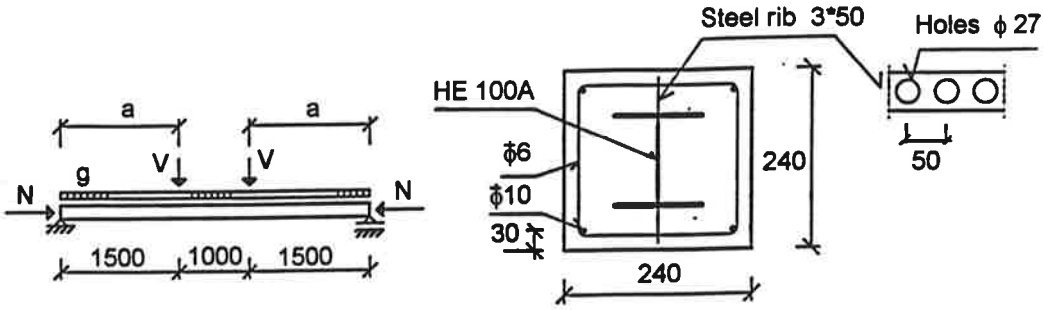

Figure 4. Loading arrangement and dimensions of the columns in the tests [6].

Columns 1/7, 2/5 and 2/6 were all tested with the same nominal eccentricity of the normal force $e_0 = 0.06$. The large difference between the test results of those columns indicates that the test of column 1/7 was unsuccesful. The comparison below shows that the strength of columns obtained by the nonlinear FEM-analysis using the model described in this paper are in a good agreement with the strengths observed in tests. The model is also relatively good in predicting the deflections of the columns.

		Ultimate limit state											
		Test results				Results of FEM-analysis				FEM/Test			
Test n:o	e_0 [m]	N [kN]	V [kN]	M(L/2) [kNm]	v(L/2) [mm]	N [kN]	V [kN]	M(L/2) [kNm]	v(L/2) [mm]	$\frac{N_{FEM}}{N_{Test}}$	$\frac{V_{FEM}}{V_{Test}}$	$\frac{M_{FEM}}{M_{Test}}$	$\frac{v_{FEM}}{v_{Test}}$
1/4	0,6	107,5	43	73,47	53,7	110,9	44,36	74,91	46,74	1,032	1,032	1,020	0,870
1/3	0,6	95	38	65,56	56,4	99,33	39,74	67,52	47,57	1,046	1,046	1,030	0,843
2/2	0,588	100	39,2	68,72	67,20	106,1	41,63	70,69	47,36	1,061	1,061	1,029	0,705
1/6	0,2	352,5	47	93,76	56,9	332,3	44,31	82,76	40,03	0,943	0,943	0,883	0,704
2/1	0,19	307,5	38,9	79,78	59,3	322,2	40,79	78,48	43,79	1,048	1,048	0,984	0,738
2/3	0,195	296	38,5	79,92	64,1	314,0	40,85	78,21	43,79	1,061	1,061	0,979	0,683
1/2	0,1	540	36	82,31	46,5	599,1	39,94	86,18	38,78	1,109	1,109	1,047	0,834
1/1	0,1	570	38	78,16	31,5	548,0	36,54	81,25	42,48	0,961	0,961	1,040	1,349
2/4	0,093	540	33,3	83,01	55,3	583,4	35,98	83,20	44,66	1,080	1,080	1,002	0,808
2/6	0,053	775	27,6	75,99	40,5	915,4	32,6	78,84	29,25	1,181	1,181	1,038	0,722
1/7	0,06	550	22	63,21	49,1	769,2	30,77	75,06	33,45	1,399	1,399	1,187	0,681
2/5	0,055	720	26,3	69,94	37,90	816,9	29,84	75,31	33,52	1,135	1,135	1,077	0,884
2/8	0,046	925	28,1	82,17	39,8	1010	30,68	74,79	25,35	1,092	1,092	0,910	0,637
1/8	0,036	950	23	64,11	27,8	1054	25,29	64,28	22,20	1,109	1,109	1,003	0,799
2/7	0,038	927	23,69	72,01	35,9	1015	25,94	67,54	25,08	1,095	1,095	0,938	0,699
1/5	0,35	154,3	36	65,96	56,8	170,2	39,71	69,94	42,28	1,103	1,103	1,060	0,744
FEM/Test		average value (excluding test 1/7)								1,070	1,070	1,003	0,801
$\frac{\text{FEM - test}}{\text{test}}$ * 100		average value (excluding test 1/7)								8,32 [%]	8,32 [%]	4,65 [%]	24,3 [%]

Table 1. Comparison of the test results [6] and the results of FEM-calculations.

The strength of materials of columns in the tests [6] were on average:

	test series 1	test series 2
Cube strength of concrete K	34 N/mm^2	33 N/mm^2
Structural steel, I-beam HE 100A, yield strength f_y	293 N/mm^2	311,2 N/mm^2
Structural steel, ribs 50*3 mm, yield strength f_y	293 N/mm^2	293 N/mm^2
Reinforcement steel bars yield strength f_y	565 N/mm^2	634 N/mm^2

3. EVALUATION OF COMPOSITE COLUMN DESIGN

A nonlinear FEM-analysis of the concrete encased composite column under combined compression and bending was carried out using the model described and verified earlier in this paper. The *M-N* interaction curve of columns was determined in the analysis by using twelve loading cases with different combinations of axial and transverse loads. In the analysis were used the dimensions and materials of the columns in test series 1 in reference [6]. The tests [6] showed that the steel ribs with holes, used as additional shear connectors in the columns, have no significant effect on the strength of the columns. In this study the ribs were not used. The results of FEM-analysis are used to evaluate the validity of the design method in the Finnish code for composite structures by comparing the strengths of columns calculated according to the code with the strengths obtained by the FEM-analysis.

3.1 Design method of code for composite structures. According to the code for composite structures [11] ultimate compressive (N_u) and bending (M_u) capacity of a composite column must fullfill following conditions:

$$N_d \le N_u = kN_p \tag{6}$$

$$M_d \le M_u \tag{7}$$

$$k = k_1 - (k_1 - k_2 - 4k_3)\frac{M_d}{M_u} - 4k_3\left(\frac{M_d}{M_u}\right)^2 \tag{8}$$

where N_u is the ultimate compressive capacity of the column, M_u is the ultimate (plastic) bending capacity, when $N = 0$, N_p is the ultimate plastic compressive capacity, N_d and M_d are the design axial force and the design bending moment.

While acting combined with the axial load, the bending moment M_d reduces the compressive strength of the column according to the formulas (6) and (8). In the case of the columns under consideration factors $k_2 = 0$ and $k_3 = 0$ and the formula (8) reduces to the form

$$k = k_1\left(1 - \frac{M_d}{M_u}\right) \tag{9}$$

The factor k_1 is also used in the code for steel structures [9] in calculating the compressive strength of an axially loaded steel column. With factor k_1 the possible instability, buckling of the column, is taken into account. Also, in factor k_1 are included possible inaccuracies in the geometry of the column and initial stresses for example due to welding. This method of calculation is based on large test programme made by the organisation of the European Convention for Constructional Steelwork (ECCS).

According to the code for composite structures [11], [12] in the calculation of a concrete encased composite column, the eccentricities of the normal force are taken into account as for the concrete column in the code for concrete structures [8]. Then the design bending moment due to the loads is

$$M_d = M_0 + \Delta M_d \tag{10}$$

where $M_0 = N*e_0$ is the primary bending moment due to the loads by first order theory, N is the normal force due to the loads, e_0 is the primary eccentricity, $\Delta M = N*(e_a + e_2)$ is the secondary bending moment due to the eccentricity $(e_a + e_2)$ of the normal force, $e_a = \frac{L}{500} + \frac{h}{20}$ is the eccentricity, which takes into account the initial geometrical imperfection of the column $\left(\frac{L}{500}\right)$ and the construction tolerances $\left(\frac{h}{20}\right)$, $e_2 = \left(\frac{\lambda}{145}\right)^2 * h$ is the eccentricity which simulates the deflection of the column at the ultimate state.

In this method the eccentricity of the normal force is taken into account twice:

- The formula (8), used in the calculation of the strength of the column under combined compression and bending, is based on the theoretical analysis and tests of the columns [7]. The equation takes into account the effect of the initial geometric imperfections and the construction tolerances and the deflection of the column and also the initial stresses.
- On the other hand, the eccentricities $(e_a + e_2)$, which are placed on the normal force due to the loads, take into account the construction tolerances and the geometric imperfection and the deflection of the column. The secondary bending moment (ΔM_d) due to the eccentric normal force is used in the formulas (10) and (8) in the calculation of the strength of column. This leads to an underestimation of the strength of the concrete encased composite columns.

The column strengths obtained by FEM-analysis with the strengths calculated according to the Finnish code for composite structures [11] is presented in the Figure 5. One can see from Figure 5, that for the small eccentricity e_0, the strengths calculated on the basis of the code for composite structures are much lower than the strengths obtained by FEM-analysis. These results confirm the observation of the earlier study [6]. The design method based on the code for composite structures underestimates the strength of columns due to overemphasizing the normal force eccentricities $(e_a + e_2)$.

3.2 Modifications to the design method. If the eccentricities $(e_a + e_2)$ are neglected in the design method based on the code for composite structures, the calculated strengths of the columns agree closely with the test results [6] and the strengths obtained by FEM -analysis, as shown in Figure 5. The neglecting of the eccentricities e_a and e_2 is supported by the facts, that already into factor k_1 in formula (8) the effect of construction tolerances and geometric imperfections and initial stresses are included, as when calculating the strength of the steel columns. Also the effect of the eccentricity due to the deflection of the column is included in formula (8), as the formula is adjusted to the test results and theoretical analysis, which takes into account second order effects. When the eccentricities are neglected, the design method would also have the same basis as the method in the ECCS model code [5] (Commentary 16.4.2 and 16.5.3 Method A).

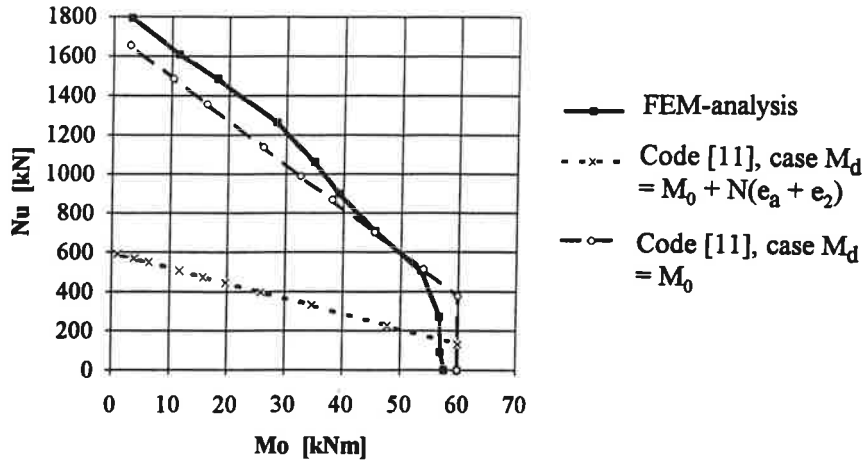

Figure 5. The M_0-N-interaction curves determined by the FEM-analysis and the code for composite structures [11].

REFERENCES

1. Bazant Zdenek P., Pan Jiaying and Pijaudier-Cabot Gilles, Softening in Reinforced Concrete Beams and Frames, Journal of Structural Engineering Vol 113 Number 12 December 1987
2. Bazant Zdenek P., Pijaudier-Cabot Gilles, and Pan Jiaying, Ductility, Snapback, Size Effect, and Redistribution in Softening Beams or Frames, Journal of Structural Engineering Vol 113 Number 12 December 1987
3. Bazant Zdenek P. and Oh Byung H., Deformation of Progressively Cracking Reinforced Concrete Beams, ACI Journal May-June 1984.
4. Chern Jenn-Chuan, You Chii-Ming, Bazant Zdenek P., Deformation of Progressively Cracking Partially Prestressed Concrete Beams, PCI Journal January-February 1992.
5. European Convention for Constructional Steelwork (ECCS), Composite Structures, The Construction Press 1981.
6. Hyttinen Esko, Hyttinen Ville, (Observations of the Strength of Composite Columns, University of Oulu, Laboratory of Structural Engineering) Havaintoja puristetun ja taivutetun liittopilarin toiminnasta, Oulun yliopisto, Rakennetekniikan laboratorio, Julkaisu 33, Oulu 1993.
7. Hyttinen V., Nonlinear FEM-analysis and Design of Composite Beam-Column, Rakenteiden mekaniikka, Vol.26 No 4, 1993, pp. 3-24
8. RIL 131-1990, (The Finnish Code for Concrete Structures) Betoninormit, Helsinki 1990.
9. RIL 173-1988, (The Finnish Code for Steel Structures) Teräsrakenteet, Rajatilamitoitusohjeet 1988, Helsinki 1988.
10. Saenz, Luis P., Discussion of "Equation for the Stress-Strain Curve of Concrete" by Prakash Desayi and S. Krishnan, ACI JOURNAL, Proceedings V. 61, No. 9 Sept. 1964, pp. 1229-1235.
11. TRY/by 26, (The Finnish Code for Composite Structures) Liittorakenteet, Suunnitteluohjeet 1988, Helsinki 1988.
12. TRY/by 36, (Commentary on the Finnish Code for Composite Structures) Liittorakenteiden sovellusohjeet, Helsinki 1991

LARGE DISPLACEMENT FINITE DIFFERENCE ANALYSIS OF RECTANGULAR WINDOW PANES IN DYNAMIC SHOCK LOADINGS

KARI IKONEN
VTT Energy
P.O. Box 1604, FIN-02044 VTT, FINLAND

ABSTRACT

Basic equations for large deformations of plates (von KARMAN, 1910) are solved by finite difference method. A code for calculating dynamic analysis of a rectangular plate with large deflections was developed. The code is applicable for both window-panes with single glass and multi-layer panes made of glass or polycarbonate. The time integration is done by straight explicit scheme. The code was verified by the results from tests made for window single glasses abroad. The results show that maximum stresses are encountered near corners in case of large deflections, whereas in case of small deflections maximum stresses appear in the middle of panes.

The code is also capable to calculate multi-panes in a wooden framework. Wooden parts are modeled as beams having large deflections and time integration of the bars is carried out simultaneously and coupled with calculating the deflections of the glass panes. In case of multi-layer panes the air pressure at every time step is calculated from the volume change between panes according to the adiabatic equation for air compression and applied as load to the panes. Different types of supporting conditions on the edges of the panes are possible to model. So called rebound effect was studied. The strength of existing window-panes under pressure loading can be estimated and the dimensioning of the window-panes can be done against pressure wave loading (explosions) in planning phase.

1. INTRODUCTION

The failure depends e.g. on the size and thickness, the distance and direction to the explosion centre, supporting of the edges and the microcracks in the material. Most of these effects can be taken into account in numerical analyses. The pressure load acting on a window can be idealized as in Fig.1. After an explosion in a typical shock pulse the pressure maximum against window is about P_s = 5 - 50 kPa and lasts about Δt = 0,01...0,1 s. The pressure over the window plate can be considered to be constant at a certain moment.

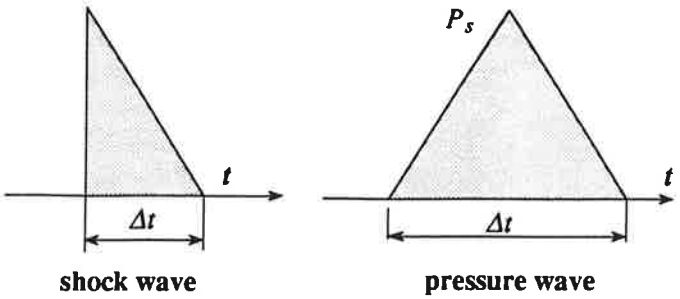

FIGURE 1. *Idealization of a pressure pulses.*

2. CALCULATION THE DYNAMIC RESPONSE OF THE WINDOW PANE BY FINITE DIFFERENCE METHOD

Because of simple geometry of a window a finite difference method was adopted making it possible to construct an efficient computer code. Tens of thousands of time steps are typically used, but the run time is small (some minutes) in modern computers.

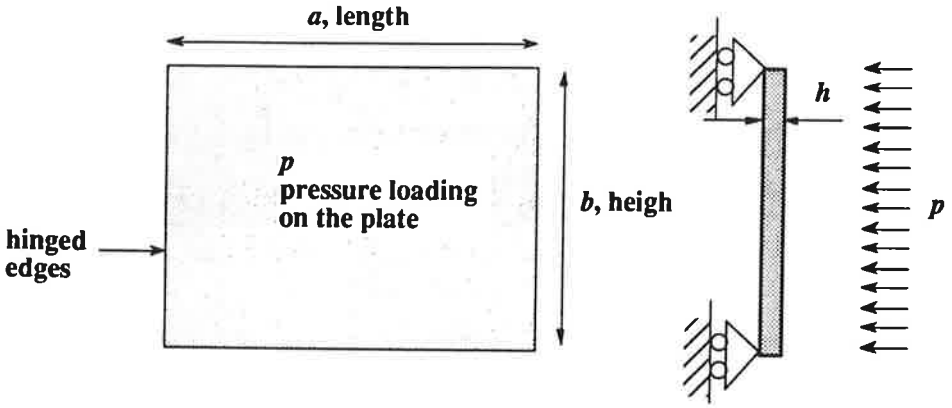

FIGURE 2. *Simply supported window plate.*

The maximum deflection w_{max} in the middle of a window is typically several centimetres. Usually $w_{max} > 0{,}10 \ldots 0{,}50h$ (h thickness of a plate) and the membrane stresses carry part of the load. Large deflection theory is thus needed. The basic differential equations for the plate are

$$\rho h \frac{\partial^2 w}{\partial t^2} = q(x,y,t) - K\left[\frac{\partial^4 w}{\partial x^4} + 2\frac{\partial^4 w}{\partial x^2 \partial y^2} + \frac{\partial^4 w}{\partial y^4}\right] + h\left[\frac{\partial^2 w}{\partial x^2}\frac{\partial^2 \Phi}{\partial y^2} + \frac{\partial^2 w}{\partial y^2}\frac{\partial^2 \Phi}{\partial x^2} - 2\frac{\partial^2 w}{\partial x \partial y}\frac{\partial^2 \Phi}{\partial x \partial y}\right], \quad (1)$$

$$\frac{\partial^4 \Phi}{\partial x^4} + 2\frac{\partial^4 \Phi}{\partial x^2 \partial y^2} + \frac{\partial^4 \Phi}{\partial y^4} = E\left[\left(\frac{\partial^2 w}{\partial x \partial y}\right)^2 - \frac{\partial^2 w}{\partial x^2}\frac{\partial^2 w}{\partial y^2}\right] \tag{2}$$

where Φ is stress function, x and y coordinates of a rectangular plate, E elasticity modulus, ρ the density, h thickness of a plate, t time, $q(x,y,t)$ time dependant pressure load and K plate constant ($K = Eh^3/[12(1-\nu^2)]$). If the time derivative on the left side of the Eq. (1) is written as

$$\frac{\partial^2 w}{\partial t^2} = \frac{w_{i,j}^{t+\Delta t} - 2w_{i,j}^{t} + w_{i,j}^{t-\Delta t}}{(\Delta t)^2} . \tag{3}$$

This makes it possible to extrapolate the deflection $w_{i,j}^{t+\Delta t}$ explicitly from the Eq. (1) for the difference points inside of the plate. The right side of the Eq. (1) is known before time step. After solving the new deflection new values of stress function are calculated from the Eq. (2). Next time step is handled in the same way. To express the spatial derivatives in Eqs. (1) and (2) with differences the plate is divided into rectangular difference mesh. Second differences of the deflection for a point i,j are

$$\begin{aligned}
\frac{\Delta^2 w}{\Delta x^2} &= \frac{w_{i-1,j} - 2w_{i,j} + w_{i+1,j}}{(\Delta x)^2} \\
\frac{\Delta^2 w}{\Delta y^2} &= \frac{w_{i,j-1} - 2w_{i,j} + w_{i,j+1}}{(\Delta y)^2} \\
\frac{\Delta^2 w}{\Delta x\, \Delta y} &= \frac{w_{i-1,j-1} - w_{i+1,j-1} - w_{i-1,j+1} + w_{i+1,j+1}}{4\Delta x \Delta y} .
\end{aligned} \tag{4}$$

The fourth differences are

$$\begin{aligned}
\frac{\Delta^4 w}{(\Delta x)^4} &= \frac{6w_{i,j} - 4(w_{i-1,j} + w_{i+1,j}) + w_{i-2,j} + w_{i+2,j}}{(\Delta x)^4} \\
\frac{\Delta^4 w}{(\Delta y)^4} &= \frac{6w_{i,j} - 4(w_{i,j-1} + w_{i,j+1}) + w_{i,j-2} + w_{i,j+2}}{(\Delta y)^4} \\
2\frac{\Delta^4 w}{(\Delta x)^2(\Delta y)^2} &= \frac{8w_{i,j} - 4(w_{i,j-1} + w_{i-1,j} + w_{i+1,j} + w_{i,j+1}) + 2(w_{i-1,j-1} + w_{i+1,j-1} + w_{i-1,j+1} + w_{i+1,j+1})}{(\Delta x)^2(\Delta y)^2}
\end{aligned} \tag{5}$$

Corresponding expressions can be written for the stress function by replacing w with Φ in Eqs. (4) and (5). In applying Eqs. (1) and (2) by turns for calculating deflection and of stress function values new deflections are straightly solved from Eq. (1) without connections between new values of deflections (explicit scheme). The values of stress function in Eq. (2) have connections leading to system of equations for unknowns. The coefficient matrix depends purely on difference mesh (Δx and Δy) being constant and symmetric. Thus the coefficient matrix $[A]$ can be reduced by Cholesky decomposition method to the form $[A] = [S]^T[S]$, where $[S]$ has nonzero elements only on and above the diagonal. A lot of computing time is saved.

3. BOUNDARY CONDITIONS

Before pressure shock at all internal and external difference points $w = \Phi = 0$. Because the edges of the plate are hinged the bending moment around the edges vanishes. This is taken into account so that the deflection on an auxiliary point is equal but of opposite sign than in the internal point. Because of no membrane stresses on free edges of the plate, the stress function Φ and its derivatives in the direction and perpendicular to the edges vanish. The condition concerning the derivatives are fulfilled, if at the auxiliary points the stress function Φ is continuously zero. The right sides of formulas (1) and (2) are vanishing on the edges having no deflections. The edges of the plates can be simply supported or fixed (free movement in the plane of the window).

4. WINDOWS WITH WOODEN FRAMEWORKS

The calculation system was enlarged by taking into account bars between window panes. It is assumed that there are no membrane forces in the plane of the plates between a bar and the plate. In Fig. 3 auxiliary points are for fulfilling the boundary conditions. The deflections of plates are antimetric. The deflections of an auxiliary point row are solved from the relation that the deflections of the plate and a bar are equal and the bending moment vanishes. If we look at a beam in y–direction we get first

$$M_x = -K\left(\frac{\partial^2 w}{\partial x^2} + \nu\frac{\partial^2 w}{\partial y^2}\right) = 0 . \tag{6}$$

At the positive edge of the plate the reduced shear force is

$$\overline{Q}_x = -K\left[\frac{\partial^3 w}{\partial x^3} + (2-\nu)\frac{\partial^3 w}{\partial x \partial y^2}\right] . \tag{7}$$

On a negative edge the minus sign on the right side is omitted. The forces acting on the edge of the plate and a beam are opposite. The deflection of the beam in y–direction is

$$EI\frac{\partial^4 w}{\partial y^4} = q(y) = -\rho A\frac{\partial^2 w}{\partial t^2} - \overline{Q}_x . \tag{8}$$

By taking into account the effects on both sides of a beam we get for a beam in y–direction the equations

$$\rho A\frac{\partial^2 w}{\partial t^2} = K\left[\frac{\partial^3 w}{\partial x^3} + (2-\nu)\frac{\partial^3 w}{\partial x \partial y^2}\right]_{\text{left plate}} - K\left[\frac{\partial^3 w}{\partial x^3} + (2-\nu)\frac{\partial^3 w}{\partial x \partial y^2}\right]_{\text{right plate}} - EI\frac{\partial^4 w}{\partial y^4}$$

$$\frac{\partial^2 w}{\partial x^2} + \nu\frac{\partial^2 w}{\partial y^2} = 0 . \tag{9}$$

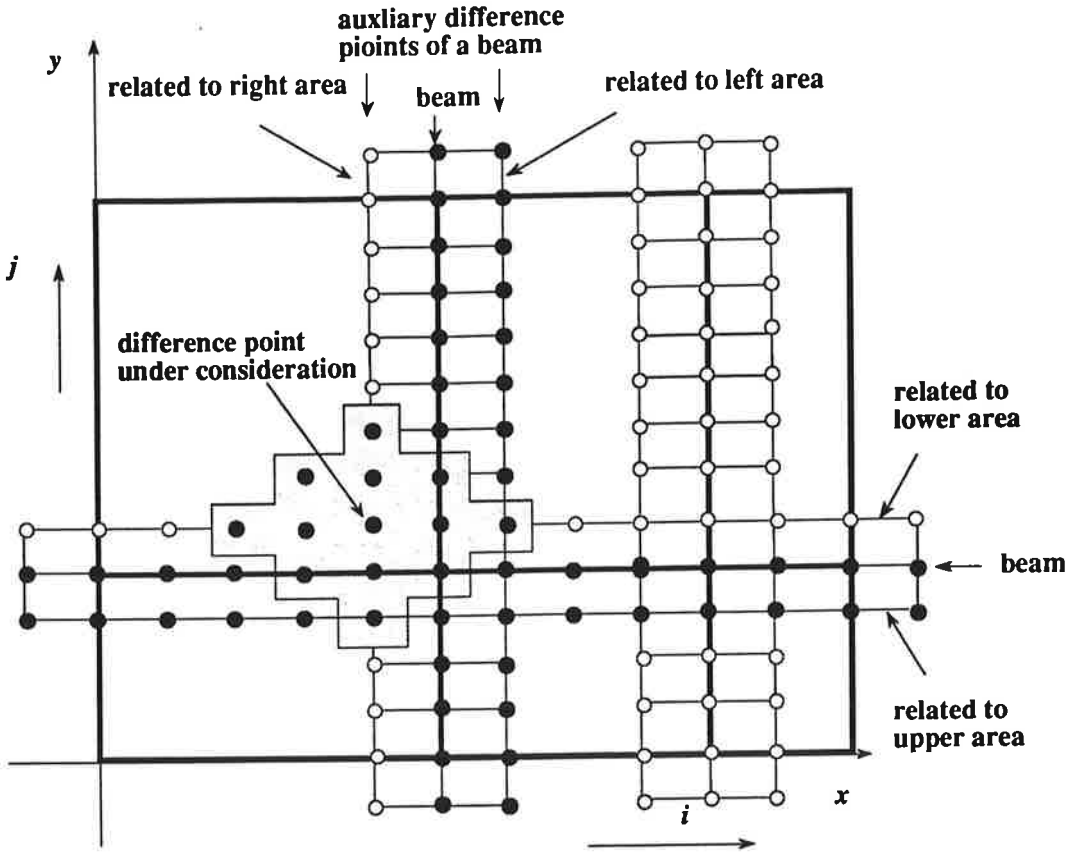

FIGURE 3. *Modelling the connection between window panes and wooden bars.*

Corresponding equation for beams in x–direction are valid. The equations are applied as follows. First from the first equation new deflections are calculated explicitly using old deflections on the right side. From the latter equation new deflections of points on the auxiliary row are calculated using new deflection values. Finally deflections of the points outside of the rectangular area are calculated. Third derivative of the deflection in Eg. (9) is extrapolated from inside direction in perpendicular direction of a bar. For example for a beam in y–direction third derivative for point $i = I, j$ approaching from left x–direction is

$$\left.\frac{\partial^3 w}{\partial x^3}\right|_{I,j} = \left(\frac{1}{2} w_{I-3,j} - 3w_{I-2,j} + 6w_{I-1,j} - 5w_{I,j} + \frac{3}{2} w_{I+1,j}\right)/\Delta x^3 \,. \tag{10}$$

The deflection of the crossing of two beams is calculated as an average on deflections

$$\begin{aligned} w_{I,J} &= \frac{1}{6}\left[4\,(w_{I-1,J} + w_{I+1,J}) - w_{I-2,J} - w_{I+2,J}\right] \\ w_{I,J} &= \frac{1}{6}\left[4\,(w_{I,J-1} + w_{I,J+1}) - w_{I,J-2} - w_{I,J+2}\right) \end{aligned} \tag{11}$$

following from the continuity requirement of the slope of the beams. As an effective stress the maximum principal stress on the surface of a plate is used and it is calculated from the equation

$$\sigma_{max} = \frac{1}{2}(\sigma_x + \sigma_y) \pm \frac{1}{2}\sqrt{(\sigma_x - \sigma_y)^2 + 4\tau_{xy}{}^2}\,, \tag{12}$$

where σ_x, σ_y are normal stress components and τ_{xy} is the shear stress. Maximum principal stress is compared to the ultimated stress of the material. The greatest principal stresses are encountered in middle of the plate, in the middle on edges or close to corners depending on the case. A typical critical value for normal glass is in dynamic loading about 70 MPa. For a hardened glass it is about three times higher.

In explicit time integration procedure the time increment Δt must be small enough. The condition for stability for a vibrating plate with small deflections is /1/

$$\Delta t \le \frac{1}{2}\sqrt{\frac{3(1-\nu^2)\rho}{E}}\,\frac{1}{h}\,\frac{1}{\frac{1}{(\Delta x)^2}+\frac{1}{(\Delta y)^2}}\,, \tag{13}$$

where E is elasticity modulus, I is the moment of inertia around an axis in the plane of the window, ρ density of glass and h the thickness. For a bar with small deflections the condition for stability is

$$\Delta t \le \frac{1}{2}\,\frac{\Delta x^2}{\sqrt{\frac{E_b I}{\rho_b A}}}\,, \tag{14}$$

where E_b is elasticity modulus of the bar, I is the inertia of moment in bending in the plane of the window, ρ_b density of of the bar material and A the cross section of the bar.

The panes can fail also in returning from the maximum deflection position, if supported unevenly form the boundaries, when there are wooden nailed beams on the edges of the panes. The computer code was enlargened to handle also this kind of so called "rebounding" -cases. It was found that failure of a pane in rebounding phase is more probable in rapid shock than in other loadings.

In case of multi-panes window the pressure between the panes is calculated from the adiabatic equation and the pressure load is applied to the panes. The volumes are calculated after every time step. The pressure between panes can be assumed to be spatially constant, because the maximum perpendicular speed of about 10 m/s is small compared to the the speed of sound (about 340 m/s) in air.

Example 1: In a single paned window the dimensions are $a = b = 1$ m and the thickness of glass $h = 5$ mm. The shape of a shock loading is as in Fig. 1 having $P_s = 11$ kPa and duration

Δt = 0,01 s. The elasticity modulus is E = 69 GPa, Poisson's ratio ν = 0,25 and density ρ = 2500 kg/m^3. The plate was divided into 10 x 10 –mesh and for a time step a value 0,00001 s was chosen. The analysis was done by small and large deflection theory. The frequency of first eigenmode was two times higher and the deflection at the middle point of the plate on half that with small deflection theory. Further, the maximum principal stress was 107,3 MPa at the middle point of the plate with small deflection theory, but 77,8 MPa with large deflection theory and close to the corners (Fig. 4).

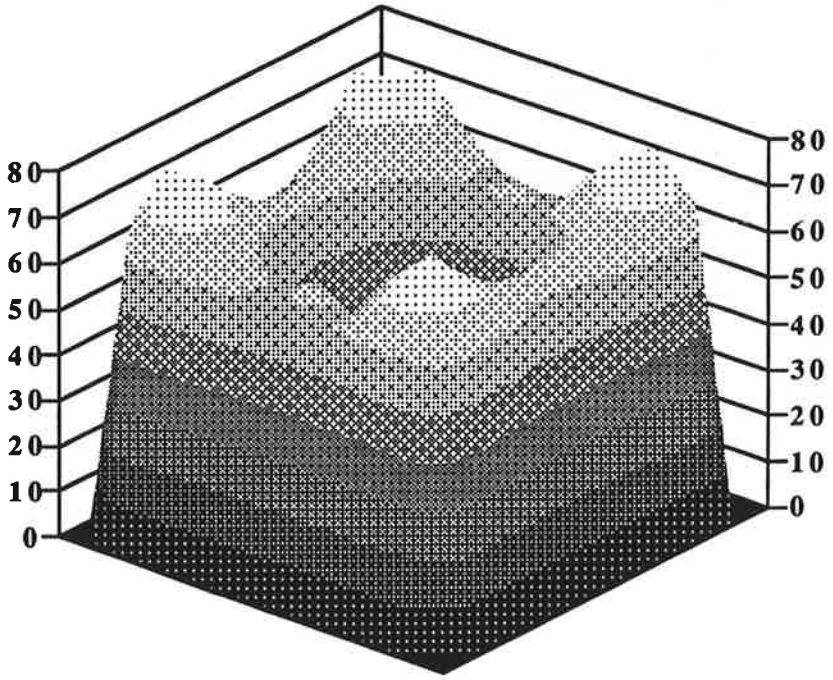

FIGURE 4. *Principal stress distribution at time 0.009 s, when the highest stress was achieved close to corners (large deflection theory).*

Example 2: In a double–panes window with identical external and internal panes, the dimensions are a = 1 m a = 1.5 m and the thickness of glass h = 3 mm. The loading and the properties of glass are as in the example 1. A window consists of six square panes mounted in a wooden framework consisting of one horizontal and two vertical bars. The elasticity modulus of wooden bar is assumed to be E_b = 12,0 GPa, the width b = 2 cm and the height h = 3 cm. The moment of inertia is $I = bh^3/12$ = 0,02·0,03^3/12 m^4 = 4,5·10^8 m^4 and bending stiffness EI = 540 Nm^2. The density is assumed to be ρ_b = 830 kg/m^3 and $\rho_b A$ = 0,5 kg/m. One pane was divided into 14 x 9 –mesh and for a time step a value 0,00001 s was chosen. The analysis was done by large deflection theory. For the outer pane the maximum principal stress was 114.0 MPa at time 0.0141 s and for the inner pane 56.3 MPa at time 0.0300 s, both close close to the corners (Fig. 5). With small deflection theory the maximum principal stress would be obtained at the middle of the panes. The maximum deflection was 25.7 mm for the outer pane at time

0.032 s and 30.8 mm at time 0.0131 s for the inner pane, both in the middle of the panes. The maximum air overpressure between the panes was 6.5 kPa about a half of the maximum external load pressure.

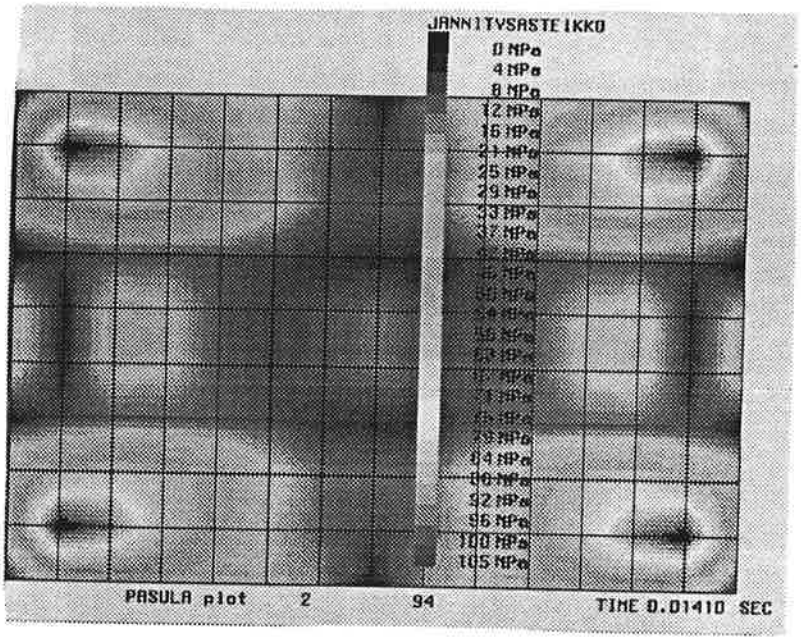

FIGURE 5. *Principal stress distribution at time 0.0141 s for the outer pane with two vertical and one horizontal wooden bars, when the highest principal stress 114,0 MPa was achieved (close to the corners).*

5. CONCLUSIONS

In the article dynamic analysis of a rectangular plate with large deflections is described. The analysis method is based on finite difference method. To perform the analyses in practice a computer code was developed. The strength of existing window–panes under shock pressure loading can be estimated and the dimensioning of the window–panes can be done against pressure wave loading in planning phase. The code is applicable for both window–panes with single glass and multi–layer panes. The intensity of an unexpected explosion can be estimated after accident from the failure rate of windows.

REFERENCE

1. Ikonen, K., Ajasta riippuvien ilmiöiden numeerisissa ratkaisuissa käytetyn aika–askeleen valinnasta. Rakenteiden Mekaniikka 14(1981), pp. 1–9.

COMPUTING AND UNDERSTANDING INTERACTIVE BUCKLING

R. KOUHIA[1], C.M. MENKEN[2], M. MIKKOLA[1] and G.-J. SCHREPPERS[2]
[1]Laboratory of Structural Mechanics, Helsinki University of Technology
Rakentajanaukio 4A, 02150 Espoo, Finland
[2]Faculty of Mechanical Engineering, Eindhoven University of Technology
P.O. 513, 5600 AM Eindhoven, The Netherlands

ABSTRACT

Non-linear interactions between buckling modes, representing one type of coupled instabilities of structures, are practically important since if these occur, the post-buckling response may differ significantly from the uncoupled situation. Analysis of structures exhibiting interactive buckling phenomena is not simple. Using conventional tools for non-linear numerical analysis, one may need several runs with different imperfection patters, in order to verify the response in the post-buckling regime. However, a shorter and usually more informative route to understand the interactive buckling behaviour is to use an asymptotic approach prior a full non-linear analysis.

In the asymptotic initial post-buckling theory, the analysis is reduced to solving a small equation system for the amplitudes of the buckling modes involved. It was developed as an analytic tool, but it can also be utilized as a part of a numerical procedure, for instance the finite element method. Due to the lack of generality and the difficulty of use, it has not gained popularity among engineers and developers of numerical software. However, it can provide some vital information about the nature of the problem and it has some connections with the continuation procedures of multiple parameter systems.

This paper shows an example of the use of the asymptotic approach in an interactive buckling phenomenon. Interaction of an overall lateral-torsional buckling and a local flange buckling in a prismatic T-beam structure is studied. Both experimental results and numerical solutions are presented.

1 INTRODUCTION

Concern with non-linear buckling mode interactions has been stimulated by increased interest in optimal structural design. Safety of a structure against collapse under buckling, is not only determined by the critical load itself, but rather by the behaviour in the post-buckling region. If the post-buckling response is stable, like in the single mode buckling of a simply supported plate, this information provides the engineer with extra safety which possibly can be utilized in the design. However, the situation is completely different in

multi-mode buckling when non-linear interactions between buckling modes occurr. These interactions can completely change the post-buckling behaviour from the uncoupled situation. A common example is a stiffened compressed plate where the 'naive' optimum design philosophy would suggest to make equal the local and overall buckling loads. Both of these buckles exhibit stable post-buckling behaviour, when appearing separately, but change to imperfection sensitive unstable behaviour when the modes interact with each other.

Koiter was the first to formulate a general theory of mode interactions for continua [1]. He established that mode interactions have a destabilizing influence, which for certain types of structures gives rise to a significant reduction of the load-bearing capacity. This in turn explained the discrepancy between critical loads obtained from bifurcation theory and critical loads observed in experiments, particularly for shells. Koiter's approach provides a strongly reduced potential energy function, the variables being the amplitudes of the relevant buckling modes. A comparable theory was developed independently by Thompson and Hunt for *a priori* discrete systems [2].

Koiter's approach was asymptotic in nature. It gives important qualitative answers of the type of post-buckling behaviour and also quantitative results for the initial post-buckling response. However, it has gained little footing in computerized buckling analyses. One of the first attempts to implement Koiter's asymptotic initial post-buckling theory was the work by Haftka, Mallett and Nachbar [3]. However, their attempt was somewhat unorthodox, focusing only to the snap-through instability. The non-linearities in the pre-buckling state were considered as generalized initial imperfections of the perfect structure. Later, implementations which are more faithful to the original theory were presented e.g. by van Erp and Menken [4].

The main stream of computer analyses of non-linear structures goes with the incremental approach. It allows the handling of fully non-linear equilibrium equations without any restrictions to the kinematics. Therefore the problem of assessing the validity of the asymptotic approach is overcome. However, it is not easy to locate the singularities and to switch onto the post-buckling branches in a reliable, robust way. In addition, the litterature deals mainly with simple critical points. Therefore it seems to be ideal to combine some of the features of the asymptotic analysis to the general continuation procedure in order to handle mode interactions.

In comparison with the widely used continuation procedure, the asymptotic approach can provide some additional information such as the shape of the worst imperfection; it also enables classification of the buckling problem in terms of catastophe theory as described, for example, by Thompson and Hunt [5], so giving insight into the mechanism of the non-linear mode-interaction.

In the original theory, the number of discrete equilibrium equations derived from the reduced potential energy expression equalled the multiplicity of the buckling load. The early analytical investigations concentrated predominantly on interaction between local and overall buckling for compressed structural members; consequently the number of discrete equilibrium equations in most cases was two [6].

When combining the asymptotic approach with a finite element discretization, many critical loads are involved. Koiter suggested a method to handle nearly coincident critical loads, while Byskov and Hutchinson presented a formulation for well separated critical loads [7]. It has also been shown experimentally that interaction between well separated critical loads can occur [8]. It was also conjectured that a limited number of modes might

suffice, an idea which is supported by the following statement of Potier-Ferry: "*The most typical feature of instability theory is that its fundamental characteristics can be found in very simple models. Moreover, any complicated structural system is equivalent in some sense to one of these simple models, at least in the neighbourhood of a critical state*" [9].

2 INTERACTIVE BUCKLING PHENOMENA

The classification of multiple bifurcation points is much more complex than in with the simple critical state. According to the theorem of Bezout, the number of emanating post-buckling branches grows (at maximum) in the power of the multiplicity of the critical point. Problems with two coincident modes fall in the category of umbilic catastrophes. One way to classify two-fold bifurcations is by their symmetry properties; either full asymmetry, symmetry in the presence of the other (semi-symmetry) or symmetry of each mode in the presence of the other (full symmetry) [5]. In the catastrophe theory the classification is more subtle. The hyberbolic and elliptic umbilic embrace both of the first two categories above, the double cusp relates to the third, and the parabolic umbilic involves symmetry in each mode independently, but broken symmetry in combination.

The example below can be classified to be a form of a parabolic umbilic catastrophe [8], which is regarded to be the most complex of the seven 'elementary' forms explicitely listed by Thom in 1975 [10]. It requires six dimensions for its complete mathematical description, two independent state variables and four dimensions of control. Thus the present discussion is only limited to one control parameter, i.e. the load parameter.

3 ASYMPTOTIC APPROACH

The basic steps of the asymptotic analysis are reviewed. The system is described by a potential energy expression that is expanded up to and including fourth order displacements terms. Bifurcation points are characterized by the vanishing of the quadratic terms of the potential energy. Thus, the first numerical step involves the solution of the linear, generalized eigenvalue problem

$$(\mathbf{K} + \lambda_i \mathbf{G})\mathbf{u}_i = \mathbf{0}, \tag{1}$$

and provides a (pre-selected) number of critical loads λ_i and pertinent buckling modes $\mathbf{u}_i$. **K** ja **S** are the linear stiffness matrix and the initial stress matrix (from unit reference load), respectively.

According to the asymptotic theory, the initial post-buckling field $\mathbf{\Delta u}$ can be written as

$$\mathbf{\Delta u} = a_i(\lambda)\mathbf{u}_i + a_i(\lambda)a_j(\lambda)\mathbf{u}(\lambda)_{ij}, \tag{2}$$

where the second order fields $\mathbf{u}_{ij}$ and the amplitudes a_i have still to be determined. It is assumed that the contribution of the second order fields is small in comparison with the first order contribution. Koiter's original formulation was based on coinciding critical loads. All pertinent modes should be inserted into (2). Thus, theoretically there was no problem of choice. The same held for the (semi)analytical analyses of uniformly compressed structural members, where at least two, sometimes three, sinusoidal modes were taken into account *a priori*. In a more general finite element analysis, however, a

whole spectrum of critical loads may occur, and the question arises which modes should be put in the linear part of the post-buckling field. This question will be discussed later.

The second numerical step involves determination of the second order fields $\mathbf{u}_{ij}$ at fixed amplitudes a_i and expansion load λ_p. Usually the following orthogonality condition

$$\mathbf{u}_k^T \mathbf{K} \mathbf{u}_{ij} = 0 \tag{3}$$

between the modes $\mathbf{u}_k$ and the second order fields $\mathbf{u}_{ij}$ is imposed. This constraint is conveniently taken into account by means of Lagrange multipliers. The requirement that the resulting Lagrangian functional be stationary leads to the following linear equation system:

$$\begin{bmatrix} \mathbf{K} + \lambda_p \mathbf{G} & \mathbf{M} \\ \mathbf{M}^T & \mathbf{0} \end{bmatrix} \begin{bmatrix} \mathbf{u}_{ij} \\ \mathbf{p}_{ij} \end{bmatrix} = \begin{bmatrix} \mathbf{f}_{ij} \\ \mathbf{0} \end{bmatrix} \tag{4}$$

where the vectors $\mathbf{p}_{ij}$ contain the Lagrange multipliers; the constraint matrix $\mathbf{M}$ and the 'load vectors' $\mathbf{f}_{ij}$ result from the potential energy expression now augmented with cubic and quartic terms. The constrain matrix follows from the orthogonality condition (3):

$$\mathbf{M} = \mathbf{K}\mathbf{U}, \qquad \mathbf{U} = \begin{bmatrix} \mathbf{u}_1 & \mathbf{u}_2 & \cdots & \mathbf{u}_M \end{bmatrix}.$$

The appearance of the stability matrix $\mathbf{K} + \lambda_p \mathbf{G}$ in this set of equations indicates that the solution requires specific care if the perturbation load factor λ_p is close to some of the critical loads λ_i. Once the second order fields have been obtained, the potential energy is only a function of the amplitudes a_i and the load parameter λ, and looks like:

$$V[a_i; \lambda] = \frac{1}{2} \sum_{I=1}^{M} (1 - \frac{\lambda}{\lambda_I}) a_I a_I + A_{ijk} a_i a_j a_k + A_{ijkl} a_i a_j a_k a_l, \tag{5}$$

where A_{ijk} and A_{ijkl} are the the cubic and quartic order coefficients of the potential energy.

The third step involves the solution of the equilibrium (amplitude) equations generated from (5). Koiter described how the direction of the equilibrium path with the steepest descent or smallest rise could be found [11].

If it is admissible to insert a small number of modes into (2) in the case of a general FE post-buckling analysis, the FE model initially comprising many degrees of freedom would be reduced to a very simple model as described by (5) too. This could correspond to the aforementioned statement of Potier-Ferry. The simple model would make the initially complicated model more tractable for interpretation; the mixed coefficients A_{ijk} and/or A_{ijkl}, for instance, indicate whether there is coupling between buckling modes or not.

4 EXAMPLE

A simply supported aluminium (E=70 GPa, ν=0.3) T-beam was analyzed as a test case (flange: width 30 mm, thickness 0.5 mm; web: height 50 mm, thickness 2 mm). Dimensions of the cross-section were chosen such that for the shorter beams local flange buckling would occur first, while buckling is initiated by an overall lateral-torsional mode for the longer ones. Dimensioning of this beam was based on estimates of the behaviour by assuming distortion free lateral-torsional buckling and sinusoidal local buckling. For

TABLE 1. Lowest buckling modes of the 520 mm and 620 mm long T-beams.

			symm. prop. w.r.t.				symm. prop. w.r.t.	
i	load	type	midspan	web	load	type	midspan	web
1	1183 N	local	symm	asymm	924 N	overall	symm	-
2	1184 N	local	asymm	asymm	975 N	local	symm	asymm
3	1211 N	local	symm	symm	976 N	local	asymm	asymm
4	1212 N	local	asymm	symm	998 N	local	symm	symm
5	1331 N	local	asymm	asymm	999 N	local	asymm	symm
6	1331 N	local	symm	asymm	1083 N	local	asymm	asymm
7	1356 N	overall	symm	-	1083 N	local	symm	asymm

experimental results see Refs. [12], [13]. Since the local buckling load is strongly influenced by the free width of the flange, the overlap between flange and web consisted of orthotropic elements having high rigidity in transverse direction. The beam was loaded by a transverse force at midspan and in the direction that induced compression in the flange.

The computational model consist of 22 spline finite strips divided into 40 sections resulting 3549 in degrees of freedom. All displacement quantities are interpolated by the basic B_3-splines in longitudinal direction. In transverse direction linear interpolation is used for membrane displacements and the cubic Hermitian polynomials for the out of plane displacement. The classical Kirchhoff-Love plate model is used.

The generalized eigenvalue problem (1) is solved using a subspace iteration method [14] where the projected eigenvalue problem is first reduced into to a standard form and the resulting matrix is tridiagonalized using Householder transformations and finally the eigenvalues are determined by using the QL-algorithm [15]. Since the procedure for selection of the initial iteration vectors in Ref.[14] is designed for wibration problems, random initial iteration vectors have been used instead in the present case.

Beams having the lengths of 520 and 620 mm were modelled, and the computed buckling loads are shown in Table 1. It is obvious that the lowest mode must be taken into account in describing the post-buckling behaviour of the perfect structure. If one looks only at the magnitude of the critical loads, at least the second mode could linearly contribute to the post-buckling field and the other modes would be 'passive' in the language of Thompson and Hunt. Table 1 shows the symmetry properties of the local modes too. In Fig.1 the two local modes 1 and 3 for the shorter beam are shown. From previous experiments (in pure bending) and the simple discrete model (with two coinciding local critical loads), it is known that local flange buckling triggered overall lateral-torsional buckling, leaving one flange half unbuckled [8]. A comparable phenomenon cannot happen by adding the second mode to the first one. Only a combination of the first and third mode can lead to a similar phenomenon. In theory the local critical loads will have the pairwise the same value. However, the numerical model produced a spectrum of nearly coinciding critical loads. Two different approaches were used for solving the reduced set of equilibrium equations:

1. The small difference between the critical loads is taken into account, leading to a

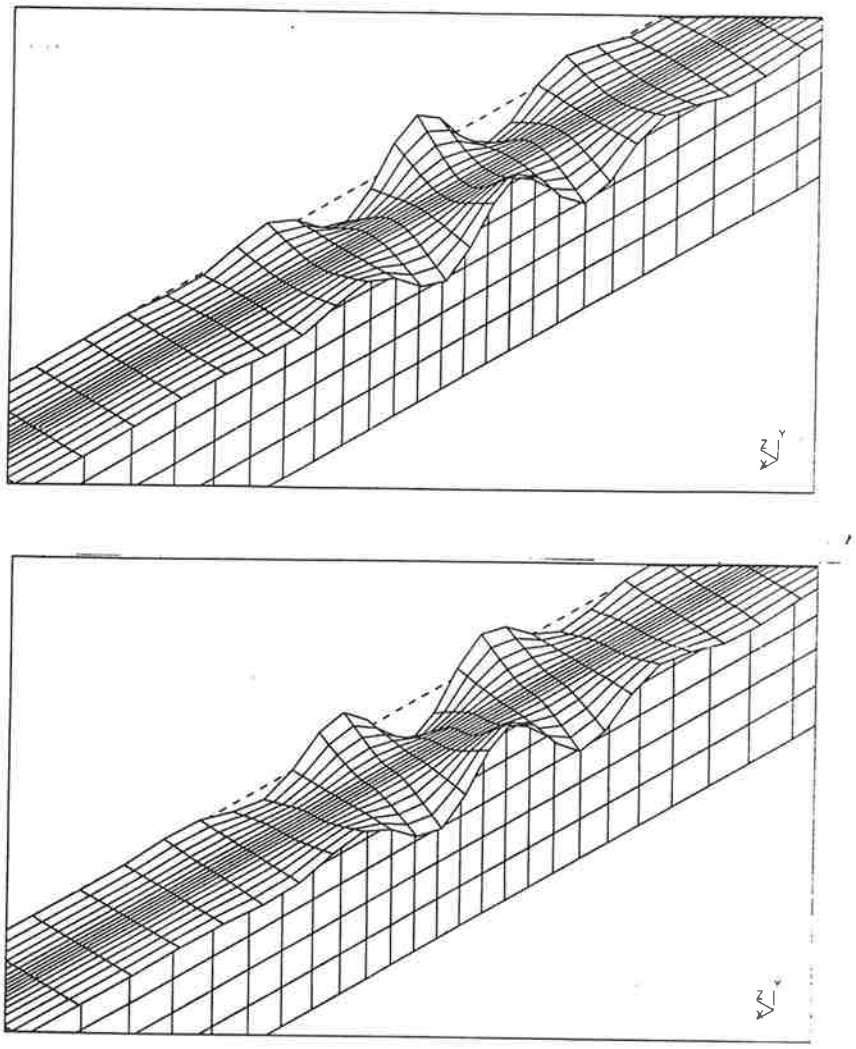

FIGURE 1. Local buckling modes 1 (below) and 3 (above) of the 520 mm beam.

secondary bifurcation on the path corresponding purely to the lowest local mode.

2. The value of the second local critical load is replaced by the value of the lowest one, leading to a compound bifurcation point.

Results of both approaches are reproduced in Fig. 2 for the case of the 520 mm beam where the results of the first approach are drawn with solid lines, while dashed lines indicate the second approach. The figure shows that the amplitudes of the asymmetric mode 1 and the symmetric mode 3 become identical, thus leaving one flange half unbuckled. It is interesting to note that the interaction between the two local modes is comparable to the behaviour of the well known Augusti model [16]. Also the amplitude paths from the 2-mode and 3-mode analyses of the 620 mm long beam are shown in Fig. 2.

The load deflection curve for the longer beam depicted in Fig. 3 shows dramatic shell like behaviour. Even though the interacting loads are quite well separated the secondary bifurcation occurs almost immediately after the first one.

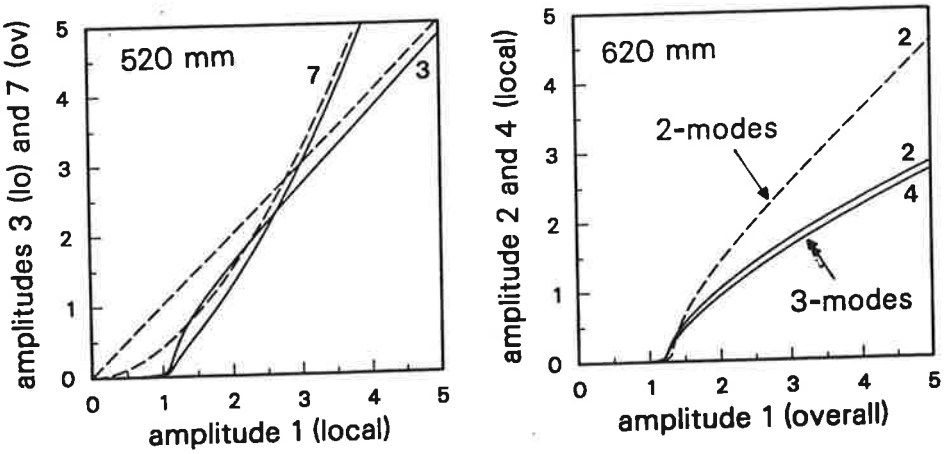

FIGURE 2. Solutions of the amplitude equations.

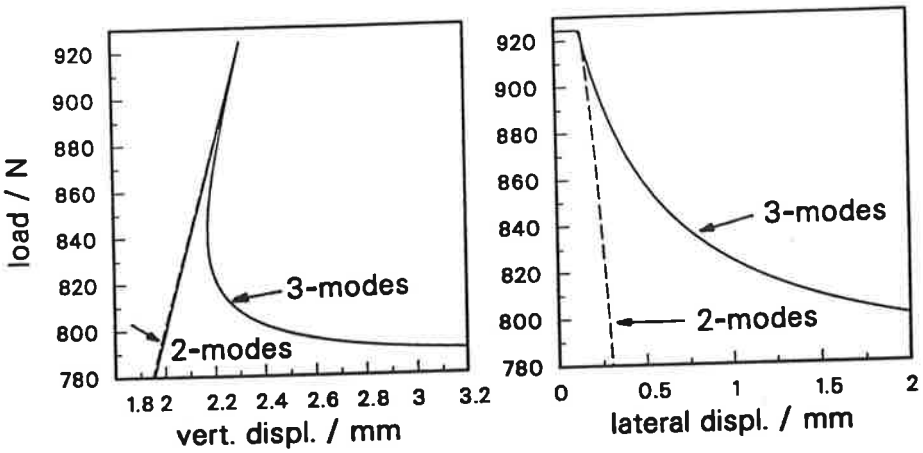

FIGURE 3. Displacements at the load point of the 620 mm beam.

Since overall buckling is also involved in this problem, it remains to be decided whether the critical load can be considered to be close to the lowest one or not. Strictly speaking, if mode interaction occurs, a mode pertaining to a separated critical load will be passive. On the other hand, one could consider this situation to be a perturbation of the case of coinciding critical loads. The latter approach was chosen and the overall mode was added into the linear combination, which after ignoring relatively small terms gave for the potential energy

$$V(a_1,a_3,a_7) = \frac{1}{2}\left[(1-\frac{\lambda}{\lambda_1})a_1^2+(1-\frac{\lambda}{\lambda_3})a_3^2+(1-\frac{\lambda}{\lambda_i})a_7^2\right]+ \\ +A_{713}a_1a_3a_7+A_{1111}a_1^4+A_{1133}a_1^2a_3^2+A_{3333}a_3^4. \qquad (6)$$

The cubic cross-term shows that all three modes are coupled.

It is numerically verified, that omission of the 'passive' global mode from the eigenmode expansion (2) lead to its appearance in the mixed second order field. However, omission of a relevat mode from the contributing eigenmodes will narrow the range of validity of

the asymptotic approach. This can be seen clearly from the figure 3, where the post-buckling paths are drawn from both 2- and 3-mode analyses which diverge rapidly after the secondary bifurcation point.

REFERENCES

1. Koiter, W.T., Over de stabiliteit van het elastisch evenwicht (in Dutch), PhD thesis, Delft University of Technology, 1945, English translations: NASA TT F10, 833 (1967) and AFFDL, TR-7025 (1970)

2. J.M.T. Thompson and G.W. Hunt, 'A General Theory of Elastic Stability', Wiley, London, 1973

3. R.T. Haftka, R.H. Mallet and W. Nachbar, Adaptation of Koiter's method to finite element analysis of snap-through buckling behaviour, International Journal of Solids and Structures, 7 (1971) 1427-1445

4. G.M. van Erp and C.M. Menken, Initial post-buckling analysis with the spline finite strip method, Computers and Structures, 40 (1991) 1185-1191

5. J.M.T. Thompson and G.W. Hunt, 'Elastic Instability Phenomena', Wiley, Chichester, 1984

6. M. Pignataro, A. Luongo and M. Rizzi, On the effect of the local-overall interaction on the post-buckling of uniformly compressed channels, Thin-Walled Structures, 3 (1986) 1470-1486

7. E. Byskov and J.W. Hutchinson, Mode interaction in axially stiffened cylindrical shells, AIAA Journal, 15 (1977) 941-948

8. C.M. Menken, W.J. Groot, and G.A.J. Stallenberg, Interactive buckling of beams in bending, Thin-Walled Structures, 12 (1991) 415-434

9. M. Potier-Ferry, Buckling and Post-Buckling, 205-223, Volume 288 of Lecture Notes in Physics, Springer-Verlag, 1987

10. G.W. Hunt, Hidden (a)symmetries of elastic and plastic bifurcation, Appl. Mech rev. 39 (1986) 1165-1186

11. W.T. Koiter, Current trends in the theory of buckling, In IUTAM Symposium on Buckling of Structures, Harvard University, Springer-Verlag, 1974, pp. 1-16

12. C.M. Menken, R. Kouhia and W.J. Groot, An investigation into non-linear interaction between buckling modes, to appear in Thin Walled Structures

13. C.M. Menken, W.J. Groot and R. Petterson, Experiments on coupled instabilities, accepted for presentation on the 10th Int. Conf. on Experimental Mech., Lisbon, 18-22.7.1994

14. K.J. Bathe and E.L. Wilson, 'Numerical Methods in Finite Element Analysis' Prentice-Hall, Englewood Cliffs, New Jersey, 1976

15. J.H. Wilkinson and C. Reinsch, 'Linear Algebra' Volume II of Handbook for Automatic Computation, Springer-Verlag, 1971

16. G. Augusti, Stabilita di strutture elastiche elementari in presenza di grandi sportamenti, *Acced. Sci. Fis. Mat.* 4(5) (1964), Napoli, Serie 34.

ACCURACY OF COMPOSITE SHELL ELEMENTS IN TRANSIENT ANALYSIS INVOLVING MULTIPLE IMPACTS

HANNU LAHTINEN and ANTTI PRAMILA
Department of Mechanical Engineering
University of Oulu
PL 444, FIN-90571 Oulu FINLAND

ABSTRACT

The accuracy of composite shell elements in linear transient analysis involving multiple impacts was studied. Results obtained by finite element method and by an analytical solution were compared with each other. The previously developed analytical solution for the impact problem was in closed form only until the end of the first contact. In this work the solution has been extended to multiple impacts in closed form. Therefore, it has been possible to solve problems with several successive impacts. Comparisons revealed that the composite shell elements of commercial FEM software give very accurate results with specially orthotropic laminates in transient analysis involving flexural and shear wave propagation. The accuracy begins to deteriorate in problems where multiple impacts occur. There are difficulties even in finding subsequent impacts. Also, it was noticed that commercially available finite element programs may have serious problems in the analysis of composite structures, e.g. in calculation of stresses.

1. INTRODUCTION

The aim of this work was to study the reliability of the composite shell elements in linear transient analysis. The properties and restrictions of the element and accuracy reached in practise were under consideration. The work was done by comparing the results obtained by FEM and an analytical solution with each other. Both of the solution methods are based on first order shear deformation theory and precisely same calculation models (geometry, boundary conditions) were used. Thus, the differences in the results are solely caused by discretization and time integration methods used.

Analytical solutions used were developed by Dobyns [1] and Christoforou and Swanson [2]. The solutions are for specially orthotropic rectangular laminated plates, which are simply supported. Dobyns solved the problem for a known force history. Christoforou and Swanson extended the solution also for an impact problem.

The solution for the impact problem was in closed form only until the end of first contact in reference [2]. In this study the closed form solution has been extended also for multiple impacts. Therefore, it has been possible to solve problems with several successive impacts. Furthermore, second shear correction factor has been added to the solution, because of obvious need of two factors with composite materials [4].

2. SOLUTION FOR MULTIPLE IMPACTS

The previously developed analytical solutions will not be presented here, because they are well documented in references [1, 2]. Solution starts from equations of motion, which are reduced to a simpler form because a crossply laminate is specially orthotropic, i.e. stiffness terms $A_{16}=A_{26}=D_{16}=D_{26}= 0$ and all coupling terms $B_{ij}= 0$. The solution is for a simply supported, rectangular plate of uniform thickness. In these solutions the shear deformation factor is assumed to be $\pi^2/12$.

The solution is based on expansions of the loads, displacements and rotations in Fourier series, which satisfy the boundary conditions of simple support. Each expression is assumed to be separable into a function of time and function of position. Furthermore, by neglecting in-plane and rotary inertia the problem becomes a second-order ordinary differential equation in time for the Fourier coefficients of the lateral deflection. The impact force is computed from the deceleration of the impactor mass. This involves the equilibrium equation between the impactor and the plate during contact. [2]

The geometry of the problem is presented in figure 1. Load of the plate is acting on a rectangular area, which size and position can be changed. Pressure load is uniform in the loading area. Also, in impact problem the loading is transferred in a similar way, except that the loading area must be located in the middle of the plate. In a real impact problem that kind of load transfer would be inadequate, but for our purpose it applies.

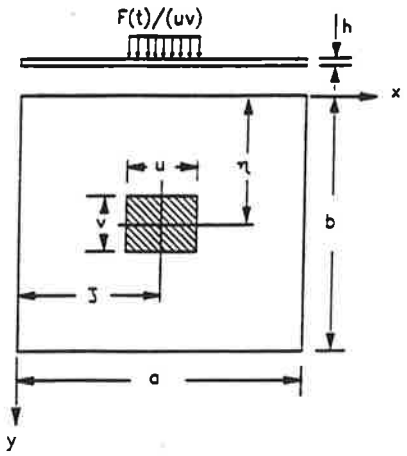

Figure 1. Geometry of the problem. [2]

The solution of the deflection response of the laminate becomes into the form

$$w(x,y,t) = \frac{ab}{uvm_1}\sum_m\sum_n \frac{P_{mn}}{\omega_{mn}}\sin\frac{m\pi x}{a}\sin\frac{n\pi y}{b}\int_0^t F(\tau)\sin\omega_{mn}(t-\tau)d\tau \quad , \qquad (1)$$

where m_1 is mass of the plate, ω_{mn} are the natural frequencies of the plate and factors P_{mn} depend on size and position of the loading area [2].

Dobyns, [1], solved the convolution integral of equation (1) for a few known force histories in closed form. Christoforou and Swanson formed an equilibrium equation between the impactor and the plate and solved the contact force by Laplace transform techniques. The response of the plate was then obtained by using the same technique as for equation (1).

In a real impact loading multiple contacts may occur between the impactor and the laminate. After the first contact, solution for laminate response is obtained from equation (1), in which the upper limit of the integral is replaced by time t_{1e} (when the first contact is lost). Now the contact force in the convolution integral is known and the equation (1) can be solved in closed form. This solution is valid until the second contact begins.

The response during the second contact can be solved in the same way as previously. To make the solution easier, a new time coordinate will be taken from the beginning of the second impact. Now, the laminate response of the first contact must also be added to the equilibrium equation between impactor and laminate. After that the solution is obtained by following the operations done in references [2, 3]. This procedure can be continued for subsequent contacts.

The solutions for the first and second contact look different. Only at the third contact the response equations find their final and general form. Therefore, general equation forms will be presented for the i'th contact. When the i'th contact begins at time t_{ib} (and will end at time t_{ie}), the impactor has a position w_0 and velocity V_0. A new time coordinate will be taken for equations concerning the i'th contact. All previous laminate responses will be superposed to the solution of i'th contact and they all have different time coordinates. The equilibrium equation at the beginning of i'th contact will be

$$
\begin{aligned}
w_0 + V_0 t - \frac{1}{m_2}\int_0^t F(\tau)(t-\tau)d\tau - \frac{F(\tau)}{K_2} = \\
\frac{ab}{uvm_1}\sum_m\sum_n \frac{P_{mn}}{\omega_{mn}}\sin\frac{m\pi}{2}\sin\frac{n\pi}{2}\int_0^{t_{1e}-t_{1b}} F(T)\sin\omega_{mn}(t+t_{ib}-t_{1b}-T)dT + \ldots + \\
\frac{ab}{uvm_1}\sum_m\sum_n \frac{P_{mn}}{\omega_{mn}}\sin\frac{m\pi}{2}\sin\frac{n\pi}{2}\int_0^{t_{(i-1)e}-t_{(i-1)b}} F(T)\sin\omega_{mn}(t+t_{ib}-t_{(i-1)b}-T)dT + \\
\frac{ab}{uvm_1}\sum_m\sum_n \frac{P_{mn}}{\omega_{mn}}\sin\frac{m\pi}{2}\sin\frac{n\pi}{2}\int_0^t F(\tau)\sin\omega_{mn}(t-\tau)d\tau \quad .
\end{aligned}
\tag{2}
$$

Here K_2 is a linearized contact area stiffness. In equation (2) the time used in the response equation for the first contact is $t+t_{ib}-t_{1b}$ and the upper limit of the integral is $t_{1e}-t_{1b}$. In the response equation for the second contact the time is $t+t_{ib}-t_{2b}$ and the upper limit is $t_{2e}-t_{2b}$ ect. Next, a Laplace transform of equation (2) will be taken and the contact force can be solved. After an inverse Laplace transform the contact force obtains the form

$$
F(t) = \sum_j (F_{1j}\sin\omega_{ij}t + F_{2j}\cos\omega_{ij}t) \quad , \tag{3}
$$

where ω_{ij} are the response frequencies and they are, of course, exactly the same as during the

first contact [2]. In every new contact only F_{1ij} and F_{2ij} must be calculated. The subscript i means the number of contact and j is the index used in summation in each contact. The subscript i is used in summation to separate different nested summations with index j. In equation (3)

$$F_{1ij} = \frac{m_2 V_0 + \frac{abm_2}{uvm_1}\sum_m\sum_n \frac{P_{mn}\omega_{ij}^2}{\omega_{mn}^2-\omega_{ij}^2}\sin\frac{m\pi}{2}\sin\frac{n\pi}{2}\,A_i}{\omega_{ij}\left[\frac{m_2}{K_2}+\frac{abm_2}{uvm_1}\sum_m\sum_n P_{mn}\sin\frac{m\pi}{2}\sin\frac{n\pi}{2}\frac{\omega_{mn}^2}{(\omega_{mn}^2-\omega_{ij}^2)^2}\right]} \tag{4}$$

and

$$F_{2ij} = \frac{m_2 w_0 + \frac{abm_2}{uvm_1}\sum_m\sum_n \frac{P_{mn}\omega_{ij}^2}{\omega_{mn}(\omega_{mn}^2-\omega_{ij}^2)}\sin\frac{m\pi}{2}\sin\frac{n\pi}{2}\,B_i}{\frac{m_2}{K_2}+\frac{abm_2}{uvm_1}\sum_m\sum_n P_{mn}\sin\frac{m\pi}{2}\sin\frac{n\pi}{2}\frac{\omega_{mn}^2}{(\omega_{mn}^2-\omega_{ij}^2)^2}}\,. \tag{5}$$

During the first contact the impactor position $w_0 = 0$ and $A_1 = B_1 = 0$, in which case also $F_{2ij} = 0$. Then equations (3) - (5) reduce to the form presented in reference [2]. For subsequent contacts

$$\begin{aligned} A_i = \sum_{k=1}^{i-1}\Bigg[\sum_j \frac{1}{2}F_{1kj}\Bigg\{ & \frac{2\omega_{kj}}{\omega_{kj}^2-\omega_{mn}^2}\cos\omega_{mn}(t_{ib}-t_{kb}) \\ & -\frac{1}{\omega_{kj}+\omega_{mn}}\cos[(\omega_{kj}+\omega_{mn})(t_{ke}-t_{kb})-\omega_{mn}(t_{ib}-t_{kb})] \\ & -\frac{1}{\omega_{kj}-\omega_{mn}}\cos[(\omega_{kj}-\omega_{mn})(t_{ke}-t_{kb})+\omega_{mn}(t_{ib}-t_{kb})]\Bigg\} \\ +\sum_j \frac{1}{2}F_{2kj}\Bigg\{ & \frac{-2\omega_{mn}}{\omega_{kj}^2-\omega_{mn}^2}\sin\omega_{mn}(t_{ib}-t_{kb}) \\ & +\frac{1}{\omega_{kj}+\omega_{mn}}\sin[(\omega_{kj}+\omega_{mn})(t_{ke}-t_{kb})-\omega_{mn}(t_{ib}-t_{kb})] \\ & +\frac{1}{\omega_{kj}-\omega_{mn}}\sin[(\omega_{kj}-\omega_{mn})(t_{ke}-t_{kb})+\omega_{mn}(t_{ib}-t_{kb})]\Bigg\}\Bigg] \end{aligned} \tag{6}$$

and

$$B_i = \sum_{k=1}^{i-1} \left[\sum_j \frac{1}{2} F_{1kj} \left\{ \frac{2\omega_{kj}}{\omega_{kj}^2 - \omega_{mn}^2} \sin\omega_{mn}(t_{ib} - t_{kb}) \right.\right.$$

$$+ \frac{1}{\omega_{kj} + \omega_{mn}} \sin[(\omega_{kj} + \omega_{mn})(t_{ke} - t_{kb}) - \omega_{mn}(t_{ib} - t_{kb})]$$

$$\left. - \frac{1}{\omega_{kj} - \omega_{mn}} \sin[(\omega_{kj} - \omega_{mn})(t_{ke} - t_{kb}) + \omega_{mn}(t_{ib} - t_{kb})] \right\} \qquad (7)$$

$$+ \sum_j \frac{1}{2} F_{2kj} \left\{ \frac{2\omega_{mn}}{\omega_{kj}^2 - \omega_{mn}^2} \cos\omega_{mn}(t_{ib} - t_{kb}) \right.$$

$$+ \frac{1}{\omega_{kj} + \omega_{mn}} \cos[(\omega_{kj} + \omega_{mn})(t_{ke} - t_{kb}) - \omega_{mn}(t_{ib} - t_{kb})]$$

$$\left.\left. - \frac{1}{\omega_{kj} - \omega_{mn}} \cos[(\omega_{kj} - \omega_{mn})(t_{ke} - t_{kb}) + \omega_{mn}(t_{ib} - t_{kb})] \right\} \right] .$$

Here the response frequencies are now denoted by ω_{kj}. During the second contact $F_{21j} = 0$, which means that only first parts of equations (6) and (7) are needed.

Next, the response of the laminate during the contact can be solved using again Laplace transformation technique with the general form of contact force (eqn (3)). The procedure used is similar to that in references [2, 3]. The solution for the i'th contact is

$$w(x,y,t) = \frac{ab}{uvm_1} \sum_m \sum_n P_{mn} \sin\frac{m\pi x}{a} \sin\frac{n\pi y}{b}$$

$$\times \sum_j \left\{ \frac{F_{1ij}}{\omega_{mn}(\omega_{ij}^2 - \omega_{mn}^2)} (\omega_{ij} \sin\omega_{mn} t - \omega_{mn} \sin\omega_{ij} t) + \frac{F_{2ij}}{\omega_{ij}^2 - \omega_{mn}^2} (\cos\omega_{mn} t - \cos\omega_{ij} t) \right\} \qquad (8)$$

$$+ \frac{ab}{uvm_1} \sum_m \sum_n \frac{P_{mn}}{\omega_{mn}} \sin\frac{m\pi x}{a} \sin\frac{n\pi y}{b} \; C_i \quad ,$$

where C_i is the contribution of previous contacts to the response. C_i is almost the same as B_i except that now $(t_{ib}-t_{kb})$ is replaced by $(t+t_{ib}-t_{kb})$.

Now, the equations during the contact has been examined. Next, the equations between the contacts are presented. The response of the laminate after any contact is obtained by substituting the contact force (eqn (3)) to equation (1). The convolution integral can be solved again in closed form. Therefore, the response of the laminate after i'th contact is

$$w(x,y,t) = \frac{ab}{uvm_1}\sum_m\sum_n \frac{P_{mn}}{\omega_{mn}}\sin\frac{m\pi x}{a}\sin\frac{n\pi y}{b}\, D_i \quad , \tag{9}$$

where D_i is again almost the same as B_i except that now the first summation is made from k = 1 to k = i and $(t_{ib}-t_{kb})$ is replaced by $(t+t_{ib}-t_{kb})$.

Once the contact between the impactor and the laminate is lost, the position of the impactor must be followed in order to find out the initiation of the possible subsequent contact. The impactor moves with constant velocity

$$w(\frac{a}{2},\frac{b}{2},t) = w_0 + V_0 t - \frac{1}{m_2}\int_0^{t_u} F(\tau)(t-\tau)d\tau \tag{10}$$

and after substitution of the contact force and integration, the position of the impactor after i'th contact is

$$w(\frac{a}{2},\frac{b}{2},t) = w_0 + V_0 t - \frac{1}{m_2}\sum_j \left[\frac{F_{1ij}t}{\omega_{ij}} + \frac{F_{2ij}}{\omega_{ij}^2} - (\frac{F_{1ij}}{\omega_{ij}^2} + \frac{F_{2ij}t_{ie}}{\omega_{ij}} - \frac{F_{2ij}t}{\omega_{ij}})\sin\omega_{ij}t_{ie} \right. \tag{11}$$
$$\left. - (\frac{F_{1ij}}{\omega_{ij}^2} + \frac{F_{2ij}t_{ie}}{\omega_{ij}} - \frac{F_{2ij}t}{\omega_{ij}})\cos\omega_{ij}t_{ie} \right] .$$

Equations presented here may look complicated. One must take care not to mix nested summations over j. However, they are quite straightforward to program for computation. There are now two factors influencing to the accuracy of results. The first one is the number of Fourier terms (m,n) used in calculation. This was discussed in [2]. The second one is the determination of the instants, when the contact will begin or end. Those instants can be searched during calculation, for example, by bisection method.

During the study the response of the plate for the multiple impact problem was solved both analytically and numerically. In the numerical solution the convolution integral was integrated by Newton-Cotes method. In the numerical solution also the time step influences the accuracy of the response. The time step will be limited such that, the more Fourier coefficients are present in calculation, the smaller time step is also needed. That makes the numerical integration inefficient compared to the analytical solution for multiple impacts.

3. COMPARISON OF RESULTS WITH FINITE ELEMENT METHOD

The analytical solution is valid only for specially orthotropic laminates. Therefore, only symmetric crossply laminates were considered in the test problems. In this case the behaviour of the laminate is simplified remarkably, because there is no coupling between bending and membrane state. In comparisons the shear correction factor $\pi^2/12$ was used, because the shear correction is not wanted to influence on the results in the same time with discretization and

time integration.

One of the problems used in comparisons is called impact problem. Standard notations are used for the material properties and the meaning of the geometric variables can be seen from figure 1.

Impact problem: Simply-supported $[0/90/0/90/0]_s$-laminate of dimensions a = b = 0.16m, h = 0.00269m, with material properties of lamina E_{11}= 141.20 GPa, E_{22}= 9.72 GPa, G_{12}= 5.53 GPa, G_{31}= 5.53 GPa, G_{23}= 3.74 GPa, ν_{12}= 0.30, ϱ = 1536 kg/m^3, is subjected to impact loading, with impactor velocity 3.00 m/s and mass 8.4 g. Contact area stiffness is 5413000.0 N/m. Analytical results at time t = 52.0 μs at position (0.04, 0.08), when number of Fourier coefficients is m = n = 300: F = 272.38 Nw = $-0.4904*10^{-5}$ mσ_{11} = -15.28 MPa

The results obtained by the finite element method were compared with the analytical solution and the percentage error was calculated from equation

$$\frac{\textit{FEM - analytical solution}}{\textit{analytical solution}}\ 100\% \ .$$

In the work the effects of the element type (program used), mesh density, length of time integration step, number of natural frequencies used and lamination parameters to the accuracy of the results were systematically studied. The field variables under consideration were displacement, strain, stress and contact force histories. Also, the computing time was one parameter considered.

Three commercial finite element programs were used; ABAQUS, ANSYS and MSC/NAS-TRAN. The purpose of the present work was to examine properties of the finite element method, test different finite element programs, investigate their solution methods and efficiency, as well as to compare the programs with each other during the analysis of transient response with multiple impacts.

The elements used were typical composite shell elements of each program, i.e. S8R5 in ABAQUS, STIF99 in ANSYS and QUAD/8 in MSC/NASTRAN. All the elements are based on the first order shear deformation theory. With S8R5-element the shear correction factor is by default 5/6 and with QUAD/8-element $\pi^2/12$. In ANSYS (and STIF99-element) the factor is 5/6 or 1/(1.0+0.2*A/(25*t^2)) (A=area and t=thickness of the element) depending on which one is smaller.

Uniform element meshes have been used to avoid numerical dispersion caused by element mesh in wave propagation problem. Also, symmetry was employed by modelling only one quarter of the laminate. This is possible due to specially orthotropic material properties, crossply laminate, symmetric boundary conditions and loading. The boundary conditions for simply-supported laminate are the same as used for the analytical solution, i.e. along edges parallel to x-axis $u_x = u_z = \theta_y = 0$ and along edges parallel to y-axis $u_y = u_z = \theta_x = 0$. Here θ_x and θ_y denote rotation about x- and y-axes, respectively. On symmetry axes the symmetric boundary conditions were used.

The impact problem was quite demanding for finite element programs. The percentage errors for contact force, displacement and stress were in ANSYS results (0.05, 0.42, 1.78) %, in ABAQUS (1.81, -14.91, -8,97) % and in MSC/NASTRAN (-0.56, -0.62, -32.72) %, respectively, when the time step was $1.0*10^{-6}$s and the number of elements was 400.

The results calculated by ABAQUS diverged as time step decreased (figure 2). Also, ANSYS had peculiar deviations in results with small time steps. MSC/NASTRAN did not show any attempt of divergence, not even with time step $0.25*10^{-6}$s. That is why, the influence of damping coefficient was examined. It was noticed that the results obtained by ABAQUS were best with maximum numerical damping.

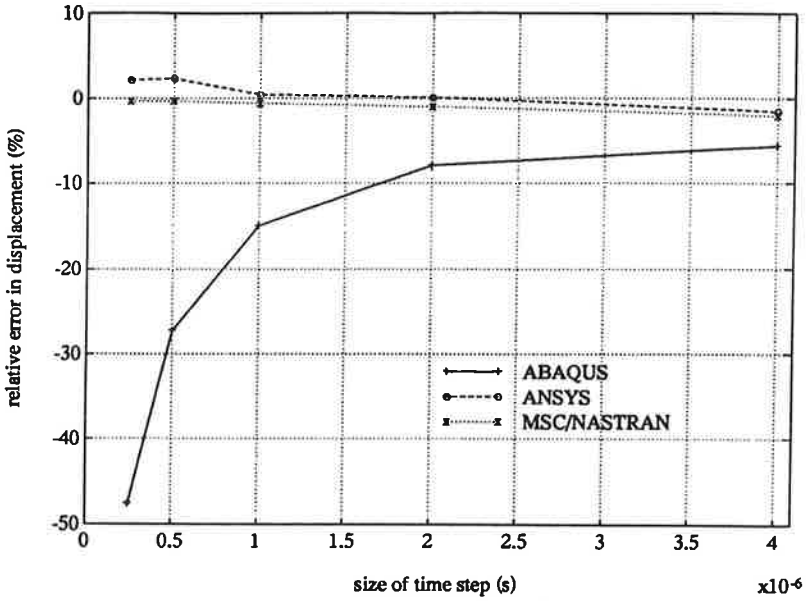

Figure 2. Errors in displacement obtained in the impact problem.

Another interesting observation was stress results obtained by MSC/NASTRAN, which had usually about 11.0 - 12.0 % error in σ_{11} and even 170.0 % in σ_{22}. These results caused some confusion and calculations were checked carefully without finding any explanation. Displacements and strains were found very accurately by MSC/NASTRAN, but stresses were always erroneous. These results were obtained with program versions V65C and V66A.

As the analysis of the impact problem continues, two separate contacts will occur. This was solved with finite element method by using a gap element and nonlinear solution procedure. ANSYS and MSC/NASTRAN found the second contact, but for some reason ABAQUS did not. The results for contact force obtained by ANSYS is shown in figure 3.

According to figure 3 the result correspond well with the analytical solution. At the maximum of the first contact the error percentage was -0.85 % with ANSYS and -1.49 % with MSC/-NASTRAN, while at the maximum of the second contact the errors were -6.69 % and -13.93 %, respectively. It seems that the longer calculation continues the larger errors occur. The errors in displacements were smaller than in stresses. There the percentage error was all the time below 2.00 %.

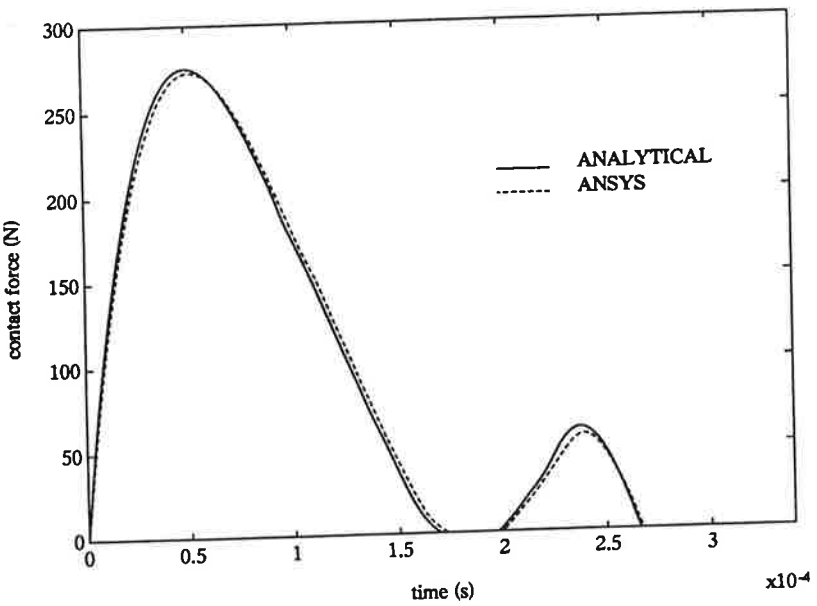

Figure 3. Contact force history.

The accuracy of the finite element results can be improved by increasing the number of natural frequencies involved in problem. Theoretically the size and the number of elements used in the model do not have any limits. However, in practice the computer resources are very often the restriction. For example, in a case when a laminate is subjected to a sudden impulse the percentage error in displacements grows significantly, but the results are still quite reasonable. Another example is the problem where three successive impacts appear. The problem was found by increasing the contact stiffness and making the laminate smaller. In this problem none of the finite element programs could follow the analytical solution with a reasonable finite element model.

4. CONCLUSIONS

In spite of observed shortcomings, it has been noticed that the composite shell elements can reach very accurate results with specially orthotropic laminates in transient analysis involving flexural and shear wave propagation. The accuracy is very good in problems where a small number of natural frequencies are present and in impact problems with low contact stiffness. Even in a problem with impulse loading, where a large number of natural frequencies are excited, the elements can reach quite good results. The accuracy begins to diminish also with problems where multiple impacts occur. There are difficulties even in finding the subsequent impact.

The finite element method programs used in comparison were ABAQUS, ANSYS and MSC/NASTRAN. They all are very well known and respected, but hardly infallible. ANSYS was the only one, which managed to solve all problems without serious errors. With MSC/NASTRAN we had problems in stress calculation and with ABAQUS in convergence of implicit time integration. Also, calculation with ABAQUS was generally time consuming. This comparison indicates that the user should be aware about the properties and shortcomings involved in the program, especially in analysis of composite structures.

REFERENCES

1. A. L. Dobyns. Analysis of simply-supported orthotropic plates subject to static and dynamic loads. AIAA Journal. Vol. 19(5), 642-650 (1981).

2. A. P. Christoforou and S. R. Swanson. Analysis of impact response in composite plates. International Journal of Solids and Structures. Vol. 27(2), 161-170 (1991).

3. A. P. Christoforou and S. R. Swanson. Analysis of simply-supported orthotropic cylindrical shells subject to lateral impact loads. Journal of Applied Mechanics vol. 57, 376-382, 1990.

4. M. Laitinen, H. Lahtinen and S.-G. Sjölind. Transverse shear correction factors for laminates in cylindrical bending. Communications in Numerical Methods in Engineering. Accepted.

AN APPLICATION OF THE GAUSS-SEIDEL ITERATION METHOD INTO THE ANALYSIS OF FLEXURAL COMPOSITE MEMBERS

Xiaohua Lu Pentti Mäkeläinen

Department of Structural Engineering
Helsinki University of Technology
Rakentajanaukio 4, FIN-02150 Espoo, Finland

ABSTRACT

The so-called Gauss-Seidel iteration method is normally used in the analysis of statically indeterminate frame structures. It is simple, avoids solving of simultaneous equations and has clear physical interpretation, which also guarantees the convergence of the iteration process. In order to utilize these advantages the authors are applying the physical principles of the Gauss-Seidel method into the analysis of the flexural behaviour of a composite member in setting up a numerical model for such kind of structural members. First description is given for the basic principles and formulations. Then an effective algorithm for accelerating the convergence is developed. Finally the possible errors of this process are briefly discussed.

1. INTRODUCTION

Steel-concrete composite flexural members, like beams and slabs, are composed of steel and concrete parts and some means of connection to activate the composite action for the two components. Generally the connection can not be fully rigid, i.e. the composite action is usually incomplete. To investigate this incomplete composite behaviour is one of the main subjects in the studies of composite structures.

In order to study the incomplete behaviour it is important to set up some analytical model for investigating load effects (i.e. stresses, strains and deflections) on the member from the commencement of loading up to the ultimate strength state of the member. Because composite members involve different material properties and steel-concrete interaction behaviour, to set up an accurate analytical model is proven to be a difficult task. In the pre-computer era, the differential equation method[3] served as a good tool. But this method is not able to deal with nonlinear material problems. This greatly degrades its practical importance because in most practical cases material nonlinearity is an important factor to be considered. Ansourian and Roderick [1] have set up a method, which may be called the equilibrium method. This

method takes equilibrium for discrete sections. The compatibility condition among all sections is realized by defining a slip strain, the interface slip rate in the axial direction of the member. In principle, this method is able to take in to account any nonlinearities, including the nonlinear steel and concrete material properties and the nonlinear load-slip relationship of connectors. But in reality to solve the simultaneous equations involving these three sources of nonlinearities is difficult. Untill these years some different ways of solving the equations have been presented [1], [2], [4] but non of these ways is universal. In order to solve the nonlinear simultaneous equations they have to satisfy some additional conditions. This leads to some limitations on the applicability of those methods. A method will be described in this article offering a way to solve the problem without losing any main parameters.

Suppose there is a composite beam of an arbitrary mono-symmetric cross-section shape (for the sake of convenience the flexural members will be referred as beams unless in case of necessary to differentiate beams and slabs) as shown in Fig. 1. Under the action of known external bending moment M(x), in a cross-section *i* the following equations must be satisfied:

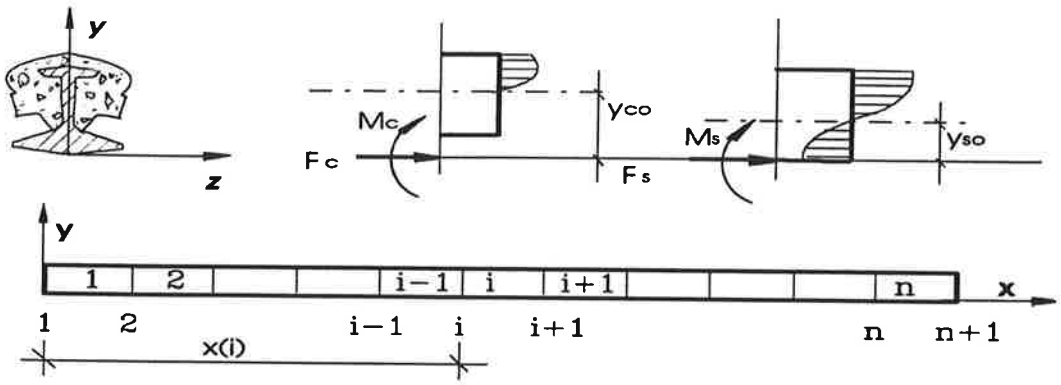

Fig. 1. A beam divided into *n* elements and the stress distribution in a section.

$$Fc(i) + Fs(i) = 0 \tag{1}$$

$$M(i) = Mc(i) + Ms(i) \tag{2}$$

$$Fc(i) = \int_{Ac} Ec \cdot \rho(i) \cdot [y - y_{c0}(i)] \cdot dA \tag{3}$$

$$Fs(i) = \int_{As} Es \cdot \rho(i) \cdot [y - y_{s0}(i)] \cdot dA \tag{4}$$

$$Mc(i) = \int_{Ac} y \cdot Ec \cdot \rho(i) \cdot [y - y_{c0}(i)] \cdot dA \tag{5}$$

$$Ms(i) = \int_{As} y \cdot Es \cdot \rho(i) \cdot [y - y_{s0}(i)] \cdot dA \tag{6}$$

where $\rho(i)$ _ Curvature of the beam at section i;

Ec, Es _Tangent moduli of concrete and steel, respectively;

$y_{c0}(i)$, $y_{s0}(i)$ _ Height of the neutral axis for concrete and steel, respectively.

In the case of complete action, equation $y_{c0}(i)=y_{s0}(i)$ holds. There are all together 6 unknowns $Fc(i)$, $Mc(i)$, $Fs(i)$, $Ms(i)$, ρ (i) and $y_{s0}(i)$ with 6 equations. The problem can be solved for any individual section. However, for incomplete composite cases $y_{c0}(i) \neq y_{s0}(i)$. Thus there are 7 unknowns with 6 equations. In these cases it is not possible to solve the problem on the basis of individual sections.

Suppose that the beam is divided into n segments of beam elements by $n+1$ sections as shown in Fig. 1. Let us define the slip strain ε_{sp} as:

$$\varepsilon_{sp}(i) = \frac{s(i) - s(i+1)}{x_{i+1} - x_i} \tag{7}$$

Assume that the concrete part and the steel part are only connected by connectors and the connectors are concentrated at those n+1 sections. Denote the connection force in connector i as $Fconn(i)$. The following relationship must exist:

$$Fc(i) = \sum_{j=1}^{i} Fconn(j) \tag{8}$$

or

$$Fconn(i) = Fc(i) - \sum_{j=1}^{i-1} Fconn(j) \tag{8'}$$

On the other hand, the connector force $Fconn(i)$ is a known function of the slip $s(i)$:

$$Fconn(i) = \varphi[s(i)] \tag{9}$$

In eq. (9) the function $\varphi[s(i)]$ can be obtained from connector tests or is defined by design specifications.

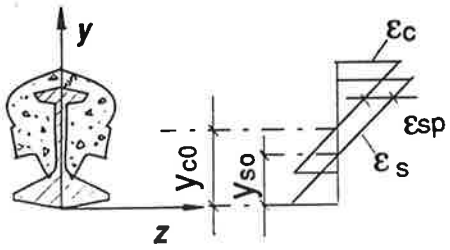

Fig. 2 Strain distribution over the cross-section.

If the commonly used Kirchhoff or Bernoulli-Navier assumption (cross-sections remain planes in bending) is adopted (Fig 2.) the following eq. (10) can be derived:

$$\Delta\varepsilon(i) = \frac{s(i) - s(i+1)}{x_{i+1} - x_i} = \varepsilon_{sp(i)}$$

$$\Delta\varepsilon(i) = \rho(i) \cdot \Delta y = \rho(i) \cdot (y_{c0}(i) - y_{s0}(i)$$

$$\therefore \quad \frac{s(i) - s(i+1)}{x_{i+1} - x_i} = \rho(i) \cdot [y_{c0}(i) - y_{s0}(i)] \tag{10}$$

Now for each section there are 2 unknowns *S(i), Fconn(i)* and 3 equations (8), (9) and (10) have been added. So the problem can be solved but the simultaneous equations coupling all the *n+1* sections are involved. Note that when steel and concrete adopt nonlinear properties the integrations in eq.(1) to eq.(6) can not have closed form. They can only be numerically integrated. If load-deformation function φ of connector is also nonlinear solving of this set of simultaneous numerical equations will be extremely difficult. That is why in previous works [1], [2], [4] some linearizations or localized linearizations have to be taken. It is seen that the difficulty of solving the problem is mainly because all sections are coupled. If a way can be found to decouple all the sections the solution will be easier.

2. APPLICATION OF THE GAUSS-SEIDEL ITERATION METHOD

In order to avoid solving nonlinear simultaneous equations, the physical principle of the Gauss-Seidel iteration method can be applied here.

a. Assume complete interaction for the whole beam, from equation (1) to (6) *Fc(i)* and $\rho(i)$ are obtained for every section. This corresponds to the 'clamping' stage in Gauss-Seidel iterations.

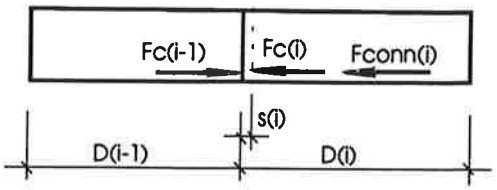

Fig. 3. Section equilibrium.

b. For each section there is an unbalanced force *Fc(i-1)-Fc(i).* This unbalanced force tends to cause section *i* to slip. If the 'clamp' is released, section *i* will slip. When section *i* has a slip increment Δ *s(i),* neutral axis of section *i* and section *i-1* are changed according to *eq.(10).* From *eq. (1)* to *(6)* the new *F(i)* and $\rho(i)$ are obtained. Condition for a stable state of section *i* is that eq.(*11)* is satisfied.

$$Fc(i-1) - Fc(i) - Fconn(i) = 0 \qquad (11)$$

This is the 'releasing' stage for section *i.*

c. Apply step b. for every section consecutively and repeat along the beam untill balance is reached for all sections. Criteria for the balance of a section is as follows:

$$Fc(i) - \sum_{j=1}^{i-1} Fconn(j) \le (\text{specified accuracy}) \cdot Fc(i) \qquad (12)$$

When (12) is satisfied for every section the process is converged. $\rho(i)$, $y_{c0}(i)$ *and* $y_{s0}(i)$ are obtained for all values of *i.*

After the convergence deflection *y(x)* of the beam can be integrated as:

$$y(x)=\int_0^x\left[\int_0^\eta \rho\cdot d\xi\right]\cdot d\eta+\int_0^x C1\cdot dx+C2 \qquad (13)$$

where C1 and C2 are constants determined by boundary conditions of the beam.

3. ACCELERATION THE CONVERGENCE

The process converges fast in cases when there are not many elements or when the stiffness of connectors is comparable with the axial stiffness of concrete component. Whenever the connector stiffness is very low or the connection level is low the process converges very slowly. It can be as slow as to make the process practically worthless. The reason for this is as follows: when a section is released all the rest sections are still fixed. Axial stiffness of the concrete part prevents the section from moving to its 'expected' place. So the slip increment in one round of iteration is very limited. In the case of low connection level slips can only propagate from the ends to the central part of the beam. In order to make this method practically valuable an algorithm accelerating the convergence of the process has to be developed. In view of this the authors have developed an algorithm to accelerate the convergence. By applying it in to different cases it has shown significant efficiency and universality.

The principle of the method is to apply the extrapolation technique in the iteration process. The algorithm predicts the final slip pattern by making use of the finished iteration results. It goes in the following way: Beginning from iteration round k let the programme iterate a further m round of iterations. Record the values of unbalanced forces $F_{unbalanced}(i)=Fc(i)-\sum_{j=1}^{i-1}Fconn(j)$ and slips *slip(i)* for every section at iteration round k and iteration round k+m. The changes in *slip(i)* during this m round of iterations are:

$$_{\Delta}slip(i)=[slip(i)]_{k+m}-[slip(i)]_k \qquad i=1,2,\ldots n+1, \qquad (14)$$

Whereas the unbalanced force changes in this m round of iterations are:

$$_{\Delta}F_{unbalanced}(i)=[F_{unbalanced}(i)]_{k+m}-[F_{unbalanced}(i)]_k, \quad i=1,2,\ldots n+1, \qquad (15)$$

The present unbalanced forces are:

$$F_{unbalanced}(i)=[F_{unbalanced}(i)]_{k+m}, \qquad i=1,2,\ldots n+1$$

Then, the expected final slips *slip(i)* are:

$$slip(i)=[slip(i)]_{k+m}+\left|\frac{_{\Delta}slip(i)}{_{\Delta}F_{unbalanced}(i)}\right|\cdot F_{unbalanced}(i), \text{ i=1,2, ... n+1, } \qquad (16)$$

In this way, a pattern of slips along the beam is prescribed. The process can go on with iteration from this prescribed pattern of slips. This process can be repeatedly used untill the convergence of the iteration. Sometimes in the calculation process $_{\Delta}F_{unbalanced}(i)$ may approach zero. In such cases just omit the second term on the right side of *eq. (16)*.

Eq. (16) works like a penalty function. It 'pulls' the slips to their equilibrium state. The value inside the absolute sign determines how much the 'fine rate' will be. Because it makes use of previous iteration results, the algorithm is robust and efficient.

Now the problem is to choose a suitable iteration interval m. If m is too small, the process may jump back and forth (finally it will converge, though) because iteration process can not give a good prediction for convergence. If m is too large, the process converges slower because less accelerating algorithms have been used. Experience of the authors shows that a value of m=5 is good for many cases except for cases of unevenly distributed connections. A value of m=10 is satisfactory for most cases.

Experience shows that the developed algorithm is very efficient. The authors have experienced a case of nonconvergence after 10000 rounds of iterations without applying the accelerating process. With the help of this algorithm convergence can be reached within 100 rounds of iterations for one load step for most cases. One other advantage of this algorithm is that it only slightly add extra work for the computer.

4. ERRORS

The errors of the process itself are controlled by the given accuracy of sectional equilibrium. It is very easy to check if eq. *(1)* to *(6)* and eq. *(8)*, *(9)* and *(10)* are satisfied. Apart from this, there are two main sources of errors for the process. The first error source is in the basic material and sectional assumptions, e.g. the Kirchhoff assumption, which is totally independent of this solving method. The second basic error source originates in the calculation of the forces *Fc(i)*.

For the convenience of calculation, steel and concrete components are assumed to be connected with each other only by connectors concentrated at discrete sections. So, *Fc(i)* is constant along element for every *i*. But the curvature along the element varies because the external moment *M(x)* is not constant. For the sake of simplicity, it is much easier to calculate $\rho(i)$ and *Fc(i)* by assuming that steel and concrete are continuously interconnected along the element, and to use *Fc(i)* and $\rho(i)$ calculated in the section on the immediate right side of section *i* for the element *i*. The errors caused by this simplification increase as the element length increases for a given load (in the case of pure bending there is no error whatever the element length is).

For slabs without actual 'connectors' like composite slabs, concentration of the connection on to every section also causes errors. Anyway, considering the physical differences between the assumption and the actual situation, it is not expected to have significant effect, especially when the element length is chosen to be small.

It must be indicated that the second source of error discussed above is not an inherent error of the described iteration method. It is an error caused by simplification of the calculation. Adoption of continuous interconnection model (for members without real connectors, like slabs) or calculation of the actual axial forces in elements (for members with connectors) does not prevent the application of this

method. It is a matter of balance between the amount of calculation work and the amount of gained accuracy. The accuracy of the simplified calculation can be increased by using smaller element length. But no matter how accurate the 'accurate' calculation is, the element length can not be chosen to be longer than the actual connector spacing. So the simplified calculation is more flexible in controlling both accuracy and amount of calculation work.

5. DISCUSSIONS

The principle of Gauss-Seidel iteration method is applied into the analysis of incomplete composite flexural members. The algorithm developed for accelerating the convergence makes this concept practically applicable. Introduction of the Gauss-Seidel iteration principle makes it possible and easy to solve the nonlinear simultaneous numerical equations. The main advantages of this method can be summarized as follows:

a. Simple and accurate
The whole process and formulations are simple. The physical idea is clear. These two together make the programming easy. Further the simplicity does not cause a lose of accuracy.

b. Broadly applicable
Former works have been specifically devoted to composite beams or composite slabs. In the process of solution there might be a need for further assumptions which are not applicable for general cases. The process introduced here can be easily applicable to both beams and slabs. No extra assumption is needed for important factors such as material properties. Factors like geometrical variations of sections along the beam axis, uneven distributions of connectors, end posts (for slabs) or endplates (for beams) and additional reinforcement can be easily taken into account.

REFERENCES

1. P. Ansourian, J. W. Roderick, 'Analysis of Composite Beams', *J. of the structural division*, ASCE, ST10, October, 1978, pp1631 - 1645.

2. M. A. Bradford, R. I. Gilbert, 'Composite Beams with Partial Interaction under Sustained Loads', *J. of Structural Engineering*, ASCE, Vol. 118, No. 7, July, 1992, pp1871 - 1883.

3. N. M. Newmark, C. P. Siess, I. M. Viest, 'Tests and analysis of composite beams with incomplete interaction', *Proc. Soc. Experimental Stress Analysis*, Vol. 9, No.1, 1951, pp75 - 92.

4 K. W. Poh, M. M. Attard, 'Calculating the Load-deflection Behaviour of Simply-supported Slabs with Interface Slip', *Engineering Structures,* Vol. 15, No. 5, 1993, pp 359 - 367.

ON THE MODELLING OF THE CORE AND THE LOCAL LOAD DISTRIBUTION IN SANDWICH PANELS

Lassi Martikainen and Paavo Hassinen
Laboratory of Structural Mechanics
Helsinki University of Technology
Rakentajanaukio 4A, FIN-02150 Espoo, FINLAND

ABSTRACT

Sandwich panels subjected to localized loads are often analyzed by modelling the locally loaded face as a beam on an elastic foundation. This paper introduces two problems related to such analysis: modelling of the core to find out the foundation parameters and a mathematical formulation of the local load. The foundation model representation of the core is formed by Vlasov's variational method. The treatment enables determination of the foundation parameters by means of the elastic constants of the isotropic core material. The degree of concentration of the localized lateral load is estimated by a function in which one constant regulates the shape of the load distribution.

1. INTRODUCTION

Sandwich panels consisting of two thin faces and a soft core which is made of plastic foam or mineral wool and glued between faces have become increasingly popular in structural applications. These panels are often subjected to localized loads such as point loads, line loads or distributed loads of high intensity. The loads can cause significant local deflections of the face associated with high stresses in the core and the face. Stress concentrations can lead to a failure of the panel due to yielding or buckling of the face or crushing of the core. These failures violate the bearing capacity of the panel and might be crucial to the safety of the whole structure.

The action of localized loads on sandwich beams with vertically flexible core is approached by considering the deflection of the loaded face against the not loaded one, i.e. the model of a beam on an elastic foundation. Different representations like Winkler`s foundation, two-parameter foundation and elastic continuum models are used to describe the behaviour of the core [1],[2],[3]. Winkler's model approximates the response of the core by linear translation springs and thus completely neglects the shear stiffness. This simple model may be contrasted with continuum models that permit an accurate description of the physical properties of the core but are mathematically rather complicate. Between these models lies a two-parameter foundation model which is physically more accurate than Winkler's model but mathematically

simpler than the elastic continuum. A two-parameter model approximates the response of the core by simple describtion in governing differential equation of the face including two foundation parameters whose determination has proved to be problematic. The first part of this paper deals with the modelling the core by Vlasov's two-parameter foundation [4],[5]. The procedure, based on the variational method allows the foundation parameters to be determined directly from the elastic properties of the core.

For the analysis of local stresses and deflections of sandwich panel the external localized load has to be modelled mathematically, also. Often the resultant and the contact area of the load is known or can well be approximated. The shape of the load distribution has a significant effect on the stresses of the sandwich panel near the loaded region. It would be desirable to find a simple function to estimate different degrees of concentration of the total load. For that, a simple mathematical formulation of the local load is introduced in the second part of the paper.

2. MODELLING THE CORE BY A TWO-PARAMETER FOUNDATION

The well known names, Filonenko-Borodich, Pasternak, Wieghardt, Reissner, Hetenyi and Vlasov [6] have proposed foundation models that involve more than one parameter for the characterization of the supporting medium. One way to develop a two-parameter model is to improve Winkler's model by introducing some kind of interaction between the springs. Another way is to simplify the continuum model by assuming certain restrictions for the displacements of the continuum. The response function of the foundation is stated using the vertical displacement w(x) on the surface of the foundation. Mathematically two-parameter models lead to the equivalent expression for the foundation pressure p(x) [7]:

$$p(x) = k_w w - k_1 \frac{d^2 w}{dx^2} \tag{1}$$

where k_w is the Winkler´s foundation modulus and k_1= the second foundation parameter. The only difference between the various two-parameter models is the definition of the second parameter. For example, Filonenko-Borodich's foundation parameter k_1 may be considered as a constant tension in the membrane that connects the tops of the springs of the Winkler foundation. In the case of Pasternak foundation the existence of shear interaction is assumed between the spring elements. The parameter k_1 characterizes the assumed shear layer. It should be noticed that Winkler's model can be recovered as a limiting case when the parameter k_1 tends to zero.

The properties of typical core materials can vary very much in different directions. Calculation models are usually based on the assumption of the isotropy, in which only two elastic constants are required. The modulus of elasticity E_c and the shear modulus G_c in the direction of the depth are often known or at least comparatively easy to determine by experiments. It could be practical to try to express the foundation parameters by means of these elastic constants. Vlasov's approach [4] to the two-parameter foundation model offers an excellent way to estimate theoretically the parametres k_w and k_1.

Vlasov and Leont'ev have based their two-parameter foundation model on the application of a variational method. By assuming some simplifying restrictions upon the displacement field in

an elastic layer, the formulation (1) for the foundation reaction can be achieved. Let us consider the state of plane strain in a system consisting of a beam and an elastic layer shown in Fig. 1. The layer is assumed to be isotropic with the modulus of elasticity E_c, the shear modulus G_c and Poisson ratio υ_c. The thickness of the layer is H. The beam has an infinite length and a bending stiffness B_f. The lateral load q(x) is distributed symmetrically with respect to the y-axis within the length of 2c along the beam.

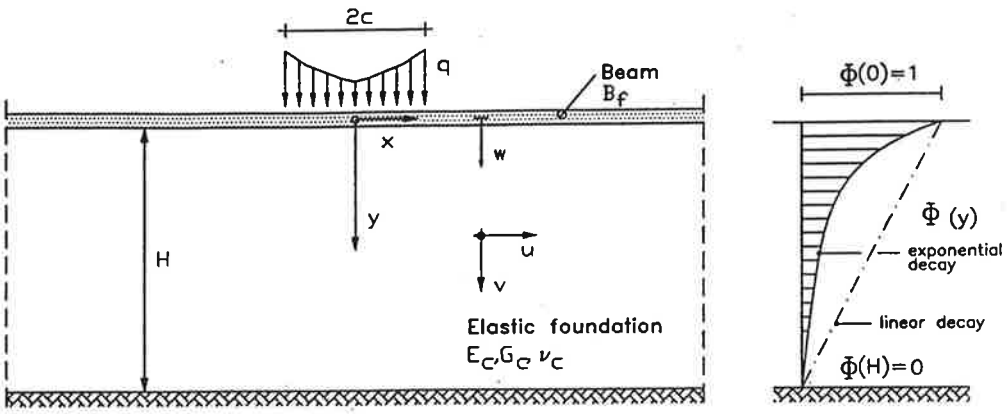

FIGURE 1. Beam on an elastic layer. Example of the vertical displacement profiles are shown in the picture; v(x,y)=w(x)Φ(y).

The use of the minimum potential energy theorem [5] is very useful when deriving the governing equations for a beam on an elastic foundation. The total potential energy of the system is

$$\Pi = \frac{1}{2}\int_{-\infty}^{\infty}(B_f w''^2)\,dx + \frac{b}{2}\int_{-\infty}^{\infty}\int_{0}^{H}(\sigma_x\varepsilon_x + \sigma_y\varepsilon_y + \tau_{xy}\gamma_{xy})\,dydx - \int_{-c}^{c}(qw)\,dx \qquad (2)$$

For brevity, the differentiation with respect to axial coordinate x is denoted by the prime. The elastic stresses in the foundation can be expressed by the constitutive equations and the kinematic relations between the displacements and strains:

$$\begin{Bmatrix}\sigma_x\\ \sigma_y\\ \tau_{xy}\end{Bmatrix} = \frac{E_0}{(1-\upsilon_0^2)}\begin{bmatrix}1 & \upsilon_0 & 0\\ \upsilon_0 & 1 & 0\\ 0 & 0 & \frac{1-\upsilon_0}{2}\end{bmatrix}\begin{Bmatrix}\frac{\partial u}{\partial x}\\ \frac{\partial v}{\partial y}\\ \frac{\partial u}{\partial y}+\frac{\partial v}{\partial x}\end{Bmatrix} \qquad (3)$$

where $E_0 = \dfrac{E_c}{(1-\upsilon_c^2)}$, $\upsilon_0 = \dfrac{\upsilon_c}{1-\upsilon_c}$ for plane strain state in the x-y plane.

The horizontal displacement u(x,y) is supposed to be negligible when compared with the displacement v(x,y) and assumed to zero everywhere in the core. The vertical displacement field v(x,y) is described by the product of two independent functions:

$$u(x,y) = 0$$
$$v(x,y) = w(x)\,\Phi(y) \tag{4}$$

The function Φ(y) describes the profile of the vertical displacement in the direction of the thickness of the foundation (Fig.1). It is chosen so that Φ(0)=1 and Φ(H)=0. An example for the function Φ(y) is given later. The function w(x) depends only on x-coordinate and can be interpreted to be the deflection of the beam.

Substituting the displacements (4) to the stress components (3) and further into the expression of the total potential energy (2), one can get

$$\Pi = \frac{1}{2}\int_{-\infty}^{\infty}(B_f w''^2)\,dx - \int_{-c}^{c}(qw)\,dx + \frac{E_c b}{2}\int_{-\infty}^{\infty}\int_{0}^{H}\left\{\frac{(1-\upsilon_c)}{(1+\upsilon_c)(1-2\upsilon_c)}w^2\left(\frac{d\Phi}{dy}\right)^2 + \frac{1}{2(1+\upsilon_c)}(w')^2\Phi^2\right\}dy\,dx \tag{5}$$

By applying variational calculus, the equilibrium condition δΠ=0 leads to the following differential equation for the beam in the region $|x| \le c$:

$$B_f w^{(4)} - k_1 w'' + k_w w = q \tag{6}$$

where the parameters k_w and k_1 are

$$k_1 = \int_0^H \frac{E_c b}{2(1+\upsilon_c)}\Phi^2 dy \tag{7}$$

$$k_w = \int_0^H \frac{E_c b(1-\upsilon_c)}{(1+\upsilon_c)(1-2\upsilon_c)}\left(\frac{d\Phi}{dy}\right)^2 dy \tag{8}$$

For $k_1 \le \sqrt{4k_w B_f}$ the general solution for the homogeneous part of the Eq. (6) can be written as

$$w = (C_1 e^{\beta_0 x} + C_2 e^{-\beta_0 x})\cos\alpha_0 x + (C_3 e^{\beta_0 x} + C_4 e^{-\beta_0 x})\sin\alpha_0 x\ , \tag{9}$$

where

$$\alpha_0 = \sqrt{\sqrt{\frac{k_w}{4B_f}} - \frac{k_1}{4B_f}}\ , \qquad \beta_0 = \sqrt{\sqrt{\frac{k_w}{4B_f}} + \frac{k_1}{4B_f}}\ . \tag{10}$$

The complete solution of Eq. (6) is obtained by superponizing the particular integral corresponding to q(x) to the solution (9). For $c < x < \infty$, where q(x) equals to zero, the solution (9) can be applied directly with no particular solution. The constants C_i in the expression for deflection can be determined from boundary conditions of the problem.

The solution of the beam subjected to a single force proves to be very useful. The solution can be expanded by integration for any distributed loading on an infinitely long beam. The expressions for the deflection and the bending moment due to a point load P at origin can be expressed as follows:

$$w(x)=\frac{Pe^{-\beta_0 x}}{4B_f\alpha_0\beta_0\sqrt{k_w B_f}}\{\alpha_0\cos\alpha_0 x+\beta_0\sin\alpha_0 x\}\qquad(x\geq 0)\tag{11}$$

$$M(x)=\frac{Pe^{-\beta_0 x}}{4\alpha_0\beta_0}\{\alpha_0\cos\alpha_0 x-\beta_0\sin\alpha_0 x\}\qquad(x\geq 0)\tag{12}$$

The vertical decay of the displacements in the continuum is still unknown. Different shape functions for the displacement are presented by Vlasov [4] including linear, hyperbolic and exponential decrease of vertical displacement. The last two are suitable for analysis of thick foundations. In the analysis of the local instability of sandwich panels the core is often treated as a semi-infinite medium (H→∞) in which the displacements decrease exponentially. Because of the localized nature of the problem studied in this paper, the exponential decay is applicable here, too:

$$\Phi(y)=e^{-\frac{\gamma}{L}y},\quad \text{where}\quad L=\sqrt[3]{\frac{2B_f(1-\upsilon_0^2)}{bE_0}}\tag{13}$$

The displacement shape function Φ(y) includes a dimensionless constant γ, which regulates the shape of the chosen displacement profile. The bending stiffness of the beam is incorporated to the shape function Φ(y) via the characteristic length L, defined by Vlasov [4].

Using the relation $E_c=2G_c(1+\upsilon_c)$ between elastic constants of an isotropic material and the exponential decay of the vertical displacement (13), the foundation parameters expressed by (7) and (8) can be written as follows:

$$k_1=\frac{bG_c}{2\gamma}\sqrt[3]{\frac{2}{b}\frac{B_f}{G_c}\frac{\xi-3}{\xi-4}}\tag{14}$$

$$k_w=\frac{\gamma bG_c}{2}\sqrt[3]{\frac{b}{2}\frac{G_c}{B_f}\left(\frac{\xi-4}{\xi-3}\right)^4}.\tag{15}$$

where $\xi=E_c/G_c$. Theoretically the ratio ξ for an isotropic medium varies between two and three according to the value of Poisson ratio of zero and a half, respectively. For typical core material, the value of ξ is closer to two than to three. The Poisson ratio $\upsilon_c=0$ (ξ=2) is chosen in many cases because of the lack of better information.

3. MATHEMATICAL FORMULATION OF THE LOCALIZED LOAD

The load distribution q(x) has to be described mathematically to apply it in Eq.(6). In practice the exact load distribution is unknown and relatively difficult to determine. However, it is often possible to determine the resultant of the local load. Also the size of the loaded area (Fig.1.; -c≤x≤c) is conceivable. Then the effect of the distribution of the load can be demonstrated through different types of pressure patterns. Thomsen [2] has taken a so called 'generalized function' to illustrate the load distribution. A 'generalized function' is a function with the ability

to approximate the Dirac Delta Function. For example, a load configuration symmetric about y-axis could be described using the function

$$q(x) = \frac{q_0\,\varepsilon}{(1-e^{-\varepsilon})} e^{-\varepsilon\left|\frac{x}{c}-1\right|} \quad , \quad q_0 = \frac{R}{2c}. \tag{16}$$

If R and c are constants, ε determines the maximum value of q(x) and its location. It should be noticed that the integral of q(x) over the length [-c,c] is independent of the parameter ε:

$$2\int_0^c q(x)dx = R\,. \tag{17}$$

One practical application for the function (16) is the description of a symmetric support pressure at the intermediate support, when R corresponds the total support reaction and q(x) is the contact stress distribution between the sandwich panel and the substructure. Thus the load (16) acts only on the length [-c,c] and is zero elsewhere. The parameter ε could be associated with the flexural stiffness of the sandwich panel and the support. In principle, the support pressure depends on the ratio of the flexural rigidities of the panel and the support plate. In the case of a very stiff substructure ($\varepsilon\to\infty$), like a steel profile or a concrete column, the distribution concentrates near the edges of the support area. Another extreme case is a very flexible support ($\varepsilon\to-\infty$) when the load is concentrated on the centerline of the support width. When the support plate and the sandwich beam have the equal stiffness ($\varepsilon\to0$), q(x) is uniformly distributed over the support width.

The load function (16) is illustrated by a numerical example of a beam on a two-parameter foundation. The deflection and the bending moment of the beam for five distributions of the total load R are shown in Fig. 2. Because of symmetry only one half of the x-axis is shown in the picture. The values of the vertical axes correspond to the ratio of the deflection (moment) and the maximum deflection (maximum moment) due to the point load R (reference load case). The numerical values used in calculations are shown also in Fig. 2. The geometry and the material data correspond to realistic properties of sandwich panels used in building applications. The foundation parameters are calculated using formulae (14) and (15). The decay factor γ is fixed and has the value of unity. The results are calculated from the solution for a point load (11) and (12) by integration.

The solutions corresponding to the five different values of ε are presented in Fig. 2. The results for ε= -100 are very close to the results obtained for a point load which is applied to the beam at x=0. In the case of ε=100 the total load is concentrated near to the edges of the loaded area and the maximum values are reduced to about a half of the case ε=-100. To illustrate the behaviour of the load function the results are calculated using the values ε=-5 and ε=5, too. The load distribution corresponding to the value $\varepsilon=10^{-5}$ resembles a uniform distribution over the width [-c,c]. The maximum of the bending moment is much less compared with other given cases. The calculated example shows the significant effect of the shape of the load distribution on the behaviour of the loaded region. By changing the degree of the concentration, i.e. the value of ε, in the load function (16), the behaviour of the sandwich panel near different load patterns can be examined.

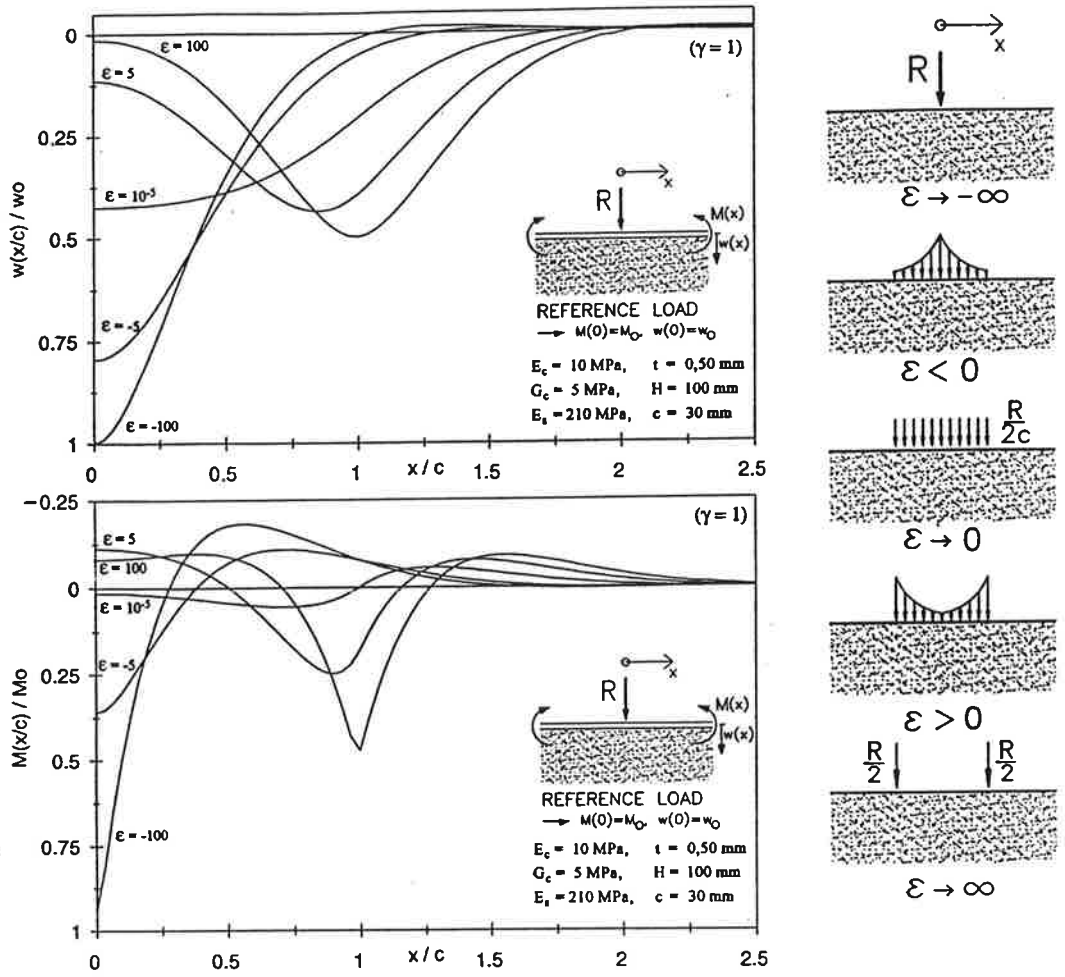

FIGURE 2. Distribution of the deflection and the bending moment of the face in the vicinity of the localized load. Different pressure shapes obtained from the function (16) based on different values of ε are shown in the figure.

4. CONCLUSIONS

Two problems related to sandwich panels subjected to localized loads are considered. The first problem concerns the modelling of the core layer when the panel is loaded in vertical direction. The Vlasov's two-parameter foundation model is applied for the analysis of local stresses and deflections of the face in a sandwich panel. Foundation parameters are derived by the variational approach using the exponential decay for the displacements in the core depth direction. The exponential decay is chosen because it is usually applied in the local buckling analyses of the face, too. Parameters are expressed as functions of the elastic properties of the sandwich panel and the decay factor γ.

In the second part of the paper a mathematical description for the localized load is presented. The total load distributed within a certain length, is expressed in the form of a generalized function. The function is capable to simulate different distributions of the load. A simple example is calculated to show that the shape of the load distribution has notable effects on the behaviour of the face close to the loaded region.

REFERENCES

1. Y. Frostig, M. Baruch, Bending of sandwich beams with transversely flexible core, AIAA Journal, 28, (1990) 523-531

2. O.T. Thomsen, "Further remarks on local bending analysis of sandwich panels using a two-parameter elastic foundation model", Aalborg University, Institute of Mechanical Engineering, Report No.40, 1992

3. D. Weissman-Berman, G.L. Petrie, M.-H. Wang, Flexural response of foam-cored FRP sandwich panels. SNAME Transactions, 96, (1988) 73-95

4. V.Z. Vlasov and U.N. Leontiev, "Beams, plates and shells on elastic foundations", Israel Program for Scientific Translations Ltd, Jerusalem, 1966

5. C.V.G. Vallabhan and Y.C. Das, Parametric study of beams on elastic foundations, Journal of Engineering Mechanics,12, (1988) 2072-2080

6. A.D. Kerr, Elastic and viscoelastic foundation models, Journal of Applied Mechanics, September, (1964) 491-498

7. F. Zhaohua and R.C. Cook, Beam-elements on two-parameter elastic foundations, Journal of Engineering Mechanics, 6, (1983) 1390-1402

RE-EXAMINATION OF THE EQUATIONS OF LATERAL BUCKLING OF THIN-WALLED BEAMS

MARTTI MIKKOLA and JUHA PAAVOLA
Laboratory of Structural Mechanics
Helsinki University of Technology
Rakentajanaukio 4A, FIN-02150 ESPOO, FINLAND

ABSTRACT

In the present paper the problem of lateral buckling of a straight beam with a thin-walled cross-section is investigated. The principle of stationary potential energy is applied in the derivation of the equilibrium equations. It is shown that the energy principle results in the equations deviating slightly from those derived traditionally by use of the equilibrium consideration. The reasons for the deviation will be speculated as well.

1. BASIC KINEMATICS

A beam with an arbitrarily shaped thin-walled cross-section is considered. As a frame a global Cartesian coordinate system x, y, z with unit vectors $\vec{e}_x, \vec{e}_y, \vec{e}_z$ is defined. The axial coordinate x coincides with the beam axis, i.e. goes through the centroid of each cross-section plane. Coordinates y and z are the principal axes of the cross-section. In addition, coordinate s with unit vector $\vec{e}_s$ follows the middle line of the cross-section's wall and coordinate n with $\vec{e}_n$ is its normal. For the simplicity, the beam is assumed to be composed of planar plates so that the cross-section is formed of piecewise straight sections as shown in Fig. 1. The displacement components of the shear center in the directions of the coordinate axes are u, v, w and the rotation of the cross-section ϕ. The displacement vector of a point of the middle surface of the wall follows from the usual assumptions made in the theory of thin-walled beams,

$$\vec{u}_o = (u - yv' - zw' - \omega\phi')\vec{e}_x + (v - (z - z_v)\phi)\vec{e}_y + (w + (y - y_v)\phi)\vec{e}_z. \qquad (1)$$

It means that the linear part of the shear strain γ_{xs} disappears at the middle surface of the wall and that the cross-section does not distort in its plane. Here, ω is the sectorial coordinate and y_v, z_v the coordinates of the shear center. The loading is assumed to include an axial centric compressive load $p_x^o(x)$ and distributed loads $p_y^o(x)$ in the principal xy-plane and $p_z^o(x)$ in the xz-plane.

FIGURE 1. Thin-walled cross-section and coordinate systems.

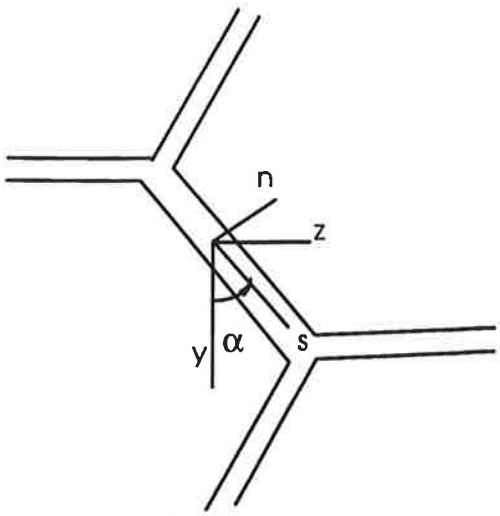

Under these assumptions the expressions of the axial normal strain ϵ_x and the shear strain γ_{xs} at the middle surface of the cross-section, including the second order terms, are

$$\begin{aligned}\epsilon_x &= \frac{\partial \vec{u}_o}{\partial x}\cdot\vec{e}_x + \frac{1}{2}\,\frac{\partial \vec{u}_o}{\partial x}\cdot\frac{\partial \vec{u}_o}{\partial x},\\ \gamma_{xs} &= \frac{\partial \vec{u}_o}{\partial s}\cdot\vec{e}_x + \frac{\partial \vec{u}_o}{\partial x}\cdot\vec{e}_s + \frac{\partial \vec{u}_o}{\partial x}\cdot\frac{\partial \vec{u}_o}{\partial s}.\end{aligned} \tag{2}$$

The derivatives needed to define the strains (2) are calculated from the displacement vector (1)

$$\begin{aligned}\frac{\partial \vec{u}_o}{\partial x} &= (u' - yv'' - zw'' - \omega\phi'')\vec{e}_x + (v' - (z-z_v)\phi')\vec{e}_y + (w' + (y-y_v)\phi')\vec{e}_z,\\ \frac{\partial \vec{u}_o}{\partial y} &= (-v' - \frac{\partial \omega}{\partial y}\phi')\vec{e}_x + \phi\vec{e}_z,\\ \frac{\partial \vec{u}_o}{\partial z} &= (-w' - \frac{\partial \omega}{\partial z}\phi')\vec{e}_x - \phi\vec{e}_y.\end{aligned} \tag{3}$$

To obtain the correspondence between the coordinate systems y, z and s, n in the cross-section plane with angle α, the unit vectors

$$\begin{aligned}\vec{e}_s &= \cos\alpha\vec{e}_y + \sin\alpha\vec{e}_z,\\ \vec{e}_n &= -\sin\alpha\vec{e}_y + \cos\alpha\vec{e}_z,\end{aligned} \tag{4}$$

and likewise the transformation between the derivatives

$$\begin{aligned}\frac{\partial}{\partial s} &= \cos\alpha\frac{\partial}{\partial y} + \sin\alpha\frac{\partial}{\partial z},\\ \frac{\partial}{\partial n} &= -\sin\alpha\frac{\partial}{\partial y} + \cos\alpha\frac{\partial}{\partial z},\end{aligned} \tag{5}$$

are required. The normal strain will get the expression

$$\begin{aligned}\epsilon_x = (u' - yv'' - zw'' - \omega\phi'') + \tfrac{1}{2}\,[&(u' - yv'' - zw'' - \omega\phi'')^2\\ &+ (v' - (z-z_v)\phi')^2 + (w' + (y-y_v)\phi')^2].\end{aligned} \tag{6}$$

The shear strain is calculated by applying the coordinate transformation in (4) and (5)

$$\begin{aligned}\gamma_{xs} = \frac{\partial \vec{u}_o}{\partial x}\cdot(\cos\alpha\vec{e}_y + \sin\alpha\vec{e}_z) + (\cos\alpha\frac{\partial \vec{u}_o}{\partial y} + \sin\alpha\frac{\partial \vec{u}_o}{\partial z})\cdot\vec{e}_x\\ + \frac{\partial \vec{u}_o}{\partial x}\cdot(\cos\alpha\frac{\partial \vec{u}_o}{\partial y} + \sin\alpha\frac{\partial \vec{u}_o}{\partial z}),\end{aligned} \tag{7}$$

which will obtain the form

$$\begin{aligned}\gamma_{xs} =&(v' - (z - z_v)\phi')\cos\alpha + (w' + (y - y_v)\phi')\sin\alpha \\ &+ (-v' - \frac{\partial\omega}{\partial y}\phi')\cos\alpha + (-w' - \frac{\partial\omega}{\partial z}\phi')\sin\alpha \\ &+ (u' - yv'' - zw'' - \omega\phi'')[(-v' - \frac{\partial\omega}{\partial y}\phi')\cos\alpha + (-w' - \frac{\partial\omega}{\partial z}\phi')\sin\alpha] \\ &+ \phi[-(v' - (z - z_v)\phi')\sin\alpha + (w' + (y - y_v)\phi')\cos\alpha].\end{aligned} \tag{8}$$

The linear part of the shear strain in the middle surface of the cross-section vanishes which is in accordance with the assumption involved in the expression of displacement (1). This can be seen directly from the definition of the sectorial coordinate

$$d\omega = -(z - z_v)dy + (y - y_v)dz, \tag{9}$$

resulting in expressions

$$\frac{\partial\omega}{\partial y} = -(z - z_v), \qquad \frac{\partial\omega}{\partial z} = (y - y_v). \tag{10}$$

Assuming further that the normals to the middle surface of the cross-section remain normal the displacement vector of the point at distance n from the middle surface is

$$\vec{u} = \vec{u}_o - nv_n'\vec{e}_x - n\phi\vec{e}_s, \tag{11}$$

Here v_n is the displacement component in the direction of the normal which can be found by use of the coordinate transformation. Then the expression (11) obtains the form

$$\vec{u} = \vec{u}_o - n[-(v' - (z - z_v)\phi')\sin\alpha + (w' + (y - y_v)\phi')\cos\alpha]\vec{e}_x - n\phi\vec{e}_s. \tag{12}$$

Using the definition of strains (2) yields additional linear terms both of normal and shear strains which describe the deformation at distance n from the middle surface

$$\begin{aligned}\epsilon_x &= n\left[(v'' - (z - z_v)\phi'')\sin\alpha - (w'' + (y - y_v)\phi'')\cos\alpha\right], \\ \gamma_{xs} &= -2n\phi'.\end{aligned} \tag{13}$$

The additional term in the normal strain is related to the bending of the walls of the cross-section and will be dropped in the continuation. The shear strain is associated with SAINT VENANT torsion.

2. PRINCIPLE OF MINIMUM POTENTIAL ENERGY

The procedure follows exactly the linearized theory, called also EULER method, presented for example by NOVOZHILOV [1] and WASHIZU [3], according to which the increment of strain energy of the beam is

$$\Delta U = U_L + U_{NL} = \frac{1}{2}\int_V (\sigma_x\epsilon_x^* + \tau_{xs}\gamma_{xs}^*)dV + \int_V (\sigma_x^o\epsilon_x^{**} + \tau_{xs}^o\gamma_{xs}^{**})dV. \tag{14}$$

Here, the linear relationship between the incremental strains ϵ_x^* and γ_{xs}^* and σ_x, τ_{xs}, respectively, is assumed so that U_L includes only the linear parts of expressions (2) for strains and the higher order terms are neglected. σ_x^o and τ_{xs}^o are the initial stresses in the initial position the stability of which will be studied and the strains ϵ_x^{**} and γ_{xs}^{**}. The expression of the strain energy is thus separated into two parts, of which the other U_L represents the energy due to the linearized deformation and the other U_{NL} takes into account the initial stresses and the second order terms in the expressions of strains. It is, of course, also assumed that the initial deflection v^o is negligible.

HOOKE's law between strains and stresses in U_L is adopted. Thus, the first variation of the strain energy U_L takes the form

$$\begin{aligned}\delta U_L &= \int_0^L dx \int_A \Big[E(u'\delta u' + y^2 v''\delta v'' + z^2 w''\delta w'' + \omega^2\phi''\delta\phi'') + 4Gn^2\phi'\delta\phi'\Big]dA \\ &= \int_0^L (EAu'\delta u' + EI_z v''\delta v'' + EI_y w''\delta w'' + EI_\omega\phi''\delta\phi'' + GI_t\phi'\delta\phi')dx,\end{aligned} \tag{15}$$

in which the familiar notations for the axial, two bending, warping and torsional rigidities

$$\int_A dA = A, \quad \int_A y^2 dA = I_z, \quad \int_A z^2 dA = I_y, \quad \int_A \omega^2 dA = I_\omega, \quad \int_A 4n^2 dA = I_t, \tag{16}$$

are introduced. In addition, due to the assumptions concerning the coordinate system the following integrals over the cross-sectional area vanish

$$\int_A y dA = \int_A z dA = \int_A \omega dA = \int_A yz dA = \int_A y\omega dA = \int_A z\omega dA = 0. \tag{17}$$

Consider the nonlinear part of strain energy U_{NL}. The part involving linear strains $U_{NL,1}$ will disappear since the stresses σ_x^o and τ_{xs}^o satisfy equations of equilibrium. The part containing nonlinear part of strains is

$$\begin{aligned}U_{NL,2} = \int_V \tfrac{1}{2}\sigma_x^o[&\underline{(u' - yv'' - zw'' - \omega\phi'')^2} + (v' - (z-z_v)\phi')^2 + (w' + (y-y_v)\phi')^2]dV \\ &+ \int_V \tau_{xs}^o\Big\{\underline{(u' - yv'' - zw'' - \omega\phi'')[(-v' - \frac{\partial\omega}{\partial y}\phi')\cos\alpha + (-w' - \frac{\partial\omega}{\partial z}\phi')\sin\alpha]} \\ &+ \phi[-(v' - (z-z_v)\phi')\sin\alpha + (w' + (y-y_v)\phi')\cos\alpha]\Big\}dV,\end{aligned} \tag{18}$$

It is easy to show, NOVOZHILOV [1], that the underlined terms above describe the effect of pure deformation. In stability analyses they usually are assumed to be small compared to the terms due to the rotations, i.e. the terms without underlining, and are neglected as insignificant. The following form for the first variation is thus obtained

$$\begin{aligned}\delta U_{NL,2} = \int_V \sigma_x^o[&(v' - (z-z_v)\phi')(\delta v' - (z-z_v)\delta\phi') \\ &+ (w' + (y-y_v)\phi')(\delta w' + (y-y_v)\delta\phi')]dV \\ &+ \int_V \tau_{xs}^o\Big\{\delta\phi[-(v' - (z-z_v)\phi')\sin\alpha + (w' + (y-y_v)\phi')\cos\alpha] \\ &+ \phi[-(\delta v' - (z-z_v)\delta\phi')\sin\alpha + (\delta w' + (y-y_v)\delta\phi')\cos\alpha]\Big\}dV,\end{aligned} \tag{19}$$

The stresses at the initial position are determined according to the simple beam theory being

$$\sigma_x^o = \frac{N^o}{A} + \frac{M_z^o}{I_z}y + \frac{M_y^o}{I_y}z, \qquad \tau_{xs}^o = \frac{Q_y^o S_z(y)}{I_z t} + \frac{Q_z^o S_y(z)}{I_y t}. \tag{20}$$

These are substituted into equation (19) resulting in the final formulation for the nonlinear part of the strain energy

$$\begin{aligned}\delta U_{NL} = \int_0^L \Big\{ & N^o[(z_v v' - y_v w' + r^2\phi')\delta\phi' + (v' + z_v\phi')\delta v' + (w' - y_v\phi')\delta w'] \\ & + M_z^o[(w' + 2\beta_y\phi')\delta\phi' + \phi'\delta w'] - M_y^o[(v' - 2\beta_z\phi')\delta\phi' + \phi'\delta v'] \\ & + Q_y^o[\beta_y(\phi'\delta\phi + \phi\delta\phi') + (w'\delta\phi + \phi\delta w')] \\ & + Q_z^o[\beta_z(\phi'\delta\phi + \phi\delta\phi') - (v'\delta\phi + \phi\delta v')]\Big\} dx.\end{aligned} \tag{21}$$

Here the notations

$$\begin{gathered}\beta_y = \frac{1}{2I_z}\int_A y(y^2+z^2)dA - y_v, \qquad \beta_z = \frac{1}{2I_y}\int_A z(z^2+y^2)dA - z_v, \\ r^2 = \frac{I_y + I_z}{A} + y_v^2 + z_v^2,\end{gathered} \tag{22}$$

arising in the integration over the cross-sectional area are used.

The increment of potential energy of the external loads is correspondingly

$$V = -\int_0^L [p_y^o(v - \tfrac{1}{2}e_y\phi^2) + p_z^o(w - \tfrac{1}{2}e_z\phi^2) + p_x^o u]dx, \tag{23}$$

in which e_y and e_z are the eccentrities of the distributed loads from the shear center. The first variation of the external potential is

$$\delta V = -\int_0^L [p_y^o(\delta v - e_y\phi\delta\phi) + p_z^o(\delta w - e_z\phi\delta\phi) + p_x^o\delta u]dx \tag{24}$$

and the variation of the total potential energy is summed up of the three terms calculated

$$\delta\Pi = \delta U_L + \delta U_{NL} + \delta V = 0. \tag{25}$$

Substituting now the expressions (15), (21) and (24) into (25), integrating twice by parts yields first the equations of equilibrium of the initial state, which are of course satisfied, and secondly

$$\begin{aligned}\int_0^L \Big\{ & \delta u[-EAu''] \\ & + \delta v[EI_z v'''' - (N^o v')' - z_v(N^o\phi')' + (M_y^o\phi')' + (Q_z^o\phi)'] \\ & + \delta w[EI_y w'''' - (N^o w')' + y_v(N^o\phi')' - (M_z^o\phi')' - (Q_y^o\phi)'] \\ & + \delta\phi[EI_\omega\phi'''' - GI_t\phi'' - z_v(N^o v')' + y_v(N^o w')' - r^2(N^o\phi')' - M_z^o w'' + M_y^o v'' \\ & - 2\beta_y(M_z^o\phi')' - 2\beta_z(M_y^o\phi')' - \beta_y(Q_y^o)'\phi + p_y^o e_y\phi - \beta_z(Q_z^o)'\phi + p_z^o e_z\phi]\Big\} dx = 0.\end{aligned} \tag{26}$$

This results in the differential equation system of lateral buckling of a thin-walled beam

$$
\begin{aligned}
&EAu'' + p_x^o = 0,\\
&EI_z v'''' - (N^o v')' - z_v(N^o\phi')' + (M_y^o\phi)'' - p_y^o = 0,\\
&EI_y w'''' - (N^o w')' + y_v(N^o\phi')' - (M_z^o\phi)'' - p_z^o = 0,\\
&EI_\omega\phi'''' - GI_t\phi'' - z_v(N^o v')' + y_v(N^o w')' - r^2(N^o\phi')' - M_z^o w''\\
&\qquad - 2\beta_y(M_z^o\phi')' + M_y^o v'' - 2\beta_z(M_y^o\phi')' + \underline{p_y^o\beta_y\phi} + p_y^o e_y\phi + \underline{p_z^o\beta_z\phi} + p_z^o e_z\phi = 0.
\end{aligned}
\tag{27}
$$

The underlined terms do not appear in the traditional equations of lateral buckling, for example in [2,5]. Integration by parts produces further the boundary conditions at the ends of the beam $x = 0$ and $x = L$, which are

$$
\begin{aligned}
if\quad \delta u \neq 0, &\qquad EAu' = 0,\\
\delta v' \neq 0, &\qquad EI_z v'' = 0,\\
\delta v \neq 0, &\qquad -EI_z v''' + N^o(v' + z_v\phi') - (M_y^o\phi)' = 0,\\
\delta w' \neq 0, &\qquad EI_y w'' = 0,\\
\delta w \neq 0, &\qquad -EI_y w''' + N^o(w' - y_v\phi') + (M_z^o\phi)' = 0,\\
\delta\phi' \neq 0, &\qquad EI_\omega\phi'' = 0,\\
\delta\phi \neq 0, &\qquad -EI_\omega\phi''' + GI_t\phi' + N^o(z_v v' - y_v w' + r^2\phi')\\
&\qquad + M_z^o(w' + 2\beta_y\phi') - M_y^o(v' - 2\beta_z\phi') + \underline{Q_y^o\beta_y\phi} + \underline{Q_z^o\beta_z\phi} = 0.
\end{aligned}
\tag{28}
$$

The corresponding additional terms are visible also in the boundary conditions. It is easy to see that the terms dropped out from (13) and (18) cannot include terms which could cancel the additional terms in (27) and (28) since they depend at least on the first derivative of the rotation.

3. EQUILIBRIUM CONSIDERATION

The equilibrium consideration is performed in a usual way, following the procedure of VLASOV [2], by separating it to stages where at first the resultants of shear forces and twisting moment due to initial stress components σ_x^o and τ_{xs}^o in the deformed configuration are evaluated. The role of these resultants is to work as a fictitious loads which are inserted into the equilibrium equations. The stress resultants due to σ_x^o are simply integrated over the cross-sectional area as

$$
\begin{aligned}
\Delta Q_z^{\sigma_x^o} &= \int_A (\sigma_x^o + \Delta\sigma_x^o)\,[w' + \Delta w' + (\phi' + \Delta\phi')(y - y_v)]\,dA - \int_A \sigma_x^o\,[w' + \phi'(y - y_v)]\,dA,\\
\Delta Q_y^{\sigma_x^o} &= \int_A (\sigma_x^o + \Delta\sigma_x^o)\,[v' + \Delta v' - (\phi' + \Delta\phi')(z - z_v)]\,dA - \int_A \sigma_x^o\,[v' - \phi'(z - z_v)]\,dA,\\
\Delta M_t^{\sigma_x^o} &= -\int_A (\sigma_x^o + \Delta\sigma_x^o)\,\{[v' + \Delta v' - (\phi' + \Delta\phi')(z - z_v)](z - z_v)\\
&\quad -[w' + \Delta w' + (\phi' + \Delta\phi')(y - y_v)]\}\,dA\\
&\quad + \int_A \sigma_x^o\,\{[v' - \phi'(z - z_v)](z - z_v) - [w' + \phi'(y - y_v)](y - y_v)\}\,dA,
\end{aligned}
\tag{29}
$$

producing after integration

$$\begin{aligned}
\Delta Q_z^{\sigma_x^o} &= \Delta(N^o w') - y_v \Delta(N^o \phi') + \Delta(M_z^o \phi'),\\
\Delta Q_y^{\sigma_x^o} &= \Delta(N^o v') + z_v \Delta(N^o \phi') - \Delta(M_y^o \phi'),\\
\Delta M_t^{\sigma_x^o} &= z_v \Delta(N^o v') - y_v \Delta(N^o w') + r^2 \Delta(N^o \phi')\\
&\quad + \Delta(M_z^o w') - \Delta(M_y^o v') + 2\beta_z \Delta(M_z^o \phi') + 2\beta_y \Delta(M_y^o \phi').
\end{aligned} \tag{30}$$

Correspondingly, the stress resultants due to the initial shear stress τ_{xs}^o are

$$\begin{aligned}
\Delta Q_y^{\tau_{xs}^o} &= -\int_A (\tau_{xs}^o + \Delta\tau_{xs}^o)(\phi + \Delta\phi)\cos(\alpha + \phi + \Delta\phi)dA + \int_A \tau_{xs}^o \phi \cos(\alpha + \phi)dA,\\
\Delta Q_z^{\tau_{xs}^o} &= \int_A (\tau_{xs}^o + \Delta\tau_{xs}^o)(\phi + \Delta\phi)\sin(\alpha + \phi + \Delta\phi)dA - \int_A \tau_{xs}^o \phi \sin(\alpha + \phi)dA,\\
\Delta M_t^{\tau_{xs}^o} &= \int_A (\tau_{xs}^o + \Delta\tau_{xs}^o)[-(z - z_v) - w - \Delta w - (\phi + \Delta\phi)(y - y_v)]\cos(\alpha + \phi + \Delta\phi)dA\\
&\quad - \int_A \tau_{xs}^o[-(z - z_v) - w - \phi(y - y_v)]\cos(\alpha + \phi)dA\\
&\quad + \int_A (\tau_{xs}^o + \Delta\tau_{xs}^o)[(y - y_v) + v + \Delta v - (\phi + \Delta\phi)(z - z_v)]\sin(\alpha + \phi + \Delta\phi)dA\\
&\quad - \int_A \tau_{xs}^o[(y - y_v) + v - \phi(z - z_v)]\sin(\alpha + \phi)dA.
\end{aligned} \tag{31}$$

The trigonometric functions are here linearized by

$$\begin{aligned}
\cos(\alpha + \phi + \Delta\phi) &\approx \cos\alpha - \phi\sin\alpha - \Delta\phi\sin\alpha,\\
\sin(\alpha + \phi + \Delta\phi) &\approx \sin\alpha + \phi\cos\alpha - \Delta\phi\cos\alpha.
\end{aligned} \tag{32}$$

The most critical term with respect to the difference between the results of the energy method and the equilibrium consideration is the twisting moment due to the initial shear, i.e. the last expression in (31). In the integration, the fact that there is no torsion in the initial state is utilized validating the condition

$$\int_A \Delta\tau_{xs}^o[-(z - z_v)\cos\alpha + (y - y_v)\sin\alpha]dA = 0. \tag{33}$$

The integration results in the relation in which the dependence on the angle of rotation disappears

$$\Delta M_t^{\tau_{xs}^o} = \int_A \tau_{xs}^o(-\Delta w\cos\alpha + \Delta v\sin\alpha)dA + \int_A \Delta\tau_{xs}^o(-w\cos\alpha + v\sin\alpha)dA. \tag{34}$$

Hence, the three additional stress resultants are

$$\begin{aligned}
\Delta Q_z^{\tau_{xs}^o} &= -\Delta(Q_y^o\phi) = -(Q_y^o\phi)'\Delta x,\\
\Delta Q_y^{\tau_{xs}^o} &= \Delta(Q_z^o\phi) = (Q_z^o\phi)'\Delta x,\\
\Delta M_x^{\tau_{xs}^o} &= -\Delta(Q_y^o w) + \Delta(Q_z^o v) = (-Q_y^o w + Q_z^o v)'\Delta x.
\end{aligned} \tag{35}$$

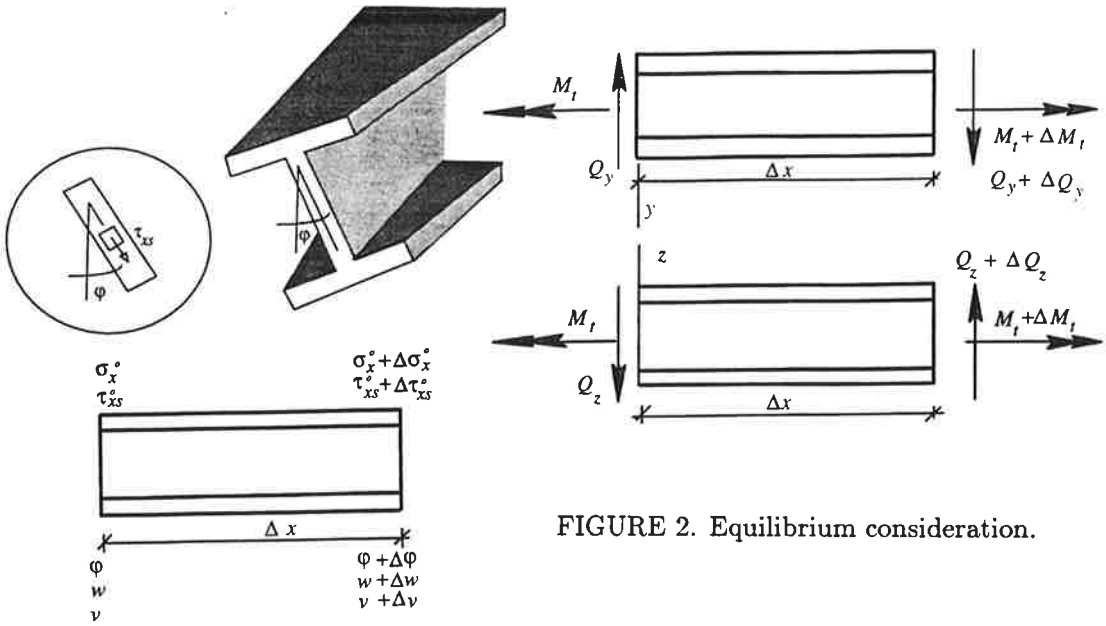

FIGURE 2. Equilibrium consideration.

According to the theory of thin-walled beams the shear forces and twisting moment due to additional displacements are

$$Q_y = -EI_z v'''; \quad Q_z = -EI_y w'''; \quad M_t = -EI_\omega \phi''' + GI_t \phi'. \tag{36}$$

Further, they must satisfy the equilibrium equations

$$\begin{aligned} \Delta(Q_y + Q_y^{\sigma_x^\circ} + Q_y^{\tau_{xs}^\circ}) &= 0, \\ \Delta(Q_z + Q_z^{\sigma_x^\circ} + Q_z^{\tau_{xs}^\circ}) &= 0, \\ \Delta(M_t + M_t^{\sigma_x^\circ} + M_t^{\tau_{xs}^\circ}) &= 0. \end{aligned} \tag{37}$$

Together with (30), (35) and (36) these yield the differential equation system (27) in which the underlined terms are absent. As a conclusion, two possible reasons for the deviation in the equations are deduced. Firstly, the equilibrium consideration in the deformed curved configuration is not complete, or secondly, the kinematics of the beam (1) is in some sense inconsistent either adding some terms in the energy approach or leaving them out in the equilibrium approach.

REFERENCES

1. V.V. Novozhilov, "Foundations of the Nonlinear Theory of Elasticity", 3rd ed., Graylock Press Rochester, New York, 1963
2. V.Z. Vlasov, "Thin-Walled Elastic Beams", Israel Program for Scientific Translations, Israel, 1963
3. K. Washizu, "Variational Methods in Elasticity and Plasticity", Pergamon Press Ltd., 2nd Edition, 1975
4. J.T. Oden, "Finite Elements of Nonlinear Continua", McGraw-Hill Book Company, Advanced engineering series, New York, 1972
5. W.F. Chen and T. Atsuta, "Theory of Beam-Columns, Volume 2 Space Behavior and Design", McGraw-Hill Book Company, New York, N.Y. 1977

ANALYSIS OF THE FIRE RESISTANCE OF COMPOSITE COLUMNS

JUKKA MYLLYMÄKI
Fire Technology
Technical Research Centre of Finland
P.O. Box 1803, FIN-02044 VTT, FINLAND

ABSTRACT

A method for the structural analysis of eccentrically loaded columns in fire conditions is presented. A pin-ended column is studied. The spatial discretization in the axial direction is carried out by uniform difference mesh. One dimensional hypo-elastic material models developed for Eurocodes and in Technical University of Brunswick are used. Integration of forces in the cross-section is carried out using finite element discretization and Gaussian quadrature.

Some experimental studies have been carried out to determine the fire resistance of loaded square hollow structural steel columns filled with reinforced concrete. Calculation results are compared with results of other programs and also with full scale fire resistance tests of composite columns and with steel column test results.

1. INTRODUCTION

Calculation of the fire resistance of column is carried out in various steps. It involves calculation of the fire temperatures to which the column is exposed, the temperatures in the column cross-sections and deformations and strength of the column during the fire exposure.

Program used in the present paper for temperature calculations is LIPA-program developed by Subnic OY. In LIPA-program finite element method in connection with conditionally stable time integration scheme is used to calculate the temperature distribution in the cross-section. Convective heat transfer is calculated by using Newton's law and radiation heat flux from surface is calculated using by Stefan-Boltzmann equation. Heat conduction is described by the heat balance equilibrium equation and with Fourier-law. Consumption of energy for vaporizing the water are taken into account in a simplified way by suitable design values for the specific heat-capacity of concrete with up to 200 °C.

In VTT Fire Technology a simple method for the structural analysis of eccentically loaded columns in fire conditions is developed. The method is valid only for pin-ended columns. Results of the thermal analysis are used as input for the method.

2. STRUCTURAL ANALYSIS

2.1 Equilibrium equations

Equilibrium equations for pin-ended column are following

$$N_i^{j+1}=N_o$$
$$M_i^{j+1}=N_o(e+v_n^j-v_i^j) \qquad (1)$$

where
- N_o is external normal force,
- v_i^j deflection at node i at Picard iteration step j
- v_n^j deflection at the end of the column at Picard iteration step j
- e eccentricity of the external load,
- N_i^j, M_i^j moment and normal force at Picard iteration step j+1

Here origin of the co-ordinate system is assumed to follow the deformed column at midspan.

2.2 Discretization of the column

The spatial discretization in the axial direction is carried out by uniform difference mesh (fig. 1), with mesh size Δx . In an arbitrary finite difference node the deflection is v_i . Normal force is increased incrementally, and to find out if an equilibrium state is possible for an axial load and a given eccentricity a Picard-type iteration is used inside the force increment step. Reasonable starting values for deflections are the deflections of the previous equilibrium state.

The curvature κ at certain point may be approximately calculated as follows:

$$\kappa = -v_i'' = -\frac{v_{i+1}-2v_i+v_{i-1}}{(\Delta x)^2} \qquad (2)$$

With boundary conditions in the middle of a pin-ended column $v_1=v_{-1}$ and $v_0=0$ we get the following recursive formulas:

$$v_1=-\frac{(\Delta x)^2\kappa_o}{2} \qquad (3)$$

$$v_{i+1}=2v_i-v_{i-1}-(\Delta x)^2\kappa_i \qquad (4)$$

Axial displacement of each point is solved by von Karman formula from the deflections

$$u_{i+1}=u_i+\Delta x\ \varepsilon_i-\frac{1}{2}\frac{(v_{i+1}-v_i)^2}{(\Delta x)^2} \qquad (5)$$

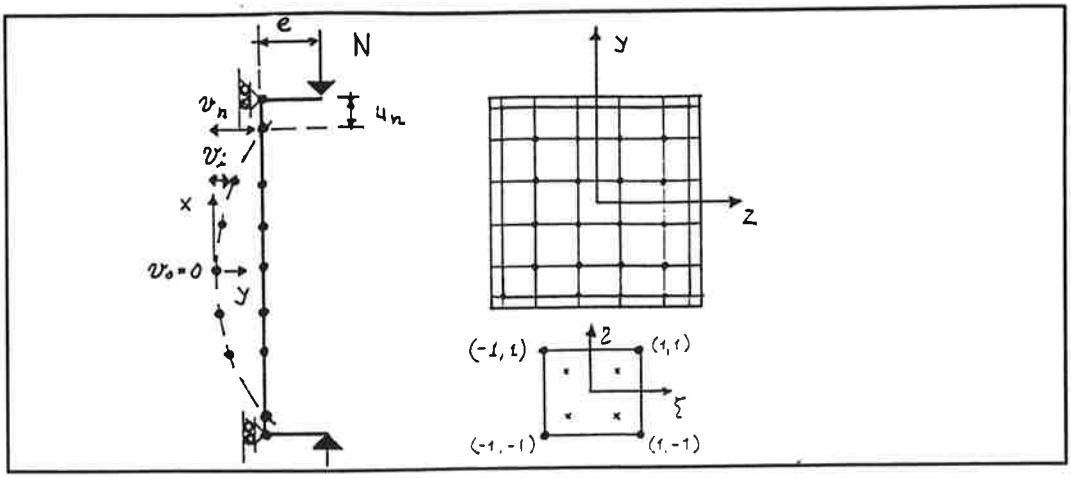

FIGURE 1. Spatial discretization of the column and its cross-section.

One quarter or one half of the column cross-section is divided to 4-node linear elements (Fig. 1) with the same element mesh as in the thermal analysis by LIPA program. Moment and normal force are calculated at each element by using one or four point Gaussian quadrature. For the temperature field $T^e(z,y,t) = \sum_j N_j(z,y)\, T_j^e(t)$ linear Serendip-type shape functions are used.

2.3 Calculation of strain

The problem is geometrically and also materially nonlinear and therefore one has to calculate iteratively the magnitude of curvature κ_1^j and strain ε_1^j at central axis of the column cross-section. This is done by using modified Newton-Raphson method in a following manner:

$$\begin{pmatrix} N_1^j - N_1^{j,k} \\ M_1^j - M_1^{j,k} \end{pmatrix} = \begin{bmatrix} \frac{\partial N_1^{j,k}}{\partial \varepsilon} & \frac{\partial N_1^{j,k}}{\partial \kappa} \\ \frac{\partial M_1^{j,k}}{\partial \varepsilon} & \frac{\partial M_1^{j,k}}{\partial \kappa} \end{bmatrix} \begin{pmatrix} \delta\varepsilon_1^{j,k+1} \\ \delta\kappa_1^{j,k+1} \end{pmatrix} \tag{6}$$

where $N_1^{j,k}, M_1^{j,k}$ are normal force and moment in finite difference node i at k:th Newton-Raphson iteration step during j: th Picard iteration step.

Inserting equations of internal forces and strain

$$\begin{aligned} N_1 &= \int_{A_1} \sigma\, dA \\ M_1 &= \int_{A_1} \sigma y\, dA \\ \varepsilon_{tot} &= \varepsilon + \varepsilon_{th} + \kappa y \end{aligned} \tag{7}$$

where
- ε_{tot} is total strain
- ε force induced strain at central axis of the cross-section
- ε_{th} is thermal strain
- κ force induced curvature

to the matrix equation (6) one gets a matrix equations (8, 9) from which strain and curvature corresponding certain moment and normal force N_1^j, M_1^j can be solved iteratively.

$$\begin{pmatrix} \delta\varepsilon_1^{j,k+1} \\ \delta\kappa_1^{j,k+1} \end{pmatrix} = \begin{bmatrix} \int_A \frac{\partial\sigma}{\partial\varepsilon} dA_1 & \int_A y\frac{\partial\sigma}{\partial\varepsilon} dA_1 \\ \int_A y\frac{\partial\sigma}{\partial\varepsilon} dA_1 & \int_A y^2\frac{\partial\sigma}{\partial\varepsilon} dA_1 \end{bmatrix}^{-1} \begin{pmatrix} N_1^j - N_1^{j,k} \\ M_1^j - M_1^{j,k} \end{pmatrix} \tag{8}$$

$$\begin{aligned} \varepsilon_1^{j,k+1} &= \varepsilon_1^{j,k} + \delta\varepsilon_1^{j,k+1} \\ \kappa_1^{j,k+1} &= \kappa_1^{j,k} + \delta\kappa_1^{j,k+1} \end{aligned} \tag{9}$$

3. CONSTITUTIVE MODELS FOR MECHANICAL PROPERTIES

In Eurocode No.4, Design of Composite Structures [2] one dimensional nonlinear elastic model for strength and deformation properties of uniaxially loaded concrete in compression at elevated temperatures is presented. Values for model parameters, relation between compressive strengths and strain are given for both siliceous and calcareous concretes. Strength and deformation properties of steel at elevated temperatures and a hypo-elastic constitutive equations are also given.

A nonlinear elastic one dimensional material model developed at Technical University of Brunswick (TUBS) is used for stress-strain calculations of both siliceous concrete and different steel qualities. Coefficients of the model for siliceous concrete and several structural and reinforcing steel qualities are given in [3]. Both models are developed based on transient tests and take into account transient creep approximately.

4. NUMERICAL EXAMPLES

4.1 Euler buckling at ambient temperature

During the calculation load is increased stepwise. Calculated axial force-displacement is dependent on the load increment that can be seen in Fig. 2, where midspan deflection w and axial deformation u of an elastic column at ambient temperature has been calculated by using two different load increments.

4.2 Axially loaded steel columns at elevated temperatures

In a paper by Vandamme and Janns [4] a series of full scale tests made at the University of Ghent as well as tests made by Olesen at Aalborg University on centrally loaded steel columns at elevated temperatures are described.

Figure 3 shows the stress results of 29 tests against the theoretical results obtained by presented method. Half of the column was discretized lengthwise with 22 finite difference points. Eurocode steel model was used.

4.3 Composite columns

In the following, results have been compared to the results calculated with LIPA-program,

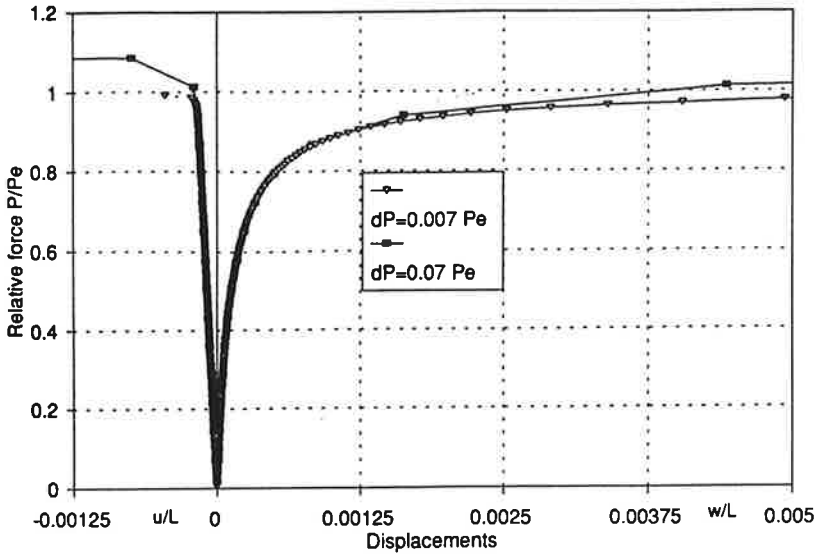

FIGURE 2. Force-displacement curves of a pin-ended column, P_e = Euler buckling load.

which adopts the European buckling curve c [2] in the analysis of composite columns. In the analysis LIPA needs functions for compression strength of concrete and yield strength of both structural steel and reinforcement. Temperature dependence of tangent modulus (for zero stress) derived from the Brunswick model has been used for both concrete and steel. Thermal properties have been those used in the Finnish Fire Technical Design Manual for Composite Columns [5]. Calculated results have also been compared to the results of FEM-program STABA [1] developed in Technical University of Brunswick. In STABA-program the Brunswick model is used.

The studied composite column is a square hollow section 300 x 300 x 12,5 mm of steel grade Fe 52 with reinforcement 8 ø 20 mm grade A500H. Following values of material parameters have been used; compression cylinder strength of concrete 34 N/mm^2, yield strength of structural steel 355 N/mm^2 and yield strength of reinforcement 500 N/mm^2. Temperature field calculated by LIPA-program at time t=30 min has been used as input data for the analysis. In Fig. 6 axial load capacities of the column for a fire grading A 30 are shown as a function of the buckling length.

4.4 Column test in NRC

Experiments of three square hollow steel columns filled with reinforced concrete and a one reinforced concrete column were carried out in the Fire Laboratory of National Research Council of Canada (NRC) in a joint research project sponsored by Rautaruukki Oy. Detailed description of the tests will be published in report [6]. All columns were 3810 mm long from end plate to end plate. The hollow structural sections and end plates consisted of steel meeting the requirements of Finnish Standard SFS 200 grade Fe 52 C. Weldable ribbed bars meeting the requirements of Standard SFS 1215 grade A 500 HW were used for the main and tie bars.

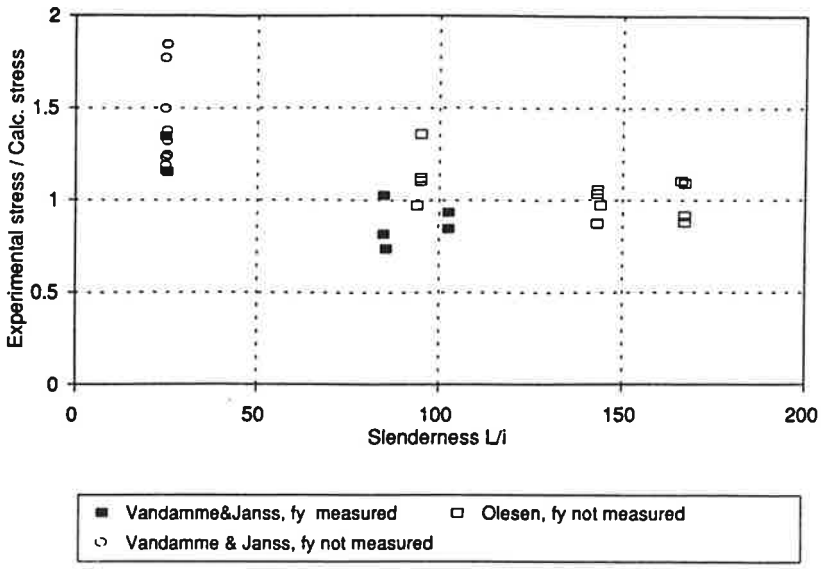

FIGURE 3. The relations of experimental and theoretical result as a function of column slenderness.

In fig. 5 the measured and calculated axial deformations of one of the composite columns are shown. In the table 1 a summary of the calculation data is given. The column was designed to fall at time 30 min. using the simple method of LIPA-program based on moment-normal force diagrams. According to calculation with finite differences column should fail at time 25 minutes. According to LIPA-program's axial deformation calculation the column i still going strong at 80 minutes. The reason for the discrepancy between calculation methods after 20 minutes is that axial deformation calculation in LIPA-program is geometrically linear.

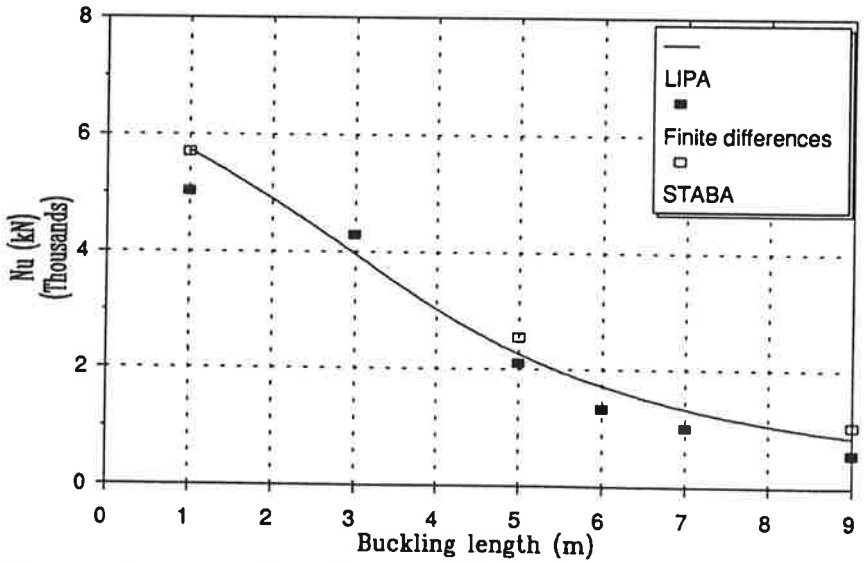

FIGURE 4. Buckling capacities of concrete filled square steel hollow section 300x300x12,5 calculated with LIPA, STABA and presented finite difference method.

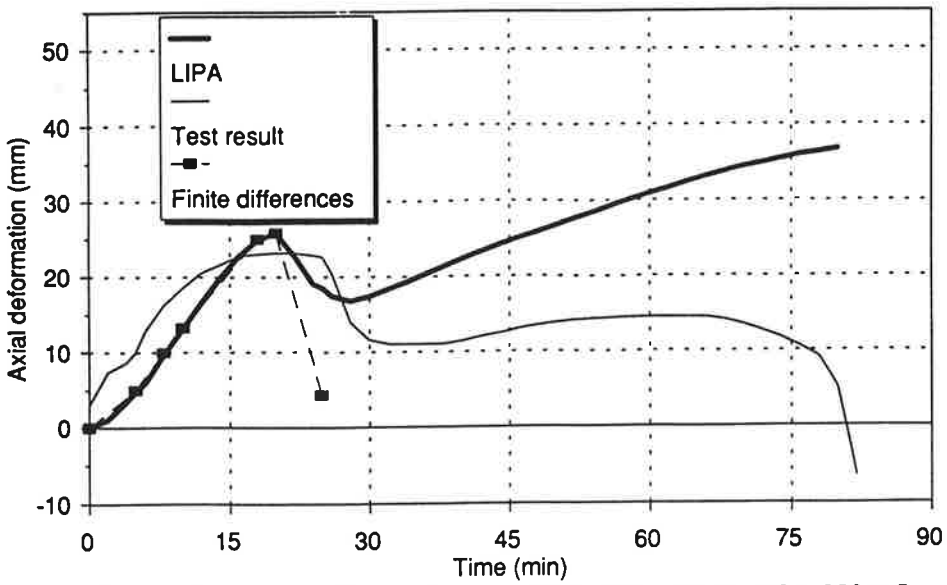

FIGURE 5. Axial deformation 3800 mm long square hollow section 150 x 150 x 5.

TABLE 1. Size and strength of 150 x 150 x 5 composite column.

Column size	Re-bars	K_{150} (28 days)	f_y (HSS)	f_y(re-bars)	Test load	Test duration
150x150x5	4 ø 12 mm	37.5 MPa	416	596 MPa	140 kN	83 min

REFERENCES

1. Hass R., Assessment of the Fire Design of Concrete Filled Hollow Section Columns. Expert's report No. G 91 401. Braunschweig 1991.

2. Eurocode No. 4, Design of Composite Structures, Part 10: Structural Fire Design, Draft April 1990. Commission of the European Communities.

3. Richter E., Spannungs/Dehnungs-Linien zur Berechnung des Trag- und Verformungsverhaltens von Konstruktionsbauteilen unter Feuerangriff.Sonderforschungsbereich 148, Arbeitsbericht 1984-1986, Teil I Band A, Braunschweig 1987.

4. Vandamme, M. & Janns, J. Buckling of Axially Loaded Steel Columns in Fire Conditions. IABSE Periodica 3 (1981).

5. Fire Technical Design Manual for Composite Columns with Concrete Filled Hollow Steel Sections 1992. Helsinki 1992, The Finnish Constructional Steelwork Association. (in Finnish)

6. Myllymäki, J., Lie, T.T., Chabot M. Fire resistance tests of square hollow steel columns filled with reinforced concrete. Ottawa , NRC Canada, Internal Report.

A METHOD FOR REFINED ANALYSIS OF BOX BEAM CROSS SECTIONS

MIKA REIVINEN*, EERO-MATTI SALONEN* and JUHA PAAVOLA**
*Laboratory of Computational Dynamics and **Laboratory of Structural Mechanics
Helsinki University of Technology
Otakaari 1, FIN-02150 Espoo, FINLAND

ABSTRACT

This article describes first steps in an effort to model monolithic junctions of plate and shell structures in a consistent way using (almost) conventional frame analysis concepts. The study here is directed towards the analysis of moderately thick-walled box beams where the cross sections are considered to act as plane frames. The corners are modelled using $n+1$ design parameters where n is the number of beams connected to a corner. For each beam one parameter gives the position of the theoretical end point of the beam. A deforming core is included in the model and its area is related to one additional design parameter. The values of the parameters are determined so that the flexibility matrix of the model is as near as possible to that of the real corner. The main points of the theory used to create the model are explained and some numerical results for a simple test problem are given.

1. INTRODUCTION

Figure 1(a) represents a typical monolithic plane frame corner or junction, (b) the kind of model to be used for it in this study and (c) some details of the model. Traditionally in plane frame analyses the beams are considered as one-dimensional structural members extending to a dimensionless node. If the axes of the members do not intersect at one single point, a small rigid nodal domain is usually employed. The stress distribution in a frame corner is complicated and the assumptions of one-dimensional beam theory of course cease to be valid in the corner region. In this study a real corner is simulated using a simple model consisting of $n+1$ adjustable parameters or so called model parameters $a_1, a_2, \cdots, a_{n+1}$ where n is the number of beams ($n \geq 2$) meeting at the corner. The parameters $a_1, a_2, \cdots, a_n$ are linear measures fixing the theoretical end points of the beam axes in the way shown in Figure 1(c). The last parameter $a_{n+1} = 1/A_c$ where A_c is the area of the so-called core region having deformations to be described shortly. If $a_{n+1} = 0$, the core is considered as rigid. The idea is to determine the model parameters so that the flexibility of the model is as near as possible to that of the real corner. The analysis of the real corner must be performed by a numerical method, say the finite element method. The final purpose is to determine the model

parameters for some common geometries in advance in tabulated forms to be used in practical analyses.

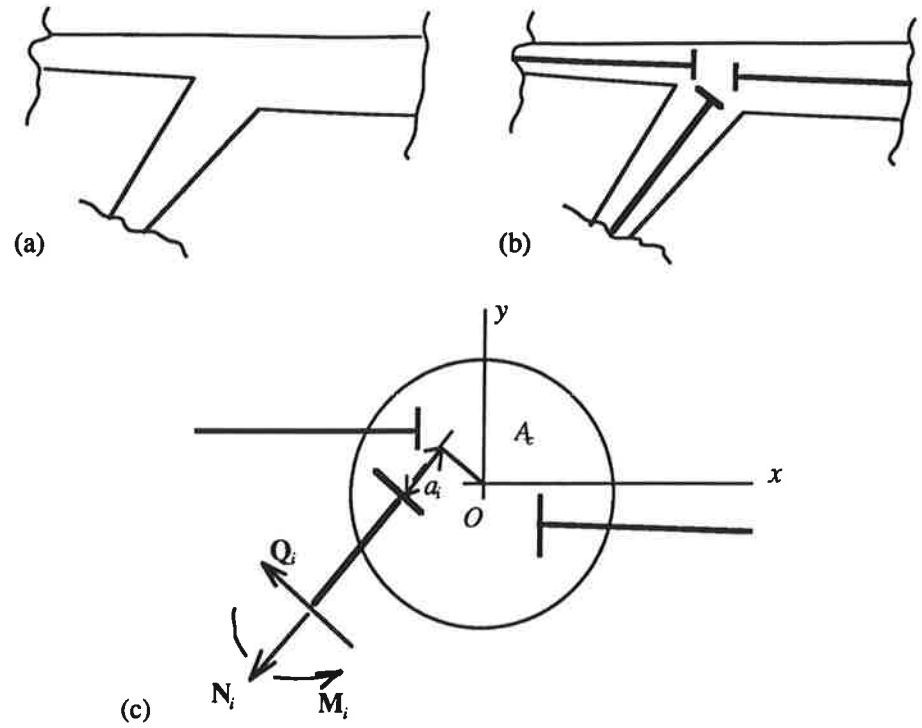

FIGURE 1(a) Frame corner. (b) Corner model. (c) Details of the model

2. JOINT DEFORMATION MODEL

The origin of a local xy-coordinate system is associated with the corner area defining a theoretical centroid of the corner (Fig.1(c)). If the extended beam axes intersect at one point, this is selected as the origin. If not, a weighted average of the intersection points is used. In the neighbourhood of the centroid the components of the displacement field

$$\boldsymbol{u} = u\boldsymbol{i} + v\boldsymbol{j} \tag{1}$$

are assumed to be of the form

$$\begin{aligned} u &= u_0 + (\frac{\partial u}{\partial x})_0 \cdot x + (\frac{\partial u}{\partial y})_0 \cdot y, \\ v &= v_0 + (\frac{\partial v}{\partial x})_0 \cdot x + (\frac{\partial v}{\partial y})_0 \cdot y, \end{aligned} \tag{2}$$

that is, to consist of truncated Taylor expansions up to the linear terms in x and y. The index 0 refers to a value at the origin. A rearrangement of the expressions gives the physically more appealing forms

$$u = u_0 - \theta \cdot y + \varepsilon_x \cdot x + \frac{1}{2}\gamma_{xy} \cdot y,$$
$$v = v_0 + \theta \cdot x + \frac{1}{2}\gamma_{xy} \cdot x + \varepsilon_y \cdot y \tag{3}$$

where

$$\theta = \frac{1}{2}\left(\frac{\partial v}{\partial x} - \frac{\partial u}{\partial y}\right) \tag{4}$$

is the average rotation of the material and

$$\varepsilon_x = \frac{\partial u}{\partial x}, \qquad \varepsilon_y = \frac{\partial v}{\partial y}, \qquad \gamma_{xy} = \frac{\partial v}{\partial x} + \frac{\partial u}{\partial y} \tag{5}$$

are the conventional engineering strain components. The displacement assumptions are considered to be valid on a certain region — called the core — surrounding the centroid. In Figure 1(c) the core region is shown as a circle but no shape is actually attached here to the core, it is only the area A_c assumed for the core which matters.

Six (master) degrees of freedom — $u_0, v_0, \theta, \varepsilon_x, \varepsilon_y, \gamma_{xy}$ — are connected thus with a corner centroid node. The first three are the conventional rigid body motion degrees of freedoms. The latter three are unconventional consisting of the core strains. To be able to use a simple frame analysis program they are calculated at this phase iteratively and appear in the analysis as given load terms. The determination of the core strains is described next. In this section the values of the model parameters are considered as known.

The position vector

$$\mathbf{r}_i = x_i \mathbf{i} + y_i \mathbf{j} \tag{6}$$

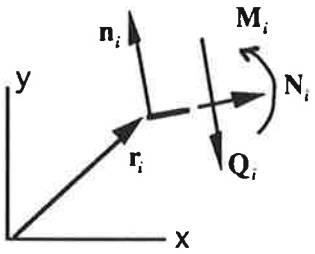

FIGURE 2 Some notations.

in Figure 2 represents the theoretical endpoint of the axis of a typical beam associated with the corner. The beams in this study are restricted to have straight axes and at most linearly

varying depths and are considered as beam elements with cubic deflection, linear axial displacement and constant shear deformation. The kinematic assumption according to the Timoshenko beam theory is used: the material fibers originally perpendicular to the beam axis remain straight but not necessarily perpendicular to the deformed axis. The beam end is now assumed to be "glued" to the core following its deformation via its normal fiber at the endpoint. The unit vector

$$\boldsymbol{n}_i = l_i \boldsymbol{i} + m_i \boldsymbol{j} \tag{7}$$

gives the direction of the normal fiber. The displacement components u_i and v_i of the beam end are obtained from expressions (3) with the coordinates x_i and y_i. The rotation of the fiber evaluated from (3) is found to be

$$\varphi_i = \theta + (\varepsilon_y - \varepsilon_x) l_i m_i + \frac{1}{2}\gamma_{xy}(l_i^2 - m_i^2). \tag{8}$$

The slave degrees of freedom of beam end i — determined by the master degrees of freedom of the centroid node — are u_i, v_i, φ_i.

Consider an analysis of a frame performed starting say with $\varepsilon_x = \varepsilon_y = \gamma_{xy} = 0$ at the cores. The stress resultants $\boldsymbol{N}_i, \boldsymbol{Q}_i, \boldsymbol{M}_i$ (Fig. 2) at the ends of each beam are now known. Here it is convenient to operate with the x- and y-force components and so the notations

$$\boldsymbol{N}_i + \boldsymbol{Q}_i = H_i \boldsymbol{i} + V_i \boldsymbol{j}, \qquad \boldsymbol{M}_i = M_i \boldsymbol{k} \tag{9}$$

are used. It is obvious that the state of stress and strain in the core region must depend somehow on the stress resultants of the beams meeting at the corner. The principle of virtual work is a suitable tool to give some sensible average values for the strains corresponding to the stress resultants.

It is assumed that the core material is isotropic and homogeneous and that plane stress state is here valid. Because of the homogeneous strain state implied by assumption (2), the stress state in the core is then also homogeneous. The principle of virtual work in the form

$$(\sigma_x \delta\varepsilon_x + \sigma_y \delta\varepsilon_y + \tau_{xy}\delta\gamma_{xy}) b A_c = \sum_{i=1}^{n} (H_i \delta u_i + V_i \delta v_i + M_i \delta\varphi_i) \tag{10}$$

is applied for the core material. The left hand side is the negative virtual work of the internal forces in the core region. Quantity b is the breadth of the frame in the z-direction and bA_c is the core volume. The right hand side is the virtual work of the external forces which is considered to consist of the work of the stress resultants at the beam ends acting through the normal fibers. Variation of expressions (3) with respect to ε_x, ε_y and γ_{xy} gives three independent virtual dispacements and homogeneous virtual strain states from which the three unknowns $\varepsilon_x, \varepsilon_y, \gamma_{xy}$ can be determined using (10). The results are

$$\varepsilon_x = \frac{1}{EbA_c}\sum_{i=1}^{n}[H_i x_i - \nu V_i y_i - (1+\nu)M_i l_i m_i],$$

$$\varepsilon_y = \frac{1}{EbA_c}\sum_{i=1}^{n}[V_i y_i - \nu H_i x_i + (1+\nu)M_i l_i m_i], \tag{11}$$

$$\gamma_{xy} = \frac{1}{2GbA_c}\sum_{i=1}^{n}[H_i y_i + V_i x_i + M_i(l_i^2 - m_i^2)]$$

where E is the Young's modulus, G the shear modulus and ν the Poisson's ratio of the material. After the core strains have been evaluated, they can be introduced in (3) as given quantities and the next analysis be performed. Good convergence is to be expected as the beam end stress resultants probably do not change much; in statically determinate cases they do not change at all and the second analysis gives the final results.

3. DETERMINATION OF THE MODEL PARAMETER VALUES

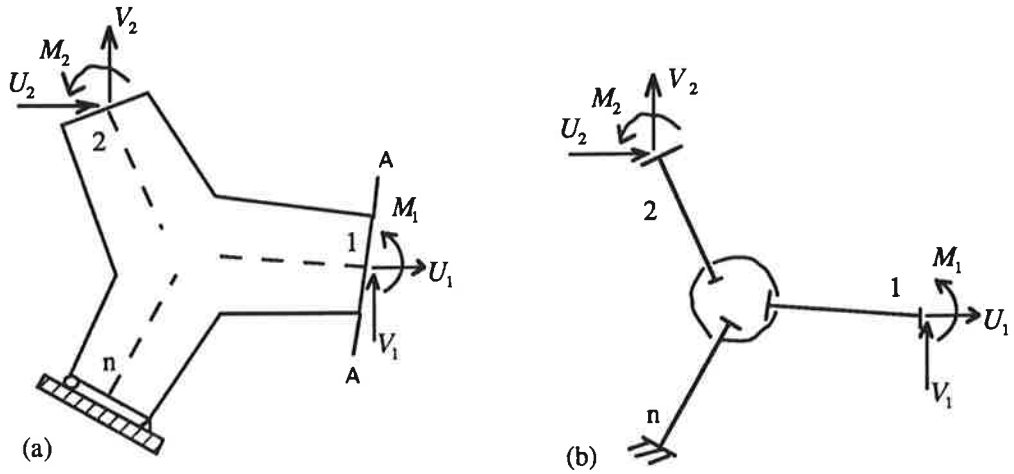

FIGURE 3(a) Corner cantilever structure. (b) Corner cantilever model.

The corner region of the frame is isolated from the rest of the structure (Fig. 3(a)) so that conventional beam theory stress distributions can be assumed to be reasonably valid at the cuts. It was estimated that a flexibility analysis based on certain beamtype tractions on the cuts would be more realistic than a stiffness analysis based on beamtype displacement distributions. The resulting cantilever type continuum structure is supported at one cut, say the one belonging to beam n, so that just the rigid body motions are prevented. Figure 3(b) describes the same configuration for the corner model. The corner model stucture has $k = 3(n-1)$ degrees of freedom $q_1 = u_1, q_2 = v_1, q_3 = \varphi_1, q_4 = u_2, \cdots$ and the corresponding generalized forces are $Q_1 = U_1, Q_2 = V_1, Q_3 = M_1, Q_4 = U_2, \cdots$. It should be noted that in this section the notations refer to the values at the cuts and not to the beam end values studied in section 2. The flexibility relationships

$$\underset{k\times 1}{\{q\}} = \underset{k\times k}{[C]}\,\underset{k\times 1}{\{Q\}} \tag{12}$$

are generated for both the continuum structure and the model. For the model this is straightforward. Quantities $Q_1, Q_2, Q_3, \cdots$ are applied consecutively as loads and the corresponding displacements give the elements of the flexibility matrix. The continuum, however, has in fact infinite number of degrees of freedom and some assumptions have to be made to proceed further. The continuum cannot accept point loads or couples; only distributed tractions.

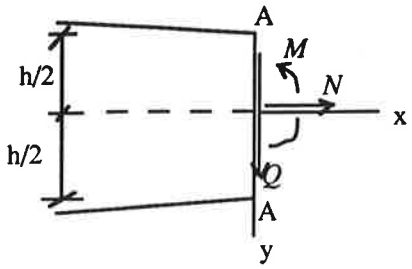

FIGURE 4 Some notations for a beam with varying depth.

A beam theory for smoothly varying beam depth [1] gives after a slight modification the stress distributions (Fig. 4)

$$\sigma_x = \frac{N}{A} + \frac{M}{I}y, \quad \tau_{xy} = \frac{Q}{A}\Psi_Q(y) + \frac{N}{A}\Psi_N(y) + \frac{M}{I}h\Psi_M(y) \tag{13}$$

where

$$\Psi_Q = \frac{3}{2} - \frac{6y^2}{h^2}, \quad \Psi_N = \frac{dh/dx}{h}y, \quad \Psi_M = \frac{3dh/dx}{2h^2}y^2 - \frac{1}{8}\frac{dh}{dx}. \tag{14}$$

The meaning of the notations should be obvious from the conventional beam theory. Tractions (13) are used in the calculation of the continuum model flexibilities. For instance for the loading case $M \neq 0$ at a cut the tractions $\sigma_x = My/I$ and $\tau_{xy} = Mh\Psi_M/I$ are used. Simultaneously the tractions corresponding to the stress resultants induced on the restrained cut must be introduced. One question still remains: what are the corresponding beamtype displacements and rotations at the cuts? The continuum does naturally not in general respond to the loadings by exactly showing the Timoshenko beam theory displacement behaviour. Using the notation of Figure 4 the following expressions for the average displacement components and average fiber rotation

$$\begin{aligned}
\bar{u} &= \int_{-h/2}^{h/2} b[u(y) + \Psi_N(y)v(y)]dy/A, \\
\bar{v} &= \int_{-h/2}^{h/2} b[\Psi_Q(y)v(y)]dy/A, \\
\bar{\varphi} &= \int_{-h/2}^{h/2} b[yu(y) + h\Psi_M(y)v(y)]dy/I
\end{aligned} \tag{15}$$

at the cuts are introduced. The distributions $u(y)$ and $v(y)$ are obtained by a finite element analysis. Expressions (15) are found by equating the work done by the tractions on the continuum displacements in a cross section to the work done by the stress resultant on the average displacements and rotation. Now the the flexibility matrix of the continuum structure can be determined. It is denoted here by the symbol $[\bar{C}]$.

The flexibility matrix elements c_{ij} of the model are functions of the model parameters: $c_{ij} = c_{ij}(a_1, a_2, \cdots, a_{n+1})$.The purpose is to select the parameters so that the flexibility matrix $[C]$ of the model structure is as close as possible to the flexibility matrix $[\bar{C}]$ of the continuum structure. For this goal the least squares expression

$$I(a_1, a_2, \cdots, a_{n+1}) = \frac{1}{2}\sum_{i=1}^{k}\sum_{j=1}^{k}(\bar{c}_{ij} - c_{ij})^2 \tag{16}$$

is formed and minimized in principle with respect to the model parameters. As the dependencies are very complicated, this must be performed numerically and iteratively. Some starting values, say zeroes, are taken for the parameters. The flexibilities are determined. Then consecutively each parameter is given a small fixed change and the altered flexibilities are determined. In this way the so-called sensitivities

$$s_{ij}^{l} = \frac{\Delta c_{ij}}{\Delta a_l}, \qquad l = 1, 2, \cdots, n+1 \tag{17}$$

can be found approximating the derivatives $\partial c_{ij} / \partial a_l$. Thereafter using obvious notations the relationships

$$c_{ij}^{\text{new}} \approx c_{ij}^{\text{old}} + \sum_{l=1}^{n+1} s_{ij}^{l} \Delta a_l \tag{18}$$

can be written down. This expression is substituted in (16) and minimization with respect to the changes Δa_l is performed leading to a linear system of equations from which the changes needed can be determined. The procedure described is repeated with the new parameter values

$$a_i^{\text{new}} = a_i^{\text{old}} + \Delta a_i \tag{19}$$

until the changes are small enough.

4. NUMERICAL EXAMPLE

In the small number of test cases gone through this far the minimization procedure has converged. Figure 5(a) shows a cantilever geometry considered here to represent a corner ($n = 2$). The structure (Poisson's ratio $\nu = 0,2$) has been analysed simply as a two-element beam just to obtain a target flexibility matrix $[\bar{C}]$. The model in Figure 5(b) consists of two uniform beams of height h. Shear correction factor value $\kappa = 5/6$ has been used. The

optimized model parameter values were $a_1 = a_2 = 0{,}038h$ and $a_3 = 43{,}7/h^2$ corresponding to a core radius $r_c = 0{,}085h$. Three iteration steps were needed for acceptable convergence.

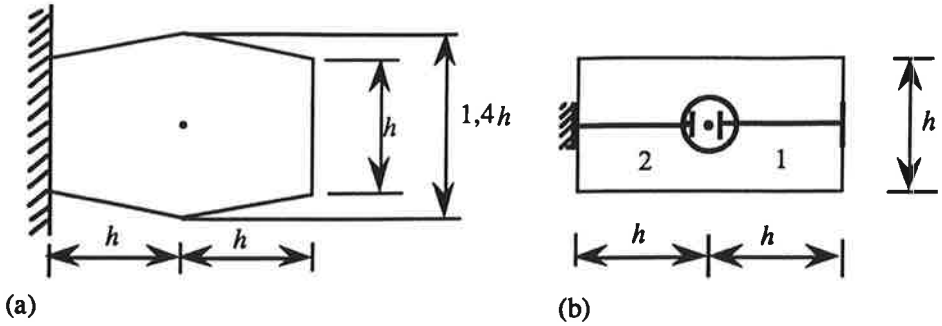

FIGURE 5 (a) Corner cantilever structure. (b) Corner cantilever model.

As a relative error measure the number

$$e = \frac{\|[\bar{C}] - [C]\|}{\|[\bar{C}]\|} \tag{20}$$

was used where $\|\cdot\|$ is the Frobenius matrix norm. With the starting parameter values $a_1 = a_2 = a_3 = 0$ the value of e was 0,48 and after the minimization only 0,0026. It should be noted, however, that for formulas (16) and (20) to be physically meaningful the flexibility coefficients must actually be represented before the calculations in a dimensionally homogeneous form. How this is done best in a logical way is not yet clear for the authors.

REFERENCE

1. J. T. Oden, "Mechanics of Elastic Structures", McGraw-Hill, New York, 1967

AN EQUIVALENT BEAM FOR CALCULATING SLENDER TRUSSES

LASSI A. SYVÄNEN
Laboratory of applied mechanics
Tampere University of Technology
P.O. Box 589 FIN-33101 Tampere, FINLAND

ABSTRACT

An equivalent beam element has been developed for calculations of 3-D slender trusses. It includes the shear deformation and the non-linear coupling between flexural and axial deformation and the non-linear coupling between torsional and axial deformation. Exact equations has been derived for the displacements and the rotations. Also the internal force vector and the tangent stiffness matrix can be calculated exactly according to the theory. An approximated solution is also presented for the axial force to obtain non-iterative formulation.

1. INTRODUCTION

Detailed modelling of trusses is not often necessary. For example the shaft of the guyed mast is quite slender, when it is compared to the height of the mast. In the present work a beam element is developed which can take the most significant effects into account in the guyed mast and other slender truss structures with only few elements.

2. THE CROSS SECTIONAL PARAMETERS FOR THE EQUIVALENT BEAM

The equivalent beam is a straight line in the center of the truss, but it must include all of the most important features of the truss. If it is assumed that only the webs carry axial and bending forces, and only the diagonals carry shearing and torsional forces, the following equivalent parameters are obtained for the cross section of the structure in the figure 1: area A, moment of inertia I (same in the y and z directions), moment of inertia in torsion I_v and shear area A_s (same in the y and z directions).

$$A=\frac{3}{4}\pi d_p^2,\quad I=\frac{3b^2A_p}{2},\quad I_v=\frac{3b^2EA_d\sin(\beta)\cos^2(\beta)}{4G}\quad\text{and}\quad A_s=\frac{3\sin(\beta)\cos^2(\beta)EA_d}{2G},\quad (1)$$

where A_p is the area of the cross section of one web, A_d the area of the cross section of one diagonal, b the distance between the center of the web and the center of the whole cross

section, E the Young's modulus, G the shear modulus and β the angle between the horizontal plane and the diagonal.

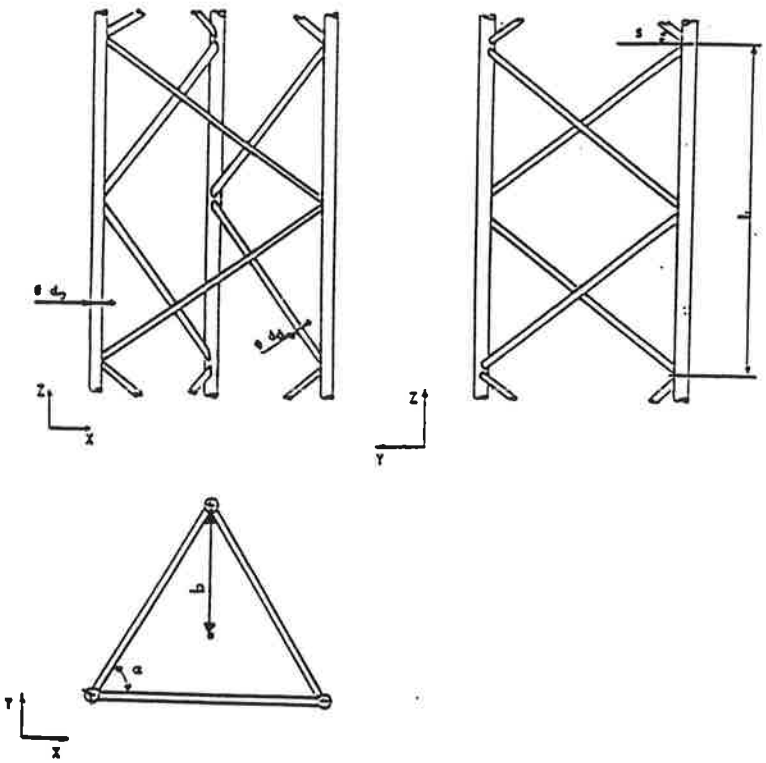

Figure 1. A typical truss structure in guyed masts

3. ADDITIONS TO CONVENTIONAL TIMOSHENKO BEAM ELEMENT

In the previous research [1] it was found that the error in the torsional deformation can be about 20% if the truss is twisted and axially loaded. Therefore the connection of the torsional and the axial deformation is included. If the length of the webs and the diagonals is assumed to maintain constant in torsion, the axial shortening per length, ε_T, of the equivalent beam can be written for the structure in the figure 1 from the deformed geometry.

$$\varepsilon_T = 1 - \sqrt{1 - 4\sin^2\left(\frac{\Phi_{,x} L}{2}\right)\left(\frac{b^2 + \varepsilon_T\left(L_d^2 - b^2\right)}{\sqrt{3}Lb}\right)^2} \quad , \tag{2}$$

where $\Phi_{,x}$ is the angle of twist per unit length and L_d the length of the diagonal. ε_T can be solved approximately by the serial expansion of the equation. If only the first term is included,

$$\varepsilon_T = \frac{b^2 \Phi_{,x}^2}{2}. \tag{3}$$

Because the radius of the gyration i_p is

$$i_p = \sqrt{\frac{I_p}{A}} = \sqrt{\frac{2(3b^2 A_p/2)}{3A_p}} = b, \tag{4}$$

the axial shortening due to the twist Δ_x can be written

$$\Delta_x = \int_0^L \frac{i_p^2}{2} \Phi_{,x}^2 dx, \tag{5}$$

which is the same result as derived in the reference [2] for the ordinary beam element.

The bowing effect must also be taken into account if the beam element is long. It is easy to show that the axial shortening due to bending in the xy-plane Δ_y and in the xz-plane Δ_z is

$$\Delta_y = \int_0^L \tfrac{1}{2} v_{,x}^2 dx, \quad \Delta_z = \int_0^L \tfrac{1}{2} w_{,x}^2 dx, \tag{6}$$

where v and w are the deflections in the y- and z-directions.

4. TOTAL POTENTIAL ENERGY FOR THE BEAM ELEMENT

The total potential energy Π is

$$\Pi = U - V, \tag{7}$$

where U is the strain energy and V is the potential of the external loads. The strain energy for the *TIMOSHENKO* beam [3] by appending the phenomena mentioned in the chapter 3, is

$$U = \frac{1}{2}\int_0^L EI_z \Psi_{,x}^2 + EI_y \Theta_{,x}^2 + GI_v \Phi_{,x}^2 + EA\left(u_{,x} + \tfrac{1}{2} v_{,x}^2 + \tfrac{1}{2} w_{,x}^2 + \tfrac{1}{2} i_p^2 \Phi_{,x}^2\right)^2 + \\ + GA_{sy}\left(v_{,x} - \Psi\right)^2 + GA_{sz}\left(w_{,x} - \Theta\right)^2 dx, \tag{8}$$

where u is the displacement in the x-direction, and Φ, Θ and Ψ are the rotations in the x-,y- and z-directions. The potential of the external loading consists the potential of the nodal forces as shown in the figure 2 and the distributed loading in the y- and z-directions q_y and q_z, now

$$V = Pu_0 - Pu_L - Q_{y0} v_0 + Q_{yL} v_L - Q_{z0} w_0 + Q_{zL} w_L - M_{y0} \Theta_0 + M_{yL} \Theta_L + \\ + M_{z0} \Psi_0 - M_{zL} \Psi_L - T\Phi_0 + T\Phi_L + \int_0^L (q_y v + q_z w) dx. \tag{9}$$

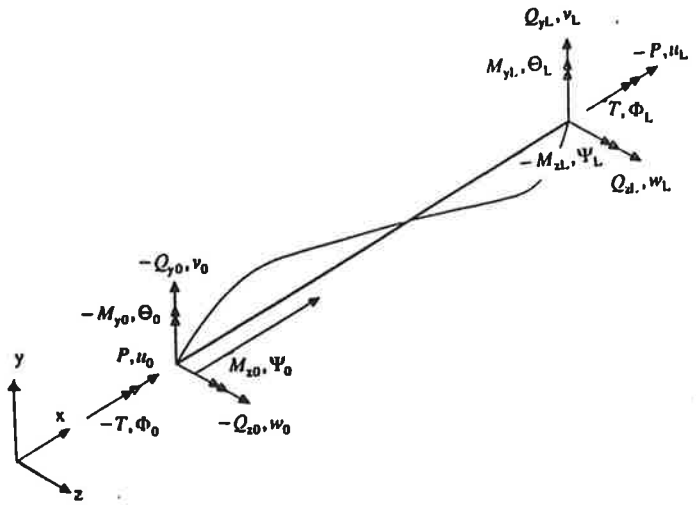

Figure 2. Coordinate system and nodal forces, displacements and rotations for the beam

5. SOLUTIONS FOR THE INTERNAL FORCE VECTOR AND THE TANGENT STIFFNESS MATRIX

Solutions for the displacement functions can be derived from the first variation of the total potential energy. The first variation $\delta\Pi$ must vanish. The variation is

$$\begin{aligned}\delta\Pi = \int_0^L \Big[& EI_z\Psi_{,x}\delta\Psi_{,x} + EI_y\Theta_{,x}\delta\Theta_{,x} + GI_v\Phi_{,x}\delta\Phi_{,x} + EA\left(u_{,x} + \tfrac{1}{2}v_{,x}^2 + \tfrac{1}{2}w_{,x}^2 + \tfrac{1}{2}i_p^2\Phi_{,x}^2\right)\cdot \\ & \cdot\left(\delta u_{,x} + v_{,x}\delta v_{,x} + w_{,x}\delta w_{,x} + i_p^2\Phi_{,x}\delta\Phi_{,x}\right) + GA_{sy}\left(v_{,x} - \Psi\right)\left(\delta v_{,x} - \delta\Psi\right) + \\ & + GA_{sz}\left(w_{,x} - \Theta\right)\left(\delta w_{,x} - \delta\Theta\right)\Big]dx + \\ & - P\delta u_0 + P\delta u_L + Q_{y0}\delta v_0 - Q_{yL}\delta v_L + Q_{z0}\delta w_0 - Q_{zL}\delta w_L + M_{y0}\delta\Theta_0 - M_{yL}\delta\Theta_L + \\ & - M_{z0}\delta\Psi_0 + M_{zL}\delta\Psi_L + T\delta\Phi_0 - T\delta\Phi_L - \int_0^L \left(q_y\delta v + q_z\delta w\right)dx = 0 .\end{aligned} \tag{10}$$

The normal force of the cross section, N, can be found from the above equation, that is

$$N = EA\left(u_{,x} + \tfrac{1}{2}v_{,x}^2 + \tfrac{1}{2}w_{,x}^2 + \tfrac{1}{2}i_p^2\Phi_{,x}^2\right). \tag{11}$$

The field equations of the displacements are found by integrating the equation (10) by parts. If the variations are non zero, then

$$
\begin{aligned}
&a)\quad EI_z\Psi_{,xx}+GA_{sy}\left(v_{,x}-\Psi\right)=0\\
&b)\quad EI_y\Theta_{,xx}+GA_{sz}\left(w_{,x}-\Theta\right)=0\\
&c)\quad GI_v\Phi_{,xx}+\left(Ni_p^2\Phi_{,x}\right)_{,x}=0\\
&d)\quad \left(Nv_{,x}\right)_{,x}+GA_{sy}\left(v_{,xx}-\Psi_{,x}\right)-q_y=0\\
&e)\quad \left(Nw_{,x}\right)_{,x}+GA_{sz}\left(w_{,xx}-\Theta_{,x}\right)-q_z=0\\
&f)\quad N_{,x}=0.
\end{aligned}
\tag{12}
$$

The boundary conditions for the beam are found from the substitution terms of the partially integrated form of the equation (10). If the variations are not zero at the nodes then

$$
\begin{aligned}
&a)\quad EI_z\Psi_{,x}(0)+M_{z0}=0\\
&b)\quad EI_z\Psi_{,x}(L)+M_{zL}=0\\
&c)\quad -EI_y\Theta_{,x}(0)+M_{y0}=0\\
&d)\quad EI_y\Theta_{,x}(L)-M_{yL}=0\\
&e)\quad GI_v\Phi_{,x}(0)+Ni_p^2\Phi_{,x}(0)-T=0\\
&f)\quad GI_v\Phi_{,x}(L)+Ni_p^2\Phi_{,x}(L)-T=0\\
&g)\quad Nv_{,x}(0)+GA_{sy}\left(v_{,x}(0)-\Psi(0)\right)-Q_{y0}=0\\
&h)\quad Nv_{,x}(L)+GA_{sy}\left(v_{,x}(L)-\Psi(L)\right)-Q_{yL}=0\\
&i)\quad Nw_{,x}(0)+GA_{sz}\left(w_{,x}(0)-\Theta(0)\right)-Q_{z0}=0\\
&j)\quad Nw_{,x}(L)+GA_{sz}\left(w_{,x}(L)-\Theta(L)\right)-Q_{zL}=0\\
&k)\quad N(0)+P=0\\
&l)\quad N(L)+P=0.
\end{aligned}
\tag{13}
$$

The functions v and Ψ can be solved from the equations (12 a&d). If the transverse loading q_y is assumed to vary linearly between the node values q_{1y} and q_{2y}, that is

$$
q_y=q_{y1}+\frac{q_{y2}-q_{y1}}{L}x, \tag{14}
$$

then the displacement v is

$$
v=A_y\sin(k_y\,x)+B_y\cos(k_y\,x)+C_yx+D_y+\frac{q_{y1}x^2}{2P}+\frac{\left(q_{y2}-q_{y1}\right)x^3}{6PL}, \tag{15}
$$

and the rotation Ψ is

$$\Psi = A_y k_y \cos(k_y x) - B_y k_y \sin(k_y x) + C_y - \frac{P\left(C_y + A_y k_y \cos(k_y x) - B_y k_y \sin(k_y x)\right)}{GA_{sy}} + \\ + \frac{C_y EI_z GA_{sy}^2 k_y^4 + \frac{q_{y2} - q_{y1}}{L}\left(GA_{sy} + EI_z k_y^2\right)^2}{GA_{sy}^2 k_y^2 \left(GA_{sy} + EI_z k_y^2\right)} + \frac{q_{y1} x}{P} + \frac{\left(q_{y2} - q_{y1}\right) x^2}{2LP}, \tag{16}$$

where the unknown constants A_y, B_y, C_y and D_y can be solved from the boundary values $v(0) = v_0$, $v(L) = v_L$, $\Psi(0) = \Psi_0$ and $\Psi(L) = \Psi_L$, and the coefficient k_y is defined by

$$k_y^2 = \frac{P}{EI_z\left(1 - \frac{P}{GA_{sy}}\right)}. \tag{17}$$

The solution can be found in the same way for u, w, Φ and Θ. The equation (12 f) shows that the normal force is constant over the beam. The compressive force P is then solved from the equations (11, 12 f, 13 k&l). By integrating the axial deformation and by using the boundary values $u(0) = u_0$ and $u(L) = u_L$, it is easy to obtain

$$P = \frac{EA}{L}\left(u_0 - u_L - \frac{1}{2}\int_0^L v_{,x}^2 + w_{,x}^2 + i_p^2 \Phi_{,x}^2 dx\right). \tag{18}$$

As we can see P depends on the deflections and the deflections depend on P, so the iterative solution is needed to solve the desired displacements. A non iterative solution is also possible, but some approximations are needed. The non iterative solution is discussed in the chapter 6.

The tangent stiffness matrix can be obtained from the second variation of the potential energy. By marking the first variation with ^ -mark and by performing the second variation yields

$$\delta^2\Pi = \int_0^L \Big[EI_z \delta\Psi_{,x} \delta\hat{\Psi}_{,x} + EI_y \delta\Theta_{,x} \delta\hat{\Theta}_{,x} + GI_v \delta\Phi_{,x} \delta\hat{\Phi}_{,x} + GA_{sy}\left(\delta v_{,x} - \delta\Psi\right)\left(\delta\hat{v}_{,x} - \delta\hat{\Psi}\right) + \\ + GA_{sz}\left(\delta w_{,x} - \delta\Theta\right)\left(\delta\hat{w}_{,x} - \delta\hat{\Theta}\right) + \delta N\left(\delta\hat{u}_{,x} + v_{,x}\delta\hat{v}_{,x} + w_{,x}\delta\hat{w}_{,x} + i_p^2 \Phi_{,x}\delta\hat{\Phi}_{,x}\right) + \\ + N\left(\delta v_{,x}\delta\hat{v}_{,x} + \delta w_{,x}\delta\hat{w}_{,x} + i_p^2 \delta\Phi_{,x}\delta\hat{\Phi}_{,x}\right)\Big] dx, \tag{19}$$

where $\delta N = EA\left(\delta u_{,x} + v_{,x}\delta v_{,x} + w_{,x}\delta w_{,x} + i_p^2 \Phi_{,x}\delta\Phi_{,x}\right)$. If the variations are written in the form

$$\delta D(i) = \frac{\partial D(i)}{\partial u_0}\delta u_0 + \frac{\partial D(i)}{\partial v_0}\delta v_0 + \frac{\partial D(i)}{\partial w_0}\delta w_0 + \frac{\partial D(i)}{\partial \Phi_0}\delta\Phi_0 + \frac{\partial D(i)}{\partial \Theta_0}\delta\Theta_0 + \frac{\partial D(i)}{\partial \Psi_0}\delta\Psi_0 + \\ + \frac{\partial D(i)}{\partial u_L}\delta u_L + \frac{\partial D(i)}{\partial v_L}\delta v_L + \frac{\partial D(i)}{\partial w_L}\delta w_L + \frac{\partial D(i)}{\partial \Phi_L}\delta\Phi_L + \frac{\partial D(i)}{\partial \Theta_L}\delta\Theta_L + \frac{\partial D(i)}{\partial \Psi_L}\delta\Psi_L, \tag{20}$$

$$\delta D_{,x}(i) = \frac{\partial D_{,x}(i)}{\partial u_0}\delta u_0 + \frac{\partial D_{,x}(i)}{\partial v_0}\delta v_0 + \frac{\partial D_{,x}(i)}{\partial w_0}\delta w_0 + \frac{\partial D_{,x}(i)}{\partial \Phi_0}\delta \Phi_0 + \frac{\partial D_{,x}(i)}{\partial \Theta_0}\delta \Theta_0 + \frac{\partial D_{,x}(i)}{\partial \Psi_0}\delta \Psi_0 + \\ + \frac{\partial D_{,x}(i)}{\partial u_L}\delta u_L + \frac{\partial D_{,x}(i)}{\partial v_L}\delta v_L + \frac{\partial D_{,x}(i)}{\partial w_L}\delta w_L + \frac{\partial D_{,x}(i)}{\partial \Phi_L}\delta \Phi_L + \frac{\partial D_{,x}(i)}{\partial \Theta_L}\delta \Theta_L + \frac{\partial D_{,x}(i)}{\partial \Psi_L}\delta \Psi_L \,, \tag{21}$$

where (i=1,..,6) and the vector D contains displacement functions $D = \{u, v, w, \Phi, \Theta, \Psi\}$. The equation (19) can be written in the following form if we collect and sum the same variations

$$\delta^2\Pi = \{\delta u_0, \delta v_0, \delta w_0, \delta \Phi_0, \delta \Theta_0, \delta \Psi_0, \delta u_L, \delta v_L, \delta w_L, \delta \Phi_L, \delta \Theta_L, \delta \Psi_L\} \cdot [K] \cdot \\ \cdot \left\{\delta \hat{u}_0, \delta \hat{v}_0, \delta \hat{w}_0, \delta \hat{\Phi}_0, \delta \hat{\Theta}_0, \delta \hat{\Psi}_0, \delta \hat{u}_L, \delta \hat{v}_L, \delta \hat{w}_L, \delta \hat{\Phi}_L, \delta \hat{\Theta}_L, \delta \hat{\Psi}_L\right\}^T , \tag{22}$$

where $[K]$ is the stiffness matrix. The developed stiffness matrix is always symmetric regardless the displacement functions. It is also exactly tangential if the same displacement functions are used in (12,13) and (20,21).

6. SIMPLIFIED EQUATIONS

The exact solution of the displacement functions must be iterated. The displacement functions can be simplified by serial expansion with respect to parameters $k_y L$ and $k_z L$. If the first two terms are maintained (that is 0th and 2nd order) in the displacement functions the compressive force P can be calculated from the third order equation directly with the *CARDANO*'s equation. The functions of the internal force vector and the tangent stiffness matrix can be also expanded into the serial form. The benefit of the serial form is also that it is not necessary to develop the solution equations for tensile force and small compression. The accuracy of the element can be viewed by calculating the value of the terms $k_y L$ and $k_z L$. In some examples the value 0.5 has been appropriate. If the value is too large, the number of the elements should be increased.

7. NUMERICAL EXAMPLE

The present element with the non iterative solution scheme has been compared to exact solution and to the results of the *ANSYS*-program with different meshes. The analysed structure is shown in the figure 3. The properties of the beam are: EA=1.2370e9 N, EI_y=9.8960e7 Nm^2, EI_z=9.8960e7 Nm^2, GA_{sy}=3.7110e7 N, GA_{sz}=3.7110e7 N, GI_v=2.9688e6 Nm^2, L=21 m and b=0.4 m. The results are presented in the figure 4, where *ans,3* means *ANSYS*-results with three *BEAM3* elements, *ans,4* and *ans,100* the same with four and 100 elements. *oma* means the present formulation with one element without iteration and *exact* means the present formulation with iterated solution.

Figure 3. The studied structure

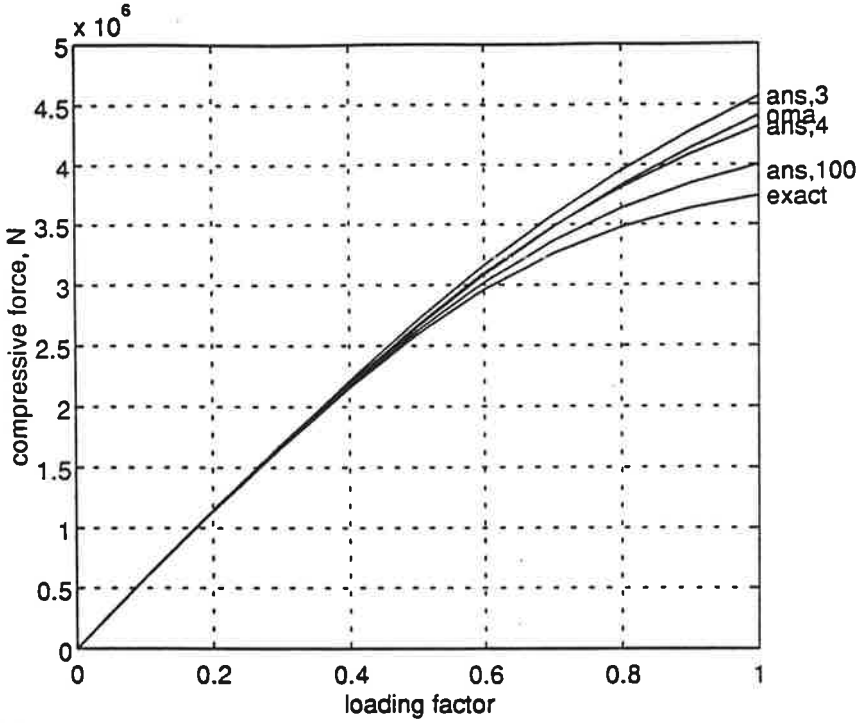

Figure 4. Results of the test example

7. CONCLUSIONS

The exact expressions for the internal force vector and the tangent stiffness matrix have been developed for the 3D equivalent beam element of the slender trusses. Conventional *TIMOSHENKO* beam is generalized to consider the flexural and torsional bowing effects and the contribution of the compressive force to the bending and torsion. Non iterative solution of the equations has been presented. The beam element with the non iterative solution is tested up to now only with one example, but it seems to correspond about three or four ordinary elements. However, the stiffness matrix for one element is full, and the expressions are quite long (without simplification), so the computational efficiency cannot be justified yet.

REFERENCES

1. L. Syvänen, Harustetun maston lujuustekninen tarkastelu, Diplomityö, TTKK/TME, 1991
2. R. S. Barsoum and R. H. Gallagher, Finite element analysis of torsional and torsional-flexural stability problems, Int. journal for num. methods in eng. 2,(1970), 335-352
3. H. Outinen, Viivarakenteet, Opintomoniste, TTKK/TME, 1991

WIND INDUCED VIBRATIONS AND THEIR INVESTIGATION IN WIND TUNNEL

LAURI HELLE
VTT Manufacturing Technology
Aerodynamics
P. 0. Box 17052, FIN-02044 VTT, FINLAND

ABSTRACT

The paper presents the main wind induced vibration types; galloping, flutter, vortex and turbulence induced vibrations. The physical background of different vibration types is described. The basic structure of wind including velocity distribution, turbulence intensity and turbulence spectra is presented. The simulation of the neutral atmospheric boundary layer in a wind tunnel is described. The new wind tunnel of VTT is presented. It is the first wind tunnel in Finland designed for wind engineering. Different wind tunnel test methods are described. They include dynamic force measurements of rigid models, section and taut strip model test of bridges and tests of full aeroelastic models.

1. INTRODUCTION

Wind induced vibrations can cause severe damage to different type of structures. Due to the complex shapes, a mathematic treatment of the flow around the structure does not give satisfactory results. Wind tunnel tests with scale models and simulated atmospheric boundary layer helps to solve these problems. The most important phenomenon in the simulation of wind is the structure of atmospheric turbulence, mainly the turbulence intensity and the spectrum.

2. VIBRATION TYPES

The main vibration types are galloping, flutter, vortex and turbulence induced vibrations. In practice a structure is affected by all these different vibration types. Galloping and flutter are caused by the deflection of the structure while vortex and turbulence induce forces to a rigid structure.

2.1 Vortex induced vibration. After the largest cross-section of a bluff body the boundary layer separates from each side of the surface and forms two free shear layers that trail aft in the flow. These two free shear layers bound the wake. A cylinder is a classical example but any structure with a sufficiently bluff trailing edge sheds vortices. The vortices induce an oscillating

force normal to the wind. Figure 1 shows a typical wake of a cylinder. The frequency of the vortex shedding is

$$f_s = SU / D$$

where

f_S	shedding frequency
S	Strouhal number
U	wind velocity
D	diameter of the cylinder

For a cylinder, the Strouhal number is about 0.2.

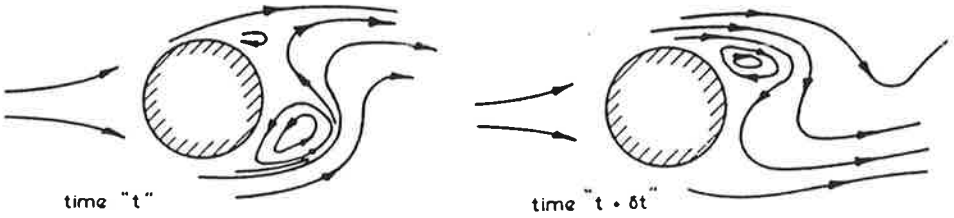

Figure 1. The wake of a cylinder [1].

If the frequency of the vortex shedding is near the nominal frequency of the cylinder, the vibration of the cylinder increases the vortex strength [2]. If the amplitude of the vibration reaches about 1 D, three vortices are formed instead of two per cycle of the stable cylinder . Thus the vortex induced forces on a cylinder are self-limiting at cylinder vibration amplitudes on the order of one diameter [3].

2.2 Galloping and flutter. If a structure vibrates in a steady flow, the flow in turn oscillates relative to the moving structure. This induces an oscillating aerodynamic force on the structure. The structure is aerodynamically unstable if the induced aerodynamic force tends to increase the vibration. Figure 2 shows one-degree-of-freedom galloping models for plunge and torsional stability.

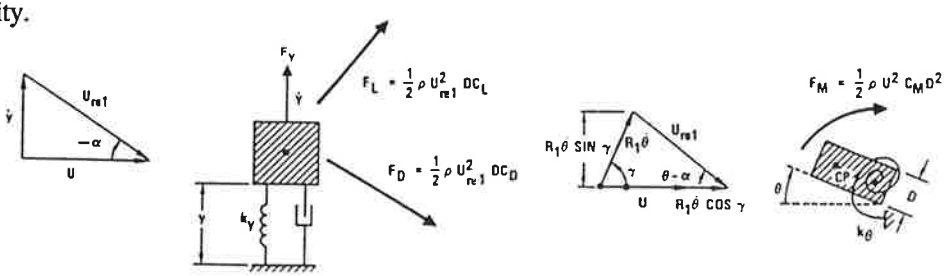

Figure 2. One-degree-of-freedom galloping models [2].

If the model has a vertical velocity $\dot{y}$, the angle of attack is

$$\alpha = atn(\dot{y} / U)$$

The velocity relative to the model is

$$U_{rel}^2 = U^2 + \dot{y}^2$$

The total vertical force per unit is

$$F_y = \tfrac{1}{2}\rho U^2 D C_y$$

The vertical force coefficient is

$$C_y = \frac{U_{rel}^2}{U^2}(C_L \cos\alpha + C_D \sin\alpha)$$

The equation of the motion is

$$m\ddot{y} + 2m\xi_y \omega_y \dot{y} + k_y y = \tfrac{1}{2}\rho U^2 D C_y$$

where the natural frequency of the model is

$$\omega_y = \sqrt{\frac{k_y}{m}}$$

For small changes in angle of attack near α=0

$$C_y = C_y(0) + \frac{\partial C_y}{\partial \alpha}(0)\cdot\alpha = C_L(0) + \left[\frac{\partial C_L(0)}{\partial \alpha} + C_D(0)\right]\frac{\dot{y}}{U}$$

The term $C_L(0)$ produces a static displacement and has no effect on the instability.

The linearized equation of motion is

$$\ddot{y} = 2\xi_T \omega_y \dot{y} + \omega_y^2 y = 0$$

where the net damping coefficient is

$$2\xi_T \omega_y = 2\xi_y \omega_y + \frac{1}{2}\frac{U\rho D^2}{m}\frac{\partial C_y(0)}{\partial \alpha}$$

The instability occurs when ξ_T becomes negative. The minimum velocity for the onset of instability is

$$\frac{U}{f_y D} = \frac{-\dfrac{4m(2\pi\xi_y)}{\rho D^2}}{\left(\dfrac{\partial C_L}{\partial \alpha} + C_D\right)}$$

For the same manner the linearized equation for the torsional motion can be formed

$$I_\theta\ddot{\theta}+2I_\theta\xi_\theta\omega_\theta\dot{\theta}+k_\theta\theta=\tfrac{1}{2}\rho U^2D^2\frac{\partial C_M(0)}{\partial\alpha}(\theta-\frac{R\dot{\theta}}{U})$$

The minimum critical velocity for the torsional instability is

$$\frac{U}{f_\theta D}=\frac{\frac{-4I_\theta(2\pi\xi_\theta)}{\rho D^3R}}{\frac{\partial C_M(0)}{\partial\alpha}}$$

In practice any real structure is a two-degree-freedom model having both plunge and torsional movements. If the two natural frequencies of the plunge-torsion system are well separated and the aerodynamic forces are small compared to inertia forces, then the aerodynamic coupling between torsion and displacement is weak [2].

Galloping is a vibration mode of cables, electrical transmission lines etc. It is most common in cold areas when icing of the cables changes very strongly the aerodynamic derivatives. Galloping of the cables of a guyed mast can induce a strong vibration to an originally stable mast.

Flutter was originally recognized in the wings of aircraft. In wind engineering it is a problem of bridges, mainly of long-span suspension bridges. Many suspended spans have been damaged by storm winds and the awakening for aerodynamic investigations did not come until the very light and slender Tacoma Narrows Bridge was destroyed by a relatively low 20 m/s wind in 1940 [4].

2.3 Vibrations induced by turbulence. The turbulence of the wind causes vibrations and if the natural frequency of the structure is near the peak of the turbulence spectrum high energy from the wind is induced to the structure.

An effective surface pressure on a slender structure is defined

$$p=\tfrac{1}{2}\rho U^2D+\rho A\dot{U}/D$$

The instantaneous velocity can be expressed

$$U=\overline{U}+u_m\sin\omega t$$

If u_m is small compared to U then

$$p=\tfrac{1}{2}\rho\overline{U}^2C_D+\rho u_m\overline{U}C_D\sin\omega t$$

The dynamic response of a structure to turbulent wind can be seen in figure 3.

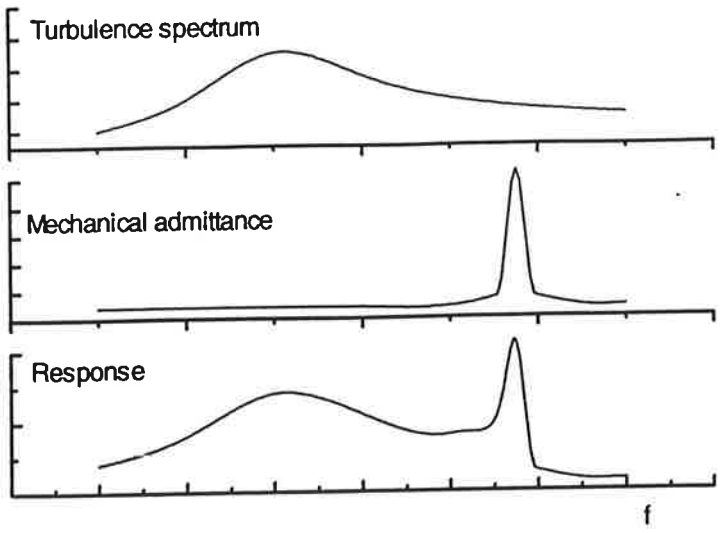

Figure 3. The response of a structure to turbulent wind.

3. THE STRUCTURE OF WIND

The wind can be divided to mesometeorological and micrometeorological parts. An idealized spectrum of the wind is presented in figure 4. Due to the friction of earth a boundary layer is developed on the lower part of the atmospheric wind Its shape and height depends on the roughness of the terrain. Figure 5 shows typical values of the atmospheric boundary layer.

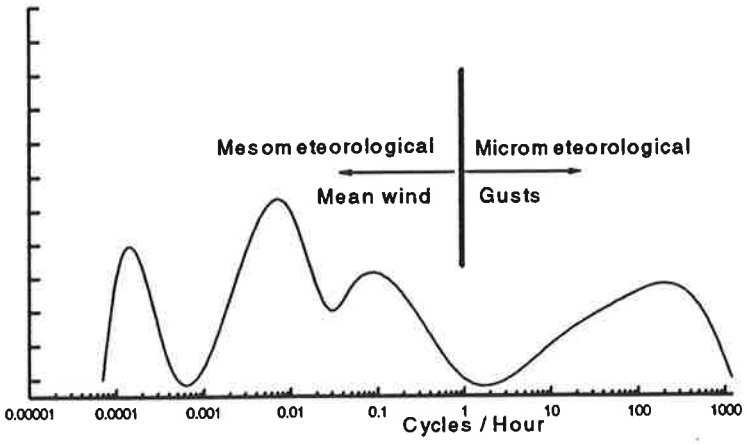

Figure 4. An idealized wind spectrum

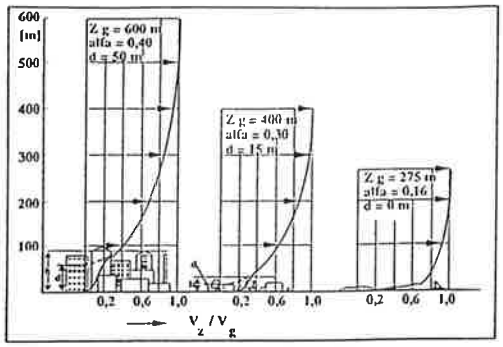

Figure 5. Velocity profiles for different terrain types

4. WIND TUNNEL SIMULATION

For proper simulation of the atmospheric wind in wind tunnel the mean velocity profile, the turbulence intensity and spectrum must be scaled. Figure 6 shows the aim of the simulation.

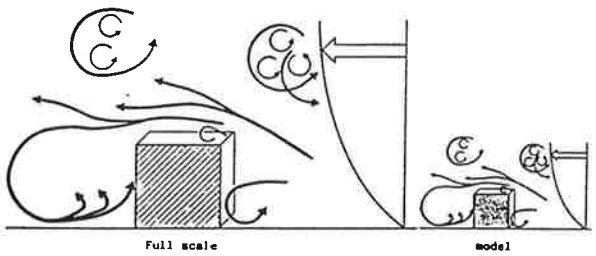

Figure 6. Similarity of flow fields.

The most common method of simulation is to use spires and roughness element in a long test section before the model. Figure 7 shows a typical arrangement. By varying the size and height of the elements different boundary layer profiles can be achieved.

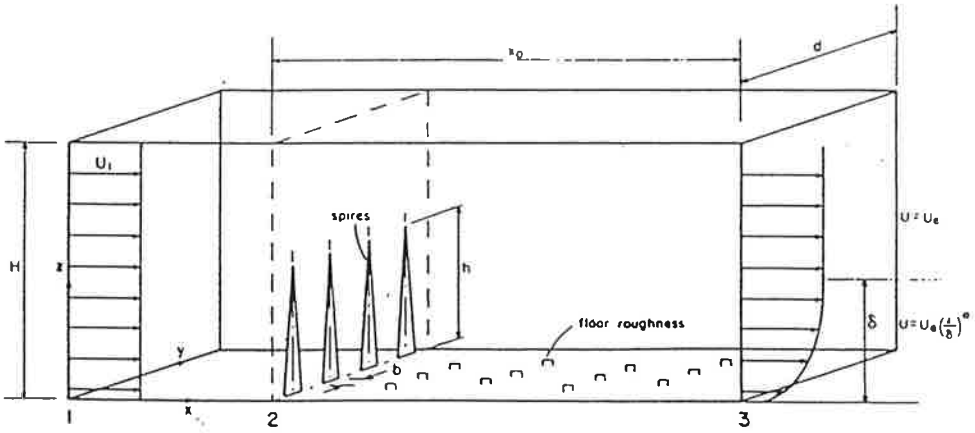

Figure 7. Arrangement for the simulation of atmospheric boundary layer.

5. VTT BOUNDARY LAYER WIND TUNNEL

The new wind tunnel of VTT Manufacturing Technology had its first test run in November 1993. It is the first wind tunnel in Finland designed for wind engineering and being capable for proper simulation of the atmospheric wind. Its test section is 12 m long, 2.5 m wide and 1.5 m high. It is driven by a ϕ2500 fan powered with a 75 kW AC-motor. Figure 8 shows the basic lay-out of the wind tunnel.

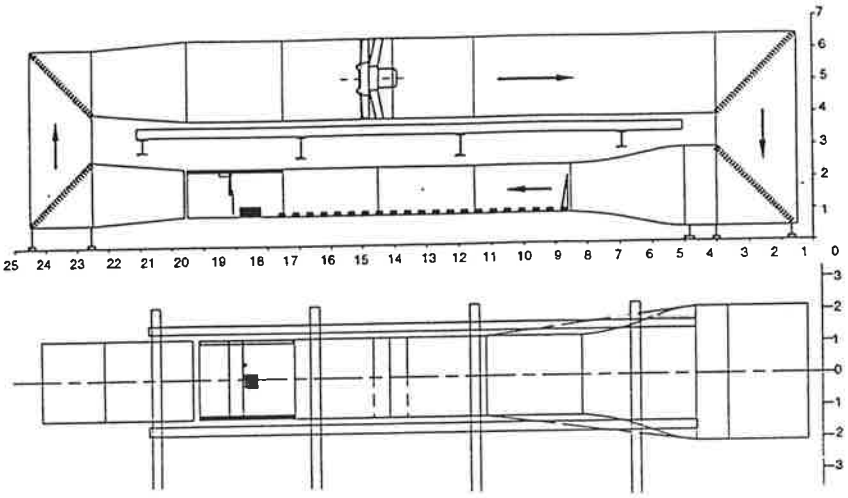

Figure 8. VTT Boundary layer wind tunnel (dimensions in meters).

The control of the wind tunnel is done with a PC. The reference velocity is measured using a differential pressure transducer, an electronic barometer, temperature and humidity probes. The wind tunnel is equipped with a turn-table and a six-component balance, a three-axis traversing mechanism, high-frequency velocity anemometer, multi-port pressure measuring system and flow visualization equipment using either smoke or helium filled bubbles. A small high-frequency balance can be mounted inside a model or under the tunnel floor.

6. TEST METHODS

The main methods in wind tunnel testing are force and motion measurements. For tests of vortex induced vibrations, the model can be rigid and connected straightly to a high-frequency balance. Galloping is not a very widely tested topic. The most challenging test area is the tests of flutter. These tests are made mainly for long span suspension bridges. The wind tunnel model can be a rigid model fastened to a spring-damper system and the motion of the model is measured. The model can be a two-dimensional part of a bridge deck or a three-dimensional model of a flexible structure.

A new technique for bridge tests is the taut-strip method. The model is an elastic two-dimensional model of the bridge deck. The structural similarity is achieved with two tight wires inside the model. The chord of the model is quite small and is chosen so that the turbulence length scale is simulated properly.

The best and unfortunately also the most expensive test method is a full aeroelastic model of the structure. The mass distribution, inertia forces and stiffness of the model are scaled using similarity laws.

7. DAMPING OF WIND INDUCED VIBRATIONS

The damping of wind induced vibrations can be done either with aerodynamic design or with conventional mechanical methods. The most common aerodynamic damping device is a helical spiral on the top of cylindrical towers and chimneys. The idea of the spiral is to break the two vortex system to smaller vortexes that separate at different time at different height of the chimney. A modified shape of the whole structure can change the aerodynamic stability derivatives so that the critical wind speed rises over the expected wind speed.

Beside the mechanical damping, hydraulic dampers have been used. A new method is a tuned liquid damper (TLD). It is a passive damper, which relies on shallow liquid sloshing in a rigid tank to suppress the horizontal vibrations [6]. In a 150 m high round hotel building the response to wind induced vibrations could be reduced to half. It was done with 30 dampers each having a stack of 9 cylindrical containers 2 m in diameter and 22 cm high. The liquid depth was 12 cm.

Also active dampers have been used. A massive bi-axial tuned mass damper has been installed on the top of Citicorp Centre in New York. The mass of the concrete block is 373 tons.

8. CONCLUSIONS

Different types of wind induced vibrations can be studied in wind tunnel. So far the mathematical treatment of complex shapes does not give satisfactory results. With good design and suitable dampers the vibrations can be reduced to acceptable level.

REFERENCES

1. B.J. Vickery, Unsteady forces in the across-wind direction in "The Application of Wind Engineering Principles to the Design of Structures". Lausanne 1987

2. R.D. Blevins, "Flow-Induced Vibrations", Robert E. Krieger Publishing Company, Malabar, Florida, 1986

3. O.M. Griffin and S.E. Ramberg, "The Vortex-Street Wakes of Vibrating Cylinders",J. Fluid Mech. 28 (19729 553-576

4. K.H. Ostenfeld and A. Larsen, Bridge Engineering and Aerodynamics in "Aerodynamics of Large Bridges",A.A. Balkema, Rotterdam, 1992

5. H.P.A.H. Irwin, "Design and Use of Spires for Natural Wind Simulation", Technical report of laboratory No LTR.LA-233, National Research Council of Canada, 1979

6. L.M. Sun et al, Modelling of Tuned Liquid Damper (TLD), J. of Wind Engineering and Industrial Aerodynamics 41-44 (1992) 1883-1894

LAGRANGIAN APPROACH TO SPINNING ASYMMETRICAL ELASTIC SHAFTS

RAIMO VON HERTZEN[1] and MARKO JORKAMA[2]

[1]Laboratory of Computational Dynamics, Helsinki University of Technology, 02150 Espoo, Finland (address correspondence to this author)
[2]Valmet Paper Machinery Inc., Wärtsilänkatu 100, 04400 Järvenpää, Finland

ABSTRACT

The increasing speed of paper machines and electric motors sets new demands on the manufacturing accuracy. The final goal is to find specifications for the fabrication process sufficient to keep the unwanted effects below a desired level. This paper concentrates on the dynamics of spinning elastic shafts, e.g. the roll tube of a paper machine or the rotor of an ultra high speed electric motor. The equations of motion for the spinning shaft, including gyroscopic coupling, asymmetrical perturbations, rigid end plates, elastic journals and non-constant spin rate, are presented. A modal analysis method employing the orthogonality of the eigenfunctions is proposed for the solution of this non-self-adjoint problem.

1. INTRODUCTION

The dynamics of spinning structures is of great technological importance in the design of rotating machinery. In the Paper Machine industry the constant demand for higher production speeds, quality and reliability arises new challenges in the roll design and manufacturing.

There are a large number of papers dealing with transverse vibration of rotating beams covering topics such as balancing of flexible rotors, asymmetrical inertia and stiffness properties, gyroscopic coupling and non-constant spin rate. The modal balancing was proposed by Bishop [1] in the 1960s and the influence coefficient balancing by Kellenberger [2] in the 1970s. Kammer [3] introduced a non-constant spin rate in the analysis of rotating beams, but his treatment was limited to small periodic disturbations around the steady-state spin rate. Bauer [4] investigated uniform rotating beams including all possible combinations of free, clamped, simply-supported and guided boundaries. Han and Zu [5] studied uniform spinning Timoshenko beams using modal expansion techniques. The formulation was based on a body-fixed axis reference system. The corresponding treatment in an inertial reference frame was given by Han and Zu in [6]. Jei and Lee [7] performed the modal analysis of a spinning, asymmetrical rotor-bearing system using the Rayleigh beam model. The effects of the gyroscopic moment were properly taken into account in the paper.

In this work a realistic approach has been made to model a spinning roll, including the asymmetrical roll tube, end plates, journals and an arbitrarily time dependent spin rate. The asymmetry of the roll tube is taken into account in a general way, allowing the variation of the principal axis and moments and products of inertia along the tube. A modal expansion technique for the solution of the equations of motion is proposed. The general orthogonality relation according to Räty *et al* [8] may be utilized to partially diagonalize the equations.

The present paper is organized as follows. In section 2 the Lagrangian function of the system is developed and in section 3 the equations of motion are presented. The modal analysis is outlined in section 4 and in section 5 the concluding remarks are drawn.

2. THE LAGRANGIAN OF THE SYSTEM

Let us consider a flexible roll tube of length l carrying rigid end plates resting on flexible journals of length a as shown in Figure 1.

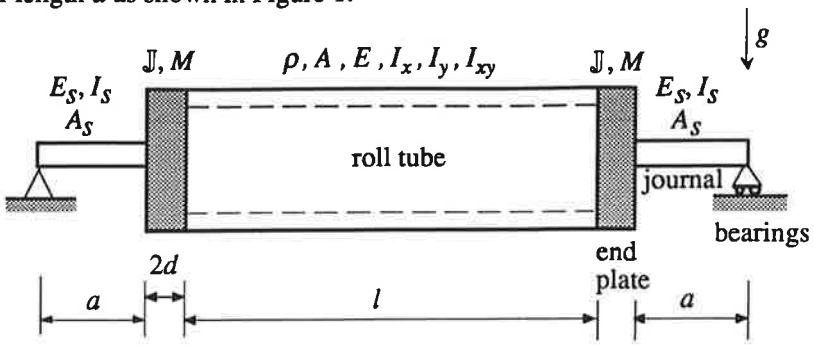

Figure 1. Spinning roll tube carrying rigid end plates resting on elastic journals.

The density, cross-sectional area and modulus of elasticity of the tube are ρ, A and E, respectively. The moments and product of area of the tube cross-section relative to the centroid of the cross-section are I_x, I_y and I_{xy}, respectively. The matrix of the inertia tensor of the end plates relative to the plate-fixed center of mass frame of reference is $\mathbb{J}$ and the mass and the thickness of the end plates are M and $2d$, respectively. The density, cross-sectional area and modulus of elasticity of the journals are ρ_s, A_s and E_s, respectively, and the diametral moment of area of the symmetrical journal cross-section is I_s. The acceleration due to gravity is g.

The generalized coordinates of the system are defined according to Figure 2.

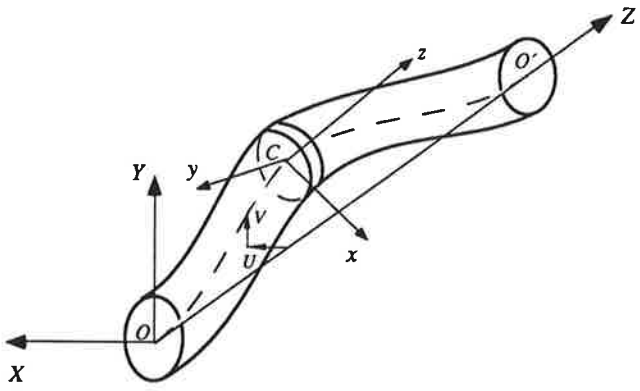

Figure 2. Coordinates used in the problem.

The displacement of the center line of the tube and the journal from the Z-axis of the inertial frame $OXYZ$ along the X- and Y-axis are U and V, respectively. The orientation of the frame $Cxyz$ fixed in the infinitesimally thin slice (or disk) of the tube relative to the frame $OXYZ$ is determined by the Euler angles α, β, ψ shown in Figure 3.

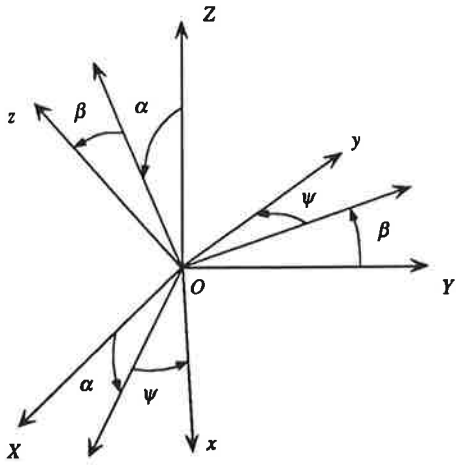

Figure 3. Definition of the Euler angles used.

The angular velocity of the disk relative to the frame *Cxyz* can be written as

$$\begin{cases} \omega_x = \dot{\alpha}\cos\beta\sin\psi + \dot{\beta}\cos\psi \\ \omega_y = \dot{\alpha}\cos\beta\cos\psi - \dot{\beta}\sin\psi \\ \omega_z = -\dot{\alpha}\sin\beta + \dot{\psi}\,, \end{cases} \tag{1}$$

where $\dot{\psi}$ is the angular speed of the shaft and α and β are the deviations of the normal of the disk from the Z-axis. For small deviations one obtains the kinematical relations

$$\alpha \cong \frac{\partial U}{\partial Z} = U'\,, \tag{2}$$

$$\beta \cong -\frac{\partial V}{\partial Z} = -V'. \tag{3}$$

We obtain for the kinetic energy of the tube in the generalized coordinates U and V the expression

$$T_{tub} = \frac{1}{2}\int_o^l \rho\Big\{A\left(\dot{U}^2 + \dot{V}^2\right) + I\left(\dot{U}'^2 + \dot{V}'^2\right) + 2I\left(\dot{\psi}^2 + 2\dot{U}'V'\dot{\psi}\right) +$$

$$+ \Delta I\left[\left(\dot{V}'^2 - \dot{U}'^2\right)\cos 2\psi - 2\dot{U}'\dot{V}'\sin 2\psi\right] +$$

$$+ I_{xy}\left[\left(\dot{U}'^2 - \dot{V}'^2\right)\sin 2\psi - 2\dot{U}'\dot{V}'\cos 2\psi\right]\Big\}dZ \tag{4}$$

and for the potential energy

$$V_{tub} = \frac{1}{2}\int_o^l \Big\{ EI\left[\left(U - U_{in}\right)''^2 + \left(V - V_{in}\right)''^2\right] + 2\rho AgV +$$

$$+\Delta I\left(\left[\left(V-V_{in}\right)''^2-\left(U-U_{in}\right)''^2\right]\cos 2\psi-2\left(U-U_{in}\right)''\left(V-V_{in}\right)''\sin 2\psi\right)+$$

$$-EI_{xy}\left(\left[\left(V-V_{in}\right)''^2-\left(U-U_{in}\right)''^2\right]\sin 2\psi+2\left(U-U_{in}\right)''\left(V-V_{in}\right)''\cos 2\psi\right)\Bigg\}dZ\,,$$

where the notations (5)

$$I_x=I+\Delta I \quad \text{and} \quad I_y=I-\Delta I\,, \tag{6), (7)}$$

displaying the asymmetry of the tube in a symmetrical way, has been used. The functions U_{in} and V_{in} define the initial displacement of the center line due to the initial lack of straightness of the tube.

The rigid end plates are rigidly attached to the tube ends at $Z = 0$ and l. It is assumed that the center line of the tube arrives at a right angle at the cross-section of the tube at $Z = 0$ and that the center of mass of the plate lies on the straight extension of the center line of the tube (see Figure 4).

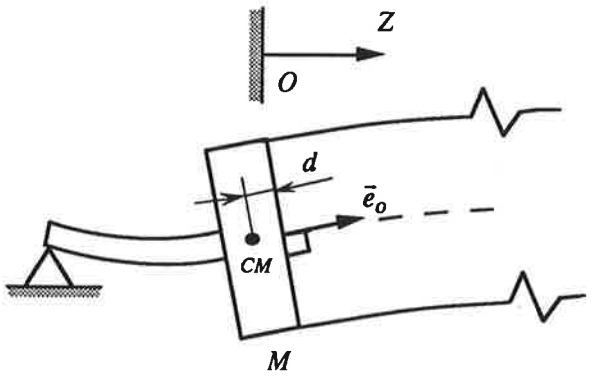

Figure 4. End plates attached rigidly to the tube ends.

The inertia matrix of the plate relative to the *CMxyz*-frame is

$$\mathbb{J}=\begin{bmatrix} J_x & J_{xy} & J_{xz} \\ J_{xy} & J_y & J_{yz} \\ J_{xz} & J_{yz} & J_z \end{bmatrix} \tag{8}$$

The center of mass *CM* of the plate is located at

$$\vec{R}_{CM}=\left(U_o-dU_o'\right)\vec{I}+\left(V_o-dV_o'\right)\vec{J}-d\vec{K}\,, \tag{9}$$

where

$$U_o=U(0,t) \quad \text{and} \quad V_o=V(0,t)\,. \tag{10}$$

We obtain for the kinetic energy of the left plate the expression

$$T_{plat} = \frac{1}{2}M\left[\dot{U}_o^2 + \dot{V}_o^2 - 2d\left(\dot{U}_o\dot{U}_o' + \dot{V}_o\dot{V}_o'\right) + d^2\left(\dot{U}_o'^2 + \dot{V}_o'^2\right)\right] +$$

$$+ \frac{1}{2}J\left(\dot{U}_o'^2 + \dot{V}_o'^2\right) + \frac{1}{2}J_z\left(\dot{\psi}^2 + 2\dot{U}_o'V_o'\dot{\psi}\right) +$$

$$+ \frac{1}{2}\Delta J\left[\left(\dot{V}_o'^2 - \dot{U}_o'^2\right)\cos 2\psi - 2\dot{U}_o'\dot{V}_o'\sin 2\psi\right] +$$

$$+ \frac{1}{2}J_{xy}\left[\left(\dot{U}_o'^2 - \dot{V}_o'^2\right)\sin 2\psi - 2\dot{U}_o'\dot{V}_o'\cos 2\psi\right] +$$

$$+ J_{xz}\dot{\psi}\left(\dot{U}_o'\sin\psi - \dot{V}_o'\cos\psi\right) + J_{yz}\dot{\psi}\left(\dot{U}_o'\cos\psi + \dot{V}_o'\sin\psi\right) \tag{11}$$

and for its potential energy

$$V_{plat} = Mg\left(V_o - dV_o'\right). \tag{12}$$

Similar expressions with $-d$ replaced by d are obtained for the right plate at the end $Z = l$.

The elasticity of the journals may be approximately modeled by equivalent linear and torsional springs. This leads to the potential energy

$$V_{jour} = \frac{1}{2}k\left(U_o^2 + V_o^2\right) + \frac{1}{2}\kappa\left(U_o'^2 + V_o'^2\right), \tag{13}$$

where the effective spring constants are

$$k = 3\frac{E_sI_s}{a^3} \quad \text{and} \quad \kappa = 3\frac{E_sI_s}{a}. \tag{14}$$

A similar expression at $Z = l$ is obtained. Since the mass of the journal is small compared to the mass of the tube and the plate, the kinetic energy of the journal is omitted here.

The Lagrangian function L of the system can now be formed by summing up the contributions of different parts of the system.

3. EQUATIONS OF MOTION

The equations of motion for the system are derived from Hamilton's principle

$$\delta\int_{t_1}^{t_2} L\,dt = 0. \tag{15}$$

A presentation using complex functions turns out to be efficient in writing the equations of motion. We employ the complex displacement field

$$\mathcal{W} = U + iV \tag{16}$$

and introduce the *complex acceleration*

$$\mathcal{A} = \ddot{\mathcal{W}} - 2i\dot{\psi}\dot{\mathcal{W}}\,, \tag{17}$$

the *complex asymmetry moment of area* of the tube

$$\Delta I = \Delta I + iI_{xy}\,, \tag{18}$$

the *complex asymmetry moment of inertia* of the end plate

$$\Delta \mathcal{J} = \Delta J + iJ_{xy}\,, \tag{19}$$

and the *complex cross moment* of the end plate

$$\mathcal{J}_{cr} = J_{xz} + iJ_{yz}\,. \tag{20}$$

Hamilton's principle (15) leads now to the following equations of motion:

$$\rho A\ddot{\mathcal{W}} - \left(\rho I\mathcal{A}'\right)' + \left[EI(\mathcal{W} - \mathcal{W}_{in})''\right]'' + i\rho Ag +$$
$$+ i\ddot{\psi}\left[\rho I(\mathcal{W} - \mathcal{W}^*)'\right]' + e^{i2\psi}\left[\rho\Delta I\,\mathcal{A}'^*\right]' - e^{i2\psi}\left[E\Delta I(\mathcal{W} - \mathcal{W}_{in})''^*\right]'' = 0\,, \tag{21}$$

$$M\ddot{\mathcal{W}}_o - Md\ddot{\mathcal{W}}_o' + k\mathcal{W}_o - \rho I\mathcal{A}_o' + \left[EI(\mathcal{W} - \mathcal{W}_{in})''\right]_o' + iMg +$$
$$+ i\ddot{\psi}\rho I\left(\mathcal{W} - \mathcal{W}^*\right)_o' + e^{i2\psi}\rho\Delta I_o\,\mathcal{A}_o'^* - e^{i2\psi}\left[E\Delta I(\mathcal{W} - \mathcal{W}_{in})''^*\right]_o' = 0\,, \tag{22}$$

$$M\ddot{\mathcal{W}}_l + Md\ddot{\mathcal{W}}_l' + k\mathcal{W}_l + \rho I\mathcal{A}_l' - \left[EI(\mathcal{W} - \mathcal{W}_{in})''\right]_l' + iMg +$$
$$- i\ddot{\psi}\rho I\left(\mathcal{W} - \mathcal{W}^*\right)_l' - e^{i2\psi}\rho\Delta I_l\,\mathcal{A}_l'^* + e^{i2\psi}\left[E\Delta I(\mathcal{W} - \mathcal{W}_{in})''^*\right]_l' = 0\,, \tag{23}$$

$$\frac{4}{3}Md^2\ddot{\mathcal{W}}_o' - Md\ddot{\mathcal{W}}_o + \kappa\mathcal{W}_o' + \frac{1}{2}J_z\mathcal{A}_o' - EI(\mathcal{W} - \mathcal{W}_{in})_o'' - ie^{i\psi}\mathcal{J}_{cr}\left(\ddot{\psi} + i\dot{\psi}^2\right) +$$
$$- i\ddot{\psi}\frac{1}{2}J_z\left(\mathcal{W} - \mathcal{W}^*\right)_o' - e^{i2\psi}\Delta\mathcal{J}\,\mathcal{A}_o'^* + e^{i2\psi}E\Delta I_o(\mathcal{W} - \mathcal{W}_{in})_o''^* = 0\,, \tag{24}$$

$$\frac{4}{3}Md^2\ddot{\mathcal{W}}_l' + Md\ddot{\mathcal{W}}_l + \kappa\mathcal{W}_l' + \frac{1}{2}J_z\mathcal{A}_l' + EI(\mathcal{W} - \mathcal{W}_{in})_l'' - ie^{i\psi}\mathcal{J}_{cr}\left(\ddot{\psi} + i\dot{\psi}^2\right) +$$
$$- i\ddot{\psi}\frac{1}{2}J_z\left(\mathcal{W} - \mathcal{W}^*\right)_l' - e^{i2\psi}\Delta\mathcal{J}\,\mathcal{A}_l'^* - e^{i2\psi}E\Delta I_l(\mathcal{W} - \mathcal{W}_{in})_l''^* = 0\,. \tag{25}$$

Equations (21) - (25) are the complete equations of motion for the tube spinning with a non-constant angular speed, treated as an asymmetrical Rayleigh beam having a small initial lack of straightness, carrying rigid end plates and supported elastically by the journals.

In the case of an ideal symmetric tube with no end plates and no angular acceleration simply supported at its ends the equations of motion reduce to the form

$$\rho A\ddot{\mathcal{W}} - (\rho I\mathcal{A}')' + [EI\mathcal{W}'']'' = 0, \tag{26}$$

$$\mathcal{W}_o = \mathcal{W}_l = 0 \quad , \quad \mathcal{W}_o'' = \mathcal{W}_l'' = 0. \tag{27) - (30)}$$

Equations (26) - (30) coincide with the equations of motion in Reference [9]. The middle term in equation (26)

$$-(\rho I\mathcal{A}')' = -\left[\rho I\left(\ddot{\mathcal{W}} - 2i\dot{\psi}\dot{\mathcal{W}}\right)'\right]' \tag{31}$$

contains the *gyroscopic coupling* term

$$2i\dot{\psi}\left(\rho I\dot{\mathcal{W}}'\right)' = 2\dot{\psi}\left[\rho I\left(-\dot{V}' + i\dot{U}'\right)\right]', \tag{32}$$

which connects the motions in X- and Y-directions.

The equations of motion (21) - (25) may readily be written in coordinates rotating with the shaft by effecting the transformation

$$\mathcal{W} = e^{i\Psi}\mathcal{W}_{rot}. \tag{33}$$

It can be seen from equations (21) - (25) that the non-autonomous parts of the equations are due to the asymmetry of the cross-section and the end plate, the non-constant spin speed and the initial bending of the tube, manifested in ΔI, ΔJ, J_{cr}, $\ddot{\psi}$ and $\mathcal{W}_{in}$, respectively. The disturbance due to ΔI and ΔJ gives rise to an excitation with an angular speed twice that of the shaft. The excitation due to the initial bending, on the other hand, has an angular speed equal to that of the shaft. This follows after putting

$$\mathcal{W}_{in} = e^{i\Psi}\mathcal{W}_{in}^{rot}, \tag{34}$$

in the equations of motion, where the initial displacement in rotating coordinates $\mathcal{W}_{in}^{rot}$ is constant in time.

4. MODAL ANALYSIS

The solution of the equations of motion using modal analysis can be performed in two different ways. One can expand the general state of the system in terms of the eigenfunctions of the idealized symmetrical problem *with* or *without* the gyroscopic coupling term. In the former case the general state can be interpreted in terms of the coupled, rotating modes giving a good insight into the rotational phenomenology of the system. However, this approach is limited to cases of constant angular speed. In a more general analysis, where the run up of the spinning shaft is also of interest, one must drop the gyroscopic coupling from the modes, thus treating the X- and Y-directions as independent from each other. The gyroscopic coupling and the asymmetry terms are then treated as external loads in the general diagonalized modal equations of motion [8].

5. CONCLUDING REMARKS

The Lagrangian approach for the problem of a spinning asymmetric elastic shaft with rigid end masses has been adopted in the paper. In this formalism the different factors of the system can elegantly be taken into account. Employing complex notation the resulting equations of motion may be written in a concise form displaying the contribution of each type of asymmetry of the system in a transparent way. In the future work the role of the different asymmetry parameters in the shaft dynamics should be accounted for.

REFERENCES

1. R.E.D. Bishop and A.G. Parkinson 1963, *Proceedings of the Institution of Mechanical Engineers* **177**, 407-426. On the Isolation of Modes in the Balancing of Flexible Shafts.
2. W. Kellenberger 1972. *Journal of Engineering for Industry, Transactions of the American Society of Mechanical Engineers* **94**, 548-560. Should a Flexible Rotor be Balanced in N or (N+2) Planes?
3. D.C. Kammer and A.L. Schlack Jr. 1987, *Journal of Applied Mechanics* **54**, 305-310. Effects of Nonconstant Spin Rate in the Vibration of a Rotating Beam.
4. H.F. Bauer 1980. *Journal of Sound and Vibration* **72**, 177-189. Vibration of a Rotating Uniform Beam. Part I: Orientation in the Axis of Rotation.
5. R.P.S. Han and J.W.-Z. Zu 1992. *Journal of Sound and Vibration* **156**, 1-16. Modal Analysis of Rotating Shafts: A Body-fixed Axis Formulation Approach.
6. R.P.S. Han and J.W.-Z. Zu 1993. *Journal of the Franklin Institute* **330**, 113-129. Analytical Dynamics of a Spinning Timoshenko Beam Subjected to a Moving Load.
7. Y.-G. Jei and C.-W. Lee 1992. *Journal of Sound and Vibration* **152**, 245-262. Modal Analysis of Continuous Asymmetrical Rotor-Bearing Systems.
8. R. Räty, J. von Boehm and M.A. Ranta 1994. *Journal of Sound and Vibration* **169**, 71-87. Non-Linearly Forced Vibrations of Elastic Systems Carrying Rigid Bodies.
9. C.W. Lee, R. Katz, A.G. Ulsoy and R.A. Scott 1988. *Journal of Sound and Vibration* **122**, 119-130. Modal Analysis of a Distributed Parameter Rotating Shaft.

DYNAMIC CHARACTERISTICS OF HYDRODYNAMIC JOURNAL BEARINGS

OLLI MAJAMÄKI
Civil Engineering Department
IVO INTERNATIONAL LTD
01019 IVO, FINLAND

ABSTRACT

When dynamics of rotating shaft lines are analysed, knowledge of the stiffness and damping coefficients of bearings is required. This paper deals with with the dynamic characteristics of hydrodynamic journal bearings. Fluid film bearing characteristics are determined from the pressure distribution of the lubricant. The pressure distribution is calculated by using the Reynolds equation derived from the Navier-Stokes equation. When the rotating shaft vibrates, an additional squeeze film pressure is generated. This pressure change determines spring and damping properties of oil film and bearing. The values of stiffness and damping coefficients are evaluated by using the perturbation technique. The results presented are calculated by the computer code COJOUR which was developed under funding by the Electric Power Research Institute (EPRI). The calculated results were compared to the tabulated values published by the Japan Society of Mechanical Engineers (JSME).

1. INTRODUCTION

A bearing is the vital tribological element of rotating machinery. According to the direction of the load, bearings that support the rotating shaft can be classified as radial type and axial type. Bearings that are supporting radial load are called journal bearings.

Fluid film journal bearings can be divided into hydrodynamic bearings, hydrostatic bearings and hybrid bearings. A hydrodynamic bearing supports the shaft by hydrodynamic pressure of the lubricant created by the rotation of the journal. In hydrostatic bearings the load is supported by the hydrostatic pressure of oil fed. Hybrid bearings are using both hydrodynamic and hydrostatic pressure to carry load.

Hydrodynamic bearings may be grouped into bearings with fixed sliding surfaces and tilting pad bearings where bearing surfaces rock with respect to the surface of the journal. Bearings with fixed sliding surfaces can be divided into cylindrical, partial arc, two lobe without or with offset and multilobe bearings, Figure 1. Tilting pad bearings can be divided into bearings in which the load is on a pad (LOP) or the load is between two pads (LBP).

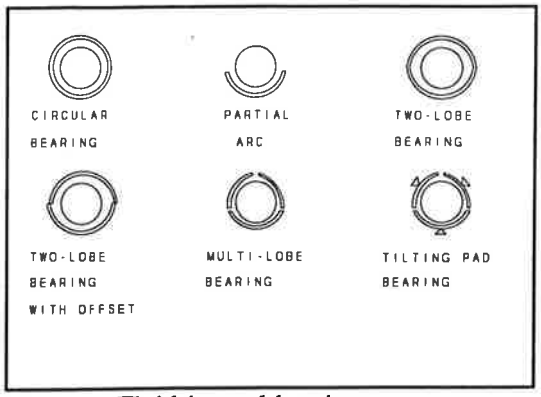

Figure 1. Fluid journal bearings.

2. REYNOLDS EQUATION

The Navier-Stokes equations of motion in Cartesian coordinates for viscous incompressible fluids are [2]

$$\begin{aligned}
\frac{\partial u}{\partial t}+u\frac{\partial u}{\partial x}+v\frac{\partial u}{\partial y}+w\frac{\partial u}{\partial z}&=f_x-\frac{1}{\rho}\frac{\partial p}{\partial x}+\frac{\mu}{\rho}\left(\frac{\partial^2 u}{\partial x^2}+\frac{\partial^2 u}{\partial y^2}+\frac{\partial^2 u}{\partial z^2}\right)\\
\frac{\partial v}{\partial t}+u\frac{\partial v}{\partial x}+v\frac{\partial v}{\partial y}+w\frac{\partial v}{\partial z}&=f_y-\frac{1}{\rho}\frac{\partial p}{\partial y}+\frac{\mu}{\rho}\left(\frac{\partial^2 v}{\partial x^2}+\frac{\partial^2 v}{\partial y^2}+\frac{\partial^2 v}{\partial z^2}\right)\\
\frac{\partial w}{\partial t}+u\frac{\partial w}{\partial x}+v\frac{\partial w}{\partial y}+w\frac{\partial w}{\partial z}&=f_z-\frac{1}{\rho}\frac{\partial p}{\partial z}+\frac{\mu}{\rho}\left(\frac{\partial^2 w}{\partial x^2}+\frac{\partial^2 w}{\partial y^2}+\frac{\partial^2 w}{\partial z^2}\right)
\end{aligned} \tag{1}$$

where u, v and w are velocity components, p is pressure, ρ is density, μ coefficient of viscosity, f_x, f_y, and f_z are body forces and t is time. For very small Reynolds numbers, the inertial forces are much smaller than the frictional force. In cases where the velocity is low, the derivates du/dx, etc, are small. The nonlinear terms udu/dx, etc, being the product of two small quantities, may be neglected in comparison with the other terms in the equation [2]. If we take steady state solution, the time derivates can be removed. In the case of bearing lubricant, the changes of the velocity profile between the shaft and the sliding pad, z direction, are dominant compared to the x and y directions. We can thus omit higher order derivates of the velocities in the x and y direction. If we assume that the fluid pressure between the shaft and the sliding pad is constant, the equations of motion of the lubricant film are

$$\frac{\partial p}{\partial x}=\mu\frac{\partial^2 u}{\partial z^2},\quad \frac{\partial p}{\partial y}=\mu\frac{\partial^2 v}{\partial z^2},\quad \frac{\partial p}{\partial z}=0 \tag{2}$$

Integrating Equations 2 twice with respect to z, we have

$$u=\frac{z^2}{2\mu}\frac{\partial p}{\partial x}+C_1(x)z+C_2(x) \quad , \quad v=\frac{z^2}{2\mu}\frac{\partial p}{\partial y}+C_3(x)z+C_4(x) \tag{3}$$

The functions from C_1 to C_4 are to be determined from the boundary conditions

$$\begin{aligned} &u=u_0, v=0,\ w=w_0 \ \textit{at}\ z=0 \quad \textit{(journal surface)} \\ &u=0,\ v=0,\ w=0 \ \textit{at}\ z=h \quad \textit{(sliding pad surface)} \end{aligned} \tag{4}$$

The oil film thickness h is not a constant but as a function of x depending on the position of the journal and the shape of the sliding pad. Applying boundary conditions to Equation 3, we get

$$u=\frac{z^2}{2\mu}\frac{\partial p}{\partial x}-\frac{h}{2\mu}\frac{\partial p}{\partial x}z-\frac{u_0}{h}z+u_0 \quad , \quad v=\frac{z^2}{2\mu}\frac{\partial p}{\partial y}-\frac{h}{2\mu}\frac{\partial p}{\partial y}z \tag{5}$$

Since the lubricant is assumed to be incompressible, the flows into and out of a small element, Figure 2, must be equal and we can integrate the continuity over the film thickness. The net flow is

$$\frac{\partial}{\partial x}\int_0^h u dz+\frac{\partial}{\partial y}\int_0^h v dz-\frac{u_0}{2}\frac{\partial h}{\partial x}+w_0=0 \tag{6}$$

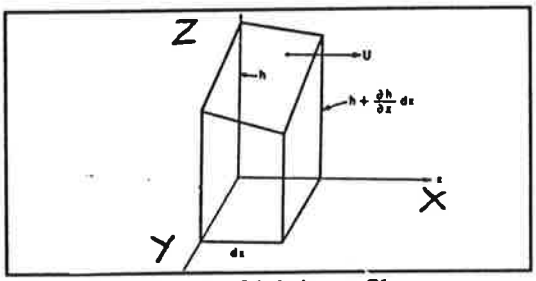

Figure 2. Element of lubricant film.

After solving Equation 6, we get for the Reynolds equation

$$\frac{\partial}{\partial x}\left(\frac{h^3}{\mu}\frac{\partial p}{\partial x}\right)+\frac{\partial}{\partial y}\left(\frac{h^3}{\mu}\frac{\partial p}{\partial y}\right)=6u_0\frac{\partial h}{\partial x}-w_0 \tag{7}$$

The relative speed u is not necessarily small. It is shown that if the thickness of the fluid is small enough compared to the width of the bearing, Equation 7 can be used [2]. A general analytical solution of the Reynolds equation has not been carried out. Analytical

solutions for bearings of infinite length perpendicular to the direction of motion and bearings of zero length are available. The film pressure at the bearing edges must be known before the Reynolds equation can be solved. In the case of the partial arc bearing with a small arc angle or tilting pad bearing, the boundary pressure is the atmospheric pressure. The case of the full cylindrical bearing is more complicated because of cavitation or separation in the oil film.

3. NUMERICAL SOLUTION OF THE REYNOLDS EQUATION

In order to solve the Reynolds equation with the computer code COJOUR [1], the finite difference method is used. Other numerical methods are the finite element method and Green's functions.

The finite difference method of the Reynolds equation at node (i,j), Figure 3, gives [4]

$$\frac{1}{\mu\Delta x^2}(h^3_{i+1,j}\cdot p_{i+1,j} - 2h^3_{ij}\cdot p_{ij} + h^3_{i-1,j}\cdot p_{i-1,j}) + \frac{1}{\mu\Delta y^2}(h^3_{ij+1}\cdot p_{ij+1} - 2h^3_{ij}\cdot p_{ij} + h_{ij-1}3\cdot p_{ij-1}) = \frac{3}{\Delta x}(h_{ij+1} - h_{ij-1}) \quad (8)$$

Because the equation is a non-linear function of pressure p, the equation must be solved by using some iterative method. The computer code COJOUR is using the secant method. The bearing edge pressure is taken as the atmospheric pressure in all cases.

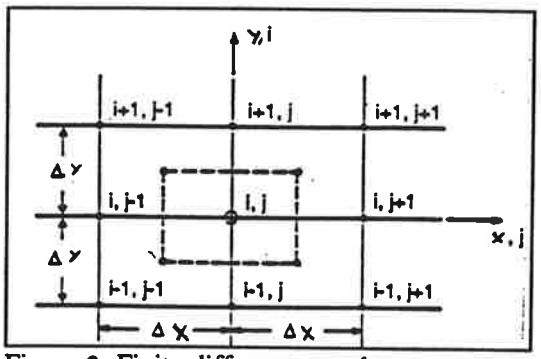

Figure 3. Finite difference mesh.

4. STATIC BEARING CHARACTERISTIC

Static characteristics of the bearing are obtained by integrating the calculated pressure distribution of the oil film determined from the Reynolds equation, Figure 4. The film rection force at the static equilibrium F_0 and its components with respect to the eccentricity direction ε and its perpendicular direction θ are

$$F_\varepsilon=\int_A p\cos\theta dA,\quad F_\theta=\int_A p\sin\theta dA,\quad F=\sqrt{F_\varepsilon^2+F_\theta^2} \tag{9}$$

Components of the film reaction force are shown in Figure 5. The attitude angle is

$$\theta=\arctan\left(-\frac{F_\theta}{F_\varepsilon}\right) \tag{10}$$

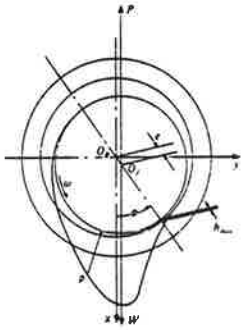

Figure 4. Pressure distribution.

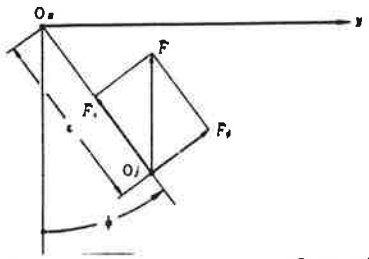

Figure 5. Components of reaction forces.

5. STIFFNESS AND DAMPING COEFFICIENTS

Vibration with small amplitude is assumed to occure in the vicinity of the static equilibrium position. When the rotating shaft vibrates, an additional squeeze film pressure is generated. This pressure change determines spring and damping properties of oil film and bearing. The values of stiffness and damping coefficients are evaluated by using the perturbation technique. When F is expanded in Taylor's series and only the first term is included, we can obtain

$$F-F_0=K(X-X_0)+C(\dot{X}-\dot{X}_0)$$

$$F=\begin{pmatrix}F_x\\F_y\end{pmatrix},\ F_0=\begin{pmatrix}F_{0x}\\F_{0y}\end{pmatrix},\ K=\begin{pmatrix}\frac{\partial F_x}{\partial x}&\frac{\partial F_x}{\partial y}\\\frac{\partial F_y}{\partial x}&\frac{\partial F_y}{\partial y}\end{pmatrix},\ C=\begin{pmatrix}\frac{\partial F_x}{\partial \dot{x}}&\frac{\partial F_x}{\partial \dot{y}}\\\frac{\partial F_y}{\partial \dot{x}}&\frac{\partial F_y}{\partial \dot{y}}\end{pmatrix},\ \dot{X}=\begin{pmatrix}\frac{dx}{dt}\\\frac{dy}{dt}\end{pmatrix},\ \dot{X}_0=\begin{pmatrix}\frac{dx_0}{dt}\\\frac{dy_0}{dt}\end{pmatrix} \tag{11}$$

F is reaction force in the vincinity of the static equilibrium point, F_0 is reaction force in the static equilibrium, K is the stiffness and C is the damping matrices, X_0 and X_0 with dot are displacement and velocity in the static equilibrium, X and X with dot are displacement and velocity in the vincinity of the static equilibrium. Perturbation is made separately in horizontal and vertical directions for displacement and velocity. Force F can then be defined from the Reynold equation. The stiffness and damping coefficients are usually presented in dimensionless form [3]

$$\bar{K}=\frac{C_p}{W}K \quad , \quad \bar{C}=\frac{C_p\omega}{W}C \tag{12}$$

where C_p is clearance, W is bearing load and ω is angular velocity of the journal.

6. EXAMPLE

The example bearing is an elliptic three lobe bearing with oil grooves. The bearing is analysed with the computer code COJOUR, which was developed under fundig by the Electric Power Research Institute (EPRI). The calculated results are compared to the tabulated values puplished by the Japan Society of Mechanical Engineers (JSME) [3]. Table 1. shows the properties of the bearing system as a function of the Sommerfeld number. The Sommerfeld number is

$$S=\frac{\mu NDL}{W}\left(\frac{C_p}{R}\right)^2 \tag{13}$$

where μ is lubricant viscosity, N is bearing load, D is the diameter and L is the length of the bearing, W is the spin speed, C_p is the machine clearance and R is the radius of the bearing.

Table 1.

lubr.visc.O	speed N	length L	diameter D	load W	clearanc C_p	Sommerf. S
lb*s/in2	rpm	in	in	lb	in	
1.50E-06	350	3.75	7.5	5000	0.005	0.027686
1.50E-06	370.2	4	8	5000	0.005	0.037908
2.00E-06	433.6	4	8	5000	0.005	0.059201
2.00E-06	615.3	4	8	5000	0.005	0.084009
2.00E-06	857	4	8	5000	0.005	0.117009
2.00E-06	1179.2	4	8	5000	0.005	0.161
2.00E-06	1640.6	4	8	5000	0.005	0.223997
2.00E-06	2359	4	8	5000	0.005	0.322082
2.00E-06	3736	4	8	5000	0.005	0.510089
2.00E-06	7764	4	8	5000	0.005	1.060045
2.50E-06	12656	4	8	5000	0.005	2.159957
2.50E-06	13000	4	8	5000	0.005	2.218667

Figure 6 shows the eccentricity ratio ε as a function of the Sommerfeld number. Eccentricity ratio is defined

$$\varepsilon=\frac{e}{C_b} \tag{14}$$

where e is eccentricity and C_b is assembly clearance. Figure 7 shows the attitude angle as a function of the Sommerfeld number. Figures 8 to 11 shows the dimensionless stiffness coefficients and Figures 12 to 15 dimensionless damping coefficients as a function of the Sommerfeld number.

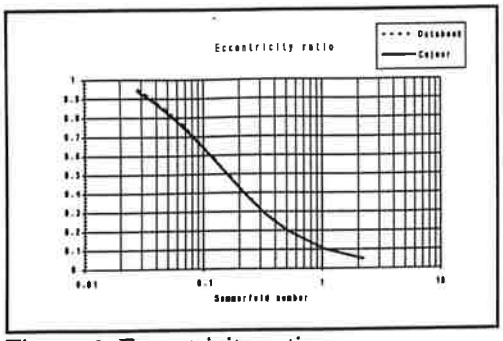

Figure 6. Eccentricity ratio

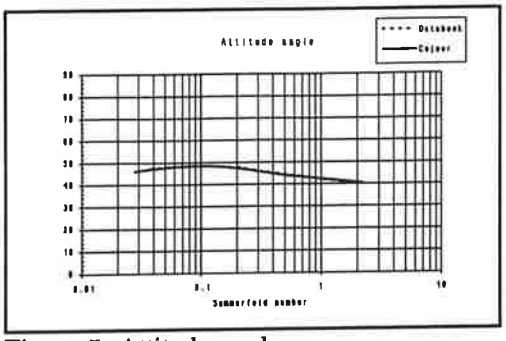

Figure 7. Attitude angle

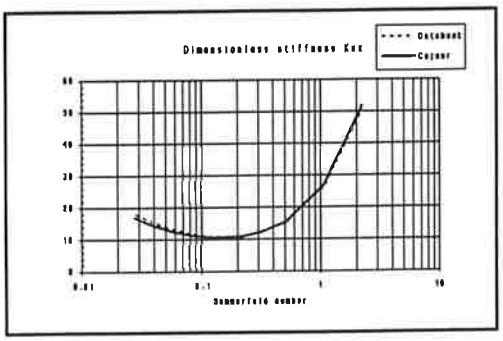

Figure 8. Kxx

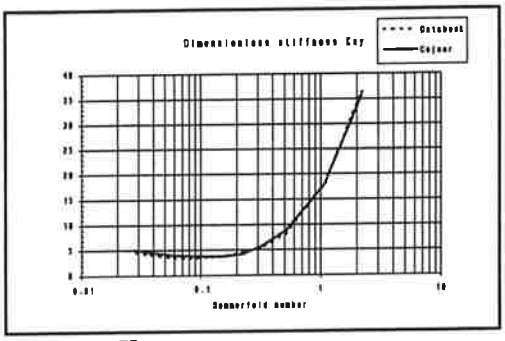

Figure 9. Kxy

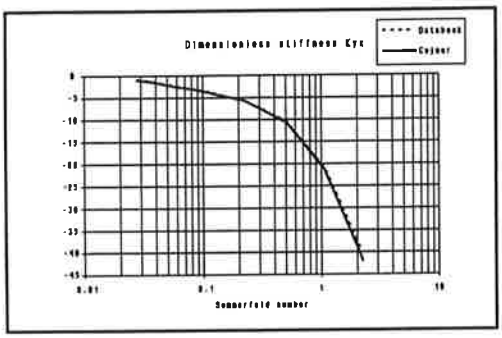

Figure 10. Kyx

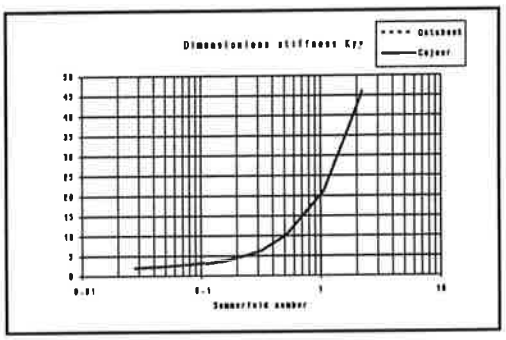

Figure 11. Kyy

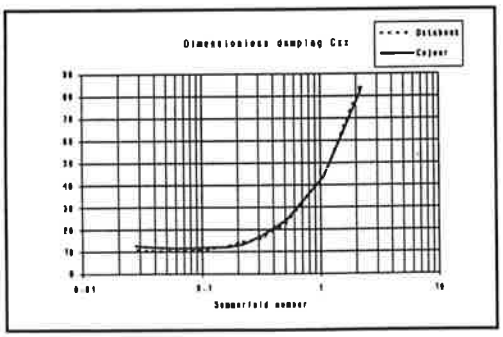

Figure 12. Cxx

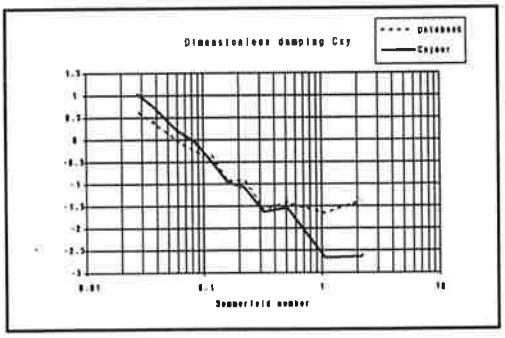

Figure 13. Cxy

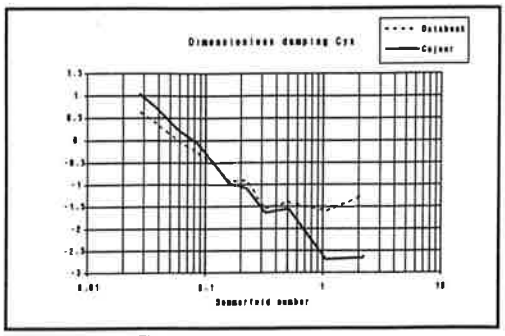

Figure 14. Cyx

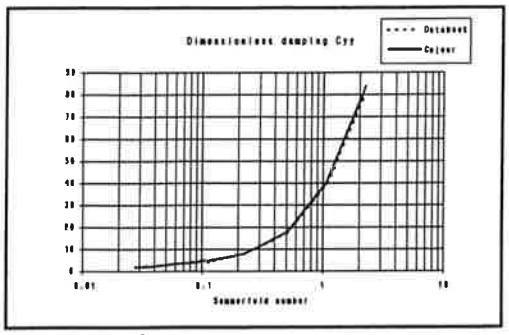

Figure 15. Cyy

7. CONCLUSION

The dynamic characteristics of the hydrodynamic journal bearings were studied by using the computer program COJOUR and the tabulated values puplished by JSME. The example shows that it is possible to get comparable values for stiffness and damping coefficients with a computer program and tables. The analysis of the fluid journal bearing is a complicated problem and there is a lot of parameters which have to be determined. Thus it is almost impossible to get exactly true dynamic parameters for a bearing by theoretical analysis. In the worst case the theoretical analysis does not give more than the magnitude of the dynamic coefficient. It is essential to carry out sensitivity analyses for parameters before obtaining the stiffness and the damping coefficients for any rotor analysis.

REFERENCES

1. EPRI, "FEATURE: Finite-Element Analysis Tool for Utility Rotordynamic Evaluation", Palo Alto, 1988

2. W. Li and S. Lam, " Principles of Fluid Mechanics", Addison-Wesley, Menlo Park, 1964

3. T. Someya, "Journal-Bearing Databook", Springer-Verlag Berlin, Heidelberg, 1989

4. Y. Zhang, "Properties of Flexible Journal Bearings", Chalmers University of Technology, Göteborg, 1988

BENDING VIBRATIONS OF ROTATING SHAFT LINES

JARI PUTTONEN
Civil Engineering
IVO INTERNATIONAL LTD
01019 IVO, FINLAND

ABSTRACT

In thermal power plants the main machines are turbines and generators, whose speeds of rotation are from 25 Hz up to about 250 Hz. A shaft-line may contain many rotors which are coupled together though designed separately. The line is supported by a thin oil film of journal bearings whose pedestals transmit bearing loads to the machine foundation. In this study, the dynamics of the shaft line is analyzed by taking into account the whole support system. The basic differences between the usual beam theory and the theory used in linear rotor dynamics have also been derived. Applications relate to the shaft-line of a turbine having a capacity of about 100 MW. Comparisons have been made between numerical and measured values.

1. KINEMATICS OF ROTOR ELEMENT

In studying the kinematics of a flexible rotor, three rotations in respect of different coordinate systems have to be considered. Two of the rotations relate to the bending of the shaft, whereas the third one is the spin of the shaft around its longitudinal axis. Without simplifications these rotations lead to quite complicated equations as shown in [1] and [2]. In analyzing complete shafts, simplifications are made and two coordinate systems, namely fixed frame and rotating frame, are used.

In Fig. 1 reference frames needed for describing the motion of a beam cross-section are given. XYZ is a fixed frame whose X-axis coincide with the original undeformed rotor axis. The rotation α about Z defines a frame $X_\alpha Y_\alpha Z$, rotation β about Y_α defines a frame $X_{\alpha\beta} Y_\alpha Z_\beta$, and finally a cross-section spin, ϕ, about $X_{\alpha\beta}$-axis, defines the frame $X_{\alpha\beta} Y_{\alpha\phi} Z_{\beta\phi}$. The orientation of a beam cross-section is defined by the Euler angles, α, β and ϕ.

The next step is to determine angular velocities for a cross-section in order to calculate the kinetic energy of the beam element. The angular velocity $\{\omega\}$ is obtained by summing up the velocities $\dot{\alpha}$, $\dot{\beta}$ and $\dot{\phi}$:

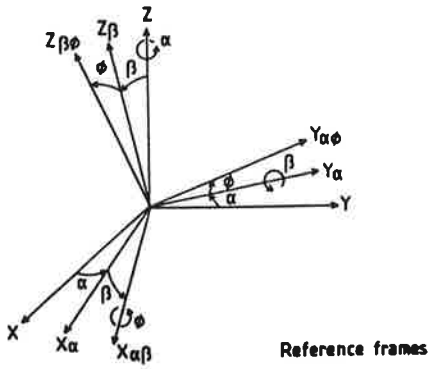

Figure 1. The reference coordinate systems used.

$$\overline{\omega}=(0,0,1)_{XYZ}\dot{\alpha}+(0,1,0)_{X_\alpha Y_\alpha Z}\dot{\beta}+(1,0,0)_{X_{\alpha\beta} Y_{\alpha\beta} Z_\beta}\dot{\phi} \qquad [1]$$

By expressing the direction vectors of rotations in the frame $X_{\alpha\beta}Y_{\alpha\phi}Z_{\beta\phi}$ the angular velocity may be written

$$\overline{\omega}=\begin{bmatrix} -\sin\beta & 1 & 0 \\ \cos\beta\sin\phi & 0 & \cos\phi \\ \cos\beta\cos\phi & 0 & -\sin\phi \end{bmatrix}\begin{bmatrix}\dot{\alpha}\\ \dot{\phi}\\ \dot{\beta}\end{bmatrix} \qquad [2]$$

The assumption that the mass centre coincides with the elastic centreline of the rotor element leads to Eq. (3) for the kinetic energy T_{rot}

$$T_{rot}=\frac{1}{2}[\omega]^T\begin{bmatrix} I_p & 0 & 0 \\ 0 & I_d & 0 \\ 0 & 0 & I_d \end{bmatrix}[\omega] \qquad [3]$$

where I_p and I_d are polar and diametral mass inertia, respectively. The substitution of Eq. (2) in Eq. (3) yields the following expression

$$T_{rot}=I_p[\dot{\alpha}^2\sin^2\beta-2\dot{\alpha}\dot{\phi}\sin\beta+\dot{\phi}^2]+I_d[\dot{\alpha}^2\cos^2\beta+\dot{\beta}^2] \qquad [4]$$

If the angles α and β are small, we may write

$$T_{rot}=I_p[-2\dot{\alpha}\dot{\phi}\beta+\dot{\phi}^2]+I_d[\dot{\alpha}^2+\dot{\beta}^2] \qquad [5]$$

Assuming a constant spin speed, Ω, and applying Hamilton's principle it can be seen that Eq. (5) gives two terms to the equilibrium equation of the beam element. One of the terms

$$M_r = I_d[\ddot{\alpha}+\ddot{\beta}] \qquad [6]$$

relates to the mass rotation of the beam element. The other describes the gyroscopic effect coupling the spin speed to the angular displacements

$$G_r = \begin{bmatrix} 0 & -I_p\Omega \\ -I_p\Omega & 0 \end{bmatrix} \begin{bmatrix} \dot{\alpha} \\ \dot{\beta} \end{bmatrix} \qquad [7]$$

The actual finite element matrices are obtained similarly by describing angular velocities as their nodal point values and shape functions. Eq. (7) shows that the gyroscopic effect is dependent on the spin speed. A consequence is complex eigenvalues which must be calculated separately for each spin speed. However, in the case of a pure gyroscopic force, the real parts of eigenvalues are zero since the force is conservative. Complete derivations of the finite beam element used in practical rotor dynamics are presented, for example, in [3] and [4]. A good general overview is given in Reference [5]

2. MODELLING OF BEARINGS

The other typical feature of rotor dynamics lies in the modelling of the bearings supporting the shaft. Large rotors are carried by journal bearings where loads are transmitted from the shaft to bearing pedestals by the pressure of a thin oil film. The oil film has two characteristic properties, namely stiffness and damping, which are modelled by separate spring and damping elements. These elements are highly frequency dependent having different values in vertical and horizontal directions accompanied by significant off-diagonal terms. The approach in modelling is based on the linearization of the oil film behaviour and is only valid for small movements around the equilibrium position. The modelling technique used has been concretized by Fig. 2.

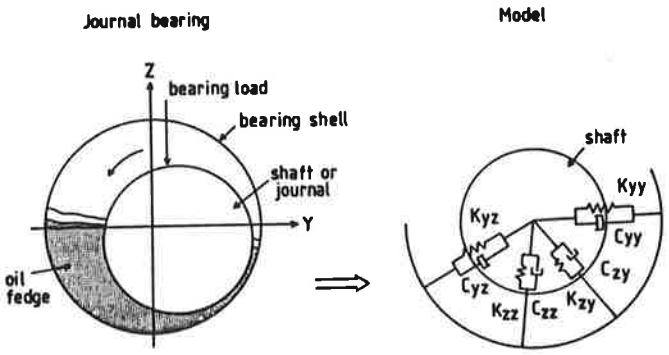

Figure 2. The modelling of a thin oil film in journal bearings.

The oil film is another frequency dependent factor leading to complex eigenvalues. In design, one indicator for the

instability is that the system has eigenvalues with positive real parts.

3. NUMERICAL APPLICATION

The example presented relates to the steam turbine whose foundation is a massive concrete plate resting on helical steel springs. The total mass carried by the springs is 792 Mg of which the mass of the machines, a turbine and a generator, is 322 Mg. Thus, the mass of the concrete foundation is 470 Mg. The average height of the foundation is 1.9 m. Its length is 16.5 m and width 8 m. The generator has an electric power of 106 MW, and a rotor whose mass is 27.3 Mg. Thus, the mass of the turbine rotor is 23.94 Mg. MSC/NASTRAN was used in the finite element calculations.

In the first phase, different techniques to model the foundation were compared. The practice being used is to describe the plate by using thick shell elements. The accuracy of this method was tested by a fully three-dimensional model where several layers of elements were in the thickness direction. In these analyses the shaft-line was included only as mass. The comparison of the foundation models was based on their eigenfrequencies. The foundation models compared have been presented in Fig. 3.

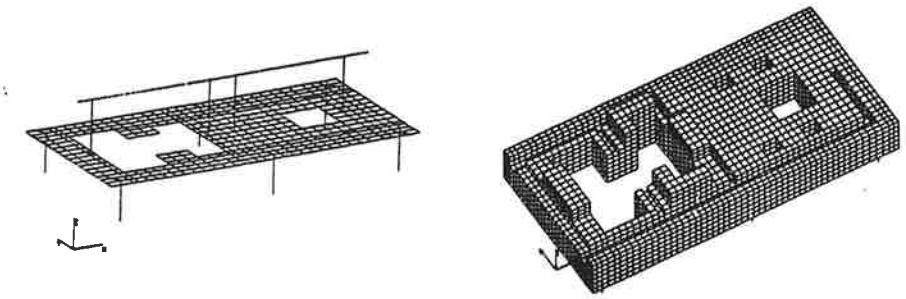

Figure 3. Compared finite element models.

Since the foundation is on the springs, there are six rigid body modes whose frequencies are between 2 and 6 Hz. The shell model gave 12.9 Hz for the first bending mode of the foundation, and 13.0 Hz was obtained by the three-dimensional model. The coincidence was not generally quite so complete, but the results obtained by different models were very similar. Some local modes given by a shell model disappeared when the thickness of the structure was described more accurately. The important fact was that the frequency contents obtained for the foundation by these two models were almost identical. The conclusion is that the model based on shell elements can be used for dynamic analyses of the foundation.

Next the shaft line was modelled discretizing it stage by stage. A total of 67 beam elements was used for the turbine rotor. The generator rotor needed 34 elements. The mass was

modelled both as part of each element and partly by 48 separate additional masses caused by blades. The lengths of the turbine and generator shafts were about 7.3 m and 9.2 m, respectively.

The bearing pedestals were assumed to be rigid, but the oil films supporting the shaft were described by spring and damping elements whose values were frequency dependent. At 50 Hz, for example, a vertical spring constant was 1.5 GN/m and a horizontal one 0.2 GN/m for the turbine front bearing. The relating damping values were 5.3 MNs/m and 0.2 MNs/m. The off-diagonal terms of springs and damping elements were unequal having values of 0.4 GN/m, -0.2 GN/m, -0.03 MNs/m and 0.2 MNs/m for the turbine front bearing at 50 Hz.

As mentioned earlier, the eigenvalues of shaft-line are complex valued. The first results are given for undamped system. In Table 1, the results obtained by analyzing the shaft-line on oil films have been represented together with the model where the foundation and its supporting springs are also taken into account. The eigenvalues are numbered according to the combined model.

Table 1. Eigenvalues [Hz] for undamped system.

EIGENVALUE	COMBINED MODEL	FOUNDATION WITHOUT SHAFT	SHAFT LINE MODEL
7	17.4	12.9	19.9
8	21.3	15.2	
9	22.8	19.8	
10	25.8	20.9	25.2
11	27.1	21.1	
12	27.3	22.5	26.8
13	29.4	31.7	28.8
14	35.6	32.7	
15	37.9	33.1	37.9
16	43.3	34.2	
17	46.5	35.7	
18	47.8	45.0	
19	56.4	46.5	

All the eigenmodes calculated by the shaft model were also found in the combined model. There are clear differences between the results of the foundation model where the shaft line was included only as a mass, and those of the combined model. From the practical point of view it is useful to notice

that even the first bending mode of the foundation, mode number 7, disappeared in the combined model, where the 7th mode relates mainly to the bending of the shaft-line.

Complex eigenvalues were calculated and measured at a frequency of 50 Hz. Table 2 shows the results. Generally, the measured values correspond quite well with the calculated ones. The combined model has more eigenvalues than observed in the measurements. The eigenmodes in which the shaft-line has a dominating role have been observed in practice since the movements relating to these modes are easily identified at the bearings. Differences are clear in the numeric values between the calculated and measured damping ratios. One explanation could be that it is difficult to measure modes with large damping in complicated systems.

Table 2. Measured and calculated eigenvalues at the operation frequency of 50 Hz.

	FREQUENCY [Hz]			DAMPING RATIO[%]		
	COMBINED MODEL	MEASURED	SHAFT MODEL	COMBINED MODEL	MEASURED	SHAFT MODEL
7	18.0	16.5-17.8	18.0	23	5.1-9.3	19
8	21.3	21.3		4.2	3.3-4.9	
9	22.8			0.0		
10	25.4	25.7	23.6	5.7	3.2-5.1	5.7
11	27.2	26.8-28.5		0.6	-	
12	27.8		27.7	14.5		20
13	29.6	29.5-29.8	29.2	2.7	3.5-4.6	6.3
14	35.9			9.3		
15	37.8	37.8-38.7	37.0	50	-	57
16	43.0		45.5	0.8		570
17	46.5			2.0		
18	48.8			0.0		
19	56.5	54.7	55.9	0.3	-	

The final phase of the analyses was to study the behaviour of the shaft line for assumed mass unbalance load. The amplitude of the load was determined by Eq. [8] where m is the mass of the rotor and Ω the spin speed of the rotor.

$$F(\Omega] = m(\frac{0.0025}{2\pi 50})\Omega^2 \qquad [8]$$

The excitation forces calculated were put in the centre of the spans of both rotors. In Fig. 4 and 5 the horizontal velocity amplitudes have been presented as a function of excitation frequency in the turbine front bearing and in the centre of the span of the generator rotor. These figures demonstrate the influence of the foundation on the dynamic behaviour of the shaft-line.

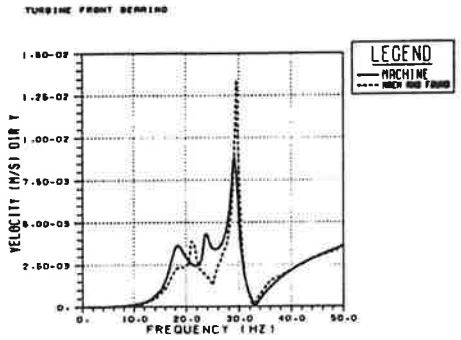

Fig. 4. The velocity amplitude in the horizontal direction at the turbine front bearing.

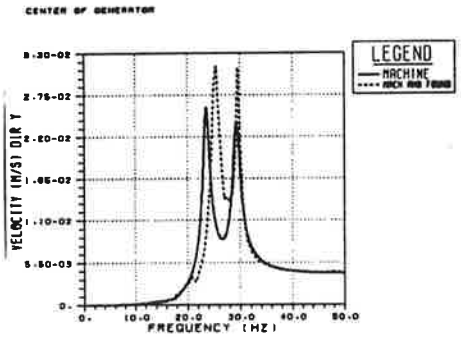

Fig. 5. The velocity amplitude in the horizontal direction at the centre of the span in the generator rotor.

Table 3 indicates calculated and measured vibration amplitudes in bearings. As it can be seen, there are differences between measurements and calculations, but the order of magnitude is the same. The result was expected since the imbalance is more or less stochastically distributed over the length of the rotors and not concentrated at the centre of the span. Concerning the measurements an interesting point was that the 50 Hz component was not dominating. High amplitudes were also measured at higher harmonics indicating partly roughness of surface and other geometrical faults.

Table 3. Measured and calculated shaft vibrations for the imbalance load at 50 Hz.

BEARING	CALCULATED	MEASURED
Turbine, front mm/s	2.64	4.61
Turbine, rear mm/s	3.94	3.54
Generator, front mm/s	1.84	1.87
Generator, rear mm/s	1.25	2.5

4. CONCLUSION

The general theory of rotor dynamics is complicated. However, if simplified assumptions are made, standard finite element programs can be utilized by adding the effect of mass rotations and gyroscopic forces into the programs.

It is obvious that concrete plates on which the turbines and generators rest can be modelled by using thick shell elements without any clear effect on the final results.

It seems to be important also to take into account the foundation when the dynamics of the coupled shaft-lines of power machines are studied. The measured and calculated eigenfrequencies coincide well, but only the order of magnitude is the same between measured and calculated vibration amplitudes.

REFERENCES

1. Y. Kang, Y.-P. Shih and A.-C. Lee, Investigation on the Steady-State Responses of Asymmetric Rotors, Jour. of Vibrations and Acoustics (ASME), Vol 114(1992), 194-208.

2. S.H. Choi, C. Pierre and A.G. Ulsoy, Consistent Modelling of Rotating Timoshenko Shafts Subject to Axial Loads, Jour. of Vibrations and Acoustics (ASME), Vol. 114(1992), 249-259.

3. H.D. Nelson and J.M. McVaugh, The Dynamics of Rotor-Bearing Systems Using Finite Elements, Journal of Engineering for Industry (ASME), May(1976), 593-600.

4. H.D. Nelson, A Finite Rotating Shaft Element Using Timoshenko Beam Theory, Journal of Mechanical Design (ASME), Vol. 102(1980), 793-803.

5. D. Childs, Turbomachinery Rotordynamics, John Wiley & Sons, New York, 1992.

SEISMIC DESIGN AND ANALYSIS METHODS

PENTTI VARPASUO
IVO INTERNATIONAL OY
Rajatorpantie 8, Vantaa
01019 IVO, FINLAND

ABSTRACT

Seismic load is in many areas of the world the most important loading situation from the point of view of structural strength.

In this study there are three areas of the center of gravity: 1) Random vibrations; 2) Soil–structure interaction and 3) The methods for determining structural response.

The solution of random vibration problems is clarified with the aid of applications in this study and from the point of view of mathematical treatment and mathematical formulations it is deemed sufficient to give the relevant sources.

In the soil–structure interaction analysis the focus has been the significance of frequency dependent impedance functions.

From the methods to determine the structural response the following four were tested: 1) The time history method; 2) The complex frequency–response method; 3) Response spectrum method and 4) The equivalent static force method. The time history method was used as reference in the evaluations of accuracy.

1. RANDOM VIBRATION APPROACH FOR EARTH QUAKE EXCITATION RESPONSE

The usual power spectrum expression for earth quake excitation is (Filtered With Noise) FWN expression. The uniformly modulated evolutionary excitation is obtained when the stationary FWN is multiplied by the time dependent modulation function. In this chapter of the study we investigate the response of the example structure given in Figure 1 for uniformly modulated FWN excitation.

The structural response is determined for uniformly modulated FWN excitation. The structural response is determined in terms of quadratic mean or variance for the response process. The variance functions are calculated to the horizontal response of points M and F which correspond to second and fifth degree of freedom of the finite element model of the structure. The variance function is calculated in 81 points over the time interval of 20 seconds. Only

the contribution of three lowest modes has been taken into account in the response calculations. The response calculations were carried out with the aid of STOCAL-program [1] for random vibration analysis of structures. The variance functions for degrees of freedom 2 and 5 are depicted in Figure 2. The square root of the variance function describes the amplitude of the oscillation above and below the zero mean value.

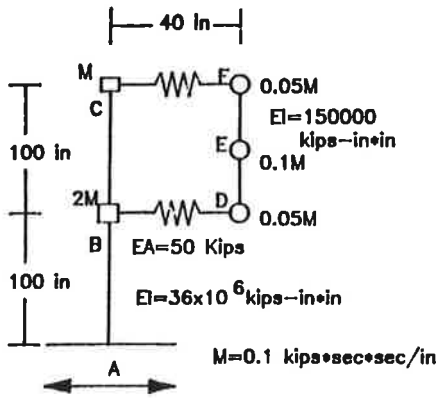

Figure 1. The example structure investigated for random vibration excitation

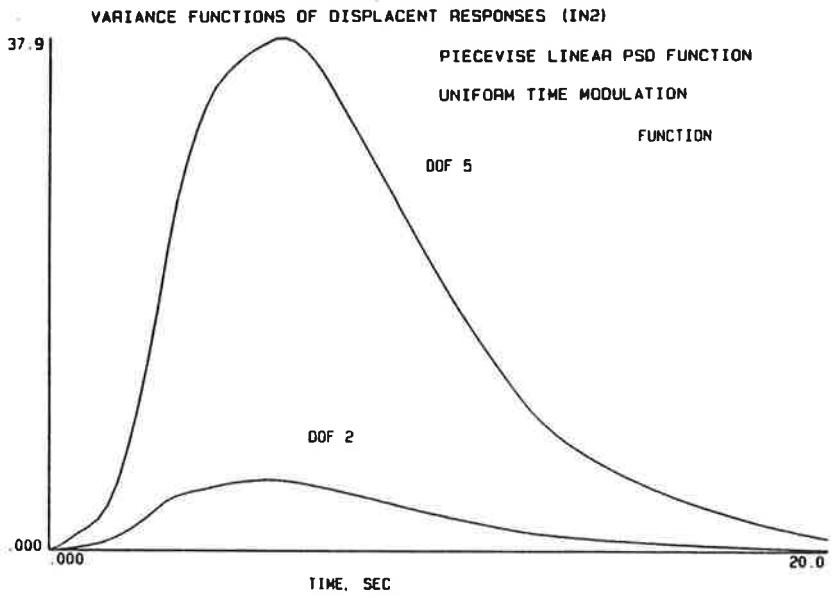

Figure 2. Variance functions of displacement responses of DOF 2 and DOF 5 of the example structure

2. SOIL–STRUCTURE INTERACTION (SSI) FOR THE EARTH QUAKE EXCITATION

Soil–structure interaction effect will be illustrated with the aid of an application example which describes the seismic response of the reactor building of the nuclear power plant. The foundation slab of the reactor building is embedded in the layered soil and the seismic excitation is determined as the motion of the free–field. The geometry of the structural model of the reactor building is depicted in Figure 3.

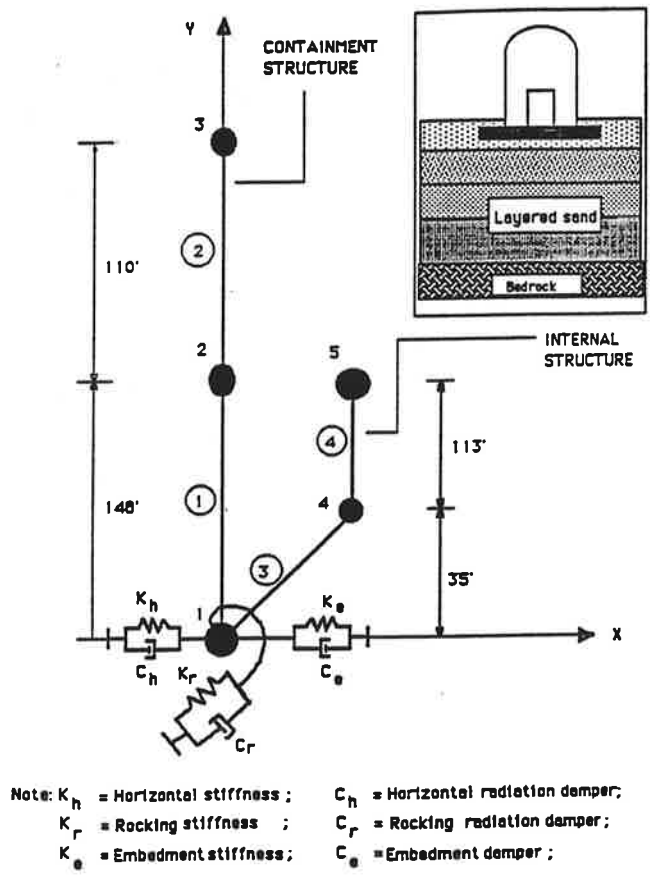

Figure 3. The soil–structure interaction model for reactor building of the nuclear power plant.

The free–field acceleration time history consistent with the USNRC 1.60 Reg.Guide [2] spectrum is the loading of the model. The SSI–analysis takes place in the frequency domain and the acceleration time history is Fourier transformed before the analysis. The result of the SSI–analysis are the acceleration time histories and in–structure response spectra in the nodal points specified by the user. The node where the response of the structure is plotted is the node 5 in this example. In this node the horizontal response spectrum with the 5 % damping ration is evaluated. The floor response spectra were calculated with the aid of frequency independent soil stiffness and damping constants and with the aid of the Beredugo–Novak–type [3] frequency dependent impedance functions. The soil structure interaction analysis was carried out using the CARES–program [3]. The results for these SSI–models are depicted in the same figure in order to facilitate the comparison of the results. In Figure 4

the horizontal response spectra are plotted for the node 5. The response spectra values are given as fractions of gravitational acceleration (g). The zero period acceleration of the input acceleration time history was 0.2 g. It can be observed from the Figure 4 that the use of frequency dependent impedance functions reduces the response. The difference in spectral ordinates in node 5 is about 25 %.

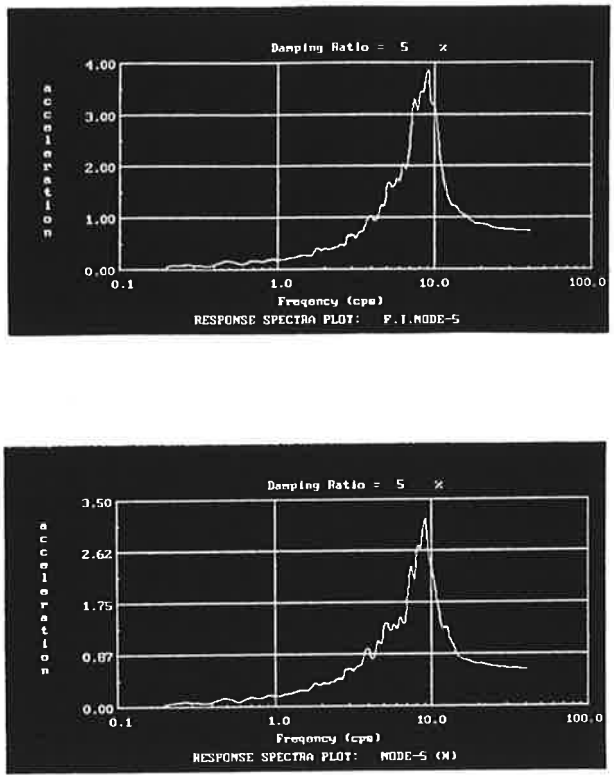

Figure 4. Acceleration response in node 5. Top figure: Frequency independent stiffness and damping parameters; Bottom figure: Beredugo–Novak impedance functions

3. THE DETERMINATION OF THE STRUCTURAL RESPONSE FOR EARTH QUAKE EXCITATION

The seismic analysis is usually carried out for three mutually perpendicular components of motion. Two of these components are horizontal and one is vertical. The directions of the motions are usually assumed to coincide with the principal axes of the building. The response of the multidegree of freedom system when excited by seismic load can be expressed with the aid of the following differential equation

$$[M]\ [\{\ddot{X}\} + \{\ddot{U}_g\}] + [C]\{\dot{X}\} + [K]\{X\} = \{0\} \qquad (1)$$

where $[M]$ = the mass matrix (n x n)
$[C]$ = the damping matrix (n x n)
$[K]$ = the stiffness matrix (n x n)
$\{X\}$ = the relative displacement vector (n x 1)

$\{\dot{X}\}$ = the relative velocity vector (n x 1)
$\{\ddot{X}\}$ = the relative acceleration vector (n x 1)
$\{\ddot{U}_g\}$ = the ground acceleration vector

Equation (1) can be solved using the time–history method based on the mode superposition. In mode superposition method the linear equation system (1) is decoupled using the transform to the so called generalized coordinates. The decoupled equations are then solved independently of each other.

In the response spectrum method the generalized response in each mode is determined from the expression

$$Y_j(max) = \Gamma_j(S_{aj}/\omega_j{}^2) \qquad (2)$$

where S_{aj} is the spectral acceleration corresponding to the frequency ω_j and Γ_j is the modal participation factor for mode j [4]. There are many different methods to combine the contributions of the individual modes.

For details of the complex frequency–response method we refer to [4]. As an application example we investigate the seismic response of VVER–91 type reactor building and its outer containment. The response was determined using four above mentioned methods. The profiles of the horizontal acceleration determined as described above are given in Figure 5.

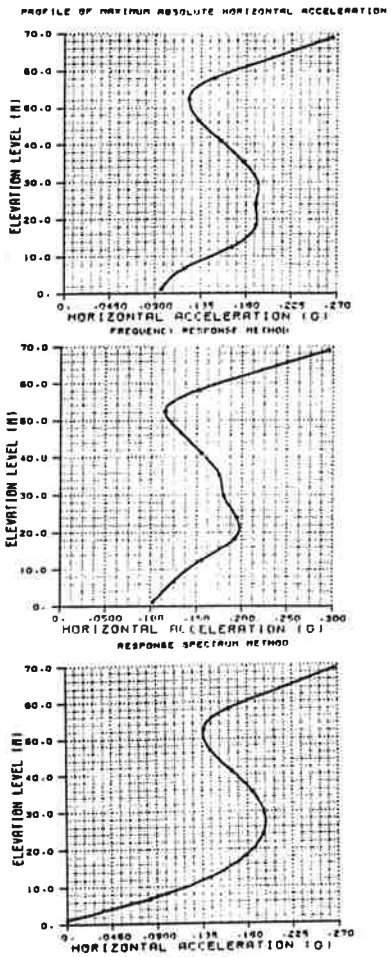

Figure 5. VVER–91 outer containment building
The distributions of horizontal acceleration
The top figure: Time–history method
The middle figure: Complex frequency–response method
The bottom figure: Response spectrum method

4. CONCLUSION

The soil structure interaction shall be always taken into account when the buildings are founded on soft soil.

In judging of the methods for determination of structural response the time–history method and the complex frequency response method seem to give very similar results. The response spectrum method gives results that do not agree perfectly with the results of two previous methods.

REFERENCES

1. C.D. Wung, A. der Kiureghian: "STOCAL II: Computer-Assisted Learning System for Stochastic Dynamics Analysis of Structures, Part I -- Theory and Development, Part II -- User's Manual", University of California at Berkeley, 1989.

2. USNRC, Regulatory Guide 1.60, "Design response Spectra for Seismic Design of Nuclear Power Plants", December 1973.

3. J. Xu et at: "Cares (Computer Analysis for Rapid Evaluation of Structures) Version 1.0, Seismic Module, Theoretical Manual Vol. 1; User's Manual Vol. 2; Sample Problems Vol. 3, Brookhaven National Laboratory, Nureg/CR - 5588, 1990.

4. ASCE STANDARD, "Seismic Analysis of Safety-Related Nuclear Structures", ASCE 4-86, 1986.

APPLICATION OF THE FINITE ELEMENT METHOD TO THE STEFAN PROBLEM IN 1-D

DJEBAR BAROUDI
VTT / Fire Technology
P.O. Box 1803, FIN-02044 VTT, FINLAND
e-mail: Djebar.Baroudi@vtt.fi

ABSTRACT

The classical Stefan problem, i.e. the two phase moving-boundary problem, is considered. A simple version of the two phase Stefan problem is the melting (solidification) of a sheet of ice (water). The material domain is at some time divided into two phases (solid/liquid) by a moving interface (discontinuousity surface) where the phase changes are assumed to occur. Changes in volume are neglected, so the density is the same in both phases. Possible convection in the liquid phase are also neglegted. The position of the discontinuousity surface is unknown and has to be solved together with the heat conduction problem.

This problem is solved using a FE-formulation where the space is discretized using a fixed mesh with one 'travelling' node to track the position of moving boundary. The global semi-discrete system of ODE together with the evolution equation of the interface are integrated using a backward-Euler scheme associated to a Picard-type iteration (a direct interation) at each time step to solve the nonlinear system of equations.

1. INTRODUCTION

The basic idea in the problem is to solve the temperature field $T_i(x,t)$ in two phases $i = 1$ and 2 and the position of the interface $S(t)$. The field equations are the diffusion equation for both phases with one constraint equation for the temperature, phase changes are assumed to happen at fixed constant temperature T^*, and a jump condition for the energy equation which gives us the evolution equation of the interface. These equations are complemented with the appropriate initial-boundary conditions to get a well-posed problem.

The Stefan problem [1] is initially semi-discretized using the standard Galerkin finite element method only with the standard 2-node linear element for the whole domain using a fixed FE-mesh. These elements are called here old elements. Assuming that at some time $t_1 > t^*$ the inteface $S(t)$ is found to reside somewhere in the old element number i. So, a simple method is used to treat and track the unknown moving boundary by introducing a 'special' moving 3-node linear element to which type the i:th element is immediately changed. This macro-element is obtained by assembling two 2-node linear elements (fig. 2). The position of the internal (third one) coincides with the moving unknown boundary. Material properties of the two phases contained by the element may be different. When the front attains at some future time $t_k > t_1$ an other old element, let say, number $i+2$ this last one is replaced by the new 3-node macro-element and the previous macro-element i is then reseted to the old one. In this way we obtain a 'fixed' FE-mesh with only one 'traveling' node to track the exact position of the moving boundary. The global DOF-enumeration is done in such a way that this moving node is given the last ordinal number $N+1$. This allows us to eliminate the DOF number $N+1$ using the constraint equation for the fixed phase change temperature in an simple way. This elimination procedure gives arise to banded symmetrical matrices with a minimal half band width.

The time-integration of the obtained global semi-discrete (ODE) equation is performed using a backward-Euler method associed with a Picard-type iteration at each time step to solve the resulting system of coupled nonlinear equations. Beside the usual possible material nonlinearity an additional nonlinearity due to the moving boundary is present.

One calculation example compared to its analytical solution is presented.

2. MATHEMATICAL FORMULATION

Let the material domain at some instant $t \in [t^*, t^{**}]$ be devided into two phases (in general there can be more than two phases). The position of the interface(s) is (are) unknown. The solid phase occupes the material domain $\Omega_1 =]0, S(t)^-[$ and the liquid phase repectively $\Omega_2 =]S^+(t), l[$. The time interval(s) $[t^*, t^{**}]$ is (are) the one(s) when phase changes take part. Outside this interval , i.e the case when only one phase is present (no phase changes) is treated as a simple heat conduction problem.

The field equations (1 - 7) are written for the case when the two phases are present. The time when this begins to happen for the first time is choosen as the origin $t^* = 0$. Initial conditions are either given explicitely at time $t^* = 0$ (when the problem is at the begining already a Stefan one) or they are the solution of the one phase heat conduction problem (1 - 4) prior to phase changes ($t < t^*$ or $t > t^{**}$). After times $t > 0$ the jump condition (6) and the constraint equation (5) are taken into account. The equations are written for the case when $t \in [t^*, t^{**}]$ [1] (see fig. 1)

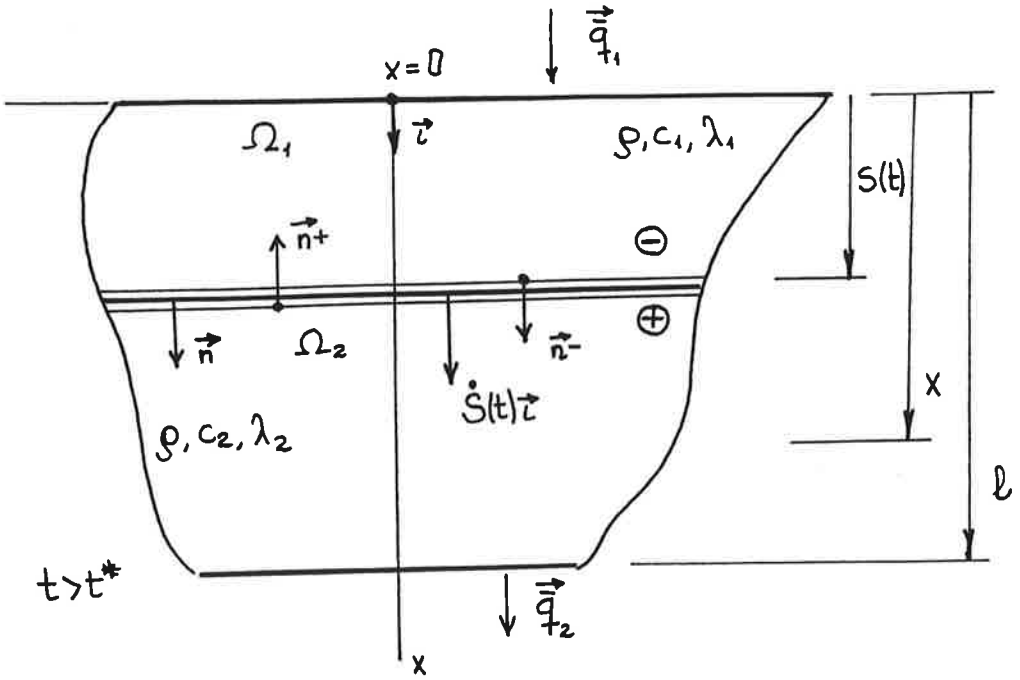

FIGURE 1. Stefan problem in 1-D.

$$\rho c_i \frac{\partial T_i(x,t)}{\partial t} - \frac{\partial}{\partial x}(\lambda_i \frac{\partial T_i(x,t)}{\partial x}) = \rho r_i, \quad x \in \Omega_i, i = 1,2 \quad t > 0, \tag{1}$$

$$T_i(x,0) = T_{i0}(x), \quad x \in \Omega_i, \quad t = 0, \tag{2}$$

$$T_1(0,t) = \bar{T}_1(t), \quad t \geq 0, \tag{3}$$

$$q_n(l,t) = \bar{q}_{n2}(t), \quad t \geq 0, \tag{4}$$

$$T_1 = T_2 = T^*, \quad x = S(t), \quad t > 0, \tag{5}$$

$$\lambda_2 \frac{\partial T_2(x,t)}{\partial x}|_{x=S^+(t)} - \lambda_1 \frac{\partial T_1(x,t)}{\partial x}|_{x=S^-(t)} = \rho L \frac{dS(t)}{dt}, \quad t > 0, \tag{6}$$

$$S(0) = \bar{S}_o \tag{7}$$

where the basic unknowns is the triplet $(T_1(x,t), T_2(x,t), S(t))$.

The Fourier heat conduction constitutive relation has already been included into equation (1). The latent heat L is negative for solidification and positive for melting. The initial condition (2) and the boundary conditions (3) and (4) given above are taken as examples. There can be other type of boundary conditions than those specified in (3) and (4).

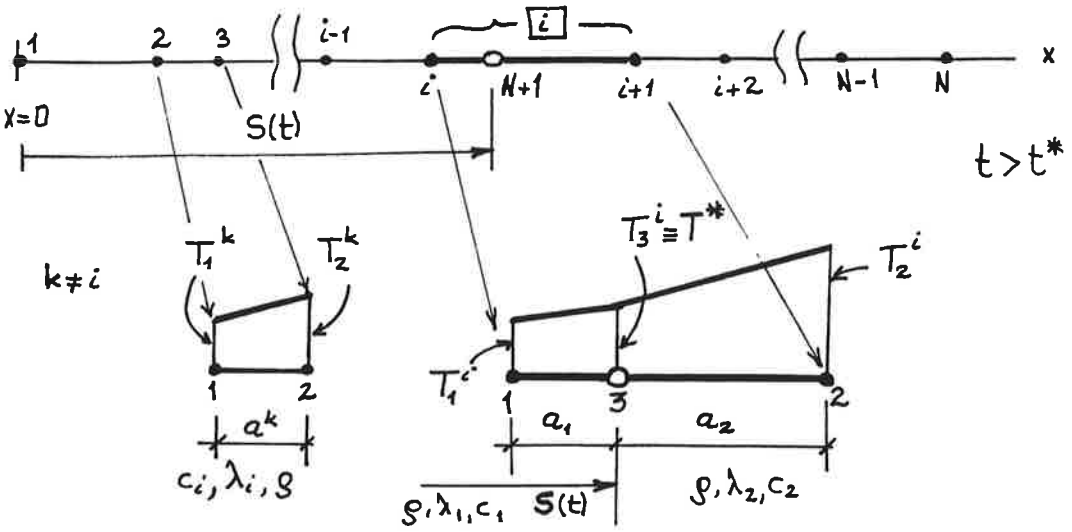

FIGURE 2. two- and three-nodes elements.

The Stefan problem is nonlinear even thought when the material properties are not depending on the temperature because of the coupling of eq. (1) and (6) via the unknown position of the moving boundary $S(t)$.

3. SEMI-DISCRETIZATION OF THE FIELD EQUATIONS

The semi-discretization of the diffusion equation (1-2) is performed using the standard Galerkin method with C^o shape functions. The space is discretized into $N-1$ elements with a FE-mesh with 2- or 3-node elements (see fig. 2). The elementary expression of the temperature field is written as $T^e(x,t) = \sum_j N_j(x) T_j^e(t)$.

Suppose that at the current time t phase changes occur somewhere inside the 3-node element number i at node $N+1$, i.e of coordinate $x_{N+1} = S(t)$. The spatial discretization is achieved by using 2-node linear elements for regions where phase changes do not occur (elements 1 ... $(i-1)$, $(i+1)$ ... $(N-1)$). The nodes 1 ... N are fixed. The two external nodes of the i:th element (with global number i and $(i+1)$) are fixed but the internal node (with the last global number $(N+1)$) coincides with the position of the interface and moves with it. This internal node divides the macro-element into two phases with different material properties. When at some future time t' this interface moves to an other element (it can also move but still stay in the same element for a while), let say, element number $(i+1)$ the 3-node element i is reseted to a 2-node element which nodes are the two external nodes of the 3-node element. Then the new element $(i+1)$ is changed to a 3-node element and so on. In this way a fixed FE-mesh with one moving node is obtained.

The moving node is given the last global number $N+1$. This allow us to get 'well' structered global matrices with minimal half band width (= 2) and to eliminate the DOF T_{N+1} from the global discrete diffusion equation using the constraint equation $T_{N+1}(t) = T^* \quad \forall t$. Before the elimination of the constraint equation (5) elimination the semi-discrete diffusion equation, a coupled nonlinear system of ODE is obtained for the case where the interface $S(t)$ in the element number i. The $N+1$:th equation which is here obtained by automatical assembling of the elementary contributions is not valid and have to be replaced by the constraint equation $T_{N+1}(t) = T^* (\Rightarrow \dot{T}_{N+1}(t) = 0)$. In this way a reduced system (8) is obtained with N unknowns DOF, the vector of the nodal temperatures $\mathbf{T}(t) = (\, T_1(t) \quad T_2(t) \quad \dots \quad T_N(t) \,)^T$ and of the interface $S(t)$. The next coupled, reduced, semi-discrete initial-boundary value problem (nonlinear ODE-system) (8) and (9)

$$\begin{aligned} &\mathbf{C}(S(t))\dot{\mathbf{T}} + \mathbf{K}(S(t))\mathbf{T} + \mathbf{f}^*(S(t)) = \mathbf{0}, \quad t > 0 \\ &\mathbf{T}(0) = \bar{\mathbf{T}}_0, \quad t = 0 \end{aligned} \tag{8}$$

$$\begin{aligned} &\lambda_2 \frac{\partial T_2(x,t)}{\partial x}|_{x=S^+(t)} - \lambda_1 \frac{\partial T_1(x,t)}{\partial x}|_{x=S^-(t)} = \rho L \frac{dS(t)}{dt}, \quad t > 0 \\ &S(0) = \bar{S}_0, \quad t = 0 \end{aligned} \tag{9}$$

is then obtained and time-integrated by a Backward-Euler scheme associated to a Picard iteration to solve the resulting nonlinear system of equations in which the essential boundary conditions are taken into account. In case when there is no phase changes the problem is a pure heat conduction one.

The global equation (8) is assembled from the contributions of the elementary matrices, capacitance $\mathbf{C}^e$, conductivity $\mathbf{K}^e$ and force vector $\mathbf{f}^e$, respectively, In the force vector the boundary term is present if the current element belongs to the boundary with given natural boundary condition.

In the case of the 3-node element the elementary matrices and vectors depend explicitely on the unknown position of the moving boundary $S(t)$ .The global equation (8) is assembled from the contributions of the elementary matrices, capacitance $\mathbf{C}^e$, conductivity $\mathbf{K}^e$ and force vector $\mathbf{f}^e$, respectively, In the force vector the boundary term is present if the current element belongs to the boundary with given natural boundary condition.

In the case of the 3-node element the elementary matrices and vectors depend explicitely on the unknown position of the moving boundary $S(t)$.

The global matrices in (8) are assembled from their respective elementary matrices using standard FE-assembling procedure. These matrices can also depend on the temperature. Their dependency on $S(t)$ is here only emphased. The nonlinearity

due to $S(t)$ is localized. These matrices are band symmetric. They are the submatrices obtained from the global matrices by omitting the $N+1$:th rows and columns. The intermidiary force vector $\mathbf{f}$ is a subvector obtained by ommiting the $N+1$:th row. The constraint is in fact (re)moved into the global reduced force vector $\mathbf{f}^*(S(t))$ for the case when the phase change front is somewhere in the element number i. This reduced force vector is obtained by 'transfering' the products of the $N+1$:th column vectors of the non-reduced capacitancy $\mathbf{C}$ and conductivity $\mathbf{K}$ matrices with the $N+1$:th component of the vectors $\mathbf{T}(t)$ and $\mathbf{T}(t)$, respectively, i.e, $\dot{T}_{N+1}(t)(=0)$ and $T_{N+1}(t)(=T^*)$ of the respectives nodal value vectors. The size of the reduced matrices is $N \times N$ and of the reduced vectors is $N \times 1$.

4. TIME-INTEGRATION OF THE ODE-SYSTEM

The time-integration of initial-value problem, equations (8) and (9), is performed using a backward-Euler scheme giving the next coupled nonlinear system of equations of $N+1$ unknowns

$$\left(\mathbf{C}(S(t_n)) + \Delta t_n \mathbf{K}(S(t_n))\right)\mathbf{T}(t_n) = -\Delta t_n \mathbf{f}^*(S(t_n)) + \mathbf{C}(S(t_n))\mathbf{T}(t_{n-1}) \qquad (10)$$

$$S(t_n) = S(t_{n-1}) + \frac{\Delta t_n}{\rho L}\left(\lambda_2 \frac{T_{i+1}(t_n) - T^*}{a_2(S(t_n))} - \lambda_1 \frac{T^* - T_i(t_n)}{a_1(S(t_n))}\right), \qquad (11)$$

to be solved at each time $t_n = t_{n-1} + \Delta t_n > 0$. This is done at each time t_n using a Picard-type iteration scheme starting from known initial conditions. Beginning from a known value (known from the previous Picard-iteration number j) of the front at time step t_n the position of the front $S_n^j = S^j(t_n)$, the temperatures $\mathbf{T}_n^j$ is solved from equation (11) by a Gaussian elimination. Then from equation (10) one gets an improved estimate S_n^{j+1} at the $j+1$:th Picard iteration. This iteration procedure is repeated for t_n untill convergence is reached ($S_n^k \to S(t_n)$ or/and $\mathbf{T}_n^k \to \mathbf{T}(t_n)$, i.e. $\|\mathbf{T}_n^{j+1} - \mathbf{T}_n^j\| \to 0$ or/and $|S_n^{j+1} - S_n^j| \to 0$.

After this we move to the next time step $t_{n+1} = t_n + \Delta t_n$ and repeat the Picard-iteration of equations (11) and (10) with starting value $S(t_{n+1}^1) = S(t_n)$ and so on. In this way a solution $(\mathbf{T}(t), S(t))$ is constructed. Using equation $T(x,t) = \mathbf{N}(x)\mathbf{T}(t)$ all the temperature field is obtained.

If, for instance for $t < 0$, we have only a pure heat conduction at the beginning of the problem the time $t = 0$ for which the phase changes begin for the first time at the node i is found from the condition that the $T_i = T^*$. Then in the first iteration of the Picard-iteration $j = 1$ at the time t_1 the equation (11) is integrated explicitely and the jump of the normal of the heat fluxes over the interface (the second term inside the parentheses in eq. (11)) is calculated at $t = 0$ as $[[q_n(t_n)]] = \frac{\lambda_2}{a^e}\left(T_{i+1}(t_{n-1}) - T^*\right)$. For $j > 1$ the time integration is continued implicitely.

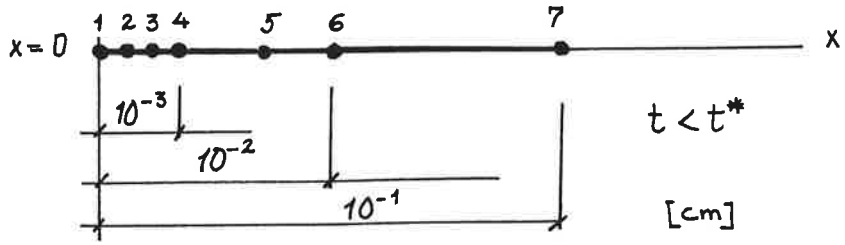

FIGURE 3. Finite element mesh used in calculations.

5. NUMERICAL EXAMPLE

An example presented in [1], chapter 11.2 pp. 283 - 286 is investigated. The example consists of the freezing (solidification) for the half space $x > 0$ initiallly liquid at constant temperature $T_0(x)$ with surface $x = 0$ maintained temperature at $\bar{T}_1(t) < T^* = 0$ for $t > 0$. The analytical solution presented for the front is

$$S(t) = 2\mu\sqrt{\kappa_1 t}$$

with $\kappa_i = \lambda_i/\rho c_i$ the thermal diffusivity of the phase i. The solid phase is idendified by the subscript 1 and the liquid one by 2. The dimensionless numerical constant $\mu = 0.056$ in our case of data (all from [1]). The intial temperature is $T_0(x) = T^* = 0 \ \ ^0C$. The boundary condition at $x = 0$ is $\bar{T}_1(t) = -1 \ \ ^0C$. The 'boundary condition' at infinity $T(x,t) \rightarrow T^{*+}$ with $x \rightarrow \infty$. The latent heat of solidification of ice $L = -308.15kJ/kg$. The thermophysical data used for the water and ice are shown in table 1.

TABLE 1. Thermophysical properties of ice and water [1].

No	Material name	λ (W/mK)	ρ (kg/m^3)	c (J/kgK)	κ (m^2/s)
1	Ice	2.219	1000	1930.1	1.148×10^{-6}
2	Water	0.603	1000	4186.8	1.144×10^{-7}

The FE-mesh is shown in fig. 3. Six 2-node elements are initially used. The time steps are respectively $0.1s, 0.05s$ and $0.01s$.

In the numerical calculations the initial temperature $T_0(x) = +0.01 \ \ ^0C$ which is near the freezing point $T^* = 0 \ \ ^0C$. The boundary condition at $x = 0$ is given 'gradually'. At $t = 0.1s$ we have $\bar{T}_1(t^*) = +0.01 \ \ ^0C$ and grows linearly to the value $\bar{T}_1(t) = -1 \ \ ^0C$ at $t = 0.1s$ where it is keeped.

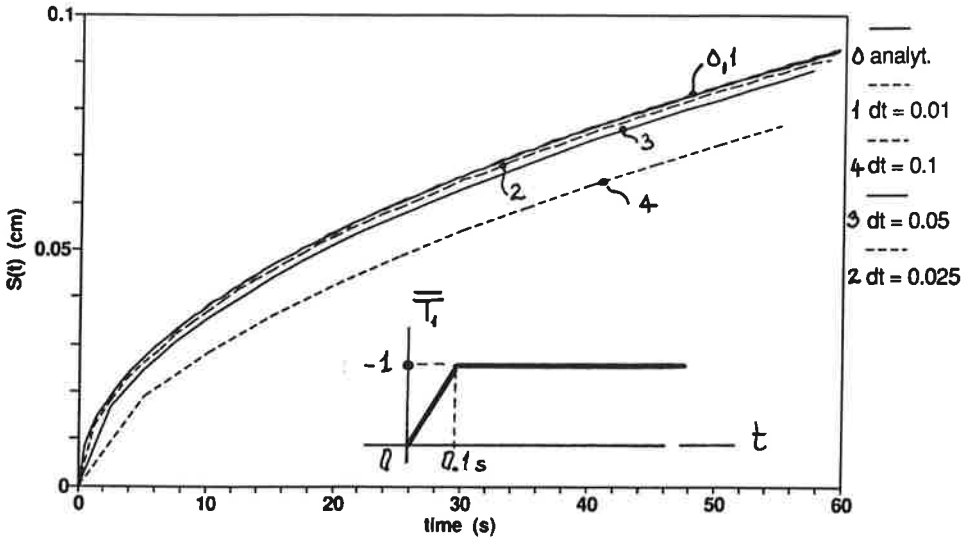

FIGURE 4. Numerical and analytical solutions $S(t)$

In fig. 4 the analytical solution and the numerical (for different length of the time steps Δt_n) obtained are shown. It is seen that there convergence to the analytical solution as the time step is reduced.

ACKNOWLEDGMENTS

The author wish to thank Juhani Pitkäranta (TKK/Mat) for fruitful discussions and Reijo Kouhia (TKK/Rak) for suggestions during the writing process.

REFERENCES

[1] H. S. Carslaw and J. C. Jaeger. Conduction of heat in solids. Oxford 1959, Oxford University Press. pp. 282-296.

A SPACE-TIME FEM FOR ELASTODYNAMICS

JOUNI FREUND , ANTTI LEMPINEN
Laboratory of Computational Dynamics
Helsinki University of Technology
Otakaari 1, SF-02150 Espoo, FINLAND

ABSTRACT

A space-time finite element method for second order hyperbolic problems is proposed. The Galerkin type of formulation makes use of weakly enforced initial conditions. No tunable problem dependent parameters or auxiliary functions are needed. The method applies well to continuum dynamics as the numerous cases arising from different kinematical assumptions and stress tensor expressions can be handled on the same footing. Numerical results are used to illustrate the convergence and stability properties in simple 1D and 2D cases.

1. INTRODUCTION

When solving hyperbolic second order problems describing elastic vibrations, one has to rely on numerical approaches, in particular, when the problem is non-linear or/and the solution domain geometry is not simple. The direct simulation may also be competitive on simple geometries when, say, the exact solution is not smooth and a large number of Fourier-series terms is needed to get an accurate enough representation.

In a conventional numerical approach the original problem is first transformed to a set of ordinary differential equations using for example the finite element method in the spatial domain only. Then the remaining initial value problem is handled separately. In the space-time finite element method no such difference is made between the spatial and temporal coordinates and the time-dependent problems are solved in the same way as the stationary ones. The only exception is that the same receipt is applied in a stepwise manner. The space-time solution method for parabolic problems –the time-discontinuous Galerkin method– is known to possess very good properties [3]. In the second order hyperbolic case it is not so clear, however, how to write a weak or residual formulation combining simplicity, stability and accuracy in a similar way (for some suggestions see [1] and [2]).

A formulation having the wanted properties to some extent is proposed here. The meth-

od can be viewed as a standard Galerkin one making use of weakly enforced initial conditions for the unknown functions and their time derivatives. It is a straightforward extension of the one used for ODE:s in [4]. In this much simpler case it is relatively easy to show that the suggested way to satisfy the initial conditions gives a method having all the properties attributed to the discontinuous Galerkin method for the first order ODE:s [5]. Due to the preliminary nature of this presentation no precise results for a given type of problem are given but the properties are illustrated by numerical experiments.

1.1 Elastodynamic problem. Figure 1(a) shows the solution domain in space and the coordinate system used. The Cartesian X,Y,Z system (Eulerian) is assumed to be at rest. The x,y,z-system (Lagrangean) is body fixed. In principle the equations of motion can be expressed in either one of the systems and it depends on the setting which one is more convenient. To keep things simple the Lagrangean approach, where the solution domain can be taken to be prismatic in space-time, is adopted here.

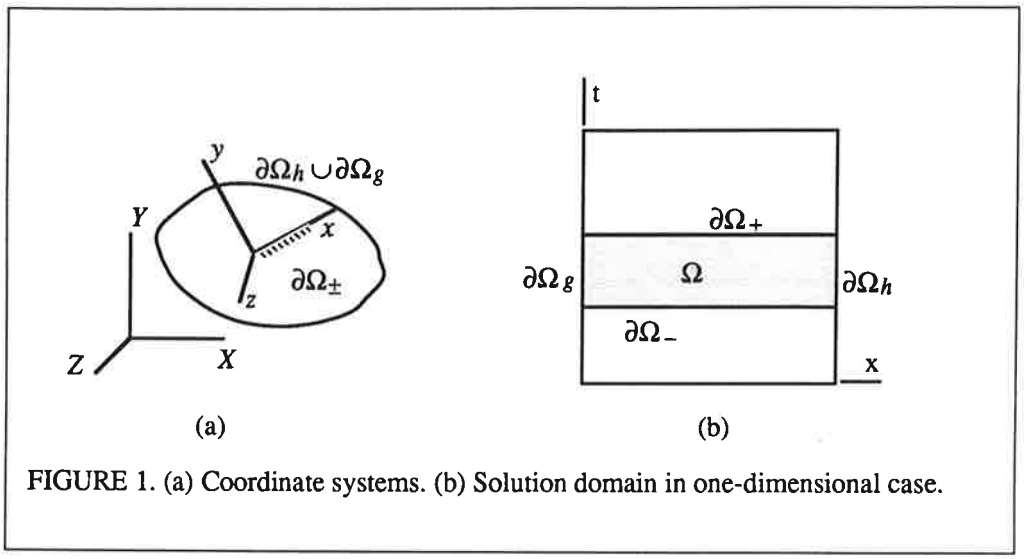

FIGURE 1. (a) Coordinate systems. (b) Solution domain in one-dimensional case.

The governing equation system for the motion of the body, i.e. the displacement field $\mathbf{u}(\mathbf{x},t)$, is

$$
\begin{aligned}
&\sigma_{ji,j} + \rho f_i - \rho u_{i,tt} = 0 && \Omega\,, \\
&u_i - \bar{u}_i = 0 && \partial\Omega_-\,, \\
&u_{i,t} - \bar{u}_{i,t} = 0 && \partial\Omega_-\,, \\
&u_i - g_i = 0 && \partial\Omega_g\,,
\end{aligned}
\tag{1}
$$

$$\sigma_{ji} n_j - h_i = 0 \qquad \partial\Omega_h ,$$

where $i,j \in \{x,y,z\}$, ρ is density, σ_{ji} the stress tensor and the solution domain Ω include both temporal and spatial domains as illustrated in Figure 1(b). The second and third equations on $\partial\Omega_-$ are the initial conditions. The subscripts g and h refer to the boundary conditions on the boundary $\partial\Omega_h \cup \partial\Omega_g$ fixing either the value of displacement or traction.

Besides equations (1), a constitutive equation relating the stress tensor to the displacement field is needed. The relationship depends on the kinematical assumptions about the displacement field as well as the material properties of the body. At this phase the exact form is, however, immaterial.

2. SOLUTION METHOD

In space-time solution methods the domain is divided into, what are called, time-slabs. A typical one with related notations is illustrated in Figure1(b). The idea is to concentrate on one time-slab at a time and determine the solution in the whole domain in a step-by step manner. Each step is carried out with the same receipt using always the obtained solution as new initial condition for the next time-slab. Consequently, it is enough to give the weak formulation for a typical slab only. The problem is to find such $\mathbf{u} - \mathbf{g} \in V$ that

$$a(\mathbf{v},\mathbf{u}) = b(\mathbf{v}) \tag{2}$$

for all $\mathbf{v} \in V$, where V is a suitably chosen space of functions (u_i , $u_{i,j}$, $u_{i,t}$ are squarely integrable in each time-slab, a proper subset will be given later). The left- and righthand side expressions are

$$\begin{aligned} a(\mathbf{v},\mathbf{u}) &= \int_\Omega \left(v_{i,j}\sigma_{ij} - v_{i,t}\rho u_{i,t}\right) d\Omega - \int_{\partial\Omega_-} \left(v_{i,t}\,\rho u_i\right) d\partial\Omega + \int_{\partial\Omega_+} \left(v_i\,\rho u_{i,t}\right) d\partial\Omega , \\ b(\mathbf{v}) &= \int_\Omega \left(v_i f_i\right) d\Omega + \int_{\partial\Omega_-} \left(v_i\,\rho \bar{u}_{i,t} - v_{i,t}\,\rho \bar{u}_i\right) d\Omega + \int_{\partial\Omega_h} \left(v_i h_i\right) d\partial\Omega . \end{aligned} \tag{3}$$

Integration by parts —assuming that the functions are smooth enough— gives clearly the original equation system. However (2) and (3) is meaningful under weaker continuity assumptions than (1) and serves well as a starting point for a numerical solution method. Similar approach is adopted for example in [1], [2], where the second equation (1) is included in the weak formulation by using the strain energy inner product. It has the obvious drawback that the rigid body part of the motion is not included without difficulties. In (3) the initial conditions are associated with the inertia term which is more correct from the physical point of view. It is easy to see that the extreme cases when either elastic or inertial effects vanish are handled correctly by (3). In the former case one obtains the standard formulation called, for example, the principle of virtual work.

2.1 About implementation. In practice it is not convenient to use totally unstructured space-time meshes as the initial values needed in a typical time-slab are obtained from the previous

slab. Thus one has to work simultaneously with two time-slabs, which makes the overall solution procedure quite complicated. Also there are startup problems due to the form of the conditions fixing the value of the function and its time derivative at the initial time level. To get an easily programmable scheme, the approximation is written in the form of a series

$$u_i(\mathbf{x},t) = \sum_k u_i^{(k)}(\mathbf{x})(t-t_+)^k / k! \,, \tag{4}$$

where the unknown $u_i^{(k)}$:s are the k:th order time derivatives of the solution at t_+. With form (4) the initial values for the next time-step are directly available. The approximations for the components $u_i^{(k)}$ are also chosen to be similar for practical reasons. The use of the approximation type (4) makes it easy to apply the method in the cases where one imposes kinematical assumptions (or dimensional reduction) to get the beam, plate etc. models. Then the continuity requirements in spatial direction for the approximation are too severe for totally unstructured space-time meshes.

The integrals over the spatial part of the domain in (3) are evaluated using a scheme where the sampling points are selected to coincide with the nodal points of the approximations $u_i^{(k)}$ in each element. Thus a certain amount of underintegration is introduced consistently in all the terms. The purpose is to add a small amount of numerical dissipation for the cases, where the exact solution is not smooth and only convergence with respect to $L_2(\partial\Omega_+)$ norm ($\|\ \|$ in the following) is to be expected. This is explained further in the next section. The selection for the integration rule can also be motivated by simple particle analogy: The elastic term can be regarded as bonding between the particles constituting a body. If it vanishes, there are no internal forces and each particle should move totally independently of the others. It is easy to see that the underintegration used disconnects the particles associated with nodes, and thus mimics the physically correct behavior.

3. NUMERICAL RESULTS

As noted above the way to enforce the initial conditions used in (3) gives a solution method with properties similar to the time discontinuous Galerkin method for first order equations [4], [5] when applied to ordinary differential equations. Some examples follow to show that the proposed selection to satisfy the initial conditions works well also in the present case. As the problems of practical interest tend to be rather complex, the numerical results are presented only for simple 1D and 2D cases, where the exact solutions are known.

3.1 Vibration of an elastic bar. To study the properties of the solution method (convergence and stability), the elastic bar problem was solved in the case where the external forces vanish, the initial velocity is zero and the initial displacement proportional to the first harmonic (for similar problem and numerical results see [1]). Unit values were specified for the length, area, density and elastic modulus E. The only non-zero displacement component is $u_x(x,t)$. Substitution of the stress-displacement relationship $\sigma_{xx} = Eu_{x,x}$ into (2) and (3) gives the weak form

$$\int_{\Omega} \left(v_{,x} E u_{,x} + v_{,tt} \rho u\right) dx dt + \int_{\partial\Omega_+} \left(v \rho u_{,t} - v_{,t} \rho u\right) dx = \int_{\partial\Omega_-} \left(v \rho \bar{u}_{,t} - v_{,t} \rho \bar{u}\right) dx \qquad (5)$$

where an additional integration by parts with respect to time is performed to show that the inertia term gives only boundary contributions when the approximation is linear in time. The form (5) is equivalent with (2) and (3) due to the restriction (4).

Figure 2 shows the error in the numerical solution as function of the spatial size of the elements. The error measures used were $\| e \|$, $\| e_{,t} \|$ and $\| e_{,x} \|$ at $\partial\Omega_+$ and the time interval studied was $T \in]0, 4[$. As it does not make much sense to study convergence with respect to either element length h or time step Δt only, the selection $\Delta t = 0.4h$ was used throughout. The bilinear space-time elements gave approximately the convergence rates h^2, h^2 and h for $\| e \|$, $\| e_{,t} \|$ and $\| e_{,x} \|$, respectively. Though the asymptotic behavior was obtained a little bit later when compared to method with exactly evaluated integrals, the use of the underintegration seemed to not affect the results considerably. The biquadratic elements gave the convergence rates about h^4, h^3 and h^2 in the same order.

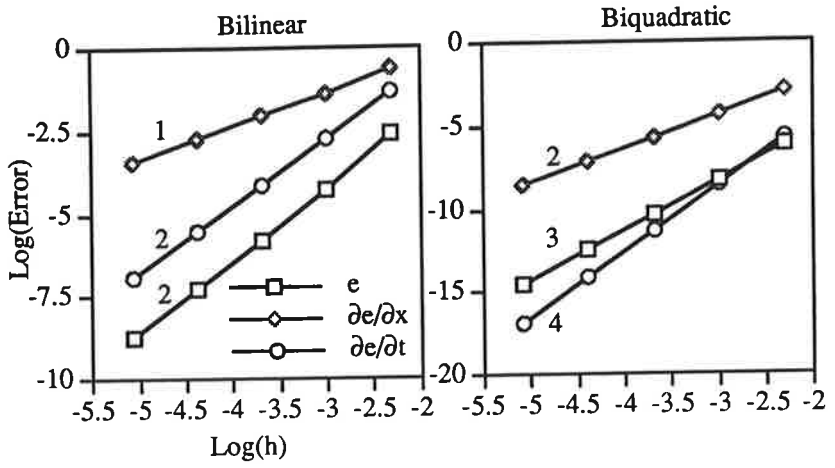

FIGURE 2. Error as function of the mesh parameter. The exact solution is $u = \sin(\pi x)\cos(\pi t)$ $x \in [0,1]$, $t \geq 0$.

When the exact solution is not smooth, the convergence rate is dominated by the smoothness of the exact solution rather than by the approximation order. In these cases spurious oscillations tend to appear near discontinuities. It is highly desirable that the spurious oscillations are localized and do not spoil the solution everywhere. To study the behavior qualitatively, two impact type problems with different smoothness in the exact solutions were solved using biquadratics. The result in Figure 3(a) shows that no problems arise when the exact solution has continuous first order derivatives. Then one can expect (viewing the figure

above) convergence for $\| e_{,x} \|$ which means in practice that no spurious oscillations arise. However, when the first order derivatives are discontinuous, one cannot expect that $\| e_{,x} \|$ stays more than bounded. The consequences can clearly be seen from Figure 3(b). At this phase one should note that the elements used were squares in space-time. For other selections the results for problem of Figure 3(b) are even worse.

Comparison shows that the method here does not localize the oscillations as well as the method in [2] containing least-squares type of stabilizing terms with tunable parameters. On the other hand it is quite clear that using terms that introduce numerical dissipation to damp the spurious oscillations means increased numerical dissipation everywhere (at least if the method is linear).

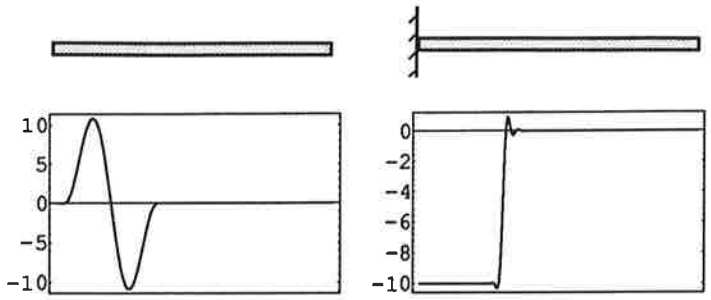

(a) (b)

FIGURE 3. Numerical results for the elastic bar problem in the case of 100 biquadratic element mesh. (a) Numerical solution for $u_{,x}$ at $t = 1.9$. The exact solution at $t = 0$ is $u = \cos^3[3\pi(x - 1/2 - t)]$ when $1/3 \le x - 1/2 - t \le 2/3$ otherwise $u = 0$. (b) Numerical solution for $u_{,x}$ at $t = 0.3$. The exact solution at $t = 0$ is $u_{,x} = 10\,(H[x - t] - 1)$ (Heaviside step).

3.2 Vibration of a membrane. The second example describes vibration of a rectangular membrane located in xy-plane. The only non-zero displacement component is $u_z(x,y,t)$. Substitution of the stress-displacement relationship ($i \in \{x,y\}$) $\sigma_{iz} = N u_{z,i}$ into equations (2) and (3) gives in this case

$$\int_\Omega \left(v_{,i} N u_{,i} + v_{,tt} \rho u\right) dxdydt + \int_{\partial\Omega_+} \left(v \rho u_{,t} - v_{,t} \rho u\right) dxdy = \int_{\partial\Omega_-} \left(v \rho \bar{u}_{,t} - v_{,t} \rho \bar{u}\right) dxdy \,, \quad (6)$$

where N is a constant. The problem can be taken as a model for more complicated systems describing the behavior of elastic waves in solids, propagation of sound etc. Both the density and the quantity N are given unit values and the boundary conditions are of homogeneous Neumann type, which means that the solution of the stationary problem is unique up to a con-

stant only.

A highly desirable property of the solution method is that the components not representable on the grid are damped out. Then, although the solution may be inaccurate, the overall behavior related to the smooth components is retained. To study the numerical damping qualitatively the problem was solved with sinusoidally varying initial condition having three components of different smoothness relative to the mesh. In all cases the initial conditions were such that the average value of the exact solution is zero all the time. The elements used were tri-linears. The results are shown in Figure 4 at $t = 0$ and $t = \sqrt{2}$ corresponding to 6 cycles of the fastest component. The number of timesteps used was 100.

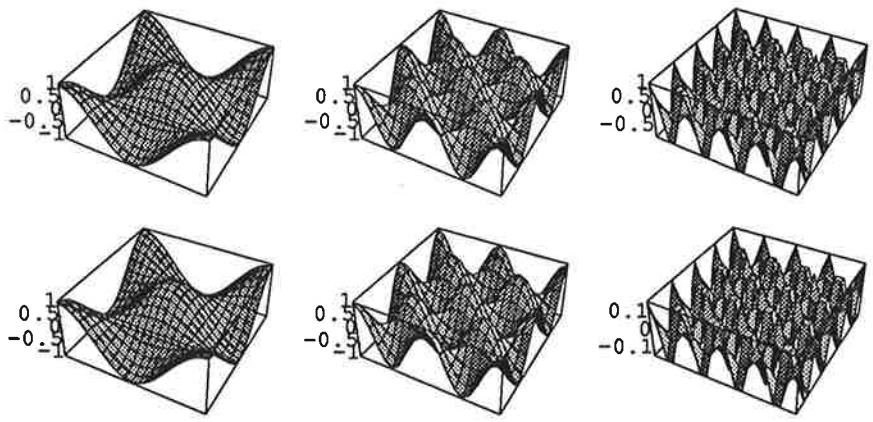

FIGURE 4. Numerical results on 20×20 element mesh. The exact solution is $u(x,y,t) = \cos(n\pi(x-1))\cos(n\pi(y-1))\cos(\sqrt{2}n\pi t)$ with $n = 2,4,6$ corresponding to the first, second and third column.

The figure shows that the components representable on the grid (loosely speaking) do not show noticeable amplitude decay. In the last case the element size becomes comparable to the wavelength, and the amplitude decay is fast. Similar behavior can be observed if the stepsize is too large to catch the solution details in the temporal direction. Consequently as any solution can be taken to be a combination of the modes like in Figure 4, one may expect unconditional stability (in energy, say) in linear cases.

4. REMARKS

The formulation described makes it possible to use a simple time-step selection method based on the jump of the solution between the time-slabs. The numerical solution has the convenient property that the error at $\partial\Omega_+$ is smaller than at $\partial\Omega_-$. Thus control over the jump at $\partial\Omega_-$ i.e

the initial condition residual gives also control over the local error at $\partial\Omega_+$, which can not be monitored directly.

In practice the use of high order approximation (quadratic etc.) in time is not tempting due to rapid increase in the problem size to be solved in each time-step. Even the method using linear approximation in time leads to a two times larger equation system than the stationary problem. However, if one wants a method which works for example in the elastic bar case with any $E,\rho \geq 0$ $E\rho \neq 0$, the doubling of the problem size seems to be unavoidable.

The solution method can easily be extended to the cases where also first order time derivative term is present by adding an initial condition contribution used in the time-discontinuous Galerkin method into equations (3) (see for example [3]). Then both parabolic and hyperbolic problems can be solved on the same footing.

The numerical results show that the proposed method works correctly in simple cases. The numerical experiments do not, however, give any idea whether the use of the approximation type (4) is essential or whether the polynomials in time could be replaced for example by another complete set. Clearly an explanation of the limitations and results obtained in the examples section would be needed.

REFERENCES

[1] Hughes, T.J.R, Hulbert, G.M, 'Space-time finite element methods for second-order hyperbolic equations, Comput. methods Appl. Mech. Eng. 84, 327-348 (1990).

[2] Hulbert, G.M, Hughes, T.J.R, 'Space-time finite element methods for elastodynamics: Formulations and error estimates, Comput. methods Appl. Mech. Eng. 66, 339-363 (1988).

[3] Johnson,C., Numerical Solution of Partial Differential Equations by The Finite Element Method, Studentlitteratur, Sweden (1987).

[4] Freund, J., A Weak Form Starting Point for ODE Integration Schemes, in Finite elements in Fluids, Eds. K.Morgan,E.Onate,J.Perioux,J.Peraire, O.C.Zienkiewicz, Pineridge Press 1993.

[5] Freund, J., A Residual Equation Based Numerical Solution Method For Initial Value Problems, In preparation.

ON MITC PLATE BENDING ELEMENTS - IMPLEMENTATION AND PRACTICAL ENGINEERING APPLICATIONS

TIMO HOLOPAINEN, KAI KATAJAMÄKI and PAUL KLINGE
Maritime Technology
VTT Manufacturing Technology
PL 1705, 02044 VTT, FINLAND

MIKKO LYLY
Faculty of Mechanical Engineering
Helsinki University of Technology
02150 Espoo, FINLAND

ABSTRACT

In this paper we discuss finite element analysis of plate structures using (stabilized) MITC plate bending elements. We will briefly review the plate bending model and introduce the MITC element family. After that, some numerical results are given for two benchmark examples and for two more complicated engineering structures. The experience of using these new elements in the SHIPFEM finite element program has been very encouraging.

1. INTRODUCTION

In VTT Manufacturing Technology (earlier in Ship Laboratory) the FEM has been applied to analyze ship and other complicated structures from late 70's. Along these calculations a FE-analysis system called SHIPFEM has been developed.

Ships are large structures with very complex behaviour on many levels of hierarchy which, in addition, are floating freely on water. Analyzing such structures is a quite complicated task and the main motivation in developing SHIPFEM has been to make these analyses faster, more flexible and reliable.

Both static and dynamic analyses can be made with SHIPFEM, but it has been developed especially for dynamic analyses of ships. It contains analysis features like: dynamic substructures [1], coupling of local and global behaviour [2], coupling of structure and fluid [3], and infinite fluid elements [4]. The basic analysis features of the system have remained about the same from the mid 80's. Since that, however, most of the code has been rewritten in order to utilize some new subsystems which have been included; the error and memory handling routines and the database [5].

A ship, as well as many other engineering structures, is composed of stiffened plates. The basis of the analysis of plate structures is a robust and reliable set of flat shell elements

- at least a set of linear and quadratic (triangular and quadrilateral) elements which are able to handle both "thin" and "thick" plates.

In the beginning of 80's the so called "shear locking" problem of the traditional thick plate elements was recognized - the elements become much too stiff if the thickness of the plate is small. The locking is usually total if linear elements ase used. For higher order methods the locking is not that severe; usually it is observed only as a decrease in the accuracy. The first solution to the locking problem in SHIPFEM context was the employment of only quadratic elements for thin plates. This was, however, not a satisfactory solution because the convegence rate, i.e., the accuracy versus degrees-of-freedom was not optimal. The second attempt to solve the problem was to apply reduced integration techniques. This led, just as before, in some cases to unsatisfactory results - due to zero energy modes and problems in solution procedures. The third approach was to modify artificially the shear energy. This was done by reducing the shear correction factor in a similar way that Fried and Yang did in their paper, cf. [6]. The disadvantage of this approach was that the so called "α-parameter" had to be determined through testing or experience.

In the late 80's and in the beginning of 90's, the locking free (stabilized) MITC (Mixed Interpolated Tensorial Components) plate bending elements were introduced, cf. e.g. [7], [8], [9], [10]. Since the Laboratory for Strength of Materials in HUT was involved in the developement of these elements, it seemed quite natural to initiate co-operation between VTT and HUT, and so bring together the theoretical results and the practical applications. This co-operaton led to the implementation of the MITC element family into the SHIPFEM package.

In the next section we will briefly review the plate bending model and introduce the MITC elements. Due to a limited space, we will concentrate on free vibration analysis of plates structures only; for static analysis we refer to [11]. After that, we will give some numerical results for two simple test examples and for two more complicated practical structures. We finally conclude the paper with some remarks corncerning the implementation and the usefulness of the new elements.

2. THE THICK PLATE MODEL AND THE FINITE ELEMENTS

Let us denote by ω and $\boldsymbol{u}(x,y) = (w, \boldsymbol{\beta})$ the natural angular frequencies and the mode shape functions of the plate. Here $w(x,y)$ and $\boldsymbol{\beta}(x,y) = (\beta_x, \beta_y)$ are the modal deflection and the two modal rotations of the normals of the plate, respectively.

In free vibration analysis of thick plates (Reissner-Mindlin plates) the variational eigenvalue problem is [12]: find ω and $\boldsymbol{u} \in \mathcal{U}_{ad}$ such that

$$\mathcal{B}(\boldsymbol{u}, \boldsymbol{v}) = \omega^2 \mathcal{D}(\boldsymbol{u}, \boldsymbol{v}) \quad \text{for all } \boldsymbol{v} = (v, \boldsymbol{\eta}) \in \mathcal{U}_{ad}. \tag{1}$$

The bilinear forms $\mathcal{B}$ and $\mathcal{D}$ are defined as

$$\mathcal{B}(\boldsymbol{u}, \boldsymbol{v}) = \frac{Et^3}{12(1-\nu^2)} a(\boldsymbol{\beta}, \boldsymbol{\eta}) + G\kappa t \int_A (\nabla w - \boldsymbol{\beta}) \cdot (\nabla v - \boldsymbol{\eta}) \, dA, \tag{2}$$

$$\mathcal{D}(\boldsymbol{u}, \boldsymbol{v}) = \rho t \int_A wv \, dA + \frac{\rho t^3}{12} \int_A \boldsymbol{\beta} \cdot \boldsymbol{\eta} \, dA, \tag{3}$$

where

$$a(\boldsymbol{\beta}, \boldsymbol{\eta}) = \int_A [(1-\nu)\boldsymbol{\varepsilon}(\boldsymbol{\beta}) : \boldsymbol{\varepsilon}(\boldsymbol{\eta}) + \nu \, \mathrm{div}\boldsymbol{\beta} \, \mathrm{div}\boldsymbol{\eta}] \, dA. \tag{4}$$

Here $\mathcal{U}_{ad}$ is the set of kinematically admissible mode shape functions for which the strain energy is finite. E, G, ν and ρ are isotropic material parameters and t is the thickness of the plate. κ is the shear correction factor. $\boldsymbol{\varepsilon}(\,\cdot\,)$ is the linear small strain operator and "div" stands for the divergence. The midsurface of the plate is denoted by A.

The finite element methods are defined as follows: the problem is to find approximate natural frequencies ω_h and the corresponding mode shape functions $\boldsymbol{u}_h = (w_h, \boldsymbol{\beta}_h) \in \mathcal{U}_{ad}^h$ such that

$$\mathcal{B}_h(\boldsymbol{u}_h, \boldsymbol{v}) = \omega_h^2 \mathcal{D}(\boldsymbol{u}_h, \boldsymbol{v}) \quad \text{for all } \boldsymbol{v} = (v, \boldsymbol{\eta}) \in \mathcal{U}_{ad}^h. \tag{5}$$

Here $\mathcal{U}_{ad}^h$ is the finite element subspace of $\mathcal{U}_{ad}$. The bilinear form $\mathcal{B}_h$ is a discrete modification of the original form $\mathcal{B}$. Both $\mathcal{U}_{ad}^h$ and $\mathcal{B}_h$ will be defined differently for each element:

2.1 The stabilized MITC3 and MITC4 elements [7], [13], [10]. These elements utilize standard isoparametric (bi)linear shape functions for the deflection and both components of the rotation vector. Hence $\mathcal{U}_{ad}^h$ is the usual finite element subspace for three or four noded thick plate elements.

The bilinear form $\mathcal{B}_h$ in the left-hand-side of (5) is defined as

$$\mathcal{B}_h(\boldsymbol{u}, \boldsymbol{v}) = \frac{Et^3}{12(1-\nu^2)} a(\boldsymbol{\beta}, \boldsymbol{\eta}) + G\kappa \sum_K \frac{t^3}{t^2 + \alpha h_K^2} \int_K (\nabla w - \boldsymbol{R}_h \boldsymbol{\beta}) \cdot (\nabla v - \boldsymbol{R}_h \boldsymbol{\eta})\, dA, \tag{6}$$

where $\boldsymbol{R}_h$ is a special "MITC reduction operator" (see e.g. [11] for the exact definition). In the shear term of (6) h_K denotes the diameter of the element K in the mesh and α is a posivite constant called the "α-parameter".

The stabilized MITC3 and MITC4 elements were first introduced and analyzed by Brezzi, Fortin and Stenberg in [10]. They considered the static analysis case and proved that the elements are stable and optimally convergent for all plate thicknesses. The numerical examples e.g. in [11] confirm that the theoretical results are in accordance with the practice.

REMARK 1. With $\alpha = 0$ one obtains the original MITC4 element of Bathe and Dvorkin [7] and the original MITC3 element of Hughes and Taylor [13] (in these papers, however, the name MITC was not used).

REMARK 2. It is possible to show that the condition number of the global stiffness matrix is $\mathcal{O}(t^{-2}h^{-2})$ and $\mathcal{O}(h^{-4})$ for the original and stabilized MITC elements, respectively. Here $h = \max h_K$ is the global mesh parameter. Since is practice $t << h$, the stabilized elements produce much better conditioned stiffness matrices than the original elements.

2.2 The MITC7 and MITC9 elements [8], [9]. These elements utilize isoparametric (bi)quadratic (serendipity type) shape functions for the deflection and both components of the rotation vector. In addition to this, the rotation space consists of hierarcical "bubble functions" for which the degrees of freedom are given, e.g., by the centre nodes of the elements. We refer to [9] for the exact definition for $\mathcal{U}_{ad}^h$.

The bilinear form B_h in the left-hand-side of (5) is now

$$\mathcal{B}_h(\boldsymbol{u}, \boldsymbol{v}) = \frac{Et^3}{12(1-\nu^2)} a(\boldsymbol{\beta}, \boldsymbol{\eta}) + G\kappa t \int_A (\nabla w - \boldsymbol{R}_h \boldsymbol{\beta}) \cdot (\nabla v - \boldsymbol{R}_h \boldsymbol{\eta})\, dA, \tag{7}$$

where, as in (6), $\boldsymbol{R}_h$ is the MITC reduction operator (cf. [8]).

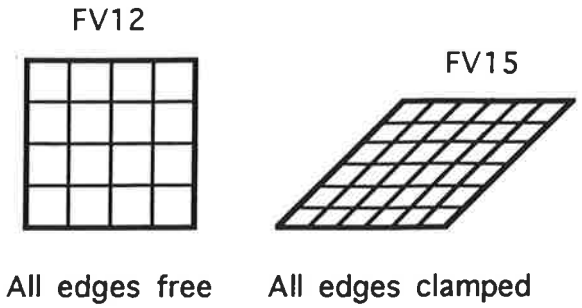

FIGURE 1: The NAFEMS tests FV12 and FV15.

REMARK 3. In this paper, the reduction operator for the MITC9 element is constructed using the so called "point tying" technique instead of the exact "integral tying", cf. [9].

3. SOME NUMERICAL TEST EXAMPLES

In this section two "standard" NAFEMS benchmark tests for free vibration analysis of thin plates are considered: the FV12 test for a free square plate and the FV15 test for a clamped skew plate [14]. A full consistent mass matrix is used and the solution is extracted using the subspace iteration techniuque.

In both test cases we choose $\alpha = 0.2$ for the stabilized MITC3 and $\alpha = 0.1$ for the stabilized MITC4. The shear correction factor is taken as $\kappa = 5/6$ and the thickness of the plate is $t = 0.05\ m$. The material parameters are $E = 200\ GPa$, $\nu = 0.3$ and $\rho = 8000\ kg/m^3$. The lenght of the edges is 10 m in both test problems. In the FV15 test the skew angle at the obtuse vertices is 135°.

In Figure 1 the 4×4 and 6×6 meshes for the MITC9 elements are shown. For the stabilized MITC4 element 8×8 and 12×12 meshes are used. The triangulations for the MITC7 and stabilized MITC3 elements are obtained from these meshes by splitting the quadrilaterals into two triangulars.

3.1 The FV12 test. In this test we calculate the nine lowest natural frequencies for the test plate. Since the plate is completely free, three rigid body modes will occur. The "exact" natural frequencies are given by the Kirchhoff plate theory. The results from the calculations are shown in Table 1. (L.O.E. and H.O.E. denote the low and high order reference elements for which the results are obtained from [14]. These elements are actually the four-noded element with selective reduced integration [15] and the eight-noded semiloof element [16]. STAB3 and STAB4 refer to the stabilized MITC3 and MITC4 elements.).

As we can see from Table 1 below, all elements perform excellently in this test. No zero energy modes occur and the accuracy of the elements is always better than 6% for the stabilized MITC3 and MITC4 and better than 3% for the MITC7 and MITC9.

3.2 The FV15 test. In this test we calculate the six lowest natural frequencies for the clamped skew test plate. The exact frequencies are again defined through the Kirchhoff model. For this test the calculated results are shown in Table 2. As we can see, especially the triangular elements surprise with their seemingly good accuracy. Also the stabilized MITC4 and the MITC9 elements work very well compared to the L.O.E. and H.O.E. elements.

TABLE 1: The errors $(\omega_h - \omega)/\omega$ for the five lowest elastic modes in the FV12 test. Frequencies 7 and 8 are identical. The three rigid body modes are not listed.

Mode	L.O.E.	STAB3	STAB4	H.O.E.	MITC7	MITC9
4	0.6 %	0.1 %	0.1 %	-5.5 %	0.0 %	-0.2 %
5	1.8 %	1.4 %	1.6 %	-0.2 %	0.2 %	-0.3 %
6	2.9 %	2.2 %	2.6 %	-2.1 %	0.3 %	-0.3 %
7	0.4 %	0.8 %	0.5 %	-2.6 %	-0.8 %	-1.6 %
9	6.0 %	5.6 %	6.0 %	-0.7 %	0.7 %	-2.8 %

TABLE 2: The errors $(\omega_h - \omega)/\omega$ in the FV15 test.

Mode	L.O.E.	STAB3	STAB4	H.O.E.	MITC7	MITC9
1	2.6 %	1.3 %	1.8 %	-0.8 %	0.1 %	-0.3 %
2	8.2 %	3.7 %	6.9 %	-2.8 %	0.5 %	0.4 %
3	11.7 %	5.3 %	9.8 %	-3.5 %	0.8 %	0.9 %
4	5.4 %	3.0 %	3.7 %	-2.1 %	0.0 %	-1.3 %
5	16.4 %	7.0 %	13.8 %	-5.4 %	0.8 %	0.7 %
6	14.8 %	6.6 %	11.9 %	-7.3 %	0.8 %	-3.9 %

4. PRACTICAL ENGINEERING APPLICATIONS

4.1 A stiffened panel. The first numerical example representing engineering structures is a stiffened panel. The vibration behaviour of this panel has been measured and calculated by FEM in a previous study [17]. The main dimensions of the panel are $3.0 \times 2.4 \times 0.45$ m, and the thickness of the plating, webs and flanges varies from 3 to 6 mm. The applied element meshes are shown in Figure 2. The detailed dimensions of the panel and the 20 lowest natural frequencies obtained using MITC9 flat shell elements (= MITC9 plate + 8-noded plane stress element [18]) and three different mesh configurations are presented in Ref. [17]. In this study the frequencies obtained by MITC9 and full integrated 9-node thick shell elements (FI9) [18] are compared. Figure 3 shows the proportional differences between the natural frequencies obtained by MITC9 elements and by the other mesh and element combinations.

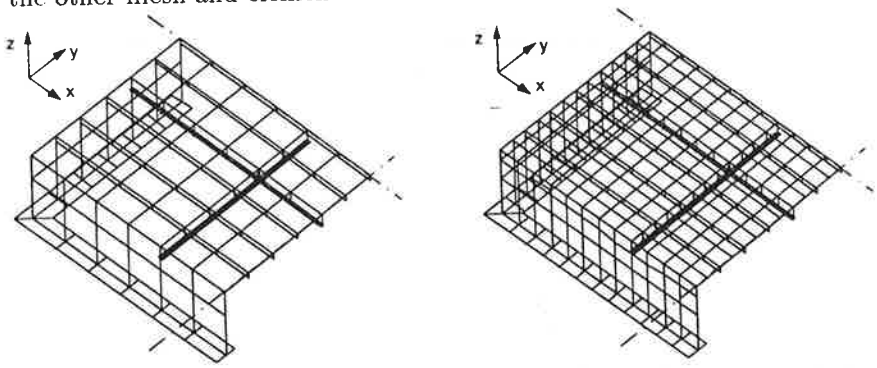

FIGURE 2: The coarse and refined element meshes. The meshes consist of 129 and 351 elements. Only one-quarter of the panel is modelled.

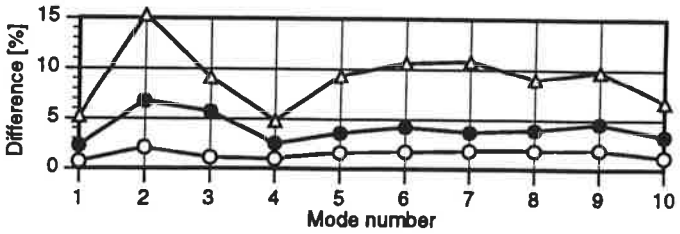

FIGURE 3: The relative differences between the natural frequencies obtained by MITC9 elements (the refined mesh) and by three other mesh and element combinations. The refined mesh and FI9 elements (○), the coarse mesh and MITC9 elements (●), the coarse mesh and FI9 elements (◇).

Figure 3 shows that the natural frequencies obtained using MITC9 elements and the refined mesh are systematically below the frequencies obtained by FI9 elements. The same is true in the case of the coarse mesh. This systematic difference results from the overly stiff behaviour (shear locking) of the full integrated thick shell elements. Although the meshes are regular and only the global behaviour (10 lowest modes) of the structure is considered, the example shows that the shear locking can reduce the accuracy considerably also in practical engineering analyses.

4.2 A cabriolet vehicle. The geometry of a car body is relatively complex and it consists of many different structural parts. As a result, the size of the calculation model easily becomes very large. Because of a limited computational capacity, relatively large elements ($t << h$) must be used. This increases the risk of shear locking or other numerical problems when traditional shell elements are applied.

In a previously accomplished co-project VTT received the finite element model of a cabriolet vehicle from Oy Saab-Valmet Ab. The model is shown in Figure 4 with hidden lines removed.

The car body has been analyzed with three different linear (3 noded) flat shell elements: the original SHIPFEM element with user defined α-parameter, the STRI3 element of ABAQUS [19] and the stabilized MITC3. We will denote the natural frequencies calculated with these elements by ω_{ORIG}, ω_{STRI3} and ω_{STAB3}, respectively.

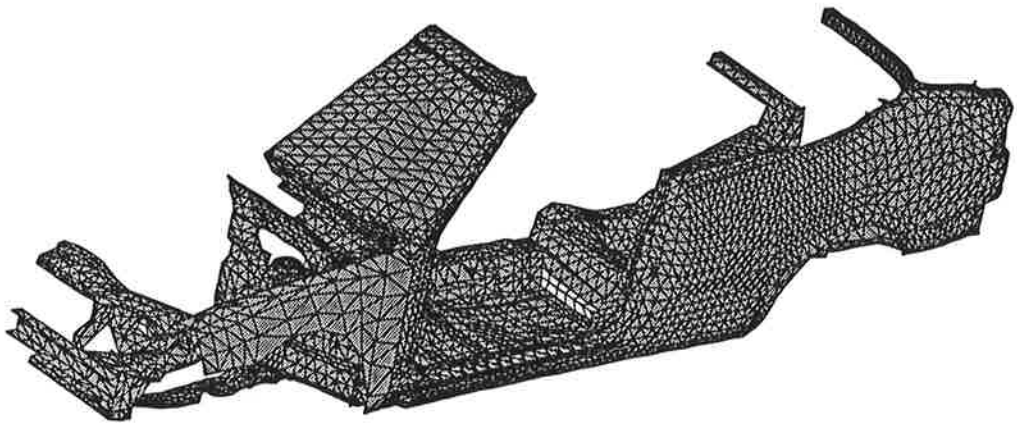

FIGURE 4: The finite element model of a car body consists of about 20,000 flat shell elements and the number of degrees-of-freedom is about 57,000.

The 10 lowest natural modes and frequencies were calculated. The results obtained using different elements are compared in Figure 5. (Unfortunately, two slightly different meshes of the same car body had to be used. First, the results obtained by elements ORIG and STRI3 were compared employing Mesh 1. Then the elements ORIG and STAB3 were compared using Mesh 2).

From Figure 5 we see that the differences between the results is relatively large if compared to the size of the model. Eventhough the results of the STRI3 and STAB3 elements can not be compared like one-to-one, they are more close to each other than to the original SHIPFEM element.

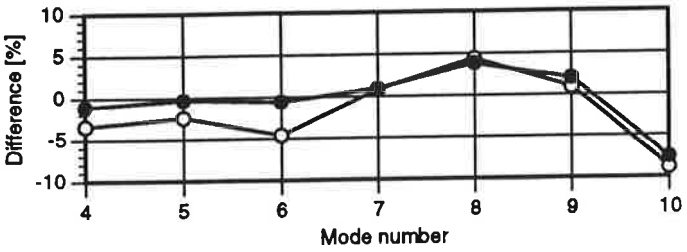

FIGURE 5: The differences $(\omega_{STRI3} - \omega_{ORIG})/\omega_{ORIG}$ (denoted by o) and $(\omega_{STAB3} - \omega_{ORIG})/\omega_{ORIG}$ (denoted by •).

5. CONCLUDING REMARKS

The results obtained using MITC elements both in simple numerical examples and practical engineering applications demonstrate the excellent predictive capability of these elements. The family of MITC elements forms a theoretically sound set both for thin and thick plate structures. The experiences in practical engineering analyses show that the MITC family is very suitable and easy to use.

The main disadvantage of the MITC elements is the relatively large programming effort which is needed to transfer these elements to a part of a larger FE-package. This results from the special configuration of the MITC elements (especially the MITC7 and MITC9).

There are some limitations related to the quadratic MITC elements presented in this study. One practical limitation is the fact that the MITC7 and MITC9 elements can not have curved boundaries. In addition, the present family of MITC elements can not be used as a variable-number-nodes element [18]. More research effort is required to enlarge the family of MITC elements to these directions.

REFERENCES

[1] S. Kivimaa. Substructure synthesis in the dynamic analysis of ship structures. In *The 4th Marine Technology Symposium, VTT Symposium 68*, pages 35–71, Espoo, 1986.

[2] M.K. Hakala. Numerical modelling of fluid-structure and structure-structure interaction in ship vibration. VTT Publications 22, Technical Research Centre of Finland, VTT, Espoo, 1985.

[3] M.K. Hakala. Application of the finite element method to fluid-structure interaction in ship vibration. Research reports 433, Technical Research Centre of Finland, VTT, Espoo, 1986.

[4] P. Klinge. Modelling of the surrounding water in ship vibration calculations. In *The 4th Marine Technology Symposium, VTT Symposium 68*, pages 73–92, Espoo, 1986.

[5] P. Klinge. The database for the structural analysis in VTT. Internal report, Technical Research Centre of Finland, VTT, Espoo, 1989.

[6] I. Fried and S.K. Yang. Triangular, nine-degrees-of-freedom, C^0 plate bending element of quadratic accuracy. *Quart. Appl. Math.*, 31:303–312, 1973.

[7] K.J. Bathe and E. Dvorkin. A four node plate bending element based on Mindlin-Reissner plate theory and mixed interpolation. *Int. J. Num. Meths. Eng.*, 21:367–383, 1985.

[8] K.J. Bathe F. Brezzi and M. Fortin. Mixed-interpolated elements for Reissner-Mindlin plates. *Int. J. Num. Meths. Eng.*, 28:1787–1801, 1989.

[9] F. Brezzi K.J. Bathe and S. W. Cho. The MITC7 and MITC9 plate elements. *Comput. Struct.*, 32:797–814, 1989.

[10] F. Brezzi, M. Fortin and R. Stenberg. Error analysis of mixed-interpolated elements for Reissner-Mindlin plates. *Mathematical Models and Methods is Applied Sciences*, 1:125–151, 1991.

[11] M. Lyly, R. Stenberg, and T. Vihinen. A stable bilinear element for the Reissner-Mindlin plate model. *Comp. Meths. in Appl. Mech. Engrg.*, 110:343–357, 1993.

[12] B. Szabó and I. Babuška. *Finite Element Analysis.* John Wiley, 1991.

[13] T. J. R. Hughes and R. L. Taylor. The triangular plate bending element. In J. R. Whiteman, editor, *The Mathematics of Finite Elements and Applications IV, MAFELAP 1981*, pages 127–142. Academic Press, 1982.

[14] R. T. Fenner G. A. O. Davis and R. W. Lewis. *Background to Benchmarks.* NAFEMS, 1993.

[15] R. L. Taylor T. J. R. Hughes and W. Kanoknukulchai. A simple and efficient finite element for plate bending. *Int. J. Num. Meth. Engrg.*, 11:1529–1543, 1977.

[16] B. Irons and S. Ahmad. *Techniques of Finite Elements.* Ellis Horwood, 1986.

[17] T. Holopainen and I. Vessonen. Experimental and numerical vibration analyses of a stiffened panel. VTT Publications 129, Technical Research Centre of Finland, VTT, Espoo, 1993.

[18] K.J. Bathe. *Finite Element Procedures in Engineering Analysis.* Prentice-Hall, New Jersey, 1982.

[19] *ABAQUS Theory Manual, Version 4.8.* Hibbitt, Karlsson & Sorensen, Inc, 1989.

ON THE SOLUTION OF NON-LINEAR DIFFUSION EQUATION

REIJO KOUHIA
Laboratory of Structural Mechanics
Helsinki University of Technology
Rakentajanaukio 4A, 02150 Espoo, Finland

ABSTRACT

Solution of the diffusion equation is usually performed with the finite element discretization for the spatial elliptic part of the equation and the time dependency is integrated via some difference scheme, often the trapezoidal rule (Crank-Nicolson) or the unconditionally stable two-step algorithm of Lees. A common procedure is to use Picard's iteration with the trapezoidal rule. However, in highly non-linear problems the convergence of Picard's iteration is untolerably slow. A simple remedy is to use consistent linearization and Newton's method. This paper concentrates on the use of quasi-Newton update schemes in solving the resulting non-linear equation system. Numerical results of highly non-linear diffusion problems are shown and the convergence of the quasi-Newton updates has been investigated. Also a note concerning temporal discretization is given.

1 INTRODUCTION

The governing energy conservation equation is

$$-\nabla \cdot \mathbf{q} + \bar{s} = c\dot{u}, \tag{1}$$

where $\mathbf{q}$ is the flux vector, which is related to the gradient of the quantity u by the constitutive law

$$\dot{\mathbf{q}} = -\mathbf{D}(u, \mathbf{g})\dot{\mathbf{g}}, \qquad \mathbf{g} = \nabla u. \tag{2}$$

Time derivatives are indicated by superimposed dots ($\partial u/\partial t = \dot{u}$). Equations (1) and (2) form a system which can be used to describe many diffusive physical phenomenas, e.g. heat conduction, seepage flow, electric fields and frictionless incompressible irrotational flow. In the case of heat conduction u stands for temperature and $\bar{s}, c, \mathbf{q}$ are the heat source, the heat capacity and the heat flux, respectively.

After finite element semidiscretization, the energy equation (1) takes the form

$$\mathbf{C}\dot{\mathbf{u}} = \mathbf{f}(t, \mathbf{u}), \tag{3}$$

in which $\mathbf{f}$ denotes the unbalance between the given source $\bar{\mathbf{s}}$ and the internal nodal 'fluxes' $\mathbf{r}$, i.e.

$$\mathbf{f} = \bar{\mathbf{s}} - \mathbf{r}.$$

The internal nodal flux vector and the source vector are computed from the element contributions

$$\mathbf{r}^{(e)} = \int_{V^{(e)}} \mathbf{B}^T \mathbf{q} dV, \qquad \bar{\mathbf{s}}^{(e)} = \int_{V^{(e)}} \mathbf{N}^T \bar{s} dV,$$

where $\mathbf{B}$ is the matrix of discretized gradient operator and $\mathbf{N}$ is the row matrix containing the finite element interpolation functions.

If the temporal discretization is performed by the one-step one-parameter method:

$$\mathbf{u}_{n+\alpha} = (1-\alpha)\mathbf{u}_n + \alpha \mathbf{u}_{n+1}, \tag{4}$$

then the fully discretized equation system is obtained from (3)

$$\frac{\alpha}{\Delta t}\mathbf{C}(\mathbf{u}_{n+\alpha} - \mathbf{u}_n) - \mathbf{f}(t_{n+\alpha}, \mathbf{u}_{n+\alpha}) = \mathbf{0}, \tag{5}$$

where $\mathbf{C}$ is the heat capasitance matrix. This one-parameter family of methods comprises both the common implicit backward Euler ($\alpha = 1$) and Crank-Nicolson ($\alpha = \frac{1}{2}$) methods and the explicit Euler forward scheme ($\alpha = 0$). In non-linear problems only the midpoint version of the trapezoidal rule is unconditionally stable [1], [2]. It is also the only one of this family which is second order accurate. In linear cases the midpoint scheme is identical with the standard trapezoidal rule.

The trapezoidal rule has no algorithmic damping. This produces spurious oscillations if the data is not smooth. A simple remedy for suppressing these oscillations is to use for the few first steps the implicit backward Euler scheme and then switch to the second order accurate midpoint rule. This has no effect on the long term accuracy.

In order to solve the non-linear equation system (5) a Newton-type linearization step is utilized and the resulting equation, at a certain step $n+1$ and iteration i, is the following:

$$\left(\frac{\alpha}{\Delta t}\mathbf{C}^i + \mathbf{K}^i\right)\delta\mathbf{u}^{i+1} = \mathbf{f}(t_{n+\alpha}, \mathbf{u}^i_{n+\alpha}) - \frac{\alpha}{\Delta t}\mathbf{C}^i \Delta \mathbf{u}^i, \tag{6}$$

where

$$\mathbf{K}^i = -\left.\frac{\partial \mathbf{f}}{\partial \mathbf{u}}\right|_{\mathbf{u}^i}$$

is the tangent matrix, and the iterative and incremental steps are defined by the equation

$$\mathbf{u}^{i+1}_{n+\alpha} = \mathbf{u}_n + \Delta \mathbf{u}^i + \delta \mathbf{u}^{i+1}.$$

The tangent matrix consists of several parts:

$$\mathbf{K}^i = \mathbf{K}^i_0 + \mathbf{K}^i_u + \mathbf{K}^i_g + \mathbf{K}^i_s + \mathbf{K}^i_r,$$

where $\mathbf{K}_0$ is the linear part, $\mathbf{K}_u$ and $\mathbf{K}_g$ come from the u and $\mathbf{g}$ dependencies of the constitutive equation (2), $\mathbf{K}_r$ from the non-linear radiation boundary condition and $\mathbf{K}_s$ from the u dependent source term. They are assembled from the element matrices

$$\mathbf{K}_0^{(e)^i} = \int_{V^{(e)}} \mathbf{B}^T \mathbf{D}^i \mathbf{B} dV, \qquad \mathbf{D}^i = \mathbf{D}(u^i, \mathbf{g}^i), \tag{7a}$$

$$\mathbf{K}_u^{(e)^i} = \int_{V^{(e)}} \mathbf{B}^T \mathbf{G}^i dV, \qquad \mathbf{G}^i = \left(\frac{\partial \mathbf{D}}{\partial u}\Big|_{u^i, \mathbf{g}^i} \right) \mathbf{g}^i \mathbf{N}, \tag{7b}$$

$$\mathbf{K}_g^{(e)^i} = \int_{V^{(e)}} \mathbf{B}^T \mathbf{D}_g^i \mathbf{B} dV, \qquad \mathbf{D}_g^i = \left(\frac{\partial \mathbf{D}}{\partial \mathbf{g}}\Big|_{u^i, \mathbf{g}^i} \right) \mathbf{g}^i, \tag{7c}$$

$$\mathbf{K}_s^{(e)^i} = \int_{V^{(e)}} \frac{\partial \bar{s}}{\partial u} \mathbf{N}^T \mathbf{N} dV, \tag{7d}$$

$$\mathbf{K}_r^{(e)^i} = \int_{S^{r(e)}} C_r^i \mathbf{N}^T \mathbf{N} dS, \tag{7e}$$

where C_r is a coefficient containing the radiation and emission coefficients of the radiating surface. All matrices, except $\mathbf{K}_u$, are symmetric. Dependency of the constitutive matrix $\mathbf{D}$ on u is common in many physical problems. However, the unsymmetric part is usually neglected in the solution of equation (6).

2 QUASI-NEWTON TECHNIQUES

2.1 Basic properties. A class of algorithms called quasi-Newton (or variable metric, variance, secant, update or modification methods) have been developed in order to speed up the convergence of the modified Newton method and which could be more efficient than the true Newton-Raphson scheme. The basic idea of these methods is to develope an update formula of the tangent matrix, i.e. a good approximation, in such a way which avoids the reforming and factorization of the global matrix.

In order to simplify the notation some abbreviations are introduced. Equation (6) can be written concisely in the following form:

$$\mathbf{H}^i \delta \mathbf{u}^{i+1} = \tilde{\mathbf{f}},$$

where

$$\mathbf{H}^i = \frac{\alpha}{\Delta t} \mathbf{C}^i + \mathbf{K}^i \qquad \tilde{\mathbf{f}} = \mathbf{f}(t_{n+\alpha}, \mathbf{u}_{n+\alpha}^i) - \frac{\alpha}{\Delta t} \mathbf{C}^i \Delta \mathbf{u}^i.$$

In the following the wavy line over the unbalanced nodal flux vector is omitted. The basic requirement for the approximation $\tilde{\mathbf{H}}^i$ is to satisfy the *secant relationship* or *quasi-Newton* equation

$$\begin{aligned} \mathbf{f}(\mathbf{q}^i) &= \mathbf{f}(\mathbf{q}^{i-1}) - \tilde{\mathbf{H}}^i (\mathbf{q}^i - \mathbf{q}^{i-1}), \\ \Rightarrow \quad \tilde{\mathbf{H}}^i \delta \mathbf{q}^i &= \delta \mathbf{f}^i \quad \text{or} \quad \tilde{\mathbf{A}}^i \delta \mathbf{f}^i = \delta \mathbf{q}^i, \end{aligned} \tag{8}$$

where[1]

$$\delta \mathbf{q}^i = \mathbf{q}^i - \mathbf{q}^{i-1}, \quad \delta \mathbf{f}^i = \mathbf{f}^{i-1} - \mathbf{f}^i, \quad \tilde{\mathbf{A}}^i = (\tilde{\mathbf{H}}^i)^{-1}.$$

In order to get a uniquely defined matrix additional requirements have to be imposed. A reasonable requirement is, that the updated matrix $\tilde{\mathbf{H}}^i$ is close to the previous matrix $\mathbf{H}^{i-1}$. This nearness is measured by matrix norms, and usually, in connection to quasi-Newton updates, the Frobenius norm or its weighted form are often used. It is also desirable that the updated matrix should inherit some properties which are characteristic

[1]Notice the difference in definition of $\delta \mathbf{q}$ and $\delta \mathbf{f}$.

to the system. In finite element applications such properties usually are symmetry and positive definiteness of the tangent matrix. So, the update $\tilde{\mathbf{H}}^i$ (or $\tilde{\mathbf{A}}$) should also satisfy:

$$\begin{aligned} &\text{if} \quad \mathbf{H}^{i-1} = (\mathbf{H}^{i-1})^T \quad \text{then} \quad \tilde{\mathbf{H}}^i = (\tilde{\mathbf{H}}^i)^T \\ &\text{if} \quad \mathbf{x}^T\mathbf{H}^{i-1}\mathbf{x} > 0 \quad \text{then} \quad \mathbf{x}^T\tilde{\mathbf{H}}^i\mathbf{x} > 0, \quad \forall \mathbf{x} \neq \mathbf{0}. \end{aligned}$$

However, it should be remembered that the new iterative change $\delta\mathbf{q}^{i+1}$ has to be easily and cost effectively computed, otherwise the benefit of this kind of update is lost since the price which is paid for omitting the full Newton step is the degradation of the convergence rate.

The quasi-Newton techniques are closely related to the conjugate-Newton methods, see Refs. [4], [5], [6]. Applications of quasi-Newton strategies to structural and fluid flow problems can be found in Refs. [7] [8], [9]

2.2 Rank-one update. A single rank update to the tangent matrix is a correction of the form

$$\tilde{\mathbf{H}} = \mathbf{H} + \alpha\hat{\mathbf{y}}\hat{\mathbf{z}}^T \quad \text{or} \quad \tilde{\mathbf{A}} = \mathbf{A} + \beta\hat{\mathbf{u}}\hat{\mathbf{v}}^T \tag{9}$$

where the unit vectors $\hat{\mathbf{y}}, \hat{\mathbf{z}}$ (or $\hat{\mathbf{u}}, \hat{\mathbf{v}}$) and the scalar α (or β) are to be determined. Substituting this expression into the quasi-Newton equation (8) and minimizing the difference between the update and the previous matrix, gives the Broyden update formula [10]:

$$\tilde{\mathbf{H}} = \mathbf{H} + \frac{(\delta\mathbf{f} - \mathbf{H}\delta\mathbf{q})\delta\mathbf{q}^T}{\delta\mathbf{q}^T\delta\mathbf{q}} \quad \text{or} \quad \tilde{\mathbf{A}} = \mathbf{A} + \frac{(\delta\mathbf{q} - \mathbf{A}\delta\mathbf{f})\delta\mathbf{f}^T\mathbf{A}}{\delta\mathbf{f}^T\mathbf{A}\delta\mathbf{f}} \tag{10}$$

Broyden's update formula does not have the property of hereditary symmetry and positive definiteness. However, it is interesting to note, that a symmetric rank one update is obtained from (9) by choosing $\mathbf{z} = \mathbf{y} = \delta\mathbf{f} - \mathbf{H}\delta\mathbf{q}$ (or $\mathbf{u} = \mathbf{v} = \delta\mathbf{q} - \mathbf{A}\delta\mathbf{f}$). Obviously in this case the closeness property is not satisfied.

The update (10) is not performing as well as symmetric rank two updates when the system possesses the symmetry property. However, it can be succesfully used in non-linear diffusion problems where the diffusion coefficients depend on u, thus producing unsymmetric tangent matrix.

2.3 Rank-two corrections. A symmetric correction of rank at most two can be written in a basic form [11]

$$\tilde{\mathbf{H}} = \mathbf{H} + \mathbf{s}\mathbf{s}^T - \mathbf{t}\mathbf{t}^T \quad \text{or} \quad \tilde{\mathbf{A}} = \mathbf{A} + \mathbf{y}\mathbf{y}^T - \mathbf{z}\mathbf{z}^T$$

and that particular form is also expressible in a symmetric product form

$$\tilde{\mathbf{H}} = (\mathbf{I} + \mathbf{u}\mathbf{v}^T)\mathbf{H}(\mathbf{I} + \mathbf{u}\mathbf{v}^T)^T \quad \text{or} \quad \tilde{\mathbf{A}} = (\mathbf{I} + \mathbf{w}\mathbf{p}^T)\mathbf{A}(\mathbf{I} + \mathbf{w}\mathbf{p}^T)^T \tag{11}$$

only if the determinant of $\tilde{\mathbf{H}}$ or $\tilde{\mathbf{A}}$ is positive.

Two most well known rank-two corrections are the Davidon-Fletcher-Powell (DFP) and the Broyden-Fletcher-Goldfarb-Shanno (BFGS) updates. These complementary formulas preserve symmetry and positive definiteness of the tangent matrix. These formulas

are:

$$\tilde{\mathbf{A}}_{BFGS} = \mathbf{A} + \frac{\delta\mathbf{q}(\delta\mathbf{q} - \mathbf{A}\delta\mathbf{f})^T + (\delta\mathbf{q} - \mathbf{A}\delta\mathbf{f})\delta\mathbf{q}^T}{\delta\mathbf{q}^T\delta\mathbf{f}} - \frac{(\delta\mathbf{q} - \mathbf{A}\delta\mathbf{f})^T\delta\mathbf{f}}{(\delta\mathbf{q}^T\delta\mathbf{f})^2}\delta\mathbf{q}\delta\mathbf{q}^T,$$

$$\tilde{\mathbf{H}}_{BFGS} = \mathbf{H} + \frac{\delta\mathbf{f}\delta\mathbf{f}^T}{\delta\mathbf{f}^T\delta\mathbf{q}} - \frac{\mathbf{H}\delta\mathbf{q}\delta\mathbf{q}^T\mathbf{H}}{\delta\mathbf{q}^T\mathbf{H}\delta\mathbf{q}}.$$

The DFP and BFGS update formulas are related to each other by the duality transformations [3]

$$\delta\mathbf{q} \longleftrightarrow \delta\mathbf{f}, \quad \mathbf{H} \longleftrightarrow \mathbf{A} = \mathbf{H}^{-1}, \quad \tilde{\mathbf{H}} \longleftrightarrow \tilde{\mathbf{A}} = \tilde{\mathbf{H}}^{-1}.$$

An alternative form of the BFGS update formula is

$$\bar{\mathbf{A}}_{BFGS} = (\mathbf{I} - \frac{\delta\mathbf{q}\delta\mathbf{f}^T}{\delta\mathbf{q}^T\delta\mathbf{f}})\mathbf{A}(\mathbf{I} - \frac{\delta\mathbf{f}\delta\mathbf{q}^T}{\delta\mathbf{q}^T\delta\mathbf{f}}) + \frac{\delta\mathbf{q}\delta\mathbf{q}^T}{\delta\mathbf{q}^T\delta\mathbf{f}}. \tag{12}$$

For detailed derivation of these equations, see Ref. [3]. The inverse update form (12) or its product form (11) are usually used in the finite element applications. There are simple recursion formulas to compute the iterative change in both cases.

3 EXAMPLES

3.1 Rheinboldt's example. A simple one-dimensional nonlinear test case is the problem [12]

$$-\frac{d}{dx}\left(\frac{u'}{1+u'}\right) + \lambda = 0, \qquad u(0) = u(1) = 0,$$

in which case the exact solution is

$$u(x) = -x + \frac{1}{\lambda}\ln\left[(\exp(\lambda) - 1)x + 1\right].$$

For growing source intensity λ this solution increases rapidly within a small interval near $x = 0$. Uniform meshes with 100 linear elements and constant load incrementation ($\Delta\lambda = 0.5$) are used. Since the flux in this example depends only on the gradient of u, the consistent tangent matrix is symmetric. Therefore, symmetric rank-two BFGS update formula is used. Convergence plots are shown in Fig. 1. It is seen from these figures, that omission of the gradient dependent term $\mathbf{K}_g$ from the stiffness matrix causes severe convergence problems, which cannot be overcome by using the BFGS update scheme. It is also worth noticing that the convergence of the true Newton's method downgrades to the level of the standard modified Newton-Raphson scheme.

3.2 Problem producing unsymmetric tangent. When the constitutive matrix $\mathbf{D}$ depends on the values of the function u, the consistent linearization produces unsymmetric tangent matrix, see equation (7). From computational point of view this is an untolerable situation. In order to avoid the assembly and factorization of an unsymmetric tangent matrix, rank-one update formula has been tested.

A model problem is again a one-dimensional equation with homogeneous boundary conditions:

$$-\frac{d}{dx}\left(D(u)\frac{du}{dx}\right) + \lambda = 0, \qquad u(0) = u(1) = 0.$$

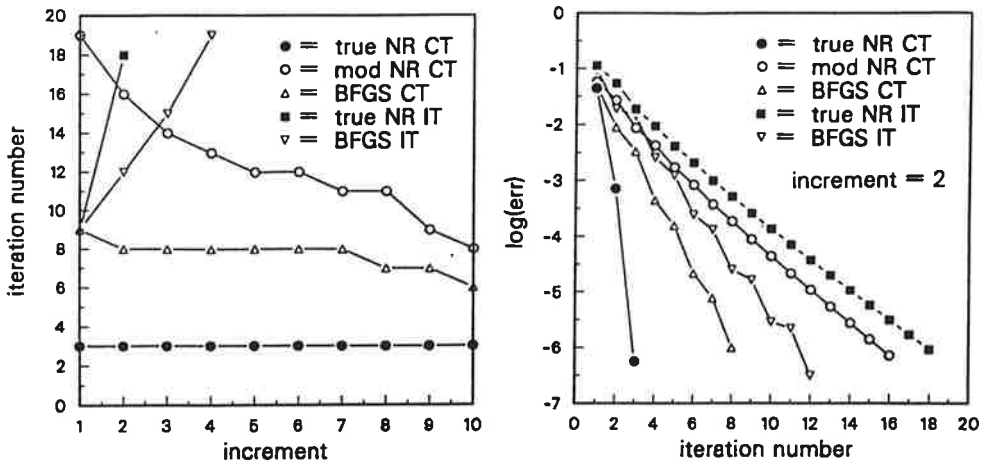

FIGURE 1. Rheinboldt's example: convergence plots, CT=consistent tangent matrix, IT=inconsistent tangent matrix ($\mathbf{K}_g$ omitted).

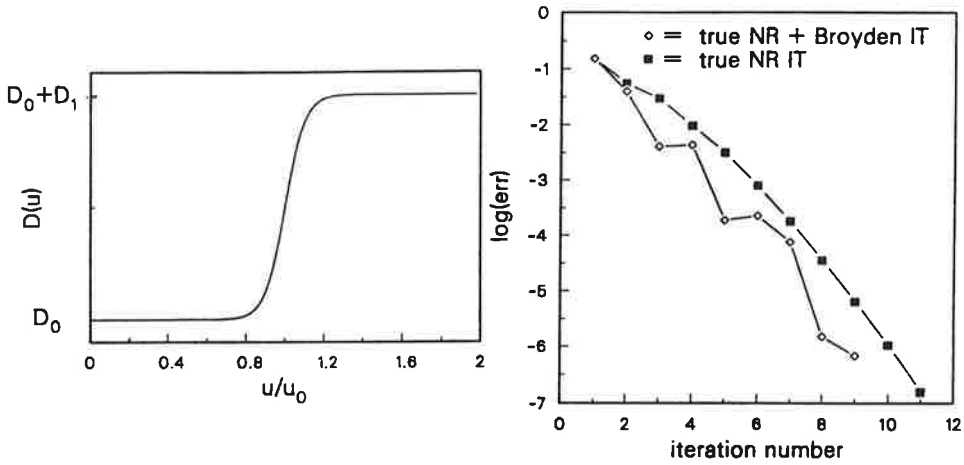

FIGURE 2. Model problem 2: diffusion coefficient as a function of u and convergence plot at the first increment, IT=inconsistent tangent matrix ($\mathbf{K}_u$ omitted).

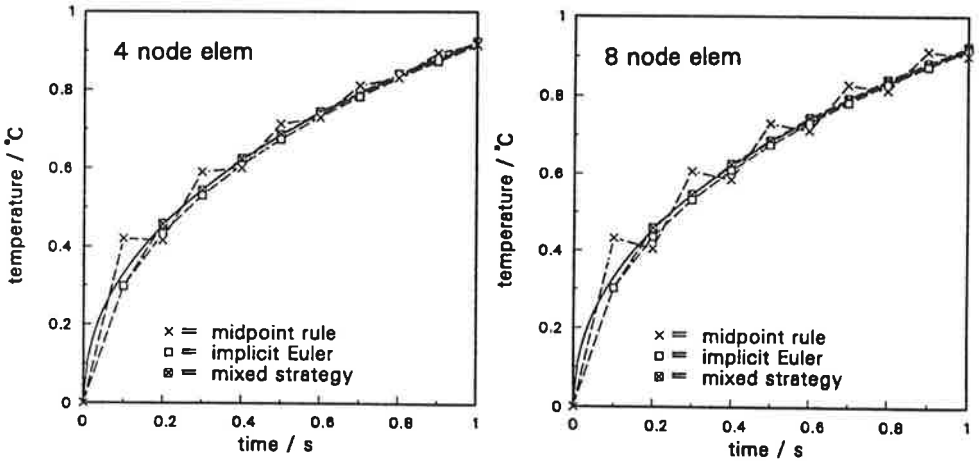

FIGURE 3. Temperature of the left end of the bar. Solid line indicates analytical solution.

TABLE 1. Temperature at the center of the cube, 64 trilinear elements.

time	exact	MPR	IE	mixed (1)	MPR (2)
0.0000	1.000000	1.00000	1.00000	1.00000	1.00000
0.0125	1.000000	1.00033	0.99999	0.99999	1.00065
0.0250	0.999954	0.99743	0.99948	0.99931	0.99420
0.0375	0.998436	1.00290	0.99578	1.00306	1.01160
0.0500	0.990637	1.01214	0.98343	1.00339	1.01268
0.0750	0.942211	0.97488	0.92748	0.95188	0.95661
0.1000	0.855496	0.88099	0.84041	0.85258	0.85355
0.2000	0.460657	0.45931	0.46261	0.44011	0.43851
0.3000	0.223432	0.21907	0.23037	0.20971	0.20884
0.4000	0.106825	0.10356	0.11286	0.09912	0.09870
0.5000	0.050973	0.04890	0.05514	0.04681	0.04661
1.0000	0.001259	0.00115	0.00153	0.00110	0.00109

(1) = First step with the implicit Euler method (IE) and the following steps with the midpoint rule (MPR).
(2) = with different initial conditions, identical to the results of Ref. [15].

A highly non-linear material model, where the diffusivity coefficient D is assumed to vary according to the equation

$$D(u) = D_0 + \tfrac{1}{2} D_1 \left[1 + \tanh\left(\frac{u - u_0}{u_1}\right)\right].$$

is adopted. With vanishing u_1 the diffusivity produces sharp transition near the value of u_0, see Fig. 2. In the computations following relations are used: $D_1 = 10D_0, u_1 = u_0/10$. Large constant increment size ($\Delta\lambda = 10$) is used. Convergence is slow and slight improvement is obtained when the Broyden update is used with the true Newton-Raphson process (symmetric matrix, $\mathbf{K}_u$ omitted).

3.3 Two-dimensional example. To demonstrate the effect of using a two-stage algorithm in order to damp the oscillations in the Crank-Nicolson scheme the following time dependent problems have been solved. The first one is a simple bar with temperature dependent isotropic material properties [13]. Both the thermal conductivity and the heat capacity are assumed to vary according to $1 + \frac{1}{2}T$ (T in $°C$). All other surfaces except the surface $x = 0$ are insulated. The initial temperature is $u = 0°C$. The loading is a unit heat input through the surface $x = 0$. The spatial domain is discretized in 15 four node bilinear or eight node reduced biquadratic (serendipity) elements. Results are shown in Fig. 3, where the time step $\Delta t = 0.1$ s has been used. Using the one step implicit Euler method before switching to the midpoint rule inhibits the oscillations completely.

3.4 Cooling of a cube. Cooling of a cube initially at constant unit temperature $T_0 = 1°C$ and subjected to zero surface temperature when $t > 0$ is considered next. The analytical solution of this problem is given in Ref. [14] and finite element solutions e.g. in

Ref. [15]. However, in their FE-analyses different initial conditions are used, in which the initial temperature varies from zero to one inside the outmost element layer. One octant has been discretized by 64 trilinear 8-node brick elements. Results are shown in Table 1. The time step has been $\Delta t = 0.0125$ s. Clearly, the use of the one step backward Euler method prior the midpoit rule does not inhibit oscillations completely as in the previous example.

REFERENCES

1. A.R. Gourlay, A note on trapezoidal methods for the solution of initial value problems, Math. Comp. 24 (1970) 629-633.

2. T.J.R. Hughes, Uncondutionally stable algorithms for nonlinear heat conduction, Comp. Meth. Appl. Mech. Engng 10 (1977) 135-139.

3. J.E. Dennis and J.J. Moré, Quasi-Newton methods, motivation and theory, SIAM Review 19 (1977) 46-89.

4. L. Bernspång, Iterative and adaptive solution techniques in computational plasticity, Chalmers Univ. of Tech., Department of Structural Mechanics, Publication 91:8 (1991).

5. B. Irons and A. Elsawaf, Proc. U.S.-German Symp. on Formulation and Algorithms in Finite Element Analysis, Eds. K.J. Bathe et al., MIT, pp. 656-672 (1977)

6. M. Papadrakakis and C.J. Gantes, Preconditioned conjugate- and secant-Newton methods for non-linear problems, Int. J. Numer. Meth. Engng 28 (1989) 1299-1316

7. H. Matthies and G. Strang, The solution of nonlinear finite element equations, Int. J. Numer. Meth. Engng, 14 (1979) 1613-1626

8. M. Geradin, S. Idelsohn and M. Hogge, Computational strategies for the solution of large nonlinear problems via quasi-Newton methods, Comput. Struct. 13 (1981) 73-81

9. M. Geradin, M. Hogge and S. Idelsohn, Implicit finite element methods, Chapter 7 in Computational Methods for Transient Analysis, Eds. T. Belytchko and T.J.R. Hughes, North-Holland (1983).

10. C.G. Broyden, A class of methods for solving nonlinear simultaneous equations, Math. Comp. 19 (1965) 577-593

11. K.W. Brodlie, A.R. Gourlay and J. Greenstadt, Rank-one and rank-two corrections to positive definite matrices expressed in product form, J. Inst. Maths Applics 11 (1973) 73-82

12. W.C. Rheinboldt, "Numerical Analysis of Parametrized Nonlinear Equations", John Wiley, New York, 1986

13. S. Orivuori, Efficient methods for solution of nonlinear heat conduction problems, Int. J. Numer. Meth. Engng 14 (1979) 1461-1476

14. H.S. Carslaw and J.C. Jaeger, "Conduction of heat in solids", Oxford University Press, 1962

15. O.C. Zienkiewicz and C.J. Parekh, Transient field problems: Two-dimensional and three-dimensional analysis by isoparametric elements, Int. J. Numer. Meth. Engng 1 (1970) 61-71

NEW AND OLD FINITE ELEMENT METHODS WITH APPROXIMATION OF THE BOUNDARY CONDITIONS

ROLF STENBERG
Faculty of Mechanical Engineering
Helsinki University of Technology
02150 Esbo, FINLAND

ABSTRACT

We discuss the stabilization of Babuškas method of approximating essential boundary conditions by using Lagrange multipliers. A simplification of earlier methods is proposed and analyzed. We also show that there is a close connection with the stabilized formulation and a classical method of Nitsche.

1. INTRODUCTION

Recently, there has been a renewed interest in a method introduced by Babuška [1] in which essential boundary conditions are approximately enforced by Lagrange multipliers. It has been proposed for domain decomposition [7], for fictitious domain methods [9] and for contact problems [11]. This, despite the fact that it may be difficult to design a stable method which satisfies the necessary "Babuška-Brezzi" conditions.

In some recent papers by Barbosa and Hughes [3, 4], Verfürth [16], and Baiocchi, Brezzi and Marini [2], it has, however, been showed that new "stabilizing" techniques can be used in order to design methods that are always stable.

The purpose of this paper is to discuss this technique. We will propose and analyze a simplification of the earlier methods. Furthermore, we will show that the stabilization in a very natural way leads to a classical method of Nitsche [12].

2. THE MODEL PROBLEM

Let Ω be a bounded domain in $\mathbb{R}^d$, $d = 2$ or 3, with a smooth boundary Γ. We consider the Dirichlet problem

$$-\Delta u = f \quad \text{in } \Omega, \tag{1}$$

$$u = g \quad \text{on } \Gamma. \tag{2}$$

This problem is chosen only for notational simplicity; our statements are also valid for other second order elliptic problems such as, e.g., the equations of linear elasticity and the Stokes problem.

The Sobolev spaces $H^s(S)$ for $S \subset \Omega$ or $S \subset \Gamma$, and $s \geq 0$, are defined in the standard way cf. [1]. The norms are denoted $\|\cdot\|_{l,S}$ with the subscript S dropped when $S = \Omega$. We will also use the space $H^{-1/2}(\Gamma)$, i.e. the dual space of $H^{1/2}(\Gamma)$, with the norm

$$\|\mu\|_{-1/2,\Gamma} = \sup_{z \in H^{1/2}(\Gamma)} \frac{\langle \mu, z \rangle}{\|z\|_{1/2,\Gamma}}, \tag{3}$$

where $\langle \cdot, \cdot \rangle$ denotes the duality pairing.

The problem is then given the following variational formulation [1]: given $f \in L^2(\Omega)$ and $g \in H^{1/2}(\Gamma)$, find $u \in H^1(\Omega)$ and $\lambda \in H^{-1/2}(\Gamma)$ such that

$$\mathcal{B}(u, \lambda; v, \mu) = (f, v) + \langle g, \mu \rangle \quad \forall (v, \mu) \in H^1(\Omega) \times H^{-1/2}(\Gamma), \tag{4}$$

with the bilinear form defined by

$$\mathcal{B}(u, \lambda; v, \mu) = (\nabla u, \nabla v) + \langle \lambda, v \rangle + \langle \mu, u \rangle. \tag{5}$$

Above $(\cdot, \cdot)$ denotes the inner product in $L^2(\Omega)$.

The problem has a unique solution, cf. [1]. By using Greens formula in (4) we get the relation

$$\lambda + \frac{\partial u}{\partial n} = 0. \tag{6}$$

3. THE FINITE ELEMENT METHODS

When discussing the finite element methods we will, for notational simplicity, consider the case when simplicial meshes are used, but we emphasize already now that the big advantage of the stabilized methods is that a very big freedom can be allowed in chosing the finite element spaces since no stability conditions are needed.

Let now $\mathcal{R}_h$ be a partitioning of the whole of $\mathbb{R}^d$ into closed simplices (i.e. triangles and tetrahedrons, respectively) and assume that the partitioning satisfies the usual requirements that the intersection of two simplices is either empty, a vertex , an edge or a face. Furthermore, the partitioning is assumed to be regular in the usual sense, cf. [6]. The partitioning of $\overline{\Omega}$ is then defined as

$$\mathcal{C}_h = \{ K \mid K = S \cap \overline{\Omega} \text{ for some } S \in \mathcal{R}_h \}. \tag{7}$$

The finite element subspace for the field variable is then defined as

$$V_h = \{ v \in H^1(\Omega) \mid v_{|K} \in P_k(K) \; \forall K \in \mathcal{C}_h \}, \tag{8}$$

where $P_k(K)$ denotes the polynomials of degree $k \geq 1$ on K.

To define the space Λ_h for the Lagrange multiplier on the boundary we proceed as follows. For $d = 2$ the finite element partitioning $\mathcal{E}_h$ of the boundary consists of segments and for $d = 3$ the elements are curved triangles. This partitioning is also assumed to satisfy the usual compatibility conditions, i.e. the intersection of two elements is assumed to be either empty, a point or a curved edge (for $d = 3$). We further assume that each element $E \in \mathcal{E}_h$ is the image of the reference element $\hat{E}$ (i.e. the unit interval or unit triangle) under a smooth mapping F_E. We then define

$$\Lambda_h = \{ \mu \in L^2(\Gamma) \mid \mu_{|E} = \hat{\mu}(F_E^{-1}(x)) \text{ for some } \hat{\mu} \in P_l(\hat{E}), \quad \forall K \in \mathcal{E}_h \}, \tag{9}$$

with $l \geq 0$.

We will also make the natural assumption that there are constants C_1, C_2 such that

$$C_1 h_K \leq h_E \leq C_2 h_K \quad \text{for all } K \in \mathcal{C}_h \text{ and } E \in \mathcal{E}_h \text{ with } K \cap E \neq \emptyset. \tag{10}$$

As usual we will denote $h = \max_{K \in \mathcal{C}_h} h_K$, and from (10) it then follows that $h_E \leq Ch$ for all $E \in \mathcal{E}_h$.

First, we will consider the original method.

Method 1 *Babuškas method of Lagrange multipliers.*

In this the variational formulation (4) is transfered to the finite element subspaces: find $(u_h, \lambda_h) \in V_h \times \Lambda_h$ such that

$$\mathcal{B}(u_h, \lambda_h; v, \mu) = (f, v) + \langle g, \mu \rangle \quad \forall (v, \mu) \in V_h \times \Lambda_h. \tag{11}$$

The convergence of the method is given by the following classical result.

Theorem 1A (Babuška [1], Brezzi [5]). *Suppose that the finite element subspaces satisfy the conditions*

$$\sup_{v \in V_h \setminus \{0\}} \frac{\langle \mu, v \rangle}{\|v\|_1} \geq C \|\mu\|_{-1/2,\Gamma} \quad \forall \mu \in \Lambda_h, \tag{12}$$

and

$$|v|_1^2 \geq C \|v\|_1^2 \quad \forall v \in \{ \, v \in V_h \mid \langle \mu, v \rangle = 0 \quad \forall \mu \in \Lambda_h \, \}. \tag{13}$$

For the solution (u_h, λ_h) to the problem (11) it then holds

$$\|u - u_h\|_1 + \|\lambda - \lambda_h\|_{-1/2,\Gamma} \leq C(h^k \|u\|_{k+1} + h^{l+3/2} \|\lambda\|_{l+1,\Gamma}), \tag{14}$$

when $u \in H^{k+1}(\Omega)$ and $\lambda \in H^{l+1}(\Gamma)$. ∎

This method has been thoroughly studied by Pitkäranta. Among other things, he showed that the stability and error analysis is most easily performed using the following meshs dependent norms (introduced in [14] with a different notation)

$$\|v\|_{1/2,h}^2 = \sum_{E \in \mathcal{E}_h} h_E^{-1} \|v\|_{0,E}^2 \quad \text{for } v \in H^1(\Omega), \tag{15}$$

and

$$\|z\|_{-1/2,h}^2 = \sum_{E \in \mathcal{E}_h} h_E \|z\|_{0,E}^2 \quad \text{for } z \in L^2(\Gamma). \tag{16}$$

For these norms it holds

$$\langle v, z \rangle \leq \|v\|_{1/2,h} \|z\|_{-1/2,h} \quad \forall (v, z) \in H^1(\Omega) \times L^2(\Gamma). \tag{17}$$

We also denote

$$\|v\|_{1,h} = \|v\|_1 + \|v\|_{1/2,h} \quad \forall v \in H^1(\Omega). \tag{18}$$

The interpolation estimates in these norms are easily proved by scaling and interpolation (cf. [14]).

Lemma 1 *For $u \in H^{k+1}(\Omega)$ it holds*

$$\inf_{v \in V_h} \|u - v\|_{1,h} \leq Ch^k \|u\|_{k+1} \,. \quad \blacksquare \tag{19}$$

Lemma 2 *For $\lambda \in H^{l+1}(\Gamma)$ it holds*

$$\inf_{\mu \in \Lambda_h} \|\lambda - \mu\|_{-1/2,h} \leq Ch^{l+3/2} \|\lambda\|_{l+1,\Gamma} \,. \quad \blacksquare \tag{20}$$

In the sequel we will also need the following inequality, which is easily proved by scaling using the condition (10).

Lemma 3 *There exist a constant C_I such that*

$$C_I \|\frac{\partial v}{\partial n}\|_{-1/2,h} \leq \|\nabla v\|_0 \quad \forall v \in V_h \,. \quad \blacksquare \tag{21}$$

In [14] the following result is proved.

Theorem 1B (Pitkäranta [14]). *Suppose that the finite element subspaces satisfy the conditions*

$$\sup_{v \in V_h \setminus \{0\}} \frac{\langle \mu, v \rangle}{\|v\|_{1,h}} \geq C \|\mu\|_{-1/2,h} \quad \forall \mu \in \Lambda_h, \tag{22}$$

and

$$|v|_1^2 \geq C \|v\|_{1,h}^2 \quad \forall v \in \{\, v \in V_h \mid \langle \mu, v \rangle = 0 \quad \forall \mu \in \Lambda_h \,\}. \tag{23}$$

For the solution (u_h, λ_h) to the problem (11) it then holds

$$\|u - u_h\|_{1,h} + \|\lambda - \lambda_h\|_{-1/2,h} \leq C(h^k \|u\|_{k+1} + h^{l+3/2} \|\lambda\|_{l+1,\Gamma}), \tag{24}$$

when $u \in H^{k+1}(\Omega)$ and $\lambda \in H^{l+1}(\Gamma)$. $\blacksquare$

In the papers [13, 14, 15] it is shown that the spaces V_h and Λ_h should be designed quite carefully in order that the stability conditions would be valid. Hence, there are reason to be quite pessimistic with regards to the general usefulness of this approach in the applications for which the methods has been proposed.

Therefore, it is natural to try to modify the method with similar techniques as those that has been successfully used for the Stokes problem [10, 8]. This has also been done by Barbosa and Hughes [3, 4]. Their methods did, however, contain terms that are not necessary for the stability. By dropping them we obtain the following method.

Method 2 *A simplification of the symmetric formulation of Barbosa and Hughes* [3, 4].

Find $(u_h, \lambda_h) \in V_h \times \Lambda_h$ such that

$$\mathcal{B}_h(u_h, \lambda_h; v, \mu) = (f, v) + \langle g, \mu \rangle \quad \forall (v, \mu) \in V_h \times \Lambda_h, \tag{25}$$

with

$$\mathcal{B}_h(u, \lambda; v, \mu) = \mathcal{B}(u, \lambda; v, \mu) - \alpha \sum_{E \in \mathcal{E}_h} h_E \langle \lambda + \frac{\partial u}{\partial n}, \mu + \frac{\partial v}{\partial n} \rangle_E \tag{26}$$

where $\mathcal{B}$ is the original bilinear form (5).

The first observation concerning this method is that it is is consistent.

Lemma 4 *For the the exact solution* (u, λ) *to* (4) *it holds*

$$\mathcal{B}_h(u, \lambda; v, \mu) = (f, v) + \langle g, \mu \rangle \quad \forall (v, \mu) \in V_h \times \Lambda_h, \tag{27}$$

provided that $\lambda \in L^2(\Gamma)$. ∎

The next observation is that the modified bilinear form is bounded with respect to the mesh dependent norms.

Lemma 5 *There is a positive constant* C *such that*

$$\begin{aligned} |\mathcal{B}_h(v, \mu; z, \eta)| \;\leq\; & C(\|v\|_{1,h} + \|\mu\|_{-1/2,h})(\|z\|_{1,h} + \|\eta\|_{-1/2,h}) \\ & \forall (v, \mu) \in H^1(\Omega) \times L^2(\Gamma),\ \forall (z, \eta) \in H^1(\Omega) \times L^2(\Gamma)\,. \end{aligned} \tag{28}$$ ∎

Next, we will prove the stability and optimal order of convergence.

Theorem 2 *Let* $(u_h, \lambda_h) \in V_h \times \Lambda_h$ *be the solution to the problem* (25) *and suppose that* $0 < \alpha < C_I$. *With* $u \in H^{k+1}(\Omega)$ *and* $\lambda \in H^{l+1}(\Gamma)$ *it then holds*

$$\|u - u_h\|_{1,h} + \|\lambda - \lambda_h\|_{-1/2,h} \leq C(h^k \|u\|_{k+1} + h^{l+3/2} \|\lambda\|_{l+1,\Gamma}). \tag{29}$$

Proof. Let us first prove the stability of the formulation. For this we let $(v, \mu) \in V_h \times \Lambda_h$ be arbitrary and we first note that the estimate of Lemma 3 gives

$$\begin{aligned} \mathcal{B}_h(v, \mu; v, -\mu) &= \|\nabla v\|_0^2 + \alpha \sum_{E \in \mathcal{E}_h} h_E \Big(\|\mu\|_{0,E}^2 - \|\frac{\partial u}{\partial n}\|_{0,E}^2 \Big) \\ &\geq (1 - \alpha C_I^{-1}) \|\nabla v\|_0^2 + \alpha \sum_{E \in \mathcal{E}_h} h_E \|\mu\|_{0,E}^2 \\ &\geq C_1 \Big(\|\nabla v\|_0^2 + \|\mu\|_{1/2,h}^2 \Big), \end{aligned} \tag{30}$$

since it was assumed that $0 < \alpha < C_I$. Next, let $\Pi_h : L^2(\Gamma) \to \Lambda_h$ be the L^2-projection. Since the functions of Λ_h are discontinuous, we can define $\bar{\mu} \in \Lambda_h$ by $\bar{\mu}_{|E} = h_E^{-1} \Pi_h v_{|E}$ forall $E \in \mathcal{E}_h$. We then have

$$\|\bar{\mu}\|_{-1/2,h} = \|\Pi_h v\|_{1/2,h} \tag{31}$$

By using (17), Lemma 3 and the Young inequality we then get

$$\begin{aligned} \mathcal{B}_h(v, \mu; 0, \bar{\mu}) &= \langle v, \bar{\mu} \rangle - \alpha \sum_{E \in \mathcal{E}_h} h_E \langle \mu + \frac{\partial v}{\partial n}, \bar{\mu} \rangle_E \\ &= \sum_{E \in \mathcal{E}_h} h_E^{-1} \|\Pi_h v\|_{0,E}^2 - \alpha \sum_{E \in \mathcal{E}_h} \langle \mu + \frac{\partial v}{\partial n}, \Pi_h v \rangle_E \\ &\geq \|\Pi_h v\|_{1/2,h}^2 - (\|\frac{\partial v}{\partial n}\|_{-1/2,h} + \|\mu\|_{-1/2,h}) \|\Pi_h v\|_{1/2,h} \\ &\geq \|\Pi_h v\|_{1/2,h}^2 - C_2(\|\nabla v\|_0 + \|\mu\|_{-1/2,h}) \|\Pi_h v\|_{1/2,h} \\ &\geq \|\Pi_h v\|_{1/2,h}^2 - \frac{C_2^2}{2}(\|\nabla v\|_0 + \|\mu\|_{-1/2,h})^2 - \frac{1}{2} \|\Pi_h v\|_{1/2,h}^2 \\ &\geq \frac{1}{2} \|\Pi_h v\|_{1/2,h}^2 - C_3(\|\nabla v\|_0^2 + \|\mu\|_{-1/2,h}^2)\,. \end{aligned} \tag{32}$$

Let now $(z,\eta) = (v, -\mu + \delta\bar{\mu})$ with $\delta > 0$. Using (30) and (32) we obtain

$$\begin{aligned} \mathcal{B}_h(v,\mu;z,\eta) &= \mathcal{B}_h(v,\mu;v,-\mu) + \delta\mathcal{B}_h(v,\mu;0,\bar{\mu}) \\ &\geq (C_1 - \delta C_3)\|\nabla v\|_0^2 + \frac{\delta}{2}\|\Pi_h v\|_{1/2,h}^2 + (C_1 - \delta C_3)\|\mu\|_{-1/2,h}^2 \qquad (33) \\ &\geq C\big(\|\nabla v\|_0^2 + \|\Pi_h v\|_{1/2,h}^2 + \|\mu\|_{-1/2,h}^2\big)\,, \end{aligned}$$

when choosing $\delta < C_1/C_3$. Now, by scaling one can prove that

$$\|\nabla v\|_0^2 + \|\Pi_h v\|_{1/2,h}^2 \geq C\|v\|_{1,h}^2\,. \qquad (34)$$

Since (31) gives

$$\|z\|_{1,h} + \|\eta\|_{-1/2,h} \leq C(\|v\|_{1,h} + \|\mu\|_{-1/2,h}) \qquad (35)$$

we have proved the stability estimate (which is optimal in view of Lemma 5)

$$\sup_{(z,\eta)\in V_h\times\Lambda_h} \frac{\mathcal{B}_h(v,\mu;z,\eta)}{\|z\|_{1,h} + \|\eta\|_{-1/2,h}} \geq C(\|v\|_{1,h} + \|\mu\|_{-1/2,h})\,. \qquad (36)$$

The asserted error estimate now follows from this, and Lemmas 4, 5, 1 and 2. ∎

The big advantage with this formulation compared to the original method of Babuška is that the finite element subspaces can be chosen completely arbitrarly.

Let us next have a closer look at the method. We note that since the functions of Λ_h are discontinuous, the variable λ_h can be eliminated locally on each boundary element. By testing with $\mu \in \Lambda_h$ in (25), we get the following expression for λ_h:

$$\lambda_{h|E} = -(\Pi_h\frac{\partial u_h}{\partial n})_{|E} + (\alpha h_E)^{-1}(\Pi_h u_h - \Pi_h g)_{|E} \quad \forall E \in \mathcal{E}_h, \qquad (37)$$

where (as before) Π_h is the L^2-projection onto Λ_h. Now, substituting this into the equation we get from (25) when testing by $v \in V_h$, we get the following symmetric (and positive definite, cf. below) system for solving the unknown u_h:

$$\begin{aligned} &(\nabla u_h, \nabla v) - \langle \Pi_h\frac{\partial u_h}{\partial n}, v\rangle - \langle \frac{\partial v}{\partial n}, \Pi_h u_h\rangle \\ &\qquad + \sum_{E\in\mathcal{E}_h} (\alpha h_E)^{-1}\langle \Pi_h u_h, v\rangle_E + \alpha \sum_{E\in\mathcal{E}_h} h_E\langle (\Pi_h - \mathrm{I})\frac{\partial u_h}{\partial n}, \frac{\partial v}{\partial n}\rangle \qquad (38) \\ &= (f,v) - \langle \Pi_h\frac{\partial v}{\partial n}, g\rangle + \sum_{E\in\mathcal{E}_h} (\alpha h_E)^{-1}\langle g, \Pi_h v\rangle_E\,. \end{aligned}$$

Now, since the space Λ_h can be chosen arbitrarly, we can choose it so big that the projection Π_h becomes the identity in the above formulation (or we can think that we choose $\Lambda_h = L^2(\Gamma)$). Then we observe that we have rediscovered a classical method:

Method 3 *Nitsches method* [12].

Find $u_h \in V_h$ such that

$$\mathcal{B}_h(u;v) = \mathcal{F}_h(v) \quad \forall v \in V_h, \tag{39}$$

with

$$\mathcal{B}_h(u;v) = (\nabla u, \nabla v) - \langle \frac{\partial u}{\partial n}, v\rangle - \langle \frac{\partial v}{\partial n}, u\rangle + \gamma \sum_{E\in\mathcal{E}_h} h_E^{-1}\langle u, v\rangle_E\,, \tag{40}$$

$$\mathcal{F}_h(v) = (f,v) - \langle \frac{\partial v}{\partial n}, g\rangle + \gamma \sum_{E\in\mathcal{E}_h} h_E^{-1}\langle g, v\rangle_E\,. \tag{41}$$

By the way we have arrived at this formulation, it is clear that we have an optimal error estimate for it. That is, however, more easily obtain directly.

Theorem 3 *Let $u_h \in V_h$ be the solution to the problem* (39) *and suppose that $\gamma > C_I^{-1}$. With $u \in H^{k+1}(\Omega)$ it then holds*

$$\|u - u_h\|_{1,h} \le Ch^k \|u\|_{k+1}\,. \tag{42}$$

Proof. The consistency of the method is immediatly seen from the formulation. The stability is proved by Schwartz, Young and Lemma 3:

$$\begin{aligned}
\mathcal{B}_h(v;v) &= \|\nabla v\|_0^2 - 2\langle v, \frac{\partial v}{\partial n}\rangle + \gamma\|v\|_{1/2,h}^2 \\
&\ge \|\nabla v\|_0^2 - 2\|v\|_{1/2,h}\|\frac{\partial v}{\partial n}\|_{-1/2,h} + \|v\|_{1/2,h}^2 \\
&\ge \|\nabla v\|_0^2 - \frac{1}{\varepsilon}\|\frac{\partial v}{\partial n}\|_{-1/2,h}^2 + (\gamma-\varepsilon)\|v\|_{1/2,h}^2 \\
&\ge (1 - \frac{1}{\varepsilon C_I})\|\nabla v\|_0^2 + (\gamma-\varepsilon)\|v\|_{1/2,h}^2 \\
&\ge C\|v\|_{1,h}^2\,,
\end{aligned} \tag{43}$$

when we choose $C_I^{-1} < \varepsilon < \gamma$.

We have thus established the stability and the consistency. The assertion then follows from Lemma 1 ∎

In view of our analysis it seems that the Nitsche method is the most straightforward method to use. Unfortunately, this method seems to be quite unknown. We think, however, that it would be worthwhile to explore it in applications such as contact problems, for fictitious domain methods and for domain decomposition.

REFERENCES

[1] I. Babuška. The finite element method with Lagrangian multipliers. *Numer. Math.*, 20:179–192, 1973.

[2] C. Baiocchi, F. Brezzi, and L.D. Marini. Stabilization of Galerkin methods and application to domain decomposition. In A. Bensoussan, editor, *Proceedings of the Conference of the Occasion of the 25th Anniversary of INRIA*. Springer-Verlag, 1992.

[3] J.C. Barbosa and T.J.R. Hughes. The finite element method with Lagrange multipliers on the boundary: circumventing the Babuška-Brezzi condition. *Comp. Meths. Appl. Mech. Eng.*, 85:109–128, 1991.

[4] J.C. Barbosa and T.J.R. Hughes. Boundary Lagrange multipliers in finite element methods: error analysis in natural norms. *Numer. Math.*, 62:1–15, 1992.

[5] F. Brezzi. On the existence, uniqueness and approximation of saddle point problems arising from Lagrangian multipliers. *RAIRO Anal. Num.*, 2:129–151, 1974.

[6] P.G. Ciarlet. *The Finite Element Method for Elliptic Problems.* North - Holland, 1978.

[7] C. Farhat and M. Geradin. Using a reduced number of Lagrange multipliers for assembling parallel incomplete field finite element approximations. *Comp. Meths. Appl. Mech. Eng.*, 97:333–354, 1992.

[8] L.P. Franca, T.J.R. Hughes, and R. Stenberg. Stabilized finite element methods. In M. Gunzburger and R.A. Nicolaides, editors, *Incompressible Computational Fluid Dynamics*, chapter 4, pages 87–107. Cambridge University Press, 1993.

[9] R. Glowinski, T.-W. Pan, and J. Periaux. A fictitious domain method for Dirichlet problems and applications. *Comp. Meths. Appl. Mech. Eng.*, 111:283–303, 1994.

[10] T.J.R. Hughes and L.P. Franca. A new finite element formulation for computational fluid dynamics: VII. The Stokes problem with various well-posed boundary conditions: Symmetric formulations that converge for all velocity/pressure spaces. *Comp. Meths. Appl. Mech. Engrg.*, 65:85–96, 1987.

[11] N. Kikuchi and J.T. Oden. *Contact Problems in Elasticity.* SIAM, 1988.

[12] J. Nitsche. Über ein Variationsprinzip zur Lösung von Dirichlet-Problemen bei Verwendung von Teilräumen, die keinen Randbedingungen unterworfen sind. *Abh. Math. Sem. Univ. Hamburg*, 36:9–15, 1970/1971.

[13] J. Pitkäranta. Boundary subspaces for the finite element method with Lagrange multipliers. *Numer. Math.*, 33:273–289, 1979.

[14] J. Pitkäranta. Local stability conditions for the Babuška method of Lagrange multipliers. *Math. Comput.*, 35:1113–1129, 1980.

[15] J. Pitkäranta. The finite element method with Lagrange multipliers for domain with corners. *Math. Comput.*, 37:13–30, 1981.

[16] R. Verfürth. Finite element approximation of incompressible Navier-Stokes equations with slip boundary condition II. *Numer. Math.*, 59:615–636, 1991.

DEVELOPING THE CONVERGENCE RATE OF A SHOOTING METHOD

PENTTI TUOMINEN
Department of Civil Engineering
University of Oulu
P.O. Box 191, FIN-90100 Oulu, FINLAND

1. INTRODUCTION

The shooting method under consideration is based on the finite difference approximations of normal forces and bending moments. The method is used to generate axisymmetric finite elements by determining first numerically the transfer matrix and loading vectors and then the stiffness matrix and nodal load vectors. Earlier reports about the aim are e.g. [1], [2] and [3].

2. DIFFERENTIAL EQUATIONS FOR ARCH STRUCTURES

In the report [1] the method was used to solve arch structures using differential equations

$$\frac{d^2v}{ds^2} + \frac{v}{r} + \frac{u}{R^2}\frac{dR}{ds} = \frac{M}{EJ} \tag{1}$$

$$\frac{du}{ds} + \frac{v}{R} = \frac{N}{EA} - \frac{1}{R}\frac{M}{EA}. \tag{2}$$

In the equations u and v are axial and normal displacement, R is the radius of the arch and N and M are the normal force and the bending moment. EA and EJ are the extensional and bending stiffnesses. All are functions of the arch length s. It is characteristic for Equations 1 and 2 that the stress resultants of the right hand side are known exactly, when the form of the arch and the loading are known. As a consequence of this the discretization error of the method can be presented using a serie of even powers as

$$e = a_2\Delta s^2 + a_4\Delta s^4 + a_6\Delta s^6 + \ldots \quad (3)$$

The accuracy of the method is increased using three or four calculation loops doubling the number of grid length Δs in each new loop. An extrapolation toward the zero grid length (known as Romberg's method) will give a high rate of convergence. The error is then proportional to the sixth or eighth power of Δs.

3. RING PLATE

3.1 Notations for the ring plate

A thin axisymmetric ring plate will be considered next. A radial line of the plate is divided into n equal segments which determine grid points from 1 to n + 1. The grid point 1 is situated at the inner boundary circle of the plate and the point n + 1 at the outer boundary. The grid points are indicated with subindeces. 'Index' i + 1/2 or a corresponding fraction is used for the mean point between grid points i and i + 1. The mesh length between two neighboring grid points is Δr. Superindeces r and t indicate radial and circumferential directions. The structure under consideration is presented in Figure 1.

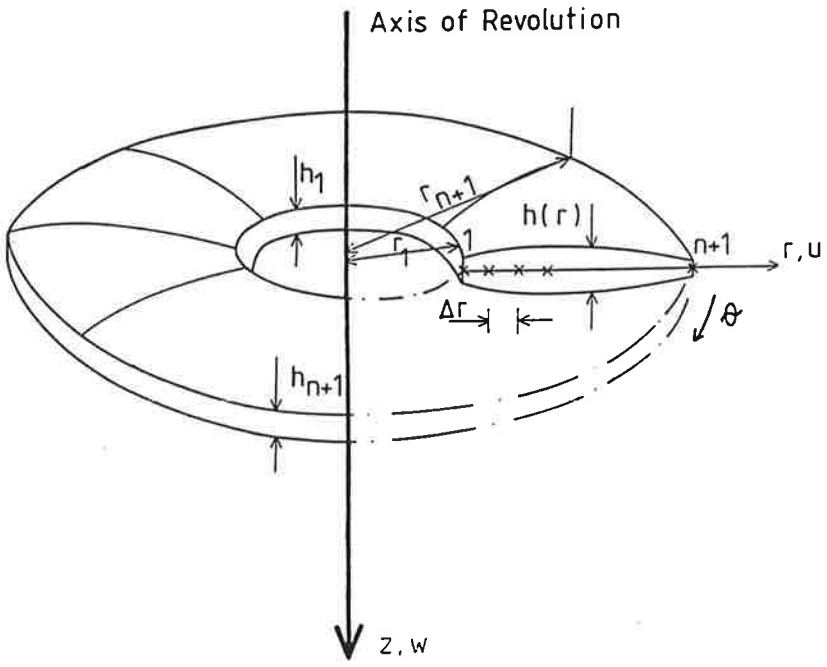

Figure 1. Dimensions, coordinates and displacements of a ring plate. All quantities are shown as positive.

Stress resultants of the ring plate under axisymmetrix loading are presented in Figure 2.

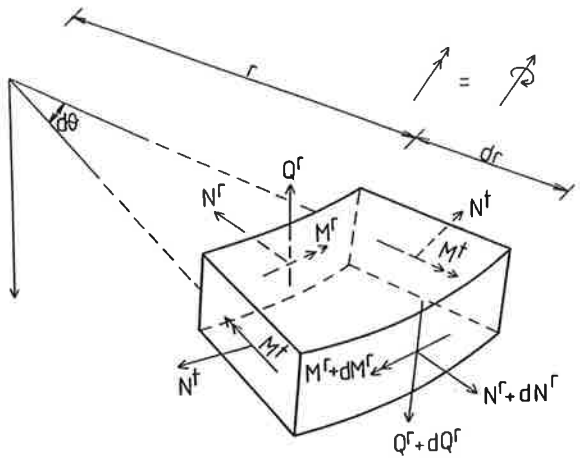

Figure 2. Stress resultants of a ring plate under axisymmetric loading

3.2 Equations for the stretching state of the ring plate

Equations for normal forces

$$N^r = C^r\left(\frac{du}{dr} + \mu\frac{u}{r}\right) \tag{4}$$

$$N^t = C^t\left(\upsilon\frac{du}{dr} + \frac{u}{r}\right) \tag{5}$$

are depending only on the radial displacement u. In Equations C^r and C^t are stretching stiffnesses and μ and υ Poisson's ratios. From Equation 4 it is obtained

$$\frac{du}{dr} + \mu\frac{u}{r} = \frac{N^r}{C^r}, \tag{6}$$

which can be approximated using finite differences and mean value of u at the mean point j = i + 1/2 as result the recursive formula

$$\left(1 + \frac{\mu_j \Delta r}{2r_j}\right)u_{i+1} = \left(1 - \frac{\mu_j \Delta r}{2r_j}\right)u_i + \Delta r\frac{N_j^r}{C_j^r} \tag{7}$$

for u_{i+1}. Normal force N^r on the right hand side of Equations 6 and 7 is now unknown otherwise than in Equations 1 and 2 for arch structures. For evaluating of it Equation

$$N_j^r = \frac{r_1}{r_j} N_1^r + \frac{1}{r_j} \int_{r_1}^{r_j} N^t dr - \frac{1}{r_i} \int_{r_1}^{r_j} X r dr \tag{8}$$

is available. The second integral with the note j = i + 1/2 will be approximated using the expression

$$\frac{1}{r_j} \int_{r_1}^{r_j} N^t dr = \frac{\Delta r}{r_j} \left(\tfrac{1}{2} N_1^t + N_2^t + \ldots + N_i^t \right). \tag{9}$$

Here the terms of summation

$$N_i^t = \mu_i N_i^r + (1 - \mu_i \upsilon_i) C_i^t \frac{u_i}{r_i}. \tag{10}$$

are obtained by eliminating du/dr from Equations 4 and 5. The approximation in Equation 9 causes decreasing of the convergence rate of the method. As before with arch structures several calculation loops with doubled numbers of grid lengths are used again. The basis for the extrapolation is assumed to be the serie

$$e = a_1 \Delta r + a_2 \Delta r^2 + a_3 \Delta r^3 + a_4 \Delta r^4 + \ldots \tag{11}$$

for the discretization error. Neville's algorithm [4, pp. 108-111] gives values

$$D_{ik} = (-D_{i-1,\,k-1} + 2^k D_{i,\,k-1}) / (2^k - 1) \tag{12}$$

for the extrapolated quantities in the scheme

$$\begin{array}{lllll}
Dr & D_{00} & & & \\
 & & D_{11} & & \\
Dr/2 & D_{10} & & D_{22} & \\
 & & D_{21} & & D_{33} \\
Dr/4 & D_{20} & & D_{32} & \\
 & & D_{31} & & \\
Dr/8 & D_{30} & & &
\end{array}$$

The use of Neville's algorithm means the eliminating of coefficients a_i after each others in 11. After four calculation loops and extrapolation the discretization error of results was now proportional to the fourth power of the grid length Δr.

3.3 A modified version of Neville's algorithm

In the third phase of the extrapolation above the new values were calculated using the formula

$$D_{i3} = (-D_{i-1,2} + 8D_{i2})/7 . \tag{12b}$$

When coefficients 8 and 7 are replaced with 16 and 15 a better convergence of results is surprisingly obtained. The discretization error is now proportional to the sixth power of Δr. The simple variation of coeffiecients means the use of Romberg's method in the third phase of Neville's algorithm. The results also tell the coefficients a_3 and a_5 to be zero in the presumption 11. The modified Neville's algorithm was first tested in generating axisymmetric cylindrical shell elements. The convergence rate was then also six when four calculation loops were used.

3.4 Equations for the bending state of the ring plate

Increasing the convergence rate in the bending state of the ring plate was more problematic than in the stretching one. It was succeeded after a discussion with associate professor Juha Paavola. In Equations of bending moments

$$M^r = -B^r\left(\frac{d^2w}{dr^2} + \frac{\mu}{r}\frac{dw}{dr}\right) \tag{13}$$

$$M^t = -B^t\left(\frac{d^2w}{dr^2} + \frac{\mu}{r}\frac{dw}{dr}\right) \tag{14}$$

B^r and B^t are bending stiffnessed. The former one gives the starting point

$$\frac{d^2w}{dr^2} + \frac{\mu}{r}\frac{dw}{dr} = -\frac{M^r}{B^r} \tag{15}$$

for the recursive formulae of deflections w_i. Using finite difference approximations and the notation $\psi = dw/dr$ the equations

$$w_2 = \Delta r\left(1 - \frac{\mu_1 \Delta r}{2r_1}\right)\psi_1 + w_1 - \frac{\Delta r^2}{2}\frac{M_1^r}{B_1^r} \tag{16}$$

$$\left(1 + \frac{\mu_i \Delta r}{2r_i}\right) w_{i+1} = -\left(1 - \frac{\mu_i \Delta r}{2r_i}\right) w_{i-1} + 2w_i - \Delta r^2 \frac{M_i^r}{B_i^r} \tag{17}$$

and

$$\Delta r\left(1 + \frac{\mu_i \Delta r}{2r_i}\right) \psi_i = \Delta r d_i \psi_i = -w_{i-1} + w_i - \frac{\Delta r^2}{2} \frac{M_i^r}{B_i^r} \tag{18}$$

are obtained for calculating deflections at each grid point. The moment equilibrium of a radial strip about the circumferential axis through point i produces the recursive formula

$$M_i^r = \frac{r_1}{r_i}\left[M_1^r + Q_1^r(r_i - r_1)\right] - \frac{1}{r_i}\int_{r_1}^{r_i} M^t dr + \frac{1}{r_i}\int_{r_1}^{r_i} Z(r_i - r) r dr \tag{19}$$

for the radial bending moment. Here the second integral was approximated with the expressions

$$\frac{1}{r_i}\int_{r_1}^{r_i} M^t dr = \frac{\Delta r}{r_i}(M_1^t + M_2^t + \ldots + M_{i-1}^t) \tag{20a}$$

$$\frac{1}{r_i}\int_{r_1}^{r_i} M^t dr = \frac{\Delta r}{r_i}(\tfrac{1}{2}M_1^t + M_2^t + \ldots + \tfrac{1}{2}M_i^t)\,. \tag{20c}$$

In the version 20b the so called midpoint rule was used. The subindeces of 20a were then 3/2, 5/2, and i - 1/2. The use of Equation 20c is the most complicated and it will be discussed in more detail. In the approximation the last couple M_i^t is unknown. For it can be found Equation

$$M_i^t = \mu_i M_i^r - \frac{(1 - \mu_i \upsilon_i)}{r_i} B_i^t \psi_i\,, \tag{21}$$

where the derivative ψ_i can be solved from Equation 18. The substitution of ψ_i into 21 and this further into Equation 20c and this finally into Equation 19 produce with some rearranging the final recursive formula

$$\begin{aligned}(1 - b_i) M_i^r = {} & \frac{r_1}{r_i}\left[M_1^r + Q_1^r(r_i - r_1)\right] + \frac{\Delta r}{r_i}\left(\tfrac{1}{2}M_1^t + M_2^t + \ldots + M_{i-1}^t\right) \\ & - c_i(-w_{i-1} + w_i) - \frac{1}{r_i}\int_{r_1}^{r_i} Z(r_i - r) r dr\end{aligned} \tag{22}$$

for the couple M_i^r. Here the shortened notations are

$$b_i = \frac{\Delta r}{2d_i r_i}\left(\mu_i + \frac{\Delta r}{2r_i}\frac{B_i^t}{B_i^r}\right) \tag{23}$$

and

$$c_i = \frac{\Delta r}{2d_i r_i}\,\frac{(1-\mu_i \upsilon_i)}{r_i}\,B_i^t \tag{24}$$

Versions 20a and 20c demand about the same CPU-times in computing, when the version 20b is somewhat slower. The most effective way of calculation is to use Equation 20c with the modified Neville's algorithm. This combination was the only one, which gave a convergence rate six after four loops calculation.

Finally a brief question: How can a convergence proportional to the eighth power of the grid length be achieved without increasing essentially the computing time? A simple way to solve the problem is to use five loops in calculations with the so called Bulirsch' queue instead of doubling the number of meridional segments in every new loop.

4. A NUMERICAL EXAMPLE

As a numerical example is considered the stretching state of an isotropic ring plate with a constant thickness h = 0.20 m. The radii of the plate are r_1 = 2 m and r_{n+1} = 5 m, Young's modulus is E = 10 000 MN/m^2 and Poisson's ratio υ = 1/3. The stiffness matrix below is obtained using 4 to 32 radial segments in four calculation loops. The deviating digits of analytical comparison results are given too.

Table 1. Stretching stiffness coefficients of a ring plate

$u_1 = 1$	$u_{n+1} = 1$
2357.134 758	-2142.853 403
42 857	6 143
-2142.853 749	3857.141 500
6 143	2 857

The error of calculations is considered using the expression

$$g = \frac{max\left|k_{ij} - a_{ij}\right|}{\sqrt{a_{ii}a_{jj}}} \cdot sgn(k_{ij} - a_{ij}) \tag{25}$$

as an error indicator. In the next table results of the upper line are obtained using the modified version and the ones of lower line with the usual Neville's algorithm.

Table 2. Values of error parameter g (Equation 25), when Neville's algorithm and its modification are used.

	n = 4 - 32 CPU-time = 4.78 s	8 - 64 9.28 s	7 - 56 8.79 s	19 - 152 20.48 s
mod.	$-0.3436 \cdot 10^{-7}$	$-0.658 \cdot 10^{-9}$	$-0.144 \cdot 10^{-8}$	-
Nev.	$0.2217 \cdot 10^{-6}$	$0.1775 \cdot 10^{-7}$	$0.2949 \cdot 10^{-7}$	$0.602 \cdot 10^{-9}$

More numerical considerations shows that the rate of convergence remains six after four calculation loops, when the thickness of the structure varies linearly or parabolically. This property however failed, when the thickness of the structure was piecewise linearly varying or the derivative of the thickness was uncontinuous.

5. CONCLUSIONS

The effect of the shooting method under consideration can be increased using a modified version of Nevilles algorithm for extrapolation. A condition of this increasing seems to be the continuity of the derivative of the structural thickness.

6. REFERENCES

1. Tuominen, P., Kaaren jäykkyyskertoimien määrittäminen jännitysresultanttien lausekkeista. II Suomen mekaniikkapäivien esitelmät (toim. Antti Pramila), Tampereen teknillinen korkeakoulu, Konetekniikan osasto, Teknillinen mekaniikka Raportti 29, Tampere 1985.

2. Tuominen, P., Generation of a Shperical Shell Element Using a Shooting Method, Domes from Antiquity to the Present, Proceedings of IASS-MSU Symposium, Istanbul 1988, Publisher Mimar Sinan University Istanbul, Istanbul, Turkey.

3. Tuominen, P., Generation of an Axisymmetric Cylindrical Shell Element Using a Shooting Method. Acta Polytechnica Scandinavica, Civil Engineering and Building Construction Series No. 93. Helsinki 1989.

4. Mäkelä, M., Nevanlinna, O. and Virkkunen J., Numeerinen matematiikka, toinen painos, Gaudeamus, Mänttä 1984.

P-CONVERGENCE IN PLATE BENDING PROBLEM

SIMO VIRTANEN
Applied Mechanics
Tampere University of Technology
P. O. Box 589, FIN-33101 Tampere, FINLAND
JENS STRUCKMANN
Department of Mechanical Engineering
Technical University of Braunschweig
Pockelsstrasse 4, D-38106 Braunschweig, DEUTSCHLAND

Abstract

This work is about the improved accuracy of finite element calculations achieved by means of the use of hierarchical shape functions. Hierarchical shape functions of higher polynomial order p are added in order to receive better results without changing the number of elements. This so-called p-convergence represents an alternative method for obtaining better results compared to the way of enlarging the number of elements (h-convergence). The polynomial order is raised up to degree 6. As an example a four-noded plate bending element is treated. For calculations a small finite element program is used. Different results are shown, when rectangular and circular elements are computed. Variations of the boundary conditions are considered for simply supported and clamped elements.

1. Introduction

Solutions of finite element calculations are always an approximation to exact solution values. The problem is that it is not possible to assess a single finite element solution, i.e., how close that solution is to the exact solution. Every single solution from a finite element calculation depends on the degree of discretization. Discretization is a measure for the finite element mesh expressed by the element size h and the polynomial degree of the element p as parameters. A sequence of discretizations, called extension, is needed. This means the creation of finite element spaces has to be executed. The purpose is to find an appropriate refinement including only a little increase of data processing. To reduce the above mentioned difference between exact and calculated solution several ways of refinement are possible (h, p and h-p).

Each calculation that is considered as not accurate enough is followed by another one until convergence is observed. Most finite element programs that are based on the principle of virtual work use the strain energy to measure the relative error between exact and FE-solution. At the end of a successful extension asymptotic behaviour for the virtual work of the error has to be reached. Equivalently, the strain energy of the error has to be minimised. Convergence of strain energy is the base of convergence for engineering data such as displacements, stress maxima, reactions, stress intensity factors, etc. [1].

An important goal in developing further steps for calculation is the ability to refer to results from the last level, i.e., the refinement includes the last solution. This kind of extension is described as "adaptive technique" or "feedback". "Self-adaptive" programs only need a minimum of user interaction because they assess the accuracy of the solution and try to reach a pre-defined tolerance or acceptance criteria automatically.

2. Hierarchical elements

2.1. P-refinement. As already mentioned, there are different ways for discretization in order to achieve more accurate results from finite element calculations. The conventional *h*-refinement is based on the reduction of the element size *h*. The drawback of this method is its need for a quite new mesh for each level of the extension. Therefore, existing nodes have to be moved and new nodes evaluating the shape of the structure have to be created both inside the element and on boundary edges. In contrast to *h*-refinement *p*-refinement always uses the same mesh for each discretization.

The results obtained from *p*-refined extensions become more and more accurate by increasing the order of polynomial degree for shape functions progressively. That means more complexity is reached by adding new equations of higher polynomial degree. During this process it is not necessary to change the polynomial order for all elements and all edges. Local refinement similar to more detailed mesh on parts of the structure during *h*-refinements is possible. As a condition common sides of neighbouring elements are forced to have the same basic functions of the same order to assure displacement compatibility and continuity for all elements of the structure.

2.2. Two dimensional shape functions. For the use of *p*-refinement the complete structure is described by basic functions $N_i(x,y)$. There are three kinds of functions appearing in the *p*-version: *nodal shape functions, side modes* and *bubble modes*. These basic functions are calculated from elemental basis functions that are obtained by mapping elemental shape functions from the general ξ,η–plane onto concrete finite elements in the x,y-plane by the use of specified mapping functions. Shape functions are defined on a standard element, e.g. equilateral, right triangles or squares in normalised size, with own co-ordinates (ξ,η).

Four-noded quadrilateral elements with four degrees of freedom per node demand sixteen nodal shape functions. These first 16 elements of the shape function matrix $\mathbf{N}^e$ are products of one-dimensional cubic Hermitian polynomials. Statements of the same type in each direction are required to fulfil the criterion of independence from co-ordinate transformations. Therefore, in case of rectangular elements symmetric statements have to be chosen. Elements treated in this work were mapped from bicubic Hermitian polynomials, which provide C^1 continuity. As an example the shape functions for the lower left corner node (node 1 [-1;-1],) are:

$$N_1 = H_{01}(\xi)\,H_{01}(\eta) \tag{1}$$
$$N_2 = H_{11}(\xi)\,H_{01}(\eta) \tag{2}$$
$$N_3 = H_{01}(\xi)\,H_{11}(\eta) \tag{3}$$
$$N_4 = H_{11}(\xi)\,H_{11}(\eta) \tag{4}$$

corresponding to the respective nodal parameters u_1, $(u_{,\xi})_1$, $(u_{,\eta})_1$ and $(u_{,\xi\eta})_1$. These shape functions are the same as for the *h*-version.

In finite element programs the Jacobian **J** contains the geometric information concerning nodal co-ordinates and mapping functions. If mapping functions and shape functions are of the same polynomial degree the mapping is called isoparametric. In this work mapping is only isoparametric for $p = 3$, i.e., in case only nodal shape functions of Hermitian type are used. If higher order polynomials are added the performance turns into subparametric, i.e., the degree of the shape functions is greater than the degree of the mapping functions.

2.3. Side modes. For *p*-refinement shape functions whose polynomial order p is greater or equal to 4 are added. These shape functions are associated with the element sides. $8(p\text{-}3)$ shape functions have to be established for quadrilateral elements what results in four degrees of freedom per corner node. Products of internal surplus functions S_i and Hermitian polynomials H_{mi} form equations for the side modes (5) and (6).

$$N_k(\xi,\eta) = H_{mi}(\xi)\,S_{p-4}(\eta) \tag{5}$$

or

$$N_k(\xi,\eta) = H_{mi}(\eta)\,S_{p-4}(\xi) \tag{6}$$

where $k > 16$ and $p > 3$. H_{mi} are Hermitian polynomials, which provide the function value or slope value 1 on the edge where the side mode is located and zero on the other edge. Equation (7) shows how the Legendre-type internal surplus function of the *i*th order is defined [2].

$$S_i = \frac{d^i}{ds^i}\left(s^2-1\right)^{i+2} \qquad i \geq 0 \tag{7}$$

In this work the polynomial degree was increased up to $p = 6 \Rightarrow$

$$S_0 = \left(s^2-1\right)^2 \tag{8}$$
$$S_1 = 3s\left(s^2-1\right)^2 \tag{9}$$
$$S_2 = (s-1)^2(s+1)^2\left(7s^2-1\right) \tag{10}$$

Required properties for this kind of function are zero values and slopes at elemental corner nodes. New degrees of freedom are produced by the implementation of side modes that are

associated with new midside nodes on element sides. Other sets of shape functions are possible, for example interpolating functions of the Peano family [3].

2.4. Internal modes. Products of the above introduced surplus functions form bubble modes. For $p > 3$ there are $(p\text{-}3)^2$ internal modes. Displacement and slope values for these shape functions are zero at every edge of the boundary because they use hierarchical functions S_i in both ξ and η direction.

$$N_k(\xi,\eta) = S_{p-4}(\eta)\, S_{p-4}(\xi) \tag{11}$$

Internal modes can be condensed already on the element level and do not have to be computed during the assemblage of the global stiffness matrix.

In the treated problem the polynomial degree of internal surplus functions is increased up to sixth order. This affects on the accuracy during the Gaussian integration. Higher polynomials required more integration points in order to receive exact results by Gaussian integration. Polynomials of 6th order in two directions deliver equations of degree 12. Therefore the number of integration points in the developed program was raised up to 7.

Shape functions used for p-convergence are based on hierarchy, i.e., new functions are added without changing the old ones. Furthermore, these additional functions do not affect on the initial set of functions in such a way that new equations provide zero values in locations where the initial set describes nodal displacements.

3. Application

In this work p-refinement is applied to the problem of the bending of thin plates. The standard test examples square and circular plates are used. The material properties for the modulus of elasticity and Poisson's ratio are $E = 210$ GPa and $\nu = 0.25$. All calculated structures have the constant thickness $t = 0.05$ m, the radius of the circular plate and the side length of the square plate are both 3 m. Point loads (30,000 N) are applied to the centre node. Further calculations applying a uniform load of 4,000 N/m^2 were examined.

Symmetry in two directions requires the modelling of one quarter of the structure only. In fact, boundary conditions replace the remaining part. Structures containing one and four elements are treated. The coarse mesh and the more refined version are examined for the case of simply supported and clamped boundary nodes.

The basic four-noded element contains 16 degrees of freedom, i.e., each node i has $u_i, (u_{,\xi})_i, (u_{,\eta})_i$ and $(u_{,\xi\eta})_i$ as its degrees of freedom, if u is the displacement of the plate in node i. More about this element is in reference [4]. The amount of variables and the practised way of numbering depending on the polynomial degree is shown in figure 1. This way of numbering is not very convenient for adapted refinements but it has its advantages in the ease of condensing the midside nodes, what is done in order to decrease the numerical effort.

4. Results

In this chapter the results obtained are presented. In general, the solution given by the used program that includes hierarchic shape functions and p-refinement is related to the exact

solution. For the treated basic problem of plate bending exact solutions can be received from standard analytic calculations. Here, formulas for flat circular plates and plates with straight boundaries of constant thickness were taken from [5]. Due to boundary conditions and applied loads u_{max} always appears as deflection of the centre node of the structure. For this reason all mentioned and pictured displacements refer to this node.

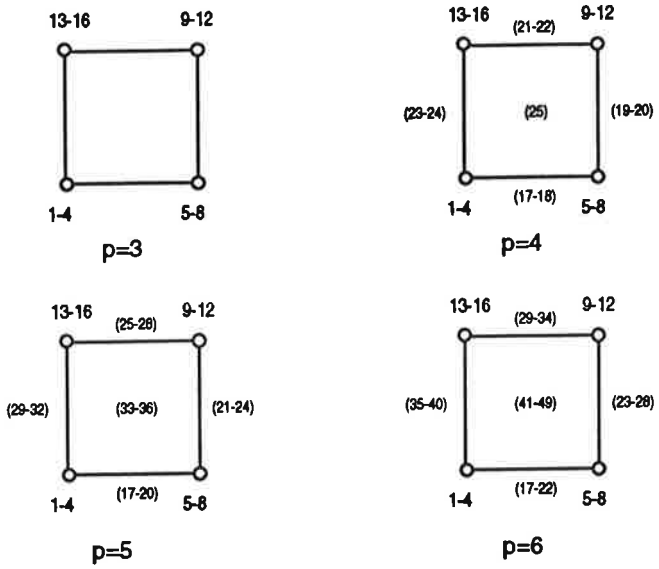

Figure 1. Nodal degrees of freedom for one element depending on the polynomial degree

In order to assess results from the treated program the same load cases and boundary conditions were examined with the aid of the commercial finite element program ANSYS. This comparison served the purpose to see how fast other programs reach convergence depending on the amount of degrees of freedom and to estimate the absolute accuracy of finite element programs, i.e., if the exact solution is exactly reached.

A real equivalent comparison between ANSYS and the program developed in this work was not possible because of ANSYS's element library. Neither hierarchical nor *p*-convergent elements are available. This is the reason why *all ANSYS convergence curves* presented in this work are *h-convergence based curves*.

ANSYS elements treated in this work are 3-D elastic quadrilateral shells that have both bending and membrane capabilities [6]. The first one is element STIF63, a four-noded linear shell. The second element used here, STIF93, is derived from STIF63. It is a 3-D isoparametric shell and has 8 nodes and six degrees of freedom at each node: translation in the nodal x, y and z directions and rotations about the nodal x, y and z axes.

4.1. Square plates. As already mentioned the deflection of the centre node was the measure for all load cases and different boundary conditions. The following figures show the relative error of this deflection depending on the degree of freedom of the structure.

Using the developed program structures containing one and four elements were examined. In case of point loaded simply supported square plates the used program gave best results for the four-element structure (see figure 2).

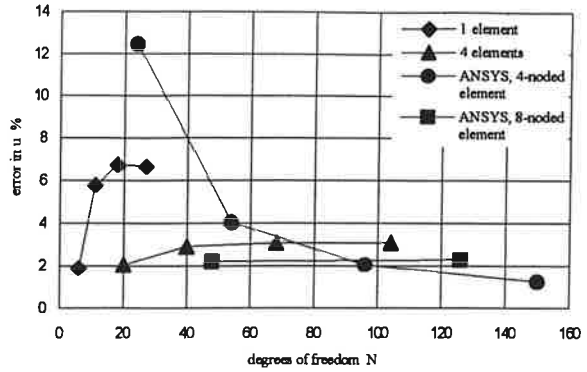

Figure 2. Error in centre deflection for point loaded simply supported square plate

Nodal displacements calculated with one-element structures reached convergence when the polynomial degree was increased to sixth order. Four-element structures show convergent behaviour already in case of polynomial degree 5. For both cases convergence required less than 50 degrees of freedom compared to 150 degrees of freedom that were necessary when ANSYS (STIF63) was used. Note that results given by the developed program come to convergence that has not the exact solution as its limit. Four-element structures include a 3.1 % error and one-element structures contain a 6 % difference between exact and FE solution.

8-noded elements from ANSYS element library (STIF93) here give accurate results within a 2.5 % difference but the amount of degrees of freedom used by ANSYS was much higher. If the number of elements is increased results obtained from STIF63 structures and STIF93 structures approached the same value. For this reason the main attention is given to ANSYS's 4-noded elements although they are much simpler and incorporate only C^0 continuity compared to elements developed in this work. For better readability 8-noded elements were only calculated for structures containing one and four elements, respectively.

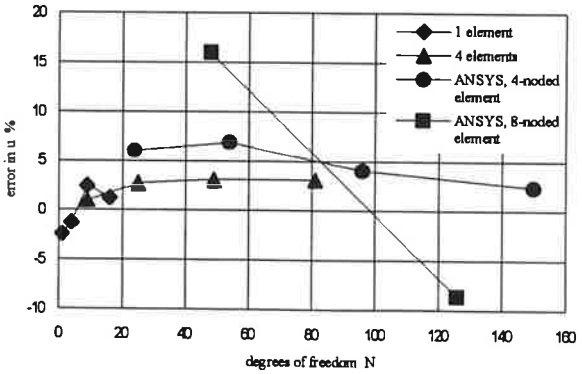

Figure 3. Error in centre deflection for point loaded clamped square plate

In case of clamped plates (figure 3.) results obtained from the developed program achieved the same accuracy (3 % deviation) as *h*-refined ANSYS structures without requiring as many degrees of freedom as ANSYS does. STIF93 elements served to compute a coarse mesh with higher order elements when using ANSYS.

In figure 4. it is obvious that the coarse mesh realised by a one-element structure is too rough to achieve good results. 13 % deviation to the exact solution is decreased down to 3 % when the amount of elements is increased up to four. ANSYS again gives accurate results but more degrees of freedom are necessary.

If square plates are clamped accuracy is obtained already for a very few degrees of freedom. The difference between exact and FE solution again amounts 3 %. In this case one-element structures and four-element structures reach the same accuracy (3.1 %).

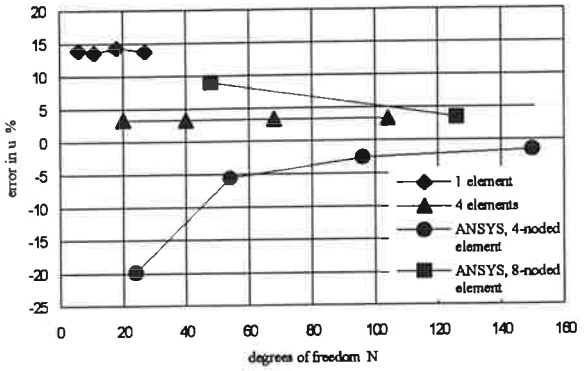

Figure 4. Error in centre deflection for uniform loaded simply supported square plate

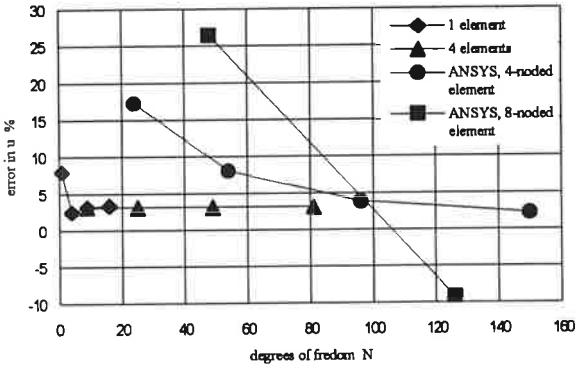

Figure 5. Error in centre deflection for uniform loaded clamped square plate

4.2. Circular plates. When plates are of circular shape ANSYS's 8-noded elements were avoided because of the above mentioned reasons. Convergence again was achieved for all load and boundary cases when using the developed program. However, point loaded simply supported plates (figure 6.) give poor results when using only one element for modelling the structure. 19.2 % deviation is the result of a poor shape approximation by using only one element for defining a quadrant of the circular plate. More discretized models containing four elements delivered results that are much closer to the exact solution (3 %).

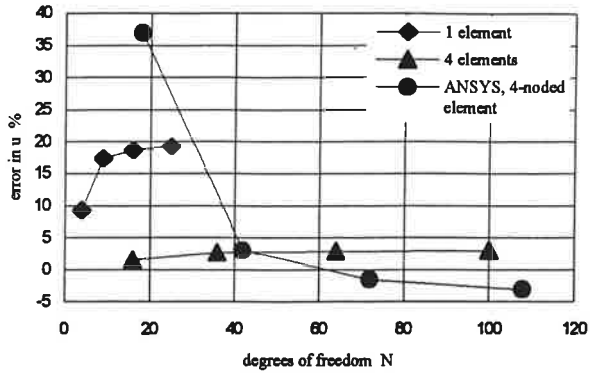

Figure 6. Error in centre deflection for point loaded simply supported circular plate

The computation of uniform load applied to simply supported plates (figure 7.) also gives acceptable convergence for structures containing at least four elements. The deviation does not exceed 3 %. One-element structures are not suited for this kind of geometry although convergent results are obtained.

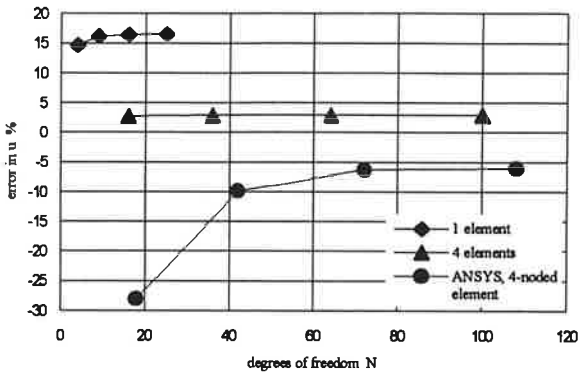

Figure 7. Error in centre deflection for uniform loaded simply supported circular plate

More details and results are given in reference [7].

5. Summary

In order to improve results' accuracy the polynomial degree of shape functions was increased while the number of elements was kept constant. This so-called *p*-refinement was practically realised by adding new functions of Legendre type. These functions must not affect on displacements in corner nodes, i.e., added internal surplus functions required hierarchical properties. The polynomial degree was raised from 3 to 6.

Convergence was observed in all cases except for circular structures containing only one element where the results approached a certain value but not the exact solution. For this reason a pure *p*-convergence is not seen to be the best way of discretization. The structure has to be

meshed sufficiently before starting the increase of polynomial degree, i.e., *h-p*-convergence seems to give best results. The average deviation between exact solution and FE solution varied between 3 % and 1.5 %. Results that equal exactly the analytic value were not obtained.

In general, the first step of refinement, a rough meshed structure of third polynomial order, already provided good results. Further refinements improved these results, i.e., a minimization of improvements from step to step could be noticed. A limit for a sensible increase of polynomial order could be observed. If p is greater than six, oscillations caused by additional degrees of freedom appear and the results do not become much better.

Results obtained from the developed program are compared to solutions given by the commercial FE program ANSYS. *H*-refined ANSYS structures that consist of C^0 continuous elements accomplish slight better results at the expense of more degrees of freedom and increased solution time. Standard deviations given by ANSYS are in the range of 2 % when the number of degrees of freedom amounts at least two times the amount needed by *p*-convergence.

References

1. *B. A. Szabo, I. Babuška*, "Finite Element Analysis", John Wiley & Sons, Inc., New York, 1991. ISBN 0-471-50273-1.
2. *R. Delpak and V. Peshkam*, A study of the influence of hierarchical nodes on the performance of selected parametric elements, International Journal for Numerical Methods in Engineering, Vol. 22, (1986) 153-171. ISSN 0023-5981.
3. *A. G. Peano, A. Pasini, R. Riccioni and L. Sardella*, Adaptive approximations in finite element structural analysis, Computers and Structures, Vol 10, (1979) 333-342. ISSN 0045-7949.
4. *S. Virtanen and A. Pramila*, A refined hermitian isoparametric plate bending element, Communications in Applied Numerical Methods, Vol. 4, (1988) 67-77. ISSN 0748-8025.
5. *R. J. Roark and W. C. Young*, "Formulas for stress and strain", 5th ed., McGraw-Hill, New York, 1975. ISBN 0-07-053031-9.
6. *G. J. De Salvo and R. W. Gorman*, ANSYS Engineering Analysis System User's Manual for ANSYS Revision 4.4, Swanson Analysis Systems Inc., Houston, 1989.
7. *J. Struckmann and S. Virtanen*, C^1 continuous *p*-hierarchical elements in plate bending problem, Report No. 56, Tampere University of Technology, Depertment of Mechanical Engineering, Institut of Applied Mechanics ,Tampere, 1994. ISSN 0356-7060.

OPTIMUM DESIGN OF STEEL FRAMES USING FATIGUE RESONANCE TESTING, DYNAMICS SIMULATION, ANALYTIC AND FEM OPTIMIZATION

Heikki Martikka
Department of Mechanical Engineering
Lappeenranta University of Technology
P.O.Box 20 SF-53851 Lappeenranta Finland

ABSTRACT

Optimization of structures is most useful from the concept design onward. But often optimizing improvements are needed when most design variables are already constrained. The present goal is to study means to ensure sufficient fatigue life in steel frames used under dynamic loading. First these were tested using resonance fatigue loading to find out surface fabrication methods to improve the fatigue life of the critically stressed parts. In the present study the design of the resonance method was analyzed using dynamics simulation based on Lagrangian dynamics. The structure was optimized using Monte Carlo optimization with weighted and fuzzy goals and with constraints on fatigue life and others with a mix of continuous, integer and discrete design variables. Also FEM optimization was tested. It concluded that each method is useful but effective integration is needed .

1 INTRODUCTION

Structural designers are increasingly pressed for better solutions in a shorter turnaround time. It has been observed that from some nine important conditions of success the most important predictor of success is ' a superior product which offers unique benefits to the user'. Therefore optimization should be used early since at the idea generation and evaluation stages most of the 'genetic' properties and costs are fixed. Correct definition of the goals and constraints is more important that their solution. If Ao alternatives have to be defined and if the design evaluation rate is L per time unit then the number of yet undefined alternatives is $A = Ao \exp(-L t)$ at time t. If the cost per evaluation of each alternative is k then the product development cost increases roughly as $C = k * Ao$ up to an allowed limit. In the specification and planning phase the goal is to understand the customer's incomplete or fuzzy requirements and translate these into engineering specifications according to Ullman [1]. One may transform these into traditional models or into fuzzy models reflecting better the customer's thinking. It has been noted often too late that the critical components should have been fully optimized, tested and verified. Some new design systems like Engineous [2] were designed with the aim to integrate and retain multidisciplinary and often incomplete design knowledge into a generic shell to

automatically iterate analysis codes. The following benefits are feasible: faster turnaround, better solutions, retaining of design expertise, reduction of human errors and reduction of labour costs. In order to reach these goals design tools have to be completed. Neittaanmäki [3] has suggested that structural optimization problems may be divided roughly into three classes; domain optimization, optimal sizing and topology optimization. The objective of the present study is to test the first two methods for optimization and dynamics simulation of some machine frames.

2 FATIGUE RESONANCE TESTING

Fatigue testing of large machine elements may be done in two ways. In the brute force method an active external excitation is applied to a passive structure. Thus large forces are required for obtaining large displacements and strains. Due to constraints the frequences have to be low and test times long. But if the structure is excited within ± 0.4 per cent of its eigenfrequency, then it will take part actively in the test. Thus only small forces are needed and frequencies can be set high and test times become short. In a previous study [4] a series of frames were tested using resonance fatigue loading to find out how fabrication methods of the critically stressed parts affect the fatigue life. The experimental set up and results of modal analysis are shown in Fig.1..

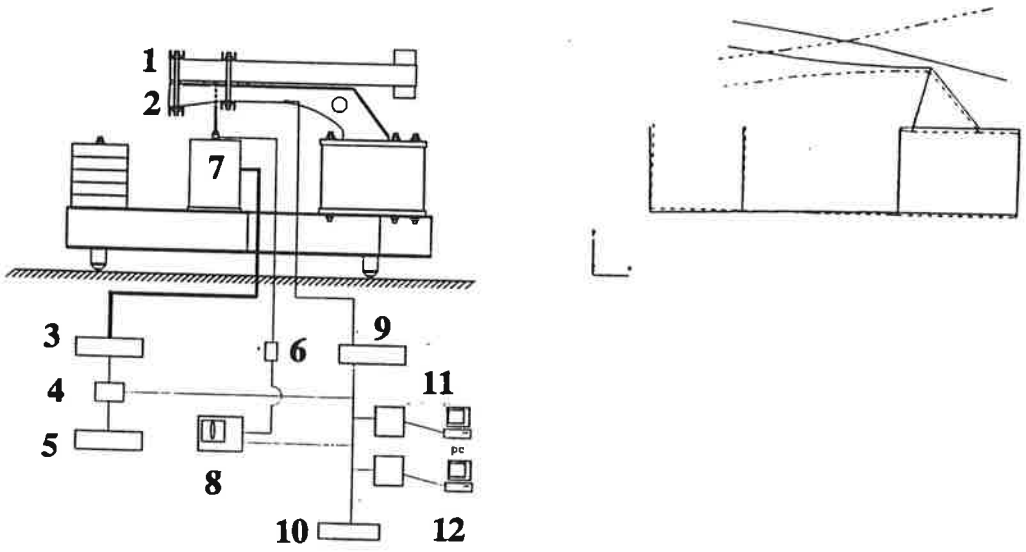

a) b)

FIGURE 1. Setup of the fatigue resonance testing [4]. a) Lay out. The numbers denote : (1) upper beam, (2) test beam, (3) power amplifier, (4) feedback, (5) function generator, (6) amplifier ,(7) electrodynamic shaker, (8) oscilloscope, (9) strain gage amplifier, (10) cycle counter, (11) rainflow counter and PC, (12) peak value collector PC. b) Results of modal analysis showing lowest eigenmode of the tested structure .

It was observed that with good machining a fatigue life of $1.46\ 10^6$ cycles was obtained with a frequency of 46.5 Hz at a stress amplitude of $\sigma_a = 160$ MPa.

3 SIMULATION OF THE DYNAMICS OF THE STRUCTURE

The simulation of the dynamics of the structure was done using the SIMNON [5] nonlinear simulation program and Lagrangian dynamics.

3.1 The kinetic energy

The dynamics model is shown in Fig.2. We select only one degree of freedom which is the the vertical defection q of the end of the beam using the method of Dimarogonas [6]. Assuming that a straight beam has a uniform cross section and a cantilever force then its static deflection at a distance x will be a polynomial shape of order 3 with zero displacement and slope at x = 0 and displacement q at x = L

$$z(x) = \frac{1}{2}\left[3\left(\frac{x}{L}\right)^2 - \left(\frac{x}{L}\right)^3\right] q \tag{1}$$

It is assumed that the motion of the beam will be

$$y(x,t) = z(x)\ q(t) \tag{2}$$

The kinetic energy of the beam b will be

$$Tb = \tfrac{1}{2} \int_0^L \dot{y}^2\ dm \tag{3}$$

where dm is mass per length .Now the the centerline of the beam is curved and its profile changes also. It is now assumed that the beam can be divided into four sections which each have constant sectional properties. The velocity of mass dm at location x is

$$\dot{y} = \frac{dy}{dt} = z(x)\ \frac{dq}{dt} \tag{4}$$

The kinetic energy of the beam is a sum

$$Tb = T1 + T2 + T3 + T4 \tag{5}$$

or

$$Tb = \tfrac{1}{2}\ Mb\ \dot{q}^2 \tag{6}$$

where Mb is the effective mass taking part in the motion of the test beam. Because the excitator frequency was restricted to about 50 Hz some additional masses were added to change the eigenfrequency of the system. The total kinetic energy of the structure is

$$T = Tb + \tfrac{1}{2}\ Mp1\ R\dot{p}1^2 + \tfrac{1}{2}\ Mp2\ R\dot{p}2^2 + \tfrac{1}{2}\ J\ \dot{\theta}^2 \tag{7}$$

where Mp1 is the mass of the upper beam and its fasteners and Mp2 is the mass at its end point , J is the moment of inertia at the center of the upper beam and Rpi are the vectors of locations of the masses respectively. The angular velocity θ is the same as the time rate of the tangent of beam deflection curve. The velocities of the masses are

$$\dot{Rp1} = RR1 \dot{q} \tag{8}$$

$$\dot{Rp2} = RR2 \dot{q} \tag{9}$$

thus the total kinetic energy is

$$T = \frac{1}{2} MM \dot{q}^2 \tag{10}$$

3.2 The potential energy and the dissipation energy of the system
The potential energy consists of the elastic energy of the beam and the gravitational energies of the mass bodies. Potential elastic energy of the beam is

$$Vb = \int_0^L E I y_{,xx} \, dx \tag{11}$$

Integrating this for the four constant elements one obtains

$$Vb = V1 + V2 + V3 + V4 = \frac{1}{2} GF q^2 \tag{12}$$

The total potential energy is obtained by adding the potential energies of the total mass of the beam at its center of gravity and others

$$V = Vb + VM + VMp1 + VMp2 \tag{13}$$

or

$$V = \frac{1}{2} GF q^2 + M g h + Mp1 g HH1 + Mp2 g HH2 \tag{14}$$

Dissipation energy was modeled as

$$D = \frac{1}{2} C1 \dot{q}^2 \tag{15}$$

3.3 The equations of motion. The Lagrangian function is

$$L = T - V \tag{16}$$

The Lagrangian equations of motion are for the coordinate q

$$\frac{d}{dt}\left[\frac{\delta L}{\delta \dot{q}}\right] - \frac{\delta L}{\delta q} + \frac{\delta D}{\delta \dot{q}} = F_q \tag{17}$$

3.4 Solution by simulation . The laboratory test force is a harmonic acting with frequency f = 46.5 Hz. Now the accuracy of the dynamics simulation model is measured by how well it reproduces the eigenfrequency of the actual structure. The vibrations were excited with initial conditions of zero displacement q = 0 and zero velocity qt = 0 and a small external step force Fq. In the simulation the method of state variables was used .

```
STATE  q   qt                                                    (18)
DER    dq  dqt
TIME   t
dq   =  qt          " = velocity       qt   =  dq/dt
dqt  =  qtt         " = acceleration   dqt  =  d(qt)/dt          (19)
qtt  =  Σ Fq /  MM  " =  Force  /  mass
```

where

ΣFq is the sum of all forces and MM is the sum of all generalized masses

3.5 Results

The following results were obtained , Fig.2 . The location of the center of gravity of the upper beam were moved by changing the parameter xL1 = x/L1 where x is distance of cantilever end of the upper beam and L1 is its length. The calculated eigenperiod T = .022 sec was rather close to the experimental period T_{exp} = 1 / 46.5 = 0.0215 sec.

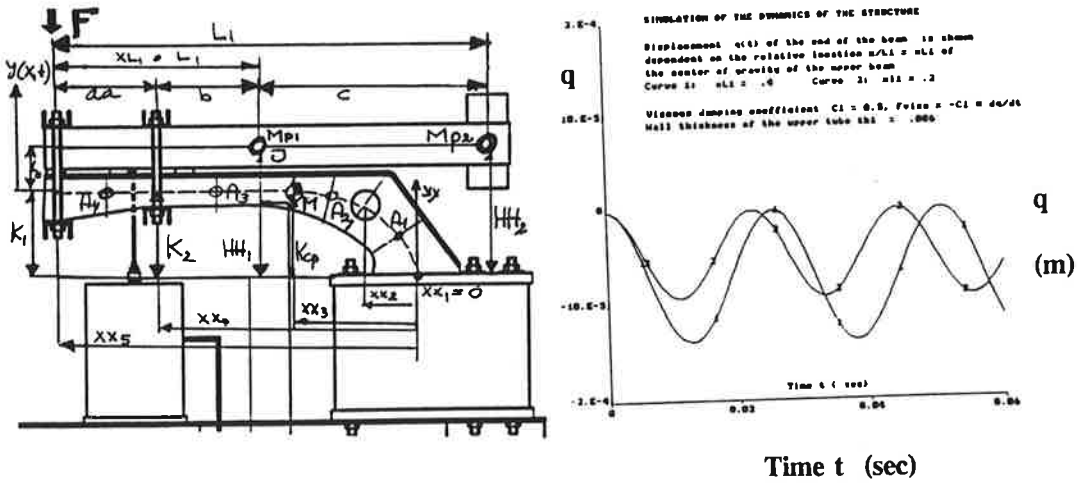

a) b)

FIGURE 2. Dynamics simulation of the structure using a simulation program and Lagrangian dynamics model.a) The simplified model b) The resulting vibration of the end of the beam q with two locations x/L1 of the upper beam mass center, curve 1: .4 and curve 2 : .2

4 OPTIMUM DESIGN OF THE STRUCTURE USING NONLINEAR MONTE CARLO OPTIMIZATION

4.1 The Algorithm. This method was based on analytical models and Monte Carlo optimization. Both continuum, integer and discrete design variables may be activated . In this program model it is possible to use for the U-beam a desired set of standard plate thickness classes , t(IT) , IT = 1,2,.. . and standard steel classes with UTS Rm(IM) , and cost C(IM) , IM = 1,2, etc . The continuous variables were the height H and width B. The objective function consisted of two terms

$$Q = Qv + Qpen \tag{20}$$

where Qv = the essential objective function
Qpen = the penalty function penalizing for violation of constraints.
If no constraints are violated then Qpen = 0. Continuous design variables were defined as

$$x(j) = xbest(j) + [\, xmax(j) - xmin(j) \,] * [\, 0.5 - RND \,] * Learn * kk \tag{21}$$

where x(j) is the continuous variable and xbest(j) is its latest best value around which the search is activated with a range which is diminished by a learning function Learn. RND is a random number 0 .. 1. Discontinuous variables were generated by

$$x(i) = INT[\, (xmax(i) - xmin(i) + 1) * RND + xmin(i) \,] \tag{22}$$

The model of the structure is shown in Fig. 3. The load force was F = 10000 N.

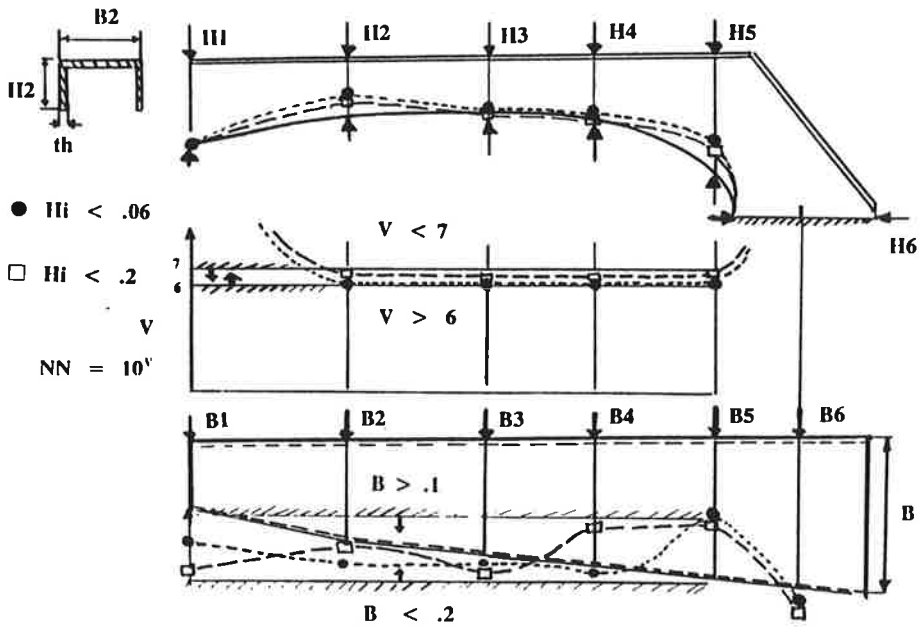

FIGURE 3. Nonlinear optimization of the beam using the fuzzy goal..Two geometric constraints were used for the mid section heights, one with Hi < .06 and the second with Hi < .2. Fatigue lives NN = 10^V were constrained by 6 < V< 7. Height H and width B were continuous variables. Width B was constrained by .1 < B < .2

4.2 Design goals. Two types of design goals were used

4.2.1 The weighted goal. The essential objective function is

$$Qv = f1\ Q1 + f2\ Q2 \tag{23}$$

Here the sum of the weight factors is one $f1 + f2 = 1$. The partial goals are dimensionless to be comparable . The first goal is the the cost minimization goal

$$Q1 = \text{cost} / \text{costo} \tag{24}$$

Here cost is the material cost and costo is the cost of a competing product. The second goal is the technical 'Taguchi' type goal modelled as the minimization of variations from desired minimum fatigue life.

$$Q2 = \sum R(i)\ R(i) \tag{25}$$

where

$$R(i) = V(i) / Vo - 1 \tag{26}$$

Here V(i) is the exponent of the fatigue life at a section number i = 1,2,3,4,5,6 and Vo is a scaling value, which was set to Vo = 6 to ensure a life of 10^6 cycles.

$$NN(i) = 10^{V(i)} \tag{27}$$

The function V(i) depends on the following stress ratios

$$Va = Sva / Rm = \text{relative effective stress amplitude} \tag{28a}$$
$$Vm = Svm / Rm = \text{relative efefctive stress mean value} \tag{28b}$$
$$Ve = Se / Rm = \text{relative fully corrected fatigue strength} \tag{28c}$$

Here R(i) is also a constraint for ensuring that a fatigue life of 10^6 is obtained. Thus it is required that $R(i) > 0$. Fatigue lives were calculated using a method proposed by Meyer [7] which combines the Haigh diagram of modified Goodman type and the S-N diagram. It has been used in axle design [8]. The ideal fatigue strength or the mean endurance limit of the rotating -bending specimes of steels is can be calculated from static strength

$$\sigma w = 0.5\ Rm \tag{29}$$

the fully corrected fatigue strength is

$$Se = C\ Cf\ \sigma w \tag{30}$$

here C and Cf = 1/Kf are the fatigue strength reduction factors, Kf = the fatigue stress - concentration factor. These factors may be changed during the manufacture within certain technical and economical limits. Now the fatigue tests showed that Se for the beams was 160 MPa .

4.2.2 The fuzzy goal. This formulation aims directly at ensuring the satisfaction of the customer to this product. A successful design event can be defined using Boolean logic . Now only intersection of events are needed

$$G = GK \text{ and } GV1 \text{ and } GV2 \text{ and } GV3 \text{ and } GV4 \text{ and } GV5 \text{ and } GV6 \tag{31}$$

The fuzzy probability of obtaining this event is the product

$$P(G) = P(GK) * P(GV1) * P(GV2) * P(GV3) * P(GV4) * P(GV5) * P(GV6) \quad (32)$$

where GK = an event of obtaining a satifactorily low cost = K
GVi = an event of obtaining a satisfactorily high fatigue life at section no i
All these can be formulated as S-formed curves or approximate straight lines. Now the fuzzy goal P(G) of obtaining a satisfactory design event can be defined as

if	K <	20	then P(GK)	= 0.001	not possible to produce	(33)
if	20 < K <	40	then P(GK)	= 1	full satisfaction is obtained	
if	40 < K <	120	then P(GK)		satisfaction changes linearly	
if	120 < K		then P(GK)	= 0.001	no satisfaction , too expensive	

Satifaction P(GV) on the fatigue life exponent V changes from 0.001 when V < Vmin = 4 to 1 when V > 5. Technical constraints were set also on fatigue life for others sections except the first and the last

$$VVmin = 6 < V(i) < 7 = VVmax \quad (34)$$

The mid section heights Hi of the actual beams were restricted to Hi < .06 by the other components of the machinery. Using the program the values H = .05 to .07 were optimal. About the same results were obtained with looser constraints Hi < .2 .. The width of the beam was constrained as .1 < B < .2 . The results are shown in Fig.3.

5 OPTIMUM DESIGN USING A FEM PROGRAM

The beam was studied using the optimization module of the I-DEAS system [9]. The model and some results are shown in Fig. 4. The actual structure is not quite symmetric but it was modelled as symmetric and one half was used.

a)

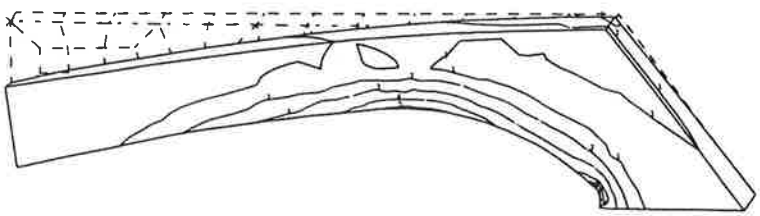

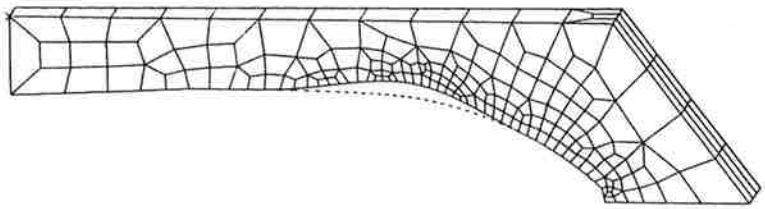

b)

FIGURE 4 Optimization of the beam under cantilever loading using FEM a) the initial model , the deformed form , Mises stress (MPa) contour codes 4: 107 5: 132 6: 157 b) the optimized form and original form (dotted line), allowed stress was 150 MPa.

6 SUMMARY AND CONCLUSIONS

Several modern testing and design methods were applied to analyze steel frames used in heavily loaded machines.They were previously tested to improve fatigue life using resonace fatigue loading. The reason for testing was that optimum design methods were not used by the original manufacturer. Nonlinear optimization proved efficient and gave global optima in a short time. Experimental dynamic testing is an efficient method for analyzing the dynamic behaviour of structures. But its experimental results can be made more useful by using theory based dynamics simulation in preliminary set up design and also in later analysis. FEM based optimization is a promising design tool but user interfaces should be made more intelligent and algorithms more robust and automatic.

Acknowledgements. The assistance of Jukka Lehmusvaara , MSc , in I-DEAS modelling is gratefully acknowledged

REFERENCES

[1] D.G.Ullman, The mechanical design process, McGraw.Hill, 1992,337 p

[2] Engineous program , GE Corporate Research and Development ,USA

[3] P.Neittaanmäki, On the computer aided optimal structural design,Proceedings of the 4th Finnish mechanics days, June 5-6, 1991, Research papers 17, Lappeenranta University of Technology, Lappeenranta , Finland, 11-23

[4] A.Verho, E Niemi,J.Lehmusvaara, J.Kainulainen, Resonanssin hyväksikäyttö ulokepalkin väsytyskokeissa, (Use of resonance in fatigue testing of a cantilever beam, Report , Symposium on Machine Design, Oulu University, 1993) Raportti 30.4.1993, Koneensuunnittelun symposiumi , Oulun Yliopisto , Oulu 1993

[5] SIMNON, Simulation Language for Nonlinear Systems, Department of Automatic Control, Lund Institute of Technology in Lund, Sweden

[6] A.D. Dimarogonas , Vibration for Engineers, Prentice Hall, Englewood Cliffs, New Jersey , 1992

[7] J.A. Meyer, Finite life under combined stress, Machine Design,August ,(1985) , 83-84

[8] H. Martikka, Akselien optimimitoitus mikrotietokoneella. (Optimum design of shafts using microcomputer), Research publication 40, Lappeenranta University of Technology, 1986

[9] I-DEAS Optimization module 1990

OPTIMIZATION OF THIN ELASTIC SHELLS OF REVOLUTION WITH AXISYMMETRIC LOADING

Esa Murtola
Tampere University of Technology / Applied mechanics
P.O. Box 589, FIN-33101 Tampere
Finland

ABSTRACT

This paper deals with the shape and thickness optimization of thin elastic axisymmetric shell structures. The objective of the design is the weight minimization of the shell material when the constraints are displacements, stresses and enclosed volume of the structure. The nodal coordinates and thicknesses of the elements are chosen as the design variables .
The finite element model used here is based on the exact solutions of the differential equations of the classical shell theory. Because of this not only the displacements but also the stresses can be obtained with great accuracy. In the design sensitivity analysis the analytical method is used and the numerical results are compared with the finite difference values. Several examples are presented illustrating optimal shape and thickness distributions for different kinds of shell structures.

1. INTRODUCTION

Axisymmetric shells are very common in technical applications such as pressure vessels, tanks, roof of structures, etc. There are also many different theories for the designers to calculate the responses of structures for various types of loadings. The method used here is based on the classical theory of thin shells created by Love and Kirchhof [1], where they have made assumptions for the thicknesses, the displacements and the material of the shell. The theory was further developped by Reissner and Meissner [1], which have shown the fundamental pair of differential equation for the thermostatics of shells of revolution in the form

$$\begin{aligned} \mathsf{L}(W) - 2f W &= \Gamma U + H \\ \mathsf{L}(W) &= -E_\theta W + G \ , \end{aligned} \tag{1}$$

which are explained more detailed e.g in the book of Krauss [1]. However the general solution of the fundamental pair (1) is

$$W = W_c + W_p \qquad U = U_c + U_p \ ,$$

where (W_p, U_p) is any of its particular solutions and (W_c, U_c) is the general solution of the corresponding homogeneous pair of differential equations

$$\begin{aligned} \mathsf{L}(W) - 2f W &= \Gamma U \\ \mathsf{L}(W) &= -E_\theta W \ . \end{aligned} \tag{2}$$

In this paper the displacements and stresses needed in the optimization program are calculated by the exact finite element method proposed by Outinen [2]. The method is based on the exact solution of the differential equations (1) in a way that leads to the normal finite element stiffness equation

$$[K]\{U\}=\{R\}. \tag{3}$$

2. OPTIMIZATION PROBLEM

The optimization problem discussed in this paper is to minimize the material volume V_m of a shell structure, when the design variables s_i are the thicknesses t_i of the elements and the nodal coordinates of the elements (x_i, y_i) shown in the figure 1. The minimization problem is subjected to constraints $g_i(\boldsymbol{s})$, which can be stress and displacement constraints for each element, a volume constraint for the inside volume V_s of the vessel and upper and lower bounds for the design variables.

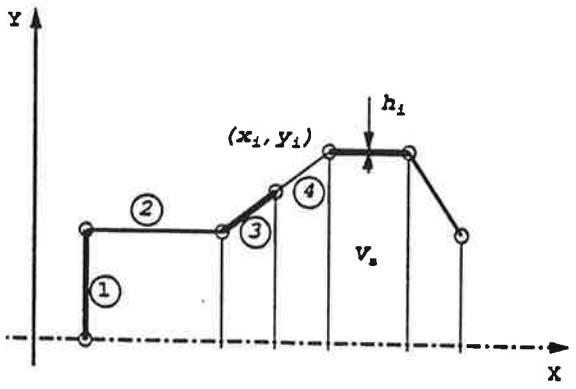

Figure 1. The design variables of the shell structure and some fundamental shell elements

The numerical method used here for the optimization problem is the sequential quadratic programming SQP [3], which is considered quite powerful for different kinds of problems.

3. STRUCTURAL ANALYSIS WITH THE EXACT FINITE ELEMENT METHOD

The basic idea for the exact finite element method [2] is to use the the particular solution of the fundamental pair (1) for different loading cases and the general solution of the corresponding homogeneous pair of the differential equations (2) to make the element stiffness matrix $[k]$ and the equivalent nodal force vector $\{r\}$ for each type of fundamental shells e.g cylinderical shell, conical shell, etc.

In this way it is possible to use fundamental shells as elements shown in the figure 1 and so the number of the elements is small. Other benefits from this method are that the nodal

displacements $\{U\}$ solved from equation (3) are exact according to the theory of thin elastic shells and also all the field functions S in the element e.g. displacements and stress resultants can be calculated exactly as a sum of S_p a particular solution of equation (1) for any field loading , S_m a particular solution of the equation (1) for the axial loading and S_c the general solution of the homogenous equation (2)

$$S = S_p + S_m + S_c \tag{4}$$

where

$$S_c = \left[\tilde{S}\right]\{A\} \tag{5}$$

where $\{A\}$ is a vector containing unknown integrations constants and matrix $\left[\tilde{S}\right]$ contains functions from the solution of equation (2) ,[2]. So there is no need for the adaptive meshing to get more accurate results e.g. in the places where strong edge effects can appear .

3.1 FORMULATION OF THE ELEMENT STIFFNESS MATRIX

The solution of homogeneous pair of the equations (2) corresponds to the element shown in the figure 2 a , where its nodal displacement vector is $\{u_c\}$ and nodal force vector is $\{F_c\}$.

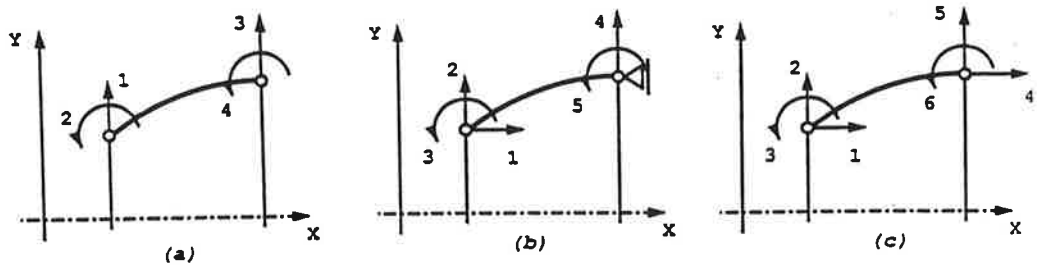

Figure 2. Different nodal degrees of freedom for shell element

According to the figure 2 a we can get the 4 x 4 flexibility matrix $[a_c]$ for the homogenious loading, which contains only radial forces and moments at the edge circles of the shell. From flexibility equation

$$\{u_c\} = [a_c]\{F_c\}\,, \tag{6}$$

with the help of the solution of the equation (2)

$$\{u_c\}=[D]\{A\} \tag{7}$$

and

$$\{F_c\}=[C]\{A\}\ , \tag{8}$$

where the matrices $[D]$ and $[C]$ contains functions from the solution of equation (2) [2], it follows that flexibility matrix for the homogenous loading is

$$[a_c]=[D][C]^{-1}. \tag{9}$$

The 5 x 5 flexibility matrix $[\bar{a}]$ for the case in the figure 2 b can be obtained with the help of the particular solution for the axial loading by adding its influence to $[a_c]$

Now the 5 x 5 element stiffness matrix $[\bar{k}]$ is

$$[\bar{k}]=[\bar{a}]^{-1} \tag{10}$$

and the 6 x 6 element stiffness matrix $[k]$ for the case in the figure 2 c can be obtained from the axial equilibrium.

3.2 FORMULATION OF THE EQUIVALENT FORCE VECTOR

The equivalent force vector for different field loads e.g. hydrostatic pressure inside a water tank can be computed exactly using the equation

$$\{r\}=[k]\{u_p\}-\{F_p\}, \tag{11}$$

where $\{u_p\}$ and $\{F_p\}$ contains the nodal displacements and the nodal forces corresponding to any particular solution of the fundamental pair (1) using the field load in question [2].

4. DESIGN SENSITIVITY ANALYSIS

One of the most important stages in the linking of the structural analysis with an optimization program is the design sensitivity analysis, which calculates the changes in the structural responses to the changes in the design variables. The methods used in the design sensitivity analyses are usually based on finite difference methods e.g. the global finite difference method or the semi-analytical method or the analytical method in which the needed derivatives are calculated analytically.

Differentiating the equation (3) with respect to the design variable s_k we have

$$[K]\frac{\partial\{U\}}{\partial s_k}+\frac{\partial\{K\}}{\partial s_k}\{U\}=\frac{\partial\{R\}}{\partial s_k} \tag{12}$$

and further

$$\frac{\partial\{U\}}{\partial s_k}=[K]^{-1}\left(\frac{\partial\{R\}}{\partial s_k}-\frac{\partial[K]}{\partial s_k}\{U\}\right). \tag{13}$$

After solving the derivatives of the displacements the derivatives of any field function can solved from the equation

$$\frac{\partial S}{\partial s_k}=\frac{\partial S_p}{\partial s_k}+\frac{\partial S_m}{\partial s_k}+\frac{\partial S_c}{\partial s_k}\ . \tag{14}$$

These derivatives can be obtained by the analytical method or by the finite difference method discussed in the chapter 4.

4.1 ANALYTICAL METHOD

In the exact finite element formulation of the thin elastic axisymmetric shell structures expressions of the element stiffness matrix, equivalent force vector and particular solutions for different field loads and axial loads are quite easy to derivate with respect to each design variable according both the thicknesses and the nodal coordinates of an element. The derivatives of the stiffness matrix $[\bar{k}]$ can be calculated from the definition

$$[\bar{k}][\bar{a}]=[I] \tag{15}$$

differating it respect to each design variable

$$\frac{\partial[\bar{k}]}{\partial s_k}=-[\bar{k}]\frac{\partial[\bar{a}]}{\partial s_k}[\bar{k}] \tag{16}$$

where $\frac{\partial[\bar{a}]}{\partial s_k}$ is calculated with the help of

$$\frac{\partial[a_c]}{\partial s_k}=\frac{\partial[D]}{\partial s_k}[C]^{-1}+[D]\frac{\partial[C]^{-1}}{\partial s_k}\ . \tag{17}$$

The derivatives of the equivalent force vector $\{r\}$ can be calculated from the equation (11), which leads to the equation

$$\frac{\partial\{r\}}{\partial s_k}=\frac{\partial\{k\}}{\partial s_k}\{u_p\}+[k]\frac{\partial\{u_p\}}{\partial s_k}-\frac{\partial\{F_p\}}{\partial s_k} \tag{18}$$

For these derivatives of the element stiffness matrix and the equivalent force vector it is needed to calculate the derivatives of the flexibility matrix $\frac{\partial[\bar{a}]}{\partial s_k}$ and the derivatives of the particular solutions for the nodal forces $\frac{\partial\{F_p\}}{\partial s_k}$ and the nodal displacements $\frac{\partial\{u_p\}}{\partial s_k}$.

The derivatives of the field functions $\frac{\partial S}{\partial s_k}$ e.g. displacements and stress resultants can be calculated from the equation (14), where the parts of the particular solutions $\frac{\partial\{S_p\}}{\partial s_k}$ and $\frac{\partial\{S_m\}}{\partial s_k}$ can be derivated easily and the part of the homogenous solution $\frac{\partial\{S_c\}}{\partial s_k}$ from the equation (5), which leads to

$$\frac{\partial\{S_c\}}{\partial s_k} = \frac{\partial[\tilde{S}]}{\partial s_k}\{A\} + [\tilde{S}]\frac{\partial\{A\}}{\partial s_k}, \tag{19}$$

where from equation (8).

$$\frac{\partial\{A\}}{\partial s_k} = \frac{\partial[C]^{-1}}{\partial s_k}\{F_c\} + [C]^{-1}\frac{\partial\{F_c\}}{\partial s_k} \tag{20}$$

4.2 THE GLOBAL FINITE DIFFERENCE METHOD

With this method is very easy to calculate the finite difference approximations of the design sensitivities, but it is computationally expensive and the accuracy of the design sensitivities depends strongly on the step size used for the perturbation of the design variables. The approximations of the design sensitivities for any field function o are

$$\frac{\partial(o)}{\partial s_k} \approx \frac{(o(s_k + \delta s_k)) - (o(s_k))}{\delta s_k}. \tag{21}$$

5. EXAMPLES

Example 1. Clamped circular plate subjected to uniformly distributed load

Problem definition. The weight of the plate with radius $r = 1\,\text{m}$ in the figure 3 is to be minimized with respect to the constraint of the maximum displacement $w_{max} = 5,5\,\text{mm}$ and to the maximum stress $\sigma_{eq} = 73.5\,\text{MPa}$. The uniform normal pressure $q = 0.0689\,\text{MPa}$ and the initial thickness $t = 25.0\,\text{mm}$. The material properties which are assumed are following Young´s modulus $E = 200\,\text{GPa}$ and poisson´s ratio $\nu = 0.3$. The design variables and the results from the optimization are shown in the figure 3. The theory of axisymmetric plates is not based on the solution of the equation (1) [2], but the stiffness equation (3) and the design sensitivity analyses is handled in the same way as in the chapters 3 and 4.

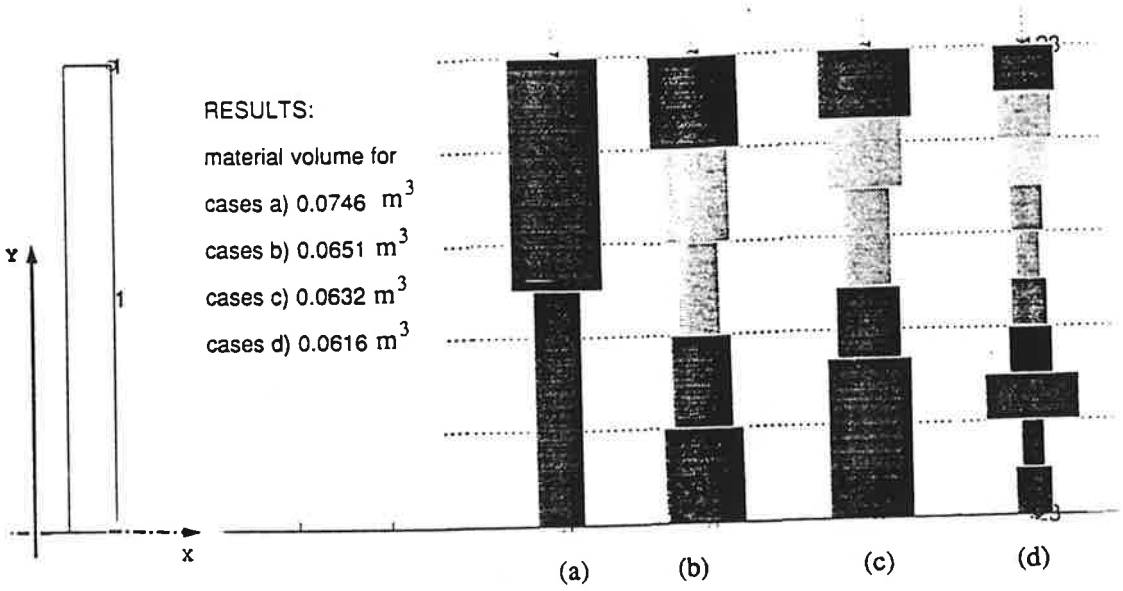

Figure 3. Clamped uniformly loaded axisymmetric plate initial design and optimum shapes

For this example it is also possible to get the exact sensitivities for the displacements and stresses. These are compared with those calculated in the way presented in chapter 4.1 and with those calculated by the finite difference method with different step values. The results are shown in the figure 4.

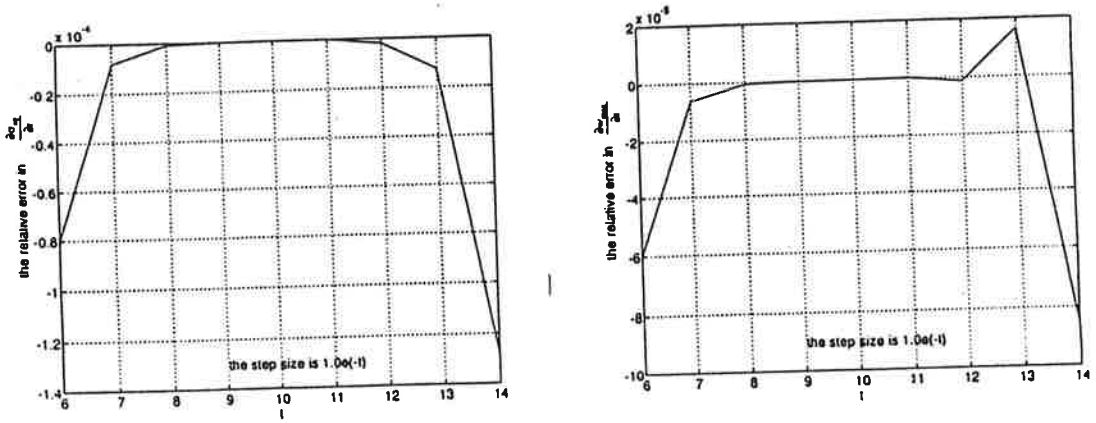

Figure 4. Comparison of the displacement and the equivalent stress sensitivities for the constant thickness plate

Example 2.
Problem definition. Symmetric pressure vessel, which is made from three fundamental shells: axisymmetric plate, cylinder and cone shown in the figure 5 is loaded with uniform pressure $q = 10\,\text{kPa}$ is to be minimized with the weight respect to the displacement constraint $\delta_{max} = 0.5\,\text{mm}$ and to the stress constraint $\sigma_{eq} = 10\,\text{MPa}$. The initial thickness $t = 8{,}0\,\text{mm}$ and the desired volume of the vessel $V_s = 1.94\,\text{m}^3$ .The material properties which are assumed are following: Young´s modulus $E = 200\,\text{GPa}$ and poisson´s ratio $\nu = 0{,}3$. The design variables and the results from the optimization are shown in the figure 5.

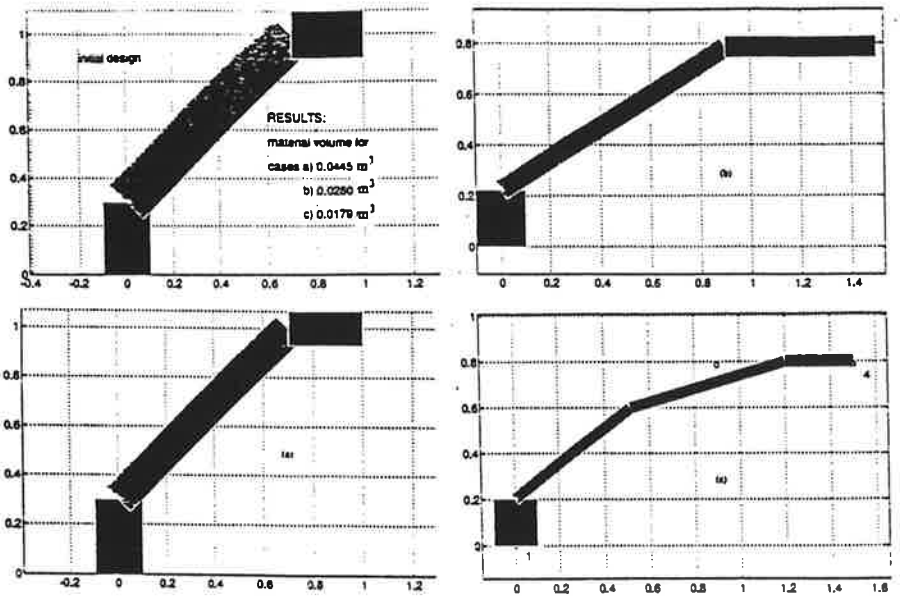

figure 5. The initial design and optimum shapes for the example 2

7. CONCLUSIONS

A new method to optimize thin elastic shells of revolution with axisymmetric loading is presented and tested with couple examples. The theory is based on the exact finite element method and so the results are exact for displacements and stresses according to the theory . It is also possible to calculate the design sensitivities analytically, which makes the optimization quite effective.

REFERENCES

1. KRAUS, H., Thin Elastic Shells. Wiley, New York, 1967

2. OUTINEN, H., Pyörähdyssymmetrisesti käyttäytyvän ohuen pyörähdyskuoren statiikka, Tampere University of Technology, Applied Mechanics, Report 27, Tampere, 1985.

3. SCHITTKOWSKI, K , What is EMP? (the manual of EMP expert system)

DISCRETE MULTICRITERION OPTIMIZATION OF A PLATE

TIMO TURKKILA
Applied Mechanics
Tampere University of Technology
P.O. Box 589, 33101 Tampere, FINLAND

ABSTRACT

The purpose of this presentation is to apply both discrete and multicriterion structural optimization to the plate structure. The multicriterion optimization problem has three criteria (the material volume of the plate, a displacement and the lowest natural frequency) and it is solved using the constraint method.

The plate is divided into several areas and thicknesses of these areas are the design variables. The discrete values of the design variables are the standard thicknesses of the steel plate. The solution of the discrete optimization problem is calculated using the Branch-and-Bound method.

1. INTRODUCTION

The general multicriterion optimization problem can be written into the form

$$\min_{\bar{x}\in\Omega} \bar{f}(\bar{x}) = \left[f_1(\bar{x}) \dots f_p(\bar{x}) \right]^T \tag{1}$$

where the feasible set is

$$\Omega = \{ \bar{x}\in\mathbb{R}^n \mid h_i(\bar{x}) = 0,\ i = 1,\dots,me,\ g_j(\bar{x}) \le 0\ j = me+1,\dots,m \} \tag{2}$$

and functions $f_1(\bar{x}),\dots, f_p(\bar{x})$ are called criteria. In the equation (2) *me* is a number of equality constrains, *m* a number of constraints and *n* number of design variables. In the multicriterion optimization the concept of Pareto optimality is used.

Definition A vector $\bar{x}^*$ is Pareto optimal for problem (1) if and only if there exists no $\bar{x}\in\Omega$ such that $f_i(\bar{x}) \le f_i(\bar{x}^*)$ for $i=1,\dots,p$ with $f_j(\bar{x}) < f_j(\bar{x}^*)$ for at least one j.

If there is only one criterion, the problem is the monocriterion problem which is part of the multicriterion problem. For example the first criterion $f_1(\bar{x})$ is the objective function and the criteria $f_2(\bar{x}),\dots, f_p(\bar{x})$ are moved to the constraints with parameters $\varepsilon_2,\dots,\varepsilon_p$. If these

parameters are fixed then there is a monocriterion optimization problem. This solution method of multicriterion optimization is called constraint method [1] and it can be written into the form

$$\begin{aligned} &\min f_1(\bar{x}) \\ &\bar{x}\in\Omega \\ &f_2(\bar{x}) \le \varepsilon_2 \\ &\vdots \\ &f_p(\bar{x}) \le \varepsilon_p. \end{aligned} \tag{3}$$

If design variables can get only values of some set, then the optimization is called discrete optimization and the feasible set is

$$\begin{aligned} &\Omega = \{\, x_k \in D_k \mid h_i(\bar{x}) = 0,\ i = 1,\dots,me,\ g_j(\bar{x}) \le 0\ j = me+1,\dots,m \,\} \\ &D_k = \{\, x_1,\dots,x_s \}\quad k = 1,\dots,n. \end{aligned} \tag{4}$$

This optimization problem can be solved using, for example, the Branch-and-Bound algorithm [2] which is a systematic way to find discrete optimum. The Basic idea is branch one design variable and then optimize. If there is a feasible set then the next design variable is branched and optimized and so on. This process continues until there is no feasible set or there is a discrete solution.

The Branch-and-Bound algorithm is suitable for a linear and a nonlinear optimization. It gives the right solution for the convex problems so the global minimum for the normal structural optimization problem is not quaranteed. But this problem is in the continuous nonlinear optimization too.

2. THE OPTIMIZATION PROGRAM

The optimization program, which has been used, is CASOP (Computer Aided Structural Optimization Program) [3],[4]. It has two different optimization routines as a black box: SQP by Schittkowski [5] and ADS by Vanderplaats [6]. All calculations of this paper have been performed with Schittkowski's SQP. The CASOP program includes also a small FE-program with four different element types: 2 and 3 dimensional bar elements, the plane stress element and the Reissner-Mindlin plate-element. All sensitivity analysises are calculated analytically without a difference method. CASOP program includes also the discrete optimization and the calculation of natural frequencies.

3. THE EXAMPLE

The example problem is a plate which loading is the uniform pressure. The plate is shown in the figure 1 and the symbol σ_{al} means allowable stress (von Mises yield condition).

The plate has twelve design variables and three objective functions. Objective functions are for minimizing the material volume V and the displacement Δ_A of the middle point A and for maximizing the lowest natural frequency ω_1. The plate is double symmetric and only

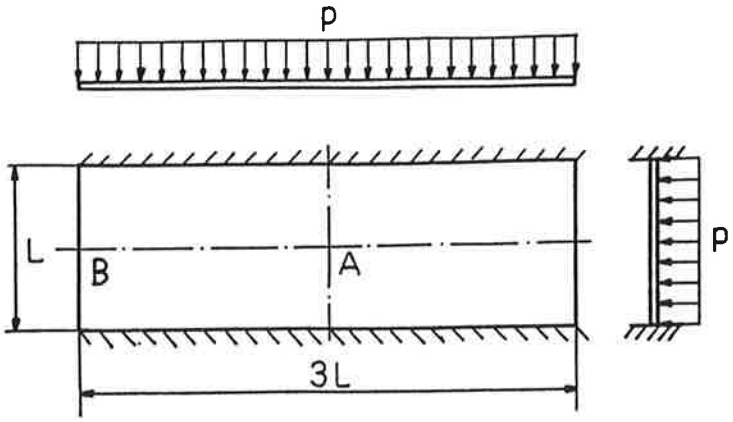

Figure 1. The plate example

one quarter of the plate is modelled. The design variables of the plate have been drawn into figure 2.

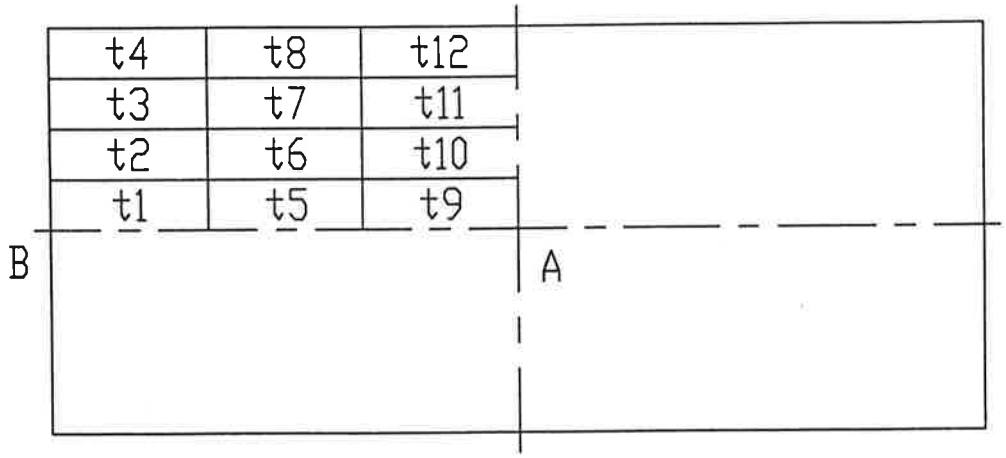

Figure 2. Design variables

The FEM-model of the plate includes 48 elements and 65 nodes. The mesh is uniform and every design variable has horisontically four elements and vertically one element. Stresses have been calculated in the middle of each element. Because it is not easy to determine where the highest stresses are, every element has the stress constraint and so there are 48 stress constraints.

The optimization problem of the plate is

$$\min \begin{pmatrix} f_1 \\ f_2 \\ f_3 \end{pmatrix} = \min \begin{pmatrix} V \\ \Delta_A \\ -\omega_1 \end{pmatrix} \qquad (5)$$

$$\sigma_i \le \sigma_{al} \quad i = 1,\ldots,48$$
$$x_k \in D \quad k = 1,\ldots,12$$

where the set of discrete values D is { 3, 4, 5, 6, 8, 10, 12, 14, 15, 16, 18, 20, 22, 25, 30, 35, 40, 50, 60 } mm [7]. These are the standard thicknesses of steel plates which routinely delivered by steel companies. There are 19 possible values for every design variable and $19^{12} \approx 2.2 \cdot 10^{15}$ different structures.

Four different Pareto optima of the problem (5) are calculated: the minimum of the displacement Δ_A, the minimum of the material volume V, the maximum of the lowest natural frequency ω_1 and an internal point where the constraints are $\Delta_A \le 0.1$ mm and $\omega_1 \ge 3000$ rad/s.

4. RESULTS

The results of Pareto optima are shown in the figures 3, 4, 5 and 6.

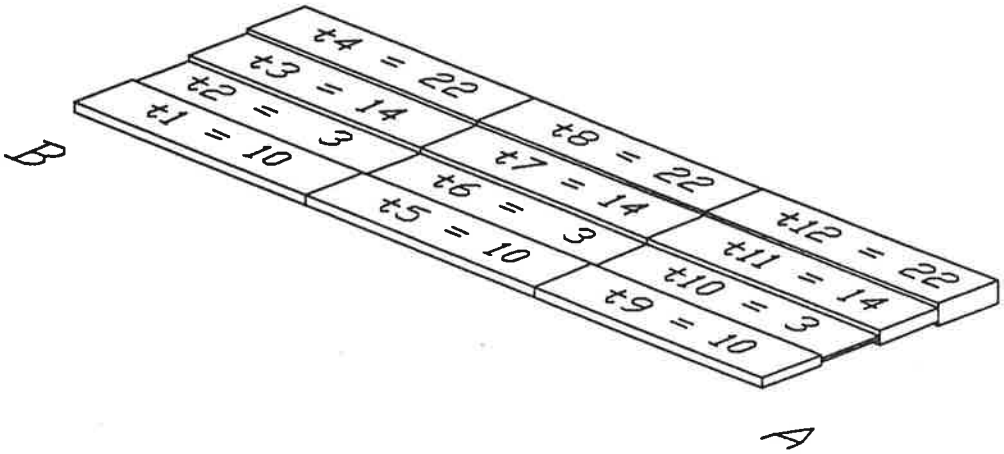

Figure 3. The minimum of the material volume. Objective functions: V=13.23 l, Δ_A=1.82 mm and ω_1=2173 rad/s.

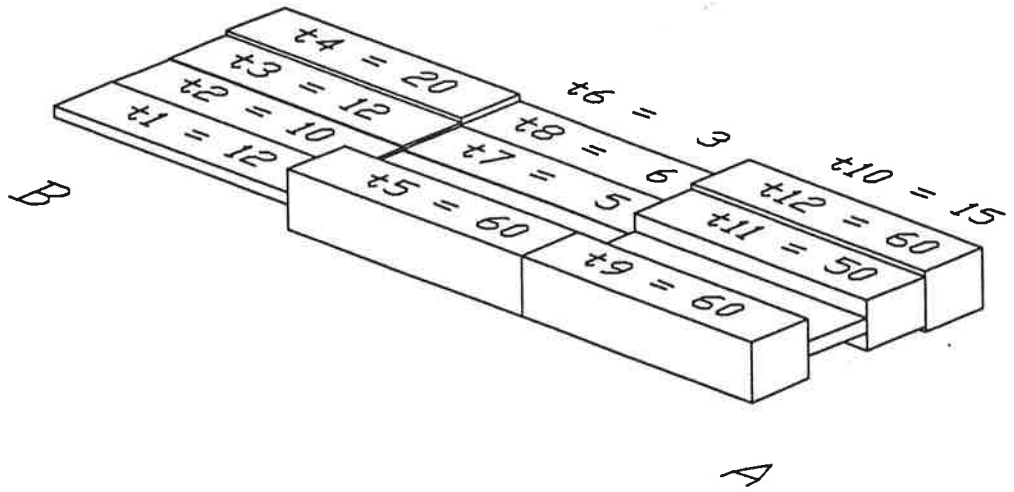

Figure 4. The minimum of the displacement in the point A. Objective functions: V=28.17 l, Δ_A=0.0209 mm and ω_1=1700 rad/s.

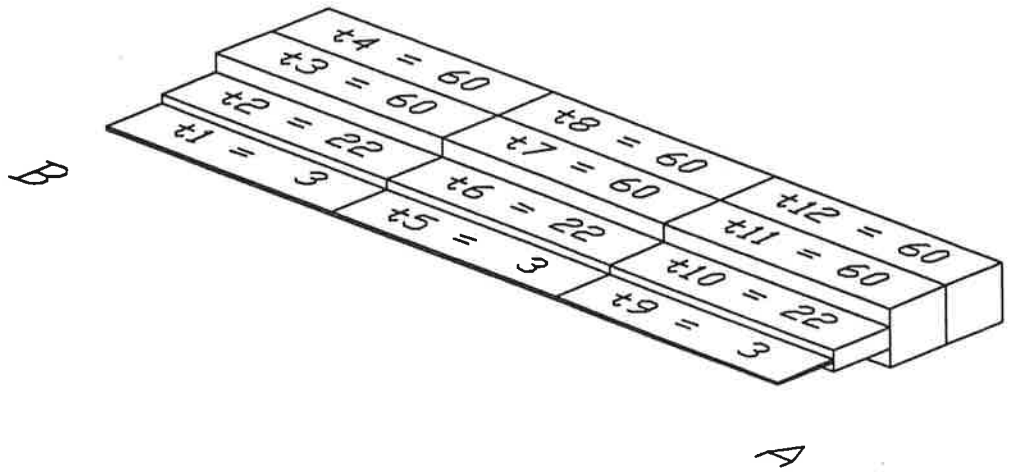

Figure 5. The maximum of the lowest natural frequency. Objective functions: V=39.16 l, Δ_A=0.149 mm and ω_1=7529 rad/s.

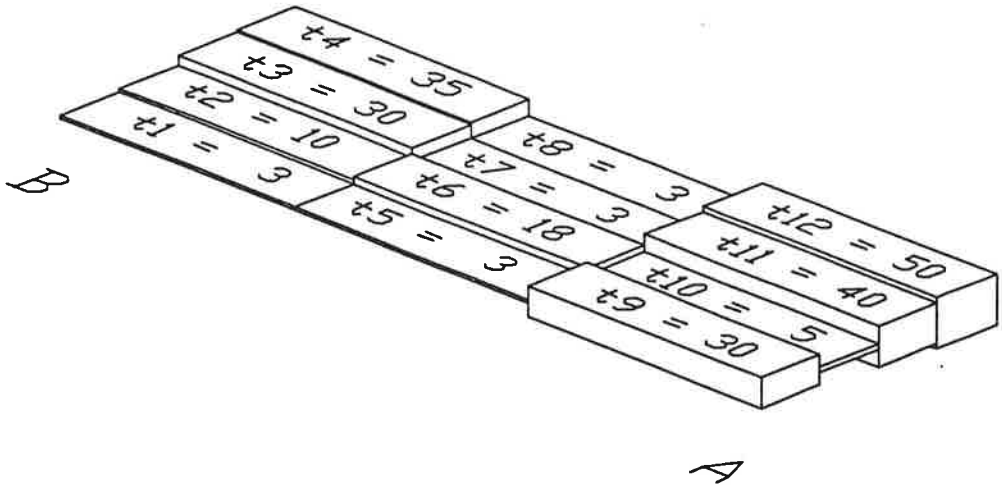

Figure 6. The internal point. Objective functions: V=20,7 l, Δ_A=0.0857 mm and ω_1=3049 rad/s.

The values of the objective functions in these four minimal solutions are written into the table 1. It is interesting that some objective functions are worse and some better in the discrete optimization than in the continuous optimization. However, it is clear that continuous problem gives better or equal results because discrete problem has extra constrains.

Table 1. The values of the objective functions in the minimal solutions. In the table below c stands for continuous and d for discrete problem.

	min V	min Δ_A	max ω_1	intern. p.
V/l	c 12.58 d 13.23	c 27.16 d 28.17	c 39.08 d 39.16	c 20.24 d 20.70
Δ_A/mm	c 2.23 d 1.82	c 0.0179 d 0.0209	c 0.151 d 0.149	c 0.1 d 0.0857
ω_1/ (rad/s)	c 2053 d 2173	c 1603 d 1700	c 7930 d 7529	c 3000 d 3049

The solutions of the problems are written in the table 2. There are some interesting aspects in this problem. First, the minimum of the displacement is not the maximum of the material volume. The maximum of the material volume has a displacement Δ_A = 0.0356 mm in the middle point of the plate. This means that if material volume is reduced then the displacement decreases. The reason for this phenomenon can be seen in the figure 7. When the displacement of point A is small then the displacement of the point B is large and opposite. When the displacement in the point B is large then the bending moments of the plate help to minimize the displacement of the point A.

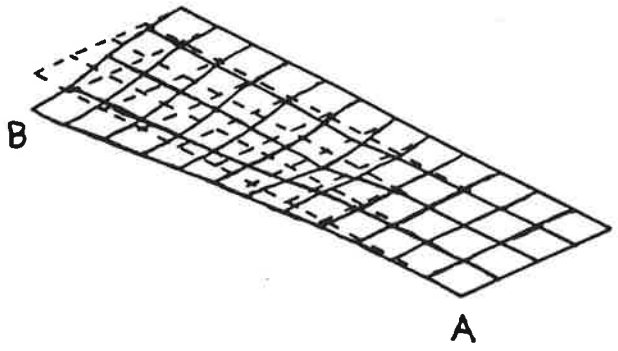

Figure 7. The displacement of the plate when the displacement of the point A is in the minimum.

Because the area of each thickness segment is equal there can be several solutions, which have the same material volume, in the discrete optimization. For example, in the internal point there is a structure which has the material volume 20.7 l, the displacement Δ_A = 0.0997 mm and the natural frequency ω_1 = 3003 rad/s. There is nothing wrong in the sense of the monocriterion optimization but it is not Pareto optimal solution because there is a structure where the material volume is equal but the displacement and the natural frequency are better.

Table 2. The solution of Pareto optima (c continuous, d discrete)

	min V	min Δ_A	max ω_1	intern. p.
t_1 / mm	c 9.94 d 10	c 12.86 d 12	c 3.00 d 3	c 3.00 d 3
t_2 / mm	c 3.00 d 3	c 10.05 d 10	c 21.64 d 22	c 9.23 d 10
t_3 / mm	c 13.52 d 14	c 11.09 d 12	c 60.00 d 60	c 31.24 d 30
t_4 / mm	c 21.18 d 22	c 19.41 d 20	c 60.00 d 60	c 35.36 d 35
t_5 / mm	c 9.38 d 10	c 60.00 d 60	c 3.00 d 3	c 3.00 d 3
t_6 / mm	c 3.00 d 3	c 3.00 d 3	c 20.72 d 22	c 17.08 d 18
t_7 / mm	c 13.08 d 14	c 3.00 d 5	c 60.00 d 60	c 3.00 d 3
t_8 / mm	c 20.70 d 22	c 9.20 d 6	c 60.00 d 60	c 3.00 d 3
t_9 / mm	c 9.38 d 10	c 53.11 d 60	c 3.00 d 3	c 29.13 d 30
t_{10} /mm	c 3.00 d 3	c 5.98 d 15	c 20.72 d 22	c 3.37 d 5
t_{11} / mm	c 13.08 d 14	c 53.98 d 50	c 60.00 d 60	c 34.79 d 40
t_{12} / mm	c 20.70 d 22	c 60.00 d 60	c 60.00 d 60	c 52.62 d 50

The discrete optimization problem is very large. The easiest problem was to minimize the lowest natural frequency. It took 104 s CPU time (Silicon Graphics Iris Indigo). The most difficult problem was the middle point problem which took 7983 s CPU time. These four minimal solutions needed totally 12,362 s CPU time. Anyway, with four points it is very difficult to imagine what the set of every minimal solutions looks like.

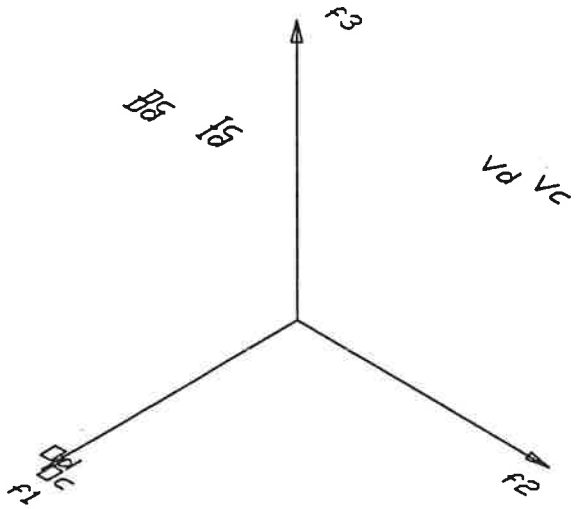

Figure 8. The calculated minimal solutions in the minimal space. In the figure V means min V, D Δ_A, O ω_1, I the internal point, c continuous optimum and d discrete optimum.

5. REFERENCES

1. D. Carmichael, Computation of Pareto Optima in Structural Design: Int. J. for Num. Meth. in Eng., 15(1980), pp. 925 - 929

2. H. A. Taha, "Integer programming theory, applications and computations", New York Academic press, 1975

3. M. Pora, Kantavien komposiittilevyjen ja -laattojen optimointi, Licentiate thesis, Tampere University of Technology, Tampere, 1994

4. T. Turkkila, Diskreettien lujuusopillisten optimointiongelmien numeerinen ratkaiseminen, Master thesis, Tampere University of Technology, Tampere, 1993

5. K. Schittkowski, What is EMP? (the manual of EMP expert system)

6. Vanderplaats, ADS version 2.01 (the manual of ADS optimization system), Engineering design optimization inc., 1987

7. Standard SFS 2142, Hot rolled steel plates. Dimensions and tolerances, 2. ed, 1987-02-23

MECHANICAL PRESSING OF SOFT POROUS MEDIA

KAI HILTUNEN

Laboratory of Scientific Computing
University of Jyväskylä
PO Box 35, FIN-40351 Jyväskylä, FINLAND

ABSTRACT. The model describing the wet-pressing of paper is presented. Focus is put on analysing the generalized version of Terzaghis principle of effective stress for soft porous media. Analysing the wet-pressing model for saturated flow gives restrictions to the parametrization of the stresses. Under these restrictions comparison between classical Terzaghis principle and phenomenological formula is made.

1. INTRODUCTION

Tests and measurements have been the traditional basis tools of the engineers designing a new product in paper making industry. Having certain demands of the efficiency, quality and costs of the product on their minds they have made the decisions of the construction of the new product. This is mainly done simply by the way of trials and errors. Nowadays the performance of the paper machine has been brought in to the level where no drastic improvements can be expected. However even very small improvements in the paper making process can save lot of money and energy. That is a reason why we need a more accurate knowledge of these processes. One very sophisticated way is to construct a mathematical modell and track paper making by computer. Compared to measurements modelling has many benefits. To make a one measurement serie on a test machine is so costly that with the same financing a group of researchers could work a year developing a computer program and with the completed simulation tool we can track these measurements using only fraction of the time and money needed for test machine. Furthermore we can foretell is it possible to make a wholy new construction. This is in many cases impossible or at least large efforts demanding using traditional way. Despite these incontestable advantages modelling is not going to replace the measurements totally. Due to the abstract reality of the models we have to have a link to reality. We must always have some comparisons between model and measurements. Also in many cases these models are using some empirical laws and relations, which are based on measurements and determination of parameters.

Paper forming process consists of four main parts. The stream of fiber suspension coming from the headbox is lead to the sheet forming section where via dewatering the suspension form the mat - called as web. The construction of the sheet forming section differs widely depending on what kind of paper we are manufacturing but in all machines the dominant mechanism in web forming is filtration. After this filtration the paper web has some kind of porous structure where the pores are filled with water. In this stage fifth of the web consists of fibers. Part of the water located in the pores is removed by squeezing the web between two pressing rolls. This stage is just after the sheet forming section and is called *pressing section*. The remaining water is removed in drying section by evaporating. This is done by contacting the paper with the series of steam-heated cylinders.

Drying section is a very long and energy-consuming part of the paper machine. So a very natural demand is to get this stage shorter. One very obvious way is to have a more efficient pressing section. Although we can not have considerable improvement in water removing without disturbing or altering the quality of the paper, only few procent growth in water removing efficiency can mean tens of meters shorter drying section. That is why we need a more comprehensive study and understanding of this wet pressing phenomena. Without any questions this study can also be extended to cover many similar physical phenomena like flows in plant tissues and perspiration of a human being for example.

Here we will just present briefly the model describing a wet pressing of paper. A more detailed description of the model is found in [1] and about the numerical solution in [2]. In this paper we are concentrating on the case of full water saturation, which leads us to a single convection-diffusion equation. From this equation we get condition for well-posedness of the problem. This condition is then used to analyse the applicability of the generalized Terzaghis principle of effective stress, introduced in [3].

2. CHARACTERIZATION OF THE PRESSING EQUIPMENT

In a conventional pressing section the water is squeezed out of the paper web into a special pressing felt by applying a pressure pulse to the paper-felt sandwich as it passes through the press 'nip'. The pressing equipment consists of two rolls, whics usually produce a short pulse with high pressure. The pressures applied varies between $2-6MPa$ and the nip residence time is order of milliseconds. Clarifying picture of the situation is seen in figure 1.

Physically the pressing phenomena is a flow of water and air in a compressible porous medium. Water and air are flowing due to external forces decelerated by viscous forces in elastic compressing porous medium.

3. MODEL FOR WET PRESSING OF PAPER

The model describing the pressing of paper web is based on volume averaged hydrodynamical equations for three phases - air, water and solid. We are looking a steady-state solution in a plane with the assumptions that the flow in horizontal direction is constant (machine velocity) and that the inertial terms are small compared to pressure gradient and terms involving mutual interaction between phases (so called Darcy approxi-

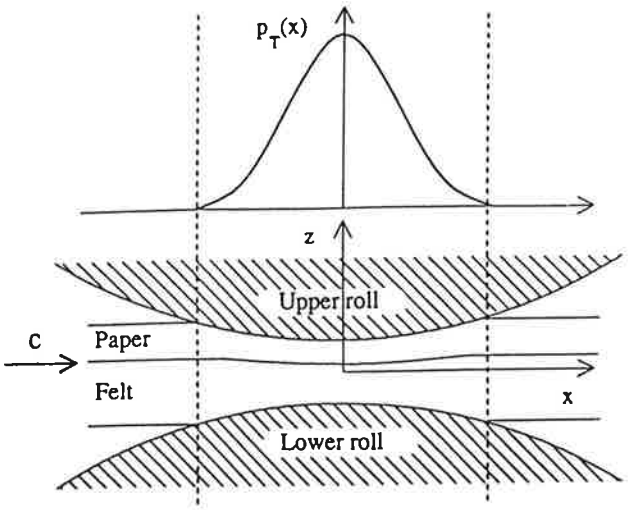

Picture 1: Schematic illustration of press nip

mation). With these assumptions we can write the equations in a following general form

$$\begin{cases} c\,\partial_x\phi_\alpha + \partial_z(\phi_\alpha v_\alpha) = 0 \qquad \alpha = s, w \\ c\,\partial_x((1-\phi_s-\phi_w)\tilde{p}_h) + \partial_z((1-\phi_s-\phi_w)\tilde{p}_h v_a) = 0 \\ \phi_\alpha \partial_z \tilde{p}_h = \bar{\Sigma}_\alpha \qquad \alpha = w, a \\ \tilde{p}_h = \tilde{p}_h(\phi_s, p_T(x)) \\ \bar{\Sigma}_\alpha = \bar{\Sigma}_\alpha(\phi_s, \phi_w, v_s - v_\alpha) \qquad \alpha = w, a. \end{cases} \tag{3.1}$$

Above c is the constant horizontal velocity, ϕ_α is the volumetric fraction and v_α is the averaged velocity of phase α. $\tilde{p}_h$ denotes the (intrinsic) hydrostatic pressure and $p_T(x)$ the total pressure applied to the porous medium. $\bar{\Sigma}_\alpha$ denotes the momentum exchange between phases. First three equations are simply the continuity equations for each phases and the following two equations are the momentum equations after Darcy approximation.

4.WATER SATURATED FLOW

In a case of water saturation system (3.1) reduces to

$$\begin{cases} c\,\partial_x\phi_s + \partial_z(\phi_s v_s) = 0 \\ c\,\partial_x\phi_s - \partial_z((1-\phi_s)v_w) = 0 \\ (1-\phi_s)F(\phi_s, p_T(x))\partial_z\phi_s = \bar{\Sigma}_w \\ \tilde{p}_h = \tilde{p}_h(\phi_s, p_T(x)) \\ \bar{\Sigma}_w = \bar{\Sigma}_w(\phi_s, v_s - v_w), \end{cases} \tag{4.1}$$

where we have used $F(\phi_s, p_T(x)) = \frac{\partial \tilde{p}_h}{\partial \phi_s}$.

Using

$$\begin{cases} \bar{\Sigma}_w = -\frac{\mu}{k(\phi_s)}(v_w - v_s) \\ (1-\phi_s)v_w = const - \phi_s v_s \end{cases}$$

gives one single convection-diffusion equation

$$c\,\partial_x \phi_s + const\,\partial_x \phi_s + \partial_z (G(\phi_s, p_T(x))\partial_z \phi_s) = 0, \tag{4.2}$$

where $G(\phi_s, p_T(x)) = k(\phi_s)/\mu\phi_s(1-\phi_s)^2 F(\phi_s, p_T(x))$. To have a well-posed problem we must now have

$$G(\phi_s, p_T(x)) \leq 0. \tag{4.3}$$

While $k(\phi_s) > 0$ this means that the condition (4.3) reduces to

$$F(\phi_s, p_T(x)) \leq 0. \tag{4.4}$$

This gives us some restrictions to the parametrization of the hydrostatic pressure $\tilde{p}_h$.

5. PARAMETRIZATION OF THE STRESSES

Rheological characteristics of porous media are determined by the microscopic structure of the solid matrices of the materials. In many cases the complexity of these structures makes it difficult to infer the macroscopic properties from the microscopic properties. It is therefore the common practice to use and rely on empirical laws and constitutive equations in describing various macroscopic phenomena in porous media. An example of such empirical relation is provided by the Terzaghis principle of effective stress, which in one dimensional compression states that the total pressure applied to a porous medium saturated by fluid is given by

$$p_T = p_s + \tilde{p}_h, \tag{5.1}$$

where p_s is the effective structural stress and $\tilde{p}_h$, as already denoted, the hydrostatic pressure of the pore fluid.

Equation (5.1) can be shown to be valid for porous media consisting of hard grains for which the intergranular contacts are pointlike. However for highly compressible porous materials, for which the contact area between the constituents is not negligibly small, the Terzaghis principle may not be applicable. That is why instead of (5.1) a more general form should be used. In [3] the pressure balance equation is written in a form

$$p_T = p_s(s) + f(s)\tilde{p}_h. \tag{5.2}$$

This parametrization is based on realization made in a case of static compression of homogeneous porous sample by a piston. The coefficient f can be interpreted as an effective areal porosity at the contact plane of the piston and the sample. Plotting a total pressure for different degrees of compression (strain s) as a function of hydrostatic pressure should lead according to (5.2) to a straight line with slope $f(s)$ and intercept $p_s(s)$. This way $f(s)$ and $p_s(s)$ can be found as functions of strain s. In figure 2 a typical functional form and the lower ($f(s) = \phi$) and upper ($f(s) \equiv 1$) limits for f are plotted.

6. RESTRICTION FOR PARAMETRIZATION

Using (5.2) in condition (4.4) gives

$$f'(s)(p_s(s) - p_T) \geq f(s)p_s'(s). \tag{6.1}$$

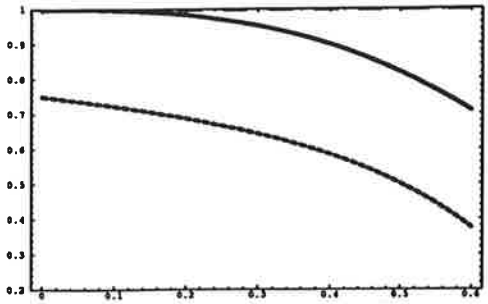

FIGURE 2. The coefficient $f(s)$

For classical Terzaghis principle (5.1) $f \equiv 1$. While $p_s'(s) \geq 0$ and $p_s(s) \leq p_T$ the condition (6.1) comes true in this case. But for functional form got for example in [3] condition (6.1) is not evidently fulfilled. Working on the measured range (in this case $p_T \in (0, 2MPa)$) (6.1) remains valid, but extending with the same functional form to the total pressure values out from the measured range, we will violate (6.1). This indicates either that the functional form choosed does not fit the reality outside measuring frame or that the theory based on contact between the compressive piston and porous medium is not applicable inside medium being just an interface phenomenon. Example of violating situation is seen in figure 3. In figure 4 is seen a limitive line in (total pressure,strain) - plane. Functional forms for $f(s)$ and $p_s(s)$ used in these figures are

$$f(s) = 1 - a\, s^b$$
$$p_s(s) = p_0 \frac{s}{s_0 - s},$$

where the parameters had the values $p_0 = 0.4$, $s_0 = 0.8$, $a = 1.1$ and $b = 2.6$. The total pressure was set to the value 3.5 in figure 3.

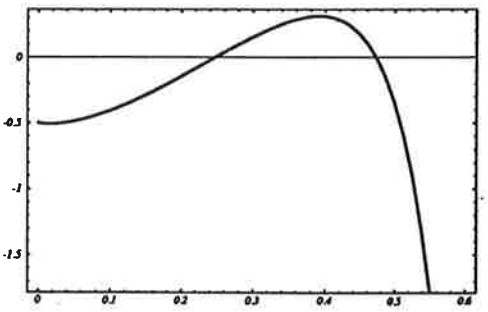

FIGURE 3. Derivative of hydrostatic pressure on strain

7. CONCLUSIONS

Equations describing the wet pressing of paper web has been briefly presented. In a case of full water saturation the system is reduced to one single convection-diffusion equation. From this equation the condition for well-posedness of the problem is deduced. Furthermore this condition is used to analyse the applicability of the empirical generalized version of Terzaghis principle of effective stress. The condition is shown to be valid for given functional forms inside measured range, but being violated outside this range.

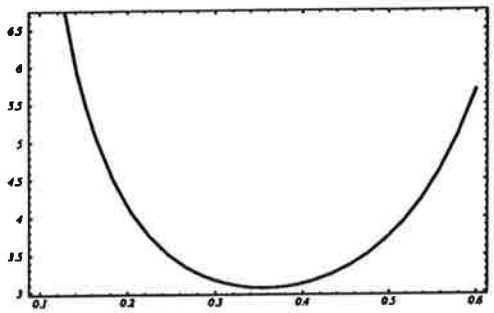

FIGURE 4: $F(s, p_T) \equiv 0$ contour in (s, p_T)-plane

ACKNOWLEDGEMENTS

This work is partially funded by the Technology Development Centre (TEKES) and by Valmet Paper Machinery at Rautpohja, Finland.

REFERENCES

1. M. Kataja, K. Hiltunen and J. Timonen, *Flow of Water and Air in Compressible Porous Medium - A Model of Wet Pressing of Paper*, J.Phys. D: Appl. Phys. **25** (1992), 1053–1063.
2. K. Hiltunen, *Modelling and Numerical Solution of Wet Pressing in a Paper Machine*, Licentiate thesis on Applied Mathematics and Computing, University of Jyväskylä (1992).
3. J. Kirmanen, M. Kataja and J. Timonen, *Rheological properties of soft porous media*, Preprint No. 17/1993, Department of Physics, University of Jyväskylä (1993).

ON THE HEADBOX FLUID FLOW MODELS

Jari Hämäläinen
Laboratory of Scientific Computing
Department of Mathematics, University of Jyväskylä
P.O. Box 35, FIN-40351 Jyväskylä, FINLAND

ABSTRACT. Fluid dynamics in a paper machine headbox have a remarkable effect on the quality of the producted paper, on basis weight and fibre orientation profiles, for example. These phenomena are desired to be studied by using numerical simulation and it requires mathematical modelling of the fluid flow. Modelling includes some special difficulties because of the complicated geometry of the headbox. Especially the manifold tubes and the turbulence generator consisting of some thousands of small tubes must be taken into account on the average. In this paper we consider some essential modelling aspects and we also give an numerical example.

1. INTRODUCTION

Fluid flow phenomena in a paper machine headbox establish a number of important paper properties, chief of which are basis weight and fibre orientation profiles, especially in the cross direction of a paper machine. Also the shape of the headbox internal flow passages and the turbulence they generate are of utmost importance.

Experimental work is very important in development of the headbox and sometimes it is the only reasonable way to research fluid flow phenomena. It has also some shortcomings. For example, optimization of the shape of the flow passages would require to build several new headboxes before an optimal construction could be chosen. There are also some technical difficulties in measuring the fluid flow inside the headbox. Besides, one problem in researching experimentally the effect of the fluid flow in the headbox on the cross directional profiles is that these profiles depend on the width of a paper machine. Because pilot machines are very narrow, about one metres wide whereas in production machines it can be up to ten metres, experiments must be done on a real scale paper machine at a paper mill.

It is also possible to study fluid flow phenomena in the headbox through mathematical modelling and numerical simulation. The headbox, with its multitude of complicated flow elements presents special difficulties in modelling the fluid flow. First of all, there can be up to some thousands of small tubes in the manifold tube bank and the turbulence

generator. If a finite element mesh were generated to represent the actual geometry, fluid flow models could be solved without any geometrical simplifications, but this would lead to huge algebraic systems and to extremely long computing times. Moreover, the flow fields of the various headbox components are interdependent, thus it is necessary to model the fluid flows in the headbox as one flow. Before continuing to these modelling aspects of the fluid flow, let us briefly describe the paper machine headbox.

The headbox is located at the wet end of a paper machine. Its function is to distribute the stock in an even layer, across the width of a paper machine. While headbox designs vary, depending on paper grades and speeds, they all have common components performing common functions. These are the header with its tube bank and equalizing chamber, a turbulence generator and a slice channel (see Fig. 1).

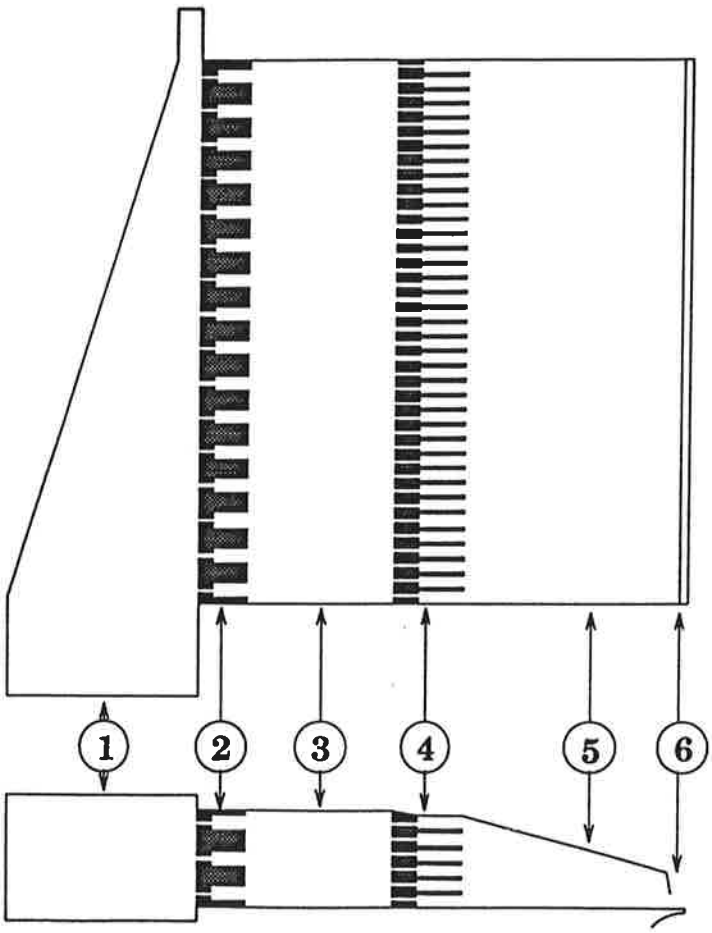

Figure 1. *Schematic representation of the headbox*

Referring to the figure, the stock enters a rectangular header (1) which distributes it equally across the machine width via a bank of manifold tubes (2). A controlled amount of the stock is recirculated at the far end of the header to provide flow control along the

header length. From the header the stock enters the manifold tubes which redirect it in machine direction and discharge it into an equalizing chamber (3). From here it enters a turbulence generator (4) comprising of a perforated plate and a bank of converging tubes, and finally into the slice channel (5) which accelerates it and deposits it onto a moving forming screen. At slice outlet there is a thin flexible lip (6) which can be profiled to control cross directional basis weight and fibre orientation profiles.

2. SOME MODELLING ASPECTS

As mentioned in Introduction, the actual geometry of the headbox is too complicated to be used in numerical simulation. Therefore the computational domain must be simplified. We proceed as follows. Firstly, using the domain decomposition method the domain is divided into three parts called as subdomains: the header and the manifold tubes, the equalizing chamber and the turbulence generator and the third one consisting of the slice channel and the free jet. Secondly, using the homogenization technique [2,4] the manifold tubes and the turbulence generator are replaced by specific outflow boundary conditions which give the same head losses as the tube systems do.

Homogenization (or averaging) of the fluid flow through the manifold tubes is based on an assumption that the flow is periodical in a thin layer near the perforated outlet wall of the header. Then it is sufficient to solve a local periodical fluid flow problem for a single tube in order to find out how the head losses in the manifold tube bank depend on the velocity and on the tube geometry. In fact, assuming that the head losses depend only on the mean velocity in the tube (the geometry is fixed), we can find an analytical expression for the head losses and thus also for the outflow boundary condition. This kind of analytical expressions are based on measurements and they are well known in hydrodynamical engineering literature. More detailed description about derivation of the homogenized outflow boundary condition is given in the references [7,9]. A similar approach is also used in modelling of the fluid flow in the equalizing chamber and in the turbulence generator [7].

The flow in the headbox is turbulent and indeed turbulence is a desirable flow phenomenon, as it contributes to fibre dispersion by breaking down fibre flocs and preventing new ones from forming. The headbox model has been developed for simulation of global time-averaged flow phenomena in the headbox, not to predict turbulence itself. Therefore it is justified to use classical k-ε turbulence model. Furthermore, when it is possible and accurate enough, also the laminar Navier-Stokes equations have been used.

One advantage of the domain decomposition is that the fluid flow in the separate subdomains can now be modelled by different kind of equations. The full system of the equations of the k-ε turbulence model have been used only for the header. For the equalizing chamber we have used two models. The first one has been introduced in [7]. The model consists of the time-averaged Reynolds equations and of a given turbulent viscosity, which was obtained by solving a local problem and using the homogenization method. Simulations have shown that the turbulent viscosity does not have any significant effect on a numerical solution. Thus it is enough to use a constant viscosity and the laminar Navier-Stokes equations for the equalizing chamber. Also the fluid flow in the slice channel has been modelled by a laminar model.

In addition to the geometrical simplifications, the fluid flow equations and the boundary conditions are averaged in the vertical direction. Dimensional reduction leads to two dimensional models and therefore it is realistic to use work stations instead of super computers in numerical simulations. The depth of the header is usually constant or it decreases in the cross direction such that the depth of the inlet tube is larger than the depth of the recirculation tube. Changes in the depth are smooth and small and they have been taken into account only via a specific continuity equation,

$$\nabla \cdot (D\vec{u}) = 0, \tag{1}$$

where D is the depth and $\vec{u}$ is the velocity vector averaged in the vertical direction. The depth of the equalizing chamber is assumed to be constant and the standard two dimensional Navier-Stokes equations can be used in modelling the equalizing chamber. The mean velocity at the inlet of the slice channel is a few m/s, but at the outlet it is order of 10 – 20 m/s. Acceleration is caused by decreasing the depth of the channel in the machine direction. At the outlet the depth is only a few centimetres. Thus it is supposed that the changes in the depth must be taken into account also in the viscous terms of the Navier-Stokes equations.

Next, the concrete fluid flow models for the headbox flow passages are given. For further information about fluid dynamics see the references [1,6] and [10,12].

3. MODELLING OF THE HEADER

The fluid flow in the domain Ω^H (i.e. the header, see Fig. 2) is modelled using the classical turbulence model consisting of the time-averaged Reynolds equations

$$-\nabla \cdot \left[\mu(\nabla\vec{u} + \nabla\vec{u}^T)\right] + \rho\vec{u} \cdot \nabla\vec{u} + \nabla p = 0, \quad \mu = \mu_0 + \mu_T,$$

of the modified continuity equation (1) and of the k-ε model

$$\begin{cases} -\nabla \cdot \left[\dfrac{\mu_T}{\sigma_k}\nabla k\right] + \rho u \cdot \nabla k = \mu_T \Phi - \rho\varepsilon, \\ -\nabla \cdot \left[\dfrac{\mu_T}{\sigma_\varepsilon}\nabla \varepsilon\right] + \rho u \cdot \nabla \varepsilon = C_1 \dfrac{\varepsilon}{k}\mu_T \Phi - \rho C_2 \dfrac{\varepsilon^2}{k}, \end{cases}$$

where the eddy viscosity is

$$\mu_T = \rho C_\mu \frac{k^2}{\varepsilon}$$

and

$$\Phi = 2\left(\frac{\partial u_1}{\partial x_1}\right)^2 + \left(\frac{\partial u_1}{\partial x_2} + \frac{\partial u_2}{\partial x_1}\right)^2 + 2\left(\frac{\partial u_2}{\partial x_2}\right)^2.$$

At the inlet Γ_{in}^H Dirichlet boundary conditions $\vec{u} = \vec{u}_{\text{in}}$, $k = k_{\text{in}}$ and $\varepsilon = \varepsilon_{\text{in}}$ are stated. Also the recirculation velocity is fixed, $\vec{u} = \vec{u}_r$ on Γ_r^H. Normal derivatives of k and ε are assumed to vanish on Γ_r^H. On the walls the standard wall boundary conditions of the k-ε model are used.

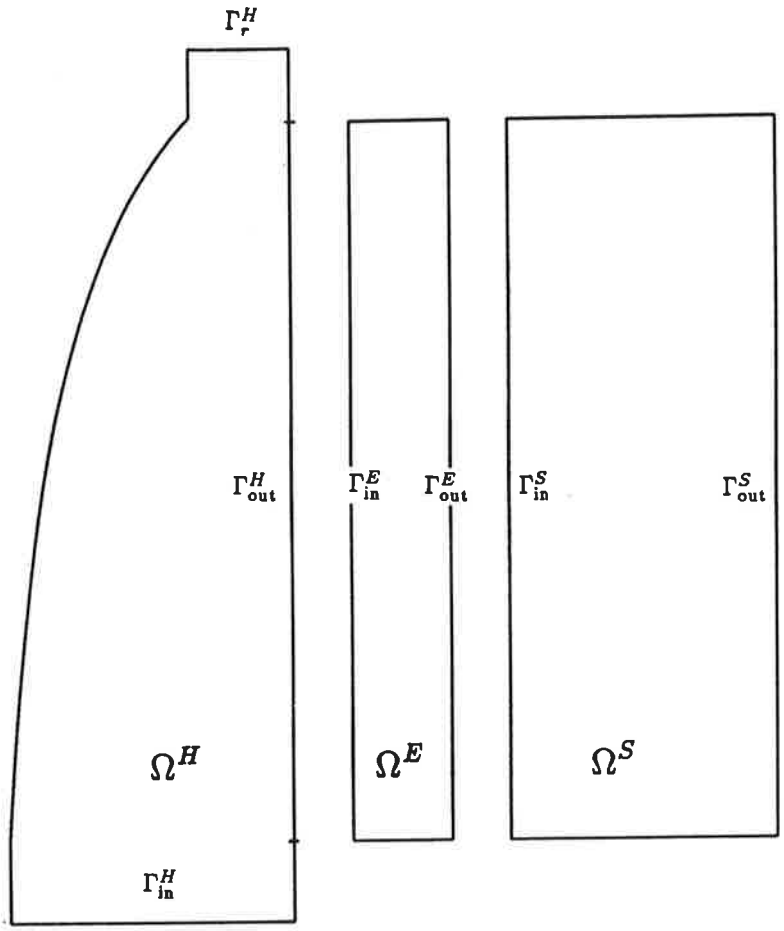

Figure 2. *Computational domain*

More interesting are boundary conditions at the outlet of the header, because they model the effect of the manifold tubes. The most important condition on Γ_{out}^H is the boundary condition for the normal force

$$\vec{\sigma}_1 \cdot \vec{n} = \sigma_{11} = -p + 2\mu\varepsilon_{11} \approx -p,$$

where $\vec{n} = (1,0)$ is the outward unit normal vector. The static pressure in the header is large compared to the viscous term and thus $2\mu\varepsilon_{11}$ is ignored. The pressure p at the outlet depends on the pressure in the equalizing chamber p_E (a solution of the equalizing chamber model) and on the head loss in the manifold tubes Δp. As mentioned earlier, based on empirical head loss formulae we get

$$p = \Delta p + p_E = \frac{1}{2}\rho F_M u_1^2 + p_E,$$

where F_M is a "friction factor" for the manifold tubes depending on the tube geometry, roughness of the walls of the tubes, etc. The head loss can also be solved numerically

as well [7]. Based on numerical simulations, a solution does not depend essentially on a tangential boundary condition and we have used either the boundary conditions $\vec{\sigma}_2 \cdot \vec{n} = \nabla k \cdot \vec{n} = \nabla \varepsilon \cdot \vec{n} = 0$ or the wall boundary conditions of the k-ε model.

4. MODELLING OF THE EQUALIZING CHAMBER

In Ω^E (the equalizing chamber) the fluid flow is modelled by the two dimensional Navier-Stokes equations

$$\begin{cases} -\nabla \cdot [(\mu(\nabla u + \nabla u^T)] + \rho(u \cdot \nabla)u + \nabla p = 0, \\ \nabla \cdot u = 0. \end{cases} \tag{2}$$

At the inlet Γ_{in}^E the velocity is given, $\vec{u} = (u_M, 0)$, where u_M is obtained as a solution of the header model. Similarly to the outflow boundary condition of the header model, we set

$$\vec{\sigma}_1 \cdot \vec{n} = -\left(\frac{1}{2}\rho F_T u_1^2 + p_S\right)$$

on Γ_{out}^E, where now F_T is the friction factor for the turbulence generator and p_S is the static pressure in the slice channel (a solution of the slice channel model). The second velocity component u_2 is zero on all the boundaries. Moreover, we set $\vec{\sigma}_1 \cdot \vec{n} = 0$ on the side walls.

5. MODELLING OF THE SLICE CHANNEL

The slice channel model is based on averaging the Navier-Stokes equations (2) in the vertical direction. The resulting equations are similar to the so-called shallow water equations, except that the depth is known in our case. The model is as follows

$$\begin{cases} -\frac{\mu}{D}\Delta(D\vec{u}) + \rho\vec{u} \cdot \nabla\vec{u} + \nabla p = 0 \\ \nabla \cdot (D\vec{u}) = 0 \end{cases} \quad \text{in } \Omega^S.$$

The velocity through the turbulence generator u_T is given by the equalizing chamber model and we set $\vec{u} = (u_T, 0)$ on Γ_{in}^S. On the side walls the tangential stress and the normal velocity are set to zero. The outflow boundary condition depends on the free jet. Assuming the contraction of the jet to be known and using the Bernoulli equations, we get that the pressure at the outlet is [7]

$$p = \frac{1}{2}\rho\left(\frac{1}{\kappa^2} - 1\right)u_1^2 = \frac{1}{2}\rho C_J u_1^2,$$

where κ is the contraction coefficient typically order of 0.7 – 0.9. Thus the outflow boundary condition is

$$\begin{cases} \frac{\mu}{D}\nabla(Du_1) \cdot \vec{n} - pn_1 = -\frac{1}{2}\rho C_J u_1^2, \\ \frac{\mu}{D}\nabla(Du_2) \cdot \vec{n} - pn_2 = 0. \end{cases}$$

6. NUMERICAL EXAMPLE

The headbox fluid flow models are solved numerically using the finite element method [3,5,8,11]. Because the solutions of the models depend on each other, an iterative procedure is used in order to simulate fluid dynamics in the whole headbox. The solution methods are not considered in this paper. We just given an example.

Typically the drying shrinkage profile is compensated by the slice lip profile such that the slice opening is smaller at the edges than in the middle. It generates cross directional velocity components towards the middle of the slice channel. Some of the simulated velocity vectors are plotted in Fig. 3. The cross directional velocity component is very small. Thus the velocity vectors and the geometry are not in real scale.

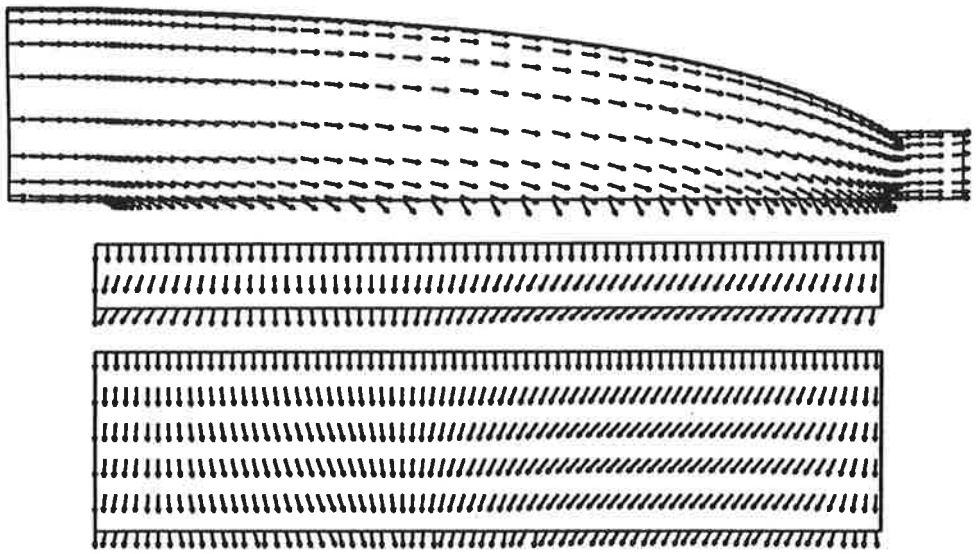

Figure 3. *Velocity field in the headbox*

CONCLUSIONS

Derivation of the models requires some assumptions and approximations. Therefore verification of the models is important before numerical simulation can be used in industrial applications. Based on the numerical tests we can conclude that the models predict at least qualitatively flow phenomena in the headbox, but further experimental measurements and development of the models are still needed.

ACKNOWLEDGEMENTS

We would like to thank Valmet Paper Machinery INC. and the Technology Development Centre (TEKES) for their financial support of this work.

REFERENCES

1. G.K. Batchelor, "An Introduction to Fluid Dynamics", Cambridge University Press, (1967)
2. A. Bensoussan, J.L. Lions and G. Papanicolaou, "Asymptotic Analysis for Periodic Structures", North-Holland, Amsterdam, (1978)
3. A.N. Brooks and T.J.R. Hughes, *Streamline Upwind/Petrov-Galerkin Formulations for Convection Dominated Flows with Particular Emphasis on the Incompressible Navier-Stokes Equations*, Computer Methods in Applied Mechanics and Engineering, vol. 32, 199-259, (1982)
4. C. Conca, *Numerical Results on the Homogenization of Stokes and Navier-Stokes Equations Modeling a Class of Problems from Fluid Mechanics*, Computer Methods in Applied Mechanics and Engineering, 53, 223–258, (1985)
5. C. Cuvelier, A. Segal and A.A. van Steenhoven, "Finite Element Methods and Navier-Stokes Equations", D.Reidel Publishing Company, Dordrecht, Holland, (1986)
6. R.W. Fox and A.T. McDonald, "Introduction to Fluid Mechanics", John Wiley & Sons, New York, USA, (1985)
7. J. Hämäläinen, "Mathematical Modelling and Simulation of Fluid Flows in the Headbox of Paper Machines", Doctoral Thesis, University of Jyväskylä, Report 57, (1993)
8. J. Hämäläinen and J. Järvinen, "Elementtimenetelmä virtauslaskennassa", CSC-Tieteellinen laskenta Oy, (1994)
9. J. Hämäläinen and T. Tiihonen, *Flow Simulation with Homogenized Outflow Boundary Conditions*, in "Finite Elements in Fluids, New Trends and Applications", K. Morgan, E. Onate, J. Periaux, J. Pereira and O.C. Zienkiewicz (Eds.), 537-545, (1993)
10. B.E. Launder and D.B. Spalding, "Lectures in mathematical models of turbulence", Academic Press, London, (1972)
11. O. Pironneau, "Finite Element Methods for Fluids", John Wiley & Sons, Masson, Paris, (1989)
12. W. Rodi, "Turbulence Models and Their Application in Hydraulics", IAHR state of the art paper, Delft, second edition (1984)

SIMULATION OF THE PAPER SHEET CURLING

REIJO PIETIKÄINEN
MATTI KURKI[1]

Laboratory of Scientific Computing, University of Jyväskylä
Seminaarinkatu 15, SF-40100 Jyväskylä, Finland

ABSTRACT. A thin plate model for humidity induced curl of copying paper is introduced. The model takes into account the profiles in the thickness direction of fiber orientation, elastic modulus and humidity expansion. In the linear theory one can derive unique and closed form expressions for the deflected surface in terms of material parameters. However, in practice the nonlinear effects can not be neglected. We show that in the the large displacement case these effects can lead to multiple solutions. We give examples of 'bifurcations' where the paper sheet takes cylindrical form whenever the humidity difference or the size of the test specimen grows beyond a critical limit. Finally we present a comparison between numerical simulation and the actual measurements.
Mathematics Subject Classification, 73B30, 73C02, 73C30, 73C50, 73K10.

1. INTRODUCTION

Curling and other dimensional changes of paper sheets are often observed during humidity and temperature variations. The nature of these deformations depend on the conditions in the environment and, of course, the properties of the paper grade under our study.

Modern printing and copying equipment require that dimensional changes in paper should be small with respect to the change in conditions induced by the device. Particularly this requirement is important in non-impact printing technology, like copying and laser printing machines. In such cases the ink is fixed by means of a hot fuser roll. As a result the paper absorbs heat, loses moisture and shrinks. Because the thermal loading and material response is non-symmetric in thickness some bending moments will develop in the paper sheet. This leads to curling unless there are sufficient displacement constrains. Figure 1 illustrates paper sheet suffering from poor dimensional stability.

Paper is generally considered as a non homogeneous and anisotropic material, [1]. Moreover, the material properties vary notably only in the thickness direction. These properties derive from the wet end operations of a paper machine. In the wet end a mixture of pulp fibres, some additives and water is first put on a broad rapidly running wire and the filtration starts. In this so called suspension phase the fibres tend to

[1]Current address: Technical Research Centre of Finland, P.O. Box 21, FIN-40101 Finland

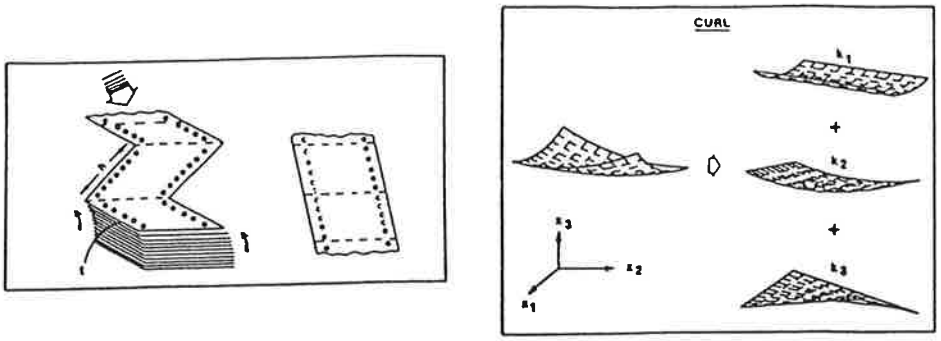

Figure 1. ***Leaning of a stack pile and curling of paper,*** [2].

orient themselves along to the direction that the suspension flow has relative to the wire. Moreover, this orientation is stronger at the bottom where the fibre suspension first meets the wire. Mainly due to this orientated structure paper exhibits anisotropic response to the thermo-mechanical loading.

Numerous authors have studied the dimensional instability and mathematical modelling of paper curling. Carlsson [3],[4] approximated the transversally inhomogeneous material properties by using a linear laminate plate model. He also gave an explicit equation predicting the curling phenomena. Shands [5] found a moderate agreement between his experiments and the Carlssons model. In [6] Carlsson proposed the Finite Element Method in analysing the bending of cardboards. A linear theory utilising FEM has been used also in the works [7],[8] and [9]. The nonlinear model has been studied by Johnson [10]. Recently the author [11] studied the nonlinear geometric effects with the solution non uniqueness and applied FEM to the inhomogeneous orthotropic plates. A rigourous mathematical theory for deformations of transversally inhomogeneous elastic plates with appropriate proofs was later accomplished in [12].

The main goal of this paper is to demonstrate the importance of the geometric nonlinear effects. Many of the papers published in the early 80's relied on the simple linear models. However, the numerical simulations [11] and experiments [14] indicate significant differences between linear and nonlinear solutions. For example, it was shown that copying paper sheets of all practical sizes curl cylindrically. The principal curvatures deviate significantly from the linear model and also from the measured values of narrow strips cut in principal directions, respectively.

Secondly, as the curling measurement has lately developed and the reliability is now reasonable it is therefore very attractive to compare the experiments and numerical simulations. For example, Niskanen [13],[14] reported that the thickness variation of fibre orientation as well as the elastic coefficients are the relevant factors in the respect of curling. Keeping this in mind we introduce theoretical analysis and numerical simulations with a set of validating measurements.

In this work we focus on the humidity induced mechanical deformations and ignore other effects like gravity. Particularly, we specialise in the slow and uniform humidity changes which is the case in drying a test sample in an oven. In this case we can expect uniform shrinking or swelling in the entire sheet. Of course, in applications like photocopying we have rapid temperature and humidity changes and the model needs to be completed with appropriate mass and heat transfer equations.

2. The asymptotic model

Consider the inhomogeneous plate where material is orthotropic so that the principal directions as well as the corresponding material parameters change in thickness. More precisely, we assume that the material properties are continuously distributed along thickness rather than strictly divided to separate layers. Note that for layered materials the properties of each layer are generally known a priori whereas in our case the distribution of thermo-elastic properties can only be measured a posteriori, often using tedious and destructive methods. By introducing asymptotic thin plate equations we can reduce the number of parameters that have to be measured.

Let us denote by $\Omega_h = \omega \times]-h, h[\subset \mathbf{R}^3$ the three dimensional body. Here h means the half thickness and $\omega \subset \mathbf{R}^2$ characterises the shape of the sheet. Material is assumed to be homogeneous within the plane and to obey the linear Hooke's law:

$$\tau_{ij} = C_{ijkl} e_{kl}. \tag{1}$$

Here τ_{ij} and e_{kl} denote the *stress* and *elastic strain* tensors. The elastic strain is a function of total deformation $\bar{\epsilon}$ and the humidity induced *initial strain* ϵ^T. In the geometrically nonlinear case we have

$$e_{ij} = \bar{\epsilon}_{ij}(u) - \epsilon^T_{ij} = \frac{1}{2}\{u_{i,j} + u_{j,i} + u_{k,i}u_{k,j}\} - \epsilon^T_{ij}, \tag{2}$$

where $u : \Omega_h \mapsto \mathbf{R}^3$ is the *displacement function* and $\bar{\epsilon}(u)$ is called *finite strain tensor.* If one assumes u to be small and neglects the nonlinear term in (2) then one obtains *the linearised strain*, usually denoted by $\epsilon(u)$, [15]. Note that we have used a notation where a repeated Latin subscript (i, j, k, l) means summation over 1 to 3 and a repeated Greek subscripts are summed over 1 to 2.

The displacement function u can be determined using the principle of minimum total potential energy. That is, the displacement field u minimises, in the certain space V of geometrically admissible displacements , the energy $\mathcal{E}$, [12]

$$\mathcal{E}(u) = \frac{1}{2}\int_{\Omega_h} \tau_{ij} e_{ij}(u)\, dx. \tag{3}$$

In the linear case $\mathcal{E}$ is continuous, strictly convex and coercive in V. Thus there exists a unique solution u in V, see [9]. In the nonlinear case the existence of a solution can be proved only in special cases.

In the following we state the main result concerning the asymptotic limit when $h \to 0$. For the sake of simplicity we treat only the linear case. The complete proofs and the nonlinear equations are given in [12]. We transform our model into a fixed geometry, i.e. we scale the x_3 coordinate: $\hat{x} = (x_1, x_2, x_3/h)$. This introduces certain scalings in displacements u and in strains ϵ, ϵ^T. Using the convention

$$E^0_{ij}(\hat{u}) = \epsilon_{ij}(\hat{u}) - \hat{\epsilon}^T_{ij} + \frac{1}{2}\hat{u}_{3,i}\hat{u}_{3,j} \tag{4}$$

the scaled energy $\mathcal{E}_h(u)$ becomes, [12]

$$\begin{aligned} &\frac{h^5}{2}\int_\omega \int_{-1}^{1} \frac{1}{h^4} C_{3333} E^0_{33}(u) E^0_{33}(u) + \frac{2}{h^2} C_{\alpha\beta 33} E^0_{\alpha\beta}(u) E^0_{33}(u) + \\ &\quad \frac{4}{h^2} C_{\alpha 3 \beta 3} E^0_{\alpha 3}(u) E^0_{\beta 3}(u) + C_{\alpha\beta\gamma\delta} E^0_{\alpha\beta}(u) E^0_{\gamma\delta}(u)\; dx_3 dx. \end{aligned} \tag{5}$$

Here we omit the ˆ-sign in variables u and x in order to simplify the notations. This energy has the unique minimiser (u^0, w) which is also the solution to the following variational problem:

$$\int_\omega \left(C^0_{\alpha\beta\gamma\delta}\epsilon_{\alpha\beta}(u^0) - C^1_{\alpha\beta\gamma\delta}w_{,\alpha\beta}\right)\epsilon_{\gamma\delta}(v)\,dx = \int_\omega \int_{-1}^{1} \bar{C}_{\alpha\beta\gamma\delta}\epsilon^T_{\alpha\beta}\epsilon_{\gamma\delta}(v)\,dx \tag{6}$$

$$\int_\omega \left(-C^1_{\alpha\beta\gamma\delta}\epsilon_{\alpha\beta}(u^0) + C^2_{\alpha\beta\gamma\delta}w_{,\alpha\beta}\right)v_{3,\gamma\delta}\,dx = \int_\omega \int_{-1}^{1} -x_3\bar{C}_{\alpha\beta\gamma\delta}\epsilon^T_{\alpha\beta}v_{3,\gamma\delta}\,dx, \tag{7}$$

where

$$C^i = \int_{-1}^{1} x_3^i \bar{C}\,dx_3, \quad \text{and } \bar{C}_{\alpha\beta\gamma\delta} = C_{\alpha\beta\gamma\delta} - \frac{C_{\gamma\delta 33}C_{\alpha\beta 33}}{C_{3333}}. \tag{8}$$

The first equation holds for all in-plane displacements $v \in V_H$ and the second one for all transversal displacements $v_3 \in V_3$, where V_H, V_3 are chosen appropriately, [12]. Variational problem (6)–(7) is the starting point for a FEM formulation.

Before going to examples we state the following remark. In the nonlinear case one starts the derivation of the variational system from the finite strains (2). This leads to a nonlinear system of equations with few additional terms compared to (6)–(7). This system can further be formulated in terms of Airy's stress functions to a *von Kármán* system. In the case of inhomogeneous material there will appear few additional terms that are not present at the standard von Kármán formulation.

Example 1. *Homogeneous, elastic material.* Let us suppose that the elastic coefficients are constant w.r.t. x_3. Then we see that $C^1 = 0$ and $C^2 = \frac{2}{3}\bar{C}$ and the transversal displacements satisfy the equation

$$\int_\omega \frac{2}{3}\bar{C}_{\alpha\beta\gamma\delta}w_{,\alpha\beta}\phi_{,\gamma\delta}\,dx = \int_\omega \bar{C}_{\alpha\beta\gamma\delta}\left(\int_{-1}^{1} -x_3\epsilon^T_{\alpha\beta}(x_3)\,dx_3\right)\phi_{,\gamma\delta}\,dx \quad \forall\phi \in V_3. \tag{9}$$

Hence $w_{,\alpha\beta} = \frac{3}{2}\int_{-1}^{1} -x_3\epsilon^T_{\alpha\beta}(x_3)\,dx_3$. Suppose that thermal expansion is orthotropic with inherent directions independent of x_3: $\epsilon^T_{\alpha\beta}(x_3) = Diag\left\{\epsilon^T_\gamma(x_3)\right\}$, $\gamma = 1, 2$. Let us write the components ϵ^T_γ in the form $\epsilon^T_\gamma(x_3) = \sum_{k=0}^{\infty}\epsilon^{Tk}_\gamma N_k(x_3)$, where N_k is the kth Legendre polynomial (remember that $\int_{-1}^{1} N_k(x_3)N_j(x_3)\,dx = 0$ if $j \neq k$). Now we get $\int_{-1}^{1} -x_3\epsilon^T_{\alpha\beta}(x_3)\,dx = \frac{2}{3}Diag\left\{\epsilon^{T1}_\gamma\right\}$, $\gamma = 1, 2$. So $w(x_1, x_2)$ is of the form

$$w(x_1, x_2) = \frac{1}{2}\left(\epsilon^{T1}_1 x_1^2 + \epsilon^{T1}_2 x_2^2\right), \tag{10}$$

where we have neglected the rigid body motions. Similarly, if we assume that ϵ^T is orthotropic and constant but under a x_3-dependent rotation, i.e $\epsilon^T(x_3) = \mathbb{D}(\theta(x_3))\hat{\epsilon}^T$, where $\mathbb{D}$ is the rotation matrix, we immediately find that the principal diagonal terms in ϵ^T will be even w.r.t. variable x_3. Thus they do not contribute to the integral over the thickness and we obtain

$$\int_{-1}^{1} -x_3\mathbb{D}(x_3)\hat{\epsilon}^T\,dx_3 = \begin{bmatrix} 0 & C \\ C & 0 \end{bmatrix}, \tag{11}$$

where $C = \left(\epsilon^T_1 - \epsilon^T_2\right)\int_{-1}^{1} -x_3\sin\theta(x_3)\cos\theta(x_3)\,dx_3$. Now, the solution will be

$$w(x_1, x_2) = Cx_1x_2, \tag{12}$$

again neglecting the rigid body motions.

Example 2. *Non-homogeneously elastic case.* If the elastic coefficients are not constant in thickness, we can write $C(x_3) = \sum_{k=0}^{\infty} \mathbb{C}^k N_k(x_3)$ and $\epsilon^T = \sum_{k=0}^{\infty} \epsilon^{Tk} N_k(x_3)$. Then

$$C^0 = 2\mathbb{C}^0, \quad C^1 = \frac{2}{3}\mathbb{C}^1, \quad C^2 = \frac{2}{3}\mathbb{C}^0 + \frac{4}{15}\mathbb{C}^2.$$

Applying this to system (7) we get

$$w_{,\alpha\beta} = -\epsilon_{\alpha\beta}^{T1} + \mathcal{F}(\epsilon_{\alpha\beta}^{T2}, \epsilon_{\alpha\beta}^{T3}, \cdots, \mathbb{C}^1, \mathbb{C}^2, \cdots). \tag{13}$$

This means that if we suppose $C = \mathbb{C}^0 + \mathbb{C}^1 x_3$ and $\epsilon^T = \epsilon^{T0} + \epsilon^{T1} x_3$ we still have $w_{,\alpha\beta} = -\epsilon_{\alpha\beta}^{T1}$. Thus the non-homogeneity of C has an effect to deformations only together with at least quadratic behaviour of thermal expansivity. This means that to first approximation we can assume C to be constant w.r.t. x_3. This is very important since the profile of C in x_3-direction can not be measured easily from materials like paper or cardboard.

3. Numerical simulation and experiments

The effect of thickness distribution of elastic parameters is very important with respect to curling. However, the measuring of this distribution from real paper sample is difficult. Therefore, for the model validation, we decided to construct our paper samples by assembling 2–4 carefully selected laminates (ordinary thin paper sheets) with using special glue. In each laminate the in-plane components of elastic parameters, thickness and the hygroreactivity were measured a priori. By stacking these laminates into a sample we could control the material parameters and therefore reliably compare true measurements and numerical simulation. The equivalent FE-model was set up using large dislacement theory and utilising anisotropic layered shell elements.

The KCL laboratories have a system in which many paper samples can be conditioned simultaneously and the curl components can be measured with an optical sensor. Samples are positioned vertically in order to avoid bending effects due to the gravity. The device can handle circular samples up to the diameter of Ø90 mm.

The preliminary simulation and the earlier analysis of rectangular plates [11] indicated that a symmetric solution turns into a non-symmetric one (bifurcation) when the dimensionless parameter $\Pi_1 = (L^2\epsilon^T)/h$ attains certain universal value. This guided us to adjust the sample size L to Ø50 mm. so that the bifurcation takes place at convenient and accurate operating scale of the tester.

Our main experiment was to attach two similar laminates together in 0/90° angle and to trace the curling when we vary the humidity conditions. The anisotropic laminates aligned in this angle create strong thickness gradients in elastic parameters. This was desired since it hides the inaccuracies of the measurements. The numerical simulation of the samples is illustrated in the figures 2 and 3. The two branches of solid line indicate the displacements of locations A and B, respectively. Humidity level 0 % RH corresponds the initial configuration before loading. As we see, the displacements at A and B develope symmetrically until approximately at 7 % RH the solution bifurcates and the sheet jumps into the cylindrical shape. This means that either A or B must become near zero but the other remains non zero: only the combinations (A_1, B_1) and (A_2, B_2) are possible. In our case the selection between these two happens randomly.

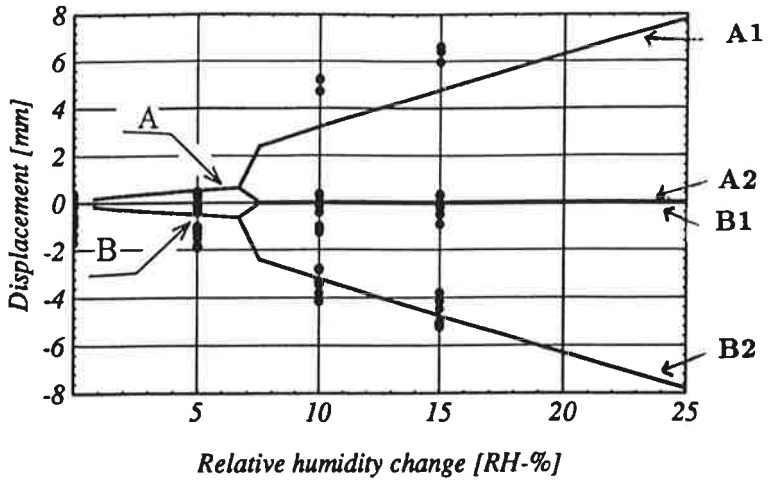

Figure 2. ***Nonlinear displacements***

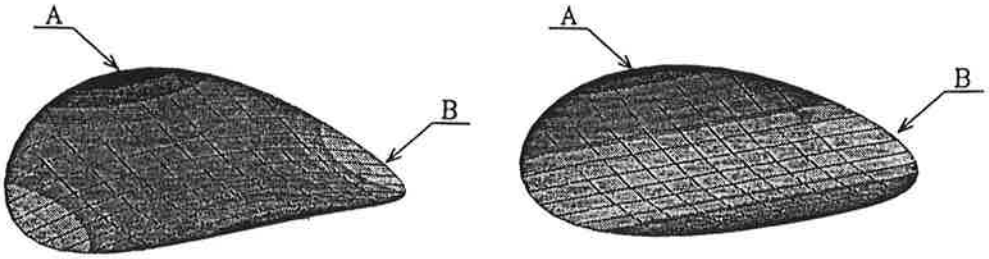

Figure 3. ***Test sheet samples at 0.75 % RH and 7.5 % RH***,[16].

Figure 2 indicates also the measurements by means of black dots. In each position a set of 10 samples were measured in the optical curl meter. However, small initial curvatures were observed on some of the samples already in the reference state. This was probably due to either poor conditioning of the samples between the preparation and the measurement event or small inaccuracies in air conditioning control of the tester.

The initial curvature effect can be seen more distinctly in another test series in figure 4. Here this initial effect was also included in the FE-model. The effect seems to prefer one of bifurcation branches and therefore the solution appears now in one branch only i.e. cylindrical curling dominates through the whole range of loading.

4. Conclusions

In linear theory we obtained that curling was presented by a parabolic surface in $\mathbb{R}^3$ and determined completely by the material parameters. Our rather general theory imposed no restrictions on structure of non homogenuity of material parameters. However, the analysis [11],[12] and the examples indicate that the nonlinear model is necessary in modelling the paper curling. The magnitude of solution can differ greatly from the linear one and the bifurcation phenomenon can be explained only by nonlinearities.

Our results indicate that the simulation performs fairly well, especially in figure 4.

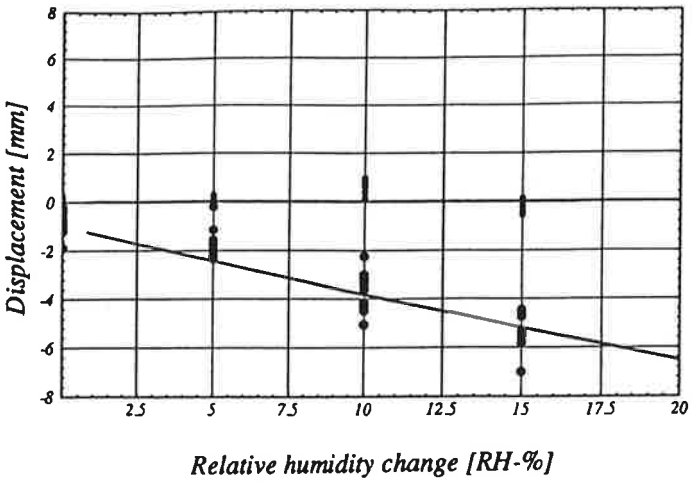

Figure 4. ***Initial curvature effects,*** [16].

The initial curvature (disturbance) promotes the sheet to follow the branch (A_2, B_2). To obtain more reliable results would require extremely accurately controlled conditions. In spite of that the local inhomogenuities in paper have their effects and we would need very large number of samples.

Acknowledgements

This reseach was supported by Valmet Paper Machinery Inc. and the Technology Development Center of Finland (TEKES). We thank Ph.D. K. Niskanen from The Finnish Pulp and Paper Research Institute (KCL), Dipl. Ing. J. Koskimies from Valmet Paper Machinery Inc. and Ph. Lic. P. Pakarinen from Technical Research Centre of Finland for advisory comments during this work.

References

[1] T. Uesaka, K. Murakami, R. Imamura, *Biaxial tensile behaviour of paper*, Tappi journal **62, No. 8** (1979), 111 – 114.

[2] T. Uesaka, *Dimensional Stability of Paper: Upgrading Paper Performance in End Use*, Journal of Pulp and Paper Science **17, No. 2** (1991), 39 – 46.

[3] L. Carlsson, C. Fellers, M. Htun, *Curl and two-sidedness of paper*, Svensk Papperstidning **No. 7** (1980), 194 – 197.

[4] L. Carlsson, *Out-Of-Plane Hygroinstability of Multiply Paperboard*, Fibre Science and Technology **14** (1981), 201 – 212.

[5] J. A. Shands, J. M. Genco, *Cross-machine variation of paper curl on a twin wire machine*, Tappi Journal **September** (1988), 165 – 169.

[6] L. Carlsson, C. Fellers, B. Westerlind, *Finite Element Analysis of the Creasing and bending of Paper*, Svensk Papperstidning **85, No. 15** (1982), 121 – 126.

[7] J. L. Thorpe, *Paper as an orthotropic thin plate*, Tappi Journal **64, No. 3** (1981), 119 – 121.

[8] I. Kajanto, *Paperin kupruilun analysointi teoreettsesti elementtimenetelmällä (in finnish)*, PSC Communications 41, Paper Science Centre, Oy Keskuslaboratorio.

[9] R. Pietikäinen, *Anisotrooppisiin materiaaleihin liittyvät laskennalliset mallit (in finnish)*, M.Sc. Thesis (1990), University of Jyväskylä, Department of Mathematics.

[10] M. W. Johnson, T. J. Urbanik, *A nonlinear theory for elastic plates with application to characterising paper properties*, Journal of Applied Mechanics **51** (1984), 146 – 152.

[11] R. Pietikäinen, *A Mathematical Model of Paper Sheet Curling Problem*, Licentiate Thesis (1993), University of Jyväskylä, Department of Mathematics.
[12] T. Tiihonen, R. Pietikäinen, *Thermal Deformations of Inhomogeneous Elastic Plates*, Mathematical Methods in Applied Sciences (submitted 8/1993).
[13] K. J. Niskanen, *Anisotropy of Laser Paper*, Paperi ja Puu - Paper and Timber **75, No. 5** (1993), 321 – 328.
[14] P. Viitaharju, K. Niskanen, *Käyryyden mittaus arkkipinoista (in finnish)*, PSC Communications 48, Paper Science Centre, Oy Keskuslaboratorio.
[15] J. Nečas, and I. Hlaváček, *Mathematical Theory of Elastic and Elastico-Plastic Bodies. An Introductio n*, Elsevier Scietific Publishing Company, 1981.
[16] M. Kurki, *Paperin kosteuskäyristymisen numeerinen simulointi ja simulointimallin kokeellinen verifiointi (in finnish)*, Report, KCL/Paper science Center, University of Jyväskylä, VTT, Valmet Paper Machinery Inc. (1993).

APPLICATION OF $k-\epsilon$ TURBULENCE MODELS IN AERONAUTICS

JAAKKO HOFFREN
Laboratory of Aerodynamics
Helsinki University of Technology
Sähkömiehentie 4, FIN-02150 Espoo, FINLAND

ABSTRACT

Chien's low-Reynolds-number $k-\epsilon$ turbulence model has been implemented in a compressible finite-volume Navier-Stokes solver, and test calculations about airfoils have been performed. The initial results are not necessarily better than the ones obtained with an algebraic model. Instead, several problems specific to the application of $k-\epsilon$ models in aeronautics emerged. The difficulties are discussed and further study subjects are suggested.

1. INTRODUCTION

In aeronautical applications, turbulent Navier-Stokes simulations have traditionally been performed using simple algebraic turbulence models, as in Ref. [1]. These models, devised for high-Reynolds-number boundary-layer flows, are well-proven and tuned to give quite accurate results in flow cases resembling their development base. Their inherent computational efficiency and the ability to define partially laminar flow in a straightforward manner are also important assets. However, the algebraic turbulence models have serious limitations in applicability. Merging or interacting turbulent layers, like wakes, cannot be properly simulated, and the modelling tends to be grid-dependent. The most serious drawback is the inability to deal with separated flow that dominates, for example, the maximum lift condition of a wing.

The range of valid flow simulations may be extended by adopting more advanced turbulence models. As a step towards generalized solvers, the aerodynamicists have recently begun to study seriously the $k-\epsilon$ model that is widely used in industrial problems. Conforming to this effort, Chien's low-Reynolds-number $k-\epsilon$ model [2] was implemented in a finite-volume Navier-Stokes code FINFLO [3].

The revised code was tested by calculations involving attached and separated flows

around airfoils and wings in subsonic and transonic conditions. However, the initial results do not show much improvement over the basic algebraic turbulence models. Instead, it became evident that there are several specific problems related to the application of a $k-\epsilon$ turbulence model in aeronautics, which are worth addressing.

In this paper, Chien's model and its implementation in FINFLO are briefly described, and some test results are given. The main emphasis lies on the subsequent discussion of the problems encountered, after which some topics for further research are suggested.

2. COMPUTATION METHOD

2.1 Main flow equations. The flow is modelled by the compressible Reynolds-averaged Navier-Stokes equations, where the main variables are the density ρ, the Cartesian momentum components ρu, ρv and ρw, and the total energy per unit volume E. The Reynolds stresses resulting from the time-averaging reduce to the modification of viscosity when the Boussinesq approximation is applied. The effective viscosity to be used in the laminar-like equations is obtained by adding an extra term to the molecular viscosity μ. When a $k-\epsilon$ turbulence model is applied, the addition, known as an eddy viscosity μ_T, is obtained from a relation

$$\mu_T = c_\mu \frac{\rho k^2}{\epsilon} \tag{1}$$

where c_μ is an empirical coefficient, k is the kinetic energy and ϵ the dissipation of turbulence. In the present implementation, the turbulence model is fully coupled to the main flow equations. This means that an apparent pressure increment of $\frac{2}{3}\rho k$ is added to the pressure p everywhere in the main flow equations. The turbulent kinetic energy is also added to the flow total energy, leading to a definition $E = p/(\gamma-1)+0.5\rho\vec{V}\cdot\vec{V}+\rho k$, where γ is the ratio of specific heats for a perfect gas, and $\vec{V} = u\vec{i} + v\vec{j} + w\vec{k}$ is the velocity vector. The main flow equations employed, not written here for brevity, are shown in detail in Ref. [4].

The introduced unknowns, the kinetic energy and dissipation of turbulence are determined by a separate set of partial differential equations which forms the turbulence model itself.

2.2 Turbulence model. There are several versions of the $k-\epsilon$ turbulence model which fall into two main categories. With the high-Reynolds-number versions, the model is not computed near solid walls where relations known as wall functions, assumed to be universally valid for turbulent boundary layers, are applied to determine the eddy viscosity. In the low-Reynolds-number versions, a modified set of equations is used in the whole flowfield, including the vicinity of solid surfaces. It can be argued that the second class of models is more general, making them more suitable for separated flows. They may also be more reliable in predicting the important skin friction, and simpler to apply without a need for special wall procedures, albeit at a cost of increased computing time.

In this work, the low-Reynolds-number $k-\epsilon$ turbulence model of Chien's [2] is adopted.

The model equations can be written in two dimensions in the following form:

$$\frac{\partial U}{\partial t} + \frac{\partial (F - F_v)}{\partial x} + \frac{\partial (G - G_v)}{\partial y} = Q \tag{2}$$

where $U = (\rho k,\ \rho\epsilon)^T$. The inviscid fluxes F, G and the viscous fluxes F_v, G_v are

$$F = \begin{pmatrix} \rho u k \\ \rho u \epsilon \end{pmatrix}, \quad G = \begin{pmatrix} \rho v k \\ \rho v \epsilon \end{pmatrix}, \quad F_v = \begin{pmatrix} (\mu + \frac{\mu_T}{\sigma_k})\frac{\partial k}{\partial x} \\ (\mu + \frac{\mu_T}{\sigma_\epsilon})\frac{\partial \epsilon}{\partial x} \end{pmatrix}, \quad G_v = \begin{pmatrix} (\mu + \frac{\mu_T}{\sigma_k})\frac{\partial k}{\partial y} \\ (\mu + \frac{\mu_T}{\sigma_\epsilon})\frac{\partial \epsilon}{\partial y} \end{pmatrix} \tag{3}$$

The source term for Chien's model is given as

$$Q = \begin{pmatrix} P - \rho\epsilon - 2\mu\dfrac{k}{y_n^2} \\ c_1\dfrac{\epsilon}{k}P - c_2\dfrac{\rho\epsilon^2}{k} - 2\mu\dfrac{\epsilon}{y_n^2}e^{-y^+/2} \end{pmatrix} \tag{4}$$

where y_n is the normal distance from the wall, and $y^+ = y_n(\rho|\nabla \times \vec{V}|/\mu)_{wall}^{1/2}$

Applying the Boussinesq approximation, the production of turbulent kinetic energy is modelled in a Cartesian coordinate system as

$$P = \mu_T\{2[(\frac{\partial u}{\partial x})^2 + (\frac{\partial v}{\partial y})^2] + (\frac{\partial u}{\partial y} + \frac{\partial v}{\partial x})^2 - \frac{2}{3}(\nabla \cdot \vec{V})^2\} - \frac{2}{3}\rho k \nabla \cdot \vec{V} \tag{5}$$

The equations for k and ϵ contain several empirical coefficients. These are given by

$$\begin{aligned} c_1 &= 1.44, & c_2 &= 1.92(1 - 0.22e^{-Re_T^2/36}) \\ \sigma_k &= 1.0, & \sigma_\epsilon &= 1.3 \\ c_\mu &= 0.09(1 - e^{-0.0115y^+}) \end{aligned}$$

where the turbulence Reynolds number is defined as $Re_T = (\rho k^2)/(\mu\epsilon)$. Chien proposed slightly different forms for c_1 and c_2. However, since our test computations performed for a flat plate boundary layer appeared to be insensitive to the modifications, the formulas above were based on the most commonly used coefficients $c_1 = 1.44$ and $c_2 = 1.92$.

2.3 Flow solver. The FINFLO flow solver [3] used in this study is a 2D/3D finite-volume code developed in the Laboratory of Aerodynamics at the Helsinki University of Technology. The fully conservative code operates on multi-block structured grids, where the unknowns are defined in the centers of the computational cells.

For the inviscid fluxes, Roe's scheme, facilitating a crisp capture of shocks, is applied [4]. The flow states at the cell faces are evaluated using a formally second- or third-order accurate upwind-biased discretization, depending on the existence of shocks. The thin-layer approximation is applied for the viscous terms that can be activated separately in each grid index direction. For their discretization, the conventional central-difference

scheme is utilized. The derivatives in the turbulence model source terms are computed in a similar manner. The continuity of the solution at grid block interfaces is ensured by the use of two layers of overlapping cells at each side of the boundary.

The steady-state solutions are sought by an implicit pseudo-time integration. The method applies an approximate factorization, and the resulting tridiagonal equations in each grid coordinate direction are further factored into simple bidiagonal sweeps for efficient implementation. Before the sweeps, a simplified implicit correction is made to the turbulence model source terms, as described in detail in Ref. [4]. Local time steps defined by a CFL condition and a diffusive stability limit are used, and the convergence is accelerated by a Jameson-type multigrid technique employing V-cycling [3].

As the boundary conditions on the solid surfaces, the flow velocity is set to zero and the wall is adiabatic. The required flow variables on the surface are extrapolated using second-order accuracy. At the farfield boundary, free-stream conditions are specified, which is sufficient if the grid is large enough.

3. TEST RESULTS

3.2 Transonic flow over an NACA 0012 airfoil. The described test cases represent typical airfoil calculations. The first example involves a transonic flow with a strong shock over an NACA 0012 airfoil at $Ma = 0.799$, $Re = 9 \times 10^6$ and $\alpha = 2.26°$. A C-type grid with 192×64 cells was used in the simulation. The outer boundary of the grid was 20 chord lengths from the airfoil, and the cell thicknesses on the surface corresponded to a y^+ value of around unity.

The results of the fully turbulent simulations are compared with results obtained using the algebraic Cebeci-Smith model and with the experiments in Fig. 1. The comparison of the pressure coefficient in Fig. 1a shows some improvement when the $k - \epsilon$ model is applied, but still the discrepancy with the measured values is large at and behind the shock. From the friction coefficient distributions in Fig. 1b it is seen that the two solutions are qualitatively different. Both models predict a shock-induced separation, but with the $k - \epsilon$ model there is a reattachment, whereas with the Cebeci-Smith model the flow remains separated. Somewhat fortuitiously, the computed lift coefficients of 0.380 for the $k - \epsilon$ model and 0.397 for the algebraic model agree fairly well with the measured value of 0.390, but the differences in the respective drag coefficients of 0.0400, 0.0394 and 0.0331 are significant.

3.2 Aerospatiale airfoil A at high lift. A different flow case is represented by an airfoil at subsonic high-lift conditions. In the present case, an Aerospatiale airfoil A is at $Ma = 0.15$, $Re = 2 \times 10^6$ and $\alpha = 13.3°$. The computational grid utilized is of the same type as in the NACA 0012 case, but the dimensions are 256×64. The flow is mainly attached, but there may be a separation bubble near the leading edge in addition to a mild trailing edge separation. The transition is fixed at 12 per cent chord on the upper surface and at 30 per cent chord on the lower surface.

The computed pressure and friction distributions are compared in Fig. 2 as in the preceeding case. It is seen that the pressure distributions obtained with the different

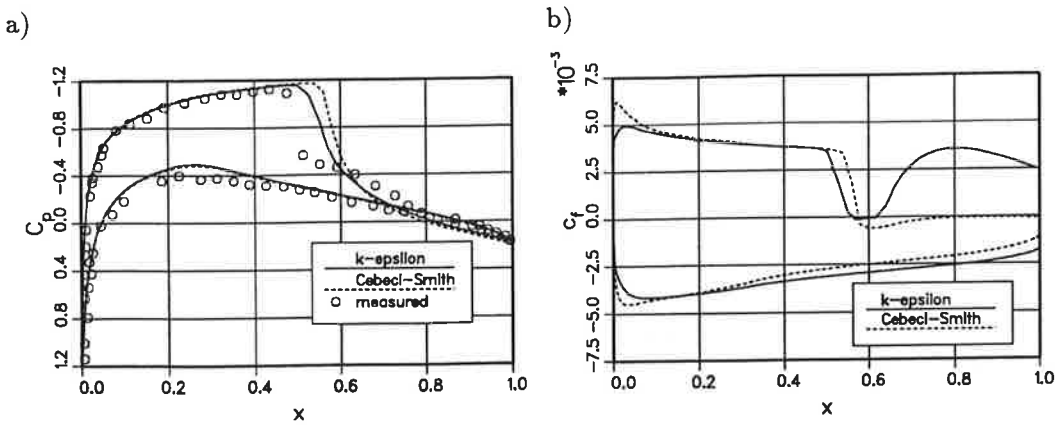

FIGURE 1. a) Pressure coefficient b) Friction coefficient distribution on the NACA 0012 at $Ma = 0.799$, $Re = 9 \times 10^6$ and $\alpha = 2.26°$.

turbulence models are practically identical. However, the friction distributions show marked differences, the result given by the algebraic model being generally in better agreement with the measurements. The integrated lift coefficients are 1.677 for the Cebeci-Smith model, 1.679 for the $k - \epsilon$ model and 1.562 for the experiments. The corresponding drag coefficients are 0.0200, 0.0238 and 0.0204, confirming the superiority of the algebraic model in this case.

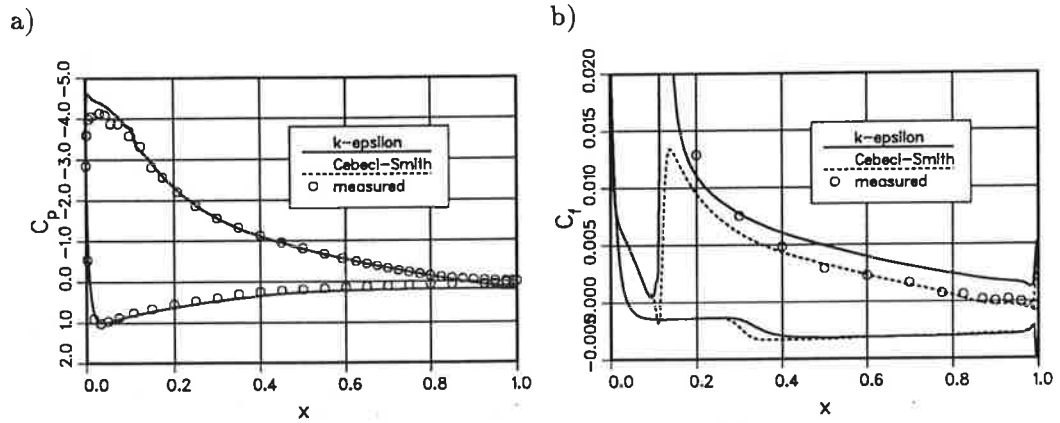

FIGURE 2. a) Pressure coefficient b) Friction coefficient distribution on the airfoil A at $Ma = 0.15, Re = 2 \times 10^6$ and $\alpha = 13.3°$.

4. SPECIFIC FEATURES OF AERONAUTICAL COMPUTATIONS

4.1 Encountered problems. Although the formulation of the $k - \epsilon$ turbulence model is relatively simple and independent of flow case, numerous problems were encountered in the test calculations requiring special attention. The problems can be largely traced back to the nature of aeronautical flows and the accuracy specifications in the field.

A typical feature in aeronautical flows are high characteristic Reynolds numbers, which means that the turbulence phenomena are concentrated in thin, strong shear layers. This

leads to large gradients that must be solved with a reasonable resolution to enable a sufficiently accurate computation of viscous stresses. Since the forces acting on the body are the main interest, in contrast to typical industrial problems, the computation must be most accurate near the solid surfaces where the nature of the turbulence changes and the low-Reynolds-number modification comes into play. For reliable force prediction, a fine grid resolution and an accurate discretization are necessary. The resulting low numerical damping, combined with k and ϵ varying several orders of magnitude within short distances, leads to stability and convergence problems.

Guided by the detected problem areas, the robustness of the code was gradually improved. The discretization of the inviscid fluxes of k and ϵ was fixed to a stable second-order fully upwinded scheme with an overshoot-inhibiting flux limiter. The maximum changes of k and ϵ at each time step are now limited to a fraction of their old values. To prevent the turbulence kinetic energy from growing nonphysically large during the iteration, it is limited to less than 10 per cent of the local total energy E. In addition, a hard upper limit of 5000μ is introduced for μ_T. On the other hand, k and ϵ may tend to become negative, requiring their free-stream values as lower limits.

Special modifications were necessary to enable the use of the multigrid scheme with the $k-\epsilon$ model. A significant improvement in robustness was achieved by lumping the eddy viscosity values to the coarse grid levels from the finest level instead of computing them. The corrections of k and ϵ interpolated from the coarse levels also need limiting based on the old state. Without the modifications, it was practically impossible to run the code in the multigrid mode. The improved code can exploit typically three or four grid levels, but the achieved convergence is still slower than that obtained with algebraic turbulence models. The results presented above require around 1000 pseudo-time steps with the Cebeci-Smith model and 3000 steps with the $k-\epsilon$ model, giving a CPU usage ratio of more than four. Typical convergence curves are shown in Fig. 3.

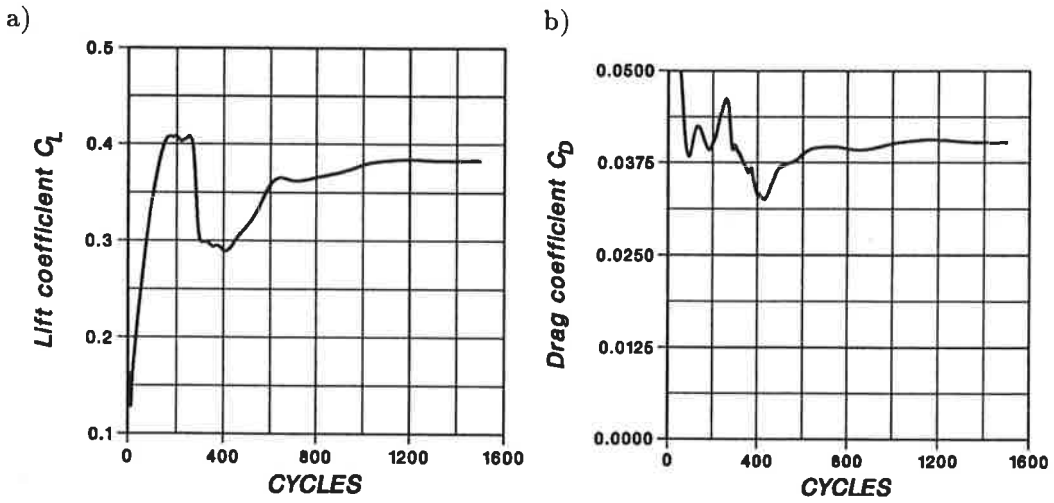

FIGURE 3. Convergence of a) the lift coefficient b) the drag coefficient of the NACA 0012 test case computed with the $k-\epsilon$ model using three multigrid levels.

The partial laminarity of typical aeronautical flows causes serious difficulties in $k-\epsilon$ simulations. Generally, the boundary layer near the wing leading edges is laminar, possibly until around the mid-chord. For realistic force predictions, it is unacceptable to run the calculations fully turbulent. However, the author is unaware of any proven and physically sound method to model or fix the transition in $k-\epsilon$ computations. The result for the airfoil A was obtained by computing a solution firstly with the Cebeci-Smith model, after which the $k-\epsilon$ run was started using the existing eddy viscosity and vorticity distributions to initiate k and ϵ. In this way, the turbulence does not extend to the laminar region since there is no turbulence production, but the transition tends to creep slowly backwards on the airfoil lower surface, see Fig. 2b.

The most unexpected problem encountered also relates to laminar flow and reveals an inherent weakness in the $k-\epsilon$ formulation. It was noted that at the boundary layer outer edges, where the turbulence should die away gradually, very high eddy viscosities emerged sporadically, leading to serious convergence problems and even failure of the runs. The origin of the problem was traced back to the definition of the eddy viscosity proportional to k^2/ϵ. In regions where both of the components decrease rapidly towards the free-stream values, their ratio may behave wildly. The situation was brought under control by the limitations discussed above, but the concept appears crude. This problem is also connected to the specification of the free-stream turbulence. During the test calculations, it was noted that varying the free-stream turbulence within reasonable bounds could change the predicted drag by several per cent, which implies difficulties in typical practical simulations.

4.2 Subjects for further study. Based on our experience with the $k-\epsilon$ model, several topics need further study to succesfully adapt the model to aeronautical problems. A few of the most obvious open questions are addressed here, most of them being related to laminar or weakly turbulent flow.

A reasonable transition mechanism should be devised. The applied method of giving a 'suitable' initial value distribution for k and ϵ could be refined and made faster, eliminating the need of preceeding calculations with an algebraic model. Another method may be the introduction of an additional surface source term that could cause the transition of an initially laminar flow.

A generally accepted free-stream turbulence should be determined. The present situation leaves too much uncertainty in the results.

The formulation of the $k-\epsilon$ model equations should be made such that the ratio k^2/ϵ behaves smoothly at turbulence layer edges and in weak turbulence in general. Additional continuous limiter functions could be developed to prevent the possible oscillations of the basic model that may completely spoil the calculations.

The accuracy of the calculations is a problem in itself. It is known that the typical $k-\epsilon$ models work poorly in flows having strong pressure gradients in the flow direction. These situations are characteristic of aeronautical flows, like the ones presented in this paper. Perhaps the results could be improved by tuning the model coefficients to better suit these types of flows.

5. CONCLUSIONS

The low-Reynolds-number $k-\epsilon$ turbulence model of Chien's has been implemented in a compressible finite-volume Navier-Stokes solver, aimed mainly at aeronautical applications. Test calculations involving flows around airfoils have been performed. The initial results do not show much improvement over the ones obtained with an algebraic turbulence model. Instead, several specific problems related to the application of $k-\epsilon$ models in aeronautics were revealed.

The accuracy requirements necessitate the use of higher-order discretization giving rise to convergence and stability problems. The calculation times are further increased by the use of dense grids near the body surfaces, necessary to determine accurately the surface friction forces. The characteristic Reynolds numbers are generally high, and the turbulence effects are confined to thin shear layers where very high gradients of k and ϵ cause special discretization problems. Especially critical are the outer boundaries of the turbulent layers, where both k and ϵ tend to zero, causing large excursions in the turbulent viscosity proportional to k^2/ϵ. Representative free-stream values must be specified for k and ϵ, which is not a trivial choice because the computed drag of an airfoil is found to be sensitive to the given free-stream conditions. More problems are caused by the typical partially laminar flow along surfaces, since the definition of transition with $k-\epsilon$ models is not straightforward. Finally, the pressure gradients along surfaces may be high, which is known to degrade the accuracy of the model.

Based on the consideration of the problems involved, it is evident that a successful application of $k-\epsilon$ turbulence models in aeronautical flow simulations requires further work to enhance the robustness and accuracy of the calculations. In their current basic forms, the $k-\epsilon$ models do not appear to offer an easy all-round method for aeronautics.

REFERENCES

1. J. Hoffren and T. Siikonen, Numerical Simulation of Transonic Flow Around Airfoils at High Reynolds Numbers Using Algebraic Turbulence Models, Helsinki University of Technology, Laboratory of Aerodynamics, Report B-29, Series B, 1990

2. K.-Y. Chien, Predictions of Channel and Boundary-Layer Flows with a Low-Reynolds-Number Turbulence Model, AIAA Journal, Vol. 20, No. 1, Jan. 1982, 33-38

3. T. Siikonen, J. Hoffren and S. Laine, "A Multigrid LU Factorization Scheme for the Thin-Layer Navier-Stokes Equations", ICAS Paper 90-6.10.3, Stockholm, Sweden, 1990

4. T. Siikonen, An Application of Roe's Flux-Difference Splitting for $k-\epsilon$ Turbulence Model, Helsinki University of Technology, Laboratory of Aerodynamics, Report A-15, Series A, 1994

THERMAL HEAT, CONVECTION, CORIUM FLUID FLOW AND STRUCTURAL ANALYSIS OF REACTOR PRESSURE VESSEL BOTTOM AND PENETRATIONS IN CORE MELTING ACCIDENTS

KARI IKONEN
VTT Energy
P.O. Box 1604, FIN-02044 VTT, FINLAND

ABSTRACT

A computing program system for calculating behaviour of pressure vessel during severe reactor accident is under development. Thermal heat conduction, heat convection and corium fluid flow are solved simultaneously and coupled. Structural behaviour and strength of a thickwalled pressure vessel wall and penetrations for control and instrument rods are to be evaluated. Problems like thermal stresses, thermo-elastic-plastic and large deformations and creeping are of essential importance. For thermo-elastic-plastic analysis 2D- and 3D-FEM codes based on isoparametric finite element formulation are developed.

Codes based on finite difference and control volume method are developed for thermal heat conduction and heat convection. Latent heat in phase changes is taken into account. Examples of applications to heating up and weakening of penetrations are presented. For flow estimation in a corium pool a code solving Navier-Stokes equations for viscous fluid flow and using k-ε-turbulence model is under development.

The purpose of the article is to describe with examples this difficult but important and challenging field including coupled phenomena of heat conduction, convection, fluid flow and structural analysis.

1. INTRODUCTION

The probability of a severe nuclear reactor accident resulting in a core damage and subsequent melting is about 10^{-4} / reactor /year. In the world there are about 400 commercial reactors. Thus one severe nuclear reactor accidents could happen at about 25 year intervals. Severe nuclear reactor accident means core melting causing very hot corium (consisting of different core materials like uranium oxide, zirkonium oxide etc., in liquid phase about over 2200...2500 K) descending on the bottom of the pressure vessel (Fig. 1). The amount of descending corium may typically be 1...15 cubic meters. To retain the integrity of pressure vessel by external and internal cooling could considerably reduce the effects to the environment. Numerical analysis

are needed to know the margins to the failure at every phase of accident and to search means to mitigate the consequences by e.g. cooling the vessel externally.

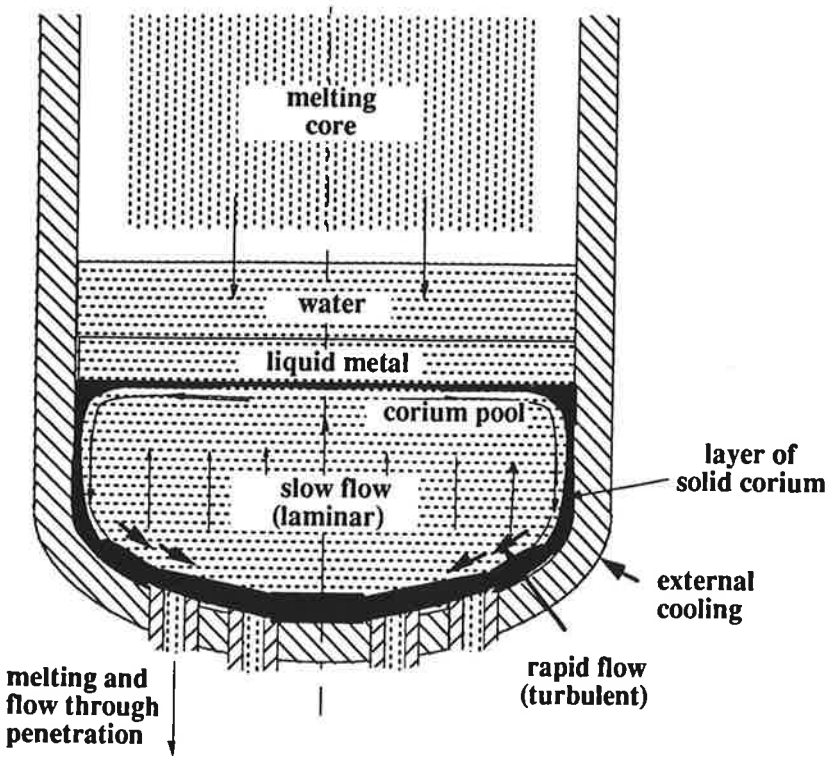

FIGURE 1. *The general layout of the nuclear reactor pressure vessel bottom area and one scenario of the core melting.*

The investigation of the Three Mile Island accident 1979 in USA, where the margin to the failure of the reactor pressure vessel was rather small, gave much information about phenomena related to core melting accident. From structural mechanics point of view there are phenomena like

- exceptionally high temperatures
- large deformations and strains
- creeping of pressure vessel steel at high temperature
- cracking of solidified corium (cooling water between gaps)

The circumstances are very exceptional and conventional calculation methods and computer programs related to thermo-elastic-plastic and creep modelling can not be applied straightly without criticism. The phase of material ranges from solidus to liquidus and structural mechanics and fluid flow problems related problems to these phases are illustrated in Fig. 2. Especially difficult zone is the transition from solidus to liquidus.

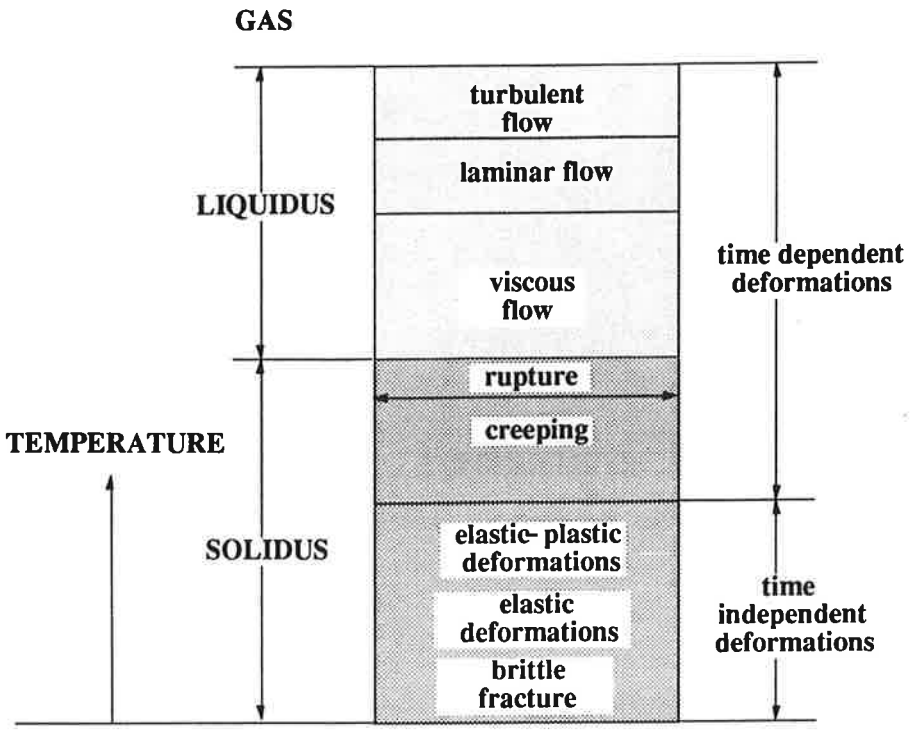

FIGURE 2. *The behaviour of materials like steel in different temperatures.*

From thermal conduction and convection and fluid flow point of view following phenomena can be listed:

- due to decay power in corium (about 100 W/kg) temperature differences are formed in the pool causing slow upwards flow in the middle area of the pool, in the upper surface outwards and downwards close the vessel wall or solid corium causing natural convection
- liquid corium streaming against the vessel wall heats and can cause erosion making the wall locally thinner and may cause burst and failure of the whole lower head of the vessel
- the melting temperature of corium is high (about 2500 K) and molten corium solidifies rather easily in cooling to ceramic crust, which may plug penetrations coming into contact with cooler materials like steel in penetrations
- essential phenomenon are phase changes and latent heat energy releasing or accumulating in them
- at high temperatures over 2500 K the dynamic viscosity μ of corium is rather small, typically μ = 0,004...0,008 kg/m/s, thus the flow is partly turbulent causing increased heat conduction and convection
- boundary layer between molten and solidified corium is not so clear as normally e.g. between water or air and solid media, thus conventional boundary layer considerations can not be applied in a straight forward way in the problem in question
- fluid flow, heat conduction and convection dependent strongly on each others

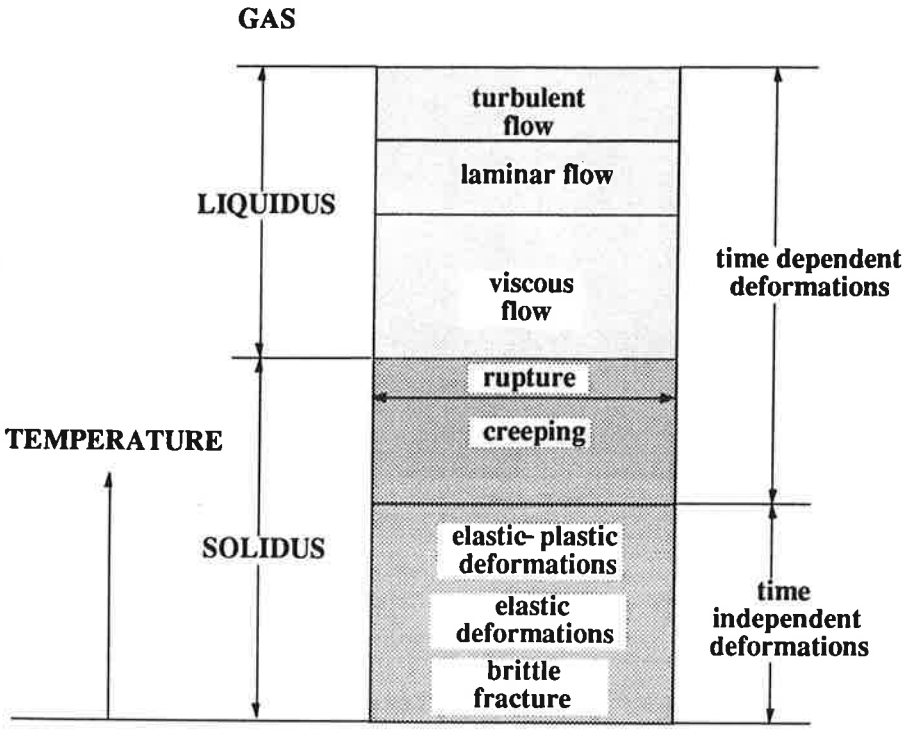

FIGURE 2. *The behaviour of materials like steel in different temperatures.*

From thermal conduction and convection and fluid flow point of view following phenomena can be listed:

- due to decay power in corium (about 100 W/kg) temperature differences are formed in the pool causing slow upwards flow in the middle area of the pool, in the upper surface outwards and downwards close the vessel wall or solid corium causing natural convection
- liquid corium streaming against the vessel wall heats and can cause erosion making the wall locally thinner and may cause burst and failure of the whole lower head of the vessel
- the melting temperature of corium is high (about 2500 K) and molten corium solidifies rather easily in cooling to ceramic crust, which may plug penetrations coming into contact with cooler materials like steel in penetrations
- essential phenomenon are phase changes and latent heat energy releasing or accumulating in them
- at high temperatures over 2500 K the dynamic viscosity μ of corium is rather small, typically μ = 0,004...0,008 kg/m/s, thus the flow is partly turbulent causing increased heat conduction and convection
- boundary layer between molten and solidified corium is not so clear as normally e.g. between water or air and solid media, thus conventional boundary layer considerations can not be applied in a straight forward way in the problem in question
- fluid flow, heat conduction and convection dependent strongly on each others

jects makes possible the verification of calculational methods by experiments and comparison of calculational results obtained by different institutions in benchmark type tests.

Example 1: A typical control rod penetration in boiling water reactor was analyzed with the computing system developed at VTT. Initial temperature of corium is about 2500 K. It is assumed that corium, whose initial temperature is about 2500 K drops suddenly on the bottom and covers the penetration area, whose initial temperature is about 400 K. Fig. 4 shows the temperature distributions

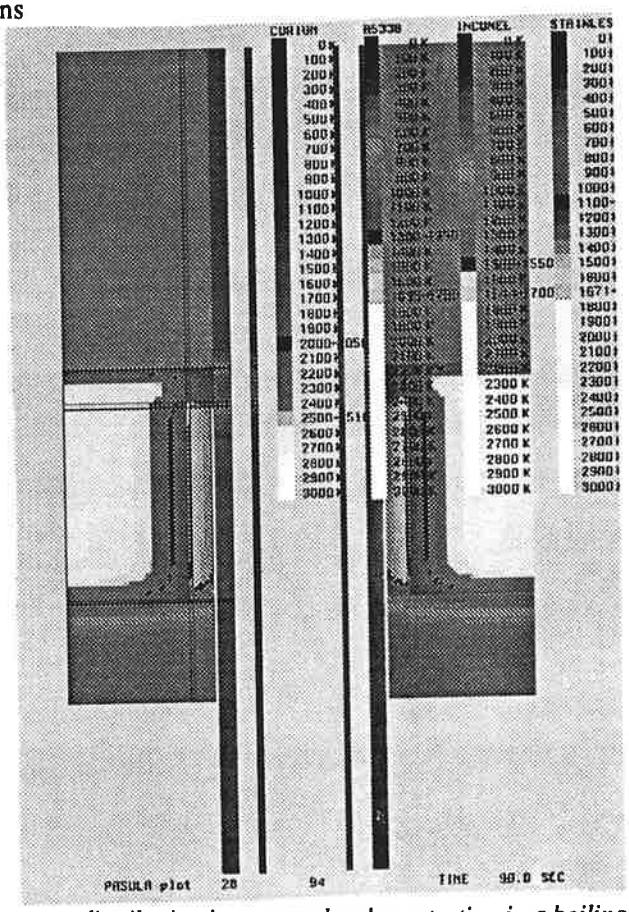

FIGURE 3. *Temperature distribution in a control rod penetration in a boiling water reactor, axisymmetric model.*

The local presence of cooling water has very essential effect on behaviour of the nozzle. If there is no water the nozzle fails, but if there is a moderate cooling effect of water and steam, the failure is prevented or, at least, delayd prominently. The calculations were done using axisymmetric models with rectangular grids. Because of simple geometry control finite difference method was adopted. In axisymmetric case and cylindrical coordinate system heat conduction equation is

$$c\frac{\partial T}{\partial t} = \frac{\partial}{\partial z}(\lambda\frac{\partial T}{\partial z}) + \frac{\partial}{\partial r}(\lambda\frac{\partial T}{\partial r}) + \frac{1}{r}\lambda\frac{\partial T}{\partial r} + \Phi\,, \qquad (2)$$

where c thermal capacity, T is the temperature, t time, z axial coordinate, r radial coordinate, λ heat conductivity and Φ heat generation. Using even difference mesh, the terms in Eq. (2) are

$$\frac{\partial}{\partial z}(\lambda \frac{\partial T}{\partial z}) = \frac{\frac{1}{2}(\lambda_{i+1,j} + \lambda_{i,j})(T_{i+1,j} - T_{i,j}) - \frac{1}{2}(\lambda_{i,j} + \lambda_{i-1,j})(T_{i,j} - T_{i-1,j})}{\Delta z^2}$$

$$\frac{\partial}{\partial r}(\lambda \frac{\partial T}{\partial r}) = \frac{\frac{1}{2}(\lambda_{i,j+1} + \lambda_{i,j})(T_{i,j+1} - T_{i,j}) - \frac{1}{2}(\lambda_{i,j} + \lambda_{i,j-1})(T_{i,j} - T_{i,j-1})}{\Delta r^2}$$

$$\frac{1}{r}\lambda \frac{\partial T}{\partial r} = \frac{1}{r_{i,j}} \lambda_{i,j} \frac{T_{i+1,j} - T_{i-1,j}}{2\Delta r} . \tag{3}$$

When calculating the sum of these terms and the heat generation term S^t at time t, a new temperature value $T_{i,j}^{t+\Delta t}$ can be solved from the equation

$$c_{i,j}^t \frac{T_{i,j}^{t+\Delta t} - T_{i,j}^t}{\Delta t} = S^t . \tag{4}$$

In practice, however, because of phase changes, instead of keeping $c_{i,j}^t$ constant, a new temperature $T_{i,j}^{t+\Delta t}$ is searched as illustrated in Fig. 4.

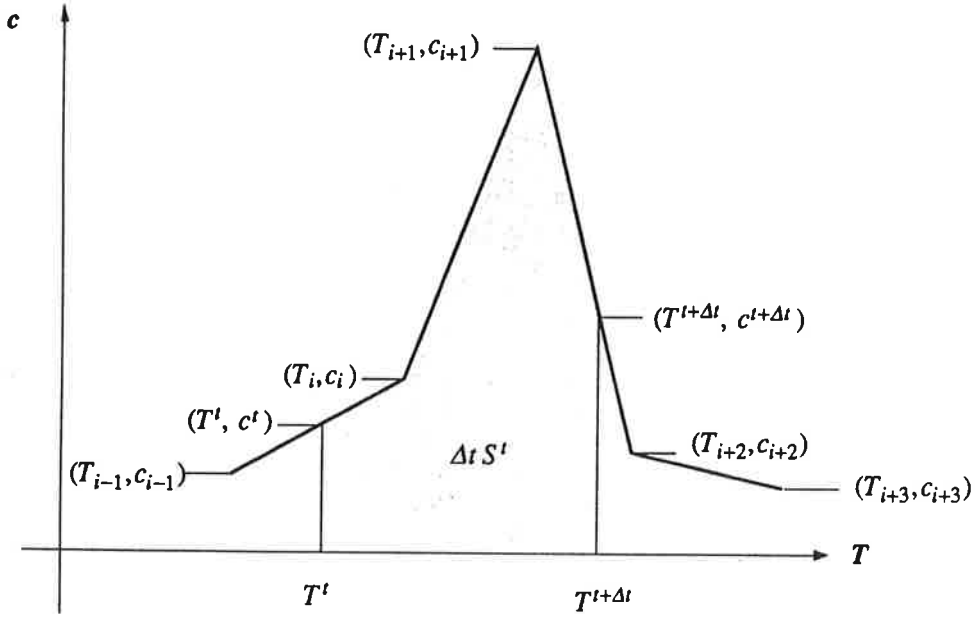

FIGURE 4. *Searching a new temperature corresponding a known enthalpy increase $\Delta t\, S^t$ (peak in the dependency heat capacity vs. temperature is due to latent heat in phase transformation).*

Because of an explicit time integration procedure, the time increment Δt must be small enough. To quarantee the stability the requirement for the time step is

$$\Delta t \le \frac{1}{2} \frac{c_{min}}{\lambda_{max}} \frac{1}{\frac{1}{(\Delta r^2)_{min}} + \frac{1}{(\Delta z^2)_{min}}} . \tag{5}$$

Flux condition from the corium surface to water is calculated from

$$\lambda \frac{\partial T}{\partial n} = \alpha (T_{water} - T_{surface}) . \tag{6}$$

$\partial T/\partial n$ is the temperature gradient perpendicular to the surface and it is calculated by using two difference nodes inside the steel or corium and the node at the surface. Heat transfer coefficient α between corium and water was strongly temperature dependant. The surface temperature T_{water} was iterated from Eq. (6). There are gaps between steel surfaces. The temperatures on the surfaces are iterated at every time step from the radiation equation

$$\lambda_- \left.\frac{\partial T}{\partial n}\right|_- = \varepsilon \sigma (T_{+0}^4 - T_{-0}^4) = \lambda_+ \left.\frac{\partial T}{\partial n}\right|_+ , \tag{7}$$

where the Stefan–Bolzman constant $\sigma = 5.67 \cdot 10^{-8}$ W/m^2/K^4 and ε is the total emissivity of the surfaces. Heat conductivity and capacity dependencies on temperature is taken into account at all phases in the calculations leading to iteration processes.

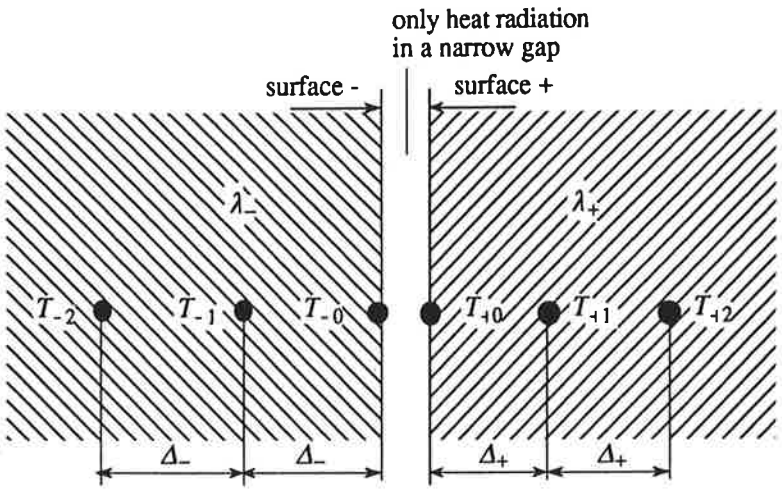

FIGURE 5. *Heat radiation over a gap between two metal surfaces.*

Example 2: A typical bottom of a pressurized water reactor without penetrations. Initial temperature of corium is about 2500 K. It is assumed that corium, whose initial temperature is about 2500 K drops suddenly on the bottom and covers it, whose initial temperature is about 400 K. Fig. 6 shows the temperature distributions after 90 seconds. In this demonstrative calculation all surfaces were insulated.

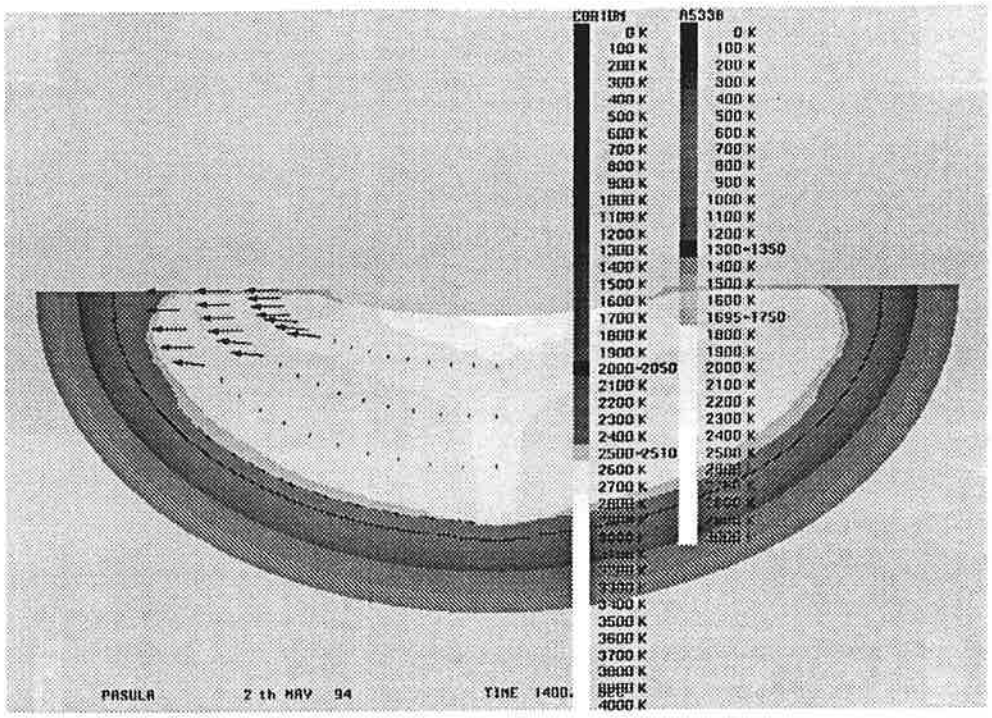

FIGURE 6. *Temperature distribution in a pressurized water reactor lower head without penetrations with forced convection.*

An oblique mesh was needed in this case. So called control volume method was applied. The basic equation for the temperature $T_{i,j}$ of a control volume $V_{i,j}$

$$c\frac{\partial T_{i,j}}{\partial t} = \frac{1}{V_{i,j}} \oint_S \lambda \frac{\partial T}{\partial n}\, dS + \Phi\,, \tag{8}$$

where c is the heat capacity of the central point of the volume calculated according to the temperature of the middle point of the volume and n is a coordinate showing outwards from the surface of the volume and Φ is internal heat generation. Explicit and implicit time integration has be applied.

CONCLUSIONS

An intensive program development work is under way at VTT ranging form structural mechanics to heat conduction, convection and fluid flow. In addition the problems described in this paper the readiness can also be used in other applications like in simulation of welding or casting processes.

SOME MECHANICAL PROBLEMS IN THIN CHANNELS

P. NEITTAANMÄKI[1], V. RIVKIND[2] AND L. SEIOUKOVA[1]

[1] Department of Mathematics
University of Jyväskylä
Jyväskylä, Finland

[2] Department of Mathematics,
St. Petersburg University
St. Petersburg, Russia

ABSTRACT

Some mechanical properties of a flow with an evaporation and durability of slots for modeling processes in valves are discussed.

0. INTRODUCTION

The valves are very important components in many fields of industry. For example in the wine preparing process one needs good valves. Valves may work in extremal conditions; with chemical active fluids, with a big jump of a pressure. Often it is very expensive to change or to repare valves (for example in the motor of rockets). There are many various physical processes which disturb work of valves: an evaporation, sedimentation (salt or occur), deformation of valves, etc. All these processes depend on hydrothermodynamical structure of the flow, material and shape design of valves (see Fig. 1). That's why it is very important to construct adequate mathematical models for mechanical properties of the flow with an evaporation and durability of slots. In Fig. 1 we see shape design for different type of valves.

In this paper we present a simple model for valves. If valves work under conditions where a jump of pressure is large, the process of an evaporation is very intensive. That's why an important problem is to calculate a process of an evaporation. We also discuss briefly the problems of durability of valves. They usually work in a periodic regime and in extremal conditions which destroy the material of valves.

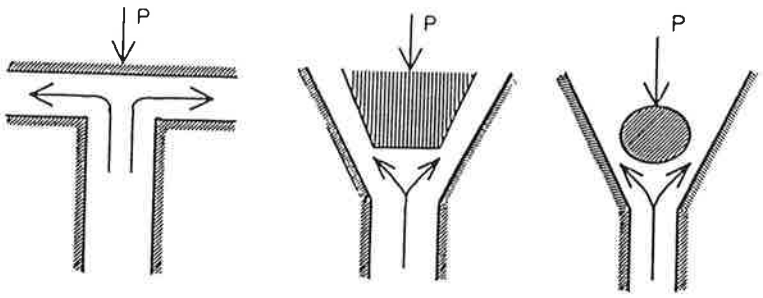

Figure 1.

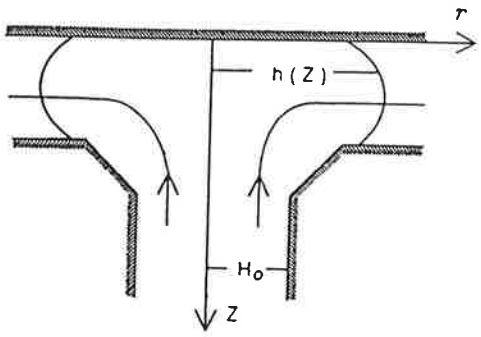

Figure 2. The scheme of the valve.

1. HYDRODYNAMICS OF FLOW

We consider flow from thin cylindrical axially symmetric channel (Fig. 2). Flow of a liquid is attended with an evaporation, a precipitation of occurs and an ice formation. We give here all equations in several curvilinear coordinates corresponding to an arbitrary Γ-shape of valves (see Figs. 1 and 3).

We suppose that our fluid contains some medium which can produce a sediment provided its concentration $c \geq c^*$ (phase transition). This fluid changes its state with $T \geq T^*$. We suppose that a liquid film is thin. That's why the temperature and the concentration in a section of film is steady with $r = r_0$. We choose for velocity and pressure the simplest approximation. The velocity u equals to $A(s)n$ where $|s|$ is a length of an arc, n is a distance from s in normal direction. We also assume that a domain, in which the evaporation on takes place as well as the process of evaporation is determined by the mass flow Q and the outside pressure P. Using these assumptions for the moment equations of the flow we obtain the conservation laws for a curved liquid film on the

The magnitude m is determined by the relation

$$m(T) = \tilde{\mu}\{p_*(T) - p_k - \alpha\overline{K}\}, \tag{1.3}$$

where p_k is the pressure over the surface, p_* is the pressure of the saturated steam, $\overline{K}$ is the curvature of Γ, $\tilde{\mu}$ is the coefficient of the accommodation. The function satisfies the Klayperon equation.

$$p_k V = MRT_k \tag{1.4}$$

where R is the specific gas constant.

The balance equation with an evaporation reads as follows:

$$\varrho_l \frac{\partial}{\partial t}(hT_l c) - \frac{\varrho_l}{\varrho}\frac{\partial}{\partial s}(qcT_l) = s_w - im\varrho_l, \qquad T_l|_{t=0} = T_{in} \tag{1.5}$$

where T_l is the liquid temperature, T_{in} is the initial temperature, ϱ_l is the density of a liquid, c is the heat capacity, γ is the specific heat of the phase transition, s_w is the warm flow from the wall. The following equations hold for s_w and for the temperature T_w of the wall

$$\begin{aligned} &\frac{\partial T_w}{\partial t} = \kappa_w \delta T_w, \\ &s_w = -\varrho_w \overline{\overline{C}}_w \kappa_w \frac{\partial T_w}{\partial n}, \end{aligned} \tag{1.6}$$

where κ_w, $\overline{C}_w$, ϱ_w are coefficients of the thermal conductivity, the heat capacity and the density of the wall.

The equation of a precipitation of occurs can be expressed as follows:

$$\frac{\partial k}{\partial t} + \frac{1}{\varrho_l}\frac{\partial}{\partial s}(c_s q) = 0. \tag{1.7}$$

Here $k = c_s + a$, c_s is the concentration of the salt, a is the height of the deposition,

$$a = \begin{cases} 0 & \text{if } c_s < c_* \\ a > 0 & \text{if } c_s = c_*, \end{cases}$$

where c_* is the limit concentration. To close the system it is necessary to consider the flow of a gas over the liquid film. This consideration provides an evaporation for the gas flow in the channel:

$$\frac{\partial M}{\partial t} = 2\pi \int_0^{s_*} mr\, dr - Q'(t), \tag{1.8}$$

where Q' is the flow of the gas ejecting from the channel per unit time, s_* is the moving point of the menisk of the film and M is the mass of gas in the channel.

The equation of balance of the heat in the channel reads

$$\frac{d}{dt}(Mc_p T_*) - Q' c_p T_k = 2\sigma \int_0^{s_*} i_0 mr\, ds, \tag{1.9}$$

where i_0 is the specific heat of an evaporation, c_p is the heat capacity in the channel. The moving point s_* is defined from the capillary angle conditions:

$$h(s_*, t) = 0, \tag{1.10}$$

$$\frac{\partial h(s_*, t)}{\partial s} = \operatorname{tg}\alpha', \tag{1.11}$$

where α' is the capillary angle.

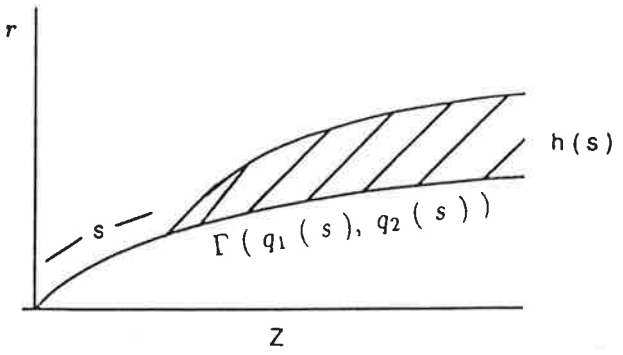

Figure 3.

surface Γ with curvature $\overline{K}$.

$$\begin{aligned}
&\frac{\partial}{\partial t}\left(\frac{Ah^2r}{2}\right)+\frac{1}{3}\frac{\partial}{\partial s}\left(A^2h^3r\right)\\
&=\nu\left\{\frac{\partial}{\partial s}\left(rh^2\frac{\partial A}{\partial s}\right)+kr(h-\frac{Ah^2}{2}k)-\left(\frac{\partial r}{\partial s}\right)^2\frac{Ah^2}{2}-rA\right\}\\
&\quad+rh\frac{\partial}{\partial s}\left(\frac{\partial r}{\partial s}\frac{\partial h}{\partial s}\right)+\alpha\left(k+\frac{\partial^2 h}{\partial^2 s}+\frac{1}{r}\left(\frac{\partial q}{\partial s}+\frac{\partial h}{\partial s}\frac{\partial r}{\partial s}\right)\right)+\frac{\partial\alpha}{\partial s}r\\
&\quad+2\nu\left\{\frac{\partial h}{\partial s}h\frac{\partial rA}{\partial s}+\frac{\partial}{\partial s}\left(h\frac{\partial}{\partial s}\left(rA\right)\right)\right\},
\end{aligned}\tag{1.1}$$

where α is the coefficient of a surface tension, v is the viscosity, r, z are cylindrical coordinates, s, n are local coordinates associated with surface $\Gamma(q(s_1), q(s_2))$, $h(s)$ is the height of a liquid film, A is a const, $u = An$, $\vec{u} = (u, w)$, u, w are components of the velocity (see Fig. 3). Our assumptions have been examined in [1]–[2] on a test example with the thin axisymmetrical flow with an evaporation. In test problem the system was governed by coupled Navier–Stokes and Stefan equations. A comparison between the solution of coupled Navier–Stokes model and the solution corresponding to the model presented here shows that it is suitable for practical things to use our simple model (1.1). We also assume that the curvature of a film does not differ essentiality from the curvature of a surface and $h \ll 1$.

The conservation law for a mass entails that

$$\frac{\partial h}{\partial t}+\frac{1}{h}\frac{\partial q}{\partial s}=-m\sqrt{1+\left(\frac{\partial h}{\partial t}\right)^2}.\tag{1.2}$$

where m is the velocity of the evaporation from the surface and q is the flow

$$q=-\int_0^h u\cdot r\,dn.$$

2. PROBLEM DURABILITY OF PERIODIC WORKING VALVES

We can describe our problem as a contact problem. The Herz theory for contact problem between two elasticity bodies can be employed for solving the durability problems of the cylindrical valves. In this case we can obtain for the energy of deformation U the following expression:

$$U = \frac{\chi d^3}{\pi}\left(\left(\frac{2d}{\chi r}\right)^2 - \frac{4}{3}\left(\frac{2d}{\chi r}\right)^2 + \frac{7}{15}\left(\frac{2d}{\chi r}\right)^2\right), \tag{2.1}$$

and the maximal d displacement is

$$d = 1.23\sqrt[3]{\frac{P}{E^2 R}},$$

where R is the radius of contact cylinder, P is the force (pressure) on the valve, $\chi = \frac{1-\nu^2}{\pi E}$, ν is the Poisson's coefficient, E is the modulus of the elasticity.

From this problem we can derive results about the dependence contact zone "d" on the outside pressure P. In the elastic case this is

$$d = 2\sqrt{\chi P R}.$$

Thereafter by means of the theory by Treska–Sen–Venan, we find the most dangerous point which is situated on the depth $z_d = .8$ for the axially symmetric case. The maximal tangent stress σ is $0.8\frac{2\pi}{\pi a}$ at this point. The maximal normal stress is at the point $z = 0.5d$. The component of stress are:

$$\sigma_r = \sigma_\phi = -0.18\frac{2\pi}{\pi d}, \quad \sigma_z = -0.8\frac{2\pi}{\pi d}, \quad r_{max} = -0.31\frac{2\pi}{\pi d}.$$

From this point the plasticity zone begins. On the boundary of contact zone the stress tension is

$$\sigma_r = \frac{1}{3}(1-2\nu)\frac{2\pi}{\pi d}.$$

At this point usually starts the destruction of material.

For definition of contact zone we can also employ the results of solving the plasticity problem. In this case we can take results for the problem of plasticity deformation of a ball which had been solved by A. Ishlinsky. Moreover, it should be taken into account the roughness of real surface which provides a microplastic deformation. This deformation leads to developing of micropress and microcracks. These produce progressive the mellowing the surface contact film by means of separating the surface into very small particles from and deteriorating the surface. This phenomena usually is being studied by means of semiempirical theories and results. Employing a simplest version of the theory we calculate a velocity of the wear of a material in the contact zone

$$w = \int_s cp(s)\,ds,$$

where $p(s)$ is possible to calculate from P.

3. NUMERICAL RESULTS

Using mathematical models presented in Chapter 1 we calculate by means of the difference method cylindrical channels of the height H_0 and with the initial temperature T_{in}.

The results of numerical experience demonstrate that accordance with H_0 and T_{in} there exists a characteristic time of the stabilisation of hydrodynamic and thermodynamic properties (see Fig. 4). If the temperature T_{in} is higher the time of stabilization is shorter. The state of the menisk is also stabilized. The edge of the menisk appears as a dangerous zone for the stable work of a valve. It is shifting to the channel if initial temperature increases. The place of the sediment is diminishing if the size and the height of the menisk are increasing. As an example we present in Fig. 4 the case $H_0 = .6\,\text{mkm}$, $T_{in} = 320°\,\text{K}$.

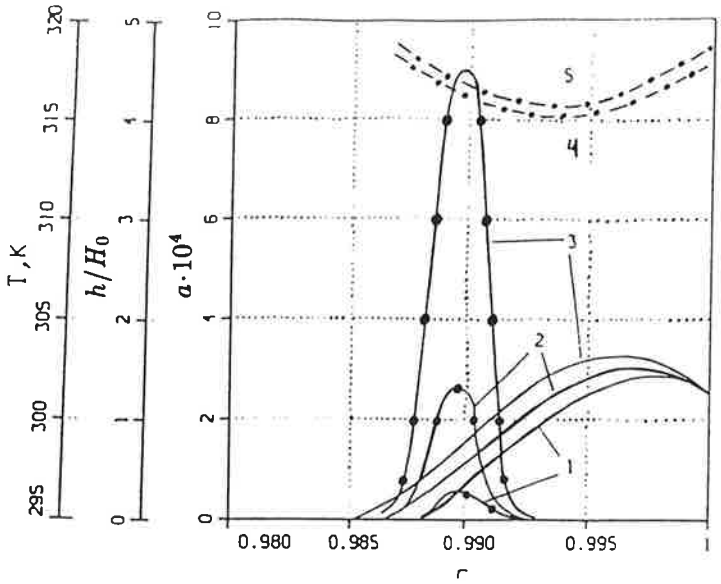

Figure 4. The shape of the menisk h/H_0 ——; the height of a sediment $a \cdot 10^4$ —●—; the temperature T - · - · - . 1) $\tau = 0.5 * 10^{-3}\,\text{s}$; 2) $\tau = 4 * 10^{-3}\,\text{s}$; 3) $\tau = 2 * 10^{-2}\,\text{s}$; 4) $\tau = 10^{-1}\,\text{s}$; 5) $\tau = 10^{2}\,\text{s}$.

The distribution of the temperature on menisk for the height of slot $H_0 = 1\,\text{mkm}$ and with different initial temperature data is given in Fig. 5. We can conclude that the character of the temperature distribution is always the same. The minimum is situated about the middle of the menisk (to be specific near .4 from the menisk and difference between T_{in} in difference points is not big $\Delta t \sim 3° - 4°$).

Finally, we note that in extremal conditions the freezing of valves may play an important role. The mathematical model suggested in Chapter 1 fits also for the descriptions of freezing process of valves.

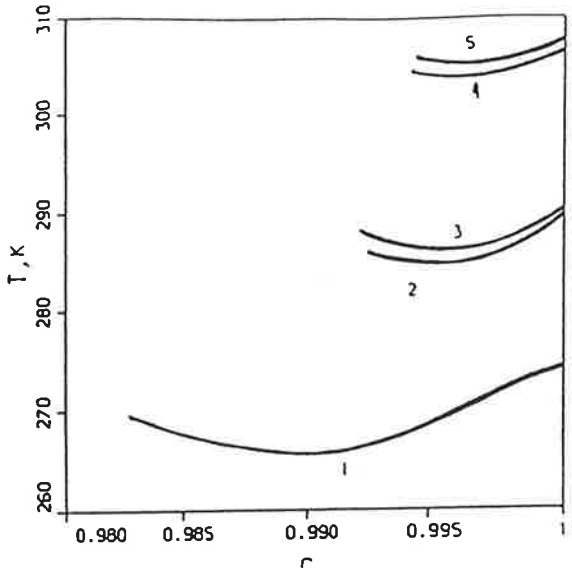

Figure 5. The distribution of the temperature on the menisk ($H_0 = 1$ mkm and for different T_{in}): 1) $T_{in} = 280°$ K, $\tau = .1$ s; 2) $T_{in} = 300°$ K, $\tau = 1$ s; 3) $T_{in} = 300°$ K, $\tau = .1$ s; 4) $T_{in} = 320°$ K, $\tau = 1$ s; 5) $T_{in} = 320°$ K, $\tau = 1.4 \cdot 10^{-1}$ s.

Equation (1.5), (1.6) can be written on this case as follows

$$\frac{\partial h}{\partial t} + \frac{\varrho_i}{\varrho_l}\frac{\partial h_i}{\partial t} + \frac{1}{r}\frac{\partial q}{\partial s} = -m\sqrt{1 + \left(\frac{\partial h_i}{\partial s}\right)^2},$$

$$\varrho_i \frac{\partial}{\partial t}(hT_i c) - \varrho_i \gamma \frac{\partial h_i}{\partial t} + \frac{\varrho_l}{r}\frac{\partial}{\partial s}(qcT_l) = s_w - im\varrho_l.$$

Above ϱ_i is the density of the ice, $h_i = 0$ if $T_l > T_*$, $h_i > 0$ if $T_l = T_*$, where T_* is a freezing point. Dynamic of the flow and freezing depends on the material of valves (metal or plastic). In the case of plastic material it is possible to obtain ice in valves. In metal valves the dynamic of the sediment is similar but the ice is absent.

REFERENCES

1. V. Rivkind and M. I. Vasenina, *Numerical solving problems of fluid films based on the full nonstationary Navier–Stokes equations*, Mathematical modelling of nonstationary problems of continuous mechanics (1986), 89–96. (Russian)

2. P. Neittaanmäki and V. Rivkind, *Mathematical modelling of liquid drops evaporation*, in "Proc. of Jyväskylä–St. Petersburg seminar on partial differential equations and numerical methods," P. Neittaanmäki and V. Rivkind (eds.), University of Jyväskylä, Department of Mathematics, Report 56, 1993, pp. 89–100.

3. V. Rivkind, *Liquid flow in a slot*, Heat Transfer Sov Res, vol. **16** (1986), no. 3, 63–71.

CHARACTERIZATION OF FREE JETS AND SPRAYS WITH A LDA /PDPA SYSTEM

TUOMAS PALOPOSKI and KARI SAARI

Helsinki University of Technology

Sähkömiehentie 4, FIN-02150 Espoo, FINLAND

ABSTRACT

Measurements with a Laser Doppler Anemometer / Phase Doppler Particle Analyzer are described in this paper. The effect of seeding particles on the accuracy of fluid velocity measurements is studied with the turbulent free jet as a test case. The characterization of drop size and velocity distributions in sprays is discussed.

1. INTRODUCTION

In this paper, we describe measurements with a modern optical instrument called LDA/PDPA. LDA is an acronym for Laser Doppler Anemometer; LDAs have been used for the measurement of fluid velocity for quite some time. PDPA is an acronym for Phase Doppler Particle Analyzer; a PDPA is a LDA which has been modified in such a way that particle size measurements can also be carried out. An Aerometrics LDA/PDPA system has been in use at Helsinki University of Technology since 1992.

The accuracy of LDA measurements in different flow conditions is rather difficult to estimate. We have used the turbulent free jet as a test case. Experimental data were obtained with various kinds of seeding particles and the measured velocities were compared with the well-known theoretical solution based on the mixing length hypothesis. Results of this exercise will be shown in our paper.

The characterization of sprays is our most important application for the particle sizing capability of the PDPA. Sprays are used in many industrial processes; for example, in the combustion of liquid fuels, in spray cooling and drying, etc. For the optimization of such processes, we need to know the sizes and velocities of the drops in the spray. This information can be used to estimate the trajectories of the drops and the heat and mass transfer between the drops and the surrounding gas. Typical results of spray drop size and velocity measurements will be shown in our paper.

2. CHARACTERIZATION OF FREE JETS WITH A LDA/PDPA SYSTEM

Any fluid flow velocity measurement with a Laser Doppler Anemometer (LDA) relies on the information obtained from seeding particles suspended in and transported with the fluid. The suspended particles flow through a fixed region in space (a measurement volume), which is monitored during a selected time interval. The measurement volume is defined by the cross-over region of two intersecting laser beams. As a particle passes through the measurement volume, it produces a Doppler burst signal. The Doppler frequency of the burst signal is then used to deduce the velocity of the particle (= velocity of the flow). Hence one basic assumption of this technique must be that the particles follow any changes of the flow immediately, i.e. with only a negligible velocity lag. While this assumption can usually be regarded as being satisfied for small to moderate acceleration or deceleration, this is not the case for large velocity gradients of the fluid and especially not for larger seeding particles.

The purpose of this paper is to present new experimental LDA data of a small turbulent free jet with two different seeding particles and with different working pressures. The results are compared with the well known solutions of Schlichting and Abramovich which are based on the mixing length theory. The velocity lag of the seeding particles can then be obtained by comparing the measured velocities with the calculated theoretical values. The measured seeding particle deceleration can then be compared with the values based on different particle drag coefficient models.

The experiments were carried out with a small cylindrical nozzle (diameter 3.6 mm) using dry air as the fluid. We used four different working pressures from 0.05 bar to 0.2 bar and measured the axial velocity at the centerline of the free jet. The axial velocities were measured at different distances from the nozzle exit (from 2.5 mm to 130 mm). The deceleration of the particles was then calculated based on the velocities at different locations.

We used dispersed potato starch (measured particle size 9.85 μm) and titanium dioxide TiO_2 (measured particle size 3.25 μm) as the seeding particles. The particle size distributions were measured with a Malvern Particle Sizer.

The velocity profile at the nozzle exit is usually considered as a plug flow, where the velocity u_0 is constant over the whole exit area. The centerline maximum velocity remains constant for about 6 to 7 diameters from the nozzle exit and then begins to decelerate very rapidly. According to Schlichting [1] the axial centerline velocity u_{max} of the cylindrical turbulent free jet is

$$\frac{u_{max}}{u_0} = 6.571\frac{d_0}{x} \tag{1}$$

where x is the distance from the nozzle exit and d_0 is the diameter of the nozzle. The results of Abramovich [2] for the axially symmetric turbulent free jet are very similar. The centerline velocity is inversely proportional to the distance from the origin, which is located not at the nozzle exit, but inside the nozzle:

$$\frac{u_{max}}{u_0} = 7.273\frac{d_0}{x + 2.197 d_0} \tag{2}$$

We assumed that the seeding particles were nondeformable spherical particles and we neglected all wall effects and collisions of the particles. The density of the particles was much larger than the density of the fluid (air). The gravitational forces were neglected since the velocity gradients in the jet were large. The static pressure at the nozzle exit was assumed to be constant. The equation of motion for a single particle in one-dimensional form can then be written as

$$\frac{\pi d_p^3}{6}\rho_p \frac{dU_p}{dt} = C_d \frac{\pi d_p^2}{4}\rho_f \frac{V^2}{2} \tag{3}$$

The velocity $V = U_p - U_f$ is the velocity lag between the particle and the fluid. The drag coefficient C_c is dependent on the particle Reynolds number which is defined by

$$\mathrm{Re}_d = \frac{V d_p}{\nu_f} \tag{4}$$

The well known Stokes` drag coefficient for a spherical particle is

$$C_d = f(\mathrm{Re}_d) = \frac{24}{\mathrm{Re}_d} \tag{5}$$

This is valid only if $\mathrm{Re}_d \leq 1$. The greater the Reynolds number becomes the more inaccurate Stokes` drag coefficient will be.

Beard and Pruppacher have studied the free falling velocity for small water droplets in saturated air. These results could be correlated as follows [3]:

$$C_d = 24\,\mathrm{Re}_d^{-1} + 2.76\,\mathrm{Re}_d^{-0.2} \qquad 2 < \mathrm{Re}_d \leq 21 \tag{6}$$

In Figures 1 and 2 we have the measured axial centerline velocity profiles of four different working pressures with potato starch and TiO_2 as the seeding particles.

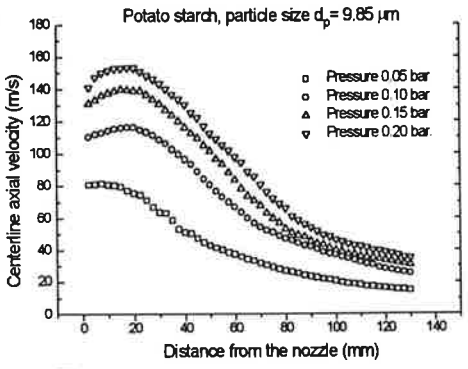

FIGURE 1 Measured centerline velocities for potato starch in 4 different working pressures

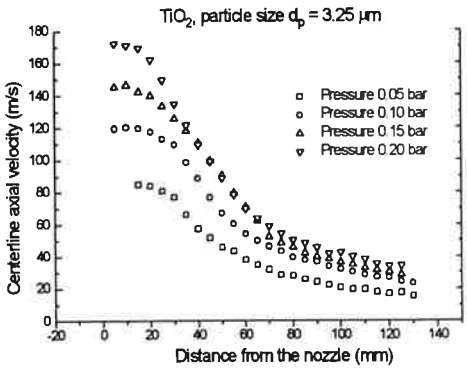

FIGURE 2 Measured centerline velocities for TiO_2 in 4 different working pressures

The case p = 0.10 bar is further analyzed in Figures 3-8. Measured and calculated velocities are compared with each other in Figures 3 and 4 and the differences can be clearly seen. The deceleration of the particles is then calculated based on the velocity lag and different drag coefficient models (Figures 5-8). It can be seen that the Stokes` model highly underestimates the drag coefficient and thus the velocity lag for potato starch, although the results for titanium dioxide particles are quite satisfactory. The model of Beard and Pruppacher gives better results especially for potato starch particles. The model of Abramovich also seems to fit the present results better than the model of Schlichting. Figures 3 - 8 show that the deceleration of axial velocity at the centerline begins closer to the nozzle exit than in the Schlichting model.

3. CHARACTERIZATION OF SPRAYS

A Phase Doppler Particle Analyzer is capable of the simultaneous measurement of the sizes and velocities of individual drops in sprays. The operation of the instrument has been described by Bachalo and Houser [4]. The Doppler burst signal caused by a drop passing through the measurement volume is detected with two or more photomultipliers placed at different locations. The Doppler frequency of the signal is then used to deduce the velocity of the drop, as in conventional laser Doppler anemometry; the phase differences between the signals detected at different locations are used to deduce the size of the drop. The name Phase Doppler Particle Analyzer (PDPA) derives from the fact that the measurement is based on the analysis of phase differences.

The use of several photomultipliers for the detection of the signals causes some problems. The locations of the photomultipliers must be carefully chosen to achieve good accuracy. The optimum locations depend on the refractive index of the liquid being sprayed; thus, the optical configuration of the instrument has to be tailored in each experiment. It has become common practice to use a single receiver unit with three photomultipliers and the user therefore only needs to choose the location and orientation of the receiver unit. It is noteworthy that the optimum configuration is always asymmetric, which is sometimes reflected in the data. This point will be discussed below. Direct backscattering cannot be employed in drop size measurements, which is unfortunate. It would be far easier from the point of view of traversing systems and optical access to the spray if the laser transmitter and receiver were built into a single component.

The data collected with a Phase Doppler Particle Analyzer can be further processed to obtain detailed information of the physical characteristics of sprays. The size of the measurement volume, the total number of drops passing through the measurement volume during the selected time interval, and the sizes and velocities of the individual drops are known; thus, one can calculate, for example, the drop concentration and the liquid volume flux, momentum flux and kinetic energy flux. Furthermore, the time of arrival of each drop is recorded and temporal variations in the structure of the spray can therefore be analyzed.

An important point is that the measurements with a Phase Doppler Particle Analyzer are essentially point measurements, that is, the size of the measurement volume is usually rather small when compared to the size of the spray itself. Thus, high spatial resolution is achieved, which is often advantageous. For example, in the combustion of liquid fuels it is important to analyze local fuel-to-air ratios in order to understand ignition, flame propagation and emissions of harmful pollutants.

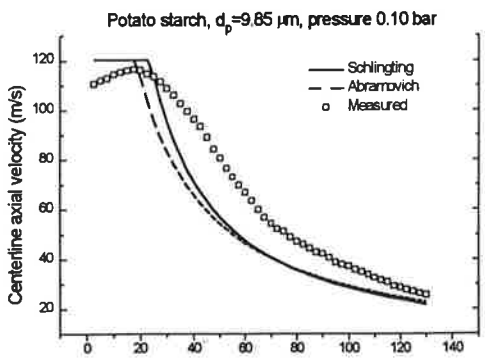

FIGURE 3 Axial centerline velocity potato starch , p = 0,1 bar

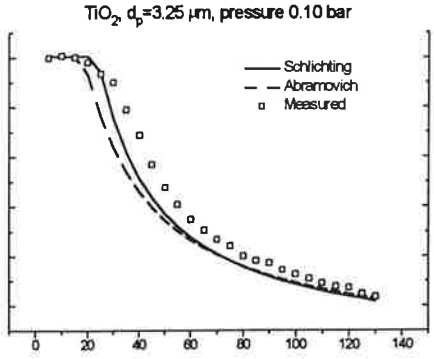

FIGURE 4 Axial centerline velocity TiO_2 , p = 0,1 bar

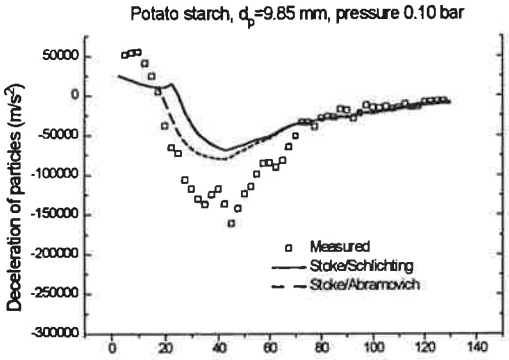

FIGURE 5 Stokes´model for potato starch

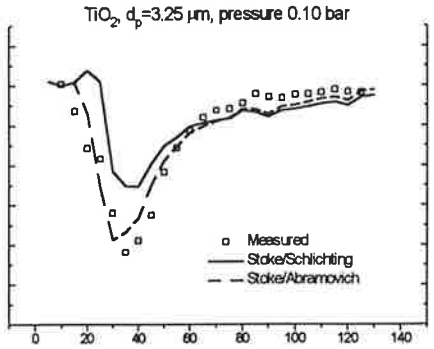

FIGURE 6 Stokes´model for TiO_2

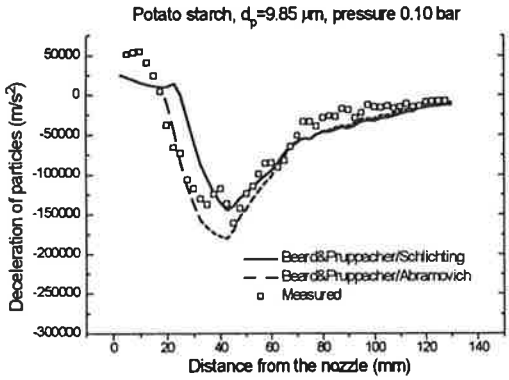

FIGURE 7 Beard & Pruppacher model for potato starch

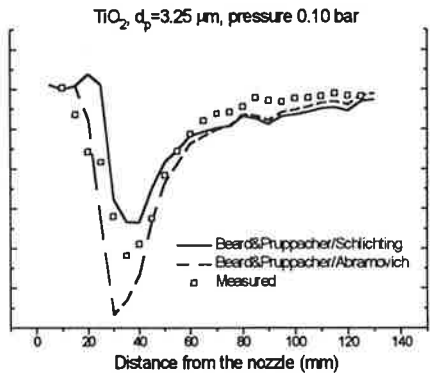

FIGURE 8 Beard & Pruppacher model for TiO_2

Phase Doppler Particle Analyzers can be built for the simultaneous measurement of one, two or three components of drop velocity. Our system can only measure one velocity component at a time. In spray studies, we are usually interested in the axial velocity of drops.

Figure 9 illustrates typical spray measurements. A water spray from a Monarch swirl pressure jet nozzle was studied in this particular experiment. The nozzle had a nominal capacity of 5.50 USgal/h and a spray cone angle of 60°. Tap water with a pressure of 6 bar and a temperature of 17 °C was used. The nozzle was mounted on a manually operated traversing table and the spray was injected co-axially into a low-velocity air stream to prevent the recirculation of drops from downstream regions back to the regions where the measurements were made.

The measurements were carried out across the spray at an axial distance of 20 mm from the nozzle. At this distance, the diameter of the spray was approximately 50 mm. The plot of the liquid volume flux vs. radial position shows a hollow-cone spray pattern, which is typical to swirl pressure jet nozzles. It can be seen that most of the liquid is concentrated in a rather narrow, ring-like region at the edge of the spray, whereas negligible liquid volume flux was observed in regions near the centerline of the spray. The plot of the liquid volume flux is not symmetric about the centerline of the spray. We believe, however, that the spray itself was symmetric and the asymmetry was a measurement artefact caused by the asymmetry of the optical configuration of the PDPA. It is of interest to note that the plots of drop mean size and drop velocity are rather symmetric. Further, it is well-known that the measurement of liquid volume flux with a PDPA is particularly susceptible to errors [5].

The plot of drop mean size vs. radial position shows both the arithmetic mean diameter and the Sauter mean diameter. The Sauter mean diameter is defined as the diameter of the drop which has the same ratio of volume to surface area as the spray as a whole. The Sauter mean diameter is often used in calculations of the evaporation and combustion of the drops. It can be seen that the arithmetic mean diameter is fairly constant across the spray whereas the Sauter mean diameter exhibits maxima in the regions of high liquid volume flux.

The plot of drop velocity vs. radial position shows both the (arithmetic) mean axial velocity and the r.m.s. velocity. Highest velocities were observed in the regions of high liquid volume flux.

Attempts were made to fit various distribution functions to the measured drop size distributions. A chi-square minimum technique developed in [6] was used in the fitting. The best fit was obtained using the log-hyperbolic distribution function developed by Barndorff-Nielsen [7]. Figure 10 shows the fitting of the log-hyperbolic distribution function to the drop size distribution measured at a radial position of 8 mm. The value of chi-square is 12.11 with 6 degrees of freedom which is well below the 5 % significance limit.

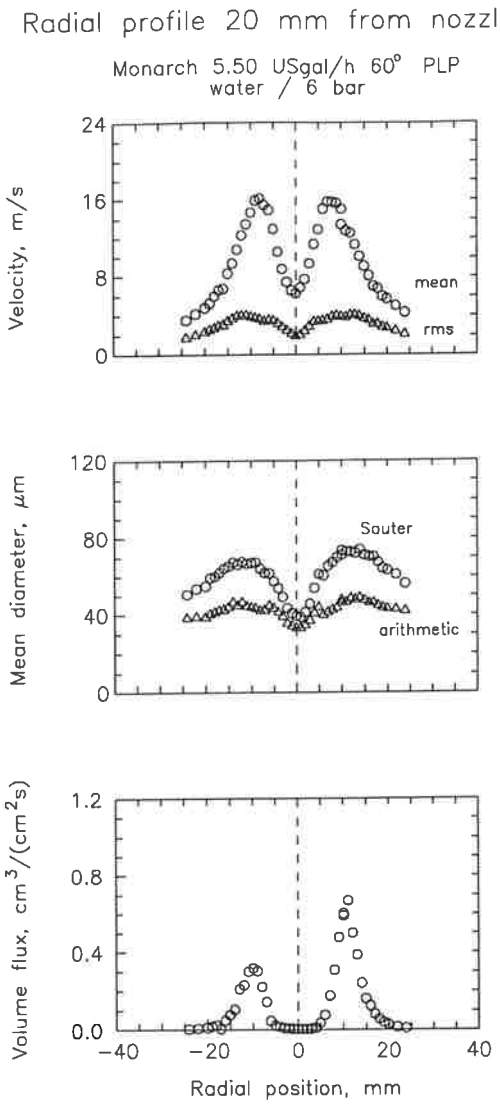

FIGURE 9 Profiles of axial velocity, mean diameter and volume flux of the drops in a water spray from a swirl pressure jet nozzle.

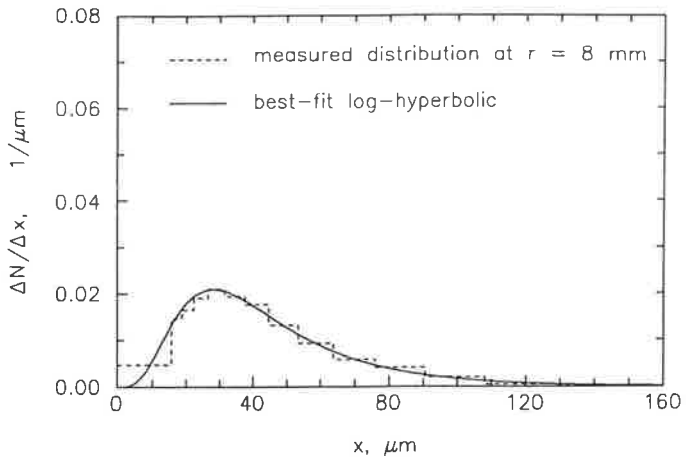

FIGURE 10 Measured drop size distribution and the best-fit log-hyperbolic distribution function at the radial position of 8 mm from the centerline of the spray.

CONCLUSIONS

The accuracy of the Laser Doppler Anemometer measurements is highly dependent on both the velocity gradient of the flow and the seeding particle size. The known drag coefficient models can be used to estimate the velocity lag between the fluid and the particles.

Phase Doppler Particle Analyzers can be used for the detailed characterization of sprays. Drop sizes and velocities can be measured with high spatial and temporal resolution. Drop concentration, liquid volume flux, and other physical characteristics of interest can be calculated from the data.

REFERENCES

1. H.Schlichting, Boundary-Layer Theory, McGraw-Hill, Seventh edition 1979
2. G.N.Abramovich, The Theory of Turbulent Jets, MIT 1963
3. M.Lampinen, Calculation Methods for Determining the Pressure Loss of Two-Phase Pipe Flow and Ejectors in Pneumatic Conveying Systems. Acta Polytechnica Scandinavica, Me 99, 1991
4. W. D. Bachalo and M. J. Houser, Phase/Doppler spray analyzer for the simultaneous measurements of drop size and velocity distributions. Opt. Engng 23 (1984) 583-590
5. C. F. Edwards and K. D. Marx, Application of Poisson statistics to the problem of size and volume flux measurement by Phase-Doppler anemometry. In "Proceedings of the 5th International Conference on Liquid Atomization and Spray Systems", H. G. Semerjian (Ed.), NIST, Gaithersburg, 1991, 653-660
6. T. Paloposki, Drop size distributions in liquid sprays. Dissertation, Helsinki University of Technology, Faculty of Mechanical Engineering. Acta Polytechnica Scandinavica Me 114, 1994.
7. O. Barndorff-Nielsen, Exponentially decreasing distributions for the logarithm of particle size. Proc. Royal Soc. Lond. A 353 (1977) 401-419

ONE-DIMENSIONAL UNSTEADY FLOW CALCULATION USING AN APPROXIMATE RIEMANN SOLVER

HUACHEN PAN
CFD-Finland Oy
Tekniikantie 17 E 213
FIN-02150 Espoo, FINLAND

ABSTRACT

One-dimensional unsteady flow calculations for a constant cross-sectional shock tube were checked with the exact solution. Several schemes with first- or second-order accuracies in temporal or in spatial discretizations were tested and compared. It is found that a combination of spatially second-order Roe's scheme with the Lax-Wendroff scheme in time marching can give the best result.

1. INTRODUCTION

One-dimensional unsteady flow calculations are often used as numerical tests for developing new schemes and testing and evaluating the available schemes. It can also be used in many practical applications. If an approximate Riemann solver such as Roe's scheme [1] is employed to treat the fluxes on the cell-faces, strong discontinuities can be handled. Then the numerical method is very suitable for such applications like compressible pipe flows with strong shocks, water pipe flows with water hammer effect and dam break flows in open channels. If a Lax-Wendroff type of scheme is used, then second-order accuracy can be obtained in time marching [2]. It would be interesting to see also the effect of the combination of Roe's scheme and Lax-Wendroff scheme. That is the question to be answered by this paper.

A classical test case for one-dimensional unsteady calculation is a shock tube flow which was probably firstly suggested by Sod [3]. The advantage of using a shock tube flow as a test case is that exact solution can be easily obtained [4]. On the other hand, the complexity flow pattern of a shock tube with a strong moving shock, an expansion wave and a moving contact discontinuous face provides a challenging case for many numerical schemes. In Sod's paper [3], a wide range of schemes available in 1970's were tested by calculating the shock tube case. Roe [1] also used this shock tube case to test its first-order upwind scheme. This shock tube case has become a standard test case which

is also found in some most recently published papers on various numerical schemes [5] [6].

In this study, this standard shock tube flow were calculated using several schemes or their combination. The purpose is to find a better numerical scheme for the other possible one-dimensional unsteady flow applications.

2. BASIC EQUATIONS

The one-dimensional, constant cross-sectional, compressible and inviscid flow can be expressed as follows:

$$\frac{\partial U}{\partial t} + \frac{\partial F}{\partial x} = 0 \tag{1}$$

where

$$U = \begin{pmatrix} \rho \\ \rho u \\ e \end{pmatrix} \tag{2}$$

and

$$F = \begin{pmatrix} \rho u \\ p + \rho u^2 \\ u(e+p) \end{pmatrix} \tag{3}$$

3. TIME MARCHING SCHEMES

We use explicit scheme for the time marching in this study. The development of $U(x,t)$ over the time interval Δt can be expressed in a Taylor series, with third-order and higher terms dropped

$$U(x,t+\Delta t) = U(x,t) + \Delta t \frac{\partial U}{\partial t} + \frac{\Delta t^2}{2}\frac{\partial^2 U}{\partial t^2} \tag{4}$$

By considering Eq.(1), Eq.(4) can be expressed as

$$U(x,t+\Delta t) = U(x,t) - \Delta t \frac{\partial F}{\partial x} + \frac{\Delta t^2}{2}\frac{\partial}{\partial x}(A\frac{\partial F}{\partial x}) \tag{5}$$

where A is the Jacobi of $F(U)$, or

$$A = \frac{\partial F}{\partial U} = \begin{pmatrix} 0 & 1 & 0 \\ \frac{\gamma-3}{2}u^2 & (3-\gamma)u & \gamma-1 \\ \frac{\gamma-2}{2}u^3 - \frac{ua^2}{\gamma-1} & \frac{3-2\gamma}{2}u^2 + \frac{a^2}{\gamma-1} & \gamma u \end{pmatrix} \tag{6}$$

Eq.(5) is called one-step Lax-Wendroff method in time marching. It retains the second-order temporal accuracy.

If the last term in Eq.(5) is dropped, it becomes a first-order scheme in time marching:

$$U(x, t+\Delta t) = U(x,t) - \Delta t \frac{\partial F}{\partial x} \tag{7}$$

4. SPATIAL DISCRETIZATION SCHEMES

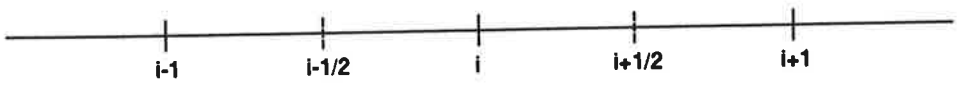

Fig.1 One-dimensional grid

In the grid shown in Fig.1, spatial derivatives in Eq.(5) and Eq.(7) can be approximated by

$$\frac{\partial F}{\partial x} \approx \frac{F_{i+\frac{1}{2}} - F_{i-\frac{1}{2}}}{x_{i+\frac{1}{2}} - x_{i-\frac{1}{2}}} \tag{8}$$

and

$$\frac{\partial}{\partial x}(A\frac{\partial F}{\partial x}) \approx \frac{A_{i+\frac{1}{2}}\frac{F_{i+1}-F_i}{x_{i+1}-x_i} - A_{i-\frac{1}{2}}\frac{F_i - F_{i-1}}{x_i - x_{i-1}}}{x_{i+\frac{1}{2}} - x_{i-\frac{1}{2}}} \tag{9}$$

we call those quantities at the locations $i+\frac{1}{2}$ and $i-\frac{1}{2}$ as the "cell-face quantities". The ways to obtain those quantities determine the quality of the solutions.

Taking fluxes F as the example, one easy way is to use simple averaging

$$F_{i+\frac{1}{2}} = \frac{1}{2}(F_i + F_{i+1}) \tag{10}$$

This is equivalent to a central difference scheme and has second-order accuracy spatially. This way of obtaining cell-face fluxes works only in Lax-Wendroff time marching as shown in Eq.(5). If it is applied in the first-order time maching scheme shown in Eq.(7), the scheme will be unstable.

A popular way to obtain the cell-face fluxes is the Roe's scheme [1], which is an approximate local Riemann solver to get upwind effect. In the Roe's scheme, the cell-face fluxes are calculated by

$$F_{i+\frac{1}{2}} = \frac{1}{2}(F_l + F_r) - \frac{1}{2}\sum_{j=1}^{3} R_j \mid \lambda_j \mid \alpha_j \tag{11}$$

where

$$\alpha_j = L_j(U_r - U_l) \tag{12}$$

and λ_j,L_j and R_j are the eigenvalues, left and right eigenvectors of the Jacobi $A_{i+\frac{1}{2}}$. $A_{i+\frac{1}{2}}$ is averaged according to the method suggested by [5]. Subscripts l and r refer to the variables on the left and right sides of the cell face $i+\frac{1}{2}$. If we simply let

$$U_l = U_i \tag{13}$$

and

$$U_r = U_{i+1} \tag{14}$$

we have Roe's scheme of first-order in spatial accuracy.

If we use MUSCL approach [7], U_l can also be obtained by linear extrapolation of U_i and U_{i-1}, and U_r by U_{i+1} and U_{i+2}, like

$$U_l = U_i + \frac{\phi(R_i)}{2}(U_i - U_{i-1}) \tag{15}$$

and

$$U_r = U_{i+1} + \frac{\phi(1/R_{i+1})}{2}(U_{i+2} - U_{i+1}) \tag{16}$$

where

$$R_i = \frac{U_{i+1} - U_i}{U_i - U_{i-1}} \tag{17}$$

and

$$\phi(R) = \frac{R^2 + R}{R^2 + 1} \tag{18}$$

Eq.(18) is called van Albada limiter [7].

Then this Roe's scheme with MUSCL approach has second-order spatial accuracy.

5. RESULTS

In this study, four schemes or scheme combination were used. They are shown in table 1.

Scheme	Spatial accuracy	Temporal accuracy	Equations used
Roe first-order upwind	first-order	first-order	(7),(11), (13),(14)
Roe second-order upwind	second-order	first-order	(7),(11), (15),(16)
Simple Lax-Wendroff	second-order	second-order	(5),(10)
Roe + Lax-Wendroff	second-order	second-order	(5),(11), (15),(16)

Table 1. Four schemes used in this study

The length of the shock tube is one. 100 computational cells are used along the tube. At the middle of the tube, i.e. $x = 0.5$, there is a membrane. The initial data for the shock tube is the same as that in the Sod's case. On the left side of the membrane, $p = 1$, $\rho = 1$ and $u = 0$; on the right side of the membrane, $p = 0.1$, $\rho = 0.125$ and $u = 0$. At the time of $t = 0$, the membrane is broken down, and the time marching or iteration begins. The iteration stops at the time of $t = 0.144$. Time step of $\Delta t = 0.0024$ is used in the iteration. This is equivalent to have a Courant number of 0.24.

The computed results are given in Fig.2, Fig.3 and Fig.4 in which pressure, density and velocity distributions of the tube at the time of $t = 0.144$ are compared with the exact solutions.

It is clearly shown that the first-order upwind Roe's scheme cannot predict the sharp gradient caused by the shock, expansion wave and the moving contacting face.

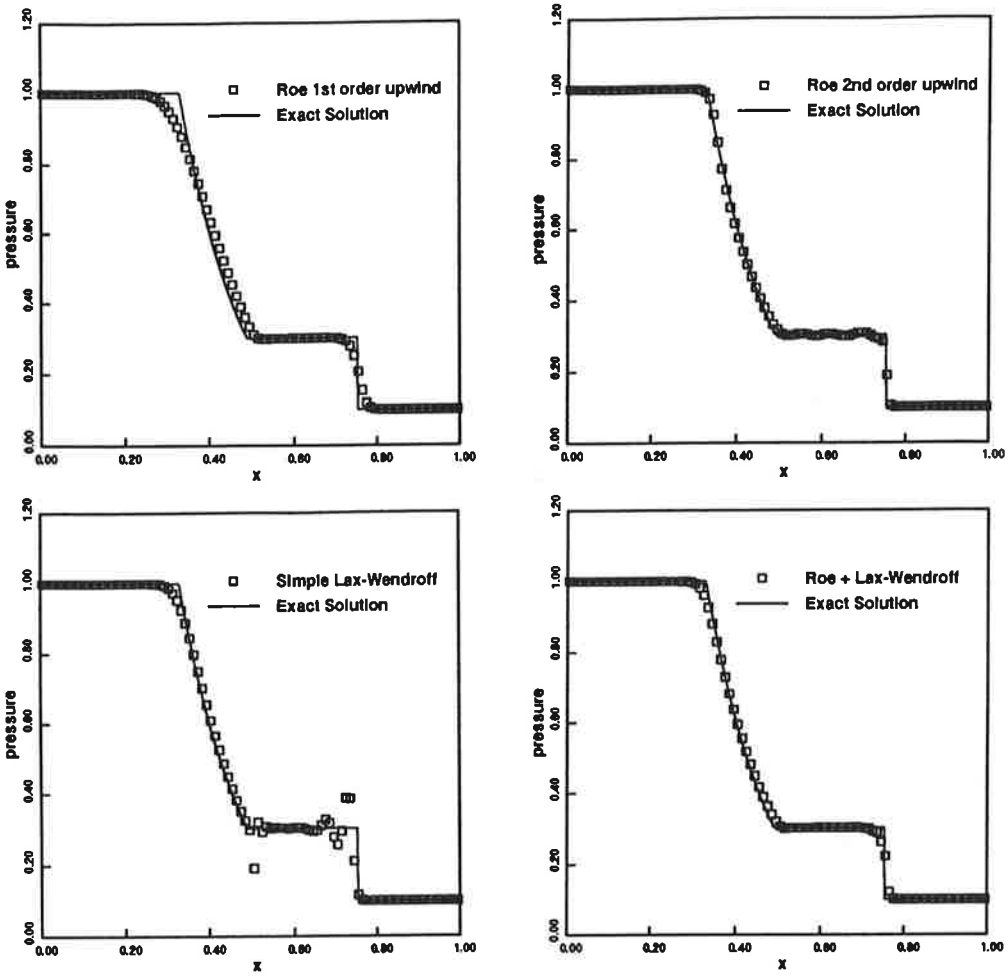

Fig.2 Pressure distributions

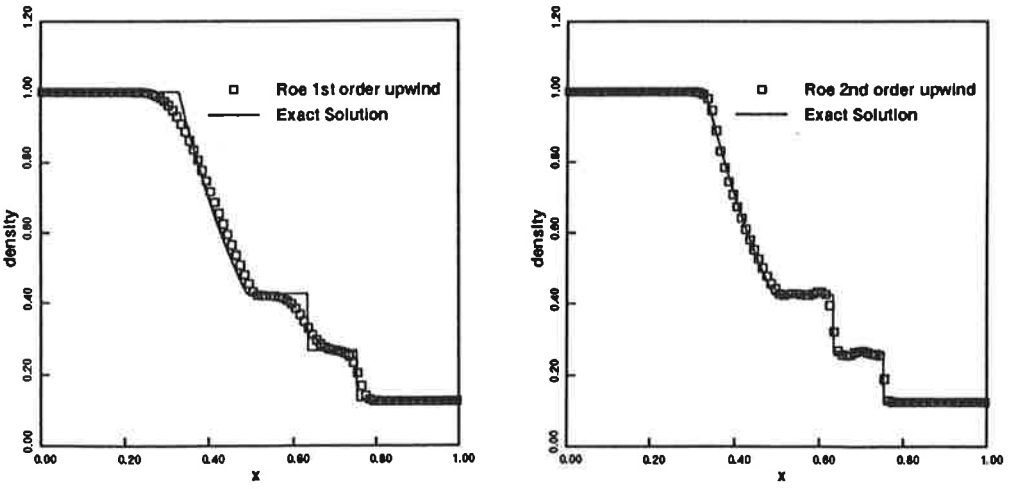

Fig.3 Density distributions (continued to the next page)

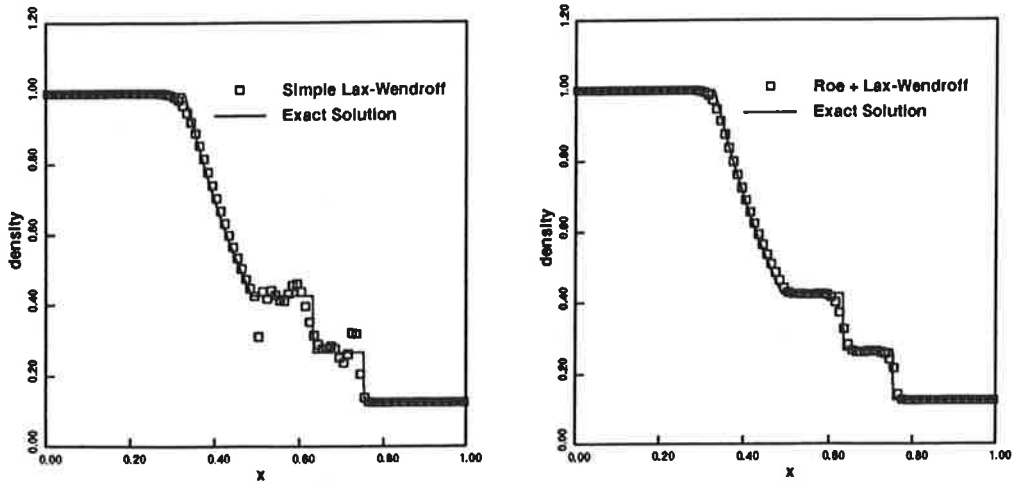

Fig.3 Density distributions

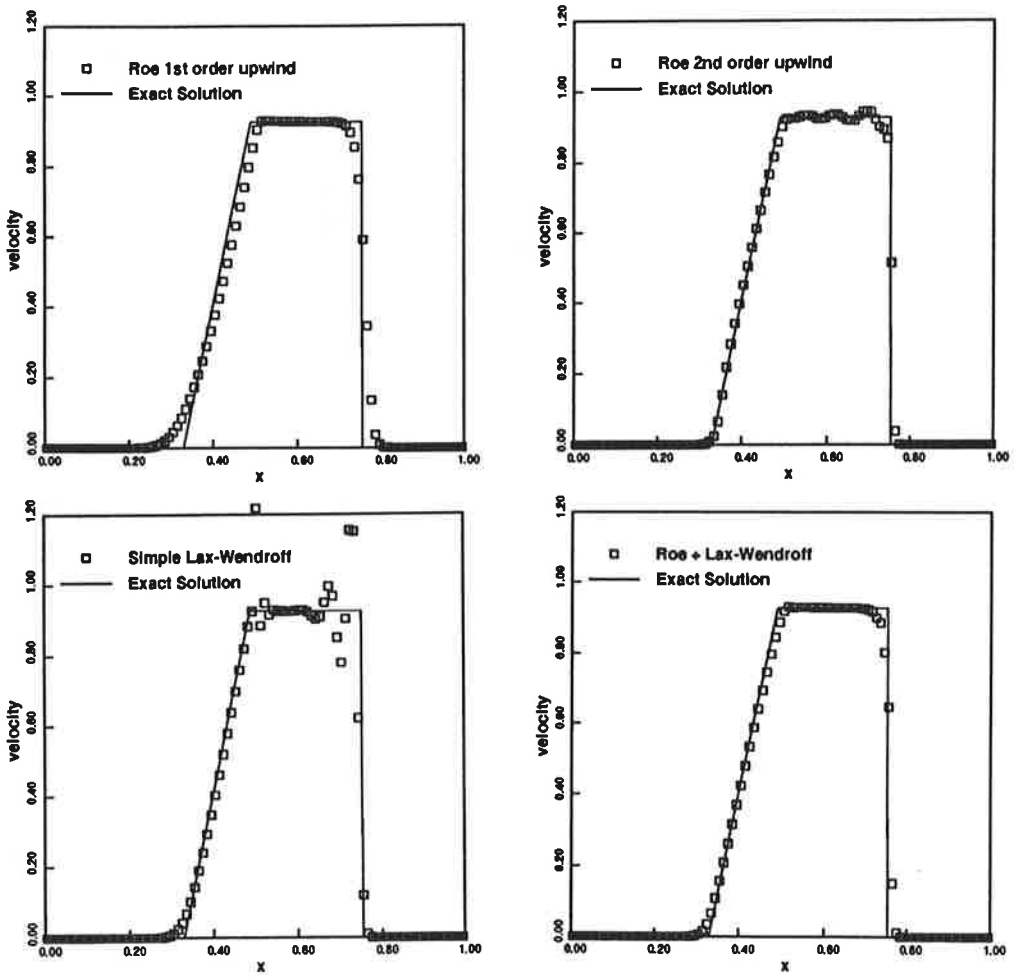

Fig.4 Velocity distributions

The simple Lax-Wendroff scheme also shows very oscillating distribution near the shock and expansion waves.

The second-order upwind Roe's scheme, although being first-order accurate in time marching, gives a quite accurate prediction of the positions of the shock and expansion waves. It also gives a sharp shock wave and sharp density jump at the moving contacting face. However, small oscillating distribution of flow variables, especially velocity, can be found.

The combination of a second-order upwind Roe's scheme for the convective term with a Lax-Wendroff type of diffusive term can give a compromised result. It gives a non-oscilating distribution, but at the expense of a slightly thicker prediction of the discontinuities. This arrangement could be the best among these four schemes.

6. CONCLUDING REMARKS

The numerical tests of the one-dimensional unsteady calculation of a shock tube indicate that the combination of a second-order upwind Roe's scheme for the convective term, with a Lax-Wendroff type of diffusive term, can give a better result than the results obtained by using simple Lax-Wendroff method, or by using the Roe's scheme with only first-order temporal accuracy.

This conclusion may be useful in developing a unsteady flow solver for one-dimensional flow with variable cross-sections or developing computational fluid dynamics programs for steady or unsteady multi-dimensional flows.

REFERENCES

(1) P.L.Roe, Approximate Riemann solvers, parameter vecters and difference schemes, J. of Comp. Phys., 43, (1981) 357-372

(2) P.D.Lax and B.Wendroff, Systems of conservation law, Comm. Pure and Applied Math., 13, (1960) 217-237

(3) G.A.Sod, A survey of several finite difference methods for systems of nonlinear hyperbolic conservation laws, J. of Comp. Phys., 27, (1978) 1-31

(4) J.D.Anderson,Jr, "Modern Compressible Flow", McGraw-Hill, 1990

(5) P.Glaister, An efficient shock-capturing algorithm for compressible flows in a duct of variable cross-section, Int. J. for Numer. Method in Fluids, 18, (1994) 107-122

(6) W.J.Rider, Methods for extending high-resolution schemes to non-linear systems of hyperbolic conservation laws, Int. J. for Numer. Method in Fluids, 17, (1993) 861-885

(7) T.Siikonen and T.Saarinen, Flux vector splitting of the one-dimensional Euler equations, Report B-11, Lab. of Aero. Helsinki Univ. of Tech., 1988

NUMERICAL SOLUTIONS FOR STEADY AND UNSTEADY REYNOLDS EQUATION FOR SPECIFIC BEARING GEOMETRIES

PEKKA SALONEN
Helsinki University of Technology
Laboratory of Machine Design
Otakaari 4, FIN-02150 Espoo, FINLAND

ABSTRACT

The purpose of this work is to find numerical solutions for 1. steady incompressible, 2. steady compressible and 3. unsteady compressible Reynolds equation with specific boundary conditions and with slider bearing geometry.

The method used to solve the problems is finite differences technique and especially central differences scheme. In order to apply the scheme, the algebraic equations are first derived into non-dimensionalized form. Several computer programs were written for different cases and as a result from them the pressure distributions and in some cases the load-carrying capacity are plotted out.

The results in 1-D steady state case agree completely with the exact solution. For the 2-D incompressible case the pressures differ only about 2% from the corresponding exact solution. In the compressible 2-D case the results match with the incompressible case when a certain parameter combination is used. The pressure peak is somewhat lower in the compressible case and also the location of the pressure peak moves slightly to the direction of the smaller film thickness.

In the unsteady compressible case the load-carrying capacity was of interest. The load-carrying capacity dropped as the time moved on, but the program written, resulted only minor drop.

1. INTRODUCTION

Reynolds equation

$$\frac{\partial}{\partial x}\left(\frac{h^3\rho}{\mu}\frac{\partial p}{\partial x}\right)+\frac{\partial}{\partial y}\left(\frac{h^3\rho}{\mu}\frac{\partial p}{\partial y}\right)=6U\frac{\partial}{\partial x}(\rho h)+12\frac{\partial}{\partial t}(\rho h) \qquad (1)$$

has no closed form solution. Yet several researhers have found solutions for (1) with certain boundary conditions and with certain approximations.

Pinkus [2] has considered already in 1961 the possibility of using computers to solve lubrication problems, which require a great deal of 'number crunching'. He has developed a numerical formula to solve Reynolds equation. He has also used the finite differences scheme, which will be the case in this work, too. The difference is that he uses the scheme already in the earlier stage of the derivation, which leads him to use finer grid and more complicated mathematical formulas. Afterwards he has printed the results for journal bearing case in numerical form. He and some others [3], [7] have derived the exact solution for slider bearing in one-dimensional incompressible case to find the load-carrying capacity.

Hamrock has made a lot of work in the area of lubrication theory of bearings. One of his books [7] covers a wide range of different types of lubrication in different types of bearings. In the slider bearing case he plots a pressure distribution of fixed-incline slider bearing. The dimensionless pressure-curves are drawn in function of dimensionless x-coordinate with different film thickness ratios (h_0/s_h). The curves show that the smaller the film thickness ratio is the higher the pressure peak goes. For instance if the ratio is 1/2 the maximum dimensionless pressure is about 1.0 and if the ratio is 1 then the maximum pressure is only like 0.3.

Walowit & Anno [8] have studied elasticity combined to lubrication problems. They have also taken into consideration the compressible gas slider bearing with a pressure difference across it. This is a one-dimensional case. Their assumption is that the density is related to the pressure by an equation of state, which means that pressure depends on the density linearly. They have developed the Reynolds equation into the form where the compressibility number plays a important role. As a result they define the limiting load support. When the speed becomes sufficiently high, the limiting load support is achieved. For example, if one machine operates ten times faster than another, this does not necessarily mean that it is a candidate for a gas bearing, since the slower machine could already be approaching the condition for limiting load support.

2. EXPERIMENTS AND RESULTS

2.1 Steady-State Incompressible Case

2.1.1 Non-dimensionalized Form for the Reynolds Equation for 2-D Case

The derivations of the following equations will start from the assumption that Reynolds equation (1) is known. The derivation of Reynolds equation is presented in [2]. For the incompressible case we may assume the density and viscosity to be constant. For the steady state case the time-dependent term cancels out leading us to

$$\frac{\partial}{\partial x}\left(h^3\frac{\partial p}{\partial x}\right)+\frac{\partial}{\partial y}\left(h^3\frac{\partial p}{\partial y}\right)=6\mu U\frac{\partial h}{\partial x} \tag{2}$$

The change in film thickness (h) in slider bearing is

$$h(x)=h_1-\frac{h_1-h_2}{B}x \tag{3}$$

In order to solve equation (2) we have to non-dimensionalize this equation. We will use the following non-dimensionalization:

$$\bar{x}=\frac{x}{B},\quad \bar{y}=\frac{y}{L},\quad \bar{h}=\frac{h}{h_2},\quad \bar{p}=\frac{p}{S} \tag{4}$$

where S is the Sommerfeld number. In addition we define the tapering (a) as

$$a=\frac{h_1}{h_2} \tag{5}$$

Using the above notation we are able to define the Reynolds equation in non-dimensionalized form

$$\frac{\partial}{\partial\bar{x}}\left(\bar{h}^3\frac{\partial\bar{p}}{\partial\bar{x}}\right)+\left(\frac{B}{L}\right)^2\frac{\partial}{\partial\bar{y}}\left(\bar{h}^3\frac{\partial\bar{p}}{\partial\bar{y}}\right)=1-a \tag{6}$$

2.1.2 Solution for 1-D Case

Now when we have derived the formula for 2-D case, it's easy to derive the equation for the 1-D case. In this case we assume that the bearing is infinitely long in y-direction (L>>B), which makes the equation (6) analytically solveable. After applying the boundary conditions for the case: 1. p=0 at x=0 and 2. p=0 at x=B we obtain an expression for the non-dimensionalized pressure,

$$\bar{p} = \frac{(a-1)\bar{x}(1-\bar{x})}{(a+1)\left[a-(a-1)\bar{x}\right]^2} \tag{7}$$

The load-carrying capacity of the bearing is

$$W = \int_A p dA \tag{8}$$

Because the pressure is constant in y-direction, we may develop the integral in the non-dimensionalized form

$$\overline{W} = \frac{W}{\frac{6\mu U B^2 L}{h_2^2}} = \frac{1}{(a-1)^2}\left[\ln a - \frac{2(a-1)}{a+1}\right] \tag{9}$$

For the bearing geometry studied, we are now able to find the pressure distribution across the bearing in x-direction. That is achieved by fixing the tapering (a) and giving different values for non-dimensionalized x-coordinate in equation (7). The load-carrying capacity for the same geometry can be calculated by using (9). A computer program was developed to do that and the results will be discussed later.

2.1.3 The Finite Differences Scheme

We can develop equation (6) even further ending up to

$$\left(\frac{\partial^2 \bar{p}}{\partial \bar{x}^2}\right) + \left(\frac{B}{L}\right)^2 \left(\frac{\partial^2 \bar{p}}{\partial \bar{y}^2}\right) + \frac{3(1-a)}{\bar{h}} \frac{\partial \bar{p}}{\partial \bar{x}} = \frac{1-a}{\bar{h}^3} \tag{10}$$

To make the finite differences notation easier we will use the following quantities

$$\frac{B}{L} = \beta \qquad \text{ja} \qquad \frac{1-a}{\bar{h}} = \alpha \tag{11}$$

In applying the finite differences scheme we will use the central differences. Substituting the scheme into (10) we can derive an expression for pressure at certain point of the bearing area. If we assume the grid to be generated over the cross sectional area, now we are able to calculate the pressure value at each grid point by using

$$\bar{p}_{i,j} = \frac{1}{2\left[1+\left(\beta\frac{\Delta\bar{x}}{\Delta\bar{y}}\right)^2\right]}\left[\left(1+\frac{3}{2}\alpha\Delta\bar{x}\right)\bar{p}_{i+1,j} + \left(1-\frac{3}{2}\alpha\Delta\bar{x}\right)\bar{p}_{i-1,j} + \left(\beta\frac{\Delta\bar{x}}{\Delta\bar{y}}\right)^2 \bar{p}_{i,j+1} + \left(\beta\frac{\Delta\bar{x}}{\Delta\bar{y}}\right)^2 \bar{p}_{i,j-1} - \frac{\alpha}{\bar{h}^2}\Delta\bar{x}^2\right] \tag{12}$$

The load-carrying capacity for this case can be evaluated from

$$W = \frac{1}{BL}\int_A \bar{p}dA \tag{13}$$

In order to integrate (13) over discretized area Simpson's rule was applied. A computer program was developed to evaluate the pressure distribution and the load-carrying capacity.

2.2 Steady-State Compressible Case

In equation (1) for the steady-state condition the last term could be left out. We know that viscosity depends more on temperature than on pressure. Then it is justified to assume that the density depends linearly from the pressure. Using the bar notation we are able to derive

$$\frac{\partial}{\partial\bar{x}}\left(\bar{p}\bar{h}^3\frac{\partial\bar{p}}{\partial\bar{x}}\right)+\left(\frac{B}{L}\right)^2\frac{\partial}{\partial\bar{y}}\left(\bar{p}\bar{h}^3\frac{\partial\bar{p}}{\partial\bar{y}}\right)=\frac{\partial}{\partial\bar{x}}(\bar{p}\bar{h}) \tag{14}$$

We introduce a new variable Q:

$$Q=(\bar{p}\bar{h})^2 \tag{15}$$

Taking the partial derivatives of Q in respect to x and y and using the relations (3), (4) and (5) we obtain:

$$\left(\frac{\partial^2 Q}{\partial\bar{x}^2}\right)-\frac{1}{\bar{h}}+\left(1-a+\frac{1}{\sqrt{Q}}\right)\frac{\partial Q}{\partial\bar{x}}+\beta^2\left(\frac{\partial^2 Q}{\partial\bar{y}^2}\right)=0 \tag{16}$$

Applying the finite differencies we achieve an expression for the quantity Q at grid point as

$$(2+2\nabla)Q_{i,j}=Q_{i+1,j}+Q_{i-1,j}-\frac{\Delta\bar{x}}{2}\frac{1-a}{\bar{h}}(Q_{i+1,j}-Q_{i-1,j})-\frac{\Delta\bar{x}}{2\bar{h}}\frac{1}{\sqrt{Q_{i,j}}}(Q_{i+1,j}-Q_{i-1,j})+\nabla(Q_{i,j+1}-Q_{i,j-1}) \tag{17}$$

where,

$$\nabla=\left(\beta\frac{\Delta\bar{x}}{\Delta\bar{y}}\right)^2 \tag{18}$$

In applying the equation (17) we calculate the Q-values (called in the first iteration round as initial Q-values). It means we have initial pressure at each grid point. Using this information we compute the next iterated values now giving to term $\sqrt{Q_{ij}}$ on the right hand side the computed previous iteration round Q-value and finding the value for the new Q on the left hand side of the equation. A computer program was developped in order to calculate the Q's and pressures respectively.

2.3 Unsteady Compressible Case

The unsteady case differs mathematically from the steady state case in the way that we have to take into account the non-linearity term on the right-hand side in (1). Assuming again the density being proportional to pressure,

$$\frac{\partial}{\partial x}(h^3 p\frac{\partial p}{\partial x})+\frac{\partial}{\partial y}(h^3 p\frac{\partial p}{\partial y})=6\mu U\frac{\partial}{\partial x}(ph)+12\mu\frac{\partial}{\partial t}(ph) \qquad (19)$$

To non-dimensionalize this, we use the former relations and additionally the non-dimensionalizing for time. Remembering that film thickness is not a function of time, we achieve

$$\frac{\partial \bar{p}}{\partial \bar{t}}=\bar{h}^2(\frac{\partial \bar{p}}{\partial \bar{x}})^2+\left[3\bar{p}\bar{h}(1-a)-1\right](\frac{\partial \bar{p}}{\partial \bar{x}})+\bar{p}\bar{h}^2\frac{\partial^2 \bar{p}}{\partial \bar{x}^2}+\beta^2\bar{h}^2(\frac{\partial \bar{p}}{\partial \bar{y}})^2+\beta\bar{p}\bar{h}^2\frac{\partial^2 \bar{p}}{\partial \bar{y}^2}-\frac{\bar{p}}{\bar{h}}(1-a) \qquad (20)$$

When we apply the finite differences scheme to this, we get the following form for time derivative:

$$\frac{\partial \bar{p}}{\partial \bar{t}}=\bar{h}_{i,j}^2\left(\frac{\bar{p}_{i+1,j}-\bar{p}_{i-1,j}}{2\Delta\bar{x}}\right)^2+\left[3\bar{p}_{i,j}\bar{h}_{i,j}(1-a)-1\right]\left(\frac{\bar{p}_{i+1,j}-\bar{p}_{i-1,j}}{2\Delta\bar{x}}\right)+\bar{p}_{i,j}\bar{h}_{i,j}^2\left(\frac{\bar{p}_{i+1,j}-2\bar{p}_{i,j}+\bar{p}_{i-1,j}}{\Delta\bar{x}^2}\right)$$

$$+\beta^2\bar{h}_{i,j}^2\left(\frac{\bar{p}_{i,j+1}-\bar{p}_{i,j-1}}{2\Delta\bar{y}}\right)^2+\beta^2\bar{p}_{i,j}\bar{h}_{i,j}^2\left(\frac{\bar{p}_{i,j+1}-2\bar{p}_{i,j}+\bar{p}_{i,j-1}}{\Delta\bar{y}^2}\right)^2-\frac{\bar{p}_{i,j}}{\bar{h}_{i,j}}(1-a) \qquad (21)$$

In order to solve (21) 4th order Runge-Kutta method was used. So called step-jump method [5] was applied. In this method the new pressure values are calculated after each time step and then the partial time derivatime does not depend explicitely on time. The delta-terms in Runge-Kutta method are then

$$\Delta p_1=\Delta t\frac{dp}{dt}(p_i) \qquad \Delta p_2=\Delta t\frac{dp}{dt}(p_i+\frac{1}{2}\Delta p_1)$$

$$\Delta p_3=\Delta t\frac{dp}{dt}(p_i+\frac{1}{2}\Delta p_2) \qquad \Delta p_4=\Delta t\frac{dp}{dt}(p_i+\Delta p_3) \qquad (22)$$

A computer program was written to apply this scheme in unsteady incompressible case.

3. DISCUSSION

Several computer programs were developed in order to find the pressure distributions in different cases described earlier. The programs were written in Fortran and compiled using MS-Fortran. As output the programs store in the harddrive the film thicknesses in different grid locations and the pressure values in each grid point. In order to decrease the iteration time the relaxation was utilized.

$$p_{i,j}^{new} = \lambda \cdot p_{i,j}^{new} + (1-\lambda) p_{i,j}^{old} \qquad (23)$$

,where the relaxation factor is denoted by creek lambda. Both under relaxation and over relaxation was tested.

3.1 Incompressible Case

For the steady-state incompressible case both in 1-D and 2-D were investigated. The pressure distributions for 1-D solutions with different taperings (a) are in complete in figure 1. For this case 9 different x-locations were taken as an example. In the figures on the legends on the right are shown the different taperings (A). From the curves can be concluded that the maximum pressure occurs with the tapering a= 2.2 - 2.3. This result agrees with the reference [2].

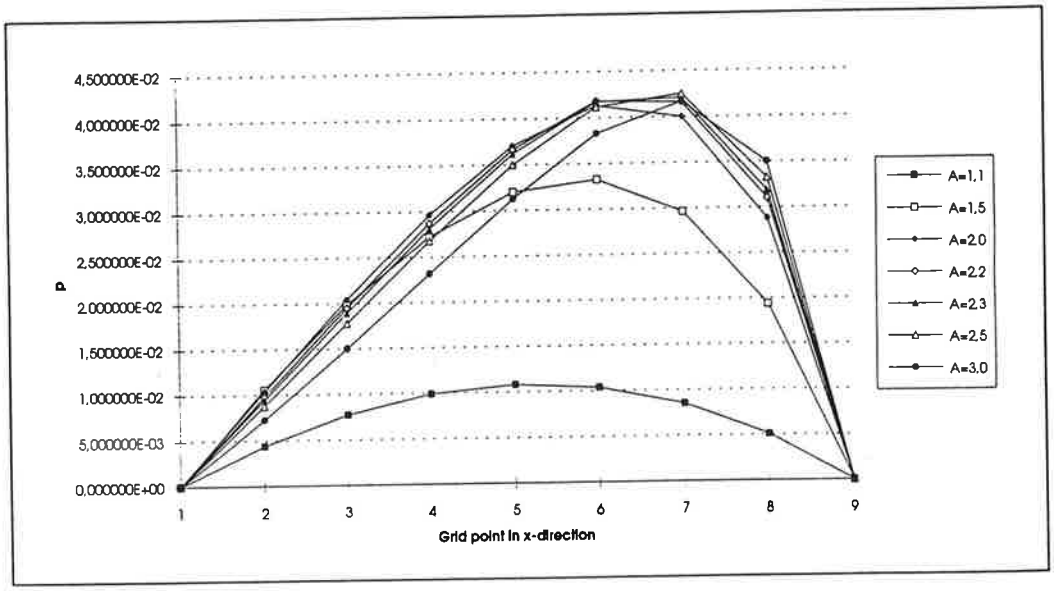

Figure 1. Pressure distributions with different taperings in 1-D.

The 2-D incompressible case the following parameters were used: grid size 9*54, tapering 2.2 and 1.5 and size factor β=0,15 (equation (11)). β was choosed this small in order to compare the results with the 1-D case. First was used overrelaxation (λ=1.5) and in the second case underrelaxation (λ=0.9). The criteria checking the

difference between the new and old pressure-value was set to 0.01. This was also later alternated.

As result the calculated load-carrying capacity (W) values between 1-D and 2-D case with these parameters showed good accuracy. In 1-D case it gave the value of $2.6707 \cdot 10^{-2}$ (fig. 2) and in 2-D case with these parameters $0.27253 \cdot 10^{-1}$. The difference in load carrying capacity values was only 2.1 %.

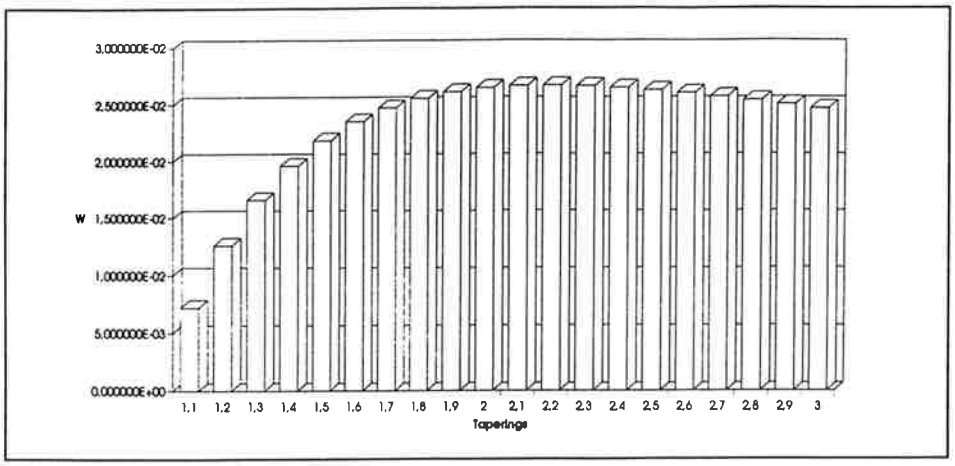

Figure 2. Load-carrying capacity with different taperings in 1-D.

The effect of relaxation factor was also tested. With λ-value of 1.5 it took 15 iteration rounds to reach the error criteria and when the factor was increased to 2.0 it reached the criterion already after 10 rounds. Only this time pressure values were also more off from the 1-D solution. With underrelaxation λ=0.9, 30 iteration rounds were needed to reach the error criterion.

If we compare the curves in fig. 1 (with a=2.2) with the curve corresponding to that in fig. 3, we recognize that the shape of the curve matches and the peak values are in both cases between 4.0 - $4.5 \cdot 10^{-2}$. Same type of phenomena can be noticed, if the fig. 4 and the fig. 1 with a=1.5 are compared. Now the dimensionless pressure peak value in both cases lies between 3.0 - $3.5 \cdot 10^{-2}$.

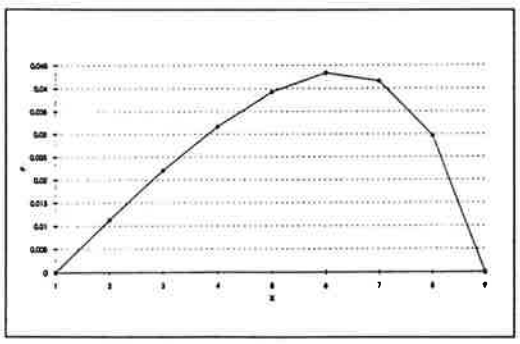

Figure 3. Pressure distribution of a slider bearing in incompressible case.

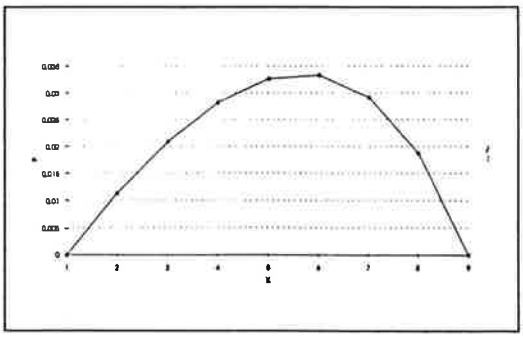

Figure 4. Pressure distribution in 2-D with tapering a=1.5.

3.2 Compressible Case

Figure 6 is achieved using the same parameters as in the figure 5 (A=2.2, λ=1.5, initial pressure values = 1.0). The results show the fact that in the compressible case (fig. 6) the peak value is slightly smaller than in incompressible case (fig. 5), only 1%. This result agrees with reference [2]. In addition the fact that the peak value moves a little to the right in compressible case is also recognizeable. This is mentioned in reference [2], too.

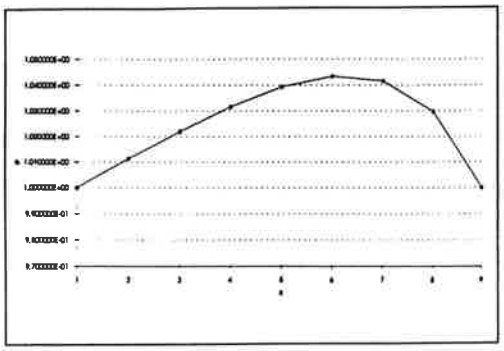

Figure 5. Pressure distribution in 2-D in incompressible case with tapering a=2.2.

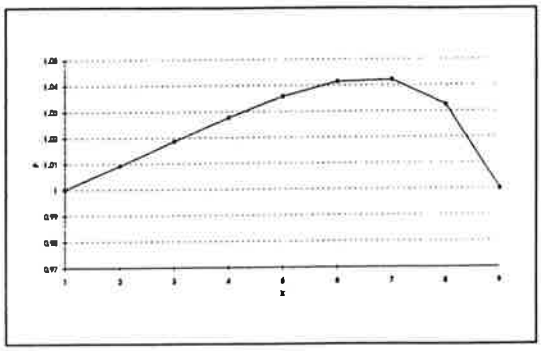

Figure 6. Pressure distribution in 2-D in in compressible case with tapering a=2.2.

3.3 Unsteady Compressible Case

The program developed for this case is not finished. The mathematical model is derived earlier in this paper, but in the time the paper had to be turned in, the computer program was not completed. The results from this part will be discussed in further similar occasions.

4. REFERENCES

[1] M.K. Jain, Numerical Solutions of Differential Equations, 2nd ed. A Halsted Press Book, John Wiley & Sons, New Delhi, 1984, 698 p.

[2] O. Pinkus, Theory of Hydrodynamic Lubrication, McGraw-Hill Book Co., York, PA, 1961, 465 p.

[3] M.C. Shaw, E.F. Macks, Analysis and Lubrication of Bearings, McGraw-Hill Book Co., York, PA, 1949, 617 p.

[4] D.D. Fuller, Theory and Practice of Lubrication for Engineers, 2nd ed., John Wiley & Sons, New York, 1984, 682 p.

[5] I. Etsion, I. Green, Dynamic Analysis of a Cantilever-Mounted Gas-Lubricated Thrust Bearing, Journal of Lubrication Technology, January 1981, vol.103, p. 157 -163.

[6] N. Tipei, Theory of Lubrication. With Applications to Liquid- and Gas-Film lubrication. Stanford University Press, Stanford, California, 1962. 566 p.

[7] B.J. Hamrock, Fundamentals of Fluid Film Lubrication. NASA, Reference Publication 1255, August 1991, 635 p.

[8] J.A. Walowit, J.N. Anno, Modern Developments in Lubrication Mechanics. John Wiley & Sons, New York-Toronto 1975, 244 p.

NUMERICAL SIMULATION OF NON-ISOTHERMAL FLOW OF POLYMER MELT IN A SINGLE-SCREW EXTRUDER

SEPPO SYRJÄLÄ AND REIJO KARVINEN
Tampere University of Technology / Thermal Engineering
P.O. Box 589, FIN-33101 Tampere, FINLAND

ABSTRACT

This paper deals with the numerical simulation of polymer flow in melt conveying zone of single-screw extruder. The mathematical model used in the simulation is based on general conservation equations of mass, momentum and energy. The rheological behaviour of polymer melt is described by the power-law viscosity model. The temperature dependence of the viscosity and the heat generation due to viscous dissipation are also incorporated in the model. The governing equations are solved using the general purpose fluid dynamics program FIDAP, which is based on finite-element method. Numerical results for three-dimensional simulation are presented in terms of the velocity, pressure, temperature and volume flow rate.

1. INTRODUCTION

Extrusion is one of the most widely used manufacturing processes in plastics industry. The most common type of extruder in use today is the single-screw version, schematically shown in Fig. 1, in which the raw material is fed into a hopper and is forced through the passage between a rotating screw and a stationary barrel. The processed material comes out through a die of a specified shape. Typically, the single-screw extruder can be divided in three zones, namely the solid conveying zone, the melting zone and the melt conveying zone, as illustrated in Fig. 1. The throughput, i.e., the volume flow rate of the polymer out of the die, depends on all of these zones, but is usually mainly controlled by the melt conveying zone.

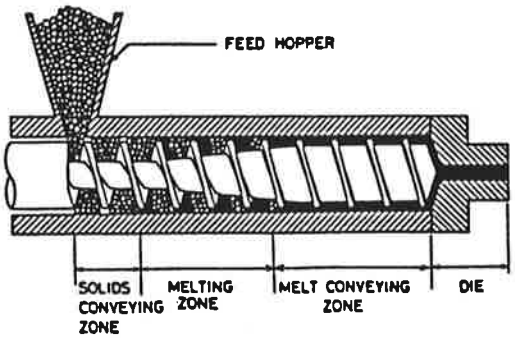

FIGURE 1. Schematic view of single-screw extruder.

The melt conveying portion of the extruder acts as a simple pump. Forward motion occurs as a result of the rotation of the screw and the helical configuration of the screw flight. If the extruder simply discharges the fluid at its downstream end from an unrestricted outlet, there would be no mechanism by which a pressure would build up in the screw channel, i.e. the pressure at the outlet equals the pressure at the inlet. In most actual extrusion operations there is, however, a shaping die of some kind at the outlet of the extruder. Consequently, in order to make it possible to overcome the flow resistance of polymer melt in the die, the production of pressure in the extruder barrel by the screw is necessary. Namely, a pressure rise in the extruder barrel must of course be equal to a pressure drop in the die. The pressure at the downstream end of the extruder is often referred to as a back pressure.

A typical overall operational diagram for a certain combination of the screw and the die is given in Fig. 2, showing the screw characteristic (i.e., the relationship of pressure rise to volume flow rate for an extruder) and the die characteristic (i.e., the relationship of pressure drop to volume flow rate for a die). As a result of intersection of screw and die characteristics, as indicated by point A in Fig. 2, the point of operation of the screw and die combination is obtained. This operation point determines the throughput and the back pressure of an extruder. If a smaller die is substituted, i.e. the flow resistance in the die is increased, the operation point is changed, as illustrated by point B in Fig. 2. Normally, the change in throughput is, however, relatively small since the screw characteristic is typically rather flat in the practical operational range. It may be summarized that the process of extrusion is the result of cooperation of the screw and the die so that the throughput of the extruder depends to a considerable extent on the screw.

The flow in screw channels has been the subject of many investigations during the past three decades. Presented analyses range from simple isothermal, Newtonian fluid-based ones to complex numerical procedures that include most important features of the process, like non-isothermal effects and non-Newtonian behaviour of polymer melt. Several reviews about the various simulation approaches for the polymer flow in single-screw extruders are available [1,2,3,4].

The objective of this study to present a three-dimensional simulation for the flow of polymer in a single-screw extruder. The analysis in this paper is restricted to the melt conveying zone only, i.e., it is assumed that the preceding solid conveying and melting zones transport and melt sufficient material so that the throughput of an extruder is controlled by the melt conveying characteristics and that there is no pressure build-up before the melt conveying zone. The theoretical background of the present simulation is in general conservation equations of mass, momentum and energy, coupled with the appropriate relation for the rheological behaviour of polymer melt. The governing equations are solved numerically by means of finite-element method using the fluid dynamics analysis package FIDAP.

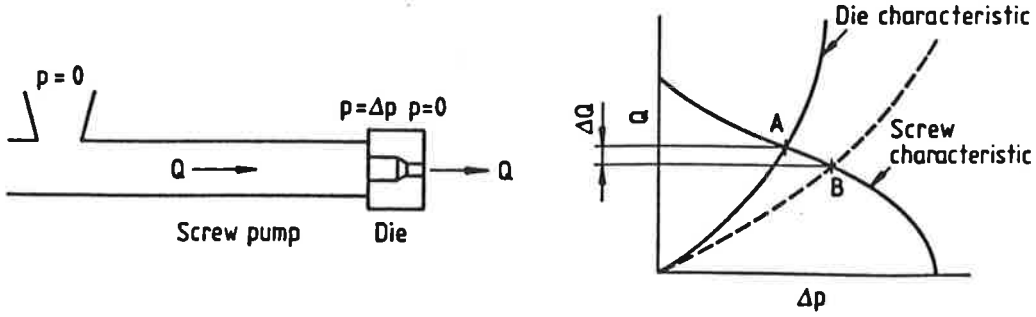

FIGURE 2. Combination of screw and die.

2. PROBLEM DESCRIPTION AND SIMPLIFYING ASSUMPTIONS

Due to helical geometry of the extruder screw and relative motions of the barrel and screw, the flow pattern of the polymer melt in the screw channel is quite complex and may be described as a "helix within a helix". Furthermore, the general set of conservation equations coupled with the constitutive relation describing the rheological behaviour of polymer melt is very complicated. Accordingly, in order to make it possible to solve this flow problem, several simplifying assumptions regarding the flow geometry, the fluid properties and the flow phenomena during the process, are required. Assumptions made in this study, and virtually in all corresponding studies, are given below in a consecutive manner. The validity of these assumptions is not discussed here, but comprehensive discussions may be found in the literature [1,2,3,4].

1) The flow is time independent

2) The fluid, i.e. the polymer melt, can be considered as incompressible.

3) The fluid can be considered as purely viscous (i.e., the viscoelastic effects are negligible)

4) The creeping flow approximation is applicable (i.e., the inertia forces resulting from acceleration of the fluid are negligible in comparison with the viscous and pressure forces)

5) The barrel can be considered to be moving with respect to a stationary screw

6) The curvature effects of the flow channel are negligible

7) The flight clearance and the consequent leakage flow is negligible

The assumption 5 and 6 mean that the actual helical channel along the rotating screw can be considered, in the theoretical analysis, as unwound to a straight rectangular channel with an infinite plate (the barrel) moving on top of the channel at constant velocity of V_b ($=\pi ND$) at an angle θ (equal to the helix angle) to the down-channel direction, as illustrated in Fig. 3. The symbols of most essential screw channel parameters are also identified in Fig. 3. The screw shown in Fig. 3 is double-flighted, i.e. there is two flow channels in parallel.

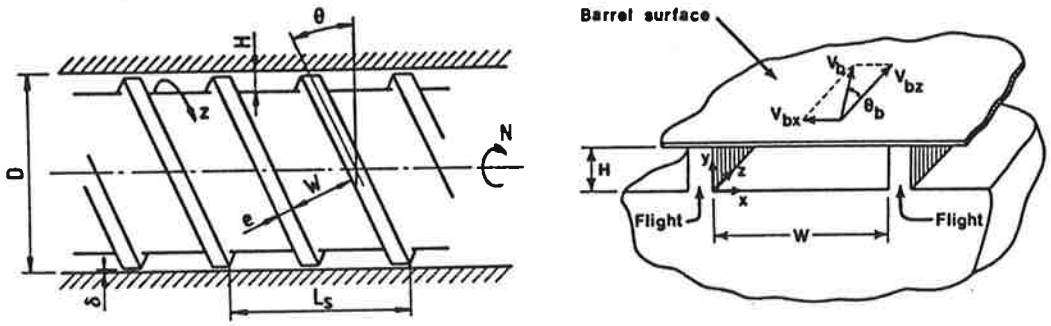

FIGURE 3. Schematic representation of the actual helical geometry and the analyzed straight unwound geometry of the screw channel. The screw channel parameters are as follows: D is the barrel diameter, H is the channel depth, W is the channel width, i.e the perpendicular distance between the flights, e is the flight width, δ is the flight clearance, i.e. the radial gap between the flight and the barrel, θ is the helix angle, N is the rotational speed of the screw, L_s is the lead of the screw, i.e. the axial distance advanced by one full rotation of the screw, V_b is the barrel velocity and V_{bx} and V_{bz} are the components of the barrel velocity in the cross-channel and down-channel directions, respectively.

3. GOVERNING EQUATIONS AND SOLUTION METHOD

Adopting the rectangular coordinate system shown in Fig. 3 and following the assumptions stated above, the equations that govern the flow of polymer melt in the channel of single-screw extruder are as follows:

Conservation of mass

$$\frac{\partial u}{\partial x}+\frac{\partial v}{\partial y}+\frac{\partial w}{\partial z}=0 \tag{1}$$

Consevation of momentum

$$\frac{\partial}{\partial x}\left(\eta\frac{\partial u}{\partial x}\right)+\frac{\partial}{\partial y}\left(\eta\frac{\partial u}{\partial y}\right)+\frac{\partial}{\partial z}\left(\eta\frac{\partial u}{\partial z}\right)=\frac{\partial p}{\partial x} \tag{2}$$

$$\frac{\partial}{\partial x}\left(\eta\frac{\partial v}{\partial x}\right)+\frac{\partial}{\partial y}\left(\eta\frac{\partial v}{\partial y}\right)+\frac{\partial}{\partial z}\left(\eta\frac{\partial v}{\partial z}\right)=\frac{\partial p}{\partial y} \tag{3}$$

$$\frac{\partial}{\partial x}\left(\eta\frac{\partial w}{\partial x}\right)+\frac{\partial}{\partial y}\left(\eta\frac{\partial w}{\partial y}\right)+\frac{\partial}{\partial z}\left(\eta\frac{\partial w}{\partial z}\right)=\frac{\partial p}{\partial z} \tag{4}$$

Conservation of energy

$$\rho C_p\left(u\frac{\partial T}{\partial x}+v\frac{\partial T}{\partial y}+w\frac{\partial T}{\partial z}\right)=\frac{\partial}{\partial x}\left(k\frac{\partial T}{\partial x}\right)+\frac{\partial}{\partial y}\left(k\frac{\partial T}{\partial y}\right)+\frac{\partial}{\partial z}\left(k\frac{\partial T}{\partial z}\right)+\eta\dot{\gamma}^2 \tag{5}$$

Here u, v and w are the velocity components in the x, y and z directions, respectively, p is the pressure, T is the temperature, η is the viscosity, ρ is the density, C_p is the specific heat, k is the thermal conductivity, and $\dot{\gamma}$ is the shear rate. Density, specific heat and thermal conductivity may, in general, depend on the temperature, but in the present study they are assumed to be temperature independent. The term $\eta\dot{\gamma}^2$ represents the heat generation due to viscous dissipation.

In the case of polymer melt the viscosity is dependent on the shear rate and usually also on the temperature. Therefore, the set of equations (2-5) must be closed with an expression that relates the viscosity to the shear rate and temperature. In this study the shear rate dependence of the viscosity is described by the power-law model

$$\eta = m\dot{\gamma}^{n-1} \tag{6}$$

where m is the consistency factor and n is the power-law index. The temperature dependence of the viscosity is entered through the consistency factor by an exponential-type of expression

$$m = Be^{-\alpha(T-T_o)} \tag{7}$$

where B and α are empirical constants and T_0 is a reference temperature. In the present case of three-dimensional velocity field the shear rate is defined as

$$\dot{\gamma} = \left[2\left(\frac{\partial u}{\partial x}\right)^2+2\left(\frac{\partial v}{\partial y}\right)^2+2\left(\frac{\partial w}{\partial z}\right)^2+\left(\frac{\partial u}{\partial y}+\frac{\partial v}{\partial x}\right)^2+\left(\frac{\partial w}{\partial y}+\frac{\partial v}{\partial z}\right)^2+\left(\frac{\partial w}{\partial x}+\frac{\partial u}{\partial z}\right)^2\right]^{1/2} \tag{8}$$

The following boundary conditions are applied in the present analysis:

Inlet: $p = 0;\ T = T_{in}$

Outlet: $p = \Delta p$

Barrel surface: $u = V_{bx} = V_b \sin\theta;\ v = 0;\ w = V_{bz} = V_b \cos\theta;\ T = T_b$

Screw surface: $u = v = w = 0;\ \frac{\partial T}{\partial n} = 0$

The boundary conditions for the velocity components at the inlet and outlet are not specified due to the fact that they are not known a priori. Actually the velocity distributions depend largely on the pack pressure, Δp. Therefore the assumption of fully developed flow is made at the inlet and outlet. The boundary conditions imposed for the temperature correspond the situation of constant barrel surface temperature and adiabatic screw surface.

The above set of governing conservation equations with the viscosity model and boundary conditions is still quite complicated despite the simplifying assumptions made. The equations are nonlinear and, in addition, the equations of momentum and energy are coupled through the temperature dependence of viscosity and viscous heat generation.

The numerical solution of the above partial differential equations is obtained by means of finite-element method using a commercially available fluid dynamics program FIDAP [6,7], which is produced by Fluid Dynamics International (FDI). In FIDAP the equations are discretized through the Galerkin formulation, which results in a set of nonlinear algebraic equations. In the present study these equations are solved in a simultaneous coupled manner using the Picard iteration method in conjunction with the direct Gaussian-type elimination for the system of linear equations. As generally known, the Newton-type methods usually offer more rapid convergence than Picard method. However, in highly nonlinear and strongly coupled flow cases like in this study, the convergence problems may be encountered with the Newton-type methods and Picard method is usually preferred. The three-dimensional elements used in this study are 27-node brick elements with quadratic interpolations for the velocity, pressure and temperature. It is worth noting that the equal-order interpolation for the velocity and pressure is possible in FIDAP due to the suitable pressure stabilization technique. The upwinding technique was applied to the temperature in order to obtain oscillation-free solutions at high Peclet numbers typical for polymer melts. The detailed theoretical background of FIDAP is found in [8].

4. RESULTS

As an application the simulation was performed for a double-flighted screw (see Fig. 3) with four leads and with the following values of parameters:

$D = 50$ mm; $H = 4.5$ mm; $W = 18$ mm; $N = 60$ rpm; $\theta = 17^{\circ}$; $T_{in} = 120^{\circ}C$; $T_b = 200^{\circ}C$.

The material properties used are (correspond a typical low-density polyethylene):

$n = 0.5$; $B = 50$ kPa s^n; $\alpha = 0.01\ 1/^{\circ}C$; $k = 0.25$ W/m°C, $C_p = 2.5$ kJ/kg°C; $\rho = 800$ kg/m^3; $T_o = 115^{\circ}C$.

The finite-element mesh used in the calculations is shown in Fig. 4. The mesh consists of 420 elements and 4675 nodal points. The calculations were carried out for six different values of back pressure, i.e., $\Delta p = 0$, 5, 10, 20, 30 and 40 MPa. The obtained pressure distributions along the screw channel for the cases of $\Delta p = 10$, 20, 30 and 40 MPa are shown in Fig. 5.

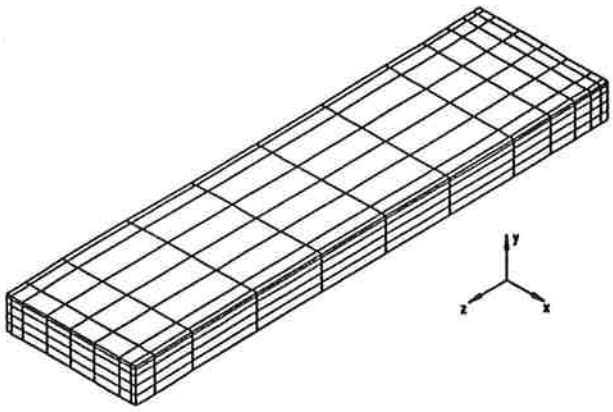

FIGURE 4. FE-mesh used in the calculations (ten times enlarged in the x and y directions).

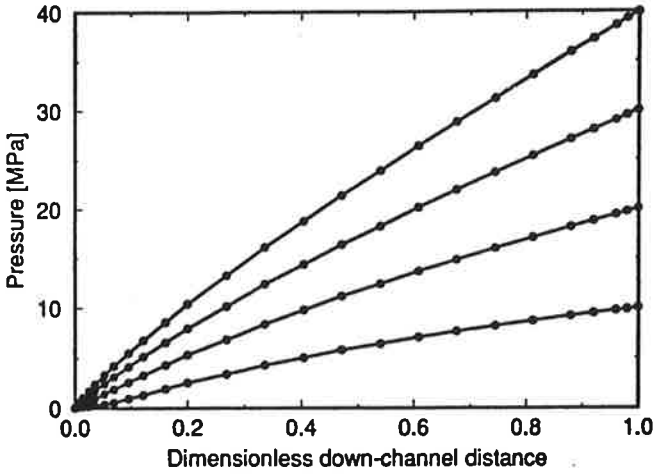

FIGURE 5. Pressure distrubutions along the screw channel for Δp = 10, 20, 30 and 40 MPa.

The temperature development along the mid-plane (x = W/2) of the screw channel is shown in Fig. 6 for different values of back pressure, Δp. The results indicate substantial temperature rise due to viscous heating especially at high values of Δp. Examples of the down-channel and cross-channel velocity profiles at the mid-plane of the channel are given in Fig. 7 for different values of Δp. It can be seen that the cross-channel velocity, u, is only slightly affected by the back pressure, whereas the influence of Δp for the down-channel velocity is clear, as can be expected. The volume flow rates for different values of Δp were calculated by integrating the down-channel velocity profiles across the cross-sectional area of the channel and are shown in Fig. 8. In order to demonstrate the overall operation of the current screw with a specified die, volume flow rate versus pressure drop data was calculated for an annular die (shown as solid lines in Fig. 8), using the following approximative relation for the isothermal annular flow of power-law fluid [5]

$$Q = \pi R_o^3 \left(\frac{R_o}{2m}\frac{\Delta p}{L}\right)^{1/n} \frac{(1-\kappa)^{(2n+1)/2}}{(2n+1)/n}\left(\frac{1+\kappa}{2}\right) \tag{9}$$

Here L is the lenght of the die, R_o is the outer radius of the annular geometry and $\kappa = R_i/R_o$, where R_i is the inner radius. The values of outer and inner radius used in the calculations were: R_o = 15 mm and R_i = 13 mm. Three different lenghts of the die was considered, i.e., L = 25, 50, 75, 100 and 125 mm. The viscosity parameters were the same as those used above at T = 200°C.

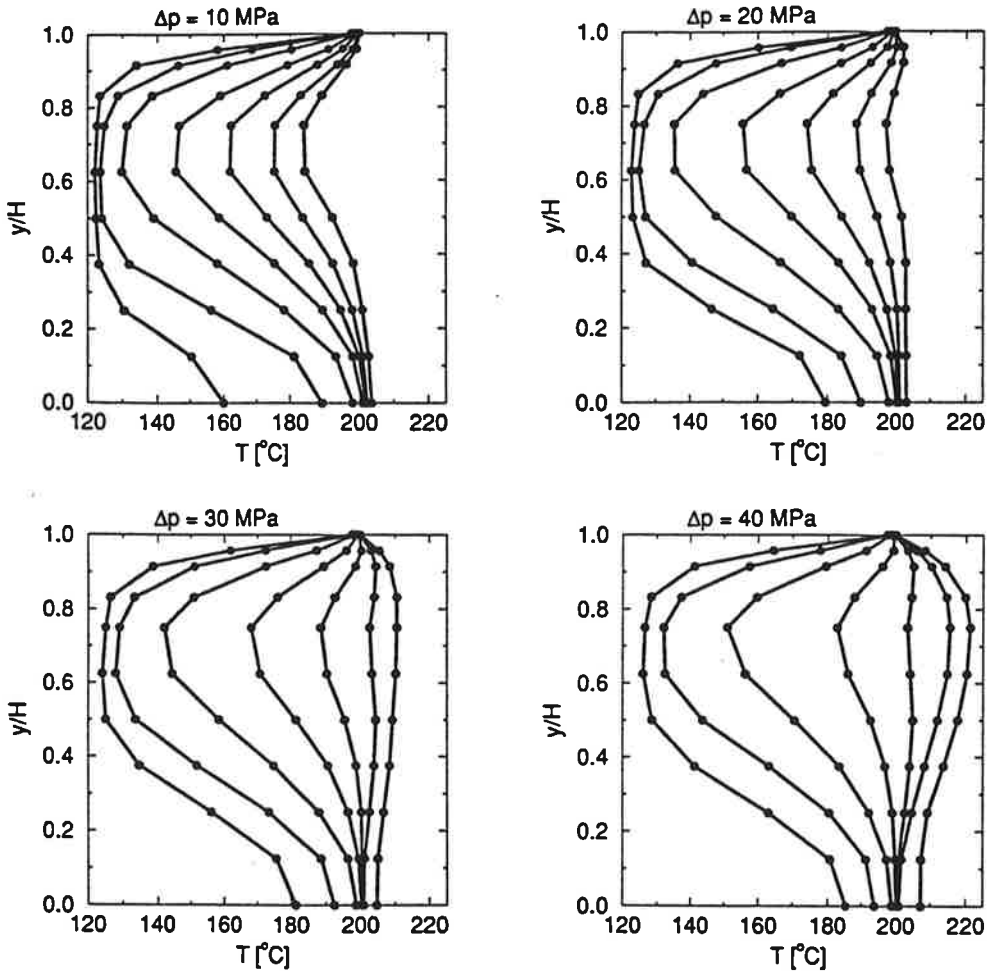

FIGURE 6. Temperature development along the mid-plane (x = W/2) of the screw channel for Δp = 10, 20, 30 and 40 MPa. The results are presented at locations ζ = 0.05, 0.1, 0.2, 0.4, 0.6, 0.8 and 1.0, where ζ is the dimensionless down-channel distance (i.e. the actual distance divided by the total lenght of the helical screw channel).

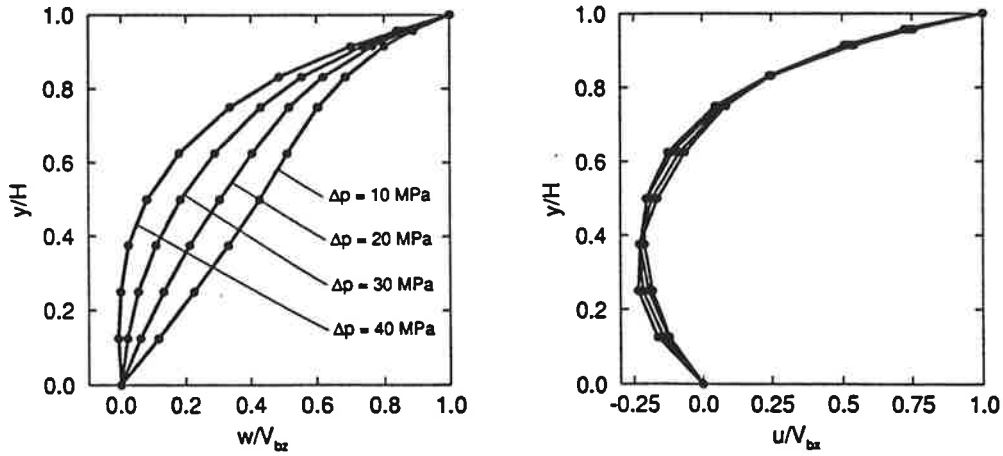

FIGURE 7. Down-channel and cross-channel velocity profiles at the mid-plane of the channel at location ζ = 0.5 for Δp = 10, 20, 30 and 40 MPa.

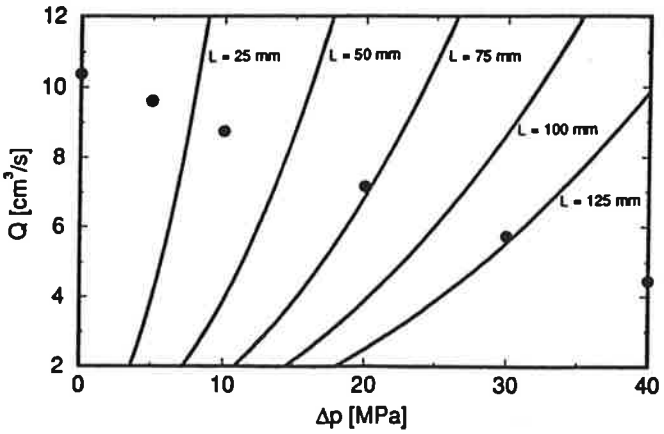

FIGURE 8. Volume flow rate data for a screw and for an annular die.

The simulations reported in this study have been run on a CONVEX C3840 located at the Centre for Scientific Computing (CSC) in Espoo. The simulations required 7-10 iterations per run to limit the relative change in the solution between iterations below 0.005 and the consequent execution time was 40-50 CPU minutes. The total storage of the problem was about 42 megabytes.

5. CONCLUSIONS

A numerical simulation of fully three-dimensional, non-isothermal flow of polymer melt in single-screw extruder has been accomplished. The simulation predicts the velocity, pressure and temperature fields for a given screw geometry, screw speed and material parameters. Furthermore, the volume flow rate in the screw channel can be related to the back pressure.

A three-dimensional finite-element flow simulation with the fully coupled solution method is expensive in terms of computer time and memory. Therefore, it might be more feasible approach to use the segregated solution method in order to reduce the storage requirements and the execution time. The segregated algorithm is available also in FIDAP, but it was not used in this study.

REFERENCES

1. R.T. Fenner, Developments in the analysis of steady screw extrusion of polymers, *Polymer*, 617-635, **18**, 1977.

2. Z. Tadmor & C.G. Gogos, *Principles of Polymer Processing*, John Wiley & Sons, 1979.

3. C. Rauwendaal, *Polymer Extrusion*, Hanser Publishers, 1986.

4. J.F. Stevenson, Extrusion of rubber and polymers, in *Comprehensive Polymer Science*, Volume 7, 303-354, Pergamon Press, 1989.

5. R.B. Bird, R.C. Armstrong & O. Hassager, *Dynamics of Polymeric Liquids*, John Wiley & Sons, 1987.

6. M.S. Engelman, FIDAP, a fluid dynamics analysis package, *Advances in Engineering Software*, **4**, 163-166, 1982.

7. *FIDAP 7.0 Users Manual*, Fluid Dynamics International Inc., 1993.

8. *FIDAP 7.0 Theory Manual*, Fluid Dynamics International Inc., 1993

PROPERTIES OF DISLOCATIONS IN METALS

J. VON BOEHM[1] AND R.M. NIEMINEN[2]
[1]Laboratory of Computational Dynamics, Helsinki University of Technology, 02150 Espoo, FINLAND
[2]Laboratory of Physics, Helsinki University of Technology, 02150 Espoo, FINLAND

ABSTRACT

The atomic arrangements and fast mass transport are studied in the [112] partial dislocation pair in Au and Cu using the canonical molecular dynamics and many-body interactions. The arrangements around the partial dislocations are found to be quite regular and relatively independent on the many-body interaction model used or the material (Au or Cu) studied. Fast mass transport along partial dislocations is found to be of vacancy-type.

1. INTRODUCTION

Dislocations play a central role in many of the basic phenomena of metals like in plastic deformation, in mass transport as fast diffusion channels or in propagation of cracks under applied force. A thorough understanding of these phenomena rests ultimately on knowledge of the atomic arrangements and movements around dislocations. For example, the (isotropic) elasticity theory gives for the total energy stored per unit length of a straight dislocation the following expression:

$$w_t = \frac{Kb^2}{4\pi}\ln\left(\frac{R}{r_0}\right) + w_0 \qquad (1)$$

where the first term on the right-hand side is the strain energy of the linear elastic field per unit length, K is a constant (energy factor), b is the magnitude of the Burgers vector, R is the outer radius of a circular cylinder within which the energy is evaluated (the dislocation line being the axis of that cylinder), r_0 is the core radius, and w_0 is the core energy per unit dislocation length [1]. When r_0 approaches zero the first term on the right-hand side diverges. This artifact is due to the neglect of the discrete atomic structure. Since there are no experimental methods one could use to measure directly these atomic arrangements or movements the only direct approach existing presently is atomistic simulation [1].

In a typical simulation (called molecular dynamics (MD)) several thousand interacting atoms move along their classical trajectories. During the last ten years both the MD methods

and the description of the interactions between the atoms have improved dramatically. For example, at present there exist well-founded MD methods to perform constant-pressure [2], constant-temperature [3,4] and constant-temperature-constant-pressure [2-4] simulations in addition to the traditional constant-energy simulations. Also, at present there exist good semiempirical methods [5,6] to describe the unavoidable many-body interactions between atoms which is a clear improvement compared to the traditional description in terms of pairwise interactions.

In this paper we study specifically the atomic arrangements in the [112] partial dislocation pairs in gold and copper as well as fast mass transport along the dislocation pair (self-pipe-diffusion) in gold using the constant-NTV MD [3,4,7] (N, T and V stand for the number of atoms, the temperature and the volume, respectively) and the many-body ATVF [8] and glue [9] forces.

The format of this paper is as follows. The constant-NTV MD methods are shortly reviewed in § 2. The geometry and the initialization of the system of the [112] partial dislocation pair are explained in § 3. The main results of the atomic arrangements and the fast mass transport are presented in § 4. The conclusions are draw in § 5.

2. CONSTANT-NTV METHODS

Nosé's equations of motion for canonical MD can be written in real variables for a monatomic system in the form

$$\frac{d^2 \mathbf{r}_i}{dt^2} = \frac{1}{m} \mathbf{f}_i - \xi \mathbf{v}_i \tag{2}$$

$$\dot{\xi} \equiv \frac{d\xi}{dt} = \frac{1}{Q}\left(\sum_i m \mathbf{v}_i^2 - n_f k_B T\right) \tag{3}$$

where $\mathbf{r}_i$, m, $\mathbf{f}_i$ and $\mathbf{v}_i$ denote the position, mass, force and velocity of nucleus i, respectively, ξ is the friction coefficient controlling absolute temperature T, Q is the thermal inertia parameter, n_f denotes the degrees of freedom and k_B is Boltzmann's constant [10,11]. The velocity-Verlet algorithm to solve Eqs. (2) and (3) consists of the following steps [7]:

1) Given $\mathbf{r}_i(t)$, $\mathbf{v}_i(t)$ and $\mathbf{a}_i(t)$ (= acceleration $\ddot{\mathbf{r}}_i$) calculate the positions (δt is the time step)

$$\mathbf{r}_i(t + \delta t) = \mathbf{r}_i(t) + \delta t\, \mathbf{v}_i(t) + \frac{1}{2} \delta t^2\, \mathbf{a}_i(t) \quad , \tag{4}$$

2) calculate the half-step velocities

$$\mathbf{v}_i\left(t + \tfrac{1}{2}\delta t\right) = \mathbf{v}_i(t) + \tfrac{1}{2}\delta t\, \mathbf{a}_i(t) \, . \tag{5}$$

3) Using $\mathbf{r}_i(t + \delta t)$ calculate the force parts of the accelerations $\frac{1}{m}\mathbf{f}_i(t + \delta t)$.

The friction coefficient $\xi(t + \delta t)$ is calculated from Eq. (3) by using Simpson's rule:

$$\xi(t + \delta t) = \xi(t) + \frac{\delta t}{6}\left[\dot{\xi}(t) + 4\dot{\xi}\left(t + \tfrac{1}{2}\delta t\right) + \dot{\xi}(t + \delta t)\right] + O\left(\delta t^5\, \xi^{(4)}\right) \tag{6}$$

where $\xi(t)$, $\dot{\xi}(t)$ and $\dot{\xi}(t+\frac{1}{2}\delta t)$ are known but $\dot{\xi}(t+\delta t)$, depending on the velocities $v_i\,(t+\delta t)$, is unknown. (An alternative would be to use $\dot{\xi}(t)$, $\dot{\xi}(t-\delta t)$, $\xi\,(t-\delta t)$ and $2\delta t$ instead of $\dot{\xi}(t+\frac{1}{2}\delta t)$, $\dot{\xi}(t)$, $\xi(t)$ and δt, respectively.) The velocities are calculated from the equation

$$v_i\,(t+\delta t) = v_i\,(t+\tfrac{1}{2}\delta t) + \tfrac{1}{2}\delta t\left[\frac{f_i\,(t+\delta t)}{m} - \xi\,(t+\delta t)\,v_i\,(t+\delta t)\right] \tag{7}$$

or by solving for $v_i\,(t+\delta t)$ from

$$v_i\,(t+\delta t) = \left[v_i\,(t+\tfrac{1}{2}\delta t) + \tfrac{1}{2}\delta t\frac{f_i\,(t+\delta t)}{m}\right] \Big/ \left[1+\tfrac{1}{2}\delta t\,\xi\,(t+\delta t)\right]. \tag{8}$$

The velocities can be eliminated from Eqs. (3), (6) and (8) to give the following equation for the friction coefficient:

$$\xi(t+\delta t) = \frac{c_1}{\left[1+\frac{1}{2}\delta t\,\xi(t+\delta t)\right]^2} + c_2 \tag{9}$$

where the constants c_1 and c_2 are calculated from the equations

$$c_1 = \frac{\delta t\, m}{6Q}\sum_i \left[v_i\,(t+\tfrac{1}{2}\delta t) + \tfrac{1}{2}\delta t\frac{f_i\,(t+\delta t)}{m}\right]^2 \tag{10}$$

and

$$c_2 = \xi(t) + \frac{\delta t}{6}\left[\dot{\xi}(t) + 4\dot{\xi}\left(t+\tfrac{1}{2}\delta t\right)\right] - \frac{\delta t\, n_f\, k_B\, T}{6Q} \tag{11}$$

including only known quantities.

We thus get for the following step:

4) Iterate the friction coefficient $\xi(t+\delta t)$ from Eq. (9) when

$$\left|-c_1\,\delta t \Big/ \left(1+\tfrac{1}{2}\delta t\,\xi\right)^3\right| < 1 \tag{12}$$

(ξ must be larger than $-2/\delta t$) or from the inverse relation

$$\xi(t+\delta t) = \frac{2}{\delta t}\left(\sqrt{\frac{c_1}{\xi(t+\delta t) - c_2}} - 1\right) \tag{13}$$

when Eq. (12) is not valid (ξ must be larger than c_2).

Step 4) is always very rapid. As the final steps we get:

5) Calculate the velocities $\mathbf{v}_i\,(t+\delta t)$ from Eq. (8),

6) calculate the accelerations $\mathbf{a}_i\,(t+\delta t)$ from the equation (see Eq. (2)):

$$\mathbf{a}_i\,(t+\delta t) = \frac{1}{m}\mathbf{f}_i\,(t+\delta t) - \xi(t+\delta t)\,\mathbf{v}_i\,(t+\delta t)\,. \tag{14}$$

The steps 1) – 6) constitute our generalization of the velocity Verlet algorithm.

As to the interactions the traditional pair-potential approximation (PPA) has following deficiences. The Cauchy ratio C_{12}/C_{44} in PPA equals 1 whereas in reality it equals 1.5...3.7 for fcc metals. The energy ratio e_v/e_c (e_v is the vacancy formation energy, e_c is the cohesion energy/atom) in short-ranged PPA equals about 1 whereas in reality it equals 0.25...0.36 for fcc metals. To describe these and also some other properties correctly one must go beyond PPA. One practical way of doing this is to use the recently derived semiempirical many-body approximations where the total energy $\mathcal{V}$ is written in the following generic form [5,6,8,9]

$$\mathcal{V} = \frac{1}{2}\sum_{i,j=1}^{N}{}' \Phi\left(\left|\mathbf{r}_i - \mathbf{r}_j\right|\right) + \sum_{i=1}^{N} U(n_i) \tag{15}$$

where

$$n_i = \sum_{j=1}^{N}{}' \rho\left(\left|\mathbf{r}_i - \mathbf{r}_j\right|\right). \tag{16}$$

In Eqs. (15) and (16) Φ is the mainly repulsive pair-potential, U is the mainly attractive many-body potential, $'$ indicates that i = j term should be omitted in the summation, n_i is the background density at nucleus i determined by the density functions ρ of the surrounding atoms. By taking the proper derivatives of Eqs. (15) and (16) we get for the force acting on nucleus i the following expression:

$$\mathbf{f}_i = -\nabla_i \mathcal{V} = -\sum_j{}' \left\{\Phi'\left(\left|\mathbf{r}_i - \mathbf{r}_j\right|\right) + \left[U'(n_i) + U'(n_j)\right]\rho'\left(\left|\mathbf{r}_i - \mathbf{r}_j\right|\right)\right\} \frac{\mathbf{r}_i - \mathbf{r}_j}{\left|\mathbf{r}_i - \mathbf{r}_j\right|} \tag{17}$$

where $'$ in Φ, U and ρ denotes a derivative with respect to the argument. We have performed simulations with the ATVF-model [8] for Au and Cu and with the glue model [9] for Au.

3. [112] PARTIAL DISLOCATION PAIR

The fcc crystal structure is shown in Fig. 1. The [112] edge dislocation (z-axis) can be formed energetically most easily because the corresponding Burgers vector $\mathbf{b} = a\,\mathbf{u}_x/\sqrt{2}$ has the smallest possible length and thus minimizes the stored energy proportional to b^2 (Eq. (1)). The $(11\bar{1})$ plane is most densely packed and acts as the glide-plane. However, since $\mathbf{b}$ contains two atomic planes, it can be further divided into two partial Burgers vectors $\mathbf{b}_1$ and $\mathbf{b}_2$:

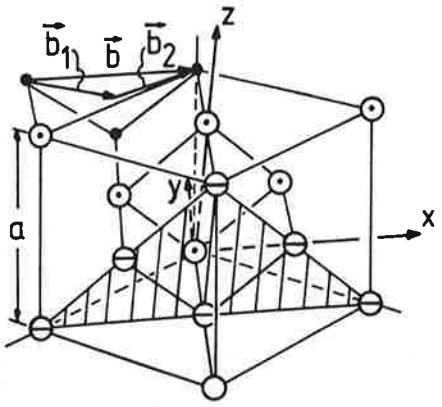

FIGURE 1. Face-centered cubic crystal structure. a denotes the lattice constant and **b** the Burgers-vector of the perfect [112] edge dislocation. $\mathbf{b}_1$ and $\mathbf{b}_2$ denote the partial Burgers-vectors. The circles with a bar represent atoms in the $(11\bar{1})$ glide-plane (shaded). The circles with a dot represent atoms in the $(11\bar{1})$-plane which contains the edges of the partial dislocations. The small filled circles represent atoms behind this plane. The open circle represents an atom in the $(11\bar{1})$-plane in front of the glide plane.

$$\mathbf{b} = \mathbf{b}_1 + \mathbf{b}_2 = \left(a\,\mathbf{u}_x/\sqrt{2} - a\,\mathbf{u}_y/\sqrt{6}\right)/2 + \left(a\,\mathbf{u}_x/\sqrt{2} + a\,\mathbf{u}_y/\sqrt{6}\right)/2 \ . \tag{18}$$

Since

$$b^2 > b_1^2 + b_2^2 \tag{19}$$

the edge dislocation containing two half-planes has a tendency to separate into two partial dislocations containing one half-plane each.

The starting geometry was prepared as follows [12]. The half-planes I and II were removed (see Fig. 1) and the half-plane III was moved by $-\mathbf{b}/2$. Then the atoms were displaced using the isotropic elasticity theory [1].

In all cases we used a rectangular geometry with periodic boundaries with the period of $1.5\cdot\sqrt{6}a$ containing 18 atom planes in the [112]-direction (z-axis in Fig. 1). The $(1\bar{1}0)$ and $(11\bar{1})$ surfaces were fixed (thickness of the fixed layer 8-10 Å).

4. RESULTS

The Au system consisting of 4683 movable and 3324 fixed atoms was allowed to relax. This was accomplished by using constant-NTV MD at T = 1 K, i.e. by solving Eqs. (2) and (3) using the modified velocity Verlet method above with $\delta t = 2.5$ fs. The top view of the middle and left part of the relaxed system obtained with the ATVF model is shown in Fig. 2. The distance of 38 Å is in a good agreement with the value 40 Å that can be estimated by using the isotropic elasticity theory [1]. The crystal is quite regular near the edge of the partial dislocation. A more detailed description of the atomic arrangements around the left partial dislocation obtained for Au with the ATVF model (Fig. 2) and with the glue model is given in [13]. The preliminary structure for Cu obtained with the ATVF model and displayed in Fig. 3 is also qualitatively very similar to the structures for Au.

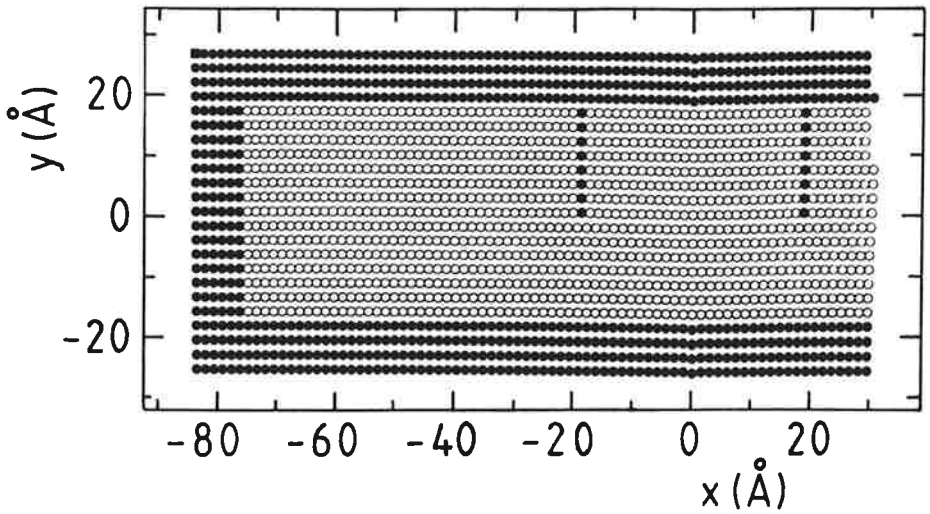

FIGURE 2. Top view of the relaxed Au system. The filled circles represent the fixed boundary atoms and the two half-planes of the partial dislocation pair.

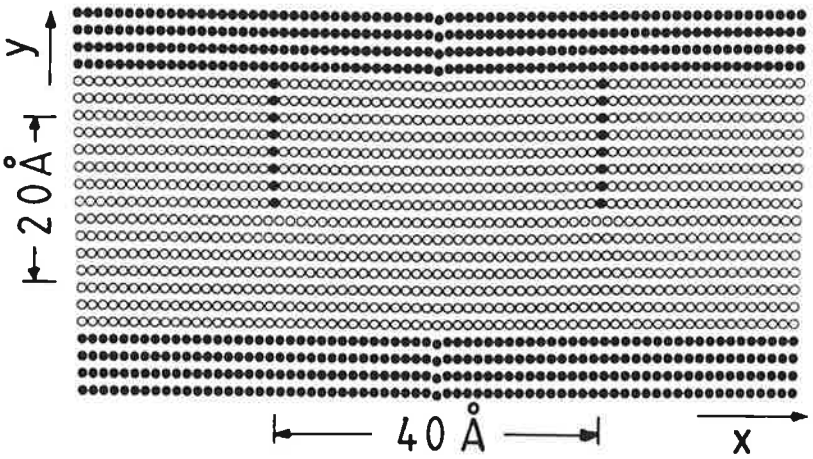

FIGURE 3. Top view of the relaxed Cu system. For further information see the caption of Fig. 2.

As to the fast mass transport along the partial dislocations the vacancy and interstitial formation energies at the edge of the partial dislocation ($E_f(v)$ and $E_f(i)$, respectively) for Au are obtained by performing constant-NTV MD at T = 1 K with the ATVF model for $N \mp 1$ particles and calculating the appropriate energy differences from the equation

$$\Delta\mathcal{V} = \mathcal{V}(N \mp 1) - (N \mp 1)\mathcal{V}(N)/N \tag{20}$$

including now all relaxations ($N = 8007$, number of movable atoms = 4683 ∓ 1). As the result we get $E_f(v) = 1.4\,eV$ and $E_f(i) = 2.7\,eV$. The formation energy difference $E_f(i) - E_f(v) = 1.3$ eV is thus significantly reduced from the value in the crystal: $E_f^{cr}(i) - E_f^{cr}(v) = 4.35\,eV - 0.96\,eV = 3.39$ eV [8].

We calculate directly the net mass transport induced by one vacancy or one interstitial. In our calculations either one atom is removed from each partial dislocation edge or one atom is added in front of each dislocation edge. The (one) vacancy and (one) interstitial diffusion constants are then calculated from the equations

$$D_v = \frac{1}{2}(D(N-2) - D(N)) \quad , \tag{21}$$

$$D_i = \frac{1}{2}(D(N+2) - D(N)) \tag{22}$$

where

$$D(N) = \lim_{t \to \infty} \frac{1}{6t} \sum_{i=1}^{N} \left(\mathbf{r}_i(t) - \mathbf{r}_i(0)\right)^2 \quad . \tag{23}$$

The calculations of ~ 1.5 ns each give the results shown in Fig. 4, presented as $\ln(D_v/D_0)$ and $\ln(D_i/D_0)$ versus $(k_BT)^{-1}$. The diffusion induced by one interstitial is 3 - 16 times as large as that induced by one vacancy. The reason for the anomalously low value of D_i (1400 K) is not clear to us but may be related to the fact that the initial configuration used at 1400 K had a significantly longer equilibration time than the initial configurations at 1150 and 1300 K. Another possibility would be that the diffusion induced by the interstitial penetrates to regions of low migration (e.g. bulk crystal; this behaviour was found in [14] for vacancies). Least squares fits to the Arrhenius law (the two lines in Fig. 4) give for the vacancy and interstitial migration energies the values $E_m(v) = 0.75\,eV$ and $E_m(i) = -0.14\,eV$, respectively. The value of $E_m(i)$ is unphysical but clearly indicates that $E_m(i)$ is very small. Nevertheless, although $E_m(i) - E_m(v) \approx -0.75\,eV$, $\Delta E_f = E_f(i) - E_f(v) = 1.3\,eV$ which makes the activation energy for interstitial self-diffusion about 0.5 eV larger than for the vacancy mechanism. Thus ΔE_f does not decrease enough at the dislocation line compared to the bulk to make the interstitial-type diffusion competitive with the vacancy-type diffusion. In this respect our result for Au differs from the MD result in PPA for Cu [14,15].

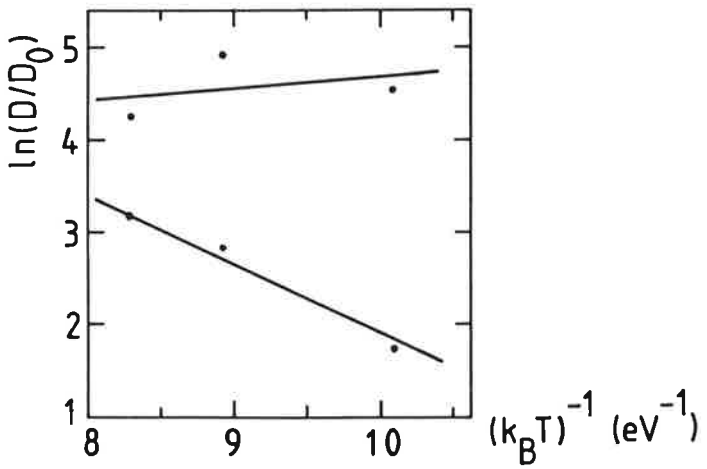

FIGURE 4. $\ln(D_v/D_0)$ (lower data points) and $\ln(D_i/D_0)$ (upper data points) versus $(k_BT)^{-1}$ where $D_0 = 4.68 \cdot 10^{-7}\,cm^2/s$. Diffusion is simulated at 1150, 1300 and 1400 K.

5. CONCLUSIONS

The atomic arrangements around the [112] partial dislocations are found to be quite regular and qualitatively similar for Au and Cu. Also the arrangements are relatively independent on the specific many-body interaction model used. Fast mass transport along the [112] partial dislocation pairs is found to be more vacancy-type than interstitial-type.

REFERENCES

1. C. Teodosiu, "Elastic Models of Crystal Defects", Springer-Verlag, 1982
2. H.C. Andersen, J. Chem. Phys. **72**, (1980) 2384
3. S. Nosé, J. Chem. Phys. **81**, (1984) 511
4. S. Nosé, Mol. Phys. **52**, (1984) 255
5. M.S. Daw and M.I. Baskes, Phys. Rev. **B29**, (1984) 6443
6. M.S. Daw, Phys. Rev. **B39**, (1989) 7441
7. J. von Boehm and R.M. Nieminen, in "Computational Physics", A. Tenner (Ed.) World Scientific, Singapore, 1991, 27
8. G.J. Ackland, G. Tichy, V. Vitek and M.W. Finnis, Phil. Mag. **A56**, (1987) 735
9. F. Ercolessi, M. Parrinello and E. Tosatti, Phil. Mag. **A58**, (1988) 213
10. W.G. Hoover, Phys. Rev. **A31**, (1985) 1695
11. D.J. Evans and B.L. Holian, J. Chem. Phys. **83**, (1985) 4069
12. R.M.J. Cotterill and M. Doyama, Phys. Rev. **145**, (1966) 465
13. J. von Boehm and R.M. Nieminen, Phys. Scr. **T33**, (1990) 216
14. J. Huang, M. Meyer and V. Pontikis, Phil. Mag. **A63**, (1991) 1149
15. J. Huang, M. Meyer and V. Pontikis, Phys. Rev. Lett. **63**, (1989) 628

CALCULATION OF FROST HEAVE USING A THERMOMECHANICAL MODEL. ONE-DIMENSIONAL CASE

J. HARTIKAINEN and M. MIKKOLA
Laboratory of Structural Mechanics
Helsinki University of Technology
Rakentajanaukio 4 A, 02150 Espoo, FINLAND

ABSTRACT

A mathematical model for the freezing of saturated soil is considered. The model is based on the basic principles of continuum mechanics and of macroscopic thermodynamics. Saturated soil is treated as a mixture of skeleton, water and ice. The model is capable of describing the cryogenic suction, the water and heat transport and the frost heave. The computer implementation of the model is carried out for the one-dimensional case. Some numerical results are presented and comparisons with experimental findings are made.

1. INTRODUCTION

Freezing soil is a multicomponent system containing mineral particles of the soil skeleton, water in its three phases: liquid water, ice and vapour, and air. The unfrozen water exists as free water and as fixed water adsorbed to the mineral particles as thin films. The free water in the pores migrates under the action of the pore water pressure and of the gravitational force, while the fixed water is strongly attached to the soil particles moving and deforming with them. The frost-susceptibility of a soil depends mainly on the grain size distribution and the permeability of the soil and on the availability of water flowing to the freezing zone.

The relevant processes in the frost phenomenon are: 1) suction and freezing of water at the water layer between ice lens and soil particles, 2) water migration from the water table to the freezing part of the soil, and 3) heat transfer process due to convection (latent heat). It has been experimentally shown that the soil contains liquid water at temperatures well below 0° C [4]. Further, it has been observed that the phase change from water to ice creates a strong depression of water, the cryogenic suction, which draws free water towards the freezing zone. The cryosuction has been explained by the decrease of the chemical potential (the Gibbs free enthalpy) of water which takes place at the phase change [4]. The flow of water in a partially frozen soil occurs in the thin layer between ice lens and soil particles.

Frémond and Mikkola [1] have presented a mathematical model of the freezing of saturated

soil based on the principles of continuum mechanics and of macroscopic thermodynamics. In their model the saturated soil is considered as a mixture of three constituents: skeleton, liquid water and ice. The constitutive equations of the porous medium are derived by the application of the method of the accompanying local equilibrium state (see e.g. [2]) choosing appropriate expressions of the free energy and of the dissipation potential. In the present paper, the one-dimensional formulation of the general model is considered and its computer implementation is described. Some preliminary numerical results are presented.

2. BASIC CONCEPTS AND NOTATIONS

A completely saturated soil is considered. The unfrozen soil is a mixture of skeleton and liquid water, and the frozen soil a mixture of skeleton, water and ice. The volume fractions of the constituents are $\beta^k, k \in \{s,w,i\}$(skeleton, water, ice), which satisfy the obvious conditions

$$\beta^s + \beta^w + \beta^i = 1, \beta^s \geq 0, \beta^w \geq 0, \beta^i \geq 0 \tag{1}$$

Introducing the porosity n and the relative amount of water χ the volume fractions can be presented in the form

$$\beta^s = 1-n, \beta^w = \chi n, \beta^i = \chi(1-n) \tag{2}$$

The densities of the constituents ρ^k are taken as constants. The velocities of the particles are denoted by $\vec{U}^k$. The relative velocity of water with respect to skeleton is $\vec{V}^w = \vec{U}^w - \vec{U}^s$. The material time derivative of a quantity f following the constituent k is denoted

$$\frac{\mathrm{d}^{(k)} f}{\mathrm{d}t} = \frac{\partial f}{\partial t} + \nabla f \cdot \vec{U}^k \tag{3}$$

3. THERMOMECHANICAL MODEL

The derivation of the model has been presented in detail by Frémond and Mikkola [1]. It is based on the balance laws of mass, momentum and energy and on the entropy inequality. A brief description of the model is given here.

The conservation of mass for the soil is

$$\theta^s = 0, \theta^w + \theta^i = 0 \tag{4}$$

where θ^k means the rate of production of the constituent k

$$\theta^k = \frac{\partial}{\partial t}\left(\rho^k \beta^k\right) + \nabla \cdot \left(\rho^k \beta^k \vec{U}^k\right) \tag{5}$$

The balance of linear momentum is

$$\vec{m}^s + \vec{m}^w + \vec{m}^i = \vec{0} \tag{6}$$

where $\bar{m}^k$ is the rate of production of the linear momentum

$$\bar{m}^k = -\nabla\cdot\sigma^k - \bar{f}^k + \rho^k\beta^k\frac{\mathrm{d}^{(k)}\bar{U}^k}{\mathrm{d}t} + \theta^k\bar{U}^k \tag{7}$$

σ^k is the stress tensor of constituent k. The total stress acting on a surface element with unit normal $\bar{n}$ is $(\sigma^s+\sigma^w+\sigma^i)\cdot\bar{n}$. In the application to the soil freezing, the inertia terms in expression (7) are neglected. The balance of energy is

$$l^s + l^w + l^i = 0 \tag{8}$$

The rate of production of energy is, neglecting the contribution of the kinetic energy,

$$l^k = \frac{\mathrm{d}^{(k)}e^k}{\mathrm{d}t} + e^k\nabla\cdot\bar{U}^k - \sigma^k : D\left(\bar{U}^k\right) + \bar{m}^k\cdot\bar{U}^k + \nabla\cdot\bar{q}^k - r^k \tag{9}$$

Above, e^k is the internal energy per unit volume, D the tensor of the rate of strain, $\bar{q}^k$ the heat flux from the body to the exterior, and r^k the rate of heat production inside the body. According to the second principle of thermodynamics, the rate of entropy production must be non-negative

$$T(\gamma^s+\gamma^w+\gamma^i) \geq 0 \tag{10}$$

The rate of production of entropy γ^k can be brought into the form

$$T\gamma^k = \sigma^k : D\left(\bar{U}^k\right) - \left[\frac{\mathrm{d}^{(k)}\Psi^k}{\mathrm{d}t} + s^k\frac{\mathrm{d}^{(k)}T^k}{\mathrm{d}t}\right] - \Psi^k\nabla\cdot\bar{U}^k - \bar{m}^k\cdot\bar{U}^k - \frac{\bar{q}^k\cdot\nabla T}{T} + l^k \tag{11}$$

In the expression above, the free energy $\Psi = e - Ts$ has been employed. s is the entropy per unit volume. In the expression of dissipation (10), it is required that both the mechanical and thermal parts are separately non-negative.

In paper [1], it has been shown that, with an appropriate choice of the expressions of the free energies of the constituents and of the potentials of the mechanical and thermal dissipations, the equations of state and the complementary constitutive equations of the freezing soil can be derived. In particular, the choice of free energies

$$\begin{aligned}
\Psi^s &= \beta^s\left\{-\rho^s C_s T\ln\left(\frac{T}{T_0}\right) + \frac{1}{2}K_s(\varepsilon^s_{ii})^2 + \mu_s\varepsilon'^s_{ij}\varepsilon'^s_{ij}\right\} \\
\Psi^w &= \rho^w\beta^w\left\{-C_w T\ln\left(\frac{T}{T_0}\right) - \frac{L(T-T_0)}{T_0} + \frac{\ell T}{T_0}f(\beta^s,\beta^w,\beta^i)\right\} \\
\Psi^i &= \beta^i\left\{-\rho^i C_i T\ln\left(\frac{T}{T_0}\right) + \frac{1}{2}K_i(\varepsilon^i_{ii})^2\right\}
\end{aligned} \tag{12}$$

and the dissipation potentials

$$\Phi_1 = \frac{\beta^i}{p}\lambda^{1-p}(K|D'^i|)^p + \frac{1}{2}k_w\left(\rho^w\beta^w\bar{V}^w\right)^2 \text{ with } |D'^i| = \sqrt{D'^i : D'^i} \tag{13}$$

$$\Phi_2 = \frac{1}{2}k_T\bar{q}^2$$

results in the following equations of state and complementary constitutive equations

$$\sigma'^s_{ij} = \beta^s\mu_s\varepsilon'^s_{ij}, \quad \sigma'^w_{ij} = 0, \quad \sigma'^i_{ij} = \beta^i\lambda^{1-p}K^p|D'^i|^{p-2}D'^i_{ij}$$

$$p^s = \beta^s\left\{-K_s\varepsilon'_{kk} + \rho^w\beta^w\frac{\ell T}{T_0}\frac{\partial f}{\partial\beta^s} + B\right\}$$

$$p^w = \beta^w\left\{\rho^w\beta^w\frac{\ell T}{T_0}\frac{\partial f}{\partial\beta^w} + B\right\}$$

$$p^i = \beta^i\left\{-K_i\varepsilon'^i_{kk} + \rho^w\beta^w\frac{\ell T}{T_0}\frac{\partial f}{\partial\beta^i} + B\right\} \tag{14}$$

$$\beta^w V^w_k = -\frac{k}{\gamma_w}\left\{\frac{\partial}{\partial x_k}\left(\frac{p^w}{\beta^w}\right) + \frac{1}{\beta^w}f^*_k - \frac{\rho^w\ell T}{T_0}\frac{\partial f}{\partial x_k}\right\}$$

$$-(C_w - C_i)T\ln\left(\frac{T}{T_0}\right) - \frac{L(T-T_0)}{T_0} + \frac{\ell T}{T_0}\left[\frac{\partial(\beta^w f)}{\partial\beta^w} - \frac{\rho^w}{\rho^i}\frac{\partial(\beta^w f)}{\partial\beta^i}\right] + B\left(\frac{1}{\rho^w} - \frac{1}{\rho^i}\right) - \frac{K_i(\varepsilon'^i_{kk})^2}{2\rho^i} = 0$$

$$q^k_i = -\kappa_k\beta^k\frac{\partial T}{\partial x_i}, k \in \{s, w, i\}$$

The function $f(\beta^s, \beta^w, \beta^i)$ in the expression of the free energy of water describes the effect of the porous medium on the behaviour of the water. Its form is based on experiments. C_k is the heat capacity, κ_k heat conductivity, and ℓ the latent heat of fusion. Besides, there are elasticity and viscoplasticity coefficients. k is the permeability of soil and $\gamma = \rho g$ the specific weight. B is the common part of pressure in each constituent. The displacement of ice is assumed to be equal with that of skeleton. The division of the second order tensors into deviatoric and spherical parts has been used, e.g. $\sigma_{ij} = \sigma'_{ij} - p\delta_{ij}$, $p = -\sigma_{kk}/3$. $\varepsilon_{ij} = u_{(j,i)}$ and $D_{ij} = U_{(j,i)}$ are the components of strain tensor and strain rate tensor, respectively.

4. ONE-DIMENSIONAL CASE

4.1 Equations. The one-dimensional formulation of the model is considered. The quantities involved depend only on time t and z-coordinate which is directed downwards. The notation can be simplified: the displacement of the skeleton is u, which is also the displacement of ice, $U^s = \partial u / \partial t$ is the velocity of skeleton and ice, and U^w the velocity of water.

The function $f(\beta^s,\beta^w,\beta^i)$ describing the effect of porous medium to the behaviour of water is taken in the form

$$f(\beta^s,\beta^w,\beta^i)=\tilde{f}(\beta^w/(1-\beta^s))=\tilde{f}(\chi)=a\left(\frac{1}{\chi}-1\right)^2 \tag{15}$$

The system of equations (4), (6), (8) is simplified to the form

$$\begin{aligned}
&-\frac{\partial n}{\partial t}+\frac{\partial}{\partial z}[(1-n)U^s]=0\\
&\frac{\partial}{\partial z}(\chi n V^w)+\frac{\partial U^s}{\partial z}-(1-\frac{\rho^i}{\rho^w})\left\{\frac{\partial}{\partial t}[(1-\chi)n]+\frac{\partial}{\partial z}\left[(1-\chi)nU^s\right]\right\}=0\\
&\frac{\partial\sigma_z}{\partial z}=-[(\gamma^s-\gamma^w)(n_0-n)+(\gamma^i-\gamma^w)(1-\chi)n]\\
&\frac{\partial}{\partial z}\left(\kappa\frac{\partial T}{\partial z}\right)-\frac{\partial}{\partial z}\left[\rho^w n\chi(C_w T+L)U^w\right]-\frac{\partial}{\partial t}\left(CT+\rho^w n\chi L\right)=0
\end{aligned} \tag{16}$$

Similarly, the equations of state and the complementary constitutive equations (14) reduce to

$$\begin{aligned}
&\sigma_z=[(1-n)M_s+n(1-\chi)K_i]\frac{\partial u}{\partial z}+n(1-\chi)\left(\frac{3\lambda}{2}\right)^{1-p}K^p\left|\frac{\partial U^s}{\partial z}\right|^{p-1}\operatorname{sgn}\left(\frac{\partial U^s}{\partial z}\right)-\\
&\quad-\frac{p^w}{n\chi}+\frac{\rho^w\ell T}{T_0}\chi(1-\chi)\tilde{f}'(\chi)\\
&p^w=n\chi\left[B+\frac{\rho^w\ell T}{T_0}\chi\tilde{f}'(\chi)\right]\\
&n\chi V^w=-\frac{k}{\gamma^w}\frac{\partial}{\partial z}\left(\frac{p^w}{n\chi}\right)-\frac{\rho^w k\ell T}{\gamma^w T_0}\tilde{f}'(\chi)\frac{\partial\chi}{\partial z}\\
&-(C_w-C_i)T\ln\left(\frac{T}{T_0}\right)-L\frac{T-T_0}{T_0}+\frac{\ell T}{T_0}\left(\chi\tilde{f}(\chi)\right)'+\left(\frac{1}{\rho^w}-\frac{1}{\rho^i}\right)B=0
\end{aligned} \tag{17}$$

Above, M_s is the compressibility modulus of the soil, K_i the bulk modulus of ice, λ, K and p viscoplastic parameters of ice, $C=(1-n)\rho^s C_s+\chi n\rho^w C_w+(1-\chi)n\rho^i C_i$ the heat capacity of soil, $\kappa=(1-n)\kappa_s+\chi n\kappa_w+(1-\chi)n\kappa_i$ the heat conductivity of soil. The total stress, the pressure of water and the displacement are changes from the initial state. The two last of equations (17) can be recognized as generalizations of Darcy's equation and the phase change equation, respectively.

The basic unknowns in equations (16) and (17) are the temperature T, the porosity n, the relative water content χ, the water pressure p^w, the displacement u and the velocity of water U^w.

For unfrozen soil the equations are still simplified

$$-\frac{\partial n}{\partial t}+\frac{\partial}{\partial z}[(1-n)U^s]=0$$

$$\frac{\partial}{\partial z}(nV^w)+\frac{\partial U^s}{\partial z}=0$$

$$(1-n)M_s\frac{\partial u}{\partial z}-\frac{p^w}{n}=-\int_0^z(\gamma_s-\gamma_w)(n_0-n)\mathrm{d}z \tag{18}$$

$$nV^w=-\frac{k}{\gamma^w}\frac{\partial}{\partial z}\left(\frac{p^w}{n}\right)$$

$$\frac{\partial}{\partial z}\left(\kappa\frac{\partial T}{\partial z}\right)-\frac{\partial}{\partial z}\left[\rho^w n(C_wT+L)U^w\right]-\frac{\partial}{\partial t}\left(CT+\rho^w nL\right)=0$$

These five equations contain as principal unknowns the temperature, the displacement of soil, the porosity, the velocity and pressure of water.

4.2 Boundary conditions. Consider the case in which the temperature at the surface z=0 is below freezing point T_0 and the lower end z=h is kept at constant temperature above freezing. Thus, the boundary conditions for the temperature are

$$T(0,t)=\overline{T}_0(t),\quad T(h,t)=\overline{T}_1 \tag{19}$$

The displacement of the skeleton at lower end is assumed to be zero, while the surface is taken as traction free, so that the boundary conditions are

$$u(h,t)=0,\quad \sigma_z(0,t)=0 \tag{20}$$

The flow of water at the surface is zero and the pressure of water at the unfrozen end remains constant $\gamma_w h$ so that the boundary conditions are

$$(n\chi V^w)(0,t)=0,\quad p^w(h,t)=(nB)(h,t)=0 \tag{21}$$

At the freezing front between the frozen and the unfrozen zones the temperature, the displacement of soil, the porosity, the normal stress, the velocity and the pressure of water and the relative water content are continuous.

4.3 Initial conditions. It is assumed that the temperature field in initial unfrozen state is uniform

$$T(z,0) = \overline{T}_1 \tag{22}$$

The initial values of stress and pressure are zero, since they are changes with respect to the initial state. The existing stress at the initial state can be computed by equilibrium consideration

$$\sigma_{z0} = -(\gamma_s - \gamma_w)(1-n_0)z - \gamma_w z \tag{23}$$

assuming the initial distribution of the porosity to be constant n_0. The value of water pressure can be recognized in the expression of the total stress

$$p_0^w / n_0 = B_0 = \gamma_w z \tag{24}$$

The displacement at the initial state equals zero as well as the velocities

$$u(z,0) = 0, \quad U^s(z,0) = 0, \quad U^w(z,0) = 0 \tag{25}$$

Finally, the initial state being unfrozen means that the relative water content equals one χ=1.

5. COMPUTATIONS

The dicretization of the equations of the one-dimensional case has been carried out using the finite element method with respect to the spatial coordinate and of the finite difference method with respect to time. Linear shape functions were used. Near to the freezing front, where the quantities vary strongly, denser mesh was employed. Numerical results for a soil specimen, described in Fig. 1, are presented in Figs. 2 and 3 together with experimental results.

Acknowledgements. The financial support given by the National Board of Roads and Waterways is gratefully acknowledged. Thanks are also due to Mr. R. Orama, Chief Inspector, and to Prof. E. Slunga for useful discussions and advice.

REFERENCES

1. M. Frémond and M. Mikkola, Thermomechanical modelling of freezing soil, in "Ground Freezing 91", Yu Xiang and Wang Changsheng (Eds.), A. A. Balkema, Rotterdam, 1991, 17-24

2. P. Germain, Q.S. Nguyen and P. Suquet, Continuum thermodynamics, J. Appl. Mech. Trans. ASME 50, (1983) 1010-1020

3. C. Duquennoi, M. Frémond and M. Levy, Modelling of thermal soil behaviour, in "Frost in Geotechnical Engineering", H. Rathmayer (Ed.), Techn. Res. Centre of Finland, 1989, 895-915

4. P. Williams, Properties and behaviour of freezing soils, Norwegian Geotechn. Inst., Publ. 72, 1967

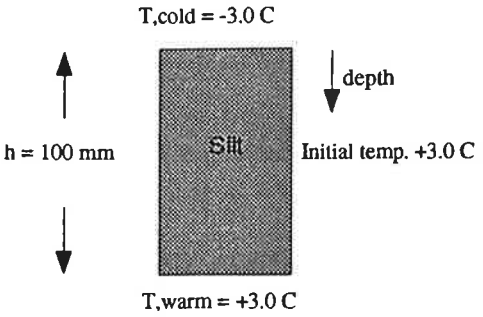

Bulk density	2726.0 kgm^{-3}
Porosity	39.0 %
Permeability	5.0 x 10^{-8} ms^{-1}
*Thermal conductivity	2.0 $Wm^{-1}K^{-1}$
*Heat capacity	900.0 $Jkg^{-1}K^{-1}$
**Unfrozen relative water cont.	
at -1.0°C	11.6 %
**Poisson's ratio	0.4
**Young's modulus	
- unfrozen	10.0 MPa
- frozen	10.0 + $Ei\beta^i$ MPa

Ei Young's modulus for pore ice 20 MPa
β^i volumetric ice content

* Average for soil solids
** Presumed for silt

Figure 1. Tested silt specimen and its physical and mechanical properties.

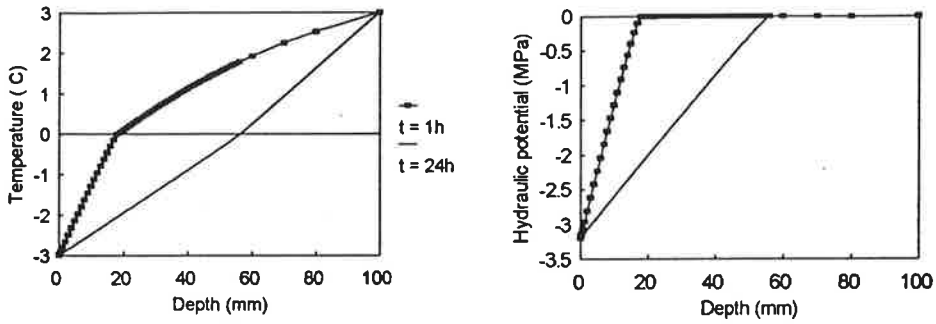

Figure 2. Computed temperature and hydraulic potential.

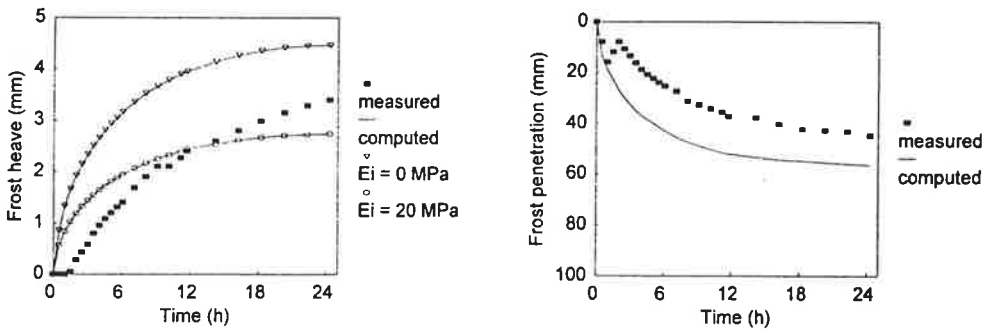

Figure 3. Computed and measured frost heave and penetration.

DETERMINATION OF VISCOELASTIC MATERIAL PARAMETERS FOR PRACTICAL USE IN TRANSIENT LOADING

MATTI TERVONEN
Engineering Mechanics Laboratory
Department of Mechanical Engineering
University of Oulu
PO Box 444, 90571 Oulu, Finland

ABSTRACT

A systematic way to find out the viscoelastic material parameters is proposed here. Practical requirements for the range of the measuring frequency and the relaxation spectrum are considered. The model parameters are found out basing on the principles of inverse problem theory and using the methods of constrained nonlinear programming. Computational and modelling selections are made automatic, building on the strategies found by performing numerical experiments with synthesized and real material data.

1. INTRODUCTION

Viscoelastic material models must often be used in transient loading conditions even for materials, which can be modelled linearly elastic in statics. Transient situations, from the material point of view, occur eg in rolling contact of cylinders covered with the so called engineering polymers. Engineering polymers include epoxies, polyesters and polypropylenes [1]. The maximum allowable strain for these materials is about 2 percent [2] which can be considered small in geometrical sense as is expressed in [11, p. 47]. For these materials, the viscoelastic model is an improvement to the commonly used elastic one, as it makes it possible, for example, to predict more accurately the energy loss and heat generation than by using, in the context of elasticity, the often guessed hysteresis loss factor. These materials, being always quite stiff, most often amorphous and cross-linked [2, 5], are the best of all polymers to be modelled as linearly viscoelastic.

The literature dealing with the viscoelasticity theory and its boundary value problems is broad, see [4,7,9,14] and the references therein, and the amount of rather new journal articles, especially on the thermoviscoelasticity, is large. However, the problem of finding out the necessary material parameters from measured data has got minor attention. Ferry [5] gives large number of measured data and interconnections between them, but not a method is presented to obtain the model parameters for a general linear material model. In [15], Vestergaard presents methods to find out nonlinear complex modulus by fitting calculated

steady state response to the measured dynamic data. Because of the steady state analysis, no attention was given for the frequency and relaxation spectra. Recently, Braat [3] described how he found out the parameters for a standard linear solid (one relaxation term). There, the loss tangent was used to fit the material model to the measured data. As it was mentioned in [3], that model can well be used for qualitative but not for quantitative calculations. The relaxation spectrum should be quite broad because of the transient state and the fact that in rolling contact problems, the loaded area is known only roughly before the analysis. Besides, the loss tangent may not be the best function to be used in a more general inverse modelling.

In this paper, a procedure based on the methods of nonlinear programming, or more generally inverse problem theory, is proposed to find out the general line-type relaxation spectrum and equilibrium modulus from the measured complex modulus. It is desired to get general strategies for, and further to automatize, as many parameter selections as possible basing on both practical simulation needs and computational requirements.

2. FOUNDATIONS AND PRACTICAL REQUIREMENTS

The material response in linear viscoelasticity can be presented in the complex modulus, in the operator (differential) or in the integral form. The Stieltjes convolution [10] is the most general of the last alternative. As it can be concluded from [4,9], a material parameter in the linear theory of viscoelasticity is completely characterized with its relaxation spectrum *N(s)* if the equilibrium modulus is included there. The general relationships between *N(s)* and the relaxation modulus *E(t)* and complex modulus E^* can be found in [9]. For a discrete, or line spectrum

$$N(s) = E_i \delta(s - \bar{s}_i)\,;\bar{s}_i = 1/\tau_i\,;i = 0\ldots\mathrm{N};\bar{s}_0 = 0$$

$$E(t) = E_0 + \sum_{i=1}^{N} E_i e^{-t/\tau_i} \tag{1}$$

$$E^*(\hat{\imath}\omega) = E_0 + \sum_{i=1}^{N} E_i \frac{(\omega\tau_i)^2}{1+(\omega\tau_i)^2} + \hat{\imath}\sum_{i=1}^{N} E_i \frac{\omega\tau_i}{1+(\omega\tau_i)^2} \equiv E_0 + \sum E_i f_i + \hat{\imath}\sum E_i g_i \equiv E'(\omega) + \hat{\imath}E''(\omega)$$

where E_0 is the equilibrium (static) modulus and the group of pairs $\{E_i,\ \tau_i\}$ forms the actual relaxation spectrum.

Incremental (differential) form, commonly used in nonlinear creeping problems is hard to use when the relaxation spectrum contains numerous terms, because the order of the equation is one more than the number of the relaxation pairs. In [13], it was shown that the integral form is powerful when the system is spatially in steady state. Complex modulus can only be used to calculate the response of a materially steady state system. It is, however, a commonly measured variable, and here we are trying to find out the material parameters using the measured complex data.

The questions that one must consider here, are: what is the band of the relaxation spectrum

needed for accurate calculations and what is the frequency range to be used in the measurements? The investigation of the base functions f_i and g_i of equations (1) and presented in figure (1) answers to the later question and give some insight to the first one.

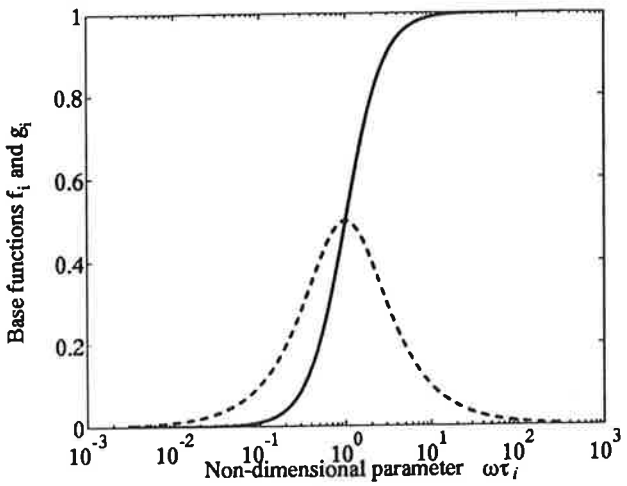

FIGURE 1. Base functions of the real (solid) and imaginary parts of the complex modulus.

If we shall have relaxation time around the point τ_0 in the spectrum, we must make measurements in the vicinity of $\omega = 1/\tau_0$. On the other hand, if the estimate for the length of the loading pulse is t_c, the relaxation terms for which $\tau \approx t_c$, have the greatest effect on the transient response. This can be predicted directly from the relaxation modulus *E(t)* (see equations (1)) or by doing simple calculations with different shapes of the loading pulse. In quasi-static response, the shape of the transient loading (including the duration) determines the width of the relaxation band needed to take completely into account the viscoelastic effects. If the loading consists of a single, smooth pulse, the needed width is about two decades below and above the centre $\tau = t_c$ as can be deduced from figure (1), from one-dimensional calculations and from the results of the rolling contact simulations done by Tervonen [13]. It is thus enough to model the material behaviour within four decades around the centre point which means that the measuring frequencies must cover the range $1/(100t_c)$ ... $100/t_c$ where t_c is the duration of the pulse. Accordingly, we can lay down bounds for the relaxation times so that all the viscoelastic effects are modelled. The relevant bounds are

$$\tau \geq \tau_{min} = 1/\omega_{max} \; ; \tau \leq \tau_{max} = 1/\omega_{min} \; . \tag{2}$$

The problem in dynamic measurements is, how to reach a frequency range that is broad enough. Usually, the system can be used to measure data over about four decades but the maximum frequency is not high enough for all practical simulations. To overcome this problem, the time-temperature equivalence (or superposition) has become a widely used practice, see eg [3,5,15]. The frequency shifting of the lower temperature data for a real material is shown in figure (2). These and many other measurements to the use of this project were done in VTT/Tampere using the DMTA equipment.

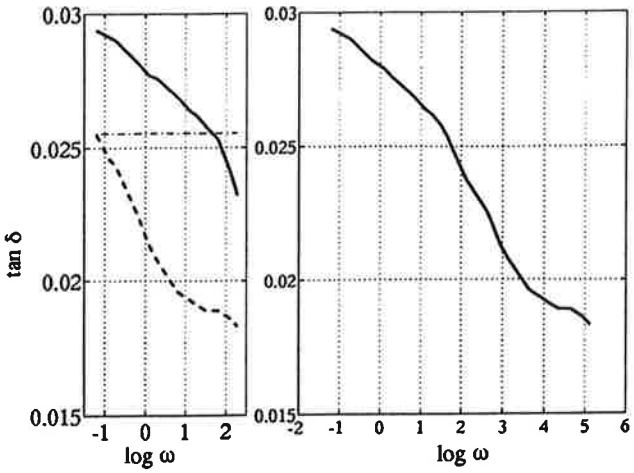

FIGURE 2. Shifting on the frequency axis according to the time-temperature equivalence.

3. DATA FITTING AND THE INVERSE PROBLEM

We are seeking the material parameters appearing in two independent functions, E' and E'' in the complex modulus form of equations (1). On physical and computational reasons, bounds must be given for the parameters. Besides the bounds in equations (2), there is a natural bound $E_i \geq 0$. On account of these facts, the problem is somewhat different from the ordinary curve fitting problem discussed for instance in [6]. Here we use the general terminology of the inverse problem theory [12]. All the material models in equations (1) could be used for the *forward modelling* and they represent *parametrizations* of the physical system. To determine numeric values for the *model parameters* $\{E_0, E_i, \tau_i\}$, we need measured data for some *observable parameters* which now are the measured values of the real and imaginary parts of the complex modulus at different measuring frequencies ω_j, or

$$\begin{aligned} \overline{E}'(\omega_j) &\equiv \overline{E}'_j \\ \overline{E}''(\omega_j) &\equiv \overline{E}''_j \end{aligned} \tag{3}$$

The model parameters are obtained with *inverse modelling*, here by using nonlinear data fitting procedure, that is, optimization methods. Loss tangent and the magnitude are the other functions of the complex data that could be used to find out the model parameters. Both parts of the modulus are used here because together they contain more information of the material than any single function. The loss tangent, for example, does not change if both parts of the complex modulus are multiplied with the same, arbitrary constant which means that we cannot obtain single-valued linear model parameters $\{E_0, E_i\}$.

Two different nonlinear optimization problems are defined and used here; the minimax (ℓ_∞) and nonlinear least squares problems. Both methods make use of the relative differences

$$Z_1(j) = \frac{E'(\omega_j)}{\overline{E}'_j} - 1$$
$$Z_2(j) = \frac{E''(\omega_j)}{\overline{E}''_j} - 1 \tag{4}$$

between the values from the forward modelling (E^* of equations (1)) and the measured (observable) data (expressions (3)). The values of Z_k at the measuring points ω_j may be arbitrarily weighted. The minimax (ℓ_∞) problem, to find the model parameters E_0, E_i and τ_i, is defined by

$$\underset{\{E_0, E_i, \tau_i\} \in \Re^{2N+1}}{\text{minimize}} \quad \max_{Z_1(j), Z_2(j)} \{|Z_1(j)|, |Z_2(j)|\}$$
$$\text{subject to} \quad \begin{cases} -\tau_i + \tau_{min} \le 0 \\ \tau_i - \tau_{max} \le 0 \\ -E_0 \le 0 \\ -E_i \le 0 \end{cases} \tag{5}$$

where $|\cdot|$ is used to mean the absolute value and N is the number of the relaxation terms. The nonlinear least squares problem reads here

$$\underset{\{E_0, E_i, \tau_i\} \in \Re^{2N+1}}{\text{minimize}} \quad \sum_{j=1}^{m} Z_1(j)^2 + \sum_{j=1}^{m} Z_2(j)^2$$
$$\text{subject to} \quad c_k(\{E_0, E_i, \tau_i\}) \le 0 \;\; ; k = 1 \ldots 3N+1 \tag{6}$$

where the constraints c_k are the same as in problem (5).

The scaling of the measured data and model parameters must be considered here because the ratio between parameters may be large. In [6], a rather thorough presentation is given on the subject. In this work, it was found that dividing the complex modulus data with the mean value of the measured real part gave good convergence results. Without scaling, numerical difficulties appeared leading frequently to a singular Hessian matrix.

The estimation of the starting point, the initial guess, is another important question. We have to decide the number of the relaxation terms, the value of the equilibrium modulus and the relaxation pairs. Because the measurements are commonly carried out using logarithmically spacing frequencies, the relaxation pairs were situated logarithmically on that axis. The minimum measured value of the real part has been used as the initial value for the static modulus. The coefficients E_i for the initial spectrum were obtained dividing by N the difference between maximum and minimum measured value of the real part.

The minimization problems (5) and (6) were solved using the optimization toolbox of the MATLAB-system [8]. MINIMAX and CONSTR functions were used, both allowing constraint optimization. They are basing on sequential quadratic programming with the BFGS update of the Hessian matrix, see [6,8] and the appropriate scripts in the optimization toolbox for details. The control function was constructed so that most parameters have built-in default values. They include the initial guess, the constraints, the termination criteria and scaling. Negligible small relaxations terms are omitted and nearby terms, having nearly the same relaxation times, are joined automatically, see also chapter 4. Last mentioned operations are crucial if we shall compute the inverse of the relaxation modulus, because small or nearby terms cause numerical difficulties in the inverse process. The inversion itself is not considered in this paper.

4. RESULTS AND DISCUSSION

Formulations (5) and (6) with appropriate computer implementations of the modelling problem have been tested with synthesized and real material data. The gradients were calculated analytically and by using finite differences.

4.1 Tests with synthesized data. The methods were tested and the effects of various algorithmic parameters were examined using synthesized data for the complex modulus. Here, we can also demonstrate how the excess relaxation terms conjoin and how we can discard some negligible terms. The synthesized material is characterized exactly with E_0 = 2 GPa, E_1 = 0.25 GPa, E_2=0.50 GPa, $\tau_1 = 3 \cdot 10^{-4}$ sec. and $\tau_2 = 5 \cdot 10^{-3}$ sec. The fitting is performed at the frequency range ω=100 - 100 00 rad/s using different starting points. The system was insensitive to the initial guess if there were enough terms. The results in table 1 show that the fit is practically exact. The physically inappropriate term E_4=$-3.94 \cdot 10^{-8}$ is within the constraint tolerance. The computation required 220 function evaluations when using the finite difference gradients and 23 evaluations plus gradient calculations with the analytic Jacobian. The total time was a little bit shorter with the numerical derivatives.

TABLE 1. The results after the minimax-procedure for the synthesized material given above and fitted to 20 logarithmically placed values.

i	Initial guess		Result		Final result	
	τ_i	E_i	τ_i	E_i	τ_i	E_i
0		$2.100\ 10^9$		$2.000\ 10^9$		$2.000\ 10^9$
1	$1 \cdot 10^{-2}$	$1.565 \cdot 10^8$	$5.0003 \cdot 10^{-3}$	$4.7012 \cdot 10^8$	$4.9978 \cdot 10^{-3}$	$5.0000 \cdot 10^8$
2	$2.154 \cdot 10^{-3}$	- " -	$4.9953 \cdot 10^{-3}$	$2.9883 \cdot 10^7$		
3	$4.642 \cdot 10^{-4}$	- " -	$3.0000 \cdot 10^{-4}$	$2.5000 \cdot 10^8$	$3.0000 \cdot 10^{-4}$	$2.5000 \cdot 10^8$
4	$1 \cdot 10^{-4}$	- " -	$2.198 \cdot 10^{-4}$	$-3.94 \cdot 10^{-8}$	------	------

The constrained least squares problem (6) gave practically same results as the minimax-procedure, but the latter took less iteration cycles.

4.2 Real materials. One of the real materials, the loss tangent of which is in figure (2), was modelled with different number of relaxation terms, N = 4 ...11. Results improved highly when N was changing from four to six and further slightly until the number of terms N was eight, but practically not at all beyond that. The fits in figure (3) are the best for each case in the sense that no better results were found by changing the initial point or by continuing the iteration. The number of iterations was 58 and 296 for the cases (a) and (b) of figure 3, respectively. An automatic selection, see chapter 3, for the initial point $\{E_0, E_i, \tau_i\}$ gave the results presented here.

(a)

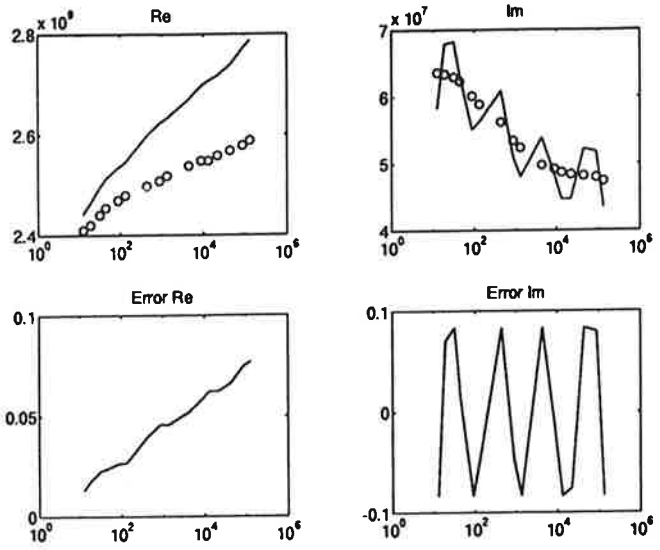

(b)

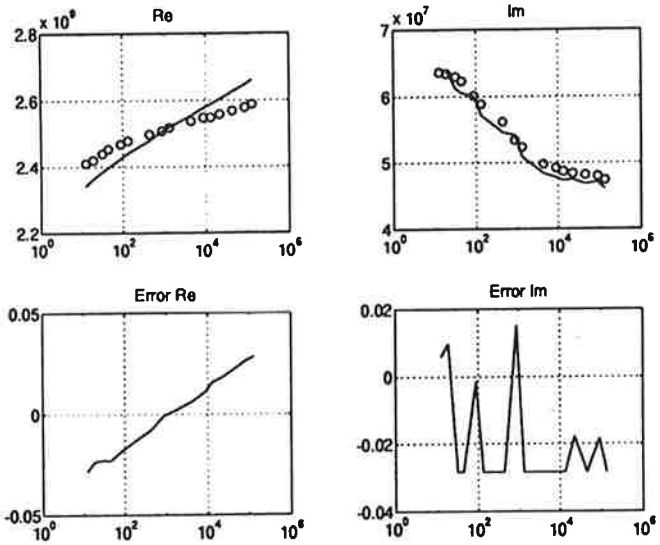

FIGURE 3. Modelling results for a real material (see figure (2)) fitted using four (a) and eight (b) relaxation terms. Measured data (o), modelled behaviour (solid line) and the relative differences between them as functions of frequency ω.

A question is, how does the relaxation spectrum alter due to those extra terms that do not better the model? The results showed that the equilibrium modulus does not change when the number of terms was six or more. This is an expected result when all the fittings were performed at the same relaxation band. From the results of figure (4), we see that negligible small and nearby terms appear when the number of terms in the initial guess is eight or higher. When we omit the small and join the nearby terms, the spectra from the models having initially eight and eleven terms are practically the same, each having finally only six different relaxation pairs. The joining was done for the terms whose relaxation times differed less than 20 percent from the mean value of them. By comparing the results we see that even if the final spectrum consists of six terms, the result is better when we have some extra terms in the initial guess.

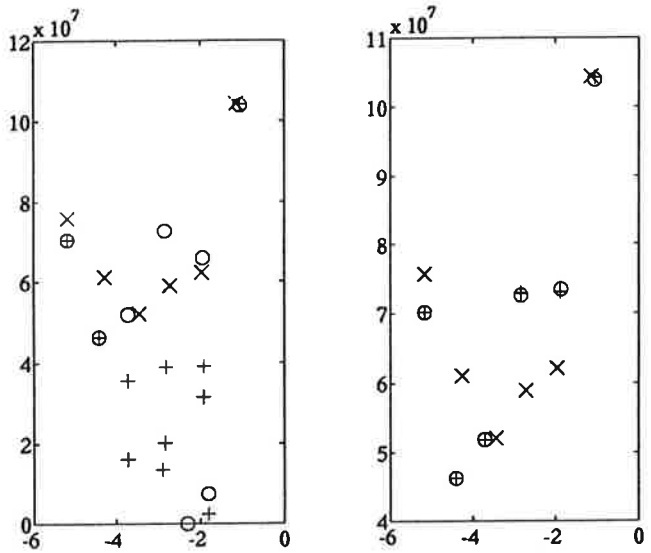

FIGURE 4. Relaxation spectra ($\log(\tau_i)$, E_i) for three different models of the real material used before: six (x), eight (o) and eleven (+) relaxation terms. Original spectra are on the left, and the spectra after omitting small and summing up the nearby terms, are on the right.

The use of a lot of terms in the starting point helps the modelling to find the best possible fit to the data and makes the modelling less sensitive to the initial guess. Computations have shown, however, that the maximum number of the relaxation pairs to be used in the initial guess is about three times the number of decades to be fitted. Numerical difficulties seem to appear after it though the system is not near the limit of underdetermination where the number of the material parameters exceeds the number of the data points. We can conclude that two to three relaxation terms are needed per decade in the initial guess. The numerical tests done here indicate also that the automatic initial guess for the spread of the spectrum is effective. The results, only a small portion of which was presented here, have shown that engineering polymers can be modelled with adequate accuracy by using the line-type relaxation spectrum. This modelling can effectively be done with strategies and methods proposed in this paper.

5. CONCLUSIONS

This paper presents how to find out the material parameters for the use of structural simulations, when the material is modelled as linearly viscoelastic and the loading is a short transient from the material point of view. It was shown that the complex modulus must be measured, perhaps by utilizing the time-temperature equivalence, over about four decades around the point where the frequency is an inverse of the load duration. Strategies are given for the automatic selection of many computational parameters, as eg the scaling and the initial guess including the number of the relaxation terms needed there. Some of the investigations done with synthesized and real data are presented as test cases. The results of these studies are the basis for the above-mentioned strategies.

REFERENCES

1. Ashby, M.F., On the Engineering properties of materials, Acra metall. 37 (1989) 1273-1293
2. Ashby, M.F., Jones, D.R.H., "Engineering Materials 2: An Introduction to Microstructures, Processing and Design", Pergamon Press, Oxford, 1988
3. Braat, G.F.M., "Theory and Experiments on Layered, Viscoelastic Cylinders in Rolling Contact", doctoral dissertation, Delft, 1993
4. Christensen, R.M., "Theory of Viscoelasticity: An Introduction", Academic Press, New York, 1982
5. Ferry, J.D., "Viscoelastic Properties of Polymers", John Wiley & Sons, Inc., New York, 1980
6. Gill, P.E., Murray, W., Wright, M.H.,"Practical Optimization", Academic Press, London, 1981
7. Golden, J.M. and Graham, G.A.C., "Boundary Value Problems in Linear Viscoelasticity ", Springer-Verlag, Berlin, 1988
8. Grace, A.,"Optimization Toolbox for use with MATLAB™; User's Guide", The Mathwoks, Inc., 1990
9. Gross, B., "Mathematical Structure of the Theories of Viscoelasticity", Hermann, Paris, 1968
10. Gurtin, M.E. and Sternberg, E., On the linear theory of elasticity, Arch. Rat. Mech. Anal. 11, (1962) 291-356
11. Lemaitre, J., Chaboche J.-L., "Mechanics of solid materials", Cambridge University Press, Cambridge, 1990
12. Tarantola, A., "Inverse Problem Theory", Elsevier, Amsterdam, 1988 (Second impression)
13. Tervonen, M., Steady State Rolling Contact of Cylinders with Viscoelastic Layers, in "Contact Mechanics: Computational Techniques", M.H. Aliabadi and C.A. Brebbia (Eds.), Computational Mechanics Publications, Southampton, 1993, 93-101
14. Tschoegl, N.W., "The Phenomenological Theory of Linear Viscoelastic Behavior", Springer-Verlag, Berlin, 1989
15. Vestergaard, B., "Identification of models for complex elastic modulus of viscoelastic materials", The Technical University of Denmark, Lungby, 1991, DCAMM report No. S 58 (in Danish)

NATURAL SYSTEM OF COORDINATES FOR ANISOTRIPIC BODY

PERTTI HOLOPAINEN
Department of Mechanical Engineering
Tampere University of Technology
P.O. Box 589, SF-33101 TAMPERE, FINLAND

ABSTRACT

The natural system of coordinates in the linear elasticity of an anisotropic body has been stated by V.V.Novozhilov (1958), but this has been presented rarely or not at all in the later professional literature. In this paper a re-examination of the natural system of coordinates is performed. In this coordinate system the number of different elastic coefficients reduces from 21 to 18. The values of elastic constants in the anisotropic body depends on the choice of the coordinate system. Only defining the natural coordinate system we can compare the elastic properties of anisotropic bodies.

PRELIMINARIES

When a material is anisotropic, linearly elastic, and deformations are small, the Hookes law in a skew curvilinear co-ordinate system is a most general form

$$\sigma^{ij} = C^{ijkl}\varepsilon_{kl}, \quad (i,j,k,l = 1,2,3) \tag{1}$$

where the σ^{ij} and ε_{kl} are components of stress tensor and deformation tensor respectively. The constants C^{ijkl} are components of materials stiffness tensor ${}^4\underline{C}$ (of fourth order). The number of its components is $3\cdot3\cdot3\cdot3 = 81$. Here the summation convention is used: The repetition of index (whether superscript or subscript) in a term will denote a summation with respect to that index over its range.

When the deformation tensor

$$\varepsilon_{kl} = \tfrac{1}{2}(u_{k|l} + u_{l|k}) \tag{2}$$

is symmetric, the summation indices in (1) can be changed, so

$$C^{ijkl} = C^{ijlk}. \tag{3}$$

When a skew infinite small element faces parallelly co-ordinate planes is in moment equilibrium, σ^{ij} is symmetric and thus

$$C^{ijkl} = C^{jikl}. \tag{4}$$

Because of (3) the number of independent components of ${}^4\underline{C}$ is 81-27=54. When the equation (4) is taken into account sufficiently, the maximum number of independent components of ${}^4\underline{C}$ is 54-18=36. When the material is linearly elastic, a strain energy density function

$$U = \tfrac{1}{2} C^{ijkl} \varepsilon_{kl} \varepsilon_{ij} \tag{5}$$

exists. But

$$\frac{\partial U}{\partial \varepsilon_{ij}} = \sigma^{ij}, \qquad \frac{\partial U}{\partial \varepsilon_{kl}} = \sigma^{kl} \tag{6}$$

and further

$$\frac{\partial^2 U}{\partial \varepsilon_{ij} \partial \varepsilon_{kl}} = C^{ijkl}, \qquad \frac{\partial^2 U}{\partial \varepsilon_{kl} \partial \varepsilon_{ij}} = C^{klij}. \tag{7}$$

When the order of differentation is immaterial, it follws from (7)

$$C^{ijkl} = C^{klij}. \tag{8}$$

When the equation (8) is taken into account sufficiently, the number of independent elastic constants is reduced to 21 as is well-known.

The strain energy density is independent of the choice of the co-ordinate system. When we known that ε_{ij} transforms tensorially, so (Table 1. Fig.1.)

TABLE 1.

	$\bar{g}_1$	$\bar{g}_2$	$\bar{g}_3$
$\bar{g}_1'$	β_1^1,	β_1^2,	β_1^2,
$\bar{g}_2'$	β_2^1,	β_2^2,	β_2^3,
$\bar{g}_3'$	β_3^1,	β_3^2,	β_3^3,

$(\bar{g}_i' = \beta_i^i, g_i)$

$(\bar{g}_i = \beta_i^{i'} g_i')$

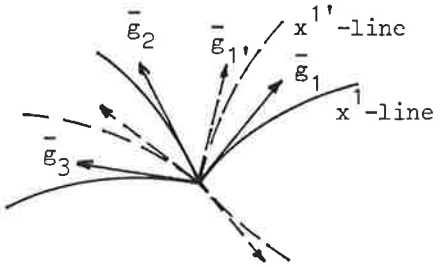

FIGURE 1.

$$\varepsilon_{ij} = \beta_i^{i'}\beta_j^{j'}\varepsilon_{i'j'}. \tag{9}$$

$$U = \tfrac{1}{2}C^{ijkl}\varepsilon_{ij}\varepsilon_{kl} = \tfrac{1}{2}C^{ijkl}\beta_i^{i'}\beta_j^{j'}\beta_k^{k'}\beta_l^{l'}\varepsilon_{i'j'}\varepsilon_{k'l'}$$

$$= \tfrac{1}{2}C^{i'j'k'l'}\varepsilon_{i'j'}\varepsilon_{k'l'} \tag{10}$$

and thus

$$C^{i'j'k'l'} = \beta_i^{i'}\beta_j^{j'}\beta_k^{k'}\beta_l^{l'}C^{ijkl}, \tag{11}$$

where

$$\beta_i^{i'} = \frac{\partial x^{i'}}{\partial x^i} \ldots \tag{12}$$

So the C^{ijkl}:s transform tensorially (11) and $^4\underline{C}$ is tensor (of fourth order).

NATURAL SYSTEM OF CO-ORDINATES

Consider the constitutive equation (1) of anisotropic material in a rectangular Cartesian co-ordinate system, when the distinction between contravariance and covariance disappears. All the indices can be subscripts (or superscripts). The constitutive equation (1) ca be written

$$\sigma_{ij} = C_{ijkl}\varepsilon_{kl}. \tag{13}$$

When σ_{ij} and ε_{ij} are symmetric and (3) and (4) are taken into account, the equation (13) can be written into matrix form

$$\begin{bmatrix}\sigma_{11}\\ \sigma_{22}\\ \sigma_{33}\\ \sigma_{23}\\ \sigma_{13}\\ \sigma_{12}\end{bmatrix} \quad \begin{bmatrix} C_{1111} & C_{1122} & C_{1133} & C_{1123} & C_{1113} & C_{1112}\\ C_{2211} & C_{2222} & C_{2233} & C_{2223} & C_{2213} & C_{2212}\\ C_{3311} & C_{3322} & C_{3333} & C_{3323} & C_{3313} & C_{3312}\\ C_{2311} & C_{2322} & C_{2333} & C_{2323} & C_{2313} & C_{2312}\\ C_{1311} & C_{1322} & C_{1333} & C_{1323} & C_{1313} & C_{1312}\\ C_{1211} & C_{1222} & C_{1233} & C_{1223} & C_{1213} & C_{1212}\end{bmatrix} \quad \begin{bmatrix}\varepsilon_{11}\\ \varepsilon_{22}\\ \varepsilon_{33}\\ 2\varepsilon_{23}\\ 2\varepsilon_{13}\\ 2\varepsilon_{12}\end{bmatrix}, \tag{14}$$

where $2\varepsilon_{ij} = \gamma_{ij}$ $(i \neq j)$ are the 'engineerin' shear strains and ε_{ij} are tensor shear strains. The order of mixed pairs of indices is chosen here so as Lekhnitskii /2/. The equation (14) can be written shortly

$$\bar{\sigma} = \bar{\bar{C}}\bar{\varepsilon} \tag{15}$$

where $\sigma_1 = \sigma_{11}$, $\sigma_2 = \sigma_{22}, \ldots$, $C_{11} = C_{1111}$, $C_{12} = C_{1122}, \ldots$ and based on

(8) the matrix $\bar{\bar{C}}$ is symmetric including 21 different elastic constants C_{ij}.

In the transformation of co-ordinates from old x_i to new $x_{i'}$, the vectors $\bar{\sigma}$ and ε transform so as

$$\sigma_{i'} = q_{i'i}\sigma_i, \quad \varepsilon_{i'} = q_{i'i}\varepsilon_i \tag{16}$$

and the matrix $\bar{\bar{C}}$

$$C_{i'j'} = q_{i'i}q_{j'j}C_{ij}, \quad (i,j = 1 \ldots 6) \tag{17}$$

$q_{i'j}$:s are not the components of rotated basevectors $\bar{i}_{i'}$, (direction cosines) $\bar{i}_i$ but their second degree homogeneous functions. So $\bar{\sigma}$, $\bar{\varepsilon}$ and $\bar{\bar{C}}$ does not transform tensorially.

It is well-known that in isotropic material the spherical defotmation

$$\varepsilon_{\underline{ii}} = \varepsilon, \quad \varepsilon_{ij} = 0, \text{ when } i \neq j \tag{18}$$

results only normal stresses

$$\sigma_{\underline{ii}} = K\varepsilon \tag{19}$$

(The notation $\varepsilon_{\underline{ii}}$, $\sigma_{\underline{ii}}$: not summed). The constant K is called the bulk modul. What stress state causes the spherical deformation (18) in anisotropic material? Substituting the spherical deformation (18) in (13) it can be obtained

$$\sigma_{ij} = C_{ijkk}\varepsilon = K_{ij}\varepsilon \tag{20}$$

The constants $K_{ij} = C_{ijkk}$ are components of the tensor of bulk modul $^2\underline{K}$ /1/. The $^2\underline{K}$ is obtainable from $^4\underline{C}$ by the contraction (german, Verjüngung, finnish, nuorentaminen) equating the idices kl → kk, and then summing.[1] The array K_{ij} is symmetric based on (4). We can see in (20) that the spherical deformation (18) causes in anisotropic material also shear stresses in rectangular Cartesian co-ordinate system with an arbitrary orientation.

But the symmetric K_{ij} has real eigenvalues λ_i and ortogonal eigenvectors $\bar{u}^{(i)}$. When the orientation of the Cartesian co-ordinate frame is parallel to eigenvectors $\bar{u}^{(i)}$ becomes the matrix of $^2\underline{K}$ diagonal

$$\bar{\bar{K}} = \lceil \lambda_1 \; \lambda_2 \; \lambda_3 \rfloor. \tag{21}$$

1) The second possible contraction gives $L_{ij} = C_{ikjk}$. The other different possibilities to contraction does not exist because of the symmetric properties of $^4\underline{C}$. The matrix of Cauchy tensor is $P_{ij}=K_{ij}-L_{ij}-\frac{1}{2}(K_1-L_1)\delta_{ij}$ where K_1 and L_1 are the first invariants of $^2\underline{K}$ and $^2\underline{L}$. The $^2\underline{P}$ gives the natural system of co-ordinates also. According to Caychy $P_{ij}=0$ always and the Poissons ratio $\nu=0{,}25$ /1/.

and thus

$$\underline{\sigma_{ii}} = \lambda_i \varepsilon. \tag{22}$$

So the spherical deformation (18) causes only normal stresses $\underline{\sigma_{ii}}$ (different values) in this special orientation of Cartesian co-ordinate system. The Cartesian co-ordinate frame whose orientation is the same as the eigenvectors of the tensor of bulk modul is called /1/ the natural co-ordinate system of anisotropic material. The directions of eigenvectors before are called the principal directions of anisotropy /1/.

When the constitutive equation (13) of anisotropic material where 21 different elastic constants are, is written in the natural co-ordinates (also C_{ijkl}:s are dependent on the orientation of co-ordinate frame (11)), become

$$C_{ijkk} = 0, \text{ when } i \neq j \tag{23}$$

without that all C_{ij11}, C_{ij22}, C_{ij33} are equal to zero. These three subsidiary conditions (23) denote that in the stiffness tensor $^4\underline{C}$ of anisotropic material has really 21-3=18 free components. When the constitutive equation (13) is transformed from the natural co-ordinate system to some other system x_i, (11) includes the components of $^4\underline{C}$ further three subsidiary conditions. When the natural co-ordinate system is defined so as presented before from the 21 elastic constants defined in some co-ordinate system experimentally, the 'fixed' elastic constants $\overset{n}{C}_{i'j'k'l'}$ are obtained by using (11). Now $\beta_{i'i} = \bar{i}_{i'} \cdot \bar{i}_i$ where $\bar{i}_{i'} = \bar{u}^{(i')}/|\bar{u}^{(i')}|$, the $\bar{i}'$:th normerad eigenvector of $^2\underline{K}$. Only the elastic constants $\overset{n}{C}_{i'j'k'l'}$ of one material are comparable to the ones of other material.

A.L.Rabinovich presents a comprehensive system of engineering constants for a fully anisotropic homogeneous body in some fixed co-ordinate system writing the constitutive equation (13) in inverted form: $\varepsilon_{ij} = D_{ijkl}\sigma_{kl}$ /2/. If the anisotropic body is non homogeneous, the elastic properties will change when going from one point to another and/or the principal directions of anisotropy will change. In anisotropic body the principal directions of $\underline{\varepsilon}$ and $\underline{\sigma}$ are different in general, i.e. when the stresses are calculated from the constitutive equation (13) or (14) written in the principal co-ordinate system of $\underline{\varepsilon}$, the principal strains results also shear stresses.

Plane stress state. The plane stress distribution is based on the assumption that

$$\sigma_{33} = \sigma_{31} = \sigma_{32} = 0 \tag{24}$$

This assumption is approximate and is used for thin flat plates loaded in the plane of the plate.

The constitutive equation (13) is written in the plane case

$$\sigma_{\alpha\beta} = C_{\alpha\beta\gamma\delta}, \quad (\alpha,\beta,\gamma,\delta = 1,2) \tag{25}$$

where the material stiffness tensor $^4\underline{C}$ has the same symmetric properties as the ones in the space stress/deformation state (3),(4) and (8). The number of different elasti constants is 6. Substituting the circle-like deformation

$$\varepsilon_{\alpha\alpha} = \varepsilon, \quad \varepsilon_{\alpha\beta} = 0, \text{ when } \alpha \neq \beta \tag{26}$$

in (25) it can be obtained

$$\sigma_{\alpha\beta} = C_{\alpha\beta\gamma\gamma}\varepsilon = K_{\alpha\beta}\varepsilon. \tag{27}$$

The $K_{\alpha\beta}$ is symmetric. By writing (27) in the principal co-ordinates of $K_{\alpha\beta}$ i.e. in the natural co-ordinate system it can be obtained

$$\sigma_{\underline{\alpha\alpha}} = \lambda_\alpha \varepsilon \tag{28}$$

where λ_α is the eigenvalue of $K_{\alpha\beta}$. In the natural co-ordinate system

$$C_{1211} + C_{1222} = 0 \tag{29}$$

which denotes that the number of free elastic constants in the plane case is 5.

REFERENCES

1. V.V.Novozhilov, Theory of Elasticity, Pergamon Press, 1961. (Translated from the 1958 Russian edition).
2. S.G.Lekhnitskii, Theory of Elasticity of an Anisotropic Body, Mir Publishers, Moscow. (Translated from the revised 1977 Russian edition).
3. Wilhelm Flügge, Tensor Analysis and Continuum Mechanics, Sprigер-Verlag, 1972.

ON HEMIVARIATIONAL INEQUALITIES AND THEIR NUMERICAL SOLUTIONS

Markku Miettinen

Department of Mathematics, University of Jyväskylä
P.O. Box 35, FIN-40351 Jyväskylä, Finland

1. INTRODUCTION

In mechanics and engineering sciences we meet problems on which constitutive laws are given by nonmonotone, multivalued relations. For example, there are mechanical problems involving such relations between reactions and displacements. The mathematical models of such kind problems lead to nonmonotone multivalued differential inclusions, the so called hemivariational inequalities. The theory of hemivariational inequalities was born only at the beginning of the last decade due to the work of Panagiotopoulos in the area of nonsmooth mechanics. He introduced the notation of a nonconvex superpotential being a generalization of the classical convex superpotential. This generalization with the notation of a generalized gradient of Clarke gave rise to hemivariational inequalities (see [8]-[14]). The aim of this paper is to present a fully discrete approximation model for hemivariational inequalities and numerical methods which can be used for solving this approximation (see more details from [3]-[6]).

The outline of this paper is as follows. In Chapter 2 we introduce the concept of hemivariational inequalities by using two examples in mechanics: an adhesive contact or a nonmonotone friction problem of a linear elastic body, nonmonotone skin friction or adhesion in plane elasticity. In Chapter 3 we present an approximation model for hemivariational inequalities, and, in Chapter 4 numerical methods for solving hemivariational inequalities.

2. APPLICATIONS OF HEMIVARIATIONAL INEQUALITIES

2.1. Adhesive contact and friction problems of a linear elastic body.

Let us denote by $\Omega \subset \mathbf{R}^3$ a bounded domain occupied by a linear elastic deformable body in its undeformed state and Γ its Lipschitz boundary. By $n = \{n_i\}$ we denote the outward unit normal vector to Γ, $\sigma = \{\sigma_{ij}\}$ the stress tensor, $\varepsilon = \{\varepsilon_{ij}\}$ the strain tensor, $S = \{S_i = \sigma_{ij} n_j\}$ the boundary force, $u = \{u_i\}$ the displacement and $f = \{f_i\}$ the volume force. Moreover, by S_T and S_N we denote the normal and tangential components of the boundary force S, respectively. In the same way, u_T and u_N are the corresponding boundary displacement components of u.

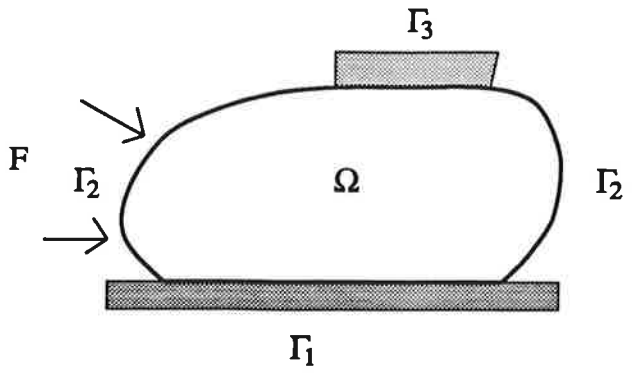

Figure 1. A linear elastic body

The boundary Γ is divided into three nonoverlapping open sets Γ_1, Γ_2 and Γ_3 such that $\Gamma = \overline{\Gamma}_1 \cup \overline{\Gamma}_2 \cup \overline{\Gamma}_3$. We assume that on Γ_1 the displacements are given, i.e.,

$$u = U, \qquad U = U(x) \text{ on } \Gamma_1.$$

For simplicity, we shall consider the homogenous boundary value problem $U = 0$ on Γ_1. The general problem ($U \neq 0$) is reduced to this by the translation $\bar{u} = u - U$. On the other hand on Γ_2 the boundary forces are given by

$$S = F, \qquad F = F(x) \text{ on } \Gamma_2. \tag{2.1}$$

On Γ_3 we have an adhesive contact boundary condition or a nonmonotone friction law:

PROBLEM (P1): We have on Γ_3 a pointwise adhesive contact condition

$$-S \in \partial j(x,u), \quad S(x), u(x) \in \mathbf{R}^3 \quad \text{on } \Gamma_3. \tag{2.2}$$

PROBLEM (P2): We have on Γ_3 a pointwise nonmonotone friction condition with given normal force

$$\begin{aligned} -S_T &\in \partial j_T(x,u_T), \quad S_T(x), u_T(x) \in \mathbf{R}^3 \quad \text{on } \Gamma_3; \\ S_N &= F_N, \quad F_N = F_N(x) \in \mathbf{R} \quad \text{on } \Gamma_3. \end{aligned} \tag{2.3}$$

The function $j\colon \Omega \times \mathbf{R}^3 \to \mathbf{R}$ satisfies the following conditions:

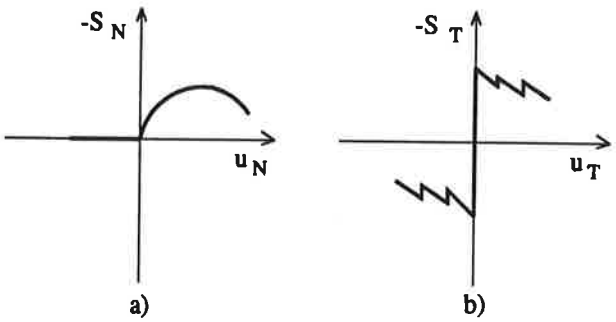

Figure 2. Nonmonotone boundary laws

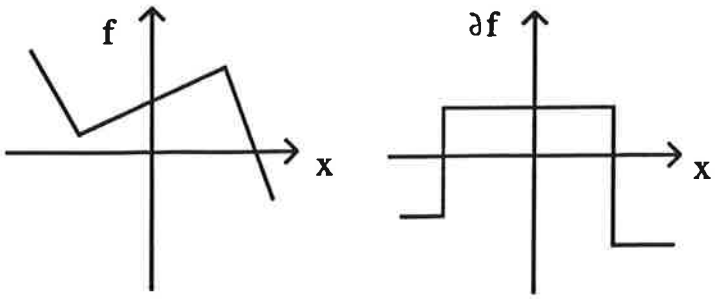

Figure 3. An example of a generalized gradient

(i) For all $\xi \in \mathbf{R}^3$ the function $x \mapsto j(x,\xi)$ is measurable on Ω.
(ii) For almost all $x \in \Omega$ the function $\xi \mapsto j(x,\xi)$ is locally Lipschitz on $\mathbf{R}^3$.
(iii) The function $j(\cdot,0)$ is finitely integrable in Ω.
(iv) For almost all $x \in \Omega$ and each $\xi \in \mathbf{R}^3$ $\eta \in \partial j(x,\xi) \implies |\eta| \le c(1+|\xi|)$ for some constant $c \ge 0$ not depending on $x \in \Omega$.
(v) It holds $j^\circ(x,\xi,-\xi) \le \alpha(x)(1+|\xi|)$ for some nonnegative function $\alpha \in L^2(\Omega)$.

Let us define what is meant by $\partial j(x,\xi)$:

DEFINITION 2.1. *Let $f\colon \mathbf{R}^M \to \mathbf{R}$ be a locally Lipschitz at $x \in \mathbf{R}^M$ and let $y \in \mathbf{R}^M$. The directional differential in the sense of Clarke of f at x in the direction y, denoted by $f^\circ(x,y)$, is defined by the relation*

$$f^\circ(x,y) = \limsup_{h \to 0+,\, z \to 0} \frac{f(x+z+hy) - f(x+z)}{h},$$

and the generalized gradient $\partial f(x)\colon \mathbf{R}^M \to \mathbf{R}^M$ by means of

$$\partial f(x) = \{y \in \mathbf{R}^M : f^\circ(x,z) \ge (y,z)_{\mathbf{R}^M} \ \forall z \in \mathbf{R}^M\}.$$

Let us derive the hemivariational inequality describing our elastic system. The equilibrium equation of the system is

$$\sigma_{ij,j} + f_i = 0 \qquad \text{in } \Omega. \tag{2.4}$$

Assuming that the displacements u are small, we have the following relation to the strain tensor ε:

$$\varepsilon_{ij} = \tfrac{1}{2}(u_{i,j} + u_{j,i}). \tag{2.5}$$

Because the material in Ω is assumed to be linear elastic, we have

$$\sigma_{ij} = C_{ijhk}\varepsilon_{hk}, \tag{2.6}$$

where $C = \{C_{ijhk}\}$, $C_{ijhk} \in L^\infty(\Omega)$, is the elasticity tensor having the well-known symmetry and ellipticity properties

$$C_{ijhk} = C_{jihk} = C_{khij},$$
$$C_{ijhk}\varepsilon_{ij}\varepsilon_{hk} \ge c\varepsilon_{ij}\varepsilon_{ij} \quad \forall \varepsilon \in \mathbf{R}^6,\ c = \text{const} > 0.$$

Then, using the Green-Gauss theorem and assuming that all the functions are sufficiently smooth, we can derive from (2.4) and (2.5) the following equilibrium condition: Find $u \in V = \{v \in [H^1(\Omega)]^3 : v = 0 \text{ on } \Gamma_1\}$ such that

$$\int_\Omega \sigma_{ij}(u)\varepsilon_{ij}(v-u)\,d\Omega - \int_\Omega f_i(v_i-u_i)\,d\Omega = \int_{\Gamma_2\cup\Gamma_3} S_i(v_i-u_i)\,d\Gamma \qquad \forall v \in V. \quad (2.7)$$

Substituting the boundary conditions (2.2) and (2.3) and the material law (2.6) to (2.7) we get for the problems (P1) and (P2) the following hemivariational inequalities: Find $u \in V$ such that

$$\begin{aligned} &\int_\Omega C_{ijhk}\varepsilon_{ij}(u)(\varepsilon_{hk}(v)-\varepsilon_{hk}(u))\,d\Omega + \int_{\Gamma_3} j^\circ(x,u,v-u)\,d\Gamma \\ &\quad \geq \int_\Omega f_i(v_i-u_i)\,d\Omega + \int_{\Gamma_2} F_i(v_i-u_i)\,d\Gamma \qquad \forall v \in V \end{aligned} \quad \text{(P1)}$$

and

$$\begin{aligned} &\int_\Omega C_{ijhk}\varepsilon_{ij}(u)(\varepsilon_{hk}(v)-\varepsilon_{hk}(u))\,d\Omega + \int_{\Gamma_3} j_T^\circ(x,u_T,v_T-u_T)\,d\Gamma \\ &\geq \int_\Omega f_i(v_i-u_i)\,d\Omega + \int_{\Gamma_2} F_i(v_i-u_i)\,d\Gamma + \int_{\Gamma_3} C_N(v_N-u_N)\,d\Gamma \qquad \forall v \in V, \end{aligned} \quad \text{(P2)}$$

respectively. The existence of at least one solution of the above problems is guaranteed by [10, Theorem 4.25].

2.2. Nonmonotone skin friction or adhesion in plane elasticity.

In this example Ω is a bounded domain of $\mathbf{R}^2$ occupied by a linear elastic body in its undeformed state. Now the boundary Γ is divided into two nonoverlapping open sets Γ_1 and Γ_2 such that $\overline{\Gamma}_1 \cup \overline{\Gamma}_2 = \Gamma$. The boundary conditions on Γ_1 and Γ_2 are the same as in the previous example. The body force f is diveded into two parts $f = f_1 + f_2$: f_1 a given body force and f_2 a body force which describes the skin effects or adhesion and it is obtained from the following relation

$$\begin{cases} -f_2 \in \partial j(x,u) & \text{on } \Omega'; \\ f_2 = 0 & \text{on } \Omega\backslash\Omega', \end{cases}$$

where Ω' is the part of the body where frictional or adhesive effects take place. The function $j\colon \Omega \times \mathbf{R}^2 \to \mathbf{R}$ satisfies the same conditions as previously, i.e., (i)-(v). The following hemivariational inequality describes the physical system: Find $u \in V = \{v \in [H^1(\Omega)]^2 : v = 0 \text{ on } \Gamma_1\}$

$$\begin{aligned} &\int_\Omega C_{ijhk}\varepsilon_{ij}(u)(\varepsilon_{hk}(v)-\varepsilon_{hk}(u))\,d\Omega + \int_{\Omega'} j^\circ(x,u,v-u)\,d\Gamma \\ &\quad \geq \int_\Omega f_i(v_i-u_i)\,d\Omega + \int_{\Gamma_2} F_i(v_i-u_i)\,d\Gamma \qquad \forall v \in V. \end{aligned} \quad \text{(P3)}$$

The existence of at least one solution of this problem is also now guaranteed by [10, Theorem 4.25].

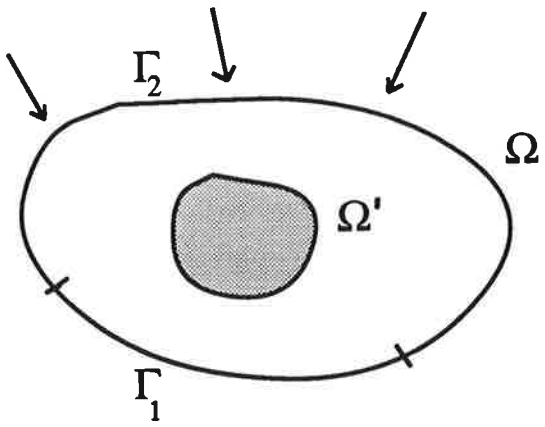

Figure 4. A plane elasticity problem

2.3. Other applications.

Other applications of hemivariational inequalities are, e.g.,

- nonlinear elasticity problems with adhesion or nonlinear friction
- nonmonotone multivalued relations in structural analysis
- adhesively connected sandwich plates
- delamination effect in laminated von Kárman plates
- rigid viscoplastic flow problems with adhesion or nonmonotone friction
- nonmonotone laws in massonry structures
- nonconvex semipermeability problems.

We refer to [10]-[14] and references therein to see more details of the applications of hemivariational inequalities.

3. APPROXIMATION OF HEMIVARIATIONAL INEQUALITIES

We shall consider the following model problem (compare to (P3)):

$$\left\{\begin{array}{l} \text{Find } u \in V \text{ and } X \in L^2(\Omega;\mathbf{R}^M) \text{ such that} \\ a(u,v) + \int_\Omega X \cdot v\,dx = \langle f, v\rangle \ (= \int_\Omega F_1 \cdot v\,dx + \int_{\Gamma_2} F_2 \cdot v\,dx) \quad \forall v \in V \\ \text{and } X(x) \in \partial j(x,u(x)) \qquad \text{a.e. } x \in \Omega. \end{array}\right. \tag{P}$$

Let us introduce the notations in the above problem. Let $\Omega \subset \mathbf{R}^N$ be a bounded domain with a Lipschitz boundary Γ, V a real Hilbert space (for example $V = \{v \in [H^1(\Omega)]^M : v = 0 \text{ on } \Gamma_1\}$) equipped with the norm $\|\cdot\|$, V' the dual space and $\langle\cdot,\cdot\rangle$ the corresponding duality. Let f be an element of V' and $a\colon V \times V \to \mathbf{R}$ be a continuous and coercive bilinear form. The function $j\colon \Omega \times \mathbf{R}^M \to \mathbf{R}$ satisfies the previous assumptions (i)-(v) ($\mathbf{R}^3$ is replaced by $\mathbf{R}^M$). We shall also assume that

$$\text{the injection } V \subset L^2(\Omega;\mathbf{R}^M) \text{ is compact;}$$
$$V \cap L^\infty(\Omega;\mathbf{R}^M) \text{ is dense in } V.$$

Under the above assumptions it is possible to show that the problem (P) is solvable.

Let us introduce the fully discrete approximation of $(\mathrm{P})_h$:

$$\begin{cases} \text{Find } u_h \in V_h \text{ and } X_h \in Y_h \text{ such that} \\ a^h(u_h, v_h) + \int_\Omega X_h \cdot P_h v_h \, dx = \langle f_h, v_h \rangle_h \qquad \forall v_h \in V_h \\ \text{and } X_h(x) \in \partial j((\hat{P}_h x)(x), (P_h u_h)(x)) \qquad \text{a.e. } x \in \Omega, \end{cases} \tag{P}_h^1$$

which can be written equivalently as follows:

$$\begin{cases} \text{Find } u_h \in V_h \text{ and } X_h \in \mathbf{R}^{m_h} \text{ such that} \\ a^h(u_h, v_h) + \sum_{i=1}^{m_h} c_h^i X_h(x_h^i) \cdot v_h(x_h^i) = \langle f_h, v_h \rangle_h \qquad \forall v_h \in V_h \\ \text{and } X_h(x_h^i) \in \partial j(x_h^i, u_h(x_h^i)) \qquad i = 1, ..., m_h. \end{cases} \tag{P}_h^2$$

Next we explain the notations used in $(\mathrm{P})_h$ and impose the assumptions needed to show the convergence of the solutions of $(\mathrm{P})_h$ to the solutions of (P). First we define finite-dimensional approximations of the spaces V and $Y = L^2(\Omega; \mathbf{R}^M)$ denoted by V_h and Y_h, respectively. The discretization parameter h is connected with the mesh size of partition of $\overline{\Omega}$ (we use the finite element method). Because we use two different partitions of $\overline{\Omega}$, we should actually have two different discretization parameters h_V and h_Y. To avoid this difficulty we assume that our families of partitions satisfy

$$h_V \to 0+ \iff h_Y \to 0+ .$$

Hence only one parameter $h = \max(h_V, h_Y)$ will be used in what follows. We shall pay more attention to the construction of Y_h, because the construction of V_h is standard, and, can be found, for example, from [1].

Let $\{V_h\}$ be a family of finite-dimensional subspaces satisfying

$$\begin{cases} V_h \subset V \cap C(\overline{\Omega}; \mathbf{R}^M), \ \dim V_h < \infty \ \forall h \in (0,1) \text{ and} \\ \forall v \in V, \ \exists \{v_h\}, v_h \in V_h : \ v_h \to v \text{ in } V. \end{cases}$$

The starting point for the construction of the approximation of Y is the approximation of the integral $\int_\Omega X \cdot v \, dx$. We shall use a quadrature formula

$$\int_\Omega X \cdot v \, dx \approx \sum_{i=1}^{m_h} c_h^i X(x_h^i) \cdot v(x_h^i) = \sum_{i=1}^{m_h} \sum_{j=1}^{M} c_h^i X_j(x_h^i) v_j(x_h^i), \tag{3.1}$$

where c_h^i are weights and $x_h^i \in \overline{\Omega}$ are nodes of a quadrature formula. From the numerical point of view is reasonable to choose the nodes x_h^i in such a way that they have some relation to the partition of V_h, for example, these can be the vertices, the midpints of the edges or the centers of the gravity of the triangles of the partition of V_h. Let us assume that (3.1) is exact for constant functions implying that $\sum_{i=1}^{m_h} c_h^i = m_N(\Omega)$, where m_N denotes the Lebesgue measure in $\mathbf{R}^N$. Then it is possible to define a partition $\mathcal{T}_h$, $h \in (0,1)$, of $\overline{\Omega}_h$, where Ω_h is another domain containing Ω. $\mathcal{T}_h$ consists of a finite number of subsets K_h^i of $\overline{\Omega}_h$, $i = 1, ..., m_h$ having the following properties:

(1) $\overline{\Omega}_h = \cup_{i=1}^{m_h} K_h^i$;
(2) $h \geq \max_{i=1,...,m_h} \{\text{diameter of } K_h^i\}$;
(3) int $K_h^i \cap$ int $K_h^j = \emptyset \ \forall i \neq j$;
(4) K_h^i is closed, convex and has a nonempty interior for any $i = 1, ..., m_h$;
(5) For each $i = 1, ..., m_h$ there is exactly one point $x_h^i \in$ int $K_h^i \cap \overline{\Omega}$;
(6) $m_N($ int $K_h^i \cap \Omega) = c_h^i \ i = 1, ..., m_h$.

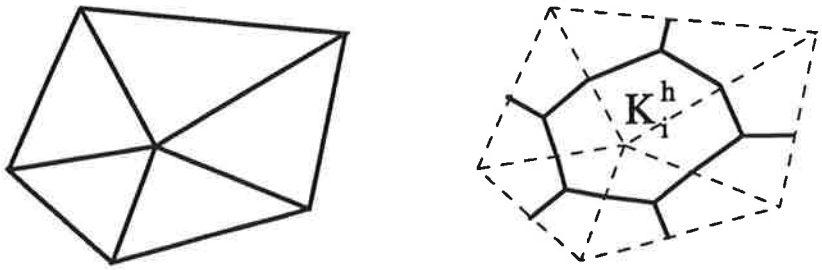

Figure 5. Partitions of V_h and Y_h

For the finite-dimensional space Y_h we will choose the space of piecewise constant functions over the partition $\mathcal{T}_h$, defined as follows:

$$Y_h = \{f \in L^\infty(\Omega; \mathbf{R}^M) : \exists \tilde{f} : \Omega_h \to \mathbf{R}^M,$$
$$\tilde{f}|_{\text{int } K_h^i} \text{ is constant } i = 1, ..., m_h, f = \tilde{f}|_\Omega\}.$$

We need also the space of piecewise continuous functions over the partition $\mathcal{T}_h$:

$$X_h = \{f \in L^\infty(\Omega; \mathbf{R}^M) : \exists \tilde{f} : \Omega_h \to \mathbf{R}^M,$$
$$\tilde{f}|_{\text{int } K_h^i} \text{ is continuous } i = 1, ..., m_h, f = \tilde{f}|_\Omega\}.$$

Let P_h be a linear mapping from X_h to Y_h defined by means of

$$(P_h f)(x) = \sum_{i=1}^{m_h} f(x_h^i)(\mathcal{X}_{\text{int } K_h^i})(x), \qquad \forall x \in \Omega,$$

where $\mathcal{X}_{\text{int } K_h^i}$ is the characteristic function of int K_h^i, and, $\hat{P}_h x$ is defined by

$$(\hat{P}_h x)(x) = \sum_{i=1}^{m_h} x_h^i(\mathcal{X}_{\text{int } K_h^i})(x), \qquad \forall x \in \Omega.$$

The following assumption concerning the consistency between the approximation spaces V_h and Y_h will be assumed:

$$y_h \rightharpoonup y \text{ in } V,\ y_h \in V_h \implies P_h y_h \to y \text{ in } L^2(\Omega; R^M).$$

The assumptions concerning approximations of a, f are standard. An approximation of a, $a^h : V_h \times V_h \to \mathbf{R}$, satisfies:

$$\exists \tilde{M} > 0 : |a^h(u_h, v_h)| \le \tilde{M}\|u_h\|\|v_h\| \ \forall u_h, v_h \in V_h,\ \forall h \in (0,1);$$
$$\exists \tilde{\alpha} > 0 : a^h(u_h, u_h) \ge \tilde{\alpha}\|u_h\|^2 \ \forall u_h \in V_h,\ \forall h \in (0,1);$$
$$u_h \rightharpoonup u,\ v_h \to v \text{ in } V,\ u_h, v_h \in V_h \implies a^h(u_h, v_h) \to a(u, v),\ a^h(v_h, u_h) \to a(v, u).$$

The symbol $\langle \cdot, \cdot \rangle_h : V_h \times V_h' \to \mathbf{R}$ denotes the duality pairing between V_h and V_h' and $f_h \in V_h'$ is an approximation of f such that

$$\exists \tilde{\beta} > 0 : |\langle f_h, v_h \rangle_h| \le \tilde{\beta}\|v_h\| \ \forall v_h \in V_h,\ \forall h \in (0,1);$$
$$v_h \rightharpoonup v \text{ in } V,\ v_h \in V_h \implies \langle f_h, v_h \rangle_h \to \langle f, v \rangle.$$

Finally we need that the function $j(x, \xi)$ is sufficiently regular with respect to x. Then it is possible to show the convergence result: the solutions of $(\mathrm{P})_h$ tend to the solutions of (P).

THEOREM 3.1. *Let $\{(y_h, X_h)\}$ be a sequence such that $(y_h, X_h) \in V_h \times Y_h$ is a solution of $(P)_h$. Then there exist subsequence of $\{(y_{h_k}, X_{h_k})\}$ and $(y, X) \in V \times Y$ such that*

$$\begin{aligned} y_{h_k} &\to y \qquad \text{in } V; \\ X_{h_k} &\rightharpoonup X \qquad \text{in } L^2(\Omega; \mathbf{R}^M). \end{aligned}$$

Moreover, (y, X) is a solution of (P).

REMARK: The reason, why we get the convergence result only for subsequences, is that in general the solutions of hemivariational inequalities are not unique due to nonmonotoness. This also implies that it is not possible to get global convergence rate estimates.

4. NUMERICAL REALIZATION

Let $h > 0$ be fixed. This enables us to skip the symbol h in many situations and instead of n_h, m_h, x_h^i,... to write n, m, x^i,... First we shall rewrite the approximation $(P)_h$ into the matrix form. Let $\{\varphi^j\}_{j=1}^n$ be the basis of V_h. We define a linear mapping $\Lambda\colon \mathbf{R}^n \to \mathbf{R}^m$ as follows:

$$\Lambda_{ij} = \varphi^j(x^i) \qquad i = 1, ..., m, j = 1, ..., n.$$

In the sequel we shall identify $y = \sum_{j=1}^n \varphi^j y_j \in V_h$ with the nodal vector $\mathbf{y} = (y_j)_{j=1}^n \in \mathbf{R}^n$. Hence $(P)_h$ is equivalent to the following problem (P):

$$\left\{ \begin{array}{l} \text{Find } \mathbf{y} = (y_1, ..., y_n) \in \mathbf{R}^n \text{ and } \mathbf{s} = (s_1, ..., s_m) \in \mathbf{R}^m \text{ such that} \\ (A\mathbf{y}, \mathbf{z})_{\mathbf{R}^n} + (\mathbf{s}, \Lambda\mathbf{z})_{\mathbf{R}^m} = (\mathbf{f}, \mathbf{z})_{\mathbf{R}^n} \qquad \forall \mathbf{z} \in \mathbf{R}^n \\ \text{and } s_i \in c_i \partial j(x^i, (\Lambda\mathbf{y})_i) \qquad i = 1, ..., m, \end{array} \right. \tag{P}$$

where $A = (a^h(\varphi^i, \varphi^j))_{i,j=1}^n$ is an $n \times n$ square matrix, $\mathbf{f} = (\langle f_h, \varphi^j \rangle_h)_{j=1}^n \in \mathbf{R}^n$ and $(\cdot,\cdot)_{\mathbf{R}^n}$, $(\cdot,\cdot)_{\mathbf{R}^m}$ denote the scalar products in $\mathbf{R}^n$, $\mathbf{R}^m$, respectively. For solving (P) we introduce two methods:

A NONSMOOTH NONCONVEX OPTIMIZATION METHOD: Let us assume that the matrix A is symmetric. Then it is possible to show that the substationary points (if $0 \in \partial L(\mathbf{y})$, $\mathbf{y}$ is a substationary point of L) of the function $L\colon \mathbf{R}^n \to \mathbf{R}$ defined by

$$L(\mathbf{y}) = \frac{1}{2}(A\mathbf{y}, \mathbf{y})_{\mathbf{R}^n} - (\mathbf{f}, \mathbf{y})_{\mathbf{R}^n} + \Psi(\mathbf{y}),$$

where

$$\Psi(\mathbf{y}) = \sum_{i=1}^m c_i j(x^i, (\Lambda\mathbf{y})_i),$$

are solutions of the problem (P). It is known that, for example, local minimum points of a locally Lipschitz function are its substationary points. Hence our problem (P) is transformed to the problem of finding a local minimum point of L, i.e.,

$$\arg\min_{\mathbf{y} \in \mathbf{R}^n} L(\mathbf{y}).$$

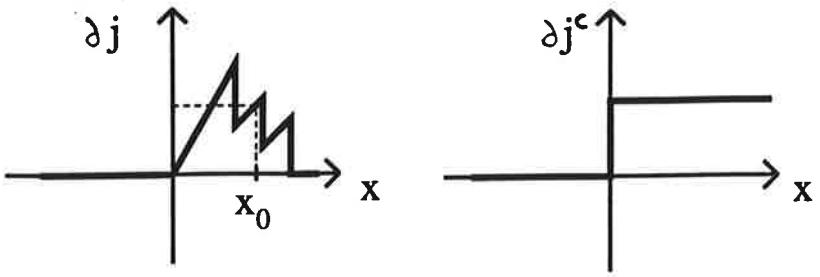

Figure 6. Nonmonotone law replaced by monotone one

To solve this problem we have to use optimization methods for nonsmooth nonconvex functions, because the function L is generally of this form (see details of those methods from [7]).

A FIXED POINT METHOD (APPROXIMATION BY MONOTONE SUBPROBLEMS): In this method we use the following iterative scheme:

$$\begin{cases} \text{on } r\text{th step find } \mathbf{y}^r \text{ such that} \\ (A\mathbf{y}^r, \mathbf{z}-\mathbf{y}^r)_{\mathbf{R}^n} + \sum_{i=1}^m c_i(j_r^c(x^i,(\Lambda \mathbf{z})_i) - j_r^c(x^i,(\Lambda \mathbf{y}^r)_i)) \\ \geq (\mathbf{f}, \mathbf{z}-\mathbf{y}^r)_{\mathbf{R}^n} + \sum_{i=1}^m c_i (E^i)_r(\mathbf{z}, \mathbf{y}^{r-1}) \qquad \forall \mathbf{z}_h \in \mathbf{R}^n, \end{cases}$$

where

$$(E^i)_r(\mathbf{z}, \mathbf{y}^{r-1}) = j_r^c(x^i,(\Lambda \mathbf{z})_i) - j_r^c(x^i,(\Lambda \mathbf{y}^{r-1})_i) - j^\circ(x_i,(\Lambda \mathbf{y}^{r-1})_i; (\Lambda \mathbf{z})_i - (\Lambda \mathbf{y}^{r-1})_i)$$

represents the error between the function j and its convex approximation j_r^c at the point $(x^i,(\Lambda \mathbf{y}^{r-1})_i)$. Thus the main idea of this method is to transform (P) to the sequence of the variational inequalities which can be solved by effective numerical methods. We refer to [6] to see the details of this method and its application to a nonmonotone friction problem.

REFERENCES

1. Ciarlet P.G., "The Finite Element Method for Elliptic Problems," North-Holland, Amsterdam, 1978.
2. Clarke F.H., "Optimization and Nonsmooth Analysis," Wiley Interscience, New York, 1983.
3. Miettinen M. and Haslinger J., Approximation of Optimal Control Problems of Hemivariational Inequalities, Numer. Funct. Anal. and Optimiz., 13(1&2), (1992), 43–68.
4. Miettinen M., "Approximation of Hemivariational Inequalities and Optimal Control Problems," PhD. Thesis, University of Jyväskylä, Department of Mathematics, Report 59, 1993.
5. Miettinen M. and Haslinger J., Approximation of Nonmonotone Multivalued Differential Inclusions, (submitted to IMA J. of Num. Anal.).

6. Mistakidis E.S. and Panagiotopoulos P.D., On the Numerical Treatment of the Nonmonotone (zigzag) Friction and Adhesive Contact Problems with Deponding. Approximation by Monotone Subproblems., (to appear in Comp. and Struct.).
7. Mäkelä M.M. and Neittanmäki P., "Nonsmooth Optimization. Analysis and Algorithms with Applications to Optimal Control," World Scientific, Singapore, 1992.
8. Naniewicz Z., On the Pseudo-Monotonicity of Generalized Gradients of Nonconvex Functions, Applicable Analysis, 47, (1992), 151–172.
9. Naniewicz Z., Hemivariational Inequalities with Functions Fulfilling Directional Growth Condition, (to appear in Applicable Analysis).
10. Naniewicz Z. and Panagiotopoulos P.D., "Mathematical Theory of Hemivariational Inequalities and Applications," (to appear).
11. Panagiotopoulos P.D., "Inequality Problems in Mechanics and Applications. Convex and Nonconvex Energy Functions.," Birkhäuser, Basel, 1985.
12. Panagiotopoulos P.D., Hemivariational Inequalities and Their Applications, in "Topics in Nonsmooth Mechanics (eds. Moreau J.J., Panagiotopoulos P.D. and Strang G.)," Birkhäuser, Boston, 1988.
13. Panagiotopoulos P.D., Coercive and Semicoercive Hemivariational Inequalities, Nonlin. Anal., 16, (1991), 209–231.
14. Panagiotopoulos P.D., "Hemivariational Inequalities. Applications in Mechanics and Engineering.," Springer Verlag, Berlin, 1993.

CURVED BEAM THEORY UTILIZING LOCAL RECTANGULAR COORDINATES

JUHA PAAVOLA* and EERO-MATTI SALONEN**
*Laboratory of Structural Mechanics and **Laboratory of Computational Dynamics
Helsinki University of Technology
FIN-02150 ESPOO, FINLAND

ABSTRACT

The present paper is concerned with the kinematics of a curved plane beam taking into account finite deformations. The most important tool in the study is a local auxiliary fixed rectangular coordinate system. This is spanned locally at each point under consideration after which all the definitions are performed in its coordinates which are not related to the geometry of the structure, at all. The method leads with no ambiguities to exact expressions for the strains which can then be systematically simplified for different purposes on the base of suitable approximations. The consideration is limited in this context to a plane beam to emphasize the simplicity of the procedure and to avoid too complicated and offputting expressions as a result.

1. INTRODUCTION

This study can be considered as a continuation to the paper presented in the Fourth Finnish Mechanics Days held in Lappeenranta, 1991 [1]. That paper enlightened the use of local rectangular coordinate systems in deriving expressions for strains in various solid systems or structures. It was emphasized in it, that the method introduced is - in the opinion of the authors - very systematic and simple and produces a novel way to study and especially to teach, for example, any curved structure in purely rectilinear coordinates.

The presentation in [1] likewise in [8] was limited to linear analysis and the aim is now to evaluate the nonlinear terms, taking into account the finite deformations in the expressions of strains. To present the main ideas in a simple context without involved formulae the consideration will be limited to the analysis of a beam curved in a plane. The paper [1] will be, at first, referred shortly on the most essential parts to recall the procedure applied.

2. MATHEMATICAL BACKGROUND

Three coordinate systems, a rectangular global Cartesian x, y with unit base vectors $\vec{i}, \vec{j}$, a rectangular local Cartesian X, Y with unit base vectors $\vec{e}_X, \vec{e}_Y$ and an orthogonal

curvilinear α, β with unit base vectors $\vec{e}_\alpha, \vec{e}_\beta$ are used. Coordinates x, y and α, β are defined for the whole structure and are employed in the traditional way. The X, Y-system is, however, used as an auxiliary tool in a way to be explained presently.

The mathematical manipulations will be performed exploiting a local Cartesian coordinate system, producing the final result, however, in the general curvilinear ones conforming to the geometry of the structure. For this purpose, the connection between derivatives evaluated in these two coordinate systems is needed. In [1], the general relationship between the derivatives in two dimensions

$$\begin{Bmatrix} \frac{\partial}{\partial X} \\ \frac{\partial}{\partial Y} \end{Bmatrix} = \begin{bmatrix} \frac{\partial \vec{r}}{\partial \alpha} \cdot \vec{e}_X & \frac{\partial \vec{r}}{\partial \alpha} \cdot \vec{e}_Y \\ \frac{\partial \vec{r}}{\partial \beta} \cdot \vec{e}_X & \frac{\partial \vec{r}}{\partial \beta} \cdot \vec{e}_Y \end{bmatrix}^{-1} \begin{Bmatrix} \frac{\partial}{\partial \alpha} \\ \frac{\partial}{\partial \beta} \end{Bmatrix} \tag{1}$$

is derived in detail. Here, $\vec{r}$ is the position vector of a generic point. In this presentation, in which the consideration is limited to beams with orthogonal curvilinear geometry, it is meaningful to orientate the unit base vectors of the local coordinate system to coincide with the unit vectors of the curvilinear system at the origin, where the local system is spanned.

3. DISPLACEMENTS AND STRAINS

The displacement vector $\vec{u}$ in two dimensions can be expressed either in a local Cartesian or in a curvilinear coordinate system, i.e.

$$\vec{u} = u_X \vec{e}_X + u_Y \vec{e}_Y, \tag{2a}$$

$$\vec{u} = u_\alpha \vec{e}_\alpha + u_\beta \vec{e}_\beta \tag{2b}$$

or in any other coordinate system. The latter one is employed in analytical calculations in curved structures. The general expressions for the rectangular strain components [3,4,5] in a X, Y-system are

$$\begin{aligned} \epsilon_X &= \frac{\partial u_X}{\partial X} + \frac{1}{2}\left\{\left(\frac{\partial u_X}{\partial X}\right)^2 + \left(\frac{\partial u_Y}{\partial X}\right)^2\right\} = \frac{\partial \vec{u}}{\partial X} \cdot \vec{e}_X + \frac{1}{2}\,\frac{\partial \vec{u}}{\partial X} \cdot \frac{\partial \vec{u}}{\partial X}, \\ \epsilon_Y &= \frac{\partial u_Y}{\partial Y} + \frac{1}{2}\left\{\left(\frac{\partial u_X}{\partial Y}\right)^2 + \left(\frac{\partial u_Y}{\partial Y}\right)^2\right\} = \frac{\partial \vec{u}}{\partial Y} \cdot \vec{e}_Y + \frac{1}{2}\,\frac{\partial \vec{u}}{\partial Y} \cdot \frac{\partial \vec{u}}{\partial Y}, \\ \gamma_{XY} &= \frac{\partial u_X}{\partial Y} + \frac{\partial u_Y}{\partial X} + \frac{\partial u_X}{\partial X}\frac{\partial u_X}{\partial Y} + \frac{\partial u_Y}{\partial X}\frac{\partial u_Y}{\partial Y} = \frac{\partial \vec{u}}{\partial Y} \cdot \vec{e}_X + \frac{\partial \vec{u}}{\partial X} \cdot \vec{e}_Y + \frac{\partial \vec{u}}{\partial X} \cdot \frac{\partial \vec{u}}{\partial Y}. \end{aligned} \tag{3}$$

The equivalence between these two formulations can be verified directly by substituting the displacement vector (2a) into the scalar product expressions on the right hand side of the equation and performing the differentiation. The unit vectors $\vec{e}_X$ and $\vec{e}_Y$ are here constant with respect to differentiation because the X, Y system is fixed.

When the unit vectors of both X, Y and α, β coordinate systems are chosen to coincide at the origin of the local coordinate system, the Jacobian matrix at that point has the diagonal form

$$\begin{bmatrix} \frac{\partial \vec{r}}{\partial \alpha} \cdot \vec{e}_X & \frac{\partial \vec{r}}{\partial \alpha} \cdot \vec{e}_Y \\ \frac{\partial \vec{r}}{\partial \beta} \cdot \vec{e}_X & \frac{\partial \vec{r}}{\partial \beta} \cdot \vec{e}_Y \end{bmatrix}^{-1} = \begin{bmatrix} H_\alpha & 0 \\ 0 & H_\beta \end{bmatrix}^{-1} = \begin{bmatrix} H_\alpha^{-1} & 0 \\ 0 & H_\beta^{-1} \end{bmatrix}. \tag{4}$$

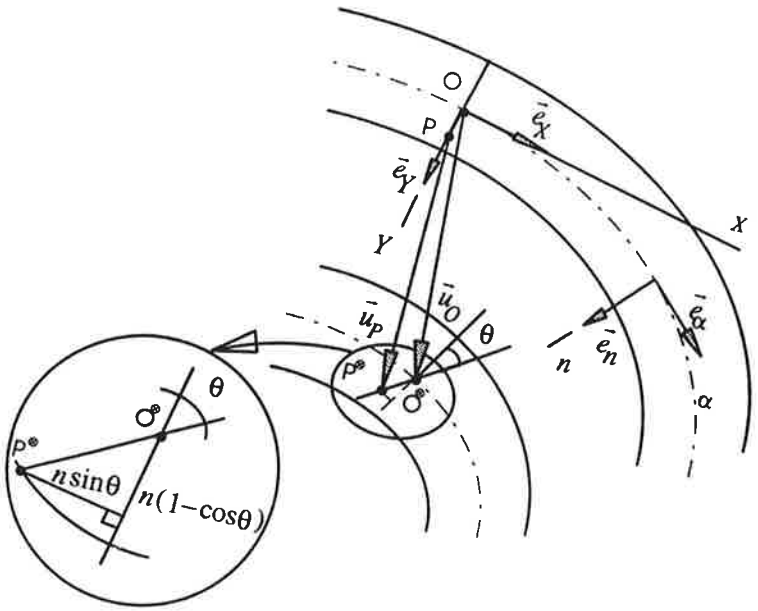

FIGURE 1. Curved beam and its deformation.

$H_\alpha = H_\alpha(\alpha,\beta)$ and $H_\beta = H_\beta(\alpha,\beta)$ are the scale factors. The derivatives of the displacement vector evaluated now with respect to the local coordinate system will get the form

$$\begin{aligned}\frac{\partial \vec{u}}{\partial X} &= H_\alpha^{-1}\left(\frac{\partial u_\alpha}{\partial \alpha}\vec{e}_\alpha + u_\alpha\frac{\partial \vec{e}_\alpha}{\partial \alpha} + \frac{\partial u_\beta}{\partial \alpha}\vec{e}_\beta + u_\beta\frac{\partial \vec{e}_\beta}{\partial \alpha}\right),\\ \frac{\partial \vec{u}}{\partial Y} &= H_\beta^{-1}\left(\frac{\partial u_\alpha}{\partial \beta}\vec{e}_\alpha + u_\alpha\frac{\partial \vec{e}_\alpha}{\partial \beta} + \frac{\partial u_\beta}{\partial \beta}\vec{e}_\beta + u_\beta\frac{\partial \vec{e}_\beta}{\partial \beta}\right).\end{aligned} \tag{5}$$

After evaluating the derivatives for the unit vectors, the expressions are substituted into the strain component formulae (3). It should still be remarked that equations (5) are valid exactly only at the origin of the auxiliary coordinate system, where the unit vectors in both systems coincide.

4. CURVED BEAM

4.1 Geometry. A curved plane beam is considered using the notation shown in Figure 1. The curvilinear coordinate α coincides with the beam axis. Symbol β is replaced here by the symbol n for the rectilinear normal coordinate measuring the distance from the beam axis. The purpose is to determine the expressions for the strain components $\epsilon_\alpha = \epsilon_X$ and $\gamma_{\alpha n} = \gamma_{XY}$ at a general point P shown in Figure 1. It is here convenient to fix the origin of the auxiliary coordinate system at the point O on the beam axis, as shown in the figure. The position vector of a point P can be represented as

$$\vec{r}(\alpha,n) = \vec{r}_O(\alpha) + n\vec{e}_n(\alpha), \tag{6}$$

where $\vec{r}_O$ is the position vector of point O on the axis. The derivatives of the unit base vectors are

$$\frac{\partial \vec{e}_\alpha}{\partial \alpha} = -\frac{H}{R}\vec{e}_n, \qquad \frac{\partial \vec{e}_n}{\partial \alpha} = \frac{H}{R}\vec{e}_\alpha, \tag{7}$$

whereas the corresponding derivatives with respect to n vanish. The reference to coordinate α is dropped out from the scale factor H and from the radius of curvature R, for brevity. Expressions (7) are obtained from the well known FRENET formulae, e.g. VÄISÄLÄ [2]. Here the radius of curvature of the beam axis is considered positive when the center of curvature is on the negative side of the n-axis. The scale factor is defined through the equation

$$\frac{\partial \vec{r}_O}{\partial \alpha} = H\vec{e}_\alpha. \tag{8}$$

If coordinate α is selected to be the arclength s - as is usual - $H = 1$. Differentiation of expression (6) gives

$$\begin{aligned} \frac{\partial \vec{r}}{\partial \alpha} &= \frac{\partial \vec{r}_O}{\partial \alpha} + n\frac{\partial \vec{e}_n}{\partial \alpha} = H\vec{e}_\alpha + n\frac{H}{R}\vec{e}_\alpha = H\Big(1+\frac{n}{R}\Big)\vec{e}_\alpha, \\ \frac{\partial \vec{r}}{\partial n} &= \vec{e}_n. \end{aligned} \tag{9}$$

It can be seen that the scale factors corresponding to coordinates α and n at a general point are $H(1+n/R)$ and 1. The relations (1) obtain thus the forms

$$\frac{\partial}{\partial X} = H^{-1}(1+\frac{n}{R})^{-1}\frac{\partial}{\partial \alpha}, \qquad \frac{\partial}{\partial Y} = \frac{\partial}{\partial n}, \tag{10}$$

which are again strictly valid only at the origin of the local coordinate system.

4.2 Displacements and strains. A general kinematics for a curved plane beam, visualized in Figure 1, is described with an equation

$$\vec{u}(\alpha, n) = [u_\alpha(\alpha) - n\sin\theta(\alpha)]\,\vec{e}_\alpha(\alpha) + [u_n(\alpha) - n(1-\cos\theta(\alpha))]\,\vec{e}_n(\alpha) \tag{11}$$

for the displacement vector of point P. This assumes that the normals to the undeformed beam axis stay straight lines with no stretcing, but do not any more form normals to the deformed axis. The unknowns are $u_\alpha(\alpha)$, $u_n(\alpha)$ and $\theta(\alpha)$ representing the displacement components of point O on the beam axis and the rotation of a material fiber originally perpendicular to the axis as positive in the clockwise direction. The derivatives of the displacement vector at point P needed for strain evaluations can be calculated directly using expressions (10) and (11) yielding

$$\begin{aligned} \frac{\partial \vec{u}}{\partial X} &= H^{-1}\left(1+\frac{n}{R}\right)^{-1}\left[\Big(\frac{\partial u_\alpha}{\partial \alpha} - n\cos\theta\frac{\partial\theta}{\partial\alpha}\Big)\vec{e}_\alpha + (u_\alpha - n\sin\theta)\frac{\partial \vec{e}_\alpha}{\partial\alpha}\right. \\ &\quad \left. + \Big(\frac{\partial u_n}{\partial\alpha} - n\sin\theta\frac{\partial\theta}{\partial\alpha}\Big)\vec{e}_n + (u_n - n(1-\cos\theta))\frac{\partial\vec{e}_n}{\partial\alpha}\right] \\ &= \Big(1+\frac{n}{R}\Big)^{-1}\left[\Big(\frac{\partial u_\alpha}{H\partial\alpha} - n\cos\theta\frac{\partial\theta}{H\partial\alpha} + \frac{u_n - n(1-\cos\theta)}{R}\Big)\vec{e}_\alpha\right. \\ &\quad \left. + \Big(-\frac{u_\alpha - n\sin\theta}{R} + \frac{\partial u_n}{H\partial\alpha} - n\sin\theta\frac{\partial\theta}{H\partial\alpha}\Big)\vec{e}_n\right], \\ \frac{\partial\vec{u}}{\partial Y} &= -\sin\theta\vec{e}_\alpha - (1-\cos\theta)\vec{e}_n. \end{aligned} \tag{12}$$

The only nonzero strain components in expressions (3) at P are ϵ_X and γ_{XY} ($\vec{e}_\alpha = \vec{e}_X$, $\vec{e}_n = \vec{e}_Y$):

$$\begin{aligned}
\epsilon_\alpha = \epsilon_X &= \Big(1+\frac{n}{R}\Big)^{-1}\Big(\frac{\partial u_\alpha}{H\partial\alpha} - n\cos\theta\frac{\partial\theta}{H\partial\alpha} + \frac{u_n - n(1-\cos\theta)}{R}\Big) \\
&\quad + \frac{1}{2}\Big(1+\frac{n}{R}\Big)^{-2}\Big\{\Big(\frac{\partial u_\alpha}{H\partial\alpha} - n\cos\theta\frac{\partial\theta}{H\partial\alpha} + \frac{u_n - n(1-\cos\theta)}{R}\Big)^2 \\
&\qquad + \Big(-\frac{u_\alpha - n\sin\theta}{R} + \frac{\partial u_n}{H\partial\alpha} - n\sin\theta\frac{\partial\theta}{H\partial\alpha}\Big)^2\Big\}, \\
\gamma_{\alpha n} = \gamma_{XY} &= \Big(1+\frac{n}{R}\Big)^{-1}\Big(-\frac{u_\alpha - n\sin\theta}{R} + \frac{\partial u_n}{H\partial\alpha} - n\sin\theta\frac{\partial\theta}{H\partial\alpha}\Big) - \sin\theta \\
&\quad - \Big(1+\frac{n}{R}\Big)^{-1}\Big\{\sin\theta\Big(\frac{\partial u_\alpha}{H\partial\alpha} - n\cos\theta\frac{\partial\theta}{H\partial\alpha} + \frac{u_n - n(1-\cos\theta)}{R}\Big) \\
&\qquad + (1-\cos\theta)\Big(-\frac{u_\alpha - n\sin\theta}{R} + \frac{\partial u_n}{H\partial\alpha} - n\sin\theta\frac{\partial\theta}{H\partial\alpha}\Big)\Big\}.
\end{aligned} \tag{13}$$

It is of certain interest to notice that though the beam undergoes no stretching in the direction of the normal, the linear part of strain component ϵ_n does not vanish. The nonlinear part cancels, however, the nonzero linear part of it.

The expression of the shear strain $\gamma_{\alpha n}$ can be simplified to the form

$$\gamma_{\alpha n} = \Big(1+\frac{n}{R}\Big)^{-1}\Big[\cos\theta\Big(\frac{\partial u_n}{H\partial\alpha} - \frac{u_\alpha}{R}\Big) - \sin\theta\Big(1+\frac{\partial u_\alpha}{H\partial\alpha} + \frac{u_n}{R}\Big)\Big], \tag{14}$$

and the normal strain, correspondingly

$$\begin{aligned}
\epsilon_\alpha &= \frac{1}{2}\Big(1+\frac{n}{R}\Big)^{-2}\Big\{\Big(\frac{\partial u_n}{H\partial\alpha} - \frac{u_\alpha}{R}\Big)^2 + \Big(1+\frac{\partial u_\alpha}{H\partial\alpha} + \frac{u_n}{R}\Big)^2 \\
&\quad + 2n\Big(\frac{1}{R} - \frac{\partial\theta}{H\partial\alpha}\Big)\Big[\cos\theta\Big(\frac{\partial u_n}{H\partial\alpha} - \frac{u_\alpha}{R}\Big) + \sin\theta\Big(1+\frac{\partial u_\alpha}{H\partial\alpha} + \frac{u_n}{R}\Big)\Big] \\
&\quad + n^2\Big(\frac{1}{R} - \frac{\partial\theta}{H\partial\alpha}\Big)^2\Big\} - \frac{1}{2}.
\end{aligned} \tag{15}$$

According to the BERNOULLI assumption or the beam theory with vanishing shear deformations the rotation function can be solved from equation (14) by setting the condition $\gamma_{\alpha n} \equiv 0$. Thus the expression

$$\tan\theta = \frac{\dfrac{\partial u_n}{H\partial\alpha} - \dfrac{u_\alpha}{R}}{1 + \dfrac{\partial u_\alpha}{H\partial\alpha} + \dfrac{u_n}{R}}. \tag{16}$$

is obtained.

In stability analyses, particularly, the nonlinear terms in the expressions of strains are adopted selectively by sustaining on the assumption, that the angles of rotation are prevailing compared to the terms of deformation, for example NOVOZHILOV [3], ODEN

[4]. Recalling the definitions of the strains (3) and performing the rearrangement of the terms results in

$$\begin{aligned}\epsilon_X &= \frac{\partial u_X}{\partial X} + \frac{1}{2}\left\{\left(\frac{\partial u_X}{\partial X}\right)^2 + \frac{1}{4}\left(\frac{\partial u_Y}{\partial X} + \frac{\partial u_X}{\partial Y} + \frac{\partial u_Y}{\partial X} - \frac{\partial u_X}{\partial Y}\right)^2\right\},\\ \gamma_{XY} &= \frac{\partial u_X}{\partial Y} + \frac{\partial u_Y}{\partial X} + \frac{1}{2}\frac{\partial u_X}{\partial X}\left(\frac{\partial u_X}{\partial Y} + \frac{\partial u_Y}{\partial X} - \frac{\partial u_Y}{\partial X} + \frac{\partial u_X}{\partial Y}\right)\\ &\quad + \frac{1}{2}\frac{\partial u_Y}{\partial Y}\left(\frac{\partial u_X}{\partial Y} + \frac{\partial u_Y}{\partial X} + \frac{\partial u_Y}{\partial X} - \frac{\partial u_X}{\partial Y}\right).\end{aligned} \tag{17}$$

By defining the rotation vector $\vec{\omega}$ which is a vector perpendicular to the plane of the beam, i.e. $\vec{\omega} = \omega_Z \vec{e}_Z$ in which

$$\omega_Z = \omega = \frac{1}{2}\left(\frac{\partial \vec{u}}{\partial X}\cdot\vec{e}_Y - \frac{\partial \vec{u}}{\partial Y}\cdot\vec{e}_X\right) = \frac{1}{2}\left(\frac{\partial u_Y}{\partial X} - \frac{\partial u_X}{\partial Y}\right). \tag{18}$$

The subscript Z has been dropped here for convenience. At point P this can further be developed to the form

$$\begin{aligned}\omega &= \frac{1}{2}\left[\left(1+\frac{n}{R}\right)^{-1}\left(-\frac{u_\alpha - n\sin\theta}{R} + \frac{\partial u_n}{H\partial\alpha} - n\sin\theta\frac{\partial\theta}{H\partial\alpha}\right) + \sin\theta\right]\\ &= \frac{1}{2}\left(1+\frac{n}{R}\right)^{-1}\left[\frac{\partial u_n}{H\partial\alpha} - \frac{u_\alpha}{R} + \sin\theta\left(1+\frac{n}{R}\right) + n\sin\theta\left(\frac{1}{R} - \frac{\partial\theta}{H\partial\alpha}\right)\right].\end{aligned} \tag{19}$$

After taking into account (18) the expressions (17) take the form

$$\begin{aligned}\epsilon_X &= \frac{\partial u_X}{\partial X} + \frac{1}{2}\left\{\left(\frac{\partial u_X}{\partial X}\right)^2 + \frac{1}{4}\left(\frac{\partial u_Y}{\partial X} + \frac{\partial u_X}{\partial Y} + 2\omega\right)^2\right\},\\ \gamma_{XY} &= \frac{\partial u_X}{\partial Y} + \frac{\partial u_Y}{\partial X} + \frac{1}{2}\left\{\frac{\partial u_X}{\partial X}\left(\frac{\partial u_X}{\partial Y} + \frac{\partial u_Y}{\partial X} - 2\omega\right) + \frac{\partial u_Y}{\partial Y}\left(\frac{\partial u_X}{\partial Y} + \frac{\partial u_Y}{\partial X} + 2\omega\right)\right\}.\end{aligned} \tag{20}$$

The nonlinear expressions can now be simplified by retaining only the terms quadratic in ω yielding finally

$$\begin{aligned}\epsilon_X &= \frac{\partial u_X}{\partial X} + \frac{1}{2}\omega^2 = \frac{\partial \vec{u}}{\partial X}\cdot\vec{e}_X + \frac{1}{8}\left(\frac{\partial \vec{u}}{\partial X}\cdot\vec{e}_Y - \frac{\partial \vec{u}}{\partial Y}\cdot\vec{e}_X\right)^2,\\ \gamma_{XY} &= \frac{\partial u_X}{\partial Y} + \frac{\partial u_Y}{\partial X} = \frac{\partial \vec{u}}{\partial Y}\cdot\vec{e}_X + \frac{\partial \vec{u}}{\partial X}\cdot\vec{e}_Y.\end{aligned} \tag{21}$$

At P these expressions obtain rather complicated form

$$\begin{aligned}\epsilon_\alpha &= \left(1+\frac{n}{R}\right)^{-1}\left[1 + \frac{\partial u_\alpha}{H\partial\alpha} + \frac{u_n}{R} + n\cos\theta\left(\frac{1}{R} - \frac{\partial\theta}{H\partial\alpha}\right)\right] - 1\\ &\quad + \frac{1}{8}\left(1+\frac{n}{R}\right)^{-2}\left[\frac{\partial u_n}{H\partial\alpha} - \frac{u_\alpha}{R} + \sin\theta\left(1+\frac{n}{R}\right) + n\sin\theta\left(\frac{1}{R} - \frac{\partial\theta}{H\partial\alpha}\right)\right]^2,\\ \gamma_{\alpha n} &= \left(1+\frac{n}{R}\right)^{-1}\left[\frac{\partial u_n}{H\partial\alpha} - \frac{u_\alpha}{R} - \sin\theta\left(1 + n\frac{\partial\theta}{H\partial\alpha}\right)\right].\end{aligned} \tag{22}$$

The assumption of EULER-BERNOULLI for the vanishing shear deformation produces a condition

$$\sin\theta\Big(1+n\frac{\partial\theta}{H\partial\alpha}\Big)=\frac{\partial u_n}{H\partial\alpha}-\frac{u_\alpha}{R}. \tag{23}$$

This result shows the angle of rotation to be dependent on coordinate n, which is against the initial assumption in the displacement kinematics (11). To avoid this discrepancy, the condition (23) could be demanded to be valid in an average sense for instance by integrating over the height of the cross-section or by considering it at the neutral axis i.e. at level $n=0$. In this context, however, (23) will be applied in its consistent form. The strain component ϵ_α is thus

$$\epsilon_\alpha=\Big(1+\frac{n}{R}\Big)^{-1}\left[\frac{\partial u_\alpha}{H\partial\alpha}+\frac{u_n}{R}+\frac{1}{2}\sin^2\theta-n\Big(\frac{1}{2R}(1-\cos\theta)^2+\cos\theta\frac{\partial\theta}{H\partial\alpha}\Big)\right]. \tag{24}$$

5. EXAMPLES

Consider at first a thin arch following the stability analysis of SIMITSES [6]. This means that the terms dependent on normal coordinate n can be dropped as insignificant or the consideration can be done on the axis of the arch. The expressions for the strains (14) and (15) are thus

$$\begin{aligned}\epsilon_\alpha&=\frac{\partial u_\alpha}{H\partial\alpha}+\frac{u_n}{R}+\frac{1}{2}\left[\Big(\frac{\partial u_n}{H\partial\alpha}-\frac{u_\alpha}{R}\Big)^2+\Big(\frac{\partial u_\alpha}{H\partial\alpha}+\frac{u_n}{R}\Big)^2\right],\\ \gamma_{\alpha n}&=\cos\theta\Big(\frac{\partial u_n}{H\partial\alpha}-\frac{u_\alpha}{R}\Big)-\sin\theta\Big(1+\frac{\partial u_\alpha}{H\partial\alpha}+\frac{u_n}{R}\Big).\end{aligned} \tag{25}$$

The strain ϵ_α which is precisely the same given by SIMITSES is independent of the angle of rotation and so EULER-BERNOULLI assumption has no meaning in this case. Instead, by applying the equations (22) and (24), gives the corresponding relations in the form

$$\begin{aligned}\epsilon_\alpha&=\frac{\partial u_\alpha}{H\partial\alpha}+\frac{u_n}{R}+\frac{1}{2}\sin^2\theta,\\ \gamma_{\alpha n}&=\frac{\partial u_n}{H\partial\alpha}-\frac{u_\alpha}{R}-\sin\theta.\end{aligned} \tag{26}$$

Applying now condition (23) for vanishing shear deformation gives for the strain component ϵ_α an expression

$$\epsilon_\alpha=\frac{\partial u_\alpha}{H\partial\alpha}+\frac{u_n}{R}+\frac{1}{2}\Big(\frac{\partial u_n}{H\partial\alpha}-\frac{u_\alpha}{R}\Big)^2. \tag{27}$$

Consider next VON KÁRMÁN's beam theory for beams and shallow arches. It is assumed that the derivative of the axial displacement is small likewise all terms containing $1/R$, TUOMALA [7]. When these are dropped the expressions (14) and (15) take the form

$$\begin{aligned}\epsilon_\alpha&=\frac{1}{2}\Big(\frac{\partial u_n}{H\partial\alpha}\Big)^2-n\frac{\partial\theta}{H\partial\alpha}\Big(\cos\theta\frac{\partial u_n}{H\partial\alpha}+\sin\theta\Big)+\frac{n^2}{2}\Big(\frac{\partial\theta}{H\partial\alpha}\Big)^2,\\ \gamma_{\alpha n}&=\cos\theta\frac{\partial u_n}{H\partial\alpha}-\sin\theta.\end{aligned} \tag{28}$$

From the latter the angle of rotation can be determined according to the EULER-BERNOULLI assumption yielding

$$\tan\theta = \frac{\partial u_n}{H\partial\alpha}, \tag{29}$$

and finally for the strain ϵ_α an expression

$$\epsilon_\alpha = \tfrac{1}{2}(u_n')^2 - 2n\frac{u_n''}{\sqrt{(1+(u_n')^2)^3}} + \tfrac{1}{2}n^2\left(\frac{u_n''}{1+(u_n')^2}\right)^2, \tag{30}$$

in which the notation $(\cdot)' = \partial(\cdot)/H\partial\alpha$ for the derivative with respect to the arch length is adopted, for brevity.

Applying then finally expressions (22) results in the relations

$$\begin{aligned} \epsilon_\alpha &= -n\cos\theta\frac{\partial\theta}{H\partial\alpha} + \frac{1}{2}\sin^2\theta, \\ \gamma_{\alpha n} &= \frac{\partial u_n}{H\partial\alpha} - \sin\theta(1 + n\frac{\partial\theta}{H\partial\alpha}). \end{aligned} \tag{31}$$

which reduce with the assumption of vanishing shear deformation, according to (24), on the beam axis to the form

$$\epsilon_\alpha = \tfrac{1}{2}(u_n')^2 - nu_n'', \tag{32}$$

REFERENCES

1. J. Paavola and E.-M. Salonen, Use of Local Rectangular Coordinates in Various Structural Analyses, in "Proceedings of the 4th Finnish Mechanics Days", E. Niemi (Ed.), Lappeenranta, Finland, 1991, 369-376
2. K. Väisälä, "Vektorianalyysi", 6th ed, WSOY, Helsinki, 1975 (in Finnish)
3. V.V. Novozhilov, "Foundations of the Nonlinear Theory of Elasticity", 3rd ed, Graylock Press, Translation, Rochester, New York, 1963
4. J.T. Oden, "Finite Elements of Nonlinear Continua", McGraw-Hill Book Company, Advanced engineering series, New York, 1972
5. L.E. Malvern, "Introduction to the mechanics of continuous medium", Prentice-Hall, New York, 1969
6. G.J. Simitses, "An Introduction to Elastic Stability of Structures", Prentice-Hall, Inc., Englewood Cliffs, New Jersey, 1976
7. M. Tuomala, "Eräiden yksinkertaisten rakenteiden staattisen ja dynaamisen vasteen analysointi elementtimenetelmällä", Teknillinen korkeakoulu, Rakennetekniikan laitos, Julkaisu 30, 1980 (in Finnish)
8. J. Paavola and E.-M. Salonen, Muodonmuutokset ja kiinteät paikalliset karteesiset koordinaatit, Rakenteiden Mekaniikka, **24**, No 3, (1992) 38-55 (in Finnish)

APPLICATION OF DIMENSIONAL ANALYSIS TO PROBLEMS OF FLUID MECHANICS

TUOMAS PALOPOSKI
Laboratory of Energy Engineering and Environmental Protection
Helsinki University of Technology
FIN-02150 Espoo, Finland

ABSTRACT

The application of dimensional analysis to a well-known example is described. The objective is to illustrate how dimensional analysis can be used to improve the physical understanding of fluid mechanics problems.

1. INTRODUCTION

Dimensional analysis is an elegant and powerful tool both in the theoretical treatment of the differential equations that govern physical phenomena and in the efforts to rationalize experimental work. It has been found out, however, that the application of dimensional analysis to practical problems often leads to failure and disillusionment. Thus, there is still a need for detailed expositions of the fundamental ideas.

In this paper, a well-known example of the application of dimensional analysis is discussed. Attention will be paid to points-of-view which may help to increase the physical understanding of fluid mechanics problems. Essentially similar lines of thought have been employed in our laboratory to solve more complex problems of current scientific and technical interest. Those results cannot be presented in this paper due to lack of space but will be presented in another publication in the near future.

2. DRAG FORCE ON A SPHERICAL BODY

Consider the following problem. A spherical body with a diameter D is immersed in a fluid stream moving with a constant velocity U. The density and viscosity of the fluid are ρ and η, respectively. We want to determine the drag force F acting on the body, that is, we are searching for a relationship of the type

$$F = f(D, U, \rho, \eta). \tag{1}$$

It has to be noted, of course, that this is not really a problem of current scientific interest. The problem has been worked out in great detail in the past and is now widely used as an example in textbooks of dimensional analysis and fluid mechanics; see, for example, [1, pp. 14–16; 2, pp. 53–55, 248–255; 3, pp. 413–414].

Let us first go through the standard procedure of dimensional analysis. The solution is obtained as follows. Note first that there are five variables (F, D, U, ρ, η) and three fundamental dimensions (mass, length, time). It can be easily shown that the rank of the dimensional matrix is three. Thus, there are $5 - 3 = 2$ dimensionless variables in a complete set and the solution can therefore be expressed as a relationship of the type

$$\Pi_1 = f(\Pi_2). \tag{2}$$

The commonly used dimensionless variables are

$$\Pi_1 = C_D = \frac{F}{\frac{\pi}{4}D^2\frac{1}{2}\rho U^2} = \frac{8}{\pi}\frac{F}{\rho U^2 D^2} \tag{3}$$

and

$$\Pi_2 = \mathrm{Re} = \frac{\rho U D}{\eta} \tag{4}$$

which can be substituted into Equation (2) to obtain

$$C_D = f(\mathrm{Re}). \tag{5}$$

Thus, the drag coefficient C_D is to be expressed as a function of the Reynolds number Re. It has indeed been confirmed by experimental investigations that a relationship of this type exists; see, for example, Fig. 1. in [1, p. 16] and Fig. 4-1. in [2, p. 54].

Two regions are of particular interest:

$$C_D = \frac{24}{\mathrm{Re}} \qquad \text{for } \mathrm{Re} < 1 \tag{6}$$

and

$$C_D \approx 0.44 \qquad \text{for } 10^3 < \mathrm{Re} < 2 \cdot 10^5. \tag{7}$$

Equation (6) is the well-known Stokes' law, which can also be derived theoretically using the creeping flow assumption; see, for example, [2, pp. 248–255]. The creeping flow assumption means that the inertial terms in the equations of motion are discarded since they are assumed to be negligible when compared with the pressure and viscous terms.

This is as far as the textbooks will take us; naturally, many more details are usually given along the way. But there is much more to be gained with some extra thoughts. Let us consider a few interesting questions.

(a) How do we know that all important variables were included in the analysis? And, on the other hand, how do we know that the variables included in the analysis are relevant?

(b) Why do we want to use C_D as the dependent dimensionless variable and Re as the independent dimensionless variable? After all, dimensionless variables can be chosen in an infinite number of ways.

(c) Do the special cases $\mathrm{Re} \ll 1$ and $\mathrm{Re} \gg 1$ have some particular physical significance? What would that be?

Question *(a)* may seem rather unnecessary since the validity of the theoretical analysis was already confirmed by the fact that the experimental data of C_D vs. Re follow a single curve. Collecting experimental data is, however, a tedious and expensive method of checking theoretical predictions. It makes sense to search for ways to refine our analysis before experimental investigations are to be undertaken.

It should first be noted that consideration of dimensional requirements may sometimes prevent gross mistakes. We know that the fundamental equations of fluid mechanics are dimensionally homogeneous and that the solutions of fluid mechanics problems can therefore be expressed by means of dimensionally homogeneous equations. Thus, one should check the list of variables to see whether it is possible to construct dimensionally homogeneous equations between the variables; if not, then at least one variable is certainly missing. For example, Langhaar [1, p. 14] has discussed a hypothetical case in which both ρ and η are disregarded in the problem described above. He pointed out that since it is impossible to construct a dimensionally homogeneous equation of the type $F = f(D,U)$, one should be warned not to proceed along this line any further. On the other hand, Kline [4, p. 6] has claimed that consideration of dimensional requirements is not likely to be of much help in practical problems.

It must also be recognized that one will not be able to know which variables are to be included in the analysis unless one has a sufficient understanding of the phenomenon being studied. According to Kline, this is the most difficult part of dimensional analysis [4, p. 6]. Bridgman emphasized the importance of a sufficient understanding [5, Ch. V] and stated that "... we are to imagine ourselves as writing out the equations of motion at least in sufficient detail to be able to enumerate the elements which enter them. ... (We use equations of motion in a general sense, applying to thermodynamic and electrical as well as mechanical systems.)" Langhaar gave some advice on the selection of variables [1, pp. 14–15], but a more detailed treatment would have been worthwhile.

At this point, it will be instructive to carry out some speculations. First, what will happen if we assume that ρ can be disregarded but η cannot? We will then be searching for a relationship of the type $F = f(D,U,\eta)$. Or, on the other hand, what will happen if we assume that η can be disregarded but ρ cannot? We will then be searching for a relationship of the type $F = f(D,U,\rho)$. Let us go through these two cases.

In the first case, we have four variables (F, D, U, η) and three fundamental dimensions. The rank of the dimensional matrix is three. Thus, there is only one dimensionless variable in a complete set and the solution can therefore be expressed as

$$\Pi = \frac{F}{\eta D U} = C \tag{8}$$

where C is a constant. Thus,

$$F = C\eta D U. \tag{9}$$

The value of C cannot be found by means of dimensional analysis; other methods are needed.

Now note that substituting Equation (9) into Equation (3) gives

$$C_D = \frac{F}{\frac{\pi}{4}D^2\frac{1}{2}\rho U^2} = \frac{8}{\pi}C\frac{\eta}{\rho U D} = \frac{8}{\pi}C\mathrm{Re}^{-1} \tag{10}$$

which becomes Stokes' law when $C = 3\pi$. Thus, the relationship $C_D \sim \mathrm{Re}^{-1}$ can be found in a simple manner using dimensional analysis and the assumption that the density of the fluid can be disregarded. Note also that the assumption that the density of the fluid can be disregarded is consistent with the creeping flow assumption.

In the second case, we have four variables (F, D, U, ρ) and three fundamental dimensions. The rank of the dimensional matrix is three. Thus, there is only one dimensionless variable in a complete set and the solution can therefore be expressed as

$$\Pi = \frac{F}{\rho D^2 U^2} = C \tag{11}$$

where C is a constant. Thus,

$$F = C\rho D^2 U^2. \tag{12}$$

The value of C cannot be found by means of dimensional analysis; other methods are needed.

Note that substituting Equation (12) into Equation (3) gives

$$C_D = \frac{F}{\frac{\pi}{4}D^2\frac{1}{2}\rho U^2} = \frac{8}{\pi}C \tag{13}$$

which becomes Equation (7) when $C = 0.173$. Thus, the relationship that C_D is independent of Re can be found in a simple manner using dimensional analysis and the assumption that the viscosity of the fluid can be disregarded.

The fact that dimensional analysis can be used to derive the results shown in Equations (10) and (13) has also been pointed out by Tritton [6, p. 94].

We are now able to move to questions *(b)* and *(c)*. Two important special cases have emerged: for $\mathrm{Re} < 1$, the viscosity of the fluid is important whereas the density of the fluid is not; for $\mathrm{Re} > 10^3$, the density of the fluid is important whereas the viscosity of the fluid is not. There is also a region where both the density and the viscosity of the fluid are important; this region is defined by $1 \leq \mathrm{Re} \leq 10^3$. Thus, Re seems to be an important parameter with obvious physical significance and it is quite natural to choose Re as the independent dimensionless variable. It should be noted, of course, that the physical significance of the Reynolds number can also be established by manipulating the equations of motion; see, for example, [2, Ch. 11]. This point will be further discussed in the next section.

Note that the words "independent" and "dependent" are used here in the meaning established in Article 16 of Langhaar's textbook [1, pp. 38–39]. Thus, the commonly used terms "independent variable" and "dependent variable" have simply been introduced into dimensional analysis. It has to be noted, however, that Langhaar has also used the term "independent dimensionless variable" in another, entirely different meaning. According to Article 7 in [1, pp. 16–18], an independent dimensionless variable is a dimensionless variable which cannot be expressed as a product of powers of the other dimensionless variables in a complete set. In this particular case, C_D is dependent in the sense that its value will depend on the value of Re and independent in the sense that C_D cannot be expressed as a power of Re. It is rather unfortunate that such confusion in terms has arisen.

3. ANALYSIS OF GOVERNING EQUATIONS

Consider the steady flow of an incompressible Newtonian fluid (neglect any body forces). The flow is governed by the equation of continuity and the equations of motion. The equations of motion are also called the Navier-Stokes equations and are of the form

$$\rho v_x \frac{\partial v_x}{\partial x} + \ldots = -\frac{\partial p}{\partial x} + \eta\left(\frac{\partial^2 v_x}{\partial x^2} + \ldots\right) \tag{14}$$

where the inertial terms are on the left-hand side and the pressure and viscous terms are on the right-hand side. For the purposes of this study, it is sufficient to consider the general form of the various terms; thus, only the x component of velocity and partial derivatives with respect to x are shown here. The complete equations can be found in textbooks of fluid mechanics.

Let us now try to develop a methodology for comparing the importance of various terms in the Navier-Stokes equations. We first non-dimensionalize the equations as follows. Choose the dimensionless variables

$$\tilde{v}_x = \frac{v_x}{U}, \quad \tilde{x} = \frac{x}{L}, \quad \tilde{p} = \frac{p}{P} \tag{15}$$

where U is the characteristic velocity, L is the characteristic length and P is the characteristic pressure. Thus, the partial derivatives can be written as

$$\frac{\partial v_x}{\partial x} = \frac{U}{L}\frac{\partial \tilde{v}_x}{\partial \tilde{x}}, \quad \frac{\partial^2 v_x}{\partial x^2} = \frac{U}{L^2}\frac{\partial^2 \tilde{v}_x}{\partial \tilde{x}^2}, \quad \frac{\partial p}{\partial x} = \frac{P}{L}\frac{\partial \tilde{p}}{\partial \tilde{x}} \tag{16}$$

and substitution of Equations (15) and (16) into Equation (14) gives the dimensionless form of the Navier-Stokes equations:

$$\begin{aligned} \tilde{v}_x \frac{\partial \tilde{v}_x}{\partial \tilde{x}} + \ldots &= -\frac{P}{\rho U^2}\frac{\partial \tilde{p}}{\partial \tilde{x}} + \frac{\eta}{\rho U L}\left(\frac{\partial^2 \tilde{v}_x}{\partial \tilde{x}^2} + \ldots\right) \\ &= -\frac{P}{\rho U^2}\frac{\partial \tilde{p}}{\partial \tilde{x}} + \frac{1}{\mathrm{Re}}\left(\frac{\partial^2 \tilde{v}_x}{\partial \tilde{x}^2} + \ldots\right). \end{aligned} \tag{17}$$

Let us assume that U, L and P have been chosen in such a way that all dimensionless variables and their all derivatives are of order unity everywhere within the system being studied. Note that this assumption is rather subtle and cannot always be satisfied; see the discussions in [2, Chs. 11 and 15; 4, pp. 101–105]. For example, in boundary layer flows there are two characteristic lengths and velocities.

The relative importance of various terms can now be compared. For $\mathrm{Re} \gg 1$, viscous terms will be negligible when compared to the inertial terms. For $\mathrm{Re} \ll 1$, inertial terms will be negligible when compared to the viscous terms. Thus, the physical significance of the Reynolds number has been established.

How should one choose P? The pressure terms in the Navier-Stokes equations are always comparable to at least one other term involving the velocity [6, p. 66]. It has been suggested by Denn [2, p. 235] that

$$P = \rho U^2 \qquad \text{for } \mathrm{Re} \ll 1 \tag{18}$$

and

$$P = \frac{\eta U}{L} \qquad \text{for } \mathrm{Re} \gg 1. \tag{19}$$

A new approach is proposed here. Let

$$P = \rho U^2 + \frac{\eta U}{L} = (\mathrm{Re}+1)\frac{\eta U}{L} \tag{20}$$

which yields

$$\frac{P}{\rho U^2} = 1 + \frac{1}{\mathrm{Re}} \tag{21}$$

and the dimensionless form of the Navier-Stokes equations becomes

$$\tilde{v}_x \frac{\partial \tilde{v}_x}{\partial \tilde{x}} + \ldots = -\left(1 + \frac{1}{\mathrm{Re}}\right)\frac{\partial \tilde{p}}{\partial \tilde{x}} + \frac{1}{\mathrm{Re}}\left(\frac{\partial^2 \tilde{v}_x}{\partial \tilde{x}^2} + \ldots\right). \tag{22}$$

For Re $\ll$ 1, Equation (22) becomes the creeping flow equation

$$-\frac{\partial \tilde{p}}{\partial \tilde{x}} + \frac{\partial^2 \tilde{v}_x}{\partial \tilde{x}^2} + \ldots = 0. \tag{23}$$

For Re $\gg$ 1, Equation (22) becomes Euler's equation of inviscid motion

$$\tilde{v}_x \frac{\partial \tilde{v}_x}{\partial \tilde{x}} + \ldots = -\frac{\partial \tilde{p}}{\partial \tilde{x}}. \tag{24}$$

Thus, the characteristic pressure given in Equation (20) seems to be a reasonable choice.

CONCLUSIONS

Successful application of dimensional analysis to problems of fluid mechanics requires good physical understanding of the problems. On the other hand, skillful application of dimensional analysis can increase the physical understanding of fluid mechanics problems.

ACKNOWLEDGEMENTS

The author would like to thank Professor Eero-Matti Salonen for helpful discussions.

REFERENCES

1. H. L. Langhaar, "Dimensional Analysis and Theory of Models", John Wiley & Sons, New York, 1951.

2. M. M. Denn, "Process Fluid Mechanics", Prentice-Hall, Englewood Cliffs, 1980.

3. L. M. Milne-Thomson, "Theoretical Hydrodynamics", 2nd ed., MacMillan and Co., London, 1949.

4. S. J. Kline, "Similitude and Approximation Theory", Springer-Verlag, Berlin, 1986.

5. P. W. Bridgman, "Dimensional analysis", Yale University Press, New Haven, 1931.

6. D. J. Tritton, "Physical Fluid Dynamics", 2nd ed., Oxford University Press, Oxford, 1988.

REDUCTION OF FRICTION BY DEVELOPING THE STRUCTURE OF SKI

MSc, Lic. Tech. Pekka Hautala
Helsinki University of technology, Laboratory of Machine Design
Otakaari 4 A
FIN-02150 Espoo, Finland

ABSTRACT

Various mechanisms contribute to the resistance to sliding over snow: plowing and compaction in front of the slider, snow deformation below the slider, deformation or fracture of the asperities, shear of the water films that support the slider's weight, capillary attraction from other water attachments, and dragging along surface dirt.

The mechanisms do not operate independently. Different mechanisms dominate under different conditions of load, speed, temperature, roughness, wetness, snow type, and slider characteristics. One of the factors that affects the above mentioned conditions, is the structure of the ski, especially as far as the plowing and compaction factors and deformation under the ski are concerned. In addition, the spreading of the surface pressure below the ski affects the tribological contact between the sole and snow.

This paper presents the measurement methods and equipment of the mechanical properties of the ski, measured results as well as conclusions are drawn from the structure of a good ski.

1. INTRODUCTION

At the moment there are two ways to ski, the traditional one and skating. The ski for the traditional skiing can construct properly well, but the ski for skating is much more complicated. The reason is that, that the traditional skiing is a two dimensional and skating is a three dimensional case.

The low friction, when the ski is sliding on the snow, is due to water film lubrication. If the sliding speed is appreciable and temperature below 0°C, the local surface melting is produced by the frictional heating of the sliding surfaces (fig. 1) /1/, /2/.

In the later investigation has been noticed, that various mechanisms contribute to the resistance to sliding over snow: plowing and compaction in front of the slider, snow deformation below the slider, deformation or fracture of the asperities, shearing of the water films that support the slider's weight, capillary attraction from other water attachments, and dragging along surface dirt /3/.

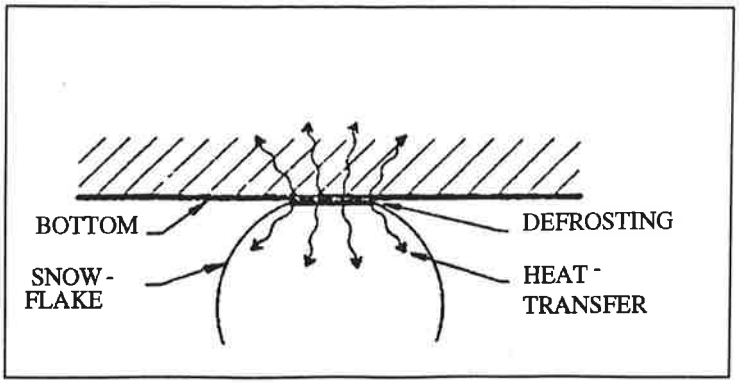

FIGURE 1. Water film lubrication /1/.

There is no water film lubrication under the tip of the ski. The contact is dry. In addition the snow compresses and it's pushed aside from that area. At the middle of the ski the snow compression, deformation and fracture of asperities, shearing of the water film, capillary attraction and drag by the surface dirt resist the sliding. If the processes operate independently, the total friction (μ) can be expressed as the sum of terms representing each mechanism /3/:

$$\mu = \mu_{plow} + \mu_{dry} + \mu_{lub} + \mu_{cap} + \mu_{dirt}$$

And when two processes interact in parallel, the total friction can be governed by:

$$1/\mu = 1/\mu_{dry} + 1/\mu_{lub}$$

The total friction depends extremely much on the contact pressure of the ski and the snow /3/. There is presented a typical pressure distribution in the fig. 2. It has been noticed by experience that the distance between pressure areas (wheel base) is long in good skating skis. Also the pressure distribution is tapered.

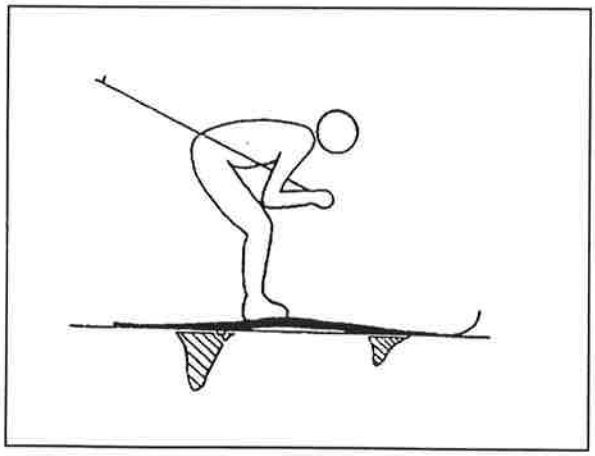

FIGURE 2. The pressure distribution under the ski /4/.

The mechanical properties of the ski have a great effect on the total friction of the ski. Also the skating skiing has created new requirements of the mechanical properties of the ski.

The goal of the research work is to find out the properties that make skating skis good to ski and to develop the ski better than ever (fig. 3).

The paper presents the measurement methods and equipment of the mechanical properties of the ski, measured results as well as conclusions are drawn from the structure of a good ski.

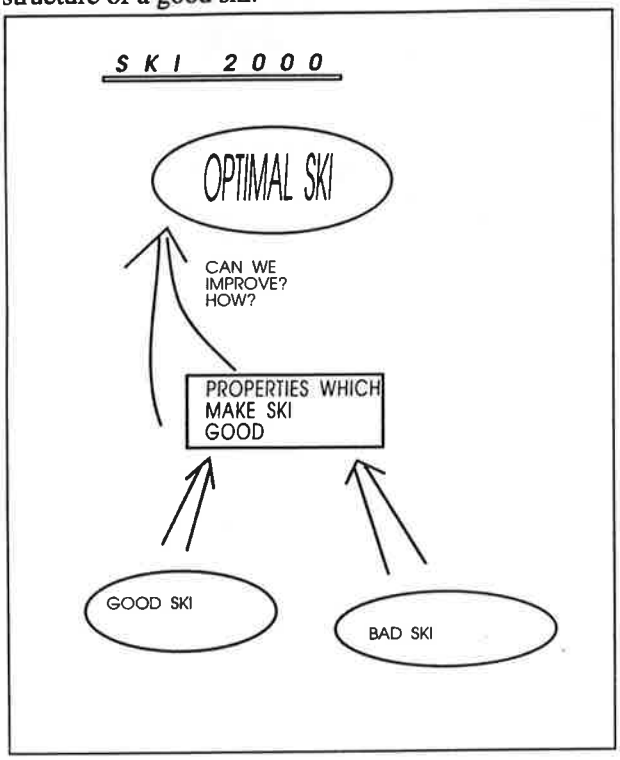

FIGURE 3. SKI-2000 research.

2. Experiment methods and equipment

2.1 Bending stiffness and shape

An equipment was developed to measure the bending stiffness and the shape of the ski (fig 4). The shape of the bottom of the ski is measured by potentiometer and the data is acquisited by computer. The equipment can define the shape with the resolution of 0,012 mm in every 0,2 mm.

First the shape is defined without the load. Then the shape is measured in three point bending position. The difference of these two is the diffraction line. The bending

stiffness distribution can be calculated from the diffraction line by the difference method.

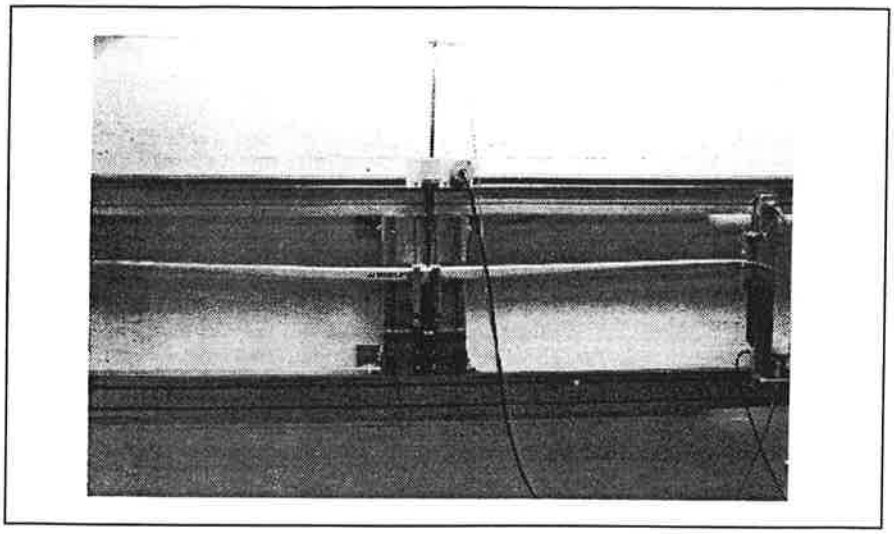

FIGURE 4. The bending stiffness measurement equipment.

2.2 Contact pressure

The theoretical relationship between bending stiffness and contact pressure is quite complicated, because the ski is non-straight beam on the elastic basis. For the reason was developed the contact pressure measurement equipment (fig. 5). In earlier investigations the contact pressure was measured by removable sensor, but this technique turned out to be unreliable.

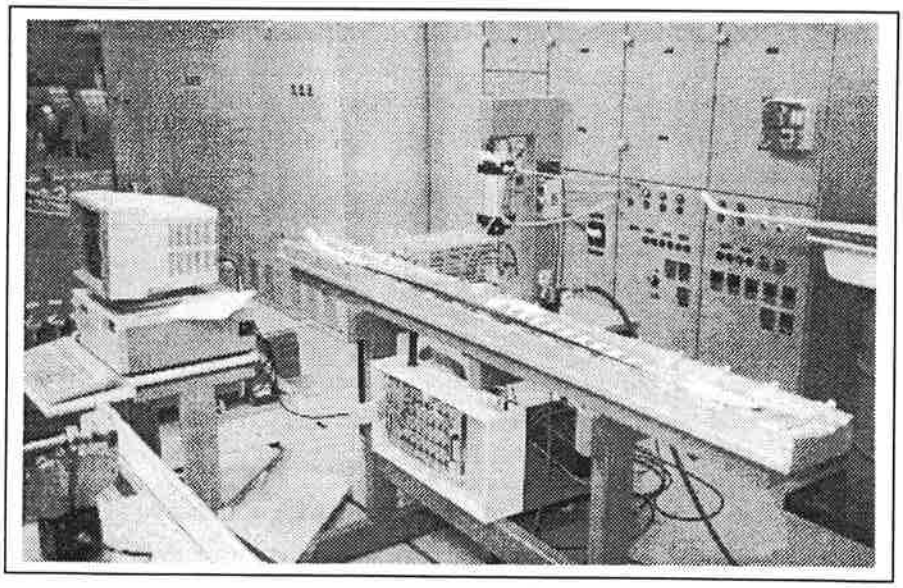

FIGURE 5. The contact pressure measurement equipment.

The current equipment consists of 34 strain-gage pressure sensors, by which the contact force can be measured in every 125 mm. The elasticity of the sensors is the same as the one of the skiing track's (fig. 6).

The ski is loaded by step-by-step increasing force. The measured data is acquisited by the computer.

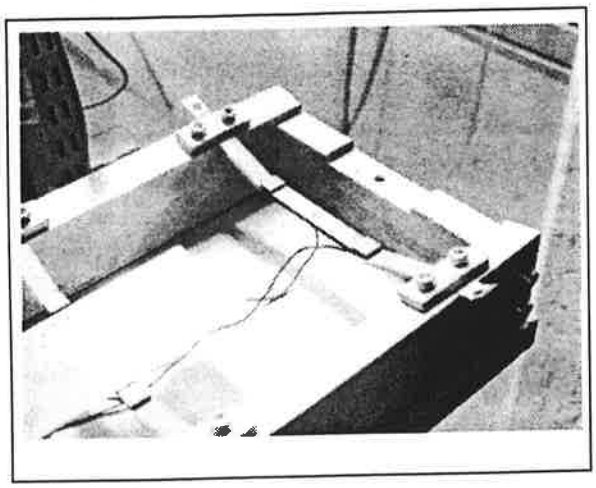

FIGURE 6. The pressure sensor.

2.3 Moment of inertia

The moment of inertia of the ski can be measured by a simple torsional pendulum (Fig. 7). The moment of inertia is calculated from the oscillation time, if the oscillation time of a sub-structure with known moment of inertia is measured.

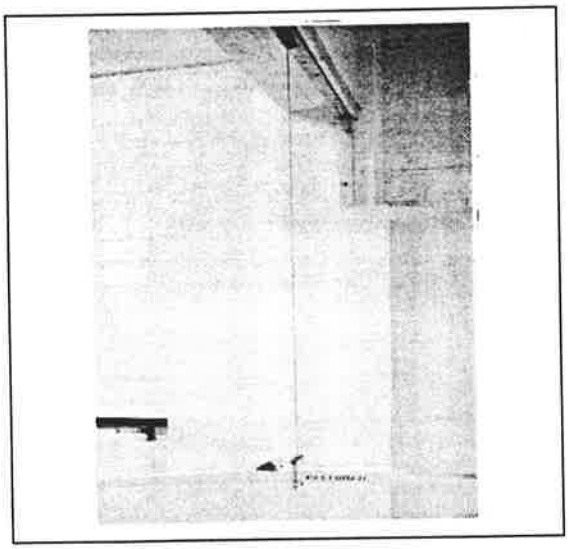

FIGURE 7. The equipment for measuring the moment of inertia.

2.4 Torsional stiffness

The torsional stiffness of the ski was detected by measuring the angle of torsion, when the ski was loaded with known torsional moment.

2.5 Vibration properties

The vibration properties of the ski were measured in the Laboratory of Strength of Materials in Helsinki University of technology. The measurements were done by GenRad 2515 real time spectra analyzator.

3. Results, Skis of the Finland's skiing team

The measured skis were selected by Finnish ski racers. They used the skis in competitions during the season 1993-1994. The skis were named A-D. The results are presented in figures 8 - 15.

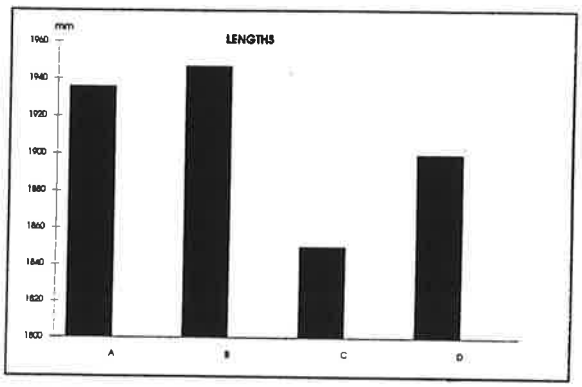

FIGURE 8. Lengths.

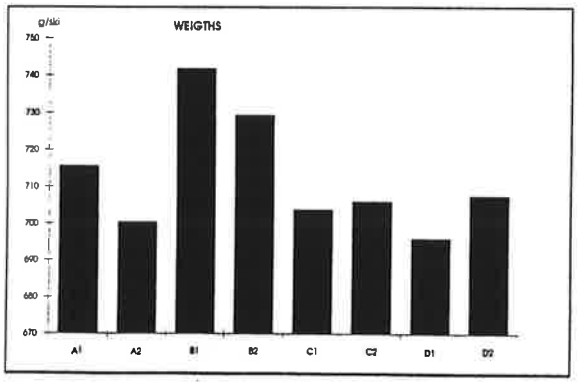

FIGURE 9. Weights.

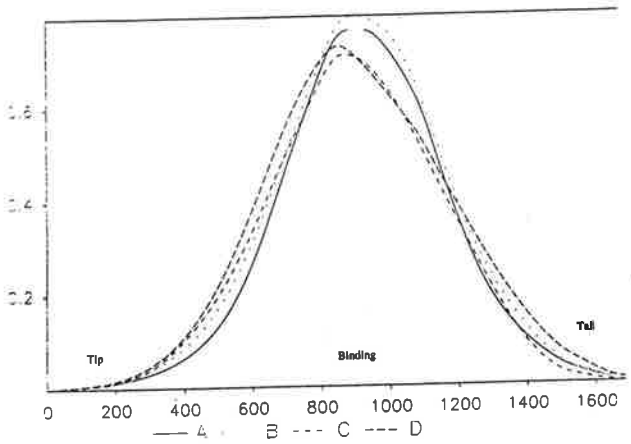

FIGURE 10. Bending stiffnesses.

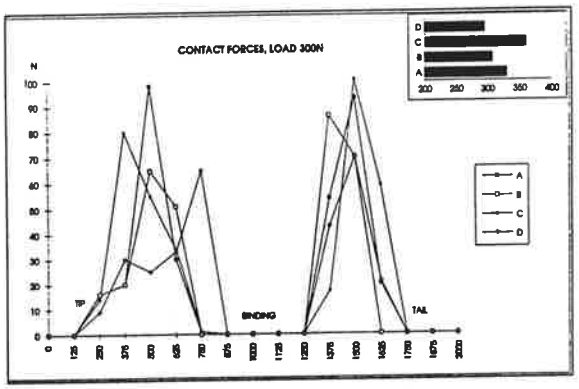

FIGURE 11. Contact forces, load 300 N.

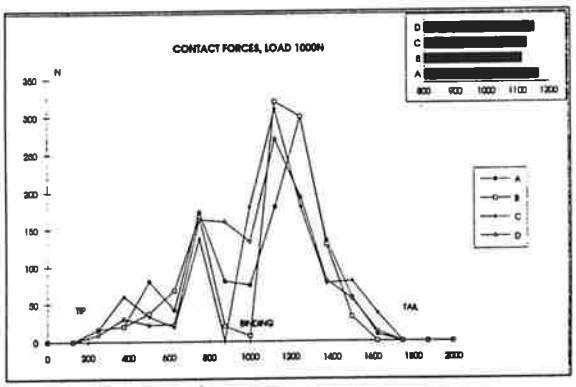

FIGURE 12. Contact forces, load 1000 N.

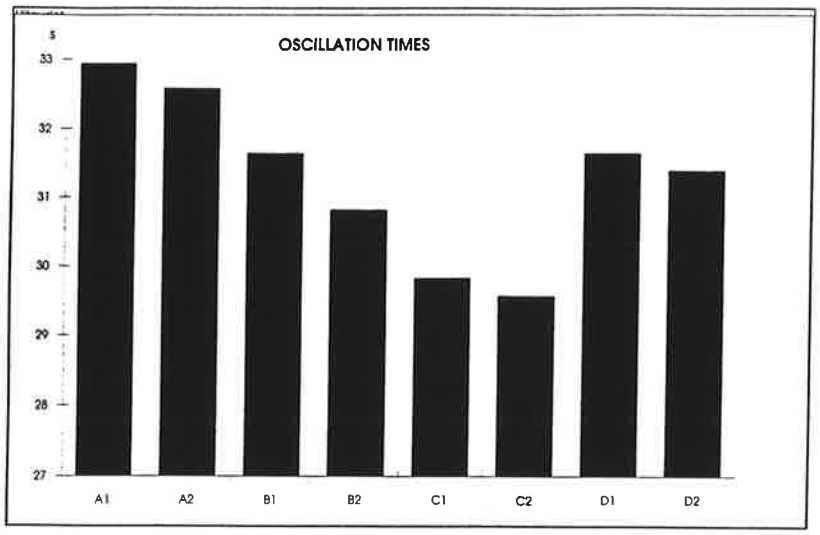

FIGURE 13. Oscillation times (Moments of inertia).

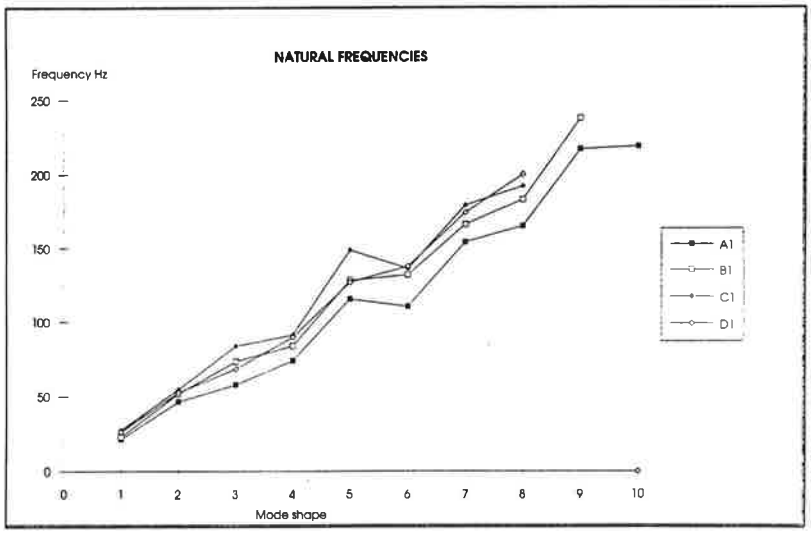

FIGURE 14. Natural frequencies.

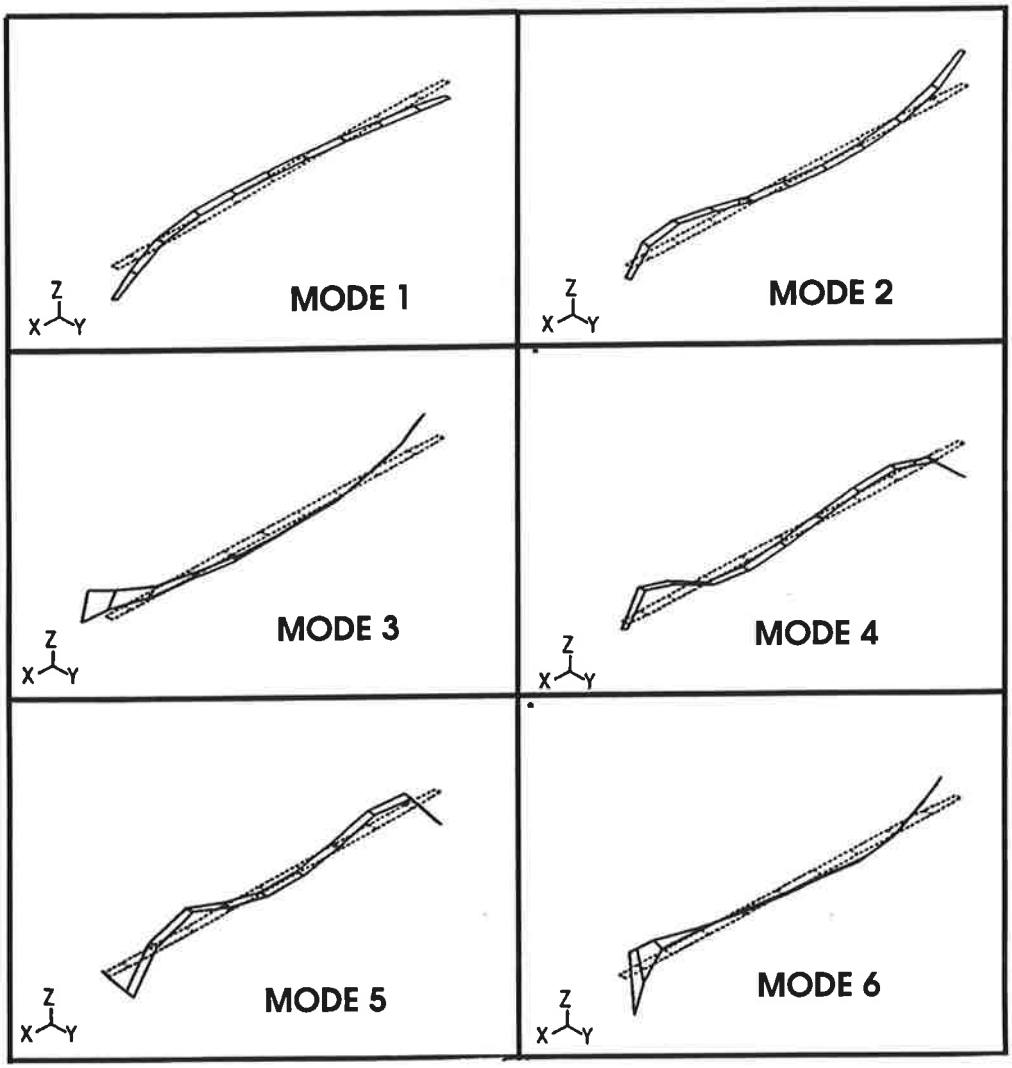

FIGURE 15. Mode shapes 1-6.

4. CONCLUSIONS

4.1 Equipment

Concluded from the measurements it can be said that the working reliability of the equipment is good. The equipment for measuring contact forces and moments of inertia were first time in use. Other equipment have been utilized earlier.

The pressure sensors in the equipment for measuring contact forces should be at the same level of heigth. The 6th sensor was obviously at lower level than the others during the measurements.

4.2 Results

The biggest differences between skis can be said to be in weights, contact forces and torsional stiffnesses. The differences in weights are partly due to differences in lengths.

The weights of the skis were measured with equal bindings. If we want to know real differences between skis, the weight of the binding (130 g) should be taken from the weight of the ski. The weight of the binding is rather big. More attention should be put in to developing lighter bindings.

In the introduction was mentioned that the distance between pressure areas (wheel base) is long in good skating skis. All the skis have this property. Obviously ski D is for lighter racer, because the ski has bigger contact forces under the binding than the other skis. It is also noticeable, that the contact force doesn't increase after the certain limit while the load still rising.

If the ski does not have enough torsional stiffness, it twists and is no more steerable. The measuring method was novel, and therefore no exact conclusions can be drawn. But obviously the ski D compensate its poor bending stiffness by the good torsional stiffness, and there fore a racer considered it as a good ski. Because the torsional stiffness is an important property of a ski, it should be developed a more accurate measurement equipment in the future.

There were only small differences between the skis in the vibration properties. The greatest differences were in the 3rd mode. The ski C had the lowest natural vibration. This was due to the camber of the ski C, which was larger than the one of the other skis'.

As a conclusion it can be stated that the distance between pressure areas (wheel base) is long in good skating ski, and it has enough bending and torsional stiffness and it should be light.

References:

1.R. Eriksson, Medens friktion mot snö och is. Meddelande n:r 34-35, Föreningen Skogsarbeten och Kungl. Domänsstyrelsens Arbetsstudieavdelning, 1949

/2/ Bowden, F. P., Friction on Sow and Ice, 1953

/3/ Colbeck, S., A Review of the Processes That Controls Snow Friction. Monograph 92-2, 1992

/4/ Lehtovaara, A., Kinetic Friction between Ski and Snow. Acta Polytechnica Scandinavica, Mechanical Engineering Series No. 93, 1989

FULL 3D STRESS FIELD ANALYSIS IS TO BECOME THE GENERALIZED FRACTURE PARAMETER

KARI IKONEN & HEIKKI RAIKO
VTT Energy
P.O. Box 1604, FIN-02044 VTT, FINLAND

ABSTRACT

Numerical results of the shallow crack effect is presented. The fracture toughness in transition area measured in J-integral is considerably increased, when crack depth or length is low. This phenomenon can be simulated using materially nonlinear FE-method and very detailed FE-mesh to get the actual value of the local stress close to the crack tip region. The cleavage fracture is assumed to take place when the maximum crack closing stress component has reached the critical value. This is, in principle, application of maybe the eldest strength hypothesis in the world, the maximum principal stress hypothesis instead of J-integral approach. The result of these kind of analyses can be used as a constraint correction parameters in fracture toughness experiments, where the specimen dimensions (size) do not fulfil the requirements to produce small scale yielding (SSY) condition. Even the very largest test specimen do not exactly produce the SSY condition, so, a numerical analysis of this kind always decreases the amount of error in test result interpretation.

1. INTRODUCTION

When making fracture mechanics tests with small or moderate size test specimen, the K_I-dominated stress field is highly disturbed in 2D-specimens close to free surfaces or in all the crack area, if the crack is shallow or ligament is small compared to other dimensions of the small specimen. All these effects are increased in significance if the plastic zone in the crack tip is large compared to the depth (a) or ligament of the crack, ref. [1], [3]. The code requirements for fracture mechanics tests (ASTM E399-83 and ASTM E813-87) define the minimum size of the test specimen as a function of flow stress and J-integral loading level. However, to know more exactly the 3D-stress state, the effect of reduced constraint at or close to free surfaces, the form and width of plastic zone, the variation of COD and J-integral in the front of crack tip, and the possible errors in interpretation of test measurements, very detailed nonlinear 3D stress analysis is needed. In the following, a short description of the FE-analysis system made for this kind of analysis is given and some numerical results are reported and discussed. The results show that a lot of error can be avoided in the interpretation of fracture mechanics test results, if a detailed 3D FE-analysis is made in addition to the

test itself with known stress-strain-relationship of the tested material and with known shape and dimensions of the test specimen and the initial crack.

2. STRESS FIELDS IN CLEAVAGE FRACTURE

If we look at stress components in front of crack tip in mathematical plane strain (MPS) condition, Fig.1, we can see that the crack closing stress component in the very tip of the crack is equal to yield strength corresponding the strain rate. This means that the stress state at the blunted crack tip is two dimensional due to the free surface of the blunted crack tip. If we go ahead in front of the tip, the stress state becomes more three dimensional and the current stress components grow much higher. The maximum of the crack closing stress component is about three times the one dimensional yield stress and the location of the maximum is about 2 - 4 times CTOD in front of the crack tip. This can be decided even by linear elastic reasoning, by FEM or by slip line theory.

The cleavage fracture is assumed to take place when the maximum crack closing stress component has reached a critical value. This is, at least in principle, application of the eldest strength hypothesis in the world, the maximum principal stress hypothesis by Rankine, Lamé, Clapeyron and Maxwell. Keeping this in mind, we can now make a correlation between the measured value of critical J-integral from a test specimen and the respective critical J-integral value in undisturbed small scale yielding field, (SSY). This kind of numerical stress analysis application can be used in the lower transition region where extensive plasticity precedes unstable fracture.

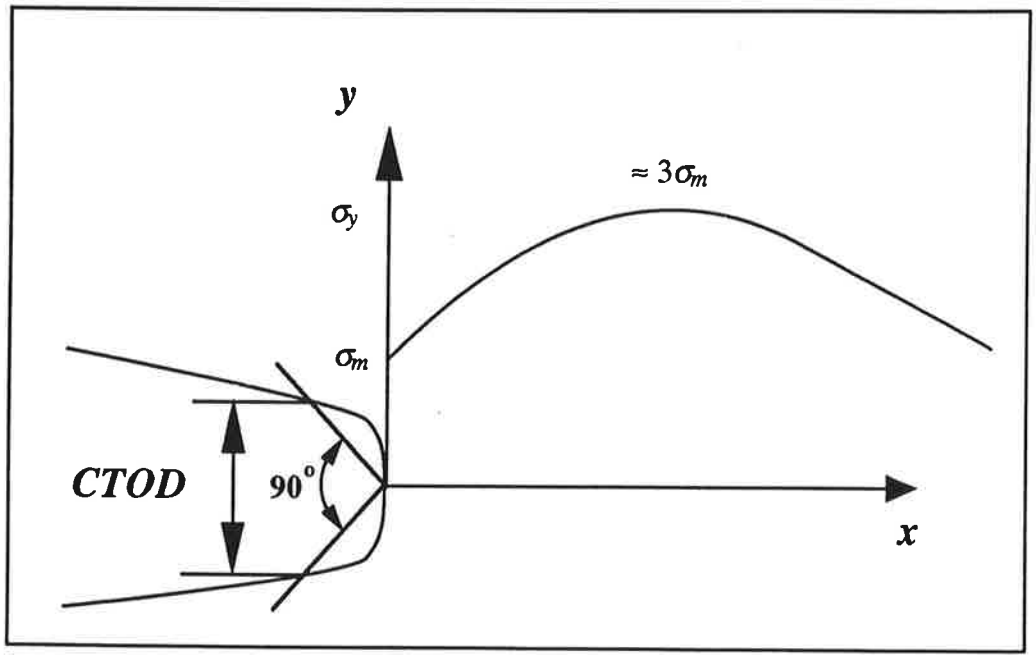

FIGURE 1. *The maximum crack closing stress component in front of a crack tip.*

3. NUMERICAL ANALYSIS PROCEDURE

A FE-method based computer code was developed at VTT Energy for special analysis purpose now in question. The basis of the program is a typical materially nonlinear FE-program. The nonlinear behavior of material is programmed according to von Mises's yielding condition and associative flow rule [4]. Due to nonlinearities the analysis process is incremental and step by step iterative. The special features needed in the FE-program for nonlinear analysis of stress fields very close to crack tip are:

- automatic node and element generation for very high density, well shaped and balanced mesh in the crack tip area,
- calculation of CTOD according to [9] in the crack front during the incremental analysis,
- calculation of J-integral in the crack front by path and domain integral method, and by a very powerful and accurate own developed method for curved crack front (eg. semielliptical cracks). The average J-integral is also calculated globally from beam deflection and reaction force,
- calculation of maximum crack closing stress component (the most positive principal stress component) in front of crack tip in the distance of about 1 to 10 CTODs during the incremental analysis,
- automatic reference case analysis (small scale yielding), where the FE-modeled crack tip area is analyzed with forced displacement boundary conditions based on analytical solution of small scale yielding infinite field [3], which gives a HRR-field close to crack tip, ref. [5], [8],
- comparison of calculated J-integral values in small scale yielding field solution and real test specimen geometry solution corresponding to equal maximum crack closing stress component in front of the crack front locating in the distance of about 2 - 4 times local CTOD, ref. [3], and
- post processing capabilities with interactive color graphics.

First a 2D FE-program was developed including the features described above. The 2D program includes the options of analyzing plane strain, plane stress and axisymmetric stress state. When doing 2D analyses it became evident that in addition to the relative shallowness (a/W) of the crack the distance of free surface at the ends of the crack in specimen also had a prominent effect in local stiffness, stresses and J-integral values. Therefore, the FE-code was expanded into 3D. In 3D program the calculation of J-integral had to be changed from line integral to domain integral method. The 3D program is able to model the effect of the partly plain stress state close to free boundary at the specimen edge. Accordingly, the possible side grooves of the specimen can be exactly modeled in the analysis. The 3D analysis gives the J-value in all calculation points of the crack front and the average J-value over the crack front can be calculated, too. Thus we are able to compare the measured average value from the test and the actual maximum value of the fracture parameter. The need of very small elements, whose dimensions are equal to order of CTOD, and the need of calculating high stresses compared to uniaxial yield strength causes frequently some numerical troubles and the iteration processes have to be continued to very high accuracy to get stable results. The updating of stiffness matrix is important for accurate and effective calculation.

4. MODELING OF THE CRACK TIP

In 2D analysis 8-noded and in 3D analysis 20-noded isoparametric elements with reduced or full Gauss quadrature were employed in the models. The mesh close to crack tip front is generated in polar coordinate system. The mesh is often generated only for a symmetric half of the structure. Circumferentially the elements are evenly distributed typically in 8 or 12 element sectors. Radially the elements are generated in a way that the radial length of the element layer is increasing in geometric series. The minimum element size close to the crack tip must be order of one COD with reasonable load level and the outside diameter of the circular mesh area must be at least ten times the plastic zone dimension. The reasonable size ratio between radial element layers is between 1 and 2. This leads to 10 to 30 radial layers of elements in the near tip field mesh. These rules yield typically to element meshes shown in Fig. 2. for three point bend specimen. There are 1092 nodes and 329 elements in the mesh. The semi circular area close to crack tip contains 30 layers of 8 elements.

In 3D models the symmetry of three point bend specimen is used in two sections; the transverse section at crack plane and the longitudinal vertical section in the axis plane of the beam. Thus only a quarter of the beam need to be modeled. The number of element layers in the half thickness dimension of the test specimen were varied from 1 to 4, which corresponds to 2 to 8 element layers in the full thickness. Two element layers give reasonable results for beam without side grooves, but a beam with V-shaped side grooves needs 3 to 4 element layers in half thickness direction to give stabile local values for the fracture parameter. The element layers have to be focused close to the free surface. In the middle part of the beam model the element layers can be thick compared to the thickness of the specimen.

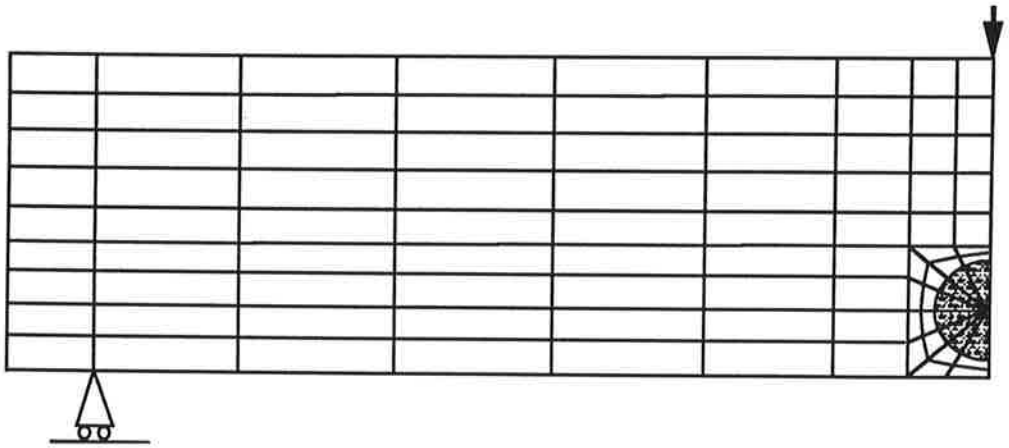

FIGURE 2. *Typical 2D mesh for three point bend test specimen.*

5. NUMERICAL RESULTS FOR THREE POINT BENDING SPECIMEN

First application of the 2D FE-analysis system was the analysis of a three point bending test specimen (W=150, B=75 and L=600 mm), refs. [6], [7]. In some actual tests the initial crack length had been a=15 mm. The material stress-strain relationship in test temperature was tested and constants for Ramberg-Osgood material model were defined.

First a reference analysis was made for the SSY-solution. A semi circular element mesh with high element density was made. The load for that was a forced displacement field at the outer boundary of the model. The displacement field is based on analytical solution of small scale yielding infinite field. The forced displacement components at radial distance R in angular coordinates θ are as follows:

$$u_x = \frac{(1+\nu)K_I}{E}\sqrt{\frac{R}{2\pi}}\,(3-4\nu-\cos\theta)\,\cos(\theta/2) \qquad (1)$$

$$u_y = \frac{(1+\nu)K_I}{E}\sqrt{\frac{R}{2\pi}}\,(3-4\nu-\cos\theta)\,\sin(\theta/2) \qquad (2)$$

The SSY reference analysis was run incrementally as far as the required J-integral level was reached. During all load increment level the J-integral, CTOD and the maximum crack closing stress component were calculated and stored.

Secondly the analysis for the test specimen was done. The element model and mesh was like in Fig. 2. The loading force F was incrementally increased and J-integral, CTOD and maximum crack closing stress component were calculated, respectively. When the maximum crack closing stress component and value of J-integral were compared in SSY analysis and the test specimen analysis, following result was received, Fig. 3. Equal analysis with the same material properties was repeated also for an other three point bending test specimen (W=100, B=50 and L=400 mm), and the result is plotted in Fig. 3, too.

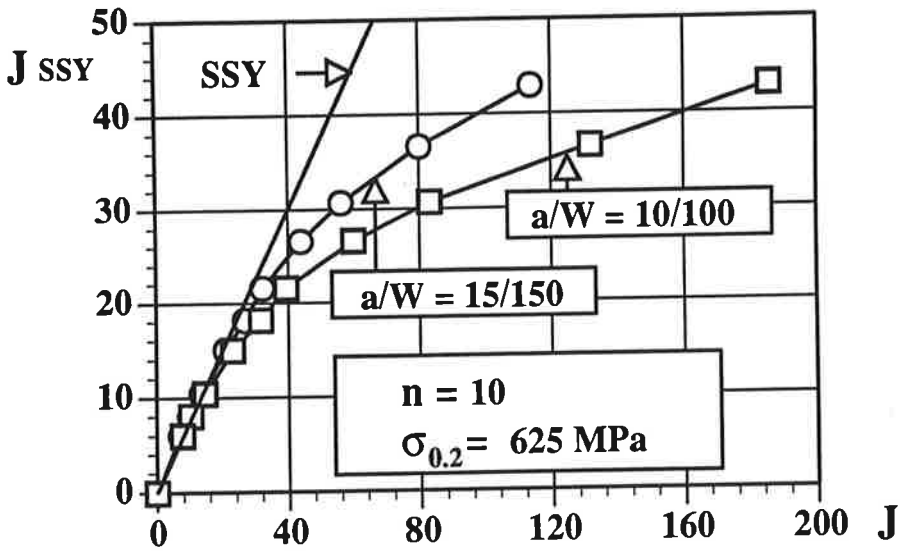

FIGURE 3. *Relation between J-integral values in test specimen and in SSY condition at loading levels which generate equal maximum crack closing stress component. Parameter "n" is the hardening exponent in Ramberg-Osgood model.*

In three dimensional analysis of the bend specimen the local variation of the fracture parameter in the crack front can be seen, Fig. 5. The reason for the changes of the parameter is that the stress state in the heavily loaded and plasticized crack tip area are changing from plane stress situation on the free surfaces of the specimen through plane strain state to complicated 3D stress state in the central part of the test beam, where the strain is clearly positive in the thickness direction of the test specimen. In addition, in small specimen with 50% crack depth the effect of the plastic zone caused by the tool bringing the external force to the specimen interacts with the plastic zone caused by the crack tip singularity. The result given in Fig. 3 were converted into temperature/stress intensity factor -coordinate system to visualize more clearly, what is the shallow crack effect in this test specimen and material property case. The J-integral values were converted to K_I-parameter values and, moreover, the K_I-parameter values corresponding to SSY condition were calibrated to a typical exponential K_{Ic}-curve. Then the calculated test specimen K_I-result could be plotted in same figure. The result is plotted in Fig. 4. There are also calculated result with the same specimen geometry but a slightly different material properties.

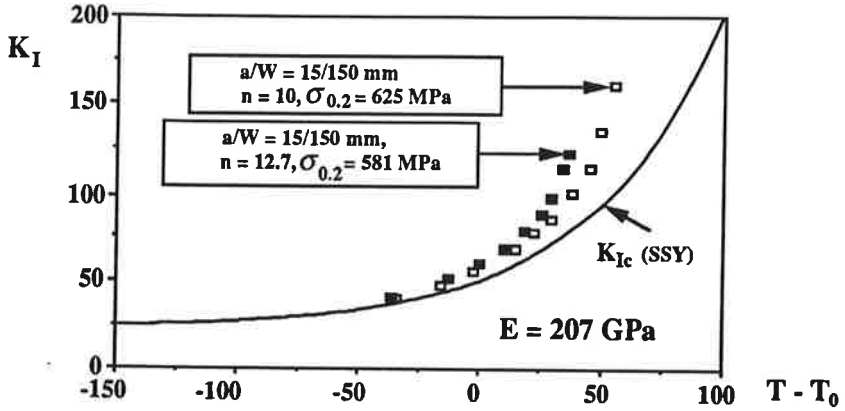

FIGURE 4. *Test specimen results and the corresponding critical K_{Ic}-values (SSY).*

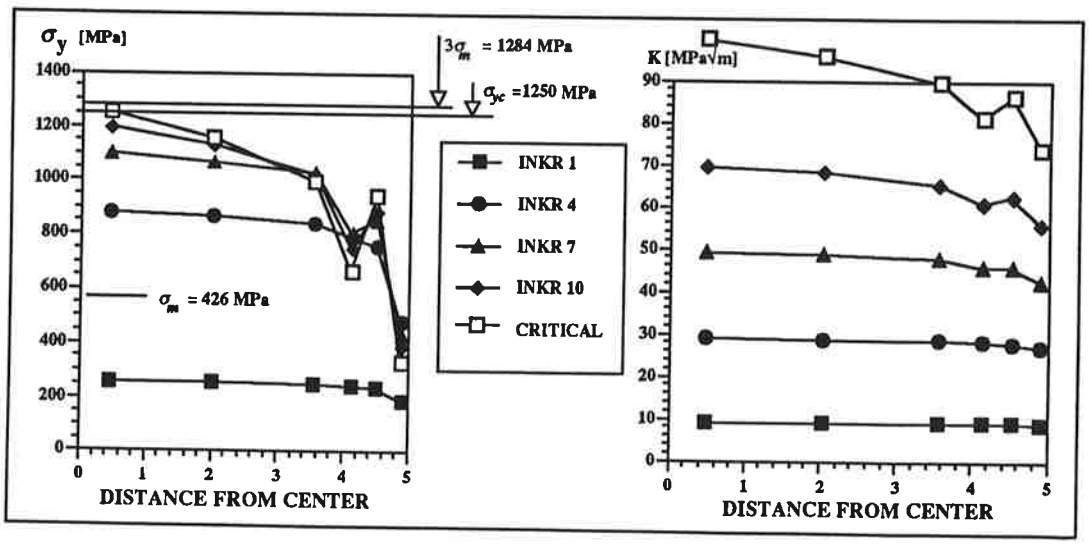

FIGURE 5. *Maximum σ_y and local fracture parameter in specimen with increasing load.*

6. THE CRACK DEPTH CORRELATION TO FRACTURE TOUGHNESS

A primary parameter in the depth effect of the crack is the size of plastic zone compared to the depth of the crack. In the regime of linear fracture mechanics the characteristic radius r_p of the plastic zone [2] in plane strain condition is

$$r_p \sim \frac{K_I^2}{\sigma_y^2} = \frac{EJ}{(1-\nu^2)\,\sigma_y^2} , \qquad (3)$$

where K_I the stress intensity factor, σ_y is the yield strength, E elasticity modulus and ν Poisson's ratio. In considering strain hardening σ_y should be substituted by some other characteristic stress. Let this be the parameter σ_o in the Ramberg-Osgood fitting function. A suitable dimensionless parameter to correlate to fracture constraint is the ratio between the radius r_p and the crack depth a. Thus we can seek the crack depth correlation in form

$$J_c = \left[1+k\left(\frac{E}{1-\nu^2}\,\frac{J}{a\sigma_0^2}\right)^m\right] J_{cSSY} . \qquad (4)$$

This fitting fulfills the requirement $J_c \rightarrow J_{cSSY}$, when $a \rightarrow \infty$. Formally it follows

$$K_{IJc} = \sqrt{1+k\left(\frac{E}{1-\nu^2}\,\frac{J}{a\sigma_0^2}\right)^m}\; K_{Ic} , \qquad (5)$$

where K_{IJc} is calculational fracture toughness.

By fitting a curve by least squares in Fig. 4 to the points calculated by FE-method in the interested area, namely below $K_{Ic} \approx 100$ MPa$\sqrt{m}$ values k = 0.993 and m = 0.889 are obtained and equation (5) will look like

$$K_{IJc} = \sqrt{1+0.993\left(\frac{K_{Ic}^2}{a\,\sigma_0^2}\right)^{0.889}}\; K_{Ic} . \qquad (6)$$

It should be emphasized that equation (6) is valid only when n = 10. For other hardening modules n the parameters k and m must be calculated accordingly.

CONCLUSION

Numerical application of FE-method is presented to correlate the size, shape and relative dimensions of the test specimen and initial crack and hardening material properties to fracture toughness in reference (SSY) condition. In addition, a correlation function procedure is proposed to eliminate the shallow crack effect in three point bending specimen.

The numerical results show that the present method is able to simulate the fracture mechanics test with good accuracy. The average J-integral values calculated either from global deflection and reaction force or from averaged local values in the crack front are both very close to those calculated according to the ASTM testing standard.

Possibility to reliable numerical simulation of strongly nonlinear material testing gives much deeper understanding on the phenomena and important factors of the material behavior in test and actual operation condition.

This kind of analyses are now able to show, why the toughness of thinner plates is better than thick plates made of same material. Secondly, this analysis procedure can be used for analysis of relatively shallow and short surface flaws in large and thick-walled real ductile structures giving results that tells that short and/or shallow surface flaws are not so dangerous in case of monotonic increasing load (concerning not high cycle fatigue) as linear elastic analysis or analytical solutions presumes.

The current activities on this procedure are focused on the analysis in case of thermal stresses and strains in 3D structures.

REFERENCES

1. T. L. Anderson, "Fracture Mechanics", CRC Press, Inc., Boca Raton, FL, 1991

2. D. Broek, "Elementary Engineering Fracture Mechanics", Martinus Nijhoff Publishers, the Hague, 1983

3. R. H. Dodds, Jr., T. L. Anderson, and M. T. Kirk, A framework to correlate a/W ratio effects on elastic-plastic fracture toughness (J_c), International Journal of Fracture 48 (1991) 1-22

4. R. Hill, "The Mathematical Theory of Plasticity", University Press, Oxford, 1958

5. J. W. Hutchinson, Singular Behavior at the End of a Tensile Crack Tip in a Hardening Material. Journal of the Mechanics and Physics of Solids 16 (1968) 13-31

6. K. Ikonen, "Murtumissitkeyden laskeminen pienen taivutuspalkin kokeesta", Finnish Centre for Radiation and Nuclear Safety, Helsinki, 1993

7. K. Ikonen and H. Raiko, Effect of Crack Depth on Crack Tip Stress Field and Crack Initiation, in "Transactions of the 12th International Conference on Structural Mechanics in Reactor Technology", K. F. Kussmaul (Ed.), Stuttgart, Germany, 1993, Volume B, 315-320

8. J. R. Rice and G. F. Rosengren, Plane Strain Deformation near a Crack Tip in a Power-Law Hardening Material. Journal of the Mechanics and Physics of Solids 16 (1968) 1-12

9. C. F. Shih, Relationships between the J-integral and crack opening displacement for stationary and extending cracks. Journal of the Mechanics and Physics of Solids 29

A RULE-BASED PROTOTYPE EXPERT SYSTEM FOR THE EVALUATION AND SELECTION OF FIBER-REINFORCED PLIES

PETRI KERE
Laboratory of Light Structures
Helsinki University of Technology
Puumiehenkuja 5 A, FIN-02150 Espoo, FINLAND

ABSTRACT

Due to its simplicity, modifiability, and flexibility in applying problem-solving knowledge, a rule-based system of AI using heuristic knowledge representation is an appropriate tool for the construction of an expert system for design purposes. A rule-based system for the evaluation and selection of fiber-reinforced plies is described. It searches feasible plies that satisfy specified requirements and ranks the plies on the basis of targets set for different ply attributes. The basic elements of an expert system are introduced.

1. BACKGROUND AND MOTIVATION

A software for analyzing composite material systems [2] is currently under development in the Laboratory of Light Structures at the Helsinki University of Technology. An expert system for searching feasible solutions is planned to be integrated in the software. The system will include tools for the ply selection, laminate creation, and laminate selection on the basis of a user defined design specification. The software is developed in the UNIX/X Window environment. Easy expandability is one of the key requirements set for the tools of the software.

A rule-based prototype expert system for the evaluation and selection of fiber-reinforced plies was developed to evaluate the feasibility of the Artificial Intelligence (AI) programming environment C Language Integrated Production System (CLIPS) in the development of an expert system for solving design problems of composite material systems. Requirements were set for the knowledge representation, modifiability, and expandability, as well as for the implementation of an explanation facility [1].

2. THE CONSTRAINT SATISFACTION PROBLEM

The constraint satisfaction problem can be established as follows. Let

$$\boldsymbol{X} = \{X_j\}, \quad j = 1,\ldots,n \tag{1}$$

be a set of attributes with values in a set of discrete and finite domains

$$\boldsymbol{D} = \{D_{ij}\}, \quad i = 1,\ldots,m, \quad j = 1,\ldots,n. \tag{2}$$

Let

$$\boldsymbol{R} = \{R_j\}, \quad j = 1,\ldots,n \tag{3}$$

be a set of constraints called *requirements*, each of which shows the values compatible for the *j*th attribute. The problem is to find a subset $\boldsymbol{S}$ of values such that all the constraints for different attributes are satisfied:

$$\boldsymbol{S} = \{S_{ij}\}, \quad i = 1,\ldots,m, \quad j = 1,\ldots,n, \tag{4}$$

where

$$S_{ij} = \begin{cases} D_{ij} \text{ if } D_{ij} \in R_j \text{ for every } j = 1,\ldots,n \\ \varnothing \text{ otherwise} \end{cases}. \tag{5}$$

Every different subset that satisfies all the constraints is called a *feasible solution.*

Besides being specified a requirement, a constraint can also be specified a *target.* A constraint is called a target if the strict satisfaction of the constraint is not required, but the constraint shows the desirable values. The distance of values from the constraint is mapped by the *quality factor function.* The quality factor function maps all elements of D_{ij} into the codomain of real number defined in the interval from 0 to 1 inclusive as

$$qf_j : \bigcup_{i=1}^{m} D_{ij} \rightarrow [0,1]. \tag{6}$$

3. AI PROBLEM-SOLVING APPROACH

The basis of rules of inference comes from deductive logic. A *syllogism* that is any valid deductive argument having two *premises* and a *conclusion* can be represented as follows:

Premise : Any element that satisfies the constraint is compatible
Premise : Element A satisfies the constraint
Conclusion : Therefore, element A is compatible

In an argument, the premises produce evidence to support the conclusion. The premises are also called the *antecedent* and the conclusion is called the *consequent.* In deductive logic, the true conclusion must follow from the premises. The advantage of using syllogisms is that they can be expressed in terms of IF-THEN rules:

IF Any element that satisfies the constraint is compatible and Element A satisfies the constraint
THEN Element A is compatible

In formal way, the general schema for representing an argument of this type is:

$$\begin{array}{l} p \rightarrow q \\ \underline{p \quad\quad} \\ \therefore\ q \end{array} \tag{7}$$

where p and q are logical variables that can represent any statements. The use of logical

variables in propositional logic allows more complex types of statements than the basic syllogistic forms. Inference schema of the propositional form is called *modus ponens* and it forms the basis of rule-based expert systems. However, in logic the conditional $p \rightarrow q$ is a logical definition defined by a truth table and can be translated into natural language in a number of ways, while in rule-based expert systems, the conditional $p \rightarrow q$ corresponds to the rule and p corresponds to the pattern that must match the antecedent for the rule to be executed.

A group of multiple inferences that connect a problem with its solution is called a *chain.* A chain that proceeds from given facts by using rules for changing state until the goal condition is satisfied, is called a data-driven search, or a *forward chain.* An alternative approach is a chain that is traversed from a conclusion back to the facts that support the conclusion. That is called a goal-driven search, or a *backward chain.* Forward chaining and backward chaining are the basic search strategies for state space search, whose definition is presented by Luger and Stubblefield [5]. The basic concept of forward chaining in a rule-based system is illustrated in Figure 1.

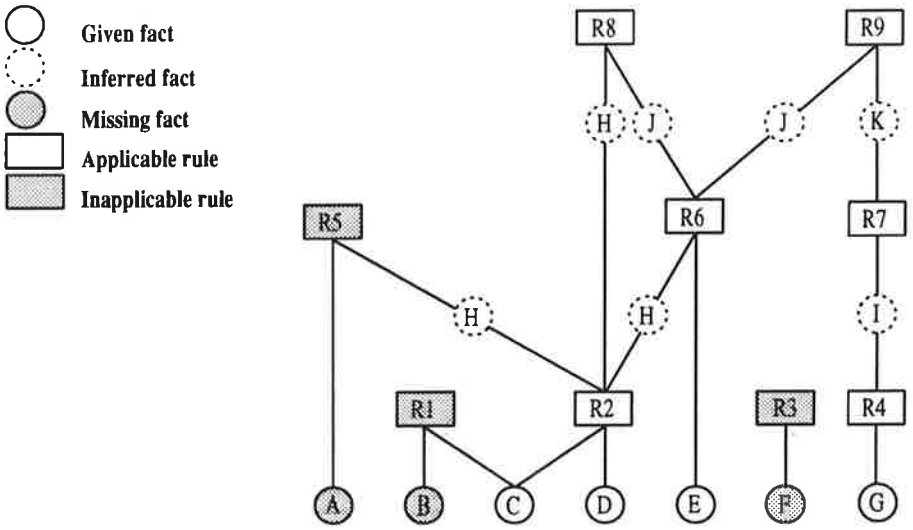

FIGURE 1. The basic concept of forward chaining in a rule-based system. Rules are triggered by the facts that satisfy their antecedent. Given that the rule R_1 has to be satisfied by facts B and C to be activated. Only fact C is present, from which follows that R_1 is not activated. Rule R_2 is activated by facts C and D which are present and so R_2 produces a new fact H. Other satisfied rules are R_4, R_6, R_7, R_8, and R_9.

4. ELEMENTS OF A RULE-BASED EXPERT SYSTEM

In the human-modelling world, condition-action rules are generally called productions. In rule-based systems a *knowledge-base* contains all the domain knowledge coded in the form of productions, called *production rules*. Each production rule represents an independent piece of knowledge and is identified by a name. Following the name is the IF part, or condition part of the rule, which is a collection of individual conditions called *patterns*. In a reasoning process, *working memory* contains a description of the current state of the problem solving process. This description is a set of patterns that is matched against the condition part of

rules to select appropriate actions for problem solving. In the beginning of the *recognize-act cycle*, working memory is initialized with the beginning problem description. The *inference-engine* controls the reasoning process as follows: the patterns are matched against the conditions of the rules; this produces a subset of the rules, called the *conflict set*, whose conditions match the patterns in working memory. The rules in the conflict set are said to be *activated*. One rule in the conflict set is then selected on the basis of the *conflict resolution strategy* and *fired*, i.e., the action part of the rule is performed, changing the contents of working memory. This control cycle is repeated until no patterns in working memory match the rule conditions. The conflict resolution strategy is based on a search algorithm. The different search algorithms are discussed by Luger and Stubblefield [5]. A schematic sketch of a rule-based system is presented in Figure 2.

The advantages of a rule-based system can be listed as follows:

1. *Separation of knowledge and the inference engine* enables easy modification of the knowledge in the knowledge-base without changing the program control.
2. *Modularity of production rules*, from which follows that the rules have no syntactic interactions. Thus, it is easy to expand the expert system by adding, deleting, and changing the knowledge in the knowledge-base.
3. It is easy to build an *explanation facility* with rules since the antecedent of a rule specifies exactly what is needed to activate a rule.

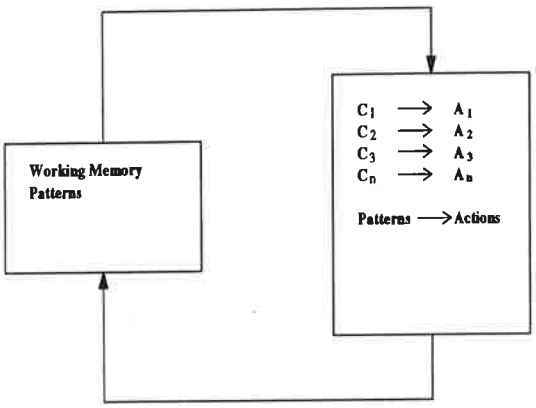

FIGURE 2. A rule-based system. The inference-engine loops until patterns in working memory no longer match the conditions of any rules.

5. THE PROTOTYPE EXPERT SYSTEM

5.1 The need for a rule-based system. Because of its simplicity, modifiability, and flexibility in applying problem-solving knowledge, a rule-based system of AI using heuristic knowledge representation is an appropriate tool for the construction of an expert system for the design of composite material systems. The need for applying symbolic reasoning and possibilities to extend the expert system into the heuristic design support the use of rule-based problem-solving techniques. Furthermore, it is characteristic of the design problem that:

1. All or most of the data are given in the initial statement of the problem.
2. The formation of the goal, or the hypothesis is difficult.
3. There are many potential goals but only a few ways to use the facts.

Thus, forward chaining is the appropriate search strategy for the design problem.

5.2 Ply evaluation and selection problem. A composite laminate is formed of plies that commonly consist of reinforcing fibers in a polymer matrix material. Ply constituents, their mutual proportions, and the form and orientation of the reinforcement specify the properties of plies, which partly define the properties of the laminate. In the evaluation and selection problem of fiber-reinforced plies, different ply properties gathered in a ply specification, called *ply attributes*, are considered design variables. The beginning problem description, i.e., the *initial state* in the prototype is formed of the ply specifications stored in the database and the design specification given by the user. The design specification may include requirements and targets set for different ply attributes. In the design specification, every different target is weighted with a *weighting factor* between 0 and 1 associating the importance of a target. Thus, the weighting factors for different ply attributes are:

$$\boldsymbol{\lambda} = \{\lambda_j \mid \lambda_j \in [0,1]\}. \tag{8}$$

The weighting factor 0 corresponds to the least important and 1 to the most important target. The value of a quality factor function is called a *quality factor*. The quality factor function is selected on the basis of the constraint. Thus, the quality factor is relative. The schematic graphs of quality factor functions are illustrated in Figure 3.

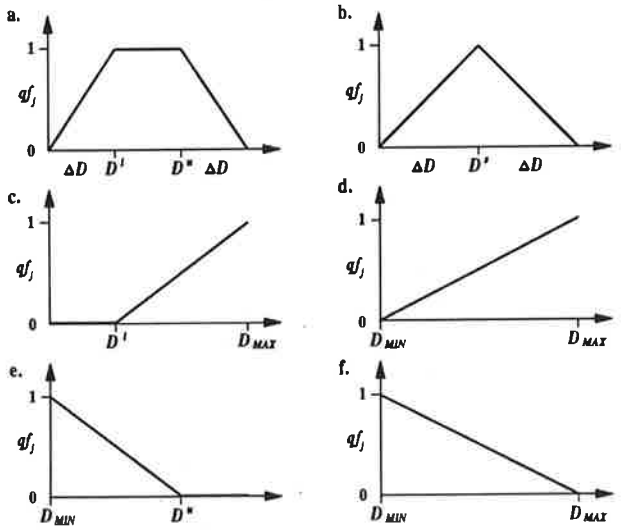

FIGURE 3. The schematic graphs of quality factor functions qf_j (D_{ij}) used in the prototype system. a) Lower and upper side constraints D^l and D^u are specified. ΔD denotes the maximum difference between the side constraints and minimum and maximum values of D_{ij}, $1 \le i \le m$. b) A certain value D^s is searched. c) The greatest value D_{MAX} is searched and lower side constraint D^l is specified. d) The greatest value D_{MAX} is searched, no side constraints are specified. e) The smallest value D_{MIN} is searched and the upper side constraint D^u is specified. f) The smallest value D_{MIN} is searched, no side constraints are specified.

When quality factors are stated in matrix form as follows

$$\boldsymbol{QF} = \{QF_{ij}\},\ i = 1,\ldots,m,\ j = 1,\ldots,n, \tag{9}$$

where

$$QF_{ij} = qf_j(D_{ij}), \tag{10}$$

a *cumulative ply quality* for each ply can be defined as

$$QF^c = \{QF_i^c\},\ i = 1,\ldots,m, \tag{11}$$

where

$$QF_i^c = \sum_{j=1}^{n} QF_{ij}\,\lambda_j. \tag{12}$$

Finally, feasible plies that satisfy all the requirements are selected and ranked on the basis of *ply quality factors* obtained by scaling cumulative ply qualities between 0 and 1:

$$QF^p = \{QF_i^p\},\ i = 1,\ldots,m, \tag{13}$$

where

$$QF_i^p = \frac{QF_i^c - \min\limits_{1\le k\le m} QF_k^c}{\max\limits_{1\le k\le m} QF_k^c - \min\limits_{1\le k\le m} QF_k^c}. \tag{14}$$

5.3 Realization of the prototype expert system. The prototype expert system is realized with CLIPS, Version 6.0, developed by the Software Technology Branch, NASA/ Lyndon B. Johnson Space Center, in the UNIX/X Window environment. CLIPS uses the efficient Rete Algorithm [3] in pattern matching and is optimized to be a forward chaining language. CLIPS provides a complete environment for developing expert systems.

The prototype consists of all the basic elements of an expert system. A *knowledge-base* with modularized structure is the storage of information. The knowledge-base contains the *design knowledge* related to the ply evaluation and selection, *explanation knowledge* used to produce the explanations, and the *process control knowledge* to control the process propagation. The knowledge in the knowledge-base consists of Object-Attribute-Value (OAV) triplets, heuristic knowledge, i.e., the production rules, and procedural knowledge including modules and functions. Modules are used to create the hierarchial structure of the knowledge-base. The interaction between the user and the prototype is realized with the CLIPS user interface. The *inference engine* and *working memory* of CLIPS control the reasoning process. The state space search is based on the forward chaining control strategy with the *depth conflict resolution* strategy. In the depth strategy newly activated rules get higher priority and the search goes deeper in the search space whenever this is possible. As soon as the goal state is reached, the ply selection tool lists feasible plies and ranks them on the basis of their ply quality factors. In the ply evaluation mode, all evaluated plies, also infeasible ones, are listed. The *explanation facility* enables the user to ask the questions *what* is being asked and what attributes are available in the knowledge-base, *why* the attribute is included in the knowledge-base, i.e., the current constraint set for the attribute, and *how* the program has reasoned to the resulting conclusion.

5.4 An example run. An example of a design variable defined heuristically in the prototype is the *ply formability*. The ply formability is a processing parameter contributed by the form of reinforcement and the thickness of a ply. The maximum formability corresponding to the hypothetical zero thickness of the ply and the change of the formability vs. ply thickness are defined heuristically in the knowledge-base for each form of reinforcement. The simplified ply formability F is defined as:

$$F = \max\left[F_{MAX} + \frac{\partial F}{\partial h}\, h, 0\right], \tag{15}$$

where F_{MAX} denotes the maximum formability, $\partial F/\partial h$ the change of the formability vs. the ply thickness, and h the ply thickness. Thus, the ply formability is a nondimensional absolute value. The default values for F_{MAX} and $\partial F/\partial h$ are shown in Figure 4c. In an example run of the prototype system shown in Figure 4a, feasible plies are searched against a simple design specification from the extended database of the LAMDA software [7] including 35 ply specifications with 34 ply attributes.

a.

```
Select ply Evaluation or Selection mode (e/s/what/why)
s
|-------------------------|
|     SELECTED PLIES      |
|-------------------------|
|   PLY-ID    |   PLY-QF  |
|-------------|-----------|
|   CEF11-02  |   0.97    |
|   CEF11-01  |   0.45    |
|   CEU11-01  |   0.34    |
|   CEU11-02  |   0.34    |
|   CEU11-03  |   0.17    |
|   CEU11-04  |   0.17    |

Select explanation (what/why/how/none)
why
Select attribute or all
all

 ATTRIBUTE formability is specified as a TARGET with WEIGHTING FACTOR 1.00
 MAXIMUM VALUE is searched for formability

 ATTRIBUTE Vf is specified as a TARGET with WEIGHTING FACTOR 0.50
 Value 60.00 is searched for Vf

 ATTRIBUTE applicability is specified as a REQUIREMENT
 Value prepreg is searched for applicability

 ATTRIBUTE reinforcement is specified as a REQUIREMENT
 Value carbon is searched for reinforcement
```

b.

Vf	h	weave	reinforcement	applicability
50	0.220	plain	carbon	prepreg
50	0.325	satin	carbon	prepreg
60	0.200	unid	carbon	prepreg
60	0.200	unid	carbon	prepreg
50	0.340	unid	carbon	prepreg
50	0.340	unid	carbon	prepreg

c.

Ply type	F_{MAX}	$\partial F/\partial z$
mat	1.0	-0.1
satin	0.8	-0.1
twill	0.6	-0.1
plain	0.4	-0.1
unid	0.2	-0.1

FIGURE 4. a) An example of the prototype expert system run. b) Ply attribute values of each selected ply. c) Default values for F_{MAX} and $\partial F/\partial h$.

The plies are selected on the basis of the requirements set for the applicability and reinforcing material (applicability refers to processing). Selected plies are ranked on the basis of the targets set for the formability and fiber volume fraction. The current design specification is explained with why all question. We can see that the ply CEF11-02 with the greatest ply quality factor corresponds best to the current design specification mainly

because of its form of reinforcement (the best formability). The ply attribute values of selected plies are shown in Figure 4b.

6. SUMMARY

A rule-based prototype expert system for the evaluation and selection of fiber-reinforced plies has been developed with CLIPS in the UNIX/X Window environment. The evaluation and selection of plies is considered as a constraint satisfaction problem. The constraint set for a ply attribute may be a requirement that must be entirely fulfilled, or a target that shows the desirable values. The selection of plies is based on requirements and the ranking of plies on targets. An example run demonstrates the use of the prototype system. The need for symbolic reasoning, as well as the need for simplicity, modifiability, and flexibility in applying problem-solving knowledge are the reasons for using rule-based techniques of AI.

REFERENCES

1. ESACOMP Analysis and Design Software of Composite Material Systems - An Expert System Prototype, Rep. No. LLS-93-T87, Revision 1, HUT, Laboratory of Light Structures, Otaniemi, Finland. 1994.

2. ESACOMP Analysis and Design of Composite Material Systems, User Requirement Document, Rep No. LLS-92-T74/URD, Issue 1, HUT, Laboratory of Light Structures, Otaniemi, Finland. 1993.

3. J. Giarratano and G. Riley, "Expert Systems: Principles and Programming", PWS-KENT, Boston, MA, USA, 1989.

4. P. Harmon, R. Maus, and W. Morrissey, "Expert Systems: Tools and Applications", Wiley, New York, NY, USA, 1988.

5. G. Luger and W. Stubblefield, "Artificial Intelligence: Structures and Strategies for Complex Problem Solving", Benjamin/Cummings, Redwood City, CA, USA, 1993.

6. S.K. Morton and J.P.H. Webber, Heuristic Methods in the Design of Composite Laminated Plates, Composite Structures 19, (1991) 207-265.

7. O. Saarela, "LAMDA-Laminate Design and Analysis: Microcomputer Software for Dimensioning Composite Laminate and Sandwich Structures", HUT, Laboratory of Light Structures, Otaniemi, Finland, 1992.

STEFAN-BOLTZMANN RADIATION FOR NON CONVEX SURFACES

TIMO TIIHONEN
Laboratory of Scientific Computing
University of Jyväskylä
P.O. Box 35, FIN-40351 Jyväskylä, FINLAND

ABSTRACT

We consider the stationary heat equation for a non convex body with Stefan-Boltzmann radiation condition on the surface. The main virtue of the resulting problem is non locality of the boundary condition. Using the technique of upper and lower solutions we prove the existence of a weak solution.

1. INTRODUCTION

Radiative heat exchange plays an important role in many situations. It has to be taken into account in general always when the temperature on a visible surface of the system is high enough or when other heat transfer mechanisms are not present (like in vacuum, for example). Apart from some simple cases like a convex radiating body and known irridation from infinity, we have to take into account the radiative heat exchange between different parts of the surface of our system. This leads to non local boundary conditions on radiating part of the boundary.

In this work we shall consider the stationary heat equation in two or three dimensional domains Ω with radiative heat transfer on $\Sigma \subset \Omega$. The typical shapes of Ω are sketched in Figure 1. The main emphasis is in analysis of a closed container, i.e. when Ω is connected but has a hole. However, we will also give some remarks on the other geometrical configurations.

The structure of the paper is as follows: First we derive the the equations for heat balance on a radiating surface and formulate them in appropriate function spaces. Some properties of the non local operator are then proved for later use. In the third chapter we consider the stationary heat equation with non local radiation boundary condition and show the existence and uniqueness under reasonable hypotheses.

NOTATIONS: We shall mainly consider geometries that belong to the class $C^{1,\delta}$. That is, domains whose boundaries can be locally represented as graphs of functions with Hölder continuous derivatives. By L^p we denote the space of measurable functions whose p:th powers are integrable. We also exploit the well known Sobolev space H^1 of L^2 functions whose derivatives are also in L^2.

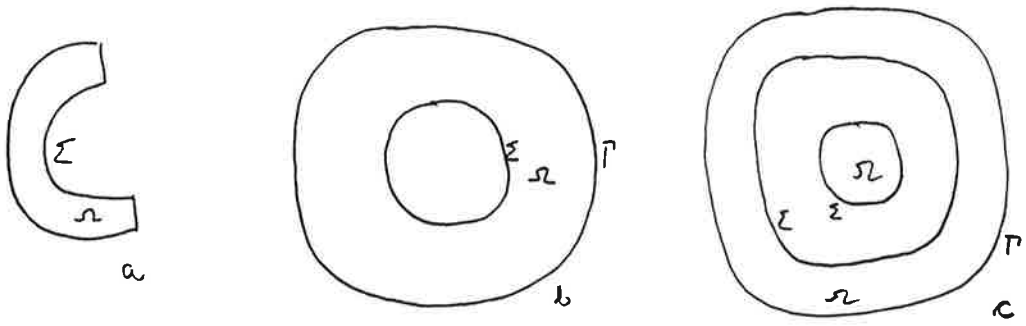

Figure 1.

2. RADIATION ON DIFFUSE GRAY SURFACES

We consider the three dimensional equivalent of the situation of Figure 1.b, where Ω is a conducting body. The domain bounded by Σ is a vacuum (transparent and non conducting). On Γ we assume, for simplicity, that temperature is known.

On Σ the heat balance reads as

$$q - R + J = 0,$$

where q is the heat brought to the surface by conduction. R denotes the radiation emitted by the surface Σ and J is the energy of incoming irridation on Σ.

For surfaces that are diffuse and gray as emitters and reflectors the intensity of emitted radiation has the representation (see [2], for example)

$$R = \epsilon\sigma T^4 + (1-\epsilon)J.$$

The first part corresponds to the Stefan-Boltzmann radiation law, the second part is the reflected part of the received irridation. In the geometry of Figure 1.b the irridation on Σ depends only on the radiation emitted by different parts of Σ itself. Infact we can write for any point $s \in \Sigma$

$$J(s) = \int_\Sigma w(s,z)R(z)dz,$$

where we call w as the view factor between points s and z of Σ. For convex three dimensional enclosures the view factor has the representation $w = w^*$ with [2]

$$w^*(s,z) = \frac{n_z(s-z)\; n_s(z-s)}{\Pi|z-s|^4}.$$

Correspondingly, in two dimensional case (cross section of an infinitely long cylinder) the view factor reads as

$$w^*(s,z) = \frac{n_z(s-z)\; n_s(z-s)}{|z-s|^3}.$$

If the enclosure is not convex we have to take into account also the visibility factor Ξ:

$$\Xi(s,z) = \begin{cases} 0, & \text{if } \overline{sz} \cap \Omega \neq \phi, \\ 1, & \text{if } \overline{sz} \cap \Omega = \phi. \end{cases}$$

The view factor can then be written as

$$w(s,z) = w^*(s,z)\Xi(s,z).$$

Let us introduce the operator $K : L^\infty(\Sigma) \to L^\infty(\Sigma)$,

$$K(f)(s) = \int_\Sigma w(s,z)f(z)dz \quad \forall s \in \Sigma, \quad \forall f \in L^\infty(\Sigma).$$

We can now write $J = K(R)$ and hence

$$R = \epsilon\sigma T^4 - (1-\epsilon)K(R) \quad \text{on } \Sigma$$

or, equivalently,

$$R = (I - (1-\epsilon)K)^{-1}\epsilon\sigma T^4.$$

Now the heat balance on Σ reads as

$$0 = q - R + J = q - G(\sigma T^4)$$

with

$$G(\sigma T^4) = (I-K)R = ((I-K)(I-(I-E)K)^{-1}E)(\sigma T^4).$$

We shall also use for G the expression

$$G = (I-H)E = (I - EK(I-(I-E)K)^{-1})E.$$

G is the infinite dimensional equivalent to the matrix of so called Gebhart factors, [2].

Let us now present some lemmas about the properties of K and G.

LEMMA 1. *Let Σ be a $C^{1,\delta}$-surface. Then $w^* \in L^\infty(\Sigma; L^p(\Sigma))$ for $p < 1/(1-\delta)$.*

PROOF: Clearly we only have to treat the situation $s \to z$ for any fixed $z \in \Sigma$. We can choose the coordinate system so that $z = (0,0,0)$ and in the neighbourhood of z Σ is a graph of a $C^{1,\delta}$ function f.

Let now $s = (x, f(x))$. Then we have

$$\frac{n_z(s-z)}{|s-z|^2} = \frac{-\nabla f(0)x + f(x)}{(1+|\nabla f(0)|^2)(|x|^2 + f(x)^2)} \leq \frac{\nabla f(0)x + \nabla f(tx)x}{|x|^2} \leq Ct|x|^{-1+\delta},$$

where $t \in (0,1)$ and C is the Hölder constant of ∇f. In a similar way we can bound also $n_s(z-s)/|z-s|^2$. Hence $w^*(z,\cdot)$ can have at z a singularity of type $|x|^{-2(1-\delta)}$ which gives the bound for p.

The above result holds clearly also for w as Ξ is in L^∞. In the two dimensional case the corresponding bound for p is $1/(1-2\delta)$.

LEMMA 2. *The operator $K \geq 0$. If $\Sigma \in C^{1,\delta}$ then K is a compact mapping from $L^p(\Sigma)$, $p > 1/\delta$ into itself and $\rho(K) = 1$.*

PROOF: For convex Σ the positivity of K is obvious. In the general case we have to notice that $\Xi(s,z) = 0$ whenever $w^*(s,z) < 0$. If $\Sigma \in C^{1,\delta}$ and $v \in L^p(\Sigma)$ then $|Kv(z)| \leq \|w^*(z,\cdot)\|_{L^{p'}(\Sigma)} \|v\|_{L^p(\Sigma)}$. The norm of $w^*(z,\cdot)$ is uniformly bounded by a constant depending on the Hölder coefficient. Hence, $Kv \in L^\infty(\Sigma) \subset L^p(\Sigma)$. As K belongs to the class of Hille-Tamarkin operators it is compact, [3].

As $\int_\Sigma w(s,z)dz = 1 \; \forall s \in \Sigma$ constant functions are eigenfunctions of K with eigenvalue 1. As K maps L^p into L^∞, the eigenvalues of K are all in L^∞. On the other hand $\|K\| = 1$ as a mapping from L^∞ into itself. Hence 1 is the maximal eigenvalue.

In the sequel we shall assume that Σ is a $C^{1,\delta}$ surface with $\delta > 0$. Hence K maps L^p into L^∞ for $p > 1/\delta$ in 3D ($p > 1/(2\delta)$ in 2D. We also denote by E the operator corresponding to multiplication with $\epsilon \in L^\infty(\Sigma)$.

LEMMA 3. *The operator $I-(I-E)K$ from $L^p(\Sigma)$, $p > 1/\delta$, into itself is invertible with non negative inverse whenever $0 < \epsilon_0 \leq \epsilon \leq 1$.*

PROOF: $(I-E)K$ is non negative and its spectral radius is bounded by $1-\epsilon_0$. Hence we can write

$$(I-(I-E)K)^{-1} = I + \sum_{i=1}^{\infty}((I-E)K)^i.$$

The series converges and its terms are all nonnegative.

LEMMA 4. *The symmetric part of operator G, $G+G^T$ from $L^p(\Sigma)$ into itself is positively semi definite.*

PROOF: Let $v \in L^p(\Sigma)$ be arbitrary. Denote by u the solution of $(I-(I-E)K)u = Ev$. Then

$$\begin{aligned}(v,(G+G^T)v) &= 2(E^{-1}(I-(I-E)K)u,(I-K)u) \\ &= 2(u,(I-K)E^{-1}(I-K)u) + 2(u,(K-K^2)u) \geq 0\end{aligned}$$

as $\rho(K) = 1$.

LEMMA 5. *Let $d \in L^s(\Sigma)$, $d \geq 0$ be given and denote by D the operator induced by d. Then if G maps $L^p(\Sigma)$ into $L^\infty(\Sigma)$, the operator GD maps $L^q(\Sigma)$ into $L^\infty(\Sigma)$ for $q \geq sp/(s-p)$. Moreover, $(x, GDx) \geq 0 \; \forall x \in L^q(\Sigma)$.*

PROOF: Let us choose a family of finite dimensional subspaces $\{V_i\}$ of $L^q(\Sigma)$ such that $V_i \subset V_{i+1}$ for all i, $L^q(\Sigma) = \cup_i V_i$ and elements of V_i:s are piecewise constant functions. Let ϕ_j, $j = 1,...,N_i$ be a basis of V_i with the property that all ϕ_j:s have pairwisely distinct supports. The finite dimensional equivalents to operators G and D are the matrices with components $G_{ij} = \int_\Sigma G(\phi_i)\phi_j$ and $D_{ij} = \int_\Sigma d\phi_i\phi_j$. D is a diagonal matrix with non negative entries. Now let λ be an eigenvalue of GD and x the corresponding eigenvector. Then denoting $y = Dx$ we have $Re(\lambda(x^TDx)) = Re(x^TDGDx) = Re(y^TGy) \geq 0$ as $G+G^T$ was positively semidefinite. Evidently, $x^TDx \geq 0$ and moreover $x^TDx = 0$ implies that $Dx = 0$ and hence $GDx = 0$. This means that $\lambda = 0$. In the case $x^TDx > 0$ we obtain immediately that $Re\lambda \geq 0$. This means that $x^TGDx \geq 0$ for all x in the finite dimensional case.

Let now $x \in L^q(\Sigma)$ be arbitrary. We can find a sequence $\{x_i\}$ such that $x_i \in V_i$ and $x_i \to x$ strongly in L^q. Then it follows easily that $Dx_i \to Dx$ strongly in L^p and consequently also $GDx_i \to GDx$ in L^∞. This implies the non negativity of $x^T GDx$ for all x in $L^q(\Sigma)$.

REMARK: The above Lemma 5 is one of the main tools in the sequel. It will be applied for the linearized version of the radiation condition. The above lemmas apply verbatim for the geometries of Figures 1.b and 1.c. In the situation like in Figure 1.a where part of the radiation can escape the operator K is, in general, contractive, $\|K\| < 1$. This implies, among other things, that G can be strictly positive definite and for $d > 0$ also GD is strictly positive definite.

3. CONDUCTION RADIATION PROBLEM

Let us now combine the radiation heat exchange with the normal heat conduction in Ω. In stationary situation the absolute temperature satisfies in Ω the boundary value problem:

$$\begin{aligned} -k\Delta T &= f \quad \text{in } \Omega, \\ T &= T^0 \text{ on } \Gamma, \\ k\frac{\partial T}{\partial n} &= -q \quad \text{on } \Sigma. \end{aligned}$$

where k is the heat conductivity and f the heat source. Combining this with the radiation law we get on Σ the nonlinear, non local condition

$$k\frac{\partial T}{\partial n} + G(\sigma T^4) = 0 \quad \text{on } \Sigma.$$

To introduce the weak formulation of our system let us define for given p

$$\begin{aligned} V^p_{T^0} &= \{v \in H^1(\Omega) \cap L^p(\Sigma) |\ \ v|_\Gamma = T^0\}, \\ V^p_0 &= \{v \in H^1(\Omega) \cap L^p(\Sigma) |\ \ v|_\Gamma = 0\}, \\ V^+_0 &= \{v \in V_0 |\ v \geq 0\}. \end{aligned}$$

Then the problem can be written as

$$a(T,v) + b(T,v) = < f, v > \qquad T \in V^p_{T^0}, \quad \forall v \in V^p_0 \tag{1}$$

with

$$\begin{aligned} a(T,v) &= \int_\Omega k\nabla T \nabla v, \\ b(T,v) &= \int_\Sigma G(\sigma|T|^3 T)v \end{aligned}$$

and $< f, v >$ is the duality pairing between V^p_0 and $(V^p_0)'$. Note that the Stefan Boltzmann law is physical only for temperatures above zero. So in order to make the mathematical model well posed we modified the law for negative (unphysical) absolute temperatures.

The space V^p_0 is a reflexive Banach space. In the three dimensional case the condition $v \in L^p(\Omega)$ is essential for $p \geq 4$ as it can not be deduced from the trace theorems. With the given definition of the spaces the weak form is well defined for $p \geq max(5, 4/\sigma)$. Moreover, we have the following result for the case without the non local term:

LEMMA 6. *[1] The problem*

$$a(T,v)+\int_\Sigma \epsilon\sigma|T|^{p-2}Tv =< f,v > \qquad \forall v\in V_0^p,\quad T\in V_{T^0}^p$$

has a unique solution $T\in V_{T^0}^p$ *for all* $f\in (V_0^p)'$.

THEOREM 1. *Let* Ω *be three dimensional. Assume that* $\Sigma\in C^{1,\delta}$, $\delta>0$, $T^0\in H^{1/2}(\Gamma)$, $f\in (V_0^p)'$ *and that there exist two functions* $\phi\le\psi$, $\phi,\psi\in H^1(\Omega)\cap L^p(\Sigma)$, $p\ge max(5,4/\sigma)$ *such that* $\phi\le T^0\le\psi$ *on* Γ,

$$\begin{aligned} a(\phi,v)+b(\phi,v)&\le < f,v > \qquad \forall v\in V_0^+,\\ a(\psi,v)+b(\psi,v)&\ge < f,v > \qquad \forall v\in V_0^+. \end{aligned}$$

Then there exists a unique solution T *for (1). Moreover,* $\phi\le T\le\psi$ *in* Ω.

The proof will be divided in two lemmas.

LEMMA 7. *Let us denote* $[u]=max((u-\psi)^+,min(0,-(\phi-u)^+))$ *and* $c(u,v)=\gamma\int_\Sigma[u]^{p-1}v$ *for some* $\gamma>0$. *Then the modified problem*

$$A(T,v):=a(T,v)+b(T,v)+c(T,v)=< f,v > \qquad T\in V_{T^0}^p,\quad \forall v\in V_0^p$$

has a unique solution.

PROOF: Let us first prove that A is monotone. Let $T_1,T_2\in V_{T^0}^p$ be arbitrary. Then

$$\begin{aligned} A(T_1,T_1-T_2)-A(T_2,T_1-T_2)&=a(T_1-T_2,T_1-T_2)+\int_\Sigma G(\sigma(T_1^4-T_2^4))(T_1-T_2)\\ &\quad+\gamma\int_\Sigma([T_1]^{p-1}-[T_2]^{p-1})(T_1-T_2)\\ &\ge\alpha\|T_1-T_2\|^2_{H^1(\Omega)}, \end{aligned}$$

where α is the coercivity constant of a. Note that we write here simply T^4 even when we actually mean $|T|T^3$. In the above the estimation of the first and the last term is clear. In the non local term we can write for some $\hat{T}$ that $T_1^4-T_2^4=4|\hat{T}|^3(T_1-T_2)$. Then

$$\int_\Sigma G(\sigma(T_1^4-T_2^4))(T_1-T_2)=\int_\Sigma G(\sigma d(T_1-T_2))(T_1-T_2)\ge 0$$

by Lemma 5 as $d=4|\hat{T}|^3\ge 0$ on Σ and G, d and p are such that the conditions of Lemma 5 are satisfied.. As A is hemicontinuous and, due to the additional term, also coercive in V^p, there exists at least one solution. Moreover, as A is strictly coercive in H^1, the solution is also unique.

LEMMA 8. *The solution of the modified problem is also a solution of the original problem.*

PROOF: We have to show that the solution T of the modified problem satisfies $\phi\le T\le\psi$ in $\Omega\cup\Sigma$, since then $c(T,v)=0$ $\forall v\in V_0^p$ and the result follows.

Let us prove that $T \leq \psi$. The other inequality follows with same technique. Subtracting the modified problem from the condition imposed for ψ we get

$$a(\psi - T, v) + b(\psi, v) - b(T, v) \geq c(T, v) \qquad \forall v \in V_0^+.$$

Now, $b(\psi, v) - b(T, v) = \int_\Sigma G(\sigma(\psi^4 - T^4))v$. As ψ and T are in $L^p(\Sigma)$, there exists a function $d \in L^{p/3}(\Sigma)$, $d \geq 0$ such that $\psi^4 - T^4 = d(\psi - T)$ on Σ. So, writing $\hat{b}(u, v) = \int_\Sigma G(\sigma du)v$ we have from above

$$a(\psi - T, v) + \hat{b}(\psi - T, v) \geq c(T, v) \qquad \forall v \in V_0^+.$$

Choosing now $v = (\psi - T)^-$ we have

$$-a((\psi - T)^-, (\psi - T)^-) - \hat{b}((\psi - T)^-, (\psi - T)^-) + \hat{b}((\psi - T)^+, (\psi - T)^-) \geq \int_\Sigma \gamma((\psi - T)^-)^p \geq 0$$

Now,

$$\hat{b}((\psi - T)^+, (\psi - T)^-) = \int_\Sigma d\sigma\epsilon(\psi - T)^+(\psi - T)^- - \int_\Sigma H(d\sigma\epsilon(\psi - T)^+)(\psi - T)^- \leq 0$$

as H is non negative. From coercivity of a and semi coercivity of $\hat{b}$ we conclude that $(\psi - T)^- = 0$.

In the two dimensional case the non linear boundary term is well defined for all H^1 temperature fields because by trace theorem the spaces V^p coincide with $H^1(\Omega)$ for all finite p. Then arguing as in the proof of Lemma 9 we obtain the

THEOREM 2. *Assume that $\Sigma \in C^{1,\delta}$, $\delta > 0$, $T^0 \in H^{1/2}(\Gamma)$ and that $f \in (V_0^p)'$. Then there exists a unique solution T for (1).*

REFERENCES

1. M.C. Delfour, G. Payre and J.P. Zolesio, Approximation of nonlinear problems associated with radiating bodies in space, SIAM J. of Numerical Analysis (1987) 1077-1094
2. F.P. Incropera and D.P. De Witt, "Fundamentals of heat and mass transfer", John Wiley & Sons, Chichester, 1985
3 K. Jörgens, "Lineare Integraloperatoren", B.G. Teubner, Stuttgart, 1970

ERROR ANALYSIS FOR MEASUREMENT OF RIGID BODY INERTIA PROPERTIES

Juha Toivola
Tampere University of Technology/Applied mechanics
P.O. Box 589, FIN-33101 Tampere, FINLAND

ABSTRACT

In this paper two methods for measuring rigid body inertia properties, which include rigid body mass, location of center of mass and components of inertia tensor, are described. Both methods are based on measured acceleration amplitudes of free rigid body, which are possible to determine from frequency response functions of flexible mounted rigid body. Methods can be divided to two stages, first the rigid body fit is used to find the acceleration of the origin and the angular acceleration of the free rigid body, and then the inertia properties are calculated from this data. In both of these two stages an overdetermined set of linear equations has to be solved. Because these equations are formed from measured data, results are random numbers. A method for estimating expected values and covariance matrix for unknowns is proposed and verified using Monte-Carlo-simulation. Errors in calculated inertia properties are measured using the estimated standard deviations.

INTRODUCTION

During the last decade several methods for measuring the rigid body inertia properties have been presented /1,...,8/. However, error analyses for these methods are lacking. In this paper error analyses for two methods are proposed. Both methods are based on measured acceleration amplitudies of free rigid body. These amplitudies are commonly called rigid body inertia restraints, and can be determined from frequency response functions of flexible mounted rigid body. There are several ways, as listed in /8/, how to calculate the rigid body inertia restraint from FRF's, but this is not the subject of this work. In this work it is assumed that expected values and variances of inertia restraints have been calculated.

Because measured data should always be taken as random, all quantities calculated from it are random. So, it is natural to measure errors in results using standard deviations or coefficients of variation /9/. When inertia properties are calculated from inertia restraints, two or three sets of linear overdeterminate equations has to be solved. For this reason the second moment analysis, used extensively in stochastic FEM, is expanded to overdeterminate case. The proposed method is verified using Monte-Carlo-simulation.

Finally, the error analysis is used to study the effects of increasing the number of response and excitation points. In all cases one method seems to be more accurate than the other.
In this work the coefficient of variation is used to measure randomness. For random variable it is the standard deviation divided by the expected value.

SECOND MOMENT ANALYSIS FOR LINEAR STOCHASTIC EQUATIONS

A set of stochastic linear equations can be written in the form

$$A\mathbf{x} = \mathbf{b}, \tag{1}$$

where $n \times m$-matrix A $(n \geq m)$ and n-vector $\mathbf{b}$ are random. In second moment analysis /9/ it is assumed that expected values and covariances between the elements of matrix A and vector $\mathbf{b}$ are known. For a matter of simplicity, the matrix A is written as column vector row-wise as

$$\mathbf{a} = \begin{bmatrix} \mathbf{a}_1^T \\ \mathbf{a}_2^T \\ \vdots \\ \mathbf{a}_n^T \end{bmatrix}, \qquad A = \begin{bmatrix} \mathbf{a}_1 \\ \mathbf{a}_2 \\ \vdots \\ \mathbf{a}_n \end{bmatrix} = \begin{bmatrix} [a_{11} & a_{12} & \cdots & a_{1m}] \\ [a_{21} & a_{22} & \cdots & a_{2m}] \\ & \vdots & & \\ [a_{n1} & a_{n2} & \cdots & a_{nm}] \end{bmatrix} \tag{2}$$

Using the above definition for vector $\mathbf{a}$, the known covariances can be written as

$$\mathrm{cov}(\mathbf{a}) = E\left[(\mathbf{a} - E[\mathbf{a}])(\mathbf{a} - E[\mathbf{a}])^T\right] \qquad (nm \times nm\text{-matrix}) \tag{3}$$

$$\mathrm{cov}(\mathbf{b}) = E\left[(\mathbf{b} - E[\mathbf{b}])(\mathbf{b} - E[\mathbf{b}])^T\right] \qquad (n \times n\text{-matrix}) \tag{4}$$

$$\mathrm{cov}(\mathbf{a},\mathbf{b}) = \mathrm{cov}(\mathbf{b},\mathbf{a})^T = E\left[(\mathbf{a} - E[\mathbf{a}])(\mathbf{b} - E[\mathbf{b}])^T\right] \qquad (nm \times n\text{-matrix}) \tag{5}$$

When solving equation (1) using the perturbation method, the matrix A and vector $\mathbf{b}$ are written in the form

$$A = A_0 + (A - A_0) = A_0 + \Delta A \approx A_0 + \varepsilon \Delta \hat{A} \tag{6}$$

$$\mathbf{b} = \mathbf{b}_0 + (\mathbf{b} - \mathbf{b}_0) = \mathbf{b}_0 + \Delta \mathbf{b} \approx \mathbf{b}_0 + \varepsilon \Delta \hat{\mathbf{b}}, \tag{7}$$

where A_0 and $\mathbf{b}_0$ are the expected values of matrix A and vector $\mathbf{b}$, respectively. The last forms in equations (6) and (7), where $\varepsilon << 1$, are based on the assumption that random disturbancies near expected values are small. Also the unknown vector $\mathbf{x}$ can be written in the form

$$\mathbf{x} \approx \mathbf{x}_0 + \varepsilon \Delta \hat{\mathbf{x}}. \tag{8}$$

Substituting expressions (6), (7) and (8) in the equation (1) and equating the equal order terms, the following equations are obtained:

$$A_0\mathbf{x}_0 = \mathbf{b}_0 \qquad \text{(from zeroth order terms)} \tag{9}$$

$$A_0\Delta\mathbf{x} = \Delta\mathbf{b} - \Delta A\mathbf{x}_0 \qquad \text{(from first order terms)} \tag{10}$$

When $n > m$, the solution of equations (9) and (10) is not so straightforward, in this work these are multiplied by Moore-Penrose-pseudoinverse of the matrix A_0, yielding

$$\mathbf{x}_0 = A_0^-\mathbf{b}_0 = D\mathbf{b}_0 \tag{11}$$

$$\Delta\mathbf{x} = A_0^-(\Delta\mathbf{b} - \Delta A\mathbf{x}_0) = D\Delta\mathbf{b} - D\Delta A\mathbf{x}_0, \tag{12}$$

because $A_0^-A_0 = I$, when the rank of matrix A_0 is full (which guarantees the unique solution). For computational reasons, the last term of the equation (12) is written in the form

$$D\Delta A\mathbf{x}_0 = \tilde{D}\Delta\mathbf{a}, \tag{13}$$

where $m \times nm$-matrix $\tilde{D}$ is

$$\tilde{D} = \begin{bmatrix} \tilde{D}_1 & \tilde{D}_2 & \cdots & \tilde{D}_n \end{bmatrix}, \tag{14}$$

where $m \times m$-matrices $\tilde{D}_i$ are of the form

$$\tilde{D}_i = \begin{bmatrix} d_{1i}x_{01} & d_{1i}x_{02} & \cdots & d_{1i}x_{0m} \\ d_{2i}x_{01} & d_{2i}x_{02} & \cdots & d_{2i}x_{0m} \\ \vdots & \vdots & \ddots & \vdots \\ d_{mi}x_{01} & d_{mi}x_{02} & \cdots & d_{mi}x_{0m} \end{bmatrix} \tag{15}$$

Finally, vector $\mathbf{x}$ is written in the form

$$\mathbf{x} = D\mathbf{b}_0 + D\Delta\mathbf{b} - \tilde{D}\Delta\mathbf{a}, \tag{16}$$

from which the expected value of vector $\mathbf{x}$ can be computed

$$E[\mathbf{x}] = E[D\mathbf{b}_0] + E[D\Delta\mathbf{b}] - E[\tilde{D}\Delta\mathbf{a}] = D\mathbf{b}_0 = \mathbf{x}_0 \tag{17}$$

and covariance-matrix for vector $\mathbf{x}$ becomes

$$\mathrm{cov}(\mathbf{x}) = E\left[(\mathbf{x} - \mathbf{x}_0)(\mathbf{x} - \mathbf{x}_0)^T\right] = \begin{bmatrix} \tilde{D} & D \end{bmatrix} \begin{bmatrix} \mathrm{cov}(\mathbf{a}) & -\mathrm{cov}(\mathbf{a},\mathbf{b}) \\ -\mathrm{cov}(\mathbf{a},\mathbf{b})^T & \mathrm{cov}(\mathbf{b}) \end{bmatrix} \begin{bmatrix} \tilde{D}^T \\ D^T \end{bmatrix} \tag{18}$$

In this work, also the covariances between the elements of vector $\mathbf{x}$ and matrix A and vector $\mathbf{x}$ and vector $\mathbf{b}$ are needed. These can be computed from

$$\mathrm{cov}(\mathbf{x},\mathbf{a}) = E\left[\left(D\Delta\mathbf{b} - \tilde{D}\Delta\mathbf{a}\right)(\Delta\mathbf{a})^T\right] = D\,\mathrm{cov}(\mathbf{a},\mathbf{b})^T - \tilde{D}\,\mathrm{cov}(\mathbf{a}) \tag{19}$$

$$\mathrm{cov}(\mathbf{x},\mathbf{b}) = E\left[\left(D\Delta\mathbf{b} - \tilde{D}\Delta\mathbf{a}\right)(\Delta\mathbf{b})^T\right] = D\,\mathrm{cov}(\mathbf{b}) - \tilde{D}\,\mathrm{cov}(\mathbf{a},\mathbf{b}). \tag{20}$$

RIGID BODY FIT

When rotations are small, the acceleration vector of point P of a rigid body is

$$\bar{a}_P = \bar{a}_O + \bar{\alpha} \times \bar{r}_{P/O}, \tag{21}$$

where $\bar{a}_O$ is acceleration of origin, $\bar{\alpha}$ is angular acceleration of the rigid body and $\bar{r}_{P/O}$ is the position vector of point P with respect to the origin. At point P the accelerometer measures acceleration to the direction of unit vector $\bar{e}_P$, so the measured acceleration is

$$a^m = \bar{e}_P \cdot \bar{a}_P. \tag{22}$$

Writing this in matrix form yields

$$\begin{bmatrix} e_x & e_y & e_z & ye_z - ze_y & ze_x - xe_z & xe_y - ye_x \end{bmatrix} \begin{bmatrix} a_{Ox} \\ a_{Oy} \\ a_{Oz} \\ \alpha_x \\ \alpha_y \\ \alpha_z \end{bmatrix} = a^m \tag{23}$$

Using at least six accelerometers an overdetermined set of equations can be formed. Because measured accelerations, coordinates of point P and components of unit vector $\bar{e}_P$ are random variables, the resulting set of equations is stochastic and can be solved using second moment analysis. Using equations (17) and (18), the expected values and the covariances for elements of the acceleration vector of the origin and the angular acceleration vector of the rigid body can be calculated.

INERTIA RESTRAINT METHODS

The equation of motion for free rigid body is

$$\begin{bmatrix} m & 0 & 0 & 0 & mz_{mk} & -my_{mk} \\ 0 & m & 0 & -mz_{mk} & 0 & mx_{mk} \\ 0 & 0 & m & my_{mk} & -mx_{mk} & 0 \\ 0 & -mz_{mk} & my_{mk} & J_{xx} & -J_{xy} & -J_{xz} \\ mz_{mk} & 0 & -mx_{mk} & -J_{xy} & J_{yy} & -J_{yz} \\ -my_{mk} & mx_{mk} & 0 & -J_{xz} & -J_{yz} & J_{zz} \end{bmatrix} \begin{bmatrix} a_{Ox} \\ a_{Oy} \\ a_{Oz} \\ \alpha_x \\ \alpha_y \\ \alpha_z \end{bmatrix} = \begin{bmatrix} F_x \\ F_y \\ F_z \\ M_{Ox} \\ M_{Oy} \\ M_{Oz} \end{bmatrix} \tag{24}$$

where vectors $\left[a_{Ox} \quad a_{Oy} \quad a_{Oz} \quad \alpha_x \quad \alpha_y \quad \alpha_z\right]^T$ and $\left[F_x \quad F_y \quad F_z \quad M_{Ox} \quad M_{Oy} \quad M_{Oz}\right]^T$ are measurable. Based on this measured data, the elements of mass matrix can be solved. Depending on the organization of unknown values, at least five different methods are possible to be found for determining the unknown inertia properties. In this work, only two of those methods are examined.

The first method, which has earlier /8/ been named as Inertia Restraint Method (IRM), starts by taking the first three equations, considering coordinates of the center of mass and the inverse of mass as unknowns, and writing them in the form

$$\begin{bmatrix} 0 & \alpha_z & -\alpha_y & F_x \\ -\alpha_z & 0 & \alpha_x & F_y \\ \alpha_y & -\alpha_x & 0 & F_z \end{bmatrix} \begin{bmatrix} x_{mk} \\ y_{mk} \\ z_{mk} \\ m^{-1} \end{bmatrix} = \begin{bmatrix} a_{Ox} \\ a_{Oy} \\ a_{Oz} \end{bmatrix} \tag{25}$$

Using at least two different excitation locations/directions an overdetermined set of equations can be formed. Because the elements of multiplying matrix and RHS vector are measured, and thereby random variables, the resulting set of equations is stochastic and can be solved using above presented second moment analysis. Thus the expected values and covariances for coordinates of c.m. and inverse of mass are obtained.

After the first step, the origin is transformed to c.m. and in last three equations of equation (24) the components of inertia tensor are considered as unknowns. So these can be written in the form

$$\begin{bmatrix} \alpha_x & 0 & 0 & -\alpha_y & -\alpha_z & 0 \\ 0 & \alpha_y & 0 & -\alpha_x & 0 & -\alpha_z \\ 0 & 0 & \alpha_z & 0 & -\alpha_x & -\alpha_y \end{bmatrix} \begin{bmatrix} J_{xx} \\ J_{yy} \\ J_{zz} \\ J_{xy} \\ J_{xz} \\ J_{yz} \end{bmatrix} = \begin{bmatrix} M_{mkx} \\ M_{mky} \\ M_{mkz} \end{bmatrix} \tag{26}$$

Again, using at least two excitation locations/directions, the set of stochastic equations is obtained. From the solution of this set, the expected values and covariances for components of inertia tensor are obtained.

There is no immediate reason for separating six equations of (24) to two sets. In (24), considering directly the unknown elements of mass matrix as unknowns, it can be written in form

$$\begin{bmatrix} a_{Ox} & 0 & -\alpha_z & \alpha_y & 0 & 0 & 0 & 0 & 0 & 0 \\ a_{Oy} & \alpha_z & 0 & -\alpha_x & 0 & 0 & 0 & 0 & 0 & 0 \\ a_{Oz} & -\alpha_y & \alpha_x & 0 & 0 & 0 & 0 & 0 & 0 & 0 \\ 0 & 0 & a_{Oz} & -a_{Oy} & \alpha_x & 0 & 0 & -\alpha_y & -\alpha_z & 0 \\ 0 & -a_{Oz} & 0 & a_{Ox} & 0 & \alpha_y & 0 & -\alpha_x & 0 & -\alpha_z \\ 0 & a_{Oy} & -a_{Ox} & 0 & 0 & 0 & \alpha_z & 0 & -\alpha_x & -\alpha_y \end{bmatrix} \begin{bmatrix} m \\ mx_{mk} \\ my_{mk} \\ mz_{mk} \\ J_{xx} \\ J_{yy} \\ J_{zz} \\ J_{xy} \\ J_{xz} \\ J_{yz} \end{bmatrix} = \begin{bmatrix} F_x \\ F_y \\ F_z \\ M_{Ox} \\ M_{Oy} \\ M_{Oz} \end{bmatrix} \quad (27)$$

Using at least two excitation locations/directions the stochastic set of equations can be set up, which is solved in the same way as earlier. This method is called Direct Inertia Restrained Method (DIRM). It is worth to note, that calculated components of inertia tensor should be transformed to coordinate frame, which has its origin in c.m.

SIMULATION AND RESULTS

For testing the proposed error analysis method, arbitrary values for rigid body mass, coordinates of c.m. and moments of inertia were chosen. From this data the acceleration amplitudes of chosen response locations were calculated for chosen excitation locations.

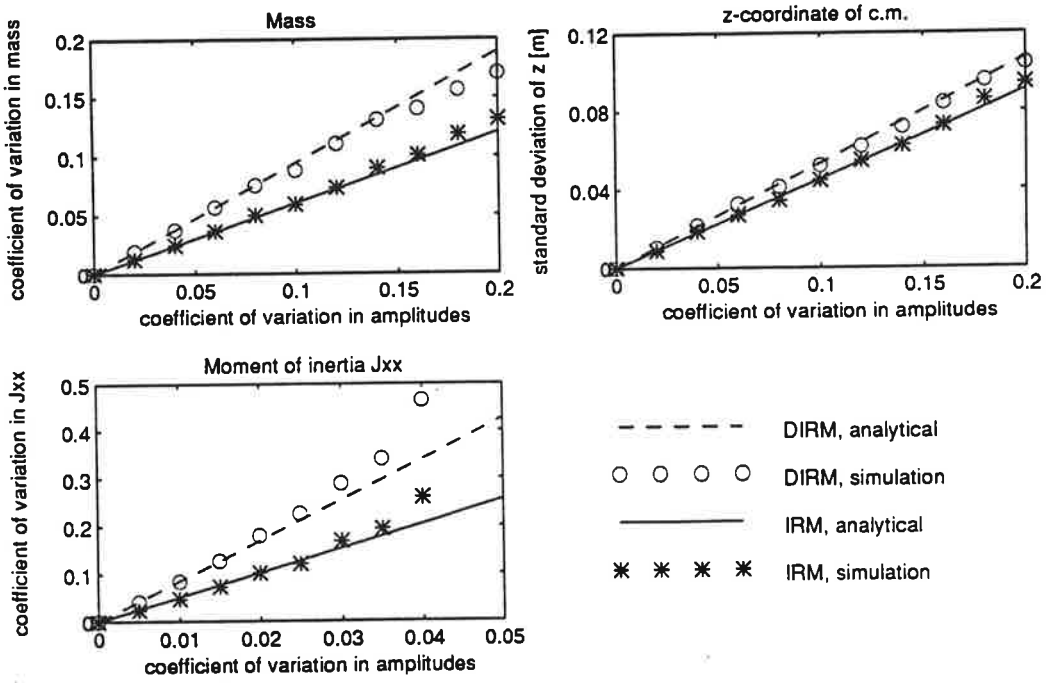

Figure 1. Analytical *vs.* simulated results when randomness in amplitudes is incresed.

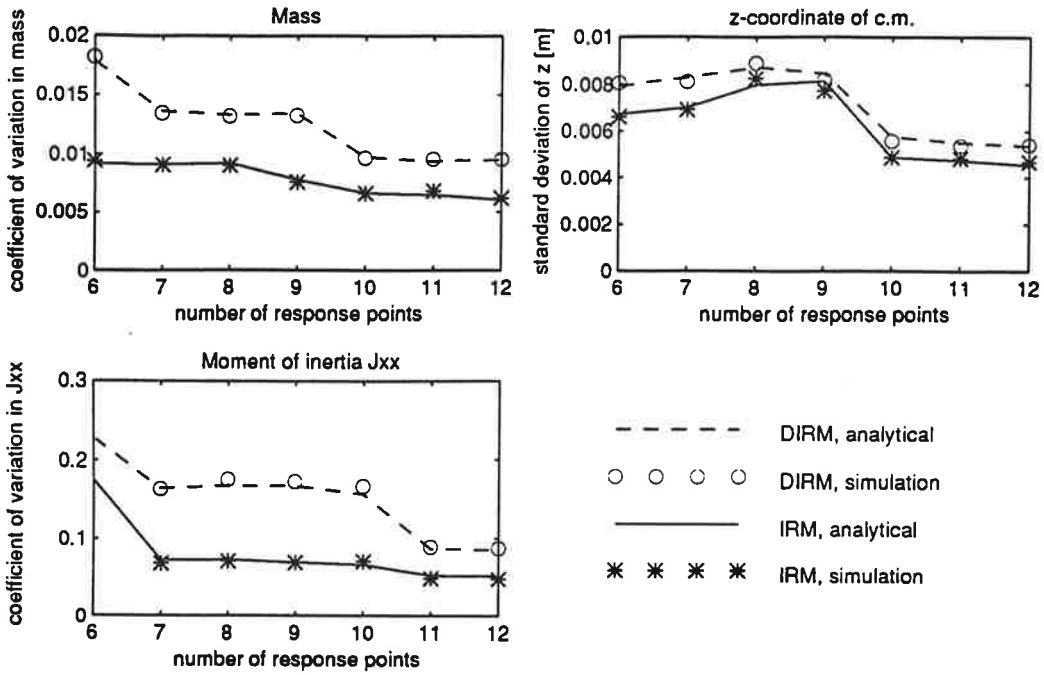

Figure 2. Analytical *vs.* simulated results when number of response locations is incresed.

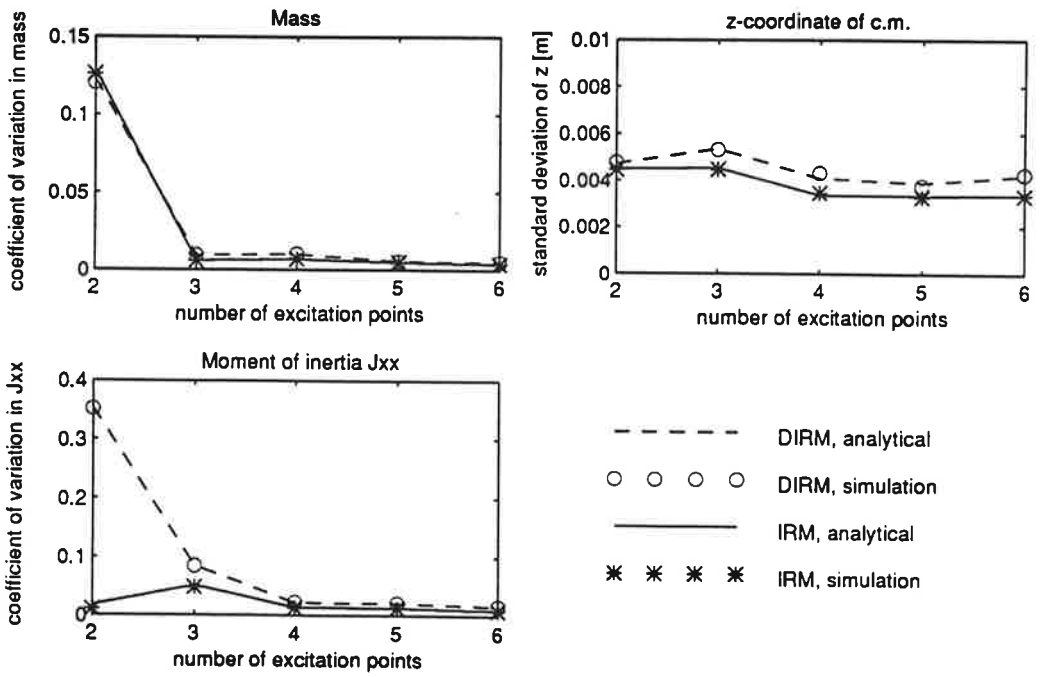

Figure 3. Analytical *vs.* simulated results when number of excitation locations is incresed.

The excitation was considered as unit force. In analytical error analysis the calculated amplitudes were taken as expected values and standard deviations, proportional to amplitudes, were assigned to these. In simulation, random amplitudes with same expected values and standard deviations as in analytical case, were generated and 1000 simulations were executed. Results, with increasing randomness in acceleration amplitudes, are shown in figure 1. It is seen that proposed error analysis works well for mass and coordinates of c.m., when coefficients of variation of acceleration amplitudes are less than 0.2. This is approximately the same limit that has been found in stochastic FEM applications. For moments of inertia the coefficients of variation of these amplitudes should be less than 0.04 for reliable error analysis results. Results of figure 1 were calculated using twelve response and three excitation locations.

Next, the effects of increasing the number of response and excitation locations were studied. The minimum number of response locations is six. The number of response locations was increased to twelve and the results are shown in figure 2. It is seen that at least 10-11 response locations are preferable. The minimum number of excitation locations is two. The number of excitation locations was increased to six, and from figure 3 it is seen that four excitation locations should be used for accurate results.

Numerous attempts were made to take into account randomness in response and excitation locations and directions. For some reason analytical error analysis presented in this paper and Monte-Carlo-simulation didn't give the same results.

CONCLUSIONS

An statistical error analysis for measurement of rigid body inertia properties was proposed and verified through Monte-Carlo-simulation. For mass and coordinates of c.m. the method works well when coefficient of variation in measured rigid body inertia restraints are less than 0.2, For moments of inertia this limiting value is 0.04. Using this error analysis some nearly optimal lower bounds for number of response and excitation locations were determined.

REFERENCES

1. N. Okubo, T. Furukawa, "Measurement of Rigid Body Modes for Dynamic Design", Proc. IMAC 2, pp. 545-549, 1984
2. J. Bretl, P. Conti, "Rigid Body Mass Properties from Test Data", Proc. IMAC 5, pp. 655-659, 1987
3. Y.S. Wei, J. Reis, "Experimental Determination of Rigid Body Inertia Properties", Proc. IMAC 7, pp. 603-606, 1989
4. M. Furusawa, "A Method of Determining Rigid Body Inertia Properties", Proc. IMAC 7, pp. 711-719, 1989
5. P. Conti, J. Bretl, "Mount Stiffnesses and Inertia Properties from Modal Test Data", Journal of Vibration, Acoustics, Stress and Reliability in Design, Vol 111, pp. 134-138, 1989
6. J. Toivola, "Jäykän kappaleen hitausominaisuuksien mittaus", Diplomityö, TTKK, 1991
7. A. Fregolent, A. Sestieri, M. Falzetti, "Identification of Rigid Body Inertia Properties from Experimental Frequency Response", Proc. IMAC 10, pp. 219-225, 1992
8. J. Toivola, O. Nuutila, "Comparison of Three Methods for Determining Rigid Body Inertia Properties from Frequency Response Functions", Proc. IMAC 11, 1993
9. M. Kleiber, T.D. Hien, "The Stochastic Finite Element Method", John Wiley & Sons, Chichester, 1992